Mass assembly of galaxies at intermediate-redshift

Vladan Markov

Vladan Markov. Mass assembly of galaxies at intermediate-redshift. Astrophysics [astro-ph]. Université Paris sciences et lettres, 2020. English. NNT : 2020UPSLO009 . tel-03277010

HAL Id: tel-03277010
https://theses.hal.science/tel-03277010
Submitted on 2 Jul 2021

PSL
UNIVERSITÉ PARIS

l'Observatoire de Paris | PSL

THÈSE DE DOCTORAT DE L'UNIVERSITÉ PSL

Préparée à l'Observatoire de Paris

L'Assemblage de masse dans des galaxies à redshift intermédiaire

Mass assembly of galaxies at intermediate redshift

Soutenue par
Vladan MARKOV
Le 28 septembre 2020

Ecole doctorale n° 127
Ecole Doctorale Astronomie et Astrophysique d'Ile de France

Spécialité
Astronomie et Astrophysique

Composition du jury :

Jacques, LE BOURLOT
Professeur HDR, Université de Paris, Observatoire de Paris
Examinateur

Vincenzo, MAINIERI
Astronome, European Southern Observatory (ESO)
Rapporteur

Bianca, POGGIANTI
Directeur de recherche, INAF-Astronomical Observatory of Padova
Rapporteur

Micol, BOLZONELLA
Chercheuse, Osservatorio di Astrofisica e Scienza dello Spazio di Bologna
Examinateur

Olivier, ILBERT
Astronome adjoint HDR, Laboratoire D'astrophysique De Marseille (LAM)
Examinateur

Simona, MEI
Professeur HDR, Université de Paris, Observatoire de Paris
Directeur de thèse

ABSTRACT

This Thesis presents my work on developing a `Python` pipeline for deriving the stellar mass function (SMF) of cluster galaxies, using the 1/V-max method and fitting the SMF with a chosen model (variations of the Schechter function), for the upcoming *Euclid Space Mission*. I test the pipeline and derive the SMF and SMF fit of the Flagship mock galaxies and COSMOS2015 galaxies over the redshift range $0.2 \leqslant z < 2.5$, i.e. the redshift range expected to be covered by the future *Euclid Mission*. Moreover, I develop a `Python` code for fitting the SMF and obtaining the best-fit parameters of the model and their uncertainties, using the MCMC algorithm and Bayesian approach.

I analyze the evolution of the SMF and stellar mass density, and confirm the results from the literature on the stellar mass build-up of different galaxy samples, over the redshift range taken into account ($0.2 \leqslant z < 2.5$). I show the mass-dependent evolution of the SMF of COSMOS2015 full sample, flattening of the SMF and sharpening of the *knee* of the function at the high-mass end around the characteristic stellar mass M^*, which is probably a consequence of *mass quenching*. The SMF of COSMOS2015 star-forming galaxies does not show any significant evolution, whereas the SMF of COSMOS2015 quiescent subsample is mass-dependent, and shows mass assembly of low and intermediate-mass galaxies at $z < 1$, possibly through *environmental quenching*, which is consistent with the *downsizing* effect. Furthermore, I split the COSMOS2015 star-forming galaxies into *high activity* ($\log(\mathrm{sSFR}) \geqslant -9.5$) and *intermediate activity* galaxies ($-9.5 > \log(\mathrm{sSFR}) \geqslant -11$). The *high activity* star-formation shifts to low and intermediate-mass galaxies at lower redshifts, in agreement with the *downsizing effect*.

I show that most of the stellar mass assembly of galaxies occurs during the stellar mass assembly and star formation epoch, i.e. the *cosmic noon* epoch $1 < z < 2.5$. After this very active phase in cosmic history, the stellar mass build-up of galaxies slows down, which is consistent with a drop of the cosmic SFR and molecular gas content of galaxies during the last cosmic epoch $z < 1$. Moreover, I show that quiescent galaxies have assembled their mass substantially over the redshift range $1 < z < 2.5$, after which their stellar mass density surpassed the stellar mass density of star-forming galaxies at $z \sim 0.75$. This shows that the star formation quenching mechanisms were very efficient during the *cosmic noon* epoch. This part of the thesis reproduces published results from Ilbert et al., (2013) and Davidzon et al., (2017).

The focus of my research is also on deriving the molecular gas content and star formation of cluster galaxies at the *cosmic noon* epoch at $z \sim 1.5$. I present the observations of the synchrotron continuum emission, detection of substantial molecular gas reservoir in the core of the CARLA J1103+3449 cluster at $z \sim 1.44$ with NOEMA, and estimation of the SFR and other properties of the cluster confirmed members (Markov et al., 2020a). I present the detection of an extended continuum emission at $\nu_{\mathrm{obs}} \sim 94.48$ GHz in the

cluster core, with the brightest peak at the position of the RLAGN, that extends towards the western radio lobe, while the fainter component is at the position of the eastern radio lobe and radio jet. The two continuum emission components visually correspond to the two radio lobes. This is consistent with the same or a connected physical origin of the two emissions. The continuum flux associated with the RLAGN, the eastern lobe and the jet, and the western radio lobe are $S_{\rm cont} = 4.6 \pm 0.2$ mJy, $S_{\rm cont} = 1.1 \pm 0.2$ mJy and $S_{\rm cont} = 0.8 \pm 0.2$ mJy, respectively. I combine the radio observations from the literature and mm observations from this work to calculate the total spectral index $\alpha = 0.92 \pm 0.02$, determined over the range of frequencies that spans over three orders of magnitude. The spectral index is consistent with optically thin synchrotron emission.

I present observations of two CO(2-1) emission lines in the center of the CARLA J1103+3449 cluster, which correspond to two extended regions. The position of the red emission peak is south-west of the RLAGN, and it encompasses the RLAGN and companion disk galaxy, while the blue emission peak is south-east of the RLAGN and it does not have an optical counterpart. The two CO(2-1) emissions are in the same direction (east-west) as the two continuum emission components and the two radio lobes, but spatially offset and less extended. The velocity integrated flux of the blue and red components are $S\Delta v = 0.88 \pm 0.14$ Jykm s^{-1} and $S\Delta v = 0.90 \pm 0.14$ Jykm s^{-1}, and molecular gas masses $M_{\rm gas} = 1.9 \pm 0.3 \times 10^{10} M_\odot$ and $M_{\rm gas} = 2.0 \pm 0.3 \times 10^{10} M_\odot$, respectively. Therefore, a total molecular gas reservoir in the cluster center is $M_{\rm gas} = 3.9 \pm 0.4 \times 10^{10} M_\odot$. We discuss several hypotheses on the most probable origin of this molecular gas reservoir, of which the most reasonable is the hypothesis of gas cooling, either from interaction of the hot ICM and AGN jets, or from the hot low-entropy gas uplifted by the AGN jets.

I show the molecular gas mass upper limits, SFR and other properties of the RLAGN and other spectroscopically confirmed cluster members which are within the NOEMA beam. The molecular gas mass upper limits and stellar masses are comparable to the expected average values of field galaxies at similar redshift. For the RLAGN host galaxy, I assume a stellar contribution to the total Hα flux in the $20 - 100\%$ range, and find $\mathrm{SFR}_{\mathrm{H}\alpha} = 30 - 140\ M_\odot \mathrm{yr}^{-1}$, consistent with the MS star-forming galaxies, while the SFR of the other cluster confirmed members are below the MS, which suggests an impact of the environment.

Throughout the Thesis Manuscript, I use *we* to refer to the contribution of my collaborators and myself, and I use *I* to mention my own involvement.

This thesis is based on, or contains non-public Euclid Consortium material or results that have not yet been endorsed by the Euclid Consortium. The work on the CARLA ALMA follow-up is preliminary and contains results that have not yet been validated and endorsed by the CARLA collaboration.

RÉSUMÉ

Cette thèse présente mon travail sur le développement d'un pipeline `Python` pour déduire la SMF (fonction de masse stelaire) des galaxies d'amas, en utilisant la méthode 1/Vmax et en ajustant la SMF avec un modèle choisi (variations de la fonction de Schechter), pour la future mission spatiale *Euclid*. Je teste le pipeline et déduis la SMF et l'ajustement de la SMF des galaxies simulées de Flagship et des galaxies de COSMOS2015 sur la plage de redshift $0.2 \leqslant z < 2.5$, c'est-à-dire la plage de redshift qui devrait être couverte par la future *Euclid Space Mission*. De plus, je développe un code `Python` pour ajuster la SMF et obtenir les meilleurs paramètres du modèle et leurs incertitudes, en utilisant l'algorithme MCMC et l'approche bayésienne.

J'analyse l'évolution de la SMF et de la densité de masse stellaire, et confirme les résultats de la littérature sur l'accumulation de masse stellaire de différents échantillons de galaxies, sur la plage de redshift prise en compte ($0.2 \leqslant z < 2.5$). Je montre l'évolution de la SMF de l'échantillon complet de COSMOS2015 en fonction de la masse, l'aplatissement de la SMF et l'accentuation du *genou* de la fonction à l'extrémité haute de la gamme de masse élevée autour de la masse stellaire caractéristique M^*, ce qui est probablement une conséquence de *mass quenching*. La SMF des galaxies à formation d'étoiles de COSMOS2015 ne montre aucune évolution significative, alors que la SMF du sous-échantillon des galaxies inactives de COSMOS2015 dépend de la masse, et montre un assemblage de masse des galaxies de masse faible et intermédiaire à $z < 1$, peut-être par la *environmental quenching*, ce qui est cohérent avec l'effet de *downsizing*. En outre, j'ai divisé les galaxies à formation d'étoiles de COSMOS2015 en galaxies de haute activité ($\log(\text{sSFR}) \geqslant -9.5$) et en galaxies d'activité intermédiaire ($-9.5 > \log(\text{sSFR}) \geqslant -11$). La formation stellaire de haute activité se déplace vers des galaxies de masse faible et intermédiaire à faible décalage à redshift plus bas, en accord avec l'effet de *downsizing*.

Je montre que la plupart de l'assemblage de masse stellaire des galaxies se produit pendant l'époque du $1 < z < 2.5$. Après cette phase très active de l'histoire cosmique, l'assemblage de la masse stellaire des galaxies ralentit, ce qui correspond à une baisse du SFR cosmique et du contenu en gaz moléculaire des galaxies pendant la dernière époque cosmique $z < 1$. De plus, je montre que les galaxies inactives ont rassemblé leur masse stellaire de manière substantielle dans la plage de redshift $1 < z < 2.5$, après quoi leur densité de masse stellaire a dépassé celle des galaxies à formation d'étoiles à $z \sim 0.75$. Cela montre que les mécanismes de tremplage de la formation stellaire étaient très efficaces à cette époque.

Mes recherches portent également sur la détermination de la teneur en gaz moléculaire et la formation d'étoiles des galaxies d'amas à des redshifts intermédiaires ($z \sim 1.5$). Je présente les observations de l'émission synchrotron continue et du réservoir substantiel de gaz moléculaire au cœur de l'amas CARLA J1103+3449 à $z \sim 1.44$ avec NOEMA, l'estimation du

SFR et des autres propriétés des galaxies membres confirmés de l'amas (Markov et al., 2020a). Je présente la détection d'une émission continue à $\nu_{\text{obs}} \sim 94.48$ GHz dans le noyau de l'amas, avec le pic le plus brillant à la position du RLAGN, qui s'étend vers le lobe radio ouest, tandis que la composante la plus faible se trouve à la position du lobe radio est, et du jet radio. Les deux composantes d'émission du continuum correspondent visuellement aux deux lobes radio. Ceci est cohérent avec une même origine physique ou une origine physique connectée des deux émissions. Le flux continu associé au RLAGN, au lobe est et au jet radio et au lobe radio ouest sont respectivement $S_{\text{cont}} = 4.6 \pm 0.2$ mJy, $S_{\text{cont}} = 1.1 \pm 0.2$ mJy et $S_{\text{cont}} = 0.8 \pm 0.2$mJy. Je combine les observations radio de la littérature et les observations mm de ce travail pour calculer l'indice spectral total $\alpha = 0.92 \pm 0.02$, déterminé sur une plage de fréquences qui s'étend sur trois ordres de grandeur. L'indice spectral correspond à une émission synchrotron optiquement mince.

Je présente les observations de deux lignes d'émission de CO(2-1) au centre de l'amas CARLA J1103+3449, qui correspondent à deux régions étendues. La position du pic d'émission rouge est au sud-ouest du RLAGN, et il englobe le RLAGN et la galaxie compagne, tandis que le pic d'émission bleu est au sud-est du RLAGN et il n'a pas de contrepartie optique. Les deux émissions de CO(2-1) sont dans la même direction (est-ouest) que les deux composantes d'émission du continuum et les deux lobes radio, mais elles sont décalées dans l'espace et moins étendues. Les flux intégrés de vitesse des composantes bleue et rouge sont $S\Delta\nu = 0,88 \pm 0,14$Jykm s^{-1} et $S\Delta\nu = 0,90 \pm 0.14$ Jykm s^{-1}, et les masses moléculaires de gaz sont $M_{\text{gaz}} = 1,9 \pm 0,3 \times 10^{10} M_{\odot}$ et $M_{\text{gaz}} = 2,0 \pm 0,3 \times 10^{10} M_{\odot}$, respectivement. Par conséquent, un réservoir de gaz moléculaire total au centre de l'amas est de $M_{\text{gaz}} = 3,9 \pm 0,4 \times 10^{10} M_{\odot}$. Nous discutons plusieurs hypothèses sur l'origine la plus probable du réservoir de gaz moléculaire, dont la plus raisonnable est l'hypothèse de refroidissement du gaz, soit par l'interaction d'ICM et des jets d'AGN, soit par le gaz chaud de faible entropie soulevé par les jets d'AGN.

Je montre les limites supérieures de la masse de gaz moléculaire, le SFR et d'autres propriétés du RLAGN et d'autres membres de l'amas confirmés par spectroscopie qui se trouvent dans le faisceau NOEMA. Les limites supérieures de la masse de gaz moléculaire et les masses stellaires sont comparables aux valeurs moyennes attendues des galaxies de champ à un redshift similaire. Pour la galaxie hôte du RLAGN, je suppose une contribution stellaire au flux total Hα dans la plage de $20 - 100\%$, et trouve $\text{SFR}_{\text{H}\alpha} = 30 - 140\ M_{\odot}\text{yr}^{-1}$, ce qui correspond aux galaxies à formation d'étoiles MS, tandis que les SFR des autres membres confirmés de l'amas sont en dessous de la MS, ce qui suggère un impact de l'environnement.

Tout au long du manuscrit de thèse, j'utilise *nous* pour faire référence à la contribution de mes collaborateurs et de moi-même, et j'utilise *je* pour mentionner ma propre participation.

Cette thèse est basée sur, ou contient du matériel ou des résultats non publiques du Consortium Euclid qui n'ont pas encore été approuvés par le Consortium Euclid. Le travail sur le suivi du CARLA ALMA est préliminaire et contient des résultats qui n'ont pas encore été validés et approuvés par la collaboration CARLA.

PUBLICATIONS

LIST OF PUBLICATIONS

Vladan Markov et al. (2020a). "Massive molecular gas reservoir around the central AGN in the CARLA J1103 + 3449 cluster at z = 1.44." In: *A&A* 641, A22, A22. DOI: `10.1051/0004-6361/202038673`. arXiv: `2007.03706 [astro-ph.GA]` (A& A, 641, 17)

ARTICLES IN PREPARATION

Tollet, É., Mamon, G., **Markov, V.**, Combes, F., Dubois, Y., Cattaneo, A., in preparation). "How fast do galaxies quench in groups and clusters? The view from Horizon-AGN."

ACKNOWLEDGEMENTS

This thesis is based on, or contains non-public Euclid Consortium material or results that have not yet been endorsed by the Euclid Consortium. The authors acknowledge the Euclid Consortium, the European Space Agency and the support of a number of agencies and institutes that have supported the development of Euclid, in particular the Academy of Finland, the Agenzia Spaziale Italiana, the Belgian Science Policy, the Canadian Euclid Consortium, the Centre National d'Etudes Spatiales, the Deutsches Zentrum für Luft- und Raumfahrt, the Danish Space Research Institute, the Fundação para a Ciência e a Tecnologia, the Ministerio de Economia y Competitividad, the National Aeronautics and Space Administration, the Netherlandse Onderzoekschool Voor Astronomie, the Norwegian Space Agency, the Romanian Space Agency, the State Secretariat for Education, Research and Innovation (SERI) at the Swiss Space Office (SSO), and the United Kingdom Space Agency. A detailed complete list is available on the Euclid web site[1].

Part of the work on the *Euclid* project is based on data products from observations made with ESO Telescopes at the La Silla Paranal Observatory under ESO programme ID 179.A-2005 and on data products produced by TERAPIX and the Cambridge Astronomy Survey Unit on behalf of the UltraVISTA consortium. The work on the CARLA ALMA follow-up is preliminary and contains results that have not yet been validated and endorsed by the CARLA collaboration.

We thank the PI of the Keck observations, Fiona Harrison, for providing these observations and Thomas Connor for assisting with the Keck observing. We thank Philip Best and Katherine Inskip for useful discussion and their kind sharing of their radio, optical and infrared observations of the central radio sources and lobes. The data reduction and mapping and most of data analysis was done by using IRAM/GILDAS free software[2], and with the assistance of the IRAM support astronomers in Grenoble, Cynthya Herrera and Melanie Krips, which we warmly thank. We would like to thank the GILDAS support team for their help and guidance for the data analysis, Sébastien Bardeau and Vincent Pietu. This work was supported by the CNES.

First of all, I would like to thank my supervisor Simona Mei for her help and support with both of my projects over the course of three years of my Thesis, for her help in finalizing the paper and Thesis Manuscript. Thanks to all of my collaborators from the *Euclid* project (S. Mei, M. Bolzonella, E. Zucca, O. Ilbert, I. Davidzon, G. Zamorani, L.Tresse, L. Pozzetti, G. Girelli) and from the NOEMA project (S. Mei, P. Salomé, F. Combes, D. Stern, A. Galametz, C. De Breuck, D. Wylezalek, S. Amodeo, E. A. Cooke, A. H. Gon-

---

[1] `http://www.euclid-ec.org`

[2] `http://www.iram.fr/IRAMFR/GILDAS/`

zalez, N. A. Hatch, G. Noirot, A. Rettura, N. Seymour, S. A. Stanford, J. Vernet) for investing their time, effort, expertize, patience and work in helping me finalize these projects. I would like to thank CARLA collaborators for taking their time to read my paper and send comments and advices on improving the paper. I would like to thank F. Combes and I. Davidzon for sending comments on some parts of the Thesis Manuscript and S. Ilic and S. Mei for their help with the translation in French.

I would like to thank M. Bolzonella, E. Zucca and other collaborators from Bologna for hosting me for a week, and all their time and help. Many thanks go to Olivier Ilbert, with whom it is always a pleasure to work, for welcoming me for two weeks in LAM, Marseille, and all his enormous help, patience, guidance and kindness.

Many thanks to Philippe Salomé, and Françoise Combes from the Paris Observatory, for guiding me through the entire NOEMA project and sharing their expertize with me. I would like to thank my friends and colleagues from the Paris Observatory, A. Audibert, B. Tabone, V. Olivares and G. Castignani for helping me with the NOEMA data mapping and analysis. I thank Valeria Olivares for her help in the data reduction and mapping of the ALMA data. I would like to thank Carolina Parroni for her help and tips regarding the MCMC algorithm and code. Also, I would like to thank F. Mannucci for his advice on the use of the new equations for metallicity in the SFR estimate.

I also thank V. Mainieri, B. Poggianti, M. Bolzonella, O. Ilbert, and J. Le Bourlot, for accepting to be members of my Thesis jury.

I would like to thank the PSL University, Doctoral School ED-127, Paris Observatory and LERMA laboratory for hosting me during the three years of my Thesis. I would also like to take this opportunity to thank the Master SPaCE programme and the Aix-Marseille University.
Thanks to everyone from the lab for their support and welcome, especially to Valeria, Ioanna, Stéphane, Gianluca, Salvo, Gaël, Stefania and others.

I appreciate all the help and support from my Comité de suivi, Anne-Laure Melchior and Veronique Buat, and also from Martina Wiedner, especially during some tough periods. I am very grateful to Veronique Buat and Olivier Ilbert who have been supporting me for many years, since my Master studies in Marseille.

I would like to thank my friends for helping, supporting and lifting me up when I was down. Special thanks go to my dear *Sagrada Familia*, Carla and Vada, who have been my pillars since my arrival in France. A big shout out goes to Igor and Damjan.

It goes without saying, many thanks go to my parents Stojmenka and Stanko, for their selfless love and support. I would also like to thank my brother Nenad, and my dear cousins Danijela, Marina, Saška, Nemanja, Andjela, ... for their love and support.

CONTENTS

LIST OF FIGURES

LIST OF TABLES

1

INTRODUCTION

ΛCDM cosmological model

In order to explain the origin, structure, evolution and future of the Universe, we use cosmological models. The current standard cosmological model based on theoretical predictions and observational constraints is the *Concordance model*: a model of a flat Universe with a non-zero cosmological constant. It is based on the *Big Bang* theory, developed by Lemaître, (1931) and Gamow and Teller, (1939), according to which the initial state of the Universe was of infinitely high temperature and density, on the cosmological principle, which is a generalization of the Copernican principle, and which states that on sufficiently large scales, the Universe is homogeneous and isotropic, and on the Einstein's theory of general relativity, in which the geometry of space-time is determined by the matter/energy distribution in the Universe (Einstein, 1916, see e.g. Weinberg, 1972; Rindler, 1977). The Friedmann-Lemaître-Robertson-Walker (FLRW) metric is used as a formal description of the flat space-time geometry and expansion of the Universe.

The current most-favored cosmological framework is the cold dark matter cosmology with a cosmological constant i.e. the ΛCDM framework. According to this framework the Universe consists of the ordinary, i.e. luminous or *baryonic* matter, dark matter, and finally dark energy ($\sim 5\%$, $\sim 25\%$ and 70% of the total universe content, respectively). However, the ΛCDM model is based on two components of generally unknown nature: dark matter and dark energy, that make $\sim 95\%$ of the Universe. The Λ term in the ΛCDM model refers to the cosmological non-zero constant in general relativity theory. This constant infers a non-static, expanding Universe, that is going through a period of accelerated expansion due to a mysterious force called dark energy (Peebles and Ratra, 1988; Steinhardt, Wang, and Zlatev, 1999). Dark energy was first confirmed observationally with studies of the luminosity distances of type Ia Supernovae (SNe) (Riess et al., 1998; Perlmutter et al., 1999).

Dark matter interacts with baryonic matter through gravitational attraction only, and it does not emit or absorb light. There is still a lack of a direct detection of dark matter, although there are numerous evidences supporting its existence, such as velocity dispersion of galaxies in the *Coma* cluster (Zwicky, 1933), flat galaxy rotation curves (Rubin, Ford, and Thonnard, 1980; Persic, Salucci, and Stel, 1996; Sofue and Rubin, 2001), strong and weak gravitational lensing (Mellier, 1999; Van Waerbeke et al., 2001; Refregier, 2003), etc. There are several possible dark matter candidates, including baryonic matter (brown dwarfs, black holes, etc.; e.g. White and Rees, 1978; Carr, Arnett, and Bond, 1982), massive neutrinos (e.g. Gershtein and Zel'dovich, 1966; Klinkhamer and Norman, 1981), non-baryonic warm dark matter (collisionless particles of ~ 1 keV energy; e.g. Peebles, 1982;

Bond and Szalay, 1983) and, presently the most favored, cold dark matter (collisionless massive particles of $\gg 1$ keV energy; e.g. Davis et al., 1985).

In order to study dark matter, dark energy, gravity, and to put constraints on cosmological parameters, we can use *cosmological probes*. For example, in order to investigate the nature of dark matter and dark energy, we can follow their effect on luminous matter, on the geometry and expansion of the Universe. Standard *cosmological probes* include Weak gravitational Lensing (WL) (Mellier, 1999; Van Waerbeke et al., 2001; Refregier, 2003; Schrabback et al., 2010), Baryonic Acoustic Oscillations (BAO) (Eisenstein et al., 2005), distribution of galaxies in groups, clusters and superclusters i.e. large-scale structures (Peacock et al., 2002), Cosmic Microwave Background (CMB) (Spergel et al., 2003; Komatsu et al., 2009; Planck Collaboration et al., 2016, 2018b), redshift space distortions and the integrated Sachs-Wolf effect (Giannantonio, Song, and Koyama, 2008). Moreover, the initial conditions of the Universe are unknown, but can be constrained by observations, such as the $\Delta T/T \sim 10^{-5}$ anisotropies present in the CMB maps of the Universe when radiation and matter first decoupled, ~ 380000 years after the Big Bang, i.e. at $z \sim 1100$ (Penzias and Wilson, 1965; Smoot et al., 1992; Bennett et al., 2003; Spergel et al., 2003; Hinshaw et al., 2007; Komatsu et al., 2009; Planck Collaboration et al., 2018a), abundance of hydrogen and helium in the Universe (Gamow, 1946; Alpher, Bethe, and Gamow, 1948) and expansion of the Universe according to the Hubble law (Hubble, 1929; Hubble and Humason, 1931).

According to the current, accepted *Concordance model* and the *Big Bang* theory, the age of the Universe is ~ 13.8 Gyr. History of the Universe can be roughly divided into several epochs (Figure 1):

- Primordial nucleosynthesis phase, in the first few minutes, when hydrogen ($\sim 75\%$), helium ($\sim 25\%$), and lithium ($< 1\%$) were produced during the nuclear reactions (Gamow, 1946; Alpher, Bethe, and Gamow, 1948; Wagoner, Fowler, and Hoyle, 1967; Walker et al., 1991; Olive, Steigman, and Walker, 2000).

- Inflationary phase, at $z > 1100$ that started with the nearly uniform, dense and hot Universe that went through exponential expansion, i.e. cosmic inflation, due to the vacuum energy that acts as a cosmological constant (Guth, 1981; Linde, 1982; see e.g. Kolb and Turner, 1990; Liddle and Lyth, 2000).

- Recombination phase, or the epoch of *dark age* of the Universe, at $14 < z < 1100$, during which the temperature of the Universe dropped, protons and electrons combined to form hydrogen and helium atoms (Peebles, 1968, 1993).

- Reionization epoch, at $6 < z < 14$, when luminous objects, i.e. first stars and quasars in galaxies produced high-energy Ultra-Violet (UV) photons that almost fully reionized the Universe (Becker et al., 2001; Fan, Carilli, and Keating, 2006; Mellema et al., 2006; Robertson et al., 2010, 2013, 2015).

- Galaxy epoch, at $0 < z < 6$ during which galaxies assembled their mass, and clustered in large-scale structures, such as groups and clusters.

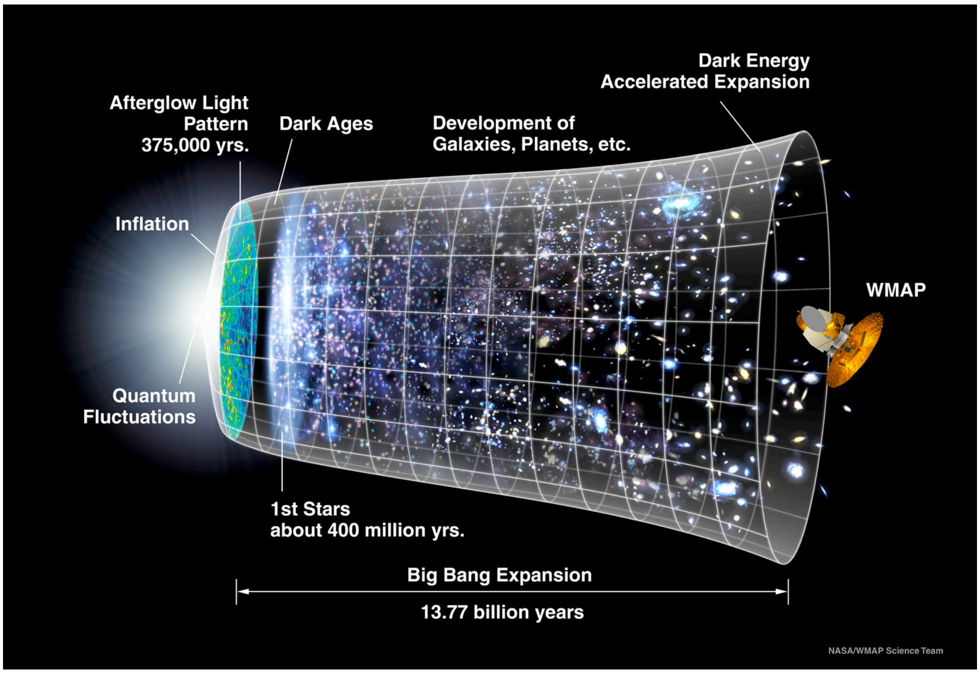

Figure 1: *A representation of the major phases in the evolution of the Universe. Credit: NASA/WMAP science team.*

Focus of this Thesis is on the last cosmic epoch, the epoch of formation and evolution of galaxies. In the following sections I give an introduction to the formation of galaxies within the ΛCDM framework (Section 1.2), a brief overview of galaxy studies (Section 1.3) with simulations (Section 1.3.1) and observations (Section 1.3.2) and fundamental galaxy properties (Section 1.3.3).

GALAXY FORMATION

According to the cosmological principle, the Universe is uniform and isotropic on large-scales. However, on smaller scales the distribution of matter in the Universe is clearly far from uniform, and we see matter distributed in structures such as galaxies. Galaxies are distributed in dense regions of galaxy clusters, and regions devoid of almost any galaxies called voids (Figure 5; Guzzo and VIPERS Team, 2013). In order to explain the existence of galaxies and galaxy clustering, we need to take into account quantum fluctuations at the very beginning of time, when the Universe was dense, hot and nearly uniform. Therefore, we need to include the inflationary theory into standard cosmology (e.g. Guth, 1981; Linde, 1982).

The ΛCDM model provides a cosmological framework to explain the formation of galaxies through mass assembly and galaxy clustering. According to this hierarchical clustering or *bottom-up* scenario, formation of the first galaxies started with small density fluctuations in the nearly uniform, and rapidly expanding early Universe, amplified exponentially through gravitational instabilities into large structures we see today (White and Rees, 1978; Peebles, 1980; Efstathiou and Silk, 1983; White and Frenk, 1991; Lacey and Cole, 1993; Kauffmann, White, and Guiderdoni, 1993; Cole et al., 1994; Cole et al., 2000). These random small fluctuations in the primordial cosmic density field were augmented over time. Once these overdensities reached critical density, they gravitationally collapsed and formed virialized objects i.e. small dark matter halos. Small dark matter halos accreted material from its surroundings or subsequently merged into larger and larger halos (Figure 2; Press and Schechter, 1974; White and Rees, 1978; Lacey and Cole, 1993; Kauffmann, White, and Guiderdoni, 1993; Stewart et al., 2008). Dark matter halos are approximately spherical or ellipsoidal objects, depending on their mass, redshift, radius, merger history, surroundings, etc. (Jing and Suto, 2002; Bailin and Steinmetz, 2005; Allgood et al., 2006). Their density distribution can be described by e.g. Navarro, Frank and White (NFW) profile (Navarro, Frenk, and White, 1996, 1997).

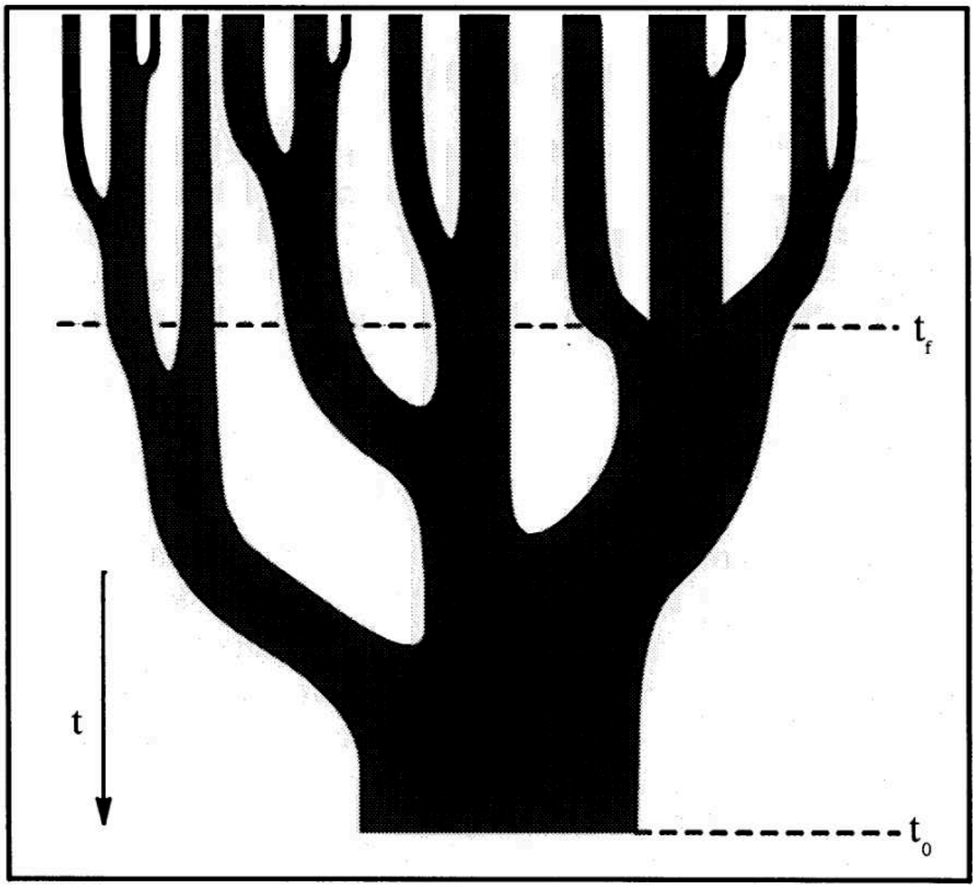

Figure 2: *Merger tree illustration of a halo at* $t = t_0$*, from Lacey and Cole, (1993). Direction of time is from top to bottom, and branch widths represent the masses of the progenitor halos.*

Baryonic matter followed the dark matter with its own physics, i.e. fluid dynamics and radiative processes. Baryonic gas associated with the dark matter halo grew through accretion and merging. During these processes, gas can be shock-heated to virial temperatures of the halo (see. e.g. Evrard, 1990; White and Frenk, 1991; Kereš et al., 2005; Mo, van den Bosch, and

White, 2010). This primordial gas was able to cool through different processes. Primary cooling process of the hot ($T > 10^6$ K) primordial gas is *bremsstrahlung*. The most important gas cooling processes of warm ionized gas at temperatures $10^4 < T < 10^6$ K are recombination and radiative de-excitation. Finally, radiative cooling in cold gas is possible though vibrational and rotational transitions (see e.g. Dalgarno and McCray, 1972; Spitzer, 1978; Mo, van den Bosch, and White, 2010; Tielens, 2010).

When gravitationally bound baryons reached a critical mass (*Jeans mass*; e.g. Gamow and Teller, 1939; Lifshitz, 1946) within the dark matter halos, they gravitationally collapsed and fragmented into stars. There are still many open questions in the theory of galaxy formation, such as: *What is the fraction of gas that collapses and the time scales of a collapse? What is the initial mass distribution of stars, i.e. the Initial Mass Function (IMF; Salpeter, 1955; Miller and Scalo, 1979; Scalo, 1986; Kroupa, 2002; Chabrier, 2003)? etc.*

Light of the first stars and quasars in (proto)galaxies is accountable for the supply of the high-energy photons responsible for reionization of the Universe (Becker et al., 2001; Fan, Carilli, and Keating, 2006; Mellema et al., 2006; Robertson et al., 2010, 2013, 2015). A complete reionization of the Universe by $z \sim 6$, requires a population of star-forming galaxies at redshifts $6 < z < 10$, and even earlier times (Ellis et al., 2013; Robertson et al., 2013). Galaxies have been confirmed spectroscopically out to $z \sim 11$ (Finkelstein et al., 2013; Oesch et al., 2016). These first galaxies were less massive, fainter, more gas rich and with a more irregular, clumpy morphology. Our knowledge on the first high-z galaxies is still quite limited, but this will change soon with the upcoming research facilities such as the *James Webb Space Telescope (JWST)* (Gardner et al., 2006), the *Euclid Space Mission* (Section 2.2.1; Laureijs et al., 2011), the European Extremely Large Telescope (E-ELT; Gilmozzi and Spyromilio, 2007), the *Wide-Field InfraRed Survey Telescope (WFIRST*; Spergel et al., 2015) and the improvements of the already existing ground facilities such as the Atacama Large Millimeter Array (ALMA).

GALAXY STUDIES

Observations of galaxies begun with the first catalogs of nebulae by Charles Messier, William Hershel and John Dreyer, at the end of the XIX century. However, it was Hubble who first proved that these nebulae are extragalactic objects, by measuring their distances using Cepheid stars in the *M31* nebula, i.e. the *Andromeda* galaxy. Furthermore, he demonstrated a relation between the radial velocities and distances of galaxies (*Hubble's law*), and thus, proved that the Universe is expanding (Hubble, 1929; Hubble and Humason, 1931).

Moreover, Hubble classified galaxies according to their morphology. This classification is still in use today and is known as Hubble classification scheme (Figure 3; Hubble, 1926). He classified galaxies into two basic morphological types: elliptical and spiral galaxies. Elliptical galaxies are ellipsoidal systems mostly supported by random motions. They are divided according to their ellipticities into subtypes E0, E1, ... , E7. In general, they are devoid of cold gas and dust, with little or no star formation and thus with an older stellar population that gives them reddish color. Spiral galaxies have a complex morphology, consisting of a disk with spiral arms, with or without a bar and often with a central bulge. They are divided in two branches: barred SB or normal spirals S, and both branches are divided further according to the relative significance of the central bulge with respect to the disk, into subtypes a, b and c. They are predominantly rotationally supported systems, and usually rich in cold gas and dust, star-forming and bluish. Furthermore, many galaxies are a combination of the two main types, smooth disk galaxies with a dominant bulge (e.g. $S0$ galaxies). Next, irregular galaxies are low-mass, gas and dust rich galaxies with no regular shape or motion. Finally, peculiar galaxies are interacting and merging galaxies with disturbed morphologies, with two or or more subcomponents, filamentary structure and tidal tails (see e.g. Mo, van den Bosch, and White, 2010).

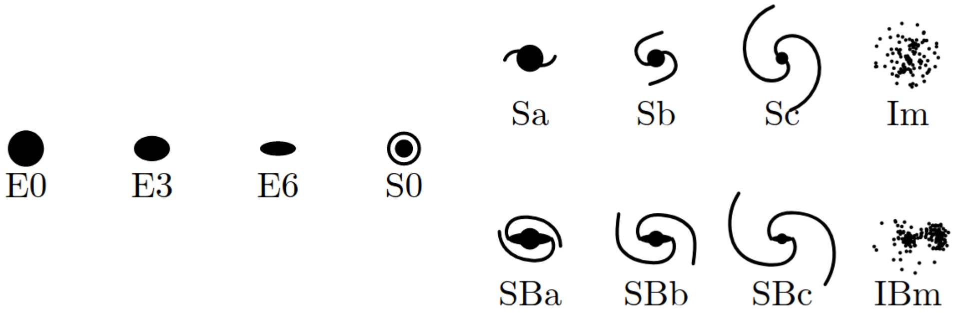

Figure 3: *The Hubble sequence tuning fork from Abraham, (1998).*

Galaxies are dynamically bound complex systems made of stars, dust, gas and dark matter. Galaxies span a wide range in mass, size, color, luminosity, star formation, Active Galactic Nuclei (AGN) activity, etc. and can be classified according to each of these properties.

Spatial distribution of galaxies in the Universe can either be in voids filaments and nods, i.e. in the *field*, small groups or massive clusters. Galaxies trace the overall distribution of matter in large-scale structures (e.g. Peacock et al., 2002). Galaxy properties such as star formation, gas and dust content, stellar population, morphology, etc. strongly depend on the local density (Section 3.1.2; e.g. Kauffmann et al., 2004; Baldry et al., 2006). Moreover, an isolated galaxy goes through a *secular* evolution, which includes aging of the stellar populations, metal enrichment through stellar and SNe feedback (De Lucia, Kauffmann, and White, 2004; Wiersma et al., 2009; Vogelsberger et al., 2013), AGN feedback (McNamara and Nulsen, 2007; Cicone et al., 2014), gas accretion (Mushotzky, 1993; Fabian, 1994), gas cooling and heating processes (e.g. Tielens, 2010), etc.

All these physical processes take part in shaping galaxies over billions of years into the galaxies we observe today. The timescales of these processes are too long, thus, it is impossible to follow the formation and evolution of a single galaxy directly. Instead, we can either study galaxies using simulations, or large galaxy surveys. Fundamental statistical tools for studying the properties of galaxy populations, star-formation history (SFH) and stellar mass assembly of galaxies, and setting constraints on the galaxy formation and evolution models are luminosity and stellar mass function (LF and SMF, respectively; Section 2.1).

Cosmological simulations

Simulations are necessary in order to make predictions of galaxy formation and evolution within the ΛCDM framework of the Universe. Moreover, simulations can be used to test alternative cosmological models (see e.g. Vogelsberger et al., 2020 for a review) and as a preparation for the upcoming observations (e.g. Carretero et al., 2017).

Numerical N-body simulations can reliably predict formation and evolution of the dominant mass component of galaxies i.e. the dark matter halos and their distribution in clumps, filaments and voids i.e. the *cosmic web* (e.g. Boylan-Kolchin et al., 2009; Potter, Stadel, and Teyssier, 2017). In simulations the dark matter is approximated by an ensemble of N collisionless *particles* of a given mass that interact only gravitationally. Therefore, objects and substructures that can be simulated are limited by the particle mass resolution. Moreover, N-body simulations do not include baryonic physical processes that are fundamental in galaxy formation and evolution, such as radiative cooling and heating of gas, star formation, stellar, SN and AGN feedback, metal enrichment, etc. In order to treat the *sub-grid* physics, it is necessary to include hydrodynamical simulations or Semi-Analytic Models (SAMs).

The first numerical simulation of gravitational clustering of cold dark matter was developed by Davis et al., (1985). In the following years, hydrodynamics and semi-analytic techniques were incorporated into N-body simulations within the CDM framework (White et al., 1987; White and Frenk, 1991; Katz and White, 1993; Springel, 2005; De Lucia and Blaizot, 2007; Klypin, Trujillo-Gomez, and Primack, 2011; Li et al., 2015; Carretero et al., 2017, etc). SAMs are based on *painting* the baryonic physics using approximate, analytic techniques, on top of the numerical simulations (e.g. White and Frenk, 1991; Kauffmann, White, and Guiderdoni, 1993; Somerville and Primack, 1999; Benson et al., 2000; Springel et al., 2005; De Lucia and Blaizot, 2007; Guo et al., 2011). Hydrodynamical simulations are more self-consistent, since they treat the gas physics for a large number of *particles* (Evrard, 1988; Katz and Gunn, 1991; Navarro, Frenk, and White, 1994; Weinberg et al., 2004;) or *cells* (Bryan and Norman, 1995; Teyssier, 2002; Li et al., 2015).

Simulations run on the most powerful supercomputers of today, but it is still not possible to have large enough volume to contain statistically representative populations of objects, and at the same time, resolve and follow small-scale processes within individual objects. Therefore, there are large-volume simulations sampling large galaxy populations and zoom simulations that resolve physical processes in a small number of galaxies (Figure 4; Vogelsberger et al., 2020). State-of-the-art dark matter simulations in large volumes include the Millennium (Springel et al., 2005), Millennium II (Boylan-Kolchin et al., 2009) and Millennium XXL (Angulo et al., 2012), Bolshoi (Klypin, Trujillo-Gomez, and Primack, 2011), Dark Sky (Skillman et al., 2014), etc., whereas hydrodynamical simulations in large volumes are the Illustris (Vogelsberger et al., 2014), Eagle (Schaye et al., 2015), Horizon-

AGN (Dubois et al., 2016), etc. Moreover, one of the best zoom dark matter simulations include Aquarius (Springel et al., 2008), GHALO (Stadel et al., 2009), ELVIS (Garrison-Kimmel et al., 2014), etc., while the zoom hydrodynamical simulations are Latte/FIRE (Wetzel et al., 2016), APOSTLE (Sawala et al., 2016), Auriga (Grand et al., 2017), etc.

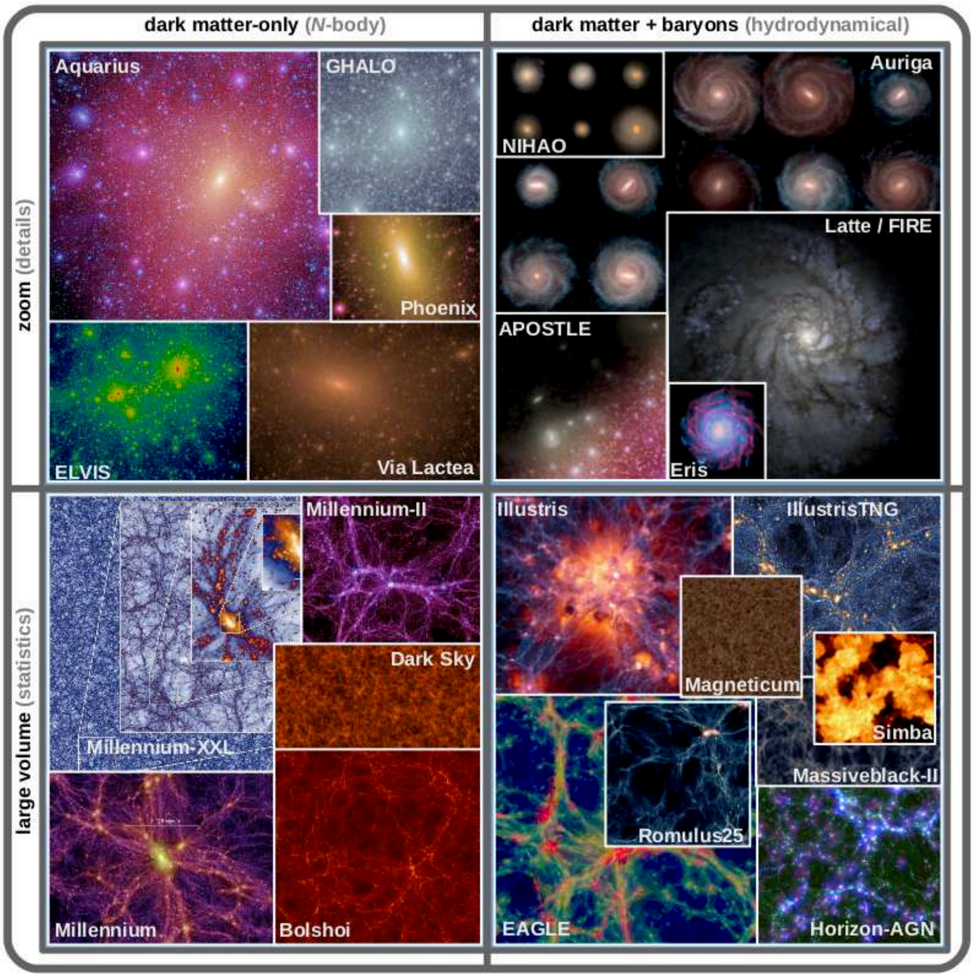

Figure 4: *Visual representations of the most important* N*-body (left panels) and hydrodynamical simulations (right panels), divided on zoom simulations (top panels) and simulations in large volume (bottom panels). Credit: Vogelsberger et al., (2020).*

A state-of-the art N-body dark matter simulation developed by Potter, Stadel, and Teyssier, (2017), with a *Euclid* Flagship mock galaxy catalog (Carretero et al., 2017) was produced for the upcoming *Euclid Space Mission* (Section 2.2.1, Section 2.2.2). I use this catalog for testing the *Euclid* pipeline for deriving the stellar mass function (SMF) of cluster galaxies (Chapter 2).

Simulations can reproduce large-scale distribution of dark matter and galaxies, i.e. the *cosmic web*, the formation and evolution of galaxies, the star formation rate density, galaxy luminosity and stellar mass function, color bimodality, morphology, metallicity etc. (e.g. White and Frenk, 1991; Somerville and Primack, 1999; White, 2002; Springel and Hernquist, 2003). However, there are still some inconsistencies between the simulated and observed universe. For instance, the missing satellites problem, i.e. simulations overpredict the number of low-mass galaxies at low redshifts (White and Frenk, 1991; Moore et al., 1999b; Boylan-Kolchin, Bullock, and Kaplinghat, 2012).

Galaxy redshift surveys

Galaxy redshift surveys are crucial in statistical studies of galaxies. We can study the evolution of galaxies by comparing their properties across cosmic time, up to the reionization epoch. We can investigate the distribution of galaxies and probe the large-scale structure. Moreover, galaxy surveys are essential in putting constraints on the galaxy formation and evolution models, testing the current cosmological models and shedding light on the nature of dark matter and dark energy.

There are two types of redshift surveys, depending on the way the redshift is obtained: spectroscopic and photometric. Spectroscopic surveys give physical properties such as galaxy star formation rate (SFR), age, metallicity, etc., while photometry gives color, morphology, size, etc. Furthermore, surveys can be divided according to the area and depth of observations into shallow and wide i.e. *all-sky* surveys, deep and narrow, and intermediate surveys. Obtaining the redshift survey data usually involves two phases: first the selected area of the sky is imaged with a low-precision photometric redshift estimates, then there is a follow-up of selected galaxies by high-precision spectroscopic redshift estimates (see Johnston, 2011 for a review).

The first crucial spectroscopic redshift survey that mapped the large-scale structure of the nearby Universe was the Center for Astrophysics (CfA) survey (Huchra et al., 1983; Geller and Huchra, 1989). The next big breakthroughs were with space telescope surveys such as Infra-Red Astronomical Satellite (IRAS) survey (Saunders et al., 2000) and especially with the *Hubble* Deep Field (HDF) (Williams et al., 1996; Fernández-Soto, Lanzetta, and Yahil, 1999) and *Hubble* Ultra Deep Field (HUDF) survey (Beckwith et al., 2006) allowing photometric redshift measurements of the faintest galaxies up to redshift $z \sim 6$. Big step forward with ground-based telescopes was the Two Degree Field Galaxy Redshift Survey (2dF-GRS; Folkes et al., 1999) that used the multi-fiber spectrograph which could estimate 400 galaxy redshifts at the same time. One of the largest all-sky galaxy surveys is the Sloan Digital Sky Survey (SDSS) (York et al., 2000; Blanton et al., 2017), which mapped more than 200 million nearby galaxies with about a million spectroscopic redshifts and characterized their physical properties and clustering in large-scale structures.

Galaxy surveys at intermediate redshift ($z \sim 1$) began with the Canada–France Redshift Survey (CFRS; Lilly et al., 1995) and Autofib-LDSS survey (Ellis et al., 1996; Heyl et al., 1997), which provided evolution of the luminosity function (LF) of galaxies at $0 < z < 1$. One of the largest intermediate-z surveys is the Deep Extragalactic Evolutionary Probe 2 (DEEP2; Davis et al., 2003), which showed that the color bimodality of galaxies is present at $z \sim 1$ and provided the evolution of the LF of the blue and red galaxies.

The VLT/VIMOS Deep Survey (VVDS) (Ilbert et al., 2005) delivered the evolution of the global LF up to $z \sim 2$. The VIMOS Public Extragalactic Redshift Survey (VIPERS) (Guzzo and VIPERS Team, 2013) is the intermediate redshift ($0.5 < z < 1.2$) equivalent of the large surveys of the nearby

Universe (SDSS and 2dF-GRS). VIPERS maps the distribution of galaxies in large scale structures and shows that the color-density relation is already present at intermediate redshifts (Figure 5). The COSMic evOlution Survey (COSMOS) (Capak et al., 2007) and the zCOSMOS follow-up (Lilly et al., 2007) combined the photometric and spectroscopic redshifts of galaxies at $0 < z < 3$. The CosmicAssembly Near-infrared Deep Extragalactic Legacy Survey (CANDELS) (Grogin et al., 2011) is designed to observe the first third of galactic evolution at $1.5 < z < 8$. The VIMOS Ultra-Deep Survey (VUDS; Le Fèvre et al., 2015) is a large spectroscopic survey of star-forming galaxies at $2 < z < 6$. I use the COSMOS2015 photometric redshift catalog (Section 2.2.3; Laigle et al., 2016; Davidzon et al., 2017) in order to test the pipeline for deriving the SMF of cluster galaxies for the upcoming *Euclid* Mission (Chapter 2).

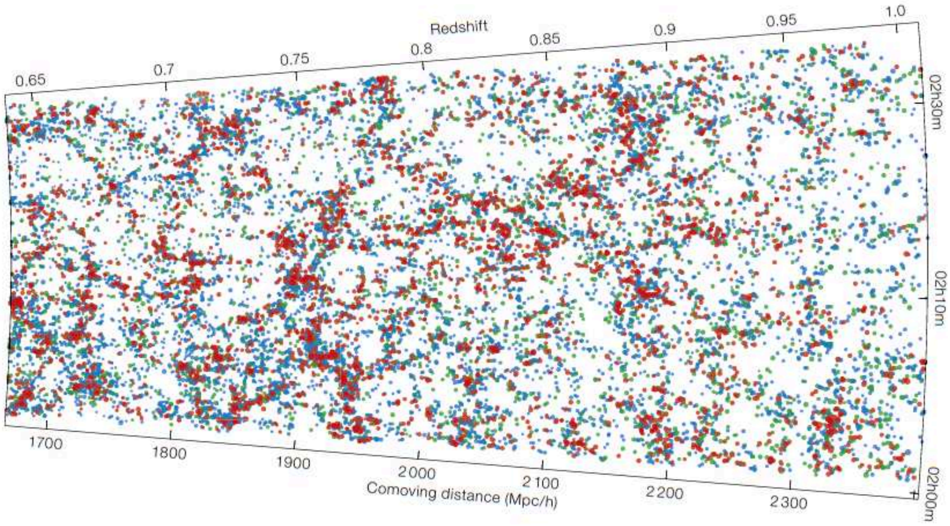

Figure 5: *Galaxies trace the large-scale structure of the Universe in the W1 field of the VIPERS survey. Galaxies are marked with different color (red, blue or green) depending on their rest-frame color. Credit:Guzzo and VIPERS Team, (2013).*

The next generation telescopes such as the *Large Synoptic Survey Telescope (LSST)* (LSST Science Collaboration et al., 2009; Ivezić et al., 2019), the *James Web Space Telescope (JWST)* (Gardner et al., 2006) and *Euclid Space Mission* (Section 2.2.1; Laureijs et al., 2011) will provide the astronomers with survey data with greater wavelength and absolute magnitude coverage.

Galaxy properties

The galaxy redshifts are essential for deriving other galaxy parameters. Furthermore, with the information on redshifts and galaxy coordinates, we can obtain a 3D map of galaxy distribution within a field of the sky (Figure 5; Guzzo and VIPERS Team, 2013) and use galaxies as cosmological probes for the geometry and expansion of the Universe (e.g. Peacock et al., 2002).

Redshifts can be derived using spectroscopy, photometry or a combination of the two. Spectroscopy is a more precise method, but more expensive in terms of the telescope time. Spectroscopic redshift z_{sp} can be computed using the spectral lines that we identify in the spectra of galaxies, by using the following equation:

$$z_{sp} = \frac{\lambda_{obs} - \lambda_{em}}{\lambda_{em}} \tag{1}$$

where λ_{obs} is the observed wavelength of a certain identified spectral line and λ_{em} is the emitted wavelength of the same spectral line. The entire spectra of distant objects (e.g. galaxies) are shifted, the shift of the spectrum increases with the distance of the object, due to the expansion of Universe. The relative shift of the spectra provides the spectroscopic redshift measurement of the galaxy.

A faster, more quantitative, but less accurate way to estimate the redshift of an object is to use photometry (Baum, 1962; Koo, 1985; Loh and Spillar, 1986; Connolly et al., 1995; Arnouts et al., 1999). Photometric redshift z_{ph} is not related to positions of specific spectral lines, but to positions of spectral features and the overall shape of the galaxy spectra, such as the Lyman break, Balmer break, 4000Å break, etc. (e.g. Connolly et al., 1995). Distant (redshifted) galaxies are redder and fainter than their counterparts at $z = 0$. Due to this effect we can estimate galaxy's redshift by comparing the observed and expected brightness of the object in different wavebands.

At intermediate and high redshifts, the photometric redshift is an essential parameter in galaxy studies (see e.g. Koo, 1999), for deriving the evolution of the LF and SMF (Subbarao et al., 1996; Wolf et al., 2003; Gabasch et al., 2004; Arnouts et al., 2007; Ilbert et al., 2013; Grazian et al., 2015; Davidzon et al., 2017), and obtaining galaxy distribution in large-scale structures (Mazure et al., 2007), etc.

Photometric redshift can be derived by Spectral Energy Distribution (SED) fitting, which is based on fitting the observed galaxy colors with those expected from the theoretical or empirical SEDs, using a χ^2 minimization procedure:

$$\chi^2(z, T, A) = \sum_{i=1}^{N_i} \left(\frac{F_{obs,i} - A \times F_{temp,i}(z, T)}{\sigma_i} \right)^2 \tag{2}$$

where $F_{obs,i}$ is the observed flux, $F_{temp,i}(z, T)$ is the flux in a given filter i for a template T at a redshift z, σ_i is the flux uncertainty in the filter i, N_i is the total number of filters used and A is the normalization constant (Lanzetta, Yahil, and Fernández-Soto, 1996; Arnouts et al., 1999, 2002; Bolzonella, Miralles, and Pelló, 2000; Ilbert et al., 2006, 2009). The z_{ph} is estimated by minimizing the χ^2. Derived photometric redshifts are generally calibrated using spectroscopic redshifts (Loh and Spillar, 1986; Arnouts et al., 1999; Bolzonella, Miralles, and Pelló, 2000; Wolf et al., 2004; Ilbert et al., 2013; Davidzon et al., 2017).

Another way of deriving the photometric redshift is by empirical fitting, where an empirical relation is derived for the z_{ph} (see e.g. Connolly et al., 1995; Brunner et al., 1997). For instance, Connolly et al., (1995) derived an empirical equation to estimate the z_{ph} as a linear function of U,B_J, R_F, I_N magnitudes for four respective bandpasses:

$$z = -0.941 - 0.147U + 0.412B_J - 0.138R_F - 0.084I_N \tag{3}$$

Moreover, they also derive empirical equations of quadratic and higher order with higher accuracy and lower dispersion σ_z. Then, the empirically computed z_{ph} values are compared to already existing spectroscopic redshifts of a subsample of galaxies (Connolly et al., 1995, 1997; Brunner et al., 1997; Firth, Lahav, and Somerville, 2003).

Both methods have been improved and extended with the use of the Bayesian statistics (Kodama, Bell, and Bower, 1999; Wolf, 2009) and neural networks (Firth, Lahav, and Somerville, 2003; Collister et al., 2007; Yèche et al., 2010). Furthermore, the two methods can be combined (Budavári et al., 2000; Benítez et al., 2004).

The accuracy of the photometric redshift estimate has been improved by increasing the number of bandpasses and using more narrow bandpasses (Wolf et al., 2003; Wolf et al., 2004; Ilbert et al., 2009), combining the photometric bandpasses and spectroscopic emission lines (Ilbert et al., 2009), etc. Photometric redshift z_{ph} can be validated using the available z_{sp} (Connolly et al., 1995; Dahlen et al., 2013; Skelton et al., 2014; Davidzon et al., 2017). Furthermore, if spectroscopic features are too faint, z_{sp} estimate can be supported by the z_{ph} estimation.

We can use the derived redshift and cosmological parameters to estimate the luminosity distance:

$$d_L = (1+z)\frac{c}{H_0}\int_0^z \frac{dz}{\sqrt{\Omega_\lambda + \Omega_m(1+z)^3}} \tag{4}$$

where Ω_m is the matter density constant, Ω_λ is the dark energy density constant, c is the lightspeed and H_0 is the Hubble constant. With the luminosity distance and the measured apparent magnitude m of our objects we can compute their K-corrected absolute magnitude:

$$\mathcal{M} = m - 5 \times \log(d_L/\mathrm{Mpc}) - m_o - K(z) \tag{5}$$

where $K(z)$ is the flux correction in the observed waveband and a fixed rest-frame waveband and m_0 is the apparent magnitude normalization i.e. zero magnitude. Absolute magnitudes can be used for deriving the LF of the observed sample of galaxies.

Stellar masses can be estimated by fitting the observed SED with the SED templates, from the Stellar Population Synthesis (SPS) models (e.g. Bruzual and Charlot, 2003; Conroy, 2013; Conroy, Gunn, and White, 2009) with different assumptions on the star formation history (SFH), IMF, stellar age, dust extinction law, metallicity, etc. for each galaxy (Ilbert et al., 2010, 2013; Grazian et al., 2015; Davidzon et al., 2017). Uncertainties in the stellar mass estimate, originate mainly from the uncertainties in photometry and photometric redshift, but also due to degeneracies of the SED parameters and systematics (Caputi et al., 2011; Ilbert et al., 2013; Grazian et al., 2015; Mobasher et al., 2015; Davidzon et al., 2017). Stellar masses can be used in order to derive the SMF of a galaxy population.

GALAXY EVOLUTION

Interplay of physical processes such as galaxy merging, star formation, gas accretion, radiative gas cooling, gas heating, feedback mechanisms, environmental effects, etc. regulate the gas content and star formation in galaxies, drive the evolution of galaxies (Kauffmann et al., 1999; Birnboim and Dekel, 2003; Kereš et al., 2005; Dekel and Birnboim, 2006; Cattaneo et al., 2006) and shape the galaxy LF and SMF (Kauffmann et al., 1999; Benson et al., 2003; Binney, 2004; Kereš et al., 2005).

Galaxies assemble their stellar mass through gravitational build-up, i.e. galaxy merging (e.g. Hopkins et al., 2008) and star formation (e.g. McKee and Ostriker, 2007). Galaxy merging is more important for the stellar mass build-up of massive galaxies ($M_* > 10^{11} M_\odot$) (Oser et al., 2010; Cattaneo et al., 2011; Lee and Yi, 2013), whereas in situ star formation contributes more for the mass build-up of low-mass galaxies (Lee and Yi, 2013; Rodriguez-Gomez et al., 2016). However, there are still many open questions such as *What is the importance of each of these processes as a function of mass, environment and cosmic epoch? What is the timescale of these processes?*, etc. In this section I give a description on the galaxy merging process (Section 1.4.1) and star formation in galaxies (Section 1.4.2) and I give an overview of the stellar mass assembly of star-forming and quiescent galaxies at different cosmic epochs (Section 1.4.3).

Galaxy merging

In the ΛCDM model, dark matter halos merge to form larger and larger halos (Section 1.2; e.g. White and Rees, 1978). Galaxies sharing the same dark matter halo, e.g. in a cluster, can interact and eventually merge with their neighboring galaxies. Their gas, dust and stars are redistributed to form a more massive galaxy with often different properties of their progenitors (Toomre and Toomre, 1972; Hopkins et al., 2006a,b, 2008; Dubois et al., 2016).

Observational evidence of merger events exists in the form of tidal tails, shells, ripples, close physical pairs, interacting and merging galaxies i.e. peculiar galaxies (Schweizer and Seitzer, 1992; Schweizer, 1996; Borne et al., 2000; Struve et al., 2010; López-Sanjuan et al., 2013; Tasca et al., 2014). These features can be modeled (e.g. Toomre and Toomre, 1972; Barnes and Hernquist, 1991; Barnes and Hernquist, 1996; Kazantzidis et al., 2008) and are also predicted by the hierarchical clustering scenario (Section 1.2; e.g. White and Rees, 1978).

Major merger is typically defined as a merger event of two galaxies with stellar mass ratio between $1:4 < M_{*,1} : M_{*,2} < 1:1$, where $M_{*,1} > M_{*,2}$ (e.g. Rodriguez-Gomez et al., 2016). It is generally believed that on average, a galaxy goes through at least one major merger event since $z \sim 1 - 1.5$, thus roughly doubling its stellar mass during this period (Oser et al., 2010; López-

Sanjuan et al., 2012, 2013). Besides having an impact on the galaxy stellar mass, a major merger has a substantial impact on other galaxy properties, such as metallicity, stellar age, morphology, size, star formation, velocity dispersion, etc. (e.g. López-Sanjuan et al., 2012). For instance, in a major merger event of two disk, star-forming galaxies, the two galaxies transform into an elliptical galaxy (Toomre and Toomre, 1972). Gas associated with the progenitors is shock-heated, settles back into the potential well of the newly formed galaxy where it cools, fragments and eventually forms stars (Barnes and Hernquist, 1991; Barnes and Hernquist, 1996). In case the two progenitors are rich in molecular gas, i.e. in a *wet* major merger event, remnant galaxy often goes through a starburst phase (Barnes and Hernquist, 1991; Mihos and Hernquist, 1994, 1996) and strong AGN activity (Di Matteo, Springel, and Hernquist, 2005) fueled by the molecular gas inflow. Over a period of time, a combination of star formation and feedback mechanisms consume the available molecular gas and galaxy moves to a more quiescent, poststarburst phase (Snyder et al., 2011; Yesuf et al., 2014). Eventually, stellar and AGN feedback disperse the remaining gas and dust and suppress star formation (Springel, Di Matteo, and Hernquist, 2005; Yesuf et al., 2014; Dubois et al., 2016). The remnant galaxy becomes a visible quasar that reddens rapidly and reaches a final stage of a *dead*, quiescent, elliptical galaxy (Figure 6; Hopkins et al., 2006a,b, 2008).

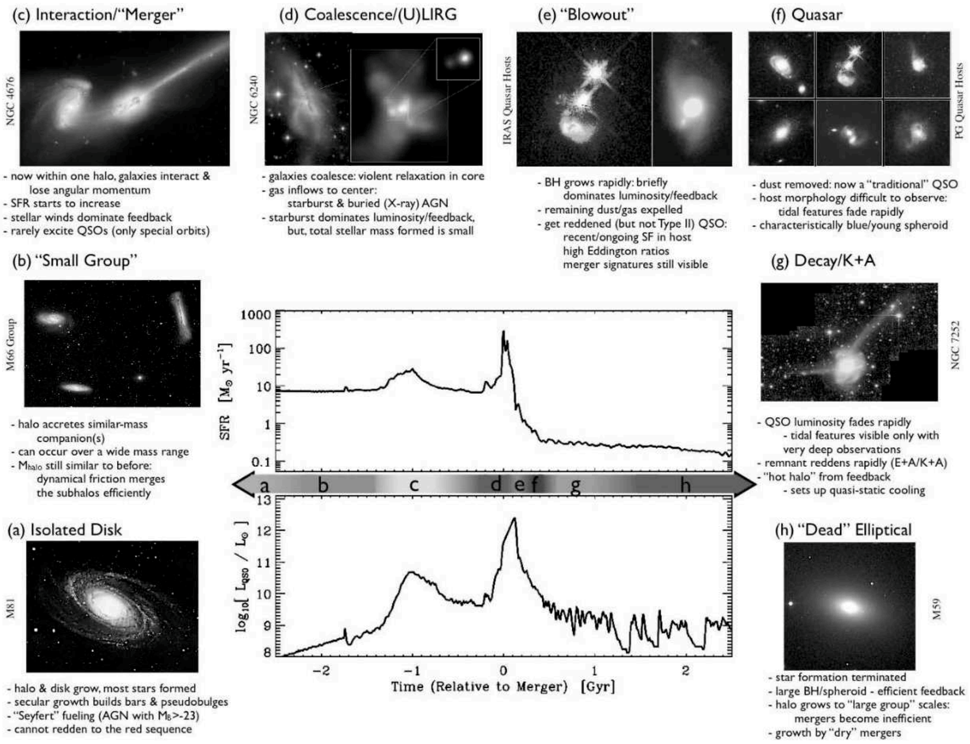

(c) Interaction/"Merger"

- now within one halo, galaxies interact & lose angular momentum
- SFR starts to increase
- stellar winds dominate feedback
- rarely excite QSOs (only special orbits)

(d) Coalescence/(U)LIRG

- galaxies coalesce: violent relaxation in core
- gas inflows to center: starburst & buried (X-ray) AGN
- starburst dominates luminosity/feedback, but, total stellar mass formed is small

(e) "Blowout"

- BH grows rapidly: briefly dominates luminosity/feedback
- remaining dust/gas expelled
- get reddened (but not Type II) QSO: recent/ongoing SF in host high Eddington ratios merger signatures still visible

(f) Quasar

- dust removed: now a "traditional" QSO
- host morphology difficult to observe: tidal features fade rapidly
- characteristically blue/young spheroid

(b) "Small Group"

- halo accretes similar-mass companion(s)
- can occur over a wide mass range
- M_{halo} still similar to before: dynamical friction merges the subhalos efficiently

(g) Decay/K+A

- QSO luminosity fades rapidly
  - tidal features visible only with very deep observations
- remnant reddens rapidly (E+A/K+A)
- "hot halo" from feedback
  - sets up quasi-static cooling

(a) Isolated Disk

- halo & disk grow, most stars formed
- secular growth builds bars & pseudobulges
- "Seyfert" fueling (AGN with M_B>-23)
- cannot redden to the red sequence

(h) "Dead" Elliptical

- star formation terminated
- large BH/spheroid - efficient feedback
- halo grows to "large group" scales: mergers become inefficient
- growth by "dry" mergers

Figure 6: *Illustration of different phases of galaxy evolution through a wet major merger. Credit: Hopkins et al., (2008).*

Wet major mergers naturally occur more often in dense regions where the probability for collisions is higher, and at higher redshifts ($z > 1.5 - 2$) when most of the galaxies were gas-rich (Hopkins et al., 2008; López-Sanjuan et al., 2013). Therefore, at higher redshift, the *wet* major remnant galaxies i.e. radio galaxies and quasars hosting powerful AGNs, can be used for identifying high-redshift galaxy protoclusters (Wylezalek et al., 2013). Moreover, these High-z Radio Galaxies (HzRG) are believed to be the progenitors of the Brightest Cluster Galaxies (BCGs) at lower redshifts (see e.g. Miley and De Breuck, 2008 for a review).

In case the two merging galaxies are gas-poor, we have a *dry* merger event. *Dry* merging of two elliptical galaxies is important in producing massive, *boxy*, elliptical galaxies at $z < 1$ (Naab, Khochfar, and Burkert, 2006; Faber et al., 2007; Peng et al., 2010; López-Sanjuan et al., 2013; Cattaneo et al., 2011).

A minor merger event, with a typical mass ratio between $1 : 10 < M_{*,1} : M_{*,2} < 1 : 4$ (Rodriguez-Gomez et al., 2016) is a less violent process, where the remnant usually keeps similar properties as its most massive progenitor, sometimes with perturbed morphology: disk thickening, bars, low-surface brightness features, etc., whereas the less massive progenitor is being completely accreted by the massive progenitor. (Velazquez and White, 1999; Kazantzidis et al., 2008; Struve et al., 2010).

Molecular gas and star formation

Dominant baryonic matter of the Universe from which galaxies form is the hot InterGalactic Medium (IGM). Ability of the hot IGM gas to cool is one of the main mechanisms that regulates molecular gas available for star formation in galaxies and it is essential for the formation of stars inside the galaxies in the center of the dark matter halos (Section 1.2; see e.g. Mo, van den Bosch, and White, 2010).

Molecular gas

Molecular gas in galaxies is assembled through cold gas accretion that is directed along the filaments (Figure 7), and (indirectly) through quasi-spherical hot gas accretion (Birnboim and Dekel, 2003; Kereš et al., 2005; Kereš and Hernquist, 2009; Kereš et al., 2009; Dekel and Birnboim, 2006; Dekel et al., 2009; Stewart et al., 2011; Bouché et al., 2013). The cold gas is directly accreted by the galaxies inside the dark matter halos with masses lower than the critical mass $M_{\mathrm{shock}} \sim 10^{11.4-12} M_{\odot}$, whereas gas entering massive halos ($M_{\mathrm{halo}} > M_{\mathrm{shock}}$) is shock-heated to virial temperatures of the halo, and part of it is eventually accreted by the galaxies within these halos (Birnboim and Dekel, 2003; Kereš et al., 2005; Kereš et al., 2009; Dekel and Birnboim, 2006; Cattaneo et al., 2006; Ocvirk, Pichon, and Teyssier, 2008; Stewart et al., 2011; Nelson et al., 2013). However, gas accretion in the massive ($M_{\mathrm{halo}} > M_{\mathrm{shock}}$), high-redshift ($z > 2 - 3$) halos is still predominantly in the cold mode (Birnboim and Dekel, 2003; Kereš et al., 2005; Kereš et al., 2009; Dekel and Birnboim, 2006; Cattaneo et al., 2006). Since gas accretion mode depends on the halo mass, it is consequently environment dependent, with the cold mode dominating low-density environments i.e. the low-mass halos, whereas the hot mode is the dominant mode in massive halos of rich galaxy groups and clusters (Kereš et al., 2005).

Fraction of the hot halo gas radiatively cools and falls towards the central galaxy in the form of a *cooling flow* (see e.g. Mushotzky, 1993; Fabian, 1994;

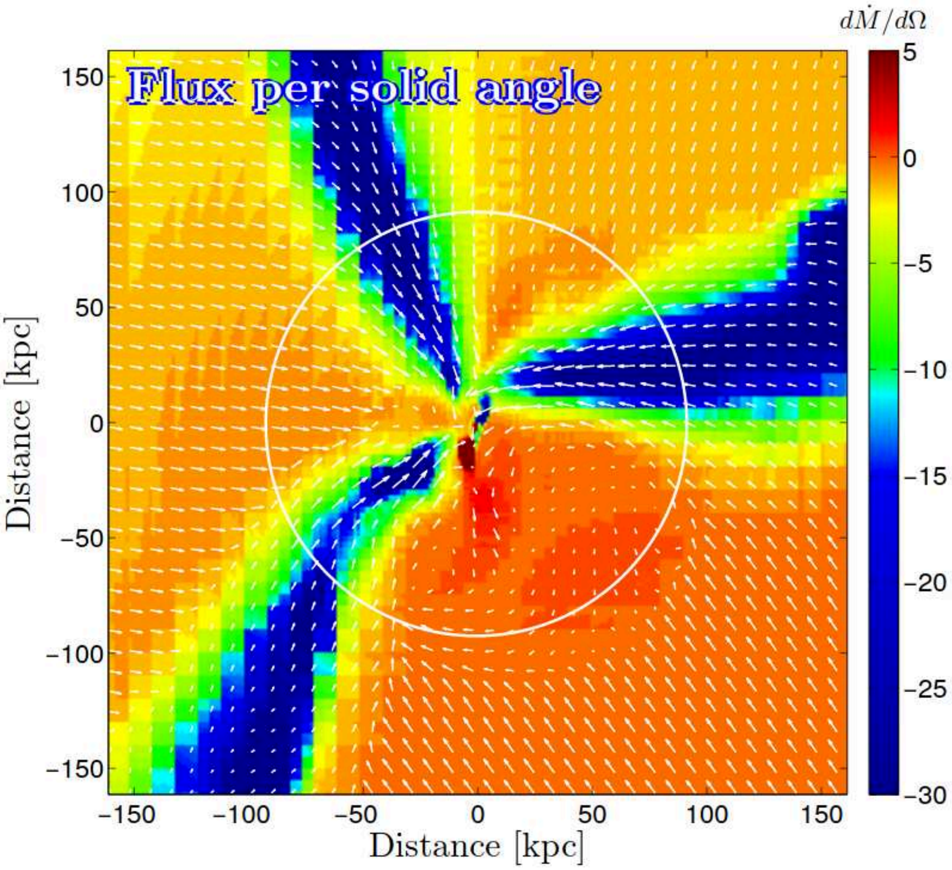

Figure 7: *Radial inward flux of cold gas flowing towards the halo center. Halo virial radius is marked as a white circle. Credit: Dekel et al., (2009).*

McNamara et al., 2000; Peterson and Fabian, 2006; Dekel and Birnboim, 2006). The cooled gas either settles inside the galaxy, fueling its star formation, or it is being accreted by the Super Massive Black Hole (SMBH), and fuels the AGN activity (Gaspari, Ruszkowski, and Sharma, 2012; Tremblay et al., 2016).

There is plenty of observational evidence supporting the existence of cooling flows in clusters, groups and massive elliptical galaxies, indicating that cooling flows are quite common (see e.g. Fabian, 1994; Peterson and Fabian, 2006 for reviews). For example, the infalling gas, shock-heated to virial temperatures ($T \sim 10^{7-8}$ K) of the massive halo is observed to radiatively cool through *bremsstrahlung* emission in the X-ray wavebands (Cowie and Binney, 1977; Edge, Stewart, and Fabian, 1992; McNamara et al., 2000; Peterson et al., 2001). Moreover, there are observations of the Near InfraRed (NIR), rovibrational emission of the warm molecular hydrogen H_2 ($T \sim 10^3$ K) probably related to cooling flows (Jaffe and Bremer, 1997; Edge et al., 2002; Jaffe, Bremer, and Baker, 2005; Lim et al., 2012). Furthermore, there are numerous optical observations of the Hα nebular emission in cooling flow clusters, that traces the warm ionized gas, that possibly cooled from the hot IntraCluster medium (ICM) (McNamara et al., 1996; Edwards et al., 2007; McDonald et al., 2010). Finally, extended molecular gas structures have been detected in the central regions of cooling flow clusters, traced by the carbon monoxide (CO) rotational lines in the (sub)mm wavebands (Edge, 2001; Edge and

Frayer, 2003; Salomé et al., 2006). The molecular gas emission is often correlated with the $H\alpha$ nebular emission, radio lobes and/or X-ray emission (Salomé et al., 2006; Olivares et al., 2019).

The hot ICM can cool radiatively and fragment into molecular gas clouds if the gas cooling time is sufficiently short $t_{ti} \leqslant 10^8$yr (e.g. McNamara et al., 2016) or if gas cooling time to free-fall time ratio is sufficiently low $t_{ti}/t_{ff} < 10$ (e.g. Li and Bryan, 2014). The expected cooling rates in massive clusters, determined from the X-ray emission, are $M_{cool} \sim 100 - 1000\ M_{\odot}yr^{-1}$ (Allen et al., 2001; Hudson et al., 2010). However, observations at lower frequencies fail to detect the expected molecular gas content and SFR. Therefore, there must be some (re)heating mechanisms that prevents the hot gas from cooling, the most popular candidate being the AGN feedback (see e.g. McNamara and Nulsen, 2007; Fabian, 2012 for reviews).

Different types of feedback mechanisms can also have a positive impact on gas cooling by shortening the gas cooling time. For instance, stellar and SNe feedback enrich the halo gas with *metals*, which shorten the gas cooling time (Wiersma et al., 2009; Fraternali, 2017). Next, AGN feedback can perturb the hot gas by compressing or lifting it to large distances where it becomes unstable and forms molecular gas filaments around the AGN jets (Section 3.1.1; e.g. Salomé et al., 2006; Werner et al., 2011).

In Chapter 3 we use the CO(2-1) rotational transition line to trace the molecular gas in two extended components around the radio loud AGN (RLAGN), possibly correlated with two radio lobes, in a galaxy cluster at $z \sim 1.44$ (Markov et al., 2020a). We discuss on several hypotheses on the most probable origin of the molecular gas, including the gas cooling hypothesis.

Star formation

There are many physical processes that lead up to star formation in galaxies. It begins with gas condensation out of the hot and warm halo gas, gas accretion by the galaxy, further cooling and formation of a neutral gas, contraction to massive gravitationally bound structures, further cooling of gas and formation of molecular clouds, fragmentation of molecular clouds into dense clumps and cores within these clumps, and finally gravitational collapse of these cores into stars (see e.g. McKee and Ostriker, 2007; Kennicutt and Evans, 2012).

Star formation is fueled by cold and dense molecular gas (see e.g. Kennicutt, 1998b; Kennicutt and Evans, 2012; Krumholz, 2014 for reviews). Galaxies rich in molecular gas are mostly star-forming, bluish, late-type spiral and irregular galaxies (e.g. Kauffmann et al., 2003; Dekel and Birnboim, 2006; Cattaneo et al., 2006). Once the galaxy is completely devoid of molecular gas through star formation, feedback or environmental mechanisms, it will stop forming new stars (Springel, Di Matteo, and Hernquist, 2005). Most stars eventually end their life with a significant release of the metal-enriched gas (De Lucia, Kauffmann, and White, 2004; Wiersma et al., 2009). Young, blue and massive stars end their life on relatively short timescales with respect to their red, low-mass counterparts. Therefore, the color of gas-depleted galaxies starts to be dominated by the color of long-lived red stars. These galaxies gradually become redder, move to the *red sequence* (e.g.

Baldry et al., 2004; Springel, Di Matteo, and Hernquist, 2005; Dekel and Birnboim, 2006), and evolve into passive, quiescent galaxies (Binney and Tremaine, 1987; Kennicutt, 1998b; Faber et al., 2007).

SFR quantifies the ongoing star formation activity in a galaxy. The SFR surface density Σ_{SFR} is tightly correlated to the molecular gas density Σ_{gas} (the star formation law, i.e. the Schmidt-Kennicutt law; Schmidt, 1959; Kennicutt, 1998a; Kennicutt et al., 2007; Schruba et al., 2011). Therefore, SFR is completely driven by the molecular gas content and density (Lada, Lombardi, and Alves, 2010). There are three distinct regimes of star formation, depending on the gas density (see e.g. Kennicutt and Evans, 2012). In the low-density regime the cold gas is predominantly neutral, the SFR is low and occurs in sparse molecular clouds. This regime is typical for early-type galaxies, dwarf galaxies, etc. In the intermediate-density regime, molecular hydrogen is the dominant component of the cold gas, the SFR is higher and SFR surface density and molecular gas density are strongly correlated (the Schmidt-Kennicutt law; Kennicutt et al., 2007). This regime is characteristic of star-forming, disk galaxies (Rodighiero et al., 2011). Finally, in the high-density or starburst regime, the molecular gas is dense and compact, the SFR is intense and it occurs on relatively short timescales. The Schmidt-Kennicutt law can be extended for starburst galaxies (e.g. Genzel et al., 2010). The starburst regime is thought to be triggered by cold gas accretion (Dekel and Birnboim, 2006), or *wet* major mergers followed by the AGN activity (Figure 6; Hopkins et al., 2008; Rodighiero et al., 2011), thus, it naturally occurs at earlier times ($z > 2$).

Most star-forming galaxies follow a tight, almost linear relation between their SFRs and stellar masses (e.g. Brinchmann et al., 2004; Elbaz et al., 2007; Peng et al., 2010; Rodighiero et al., 2011; Tasca et al., 2015; Schreiber et al., 2015). However, a small population of starburst galaxies lie above this *main sequence (MS)* (Rodighiero et al., 2011). Moreover, below the *MS* is a growing population of mostly massive galaxies going through star formation quenching (Elbaz et al., 2007; Tanaka et al., 2013; Tasca et al., 2015). The $\mathrm{SFR} - M_*$ relation evolves with redshift, and the *MS* galaxies at high-z, have on average higher SFR than their local counterparts (Tasca et al., 2015; Schreiber et al., 2015; Tomczak et al., 2016). The specific star formation rate $\mathrm{sSFR} = \mathrm{SFR}/M_*$ of star-forming galaxies is increasing with redshift (Peng et al., 2010; Karim et al., 2011; Sargent et al., 2012, 2014; Behroozi, Wechsler, and Conroy, 2013; Scoville et al., 2013; Ilbert et al., 2013; Tasca et al., 2015; Schreiber et al., 2015; Darvish et al., 2016). Moreover, the sSFR is on average lower for more massive galaxies than their low-mass counterparts (Brinchmann et al., 2004; Elbaz et al., 2007; Karim et al., 2011; Muzzin et al., 2012; Hatch et al., 2017).

The most common location of active star formation and rapid stellar mass assembly shifts from more massive galaxies at early epochs, to intermediate and low-mass galaxies at later epochs (the so called *downsizing* scenario; Cowie et al., 1996; Brinchmann and Ellis, 2000; Heavens et al., 2004; Juneau et al., 2005; Bundy et al., 2006; Panter et al., 2007; Vergani et al., 2008; Pérez-González et al., 2008; Ilbert et al., 2010; Muzzin et al., 2012; Pacifici et al., 2016).

Star Formation Rate Density (SFRD) is defined as SFR per unit volume. The SFRD can be derived from the luminosity density (Equation 6), measured in the UV rest-frame (Madau, Pozzetti, and Dickinson, 1998). The SFRD characterizes the star formation activity across cosmic time, i.e. the cosmic star formation history (Madau et al., 1996; Cucciati et al., 2012; Guglielmo et al., 2015; see e.g. Madau and Dickinson, 2014 for a review). The SFRD increased by more than an order of magnitude since the end of the reionization epoch ($z \sim 6-8$), to the so-called galaxy mass assembly epoch or *the cosmic noon epoch* at $1 < z < 3$, with a peak around $z \sim 2$ (Cucciati et al., 2012; Guglielmo et al., 2015; Bouwens et al., 2015). Since then, the SFRD has been progressively declining, with the present day SFRD on average an order of magnitude lower than at its peak (Figure 8, top panel; see Madau and Dickinson, 2014 and references therein). The rise and fall of the cosmic SFRD corresponds to the evolution of the cosmic molecular gas density $\rho(H_2)$ (Walter et al., 2014; Walter et al., 2019; Decarli et al., 2019), although the uncertainties are significant at higher redshifts (Figure 8, bottom panel; Walter et al., 2019). Moreover, the decrease in SFRD matches the decrease in molecular gas fraction (M_{gas}/M_{*}) since $z \sim 2$ (Tacconi et al., 2013, 2018).

Star formation quenching

There are several physical processes responsible for shutting down (quenching) of star-formation in galaxies. Each of them plays a different role in cold molecular gas depletion, at different epochs and with different time scales (see e.g. Boselli and Gavazzi, 2006 for a review). These quenching mechanisms can be internal i.e. mass-driven or external i.e. environment-driven (Peng et al., 2010, 2012, 2014; Muzzin et al., 2012; Darvish et al., 2016; Darvish et al., 2018b; Cora et al., 2018), with the two effects being independent up to $z < 1$ (Peng et al., 2010, 2012). Mass quenching dominates massive central galaxies, while both mass quenching and environmental quenching affect low-mass, satellite galaxies (Peng et al., 2010, 2012). Environmental quenching becomes more relevant at lower redshift ($z < 1$), when large-scale structures become denser and better differentiated (Peng et al., 2010, Scoville et al., 2013, Darvish et al., 2016), whereas mass quenching is more important at higher redshifts (Muzzin et al., 2012; Darvish et al., 2016). However, some works found that the mass and environmental quenching are simply two different manifestations of the same process related to the galaxy halo mass (Knobel et al., 2015; Carollo et al., 2016).

Massive galaxies assemble their mass and quench earlier than their low-mass counterparts (Thomas et al., 2005; Bundy et al., 2006; Vergani et al., 2008; Peng et al., 2010, 2012; Ilbert et al., 2010, 2013; Guglielmo et al., 2015; Pacifici et al., 2016; Tomczak et al., 2016; Sklias et al., 2017). For instance, AGN feedback is an internal feedback mechanism that unleashes vast amounts of energy that can disrupt star formation in massive galaxies (Begelman, de Kool, and Sikora, 1991; McNamara et al., 2000; Springel, Di Matteo, and Hernquist, 2005; Croton et al., 2006; see e.g. McNamara and Nulsen, 2007; Fabian, 2012 for reviews). Moreover, blasts and radiation from SNe explosion can release energy sufficient for quenching the low-mass galax-

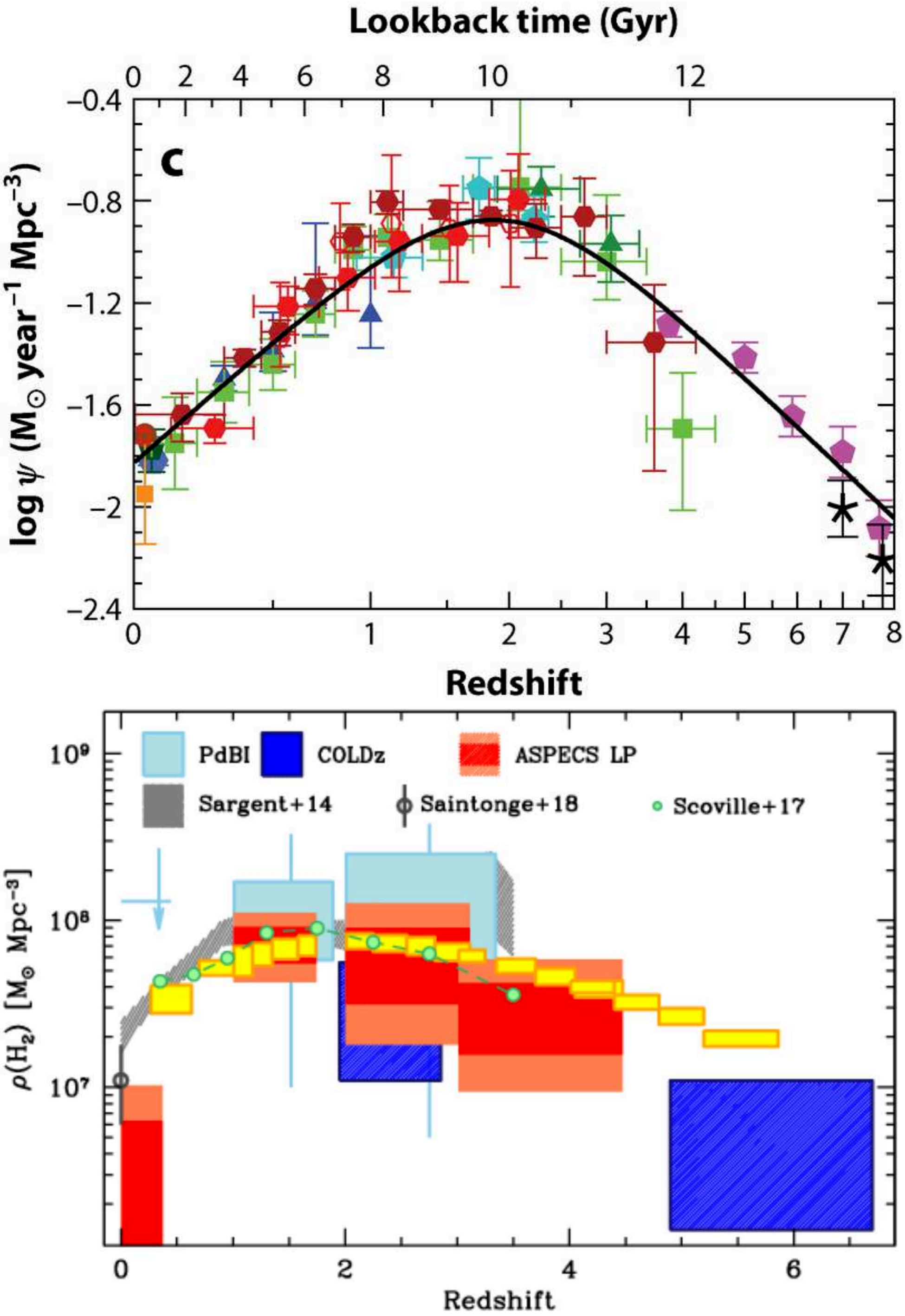

Figure 8: *Rise and fall of the SFRD (top panel; credit: Madau and Dickinson, 2014) and molecular gas density (bottom panel; credit: Walter et al., 2019) with redshift.*

ies (Heckman, Armus, and Miley, 1990; Martin, 1999; Benson et al., 2003; Strickland and Heckman, 2009; Hopkins et al., 2014). Finally, star formation of the intermediate-mass galaxies seem to be least affected by different types of feedback, and possibly other quenching mechanisms (Figure 9; Silk, 2011; Silk and Mamon, 2012; Mutch, Croton, and Poole, 2013; Davidzon et al., 2017). Therefore, the shape and evolution of the LF and SMF are determined by quenching mechanisms (Pozzetti et al., 2010; Peng et al., 2010, 2012).

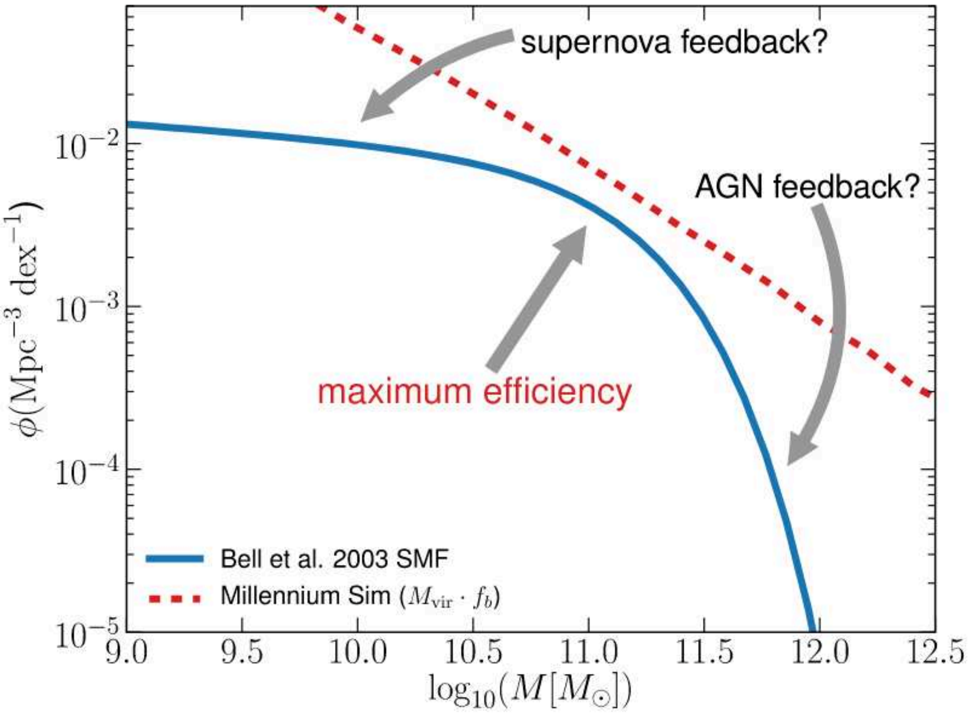

Figure 9: *Galaxy SMF (blue solid line) and halo mass function (dashed red line). The SNe and AGN feedback affect the low-mass and high-mass end of the SMF. Credit: Mutch, Croton, and Poole, 2013.*

Observations of galaxies of the same stellar mass show that the evolution from star-forming to quiescent phase is more rapid for cluster galaxies than for their field counterparts (Kauffmann et al., 2004; Bundy et al., 2006; Strazzullo et al., 2013; Scoville et al., 2013; Delaye et al., 2014; Guglielmo et al., 2015; Hatch et al., 2017; Foltz et al., 2018), due to the additional environmental mechanisms. For instance, tidal stripping is a gravitational effect and affects both dark and baryonic matter. Galaxies in groups and clusters interact with their neighbors and their outer regions can be stripped off its dark matter, gas, dust and stars by tidal forces. (Farouki and Shapiro, 1981; Moore et al., 1999a; Cooper et al., 2010; Carleton et al., 2018). Moreover, satellite galaxies entering groups and clusters, experience ram-pressure stripping by the hot halo gas (Abadi, Moore, and Bower, 1999: McCarthy et al., 2008; Merluzzi et al., 2013; Jaffé et al., 2018), and *strangulation* (Larson, Tinsley, and Caldwell, 1980; Balogh and Morris, 2000; Van den Bosch et al., 2008; Peng, Maiolino, and Cochrane, 2015; Maier et al., 2016). Finally, galaxy mergers can be violent processes that play an important role in star formation quenching (Section 1.4.1; Hopkins et al., 2006b, 2008; Struve et al., 2010; Rodriguez-Gomez et al., 2016; Dubois et al., 2016).

Stellar mass assembly

Besides the SFRD and molecular gas density $\rho(\mathrm{H_2})$ which quantify the star formation activity and molecular gas content of galaxies, respectively, another key parameter is the stellar mass density ρ_*, that quantifies the stellar mass assembly of galaxies. We can investigate the stellar mass assembly of different galaxy samples, by deriving the evolution of ρ_* over cosmic time. Moreover, evolution of the ρ_* corresponds with the evolution of the SFRD and $\rho(H_2)$ with redshift and provides complementary information on the overall galaxy evolution (see Madau and Dickinson, 2014, for a review). For instance, at $z < 1$, the ρ_* shows relatively modest evolution (Figure 10; Brinchmann and Ellis, 2000; Fontana et al., 2004; Ilbert et al., 2010, 2013; Moustakas et al., 2013), corresponding to a sharp decline of the SFRD and $\rho(H_2)$ over the same redshift range (Figure 8). Moreover, at the *cosmic noon* epoch $1 < z < 4$, the strong evolution of the ρ_* implies a very active phase in the mass build-up of galaxies (Figure 10; Ilbert et al., 2013), corresponding to the peak of the SFRD and $\rho(H_2)$ (Figure 8) see Madau and Dickinson, 2014 for a review). Finally, at high redshift $z > 4$, the ρ_* shows consistent growth since $z \sim 8-9$, although uncertainties are still large (e.g. Stark et al., 2013; Grazian et al., 2015; see Madau and Dickinson, 2014 for a review).

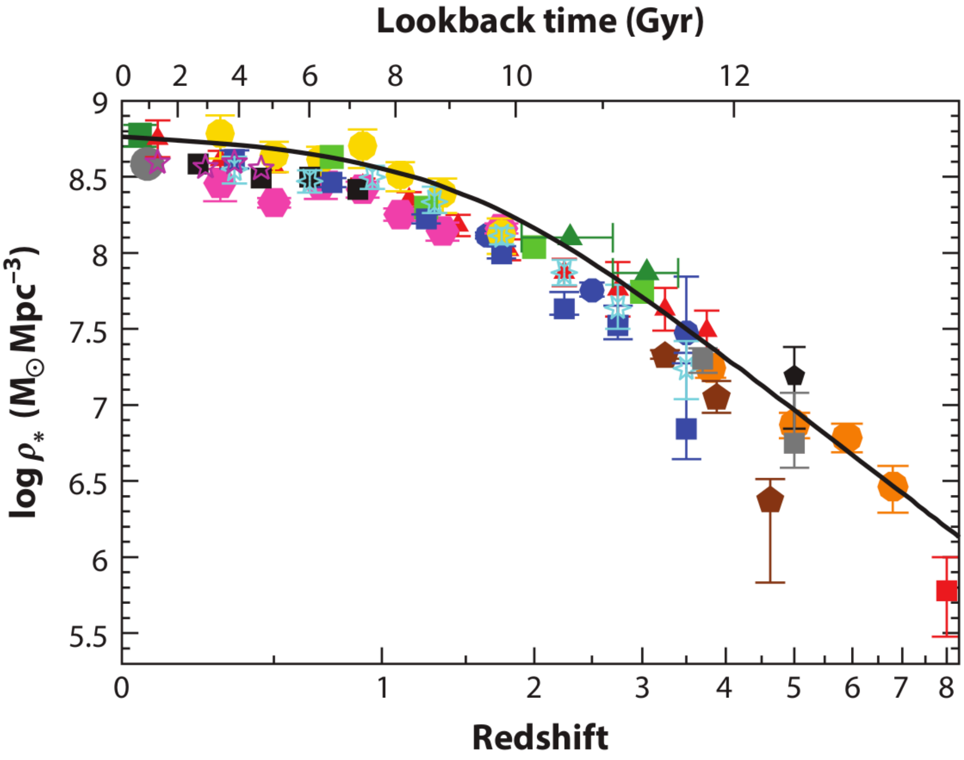

Figure 10: *The evolution of the stellar mass density over cosmic time, from the work of Madau and Dickinson, (2014).*

The ρ_* can be derived from the integral of the SMF (Equation 7 e.g. Wilkins, Trentham, and Hopkins, 2008; Ilbert et al., 2010, 2013; Davidzon et al., 2017), from the integral of the SFRD (e.g. Wilkins, Trentham, and Hopkins, 2008; Behroozi, Wechsler, and Conroy, 2013), or from the luminosity density and mass to light ratio (Arnouts et al., 2007), (see Madau and Dickinson, 2014 for a review).

Studies on the stellar mass assembly of galaxies at high redshift $z > 4$ are still inconclusive, due to biased sample selection and large uncertainties (Caputi et al., 2011, 2015; Grazian et al., 2015; Davidzon et al., 2017; see Madau and Dickinson, 2014 for a review). A consistent picture of the stellar mass assembly of galaxies exists out to $z \sim 4$ (e.g. Marchesini et al., 2009; Fontana et al., 2009; Muzzin et al., 2013b; Ilbert et al., 2013; Tomczak et al., 2016; Davidzon et al., 2017). At $3 < z < 4$ there is already evidence of quenching of the most massive star-forming galaxies, and consequently an emergence of a population of early-type, quiescent galaxies (Pérez-González et al., 2008; Fontana et al., 2009; Muzzin et al., 2013b; Buitrago et al., 2013; Straatman et al., 2014; Spitler et al., 2014; Davidzon et al., 2017).

Quiescent galaxies assembled most of their stellar mass during the peak of the mass assembly epoch (the so-called *cosmic noon* epoch), at $1 < z < 3$, with a substantial increase in a population of quiescent galaxies of all masses, which indicates that star formation quenching is very efficient at this epoch (Muzzin et al., 2013b; Ilbert et al., 2013; Davidzon et al., 2017). This is in agreement with the previous works in the literature at lower redshifts (out to $z \sim 2$), who found that the key epoch in the stellar mass assembly of quiescent galaxies is at $1 < z < 2$, when a large fraction of massive, star-forming galaxies turn quiescent (McCarthy et al., 2004; Juneau et al., 2005; Arnouts et al., 2007; Williams et al., 2009; Ilbert et al., 2010).

Galaxy bimodality, i.e. a population of star-forming, blue, mostly spiral and irregular galaxies (*blue cloud*) and quiescent, red, mostly elliptical galaxies (*red sequence*) is already present as early as $z \sim 2$ (Cattaneo et al., 2006; Williams et al., 2009; Ilbert et al., 2010; Tanaka et al., 2013; Strazzullo et al., 2013; Tomczak et al., 2014). At $z \sim 1$ a significant fraction of both star-forming (mostly late-type) and quiescent (mostly early-type) galaxies is already assembled (Brinchmann and Ellis, 2000; Pozzetti et al., 2003, 2010; Bell et al., 2004; Fontana et al., 2004; Arnouts et al., 2007; Pérez-González et al., 2008; Ilbert et al., 2010).

During the last cosmic epoch ($0 < z < 1$), both star-forming and quiescent galaxies continue to evolve, but at a slower pace (Fontana et al., 2004; Arnouts et al., 2007; Ilbert et al., 2010, 2013), which is consistent with a decrease of the cosmic molecular gas density and SFR at lower redshifts (Figure 8). Star-forming galaxies show modest evolution (Bundy et al., 2006; Arnouts et al., 2007; Faber et al., 2007; Ilbert et al., 2010; Pozzetti et al., 2010), while the evolution of quiescent galaxies is mass dependent (Pozzetti et al., 2010; Ilbert et al., 2010, 2013; Davidzon et al., 2017). Massive quiescent elliptical galaxies do not experience significant evolution (Pozzetti et al., 2003, 2010; Vergani et al., 2008; Ilbert et al., 2010, 2013). On the other hand, there is a mass-build up of low and intermediate-mass quiescent galaxies and a flattening of a SMF, probably due to a fact that low-mass star-forming galaxies experience star formation quenching and a morphological transformation, and migrate to the *red sequence* (Juneau et al., 2005; Pozzetti et al., 2010; Peng et al., 2010, 2012; Ilbert et al., 2010, 2013; Davidzon et al., 2017). Therefore, at this epoch, quiescent, mostly early-type galaxies start to dominate the high-mass end of the SMF (Pozzetti et al., 2003; Fontana et al., 2004, 2009; Williams et al., 2009; Ilbert et al., 2010; Buitrago et al., 2013). Galaxy mass assembly still continues today. In the local Universe, the Magellanic Clouds are being accreted by the Milky Way galaxy and the Milky Way and Andromeda galaxy are approaching and will eventually collide and merge in approximately four billion years.

In Chapter 2 we derive the SMF of Flagship mock galaxies (the full sample and star-forming and quiescent subsamples). Next, we derive the SMF and ρ_* of the COSMOS2015 full sample, star-forming (including the *high activity* and *intermediate activity* subsamples) and quiescent galaxies, over the redshift range $0.2 \leqslant z < 2.5$. We discuss the evolution of the SMF, and ρ_* over cosmic time and investigate the stellar mass assembly of these galaxies over cosmic time.

Goal of the Thesis

General framework for building the theory of galaxy formation and evolution is already present. However, this theory is still far from complete, and there are many open questions, such as: *How and when did different galaxy populations assemble most of their mass? What are the molecular gas content and star formation rate of galaxies at intermediate redshift? How are galaxy properties affected by feedback mechanisms and environment?* I address some of these questions in the following chapters. The main focus of my research is on developing `Python` code written to compute the SMF of cluster galaxies, study on the stellar mass assembly of galaxies at $0 < z < 2.5$ (Chapter 2) and the molecular gas content and star formation of cluster galaxies at the *cosmic noon* epoch $z \sim 1.5$ (Chapter 3). In Chapter 2 I describe the work on developing and testing a `Python` pipeline for computing the SMF of cluster galaxies for the future *Euclid Mission*. I test the pipeline and derive the SMF of Flagship mock galaxies and COSMOS2015 galaxies over the redshift range $0.2 \leqslant z < 2.5$. In Chapter 3 I present the work on detecting the molecular gas in the cluster center and estimating the molecular gas, star formation and other properties of the CARLA J1103+3449 cluster member galaxies at $z \sim 1.44$ with NOEMA interferometer (Markov et al., 2020a). Moreover, in Appendix A, I present the preliminary results of the CO(2-1) emission in two other CARLA clusters at $z \sim 1.5$ with ALMA. Finally, the Thesis summary, concluding remarks and future prospects are in Chapter 4.

In this Thesis I use the term *dex* for the antilogarithm, e.g. $1\mathrm{dex} = 10^1$.

2

EUCLID PIPELINE FOR DERIVING THE STELLAR MASS FUNCTION

LUMINOSITY AND STELLAR MASS FUNCTION

The luminosity function (LF) and stellar mass function (SMF) represent a distribution of objects (e.g. stars, galaxies, etc.) by their luminosity and stellar mass, respectively. Specifically, LF and SMF represent a comoving number density binned in luminosity or stellar mass, in a chosen redshift range. The LF and SMF are essential statistical tools for studying galaxy evolution and probing galaxy populations. For instance, evolution of the galaxy SMF gives an indication on stellar mass assembly of galaxies. (Arnouts et al., 2007; Ilbert et al., 2013; see also a review of Johnston, 2011).

We can investigate the stellar mass assembly of different subsamples of galaxies by splitting the full galaxy sample according to a galaxy property. For instance, we can split galaxies according to their morphological type (Marzke et al., 1998; Bell et al., 2003; Mortlock et al., 2015), environment (Croton et al., 2005; Bolzonella et al., 2010; McNaught-Roberts et al., 2014; Mortlock et al., 2015; Davidzon et al., 2016), color (Lilly et al., 1995; Lin et al., 1999; Ilbert et al., 2010, 2013; McNaught-Roberts et al., 2014; Mortlock et al., 2015), sSFR (Ilbert et al., 2010; Domínguez Sánchez et al., 2011; Weigel, Schawinski, and Bruderer, 2016; see also Section 2.6) and other galaxy properties, such as halo mass, central/satellite, etc. (Weigel, Schawinski, and Bruderer, 2016).

The most used classification in the literature is the one that divides galaxies in two main classes, *active*, i.e. star-forming and *passive*, i.e. quiescent galaxies. There are different procedures used for splitting the galaxy sample, such as the SED fitting procedure (Arnouts et al., 2007), color-magnitude diagram (Lilly et al., 1995; Bell et al., 2004; Faber et al., 2007) and color-color diagrams (Williams et al., 2009; Ilbert et al., 2010, 2013; Davidzon et al., 2017). Unlike the color-magnitude diagram, the color-color diagram is able to differentiate between the dust-obscured star-forming and quiescent galaxies. Moreover, a direct way to separate the two galaxy populations is to use the specific star formation rate (sSFR), i.e. the SFR to stellar mass ratio (see Section 2.6; Pozzetti et al., 2010; Ilbert et al., 2010; Domínguez Sánchez et al., 2011). According to Ilbert et al., (2013), both of their color-color and the sSFR techniques provide similar results for the UltraVISTA data. However, at higher redshift, the sSFR technique is more restrictive in selecting quiescent galaxies with respect to the color-color method in selecting red galaxies.

By integrating the LF we obtain the luminosity density function, which is related to the SFRD and star formation history of a given galaxy sample (Schiminovich et al., 2005; Arnouts et al., 2007; Faber et al., 2007):

$$\rho_L = \int_0^\infty L\Phi(L)dL \tag{6}$$

Furthermore, integral of the SMF gives the stellar mass density ρ_* (e.g. Wilkins, Trentham, and Hopkins, 2008; Mortlock et al., 2015):

$$\rho_* = \int_0^\infty M\Phi(M)dM \tag{7}$$

which can be used to infer the stellar mass assembly of a certain galaxy population (see Madau and Dickinson, 2014 for a review).

Schechter function

The number of galaxies per unit mass approximately declines as a power law up to a cut-off point, beyond which it declines almost exponentially. One of the best-known models that captures the power law behavior and the exponential decline at the bright i.e. high-mass end of the LF i.e. SMF is the Schechter function (Schechter, 1976):

$$\Phi(L)dL = \Phi^* e^{-L/L^*}\left(\frac{L}{L^*}\right)^{\alpha}\frac{dL}{L^*} \tag{8}$$

where $\Phi(L)$ is the galaxy luminosity number density, L is the luminosity, Φ^* is the normalization factor in units of h^3 Mpc^{-3}, L^* is the characteristic luminosity and α is the faint-end slope of the function. The Schechter function can be expressed as a function of absolute magnitude $\mathcal{M}$:

$$\begin{aligned}\Phi(\mathcal{M})d\mathcal{M} = 0.4\ln(10)\Phi^* 10^{-0.4(\mathcal{M}-\mathcal{M}^*)(\alpha+1)} \\ \exp(-10^{-0.4(\mathcal{M}-\mathcal{M}^*)})d(\mathcal{M})\end{aligned} \tag{9}$$

where $\mathcal{M}^*$ is the characteristic absolute magnitude. Finally, the Schechter function can be used for modeling the stellar mass distribution:

$$\Phi(M)dM = \Phi^* e^{-M/M^*}\left(\frac{M}{M^*}\right)^{\alpha}\frac{dM}{M^*} \tag{10}$$

where $\Phi(M)$ is the stellar mass number density, M is the stellar mass, the normalization function Φ^* and the characteristic stellar mass M^*, determine a change in the slope α of the SMF (the so-called *knee* of the function). The SMF can also be fitted by a double Schechter function (Pozzetti et al., 2010):

$$\Phi(M)dM = e^{-M/M^*}\left[\Phi_1^*\left(\frac{M}{M^*}\right)^{\alpha_1} + \Phi_2^*\left(\frac{M}{M^*}\right)^{\alpha_2}\right]\frac{dM}{M^*} \tag{11}$$

where α_1 and α_2 are the slopes of the Schechter function and Φ_1^* and Φ_2^* are normalization functions.

Schechter models have been widely used and are robust in representing the LF and SMF for many types of survey data. However, shape of the SMF depends on the redshift, galaxy type, color, environment, etc. (Peng et al., 2010; Bolzonella et al., 2010; Ilbert et al., 2010, 2013; Davidzon et al., 2017). For instance, when fitting the SMF with a model, it is possible to assume a power law model at the reionization epoch (at $z \sim 10$ Peng et al., 2010; at $z > 5$ Davidzon et al., 2017). At high redshifts, galaxies start to accumulate at the high-mass end around the specific stellar mass M_*, with a exponential cutoff at $M > M_*$, due to the mass quenching (Peng et al., 2010). Thus, a single Schechter model is a better fit to the SMF over this redshift range (at $3 < z < 5$ Davidzon et al., 2017). Finally, at intermediate and low redshifts, a population of low-mass quiescent galaxies starts to appear, due to the environmental quenching (Peng et al., 2010). Therefore, a double Schechter model is a better fit to the SMF over this redshift range (at $z < 2-3$ Ilbert et al., 2013; Tomczak et al., 2014; Davidzon et al., 2017).

There are other models used for fitting the SMF of specific objects or data. For instance, the log-Gaussian form derived for IRAS data by Saunders et al., (1990), the broken power-law for IRAS by Sanders et al., (2003), and for *Spitzer* observations by Magnelli et al., (2009, 2011), the Gaussian function for early-type galaxies by Bernardi et al., (2003), and many more.

Estimators

Deriving an accurate LF or SMF is a tricky and complex task, due to the observational limits on any survey data. In a flux-limited survey, a galaxy i is observable inside a redshift ($z_{\mathrm{min}} \leqslant z_i < z_{\mathrm{max}}$) and absolute magnitude ($\mathcal{M}_{\mathrm{bright}} \leqslant \mathcal{M}_i < \mathcal{M}_{\mathrm{faint}}$) range (Figure 11; Ilbert et al., 2004).

If we want to observe distant, high-redshift galaxies, we will be able to detect only the brightest objects and a substantial number of faint objects is going to be missed in our sample. The incompleteness of our sample due to observational constraints can lead to an incorrect estimation of the LF and SMF. This is the so-called Malmquist bias (Malmquist, 1920).

When deriving the LF and SMF, we use different statistical estimators in order to correct for observational bias. There are numerous statistical estimators (or methods) developed over the years for deriving the correct LF and SMF (see a review of Johnston, 2011 or a book of Wall and Jenkins, 2003). For instance, the LF and SMF can be derived by binning the data according to their luminosity (or absolute magnitude) and stellar mass, respectively. These are non-parametric methods, which do not require an assumption of a shape of the LF and SMF. In addition, there are parametric methods where we need to model the luminosity and stellar mass distribution. In this section I give short introduction of the most important and the most frequently used statistical estimators, including the 1/Vmax method that is used in this Thesis project. The procedure for deriving the LF and SMF is the same, except for the obvious difference in the function arguments, i.e. the absolute magnitudes and stellar masses, respectively.

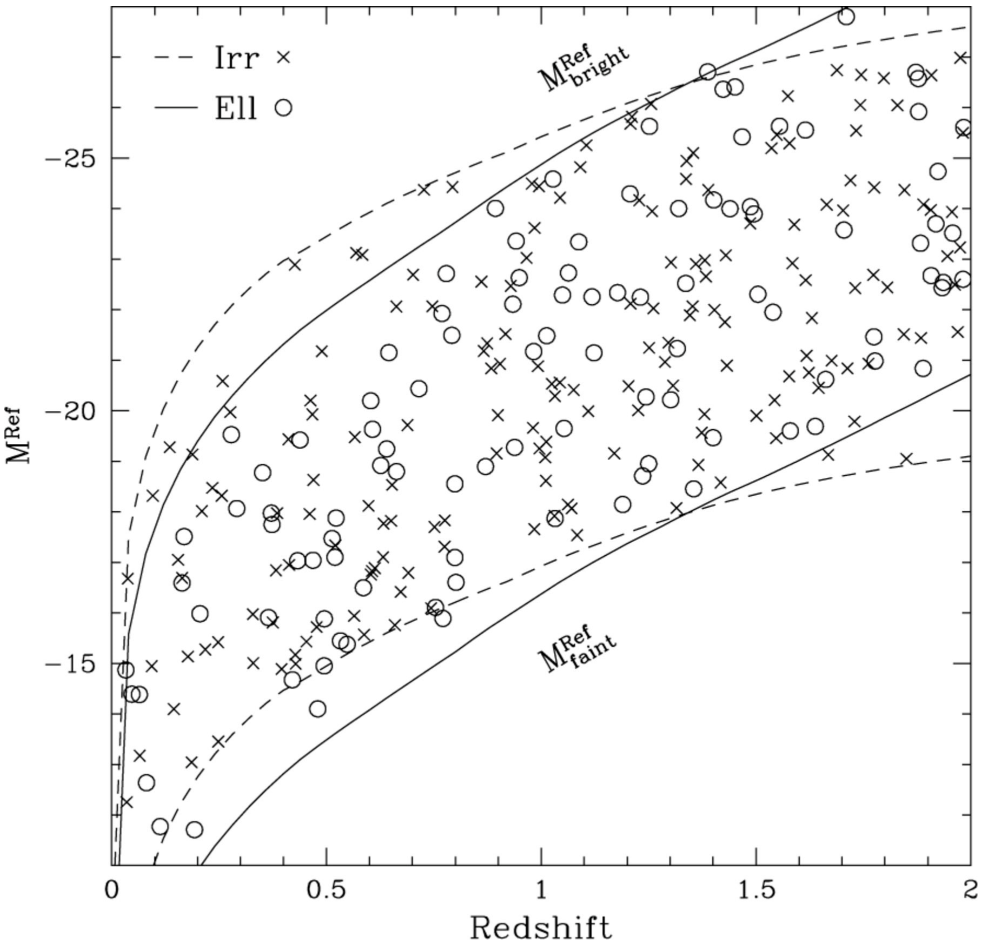

Figure 11: *Example of the observable absolute magnitude-redshift* ($\mathcal{M} - z$) *plane for irregular (crosses) and early-type galaxies (open circles), from the work of Ilbert et al., (2004).*

1/Vmax method

The 1/Vmax method (Schmidt, 1968) is one of the classical non-parametric estimators. It remains one of the most widely used estimators due to its simplicity. The 1/Vmax method implements the correction for the Malmquist bias. According to Schmidt, (1968) and Felten, (1976), the SMF can be derived as a number of objects N_g in each stellar mass bin k, normalized by the maximum comoving volume V_{max}, in which we are still able to observe an object of a given stellar mass M in a given stellar mass and redshift range:

$$\phi_k(M) = \sum_{i=1}^{N_g} \frac{1}{V_{max,i}} \tag{12}$$

If we suppose Poissonian fluctuations and a uniform galaxy distribution, statistical uncertainty can be computed using the following equation (Condon, 1989; Croom et al., 2009):

$$\sigma_i = \left[\sum_{i=1}^{N_g} \frac{1}{V_{max,i}}^2 \right]^{1/2} \tag{13}$$

The first step is to compute the maximum comoving volume in which a galaxy i can still be detected, and it can be computed with the following equation (e.g. Ilbert et al., 2004):

$$V_{max,i} = \int_{\omega} \int_{z_{min,i}}^{z_{max,i}} \frac{d^2V}{d\omega dz} dz d\omega \tag{14}$$

where ω is the effective solid angle of the survey and $z_{min,i}$ and $z_{max,i}$ are the minimum and maximum redshifts in which a galaxy i can still be detected.

The 1/Vmax method is non-parametric method, which means the SMF is discretized in stellar mass bins:

$$\phi(M) = \sum_{k=1}^{N_{bin}} \phi_k W(M_k - M) \tag{15}$$

where ϕ_k is the number density of objects in the k bin, M_k is the mean or median stellar mass of a given bin k and W is the window function defined as:

$$W(M_k - M) = \begin{cases} 1 & \text{if } -dM/2 \leqslant M_k - M < dM/2 \\ 0 & \text{otherwise} \end{cases} \tag{16}$$

ϕ_k is derived for each bin k as:

$$\phi_k dM = \frac{1}{V_{\text{total}}} \sum_{i=1}^{N_g} \frac{V_{\text{total}}}{V_{max,i}} W(M_k - M_i) \tag{17}$$

where V_{total} is the total comoving volume in a given redshift range $z_{\text{min}} \leqslant z < z_{\text{max}}$, M_i is the stellar mass of an individual galaxy i and dM is the bin width. The $V_{\text{total}}/V_{max,i}$ term is a weight applied for each galaxy i in order to take into account the sample (in)completeness and is essential for deriving the correct SMF. The LF is derived in a similar way, by binning the galaxies according to their absolute magnitude bins.

Advantage of the 1/Vmax estimator is that it gives the normalization of the SMF from the assumption of a uniform spatial distribution of the galaxies. However, this is also a downside of the 1/Vmax estimator, since it can create a bias when taking into account survey data with a varying distribution of objects, such as galaxies in clusters and voids (Takeuchi, Yoshikawa, and Ishii, 2000). Nevertheless, the 1/Vmax estimator has been generalized over the years to handle the survey data of different density distribution (Eales, 1993; Qin and Xie, 1997, 1999; Cole, 2011).

C^+ *method*

C^+ is a modification of the non-parametric, maximum likelihood method C^- (Lynden-Bell, 1971) developed by Zucca et al., (1997) and implemented in the Algorithm for Luminosity Function (ALF) tool of Ilbert et al., (2005). Here I give a brief introduction to the C^+ method for estimating the SMF. According to the C^+ method, the contribution of each galaxy i to the total cumulative function is:

$$\psi(M_i) = \frac{1 - \sum_{j=1}^{i-1} \psi(M_j)}{C^+(M_i)} \tag{18}$$

where galaxies are sorted according to their stellar masses, from the lowest ($j = 1$) to the highest stellar mass ($j = i - 1$), and C^+ is the number of galaxies in the stellar mass $M < M_i$ and redshift range $z_{\mathrm{min},i} \leqslant z \leqslant z_{\mathrm{max},i}$. Φ_k is derived as the sum of the contributions $\psi(M_i)$ of all galaxies inside the stellar mass bin k:

$$\Phi_k(M)dM = A \sum_{i=1}^{N_g} \psi(M_i) W(M_k - M_i) \tag{19}$$

where A is the absolute normalization, that can be obtained following the procedure from Efstathiou, Ellis, and Peterson, (1988). The statistical uncertainties of the C^+ method can be estimated by assuming Poissonian errors (Ilbert et al., 2004).

STY method

The STY estimator (Sandage, Tammann, and Yahil, 1979) is a parametric maximum likelihood method. The principle is to maximize the likelihood $\mathcal{L}$ of obtaining a galaxy sample within the observational limits. The probability density of detecting a galaxy i at redshift z_i with the stellar mass M_i is:

$$p(M_i, z_i) = \frac{\Phi(M_i)}{\int_{M_{\mathrm{max}}(z_i)}^{M_{\mathrm{min}}(z_i)} \Phi(M')dM'} \tag{20}$$

where M_{max} and M_{min} are the stellar mass limits at redshift z_i. The total likelihood is then given as the product of probabilities of observing each galaxy i of a stellar mass M_i:

$$\mathcal{L} = \prod_{i=1}^{N_g} p(M_i, z_i) = \prod_{i=1}^{N_g} \frac{\Phi(M_i)}{\int_{M_{\mathrm{max}}(z_i)}^{M_{\mathrm{min}}(z_i)} \Phi(M)dM} \tag{21}$$

Relevant improvements of the STY method include the works of Davis and Huchra, (1982) who implemented the normalization and Efstathiou, Ellis, and Peterson, 1988 who provided the error estimates.

STY estimator assumes a parametric shape of the LF or SMF. In this way, the STY avoids issues on binning galaxies. In general, the Schechter function (Section 2.1.1) is used as the LF (SMF) model due to its robustness to different survey data.

SWML method

The Step-Wise Maximum Likelihood (SWML) method (Efstathiou, Ellis, and Peterson, 1988) is an extension of the STY method. Along with the 1/Vmax, the SWML estimator is one of the most widely used methods. Unlike the STY, the SWML method is a non-parametric method, and stellar masses are sorted into bins (as in Equation 15). The total likelihood is given as:

$$\mathcal{L}(\Phi_k, M_i) = \prod_{i=1}^{N_g} \frac{\sum_{j=1}^{N_{bin}} W(M_j - M_i)\phi_j}{\sum_{j=1}^{N_{bin}} \phi_j H(M_{max(z_i)} - M_k) H(M_k - M_{min(z_i)}) dM} \tag{22}$$

where ϕ_k is a number density of objects in the bin k (Equation 15), W is the window function (Equation 16), M_k is the stellar mass of a given bin k, and $H(x)$ is defined as:

$$H(x) = \begin{cases} 1, & \text{if } x \leqslant -\Delta M/2 \\ (1/2 - x/\Delta M), & \text{if } -\Delta M/2 \leqslant x \leqslant \Delta M/2 \\ 0, & \text{if } x \geqslant \Delta M/2 \end{cases} \tag{23}$$

Finally, the ϕ_k values are derived iteratively, with the following equation:

$$\phi_k \Delta M = \frac{\sum_{i=1}^{N_g} W(M_i - M_k)}{\sum_{i=1}^{N_g} \frac{H(M_{max(z_i)} - M_k) H(M_k - M_{min(z_i)})}{\sum_{j=1}^{N_{bin}} \phi_j dM H(M_{max(z_i)} - M_k) H(M_k - M_{min(z_i)})}} \tag{24}$$

The errors of the ϕ_k can be estimated using the covariance matrix (Efstathiou, Ellis, and Peterson, 1988).

Unlike the 1/Vmax, other three maximum likelihood methods (the C^+, STY and SWML) do not require any assumption on the uniform distribution of galaxies, and therefore, are not subject to the bias associated to it. Furthermore, the normalization is not derived for the three methods, so it has to be calculated independently.

Besides the classical methods, there are a couple of recent methods that try to avoid the pitfalls of the classical methods. For example, the semi-parametric method developed by Schafer, (2007), a Bayesian approach for constraining the LF, which is parametrized by a combination of Gaussian functions by Kelly, Fan, and Vestergaard, (2008), and a Gaussian *copula* function to derive a bivariate LF by Takeuchi, (2010) and many more.

All the estimators have both advantages and drawbacks. Therefore, it is preferable to use more than one estimator in deriving the LF and SMF in order to check for consistency between the different estimators and to estimate the bias. Advantage of using more than one estimator when estimating the LF or SMF lies in the fact that different estimators are often not affected in the same way by the bias. Therefore, if at a certain point the estimated LF or SMF start to diverge, it is an indication of a bias presence in the measurements (Ilbert et al., 2004).

Comparison of different estimators on different observational and simulated data have been performed by Willmer, (1997), Takeuchi, Yoshikawa, and Ishii, (2000), Ilbert et al., (2004) and Weigel, Schawinski, and Bruderer, (2016), with sometimes different conclusions. For example, Willmer, (1997) found that the most robust estimator is the C^{-}, followed by the slightly biased STY estimator. Takeuchi, Yoshikawa, and Ishii, (2000) recommended the Chołoniewski estimator (Choloniewski, 1986) since it is the fastest due to its simplicity and it determines the shape of the LF and normalization. Weigel, Schawinski, and Bruderer, (2016) derived the SMF using the 1/Vmax, SWML and STY estimator, and found that the STY and SWML methods are more successful in retrieving the SMF than the 1/Vmax method.

Ilbert et al., (2004) investigate a specific intrinsic bias that appears at the faint-end slope of the LF for high redshift galaxies and is related to K corrections. They tested the 1/Vmax, C^{+}, SWML and STY estimator, on both simulated (multicolor mock catalogs derived in Arnouts et al., 1999) and observed (HDF-North and HDF-South survey from Arnouts et al., 1999, 2002) data. They found that galaxies of different morphological types (elliptical, spiral and irregular) at a given redshift range and absolute magnitude range can have different absolute magnitude limits within which they are observable. Therefore, all galaxy types would not be observable at the same absolute magnitude and this will lead to an overestimate or underestimate of the global LF, depending on the statistical estimator (Figure 12, top panels).

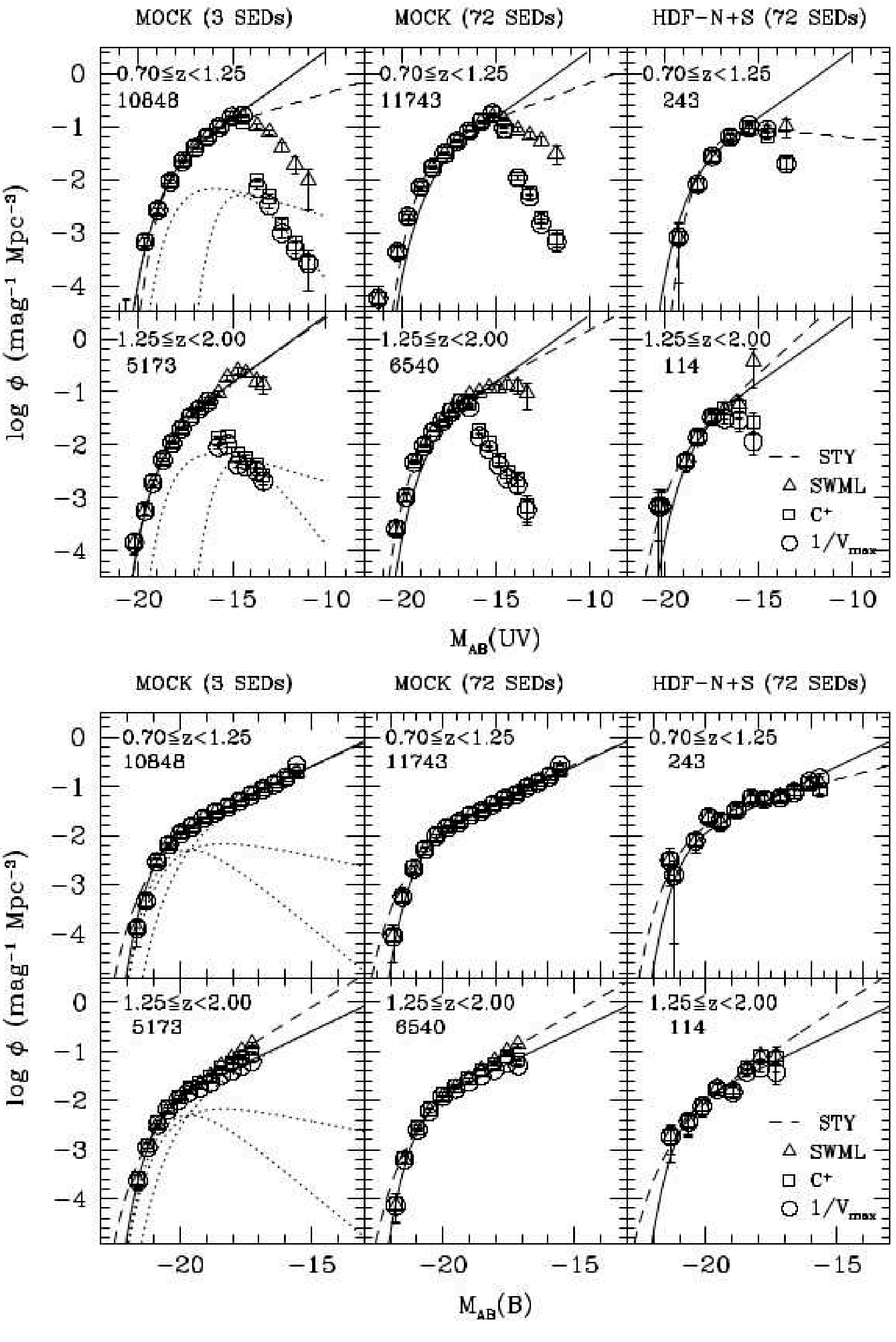

Figure 12: *Examples of the global LF and recovered LF from the work of Ilbert et al., (2004), using the 1/Vmax, (circles),* C$^+$ *(squares), STY (dashed line) and SWML method (triangles) in the UV-FOCA [2000Å] (top panel set) and the B-HST [4500Å] (bottom panel set). LFs are derived on simulations with 3 SED templates (left panels), 72 SED templates (middle panels) and the HDF North and South surveys (right panels). The global LF corresponds to the sum of all the three input LFs (solid line). Three LFs corresponding to three input SEDs for three galaxy types: irregular, spiral and elliptical galaxies, are represented as dotted lines, from the steepest to the shallowest slope, respectively (left panels). Redshift intervals and number of galaxies are given at the top left of each panel.*

Uncertainties

When deriving the SMF there are uncertainties that need to be taken into account, depending on the type of the statistical estimator. In general, there are two categories of uncertainties: statistical (random) and systematic uncertainties (see e.g. Barlow, 1989; Lupton, 1993; Taylor, 1997; Squires, 2001).

Statistical uncertainties

Statistical uncertainties are random scatter of measurements of an otherwise constant quantity. Origins of statistical uncertainties are coming from random small variations of a measured quantity, variations inside the instruments (e.g. telescope), fluctuations of conditions during measurements, in case of observations, and they can be estimated using multiple simulation runs in case of simulated data (see Barlow, 1989; Taylor, 1997; Squires, 2001).

Probability distribution of N measurements is normal (Gaussian) if it is symmetrical and if the distribution mean and maximum values are equal. Normal distribution is important since any distribution of N independent random measurements can be approximated by a normal (Gaussian) distribution if $N \longrightarrow \infty$ (the central limit theorem; e.g. Barlow, 1989).

On the other hand, if nature of the measurement is such that it generates discreet measured values or if measurements are sorted into bins (e.g. when we count galaxies and sort them in stellar mass bins) they follow a Poissonian distribution (e.g. Bevington and Robinson, 2003). Poissonian distribution is equal to the probability of obtaining N events in a given interval (e.g. number of galaxies in a stellar mass bin) if the average value of events is λ (see e.g. Beyer and Company, 1968; Barlow, 1989; Taylor, 1997):

$$P_\lambda(N) = e^{-\lambda}\frac{\lambda^N}{N!} \tag{25}$$

POISSONIAN UNCERTAINTY (i.e. or number counts uncertainty) is characterized by the standard deviation σ_p of the Poissonian distribution and it is equal to the square root of the mean (average) number of the events (λ).

$$\sigma_p = \sqrt{\lambda} \tag{26}$$

In astronomy, the number of measurements is often quite small, measured event can be rare or unpredictable, measurements are often too expensive in terms of telescope time, computer memory, etc. In case there is only one measurement of the number of events N, the mean is simply $\lambda = N$. Then, the Poissonian error is simply given as (see e.g. Taylor, 1997; Bevington and Robinson, 2003):

$$\sigma_p = \sqrt{N} \tag{27}$$

Poissonian error is the dominant source of uncertainty for a low number counts, i.e. when the number of objects per bin approaches zero (Trenti and Stiavelli, 2008). Poissonian uncertainties arise from statistical variations when dealing with a limited number of counts in a limited unit interval (see e.g. Bevington and Robinson, 2003). For instance, when deriving the SMF using a non-parametric estimator such as the 1/Vmax, which is based on counting galaxies and sorting them into stellar mass bins, Poissonian errors need be taken into account for estimating the statistical uncertainty (Section 2.1.2; Ilbert et al., 2004, 2005).

Spatial distribution of galaxies is not uniform and there are different types of cosmic environments such as galaxy clusters, groups and voids. Therefore, the distribution of galaxies does not follow simple Poissonian statistics and there is an additional uncertainty called cosmic variance that needs to be taken into account.

COSMIC VARIANCE arises from large-scale density fluctuations in the universe. There are several ways of calculating cosmic variance (see e.g. Peebles, 1980, Trenti and Stiavelli, 2008; Moster et al., 2011). Moster et al., (2011) derived the cosmic variance with the following equation:

$$\sigma_{cv}(z, M_*) = b(z, M_*)\sigma_{dm}(z) \tag{28}$$

where $b(z, M_*)$ is the galaxy bias, which depends on the redshift and stellar mass, and $\sigma_{dm}(z)$ is the dark matter cosmic variance that can be computed with the following equation:

$$\sigma^2_{dm}(z) = \frac{1}{V^2}\int_0^R \xi_{dm}(|\vec{r_1} - \vec{r_2}|, z)dV_1 dV_2 \tag{29}$$

where V is the sample volume, ξ_{dm} is the dark matter two-point correlation function, Galaxy bias is defined as:

$$b(\bar{z}, M_*) = b_0(\bar{z} + 1)^{b_1} + b_2 \tag{30}$$

where $\langle z \rangle$ is the mean redshift of the sample, and b_0, b_1, b_2 are parameters given in Moster et al., (2011).

Cosmic variance depends on the luminosity, i.e. the stellar mass (Moster et al., 2011; Grogin et al., 2011; Bowler et al., 2014; Ilbert et al., 2013; Davidzon et al., 2017), environment (Hoyle et al., 2005), survey area size and geometry (Newman and Davis, 2002; Somerville et al., 2004; Driver and Robotham, 2010). For small-area fields, cosmic variance has the largest contribution to the total uncertainty, whereas for shallow and large area surveys its contribution is smaller (Somerville et al., 2004; Trenti and Stiavelli, 2008; Moster et al., 2011). Thus, for the *Euclid all-sky* survey, the expected contribution of the cosmic variance to the total uncertainty should be negligible.

UNCERTAINTY IN THE PHOTOMETRIC REDSHIFT ESTIMATE σ_z arises from the photometric uncertainties, i.e. uncertainties in magnitude measurements (Connolly et al., 1995; Subbarao et al., 1996; Bolzonella, Miralles, and Pelló, 2000; Wolf et al., 2004).

The photometric redshift uncertainty σ_z depends on the method used for deriving the photometric redshift z_{ph}, i.e. the SED or empirical fitting (Section 1.3.3; e.g. Loh and Spillar, 1986 and Connolly et al., 1995). For instance, the uncertainty in the SED fitting leads to a redshift probability distribution function (Loh and Spillar, 1986; Arnouts et al., 2002; Ilbert et al., 2006, 2009):

$$P(z) = A \times \exp\left(-\frac{\chi^2(z)}{2}\right) \tag{31}$$

σ_z uncertainty can be estimated by:

$$\chi^2(z) = \chi^2_{min} + \Delta\chi^2 \tag{32}$$

where $\chi^2_{min}(z)$ is the best value obtained at redshift z and $\Delta\chi^2 = 1$ for 1σ error (Bolzonella, Miralles, and Pelló, 2000; Arnouts et al., 2002; Ilbert et al., 2006, 2009). The σ_z uncertainty depends on the spectral coverage of the Balmer and Lyman breaks, spectral resolution (Connolly et al., 1995; Bolzonella, Miralles, and Pelló, 2000; Wolf et al., 2003, 2004; Ilbert et al., 2006, 2009), galaxy magnitude (Connolly et al., 1995; Bolzonella, Miralles, and Pelló, 2000; Wolf et al., 2004; Ilbert et al., 2006, 2009; George et al., 2011; Bezanson et al., 2016) (stellar mass), galaxy color i.e. spectral type (Koo, 1985; Connolly et al., 1995; Wolf, Meisenheimer, and Röser, 2001; Ilbert et al., 2006; Dahlen et al., 2013) and redshift (Ilbert et al., 2006, 2009, 2013; Caputi et al., 2011; Dahlen et al., 2013; Ascaso, Mei, and Benítez, 2015; Bezanson et al., 2016).

UNCERTAINTY DUE TO THE PROBABILITY OF A GALAXY BEING A CLUSTER MEMBER. Castignani and Benoist, (2016) derived an expression for a probability of a galaxy g of a magnitude m'_g, at a spectroscopic redshift $z'_{sp,g}$ to be a member of a group or cluster c at a redshift z'_c:

$$P_{mem}(g \in c|\Pi) = \int \left[1 - \frac{N^{loc}_{bkg,c}(m'_g, z'_c)}{N_{tot,c}(m'_g, z'_c, r_{c,g})}\right] \times \phi(z'_c, z'_{sp,g}) dP(z'_c, z'_{s,g}, m'_g|\Pi) \tag{33}$$

where Π consists of all the information on assigning a galaxy to a cluster or group, $N^{loc}_{bkg,c}$ is the local background density, $N_{tot,c}$ is the local number density, $\phi(z'_c, z'_{sp,g})$ is a general positive function $\leqslant 1$ and $r_{c,g}$ is the distance between the galaxy and cluster center. It can be seen that the membership probability is equal to the number excess β and the probabilities of galaxy and cluster being at the same redshift z_i:

$$P_{mem}(g \in c|\Pi) \simeq (1-\beta) \sum_i P_g(z_i) P_c(z_i) \tag{34}$$

In order to take into account the membership probability P_{mem} when deriving the SMF of cluster galaxies, we can weight each galaxy by P_{mem} (as suggested by George et al., 2011 and Castignani and Benoist, 2016). Accuracy in assigning a galaxy membership to a certain cluster or a group depends mostly on the accuracy in determining galaxy position and distance compared to the cluster center, i.e. determining galaxy and cluster redshifts (Brunner and Lubin, 2000; George et al., 2011; Castignani and Benoist, 2016). Besides, uncertainties in photometric colors (Rozo et al., 2015), galaxy magnitude (Castignani and Benoist, 2016), distance from the halo center (George et al., 2011; Castignani and Benoist, 2016) and halo properties (Castignani and Benoist, 2016) also affect the galaxy membership uncertainties.

Finally, the total statistical uncertainty in deriving the LF and SMF of cluster galaxies can be calculated by combining all the above mentioned uncertainties:

$$\sigma_{\mathrm{tot}} = \sqrt{\sigma_{\mathrm{p}}^2 + \sigma_{\mathrm{cv}}^2 + \sigma_{\mathrm{z}}^2 + \sigma_{\mathrm{cm}}^2} \tag{35}$$

where σ_{p} is the Poissonian uncertainty, σ_{cv} is the cosmic variance, σ_{z} is the photometric redshift uncertainty and σ_{cm} is the cluster membership uncertainty.

Systematic uncertainties

Systematic uncertainties (i.e. biases or offsets) appear as consistent divergence from the true value and are therefore, harder to detect. Sources of systematic uncertainties come from unknown factors such as defects and inaccuracies in measurements, instruments (e.g. incorrect calibration), or observational methods (see e.g. Barlow, 1989; Taylor, 1997; Squires, 2001; Bevington and Robinson, 2003). There are many systematic uncertainties involved in the SMF estimate. Main systematic uncertainties that need to be taken into account are:

z_{ph} SYSTEMATIC UNCERTAINTIES. Systematic errors that contribute to the z_{ph} estimate are zero point offset, i.e. uncertainties in calibration of the photometric *zero-points* (Wolf et al., 2004; Ilbert et al., 2006, 2009; Dahlen et al., 2013; Grazian et al., 2015), color offset, i.e. a mismatch in fitting the observations with the SED templates, due to an incomplete set of templates, an incorrect dust extinction law, etc. (Wolf et al., 2004; Ilbert et al., 2006, 2009; Dahlen et al., 2013; Grazian et al., 2015), color uncertainties, due to an atmospheric emission or contamination from a close neighbor (Loh and Spillar, 1986).

EDDINGTON BIAS The Eddington bias (Eddington, 1913) is a systematic uncertainty that causes an asymmetric scatter in galaxy stellar masses, when deriving the SMF. Galaxies scatter to different stellar mass bin, due to stellar mass uncertainties. At the high-mass end of the SMF, where the galaxy number density exponentially decreases, galaxies scatter more to higher bins, and we overestimate the number density of the most massive galaxies (Caputi et al., 2011).

In order to take into account the Eddington bias, we convolve the SMF model Φ (e.g. a Schechter function), with the stellar mass uncertainties σ_m:

$$\Phi_{conv}(z, M) = \int \Phi(m) * \sigma_m(z, M) dm \tag{36}$$

The Eddington bias has the strongest effect at high-z and at high-mass end of the SMF where the number of galaxies is low and stellar mass uncertainties are higher (Caputi et al., 2011; Ilbert et al., 2013; Grazian et al., 2015; Davidzon et al., 2017), but also at the low-mass end of the SMF, where galaxies are fainter and photometric uncertainties are larger (Grazian et al., 2015).

The goal of the project

While working on this Thesis project, I was a member of an international collaboration, including S. Mei, M. Bolzonella, E. Zucca, O. Ilbert, I. Davidzon, G. Zamorani, L.Tresse, L. Pozzetti, G. Girelli and myself. General idea behind this project is to develop a pipeline that will produce the LF and SMF of different galaxy samples (passive, star-forming, Hα emitters, cluster galaxies etc.), and fit the LF and SMF using different models (e.g. a single Schechter model (Schechter, 1976), a double Schechter model (Baldry, Glazebrook, and Driver, 2008; Pozzetti et al., 2010), etc.), for the upcoming *Euclid Space Mission* (Section 2.2.1; Laureijs et al., 2011) and possibly to generalize the pipeline for other survey data. Basic information on the input/output of the pipeline is contained in the *Euclid* internal documents and summarized in Figure 13. Basic necessary inputs are the object type, redshifts, statistical weights, absolute magnitudes, stellar masses, cluster membership (for the SMF of cluster galaxies) and the outputs are the luminosity and stellar mass function.

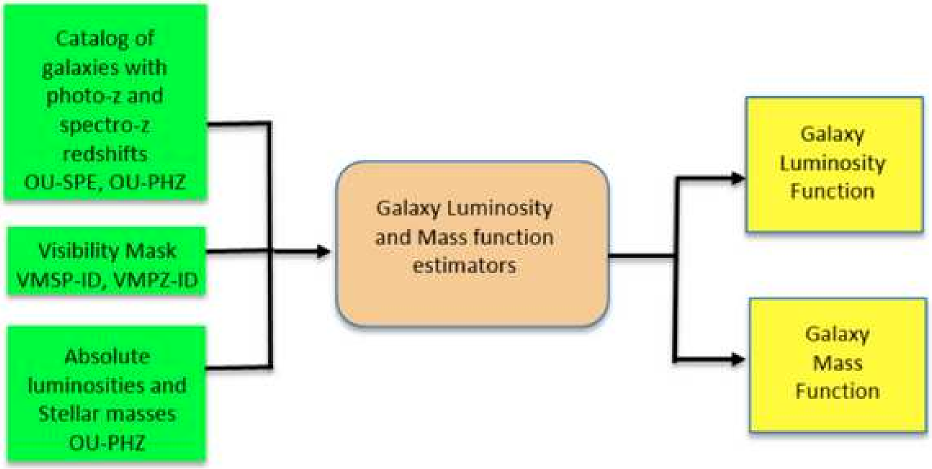

Figure 13: *The input (green) and output (yellow) information of the galaxy luminosity and stellar mass function code.*

The goal of this Thesis project is to develop a pipeline that will derive the SMF of cluster galaxies and fit the SMF with a chosen model, for the upcoming *Euclid Mission*. The pipeline algorithm outline is to:

- Derive the stellar mass function using standard statistical estimators (Section 2.1.2). For instance, the 1/Vmax estimator is one of the simplest methods. The 1/Vmax gives number of galaxies per stellar mass bin, normalized by the bin width and the maximum comoving volume (Section 2.1.2.1; Schmidt, 1968). Next, the Step-Wise Maximum Likelihood (SWML) (Section 2.1.2.4; Efstathiou, Ellis, and Peterson, 1988) and STY estimator (Section 2.1.2.3; Sandage, Tammann, and Yahil, 1979, etc.) are maximum likelihood methods often used in combination with the 1/Vmax method (Ilbert et al., 2004).

- Take into account the statistical uncertainties in the SMF estimate (Section 2.1.3.1). The Poissonian errors are fundamental statistical uncertainties that should be derived when deriving the SMF using the 1/Vmax method. The Poissonian errors are given by the square root of the number of objects per stellar mass bin normalized by the bin width and the maximum comoving volume (Equation 27; see e.g. Bevington and Robinson, 2003). Next, the cosmic variance can be derived following the work of Moster et al., (2011) (Equation 28). Finally, the uncertainty of assigning a galaxy membership to a cluster is essential when deriving the SMF of cluster galaxies (Castignani and Benoist, 2016).

- Fit the SMF using a chosen model: a single Schechter function (Schechter, 1976), or a double Schechter function (Pozzetti et al., 2010), deconvolved by the stellar mass uncertainties in order to take into account the Eddington bias (Ilbert et al., 2013) (Section 2.3.2.1). In order to obtain the best-fit parameters of the Schechter function, we use the maximum likelihood method and the `scipy` minimization function (Section 2.3.2) and the Bayesian analysis with the Markov Chain Monte Carlo (MCMC) (Section 2.4).

.

We test the pipeline using the *Euclid* Flagship mock galaxy catalog (Section 2.2.2; Carretero et al., 2017) and COSMOS2015 photometric redshift catalog (Section 2.2.3; Laigle et al., 2016; Davidzon et al., 2017). This chapter is organized as follows. First the *Euclid Space Mission*, the Flagship mock galaxy catalog and COSMOS2015 photometric catalog are briefly presented in Section 2.2. The methodology for deriving the SMF and fitting the SMF using the *Euclid* pipeline and the MCMC Python code are given in Section 3.3.5 and Section 2.4. The results of the derived SMF and SMF fit of the Flagship mock galaxies and COSMOS2015 galaxies are presented in Section 2.5. The discussion on the evolution of the SMF, best-fit Schechter parameters and stellar mass density are in Section 2.6. Finally, a short summary and following work of this chapter is in Section 2.7.

DATA

Euclid Space Mission

European Space Agency (ESA) *Euclid Space Mission* (Laureijs et al., 2011; Racca et al., 2016) is the next ESA cosmology mission after *Planck* (Adam et al., 2015). It is to be launched in 2022, with an expected duration of six years. During this time it will survey 15000 $\deg^2$ of the extragalactic sky to map the distribution of billions of galaxies in the optical, and provide photometry for these galaxies and spectra for millions of galaxies in the near infrared (NIR) range. The *Euclid* deep survey with two 20 $\deg^2$ deep fields is two magnitudes deeper and will observe thousands of galaxy and quasar candidate objects at high redshifts ($z > 6$). The goals of the *Euclid Mission* are to:

- Map the cosmic history of structure formation and evolution of large-scale structures covering the last 10 billion years. *Euclid* will test the General Relativity theory by estimating the structure growth over cosmic times.

- Measure the baryonic and dark matter distribution in the Universe with high precision, by using cosmological probes such as weak lensing and galaxy clustering.

- Estimate the accelerated expansion of the Universe at different redshifts using galaxy clustering. This will shed light on the nature and characteristics of dark energy.

- Produce a legacy dataset with an unmatched spatial resolution (0.2 arcsec) and depth, covering a large area of the celestial sky. It will provide morphologies, redshifts, masses, SFR, etc. for nearby and distant galaxies out to $z \sim 2$.

The *Euclid* satellite consists of a three-mirror Korsch type telescope with a diameter of $1.2\ \mathrm{m}$ and a focal length of $F = 24.5\ \mathrm{m}$. Observations will be carried out with two different instruments: the Visible Imager (VIS) and the Near-Infrared Spectrometer Photometer (NISP). The VIS instrument is an optical camera made of 36 charge-coupled devices (CCDs) with a field of view of $0.57\ \deg^2$, in a broad $r + i + z$ band, in the optical range ($550\ \mathrm{nm} - 900\ \mathrm{nm}$). VIS will be used for imaging 1.5×10^9 galaxies down to a magnitude of 24.5 with a SNR > 10 at $0 < z < 2.3$ (Figure 15, top panel; Cropper et al., 2016). It will image the sky with quality approaching that of the *Hubble* Ultra Deep Field (UDF) image (Figure 14). Furthermore, the VIS will derive accurate galaxy shapes and estimate gravitational lensing effects from the distortion of galaxy shapes, that will be used for mapping the dark matter distribution in the Universe and evolution of the dark matter distribution over cosmological times.

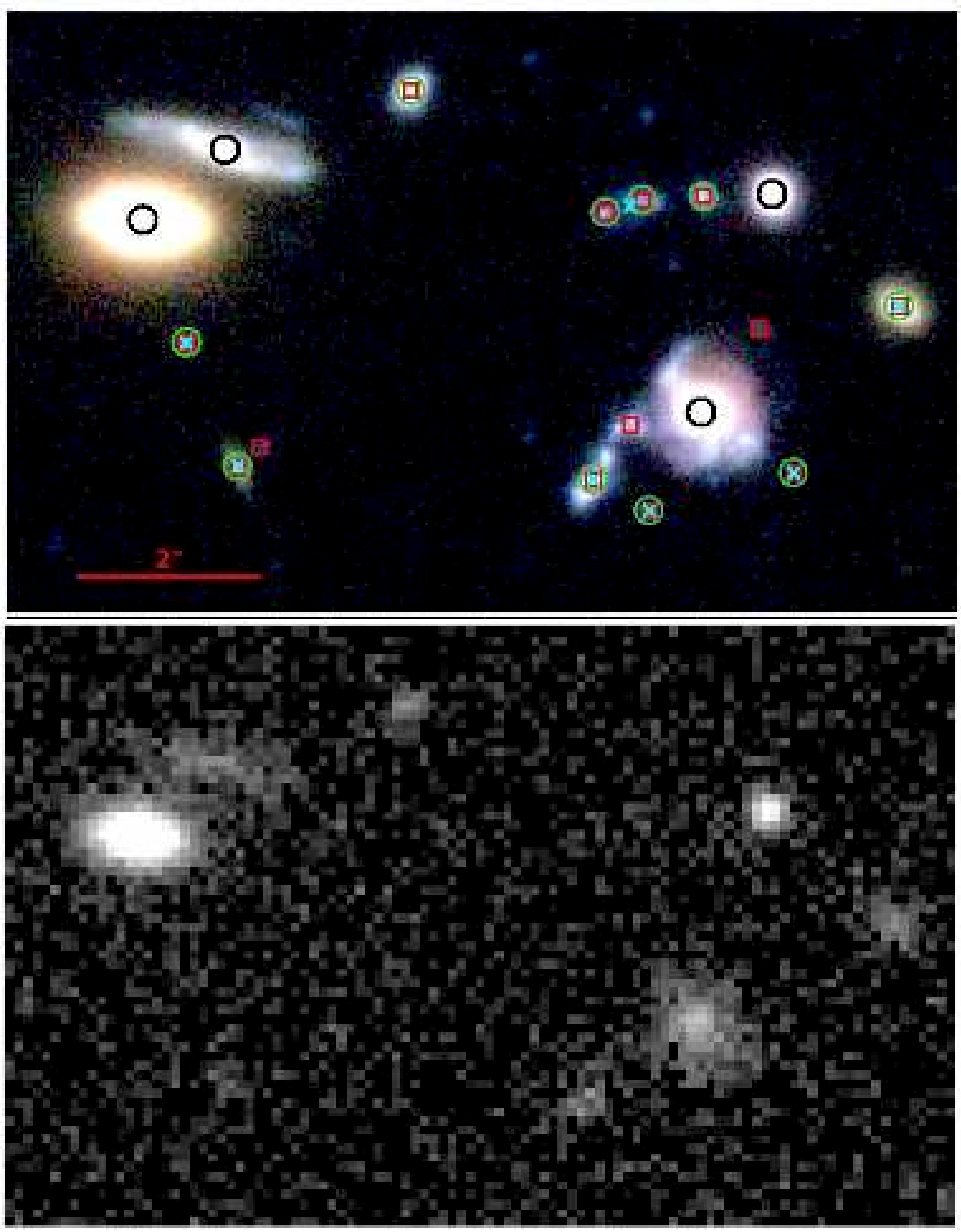

Figure 14: *Top: HST UDF color image with galaxies brighter than 24.5 magnitude (black circles), and fainter neighboring galaxies (cyan cross, green circle or red square). Bottom: Expected Euclid VIS image. Figures are from the work of Euclid Collaboration et al., (2019).*

The NISP instrument consists of detectors covering a 0.53 deg^2 field of view, in the NIR range (900 $\mathrm{nm}-2000$ nm) (Maciaszek et al., 2016). The NISP will provide photometric observations in the Y (900 $\mathrm{nm}-1192$ nm), J (1192 $\mathrm{nm}-1544$ nm) and H (1544 $\mathrm{nm}-2000$ nm) broad bands that will be used for estimating the photometric redshifts and approximate distances for billions of galaxies observed with the VIS instrument, down to a magnitude of 24 with a SNR $> 5\sigma$. Moreover, the NISP will provide low resolution spectra ($R = 380$ for a 0.5 arcsec source) with three *red* (1250 $\mathrm{nm}-1850$ nm) and one *blue* grism (920 $\mathrm{nm}-1850$ nm) that will be used for deriving the precise spectroscopic redshifts and galaxy positions for millions of galaxies in the same NIR range and at $0.8 < z < 1.9$ (Figure 15, middle panel). The NISP spectroscopic data will mainly be utilized for estimating galaxy clustering and large scale structures and the evolution of these structures over cosmic time due to the effects of gravity, the dark matter and dark energy.

These instruments are developed by the *Euclid* Consortium (EC), an international team of more than 1000 scientists from 14 European countries, Canada and United States, with the goal to produce big and complex datasets, and to perform data reduction, imaging, and data analysis. In order to prepare for the scientific exploitation of the *Euclid* observations, the EC is developing the software needed for the data processing and science analysis. The specific role of the science working group of LERMA (Laboratoire d'Etudes du Rayonnement et de la Matière en Astrophysique et Atmosphères) and an international collaboration gathered around this *Euclid* project is to develop a pipeline that will produce the SMF of cluster galaxies. For a full overview on the *Euclid Mission*, see the *Euclid Red Book* (Laureijs et al., 2011).

Euclid Flagship mock galaxy catalog

The key role in the preparation for the upcoming *Euclid* data is development of simulated observations that mimic the expected complexity and size of the real future *Euclid* survey data. The EC developed the largest simulated galaxy catalog up to date, the *Euclid* Flagship mock galaxy catalog (Carretero et al., 2017), based on a N-body cosmological simulation (Potter, Stadel, and Teyssier, 2017). The simulation is based on the ΛCDM cosmological model, with the following cosmological parameters: the total matter density $\Omega_m = 0.319$, baryonic mass density $\Omega_b = 0.049$, dark matter density $\Omega_\Lambda = 0.681$, root-mean-square matter fluctuation $\sigma_8 = 0.83$, scalar spectral index $n_s = 0.96$ and Hubble constant $h = 0.67$.

The dark matter catalog consists of more than 2×10^{12} dark matter particles (with a possibility to reach 8×10^{12}), with a mass of $m_p \sim 10^9 M_\odot h^{-1}$, evolving in the redshift range $0 \leqslant z < 49$ and forming the cosmic web (Potter, Stadel, and Teyssier, 2017). Moreover, the dark matter halo catalog contains 4×10^{10} halos covering the full sky in the redshift range $0 \leqslant z < 2.4$, inside a box of 3.78 Gpc h^{-1}.

Carretero et al., (2017) use the dark matter halo population as input in order to generate a mock galaxy catalog with 2.6×10^9 galaxies over 1/8th of the sky, covering an area of 5000 deg² in the redshift range $0 \leqslant z < 2.3$ (Figure 15). This catalog is constructed using the halo occupation distribution

(HOD) and halo abundance matching (HAM) in order to relate the dark matter and baryonic matter particles. It is the largest mock galaxy catalog today and it successfully reproduces galaxies of different morphologies, colors and luminosities. Furthermore, it reproduces global galaxy properties observed in galaxy surveys, such as galaxy clustering, weak lensing, etc.

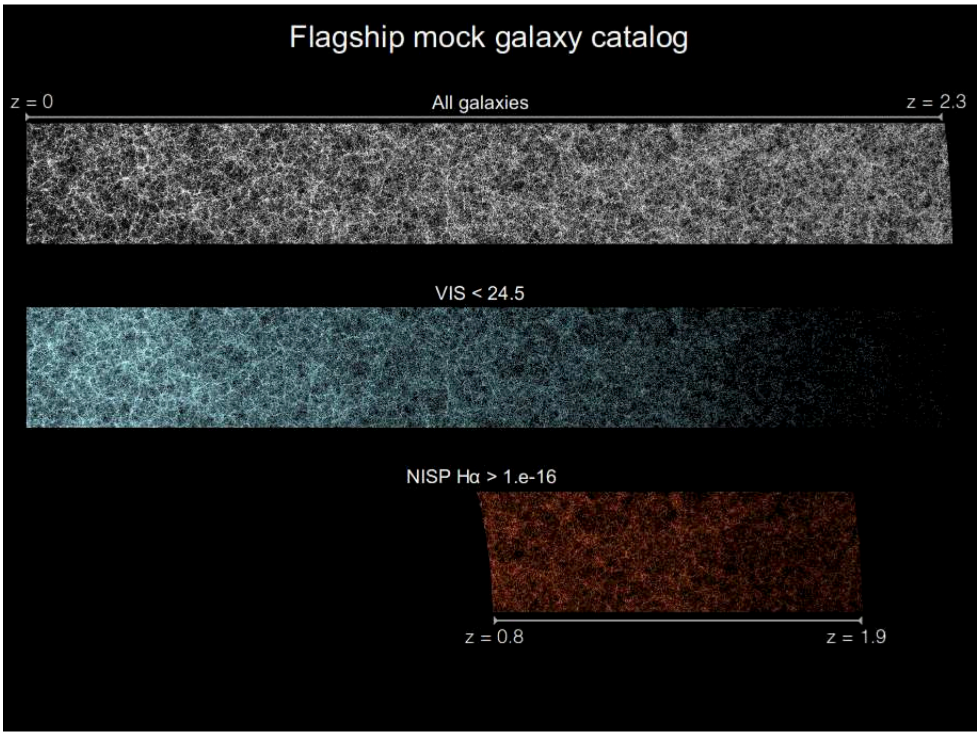

Figure 15: *Euclid Flagship mock galaxy catalog: Slice of the light-cone simulation of mock galaxies in the Euclid survey. Top: The entire mock galaxy sample of galaxies. Middle and bottom: The sub-samples expected to be observed with the VIS and NISP-Hα channels, respectively. Figure is from the work of Carretero et al., (2017).*

COSMOS2015 photometric redshift catalog

The COSMOS2015 (Laigle et al., 2016; Davidzon et al., 2017) is a catalog of photometric redshifts and stellar masses in the redshift range $0 \leqslant z < 6$ and magnitude limits $K_s = 24.7$ and $[3.6\mu m] = 25.5$ in a 3 arcsec aperture, inside the COSMOS field (Scoville et al., 2007), covering a total area of 2 deg^2 (dark blue contours in Figure 16 top panel). The catalog contains $\sim 6 \times 10^5$ objects within 1.5 deg^2 reaching 3σ magnitude limit of $Mag\_K_s = 24.0$ in the *Deep* area (orange contours in Figure 16, top panel). Moreover, it contains $\sim 1.5 \times 10^5$ objects in the *Ultra-Deep* area of 0.62 deg^2 reaching a 3σ magnitude limits of $Mag\_K_s = 24.7$ (light green contours in Figure 16, top panel).

The catalog consists of the UltraVISTA-DR2 survey (McCracken et al., 2012) in the near infrared (NIR) (Y, J, H, K_s bands), the *Spitzer* Large Area Survey with Hyper-Suprime-Cam (SPLASH, Capak et al., 2012) in the medium IR (MIR) (4 channels at 3.6μm, 4.5μm, 5.8μm and 8.0 μm), and the z^{++} band of the Subaru/Hyper-Suprime-Cam (HSC) survey (Miyazaki et al., 2012). Moreover, in the NIR, the UltraVISTA bands are supplemented by the H

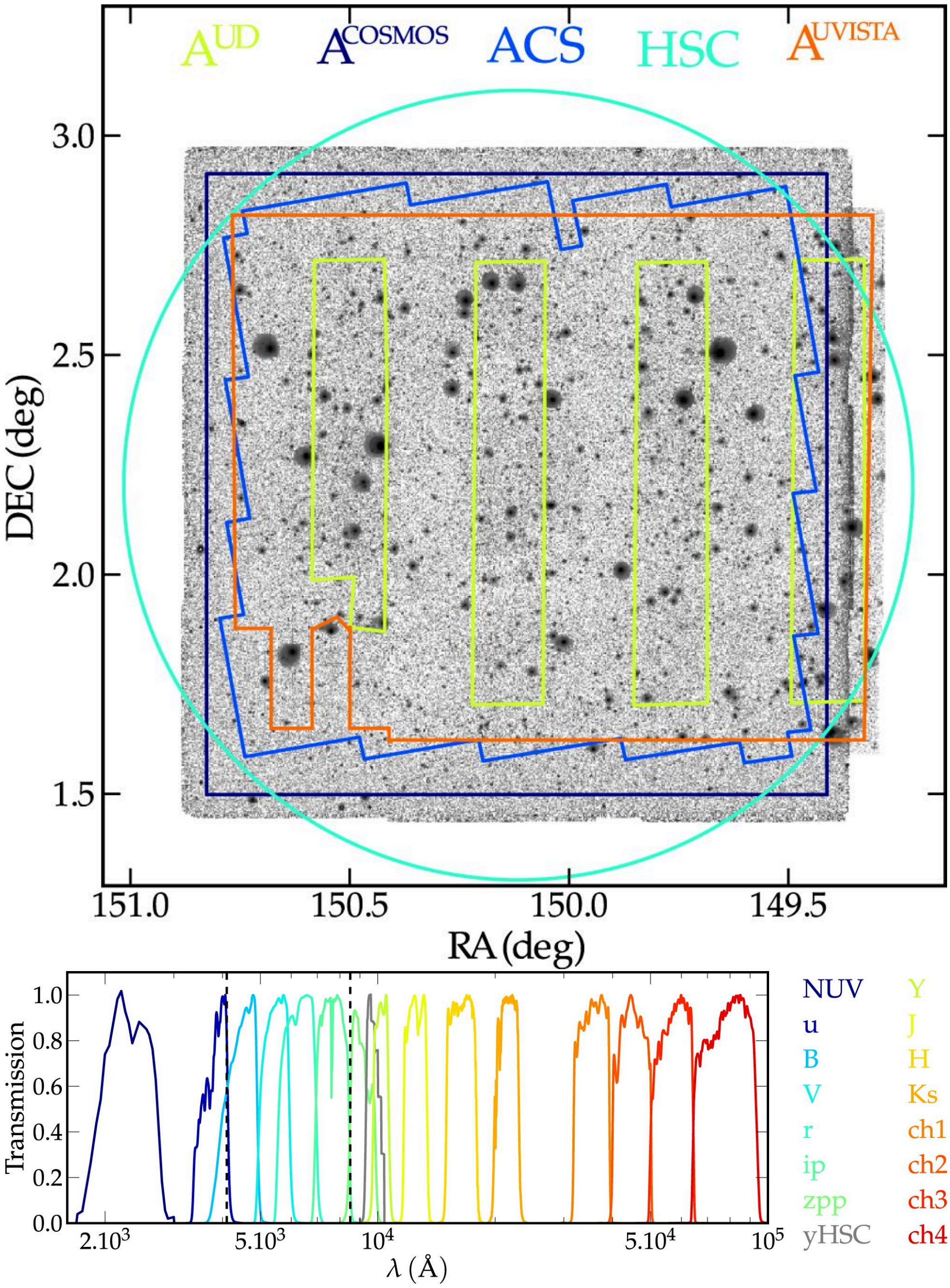

Figure 16: *Top: The COSMOS field with the observations of the COSMOS2015 catalog. The background image is from the* YKHK$_s$z^{++} *bands. The areas covered by observations are: 2* deg² *COSMOS field (dark blue), the UltraVISTA-DR2 (orange), and the UltraVISTA-DR2 deep stripes (light green), HST/ACS data (blue) and the Subaru/HSC. Bottom: Transmission curves of the photometric bands. Figures are from the work of Laigle et al., (2016).*

and K$_s$ bands of the Canada-France-Hawaii Telescope (CFHT)/WIRCAM (McCracken et al., 2010) and Y band observations of the Subaru/Hyper-Suprime-Cam (HSC) (Miyazaki et al., 2012). Furthermore, the catalog includes the near-UV and optical data (GALEX, Zamojski et al., 2007), u* band from the CFHT/MegaCam and the COSMOS-20 survey (Taniguchi et al., 2007; Taniguchi et al., 2015), while X-ray bands were excluded due to the possible contamination from the AGN. Total number of bands used for the catalog is 30. The areas of the optical and NIR observations from the surveys and transmission curves are shown in Figure 16. More details on the COSMOS2015 catalog can be found in Laigle et al., (2016) and Davidzon et al., (2017).

Davidzon et al., (2017) estimate the SMF and stellar mass density of galaxies in the COSMOS field, covering the last ~ 13 Gyrs of galaxy evolution ($0 \leqslant z < 6$). They use the combined UltraVISTA, SPLASH and Subaru/Hyper-Suprime-Cam survey data (orange and light green contours less the area outside of dark blue square of the COSMOS field in Figure 16, respectively), in the $0 \leqslant z < 6$ redshift and $15.0 < \text{Mag\_K}_s < 24.7$ magnitude range. They split their galaxy sample into active and passive subsamples, using the color-color selection method (Arnouts et al., 2013). They produce the SMF of galaxies using the 1/Vmax, STY and SWML methods with the ALF code (Ilbert et al., 2005), and they fit the SMF with different Schechter functions deconvolved by the stellar mass uncertainties. They present an evolution of the SMF of the full sample of galaxies in the $0.2 \leqslant z < 5.5$ range, and active and passive galaxies in the $0.2 \leqslant z < 4.0$ range (Figure 17, top, middle and bottom panels, respectively).

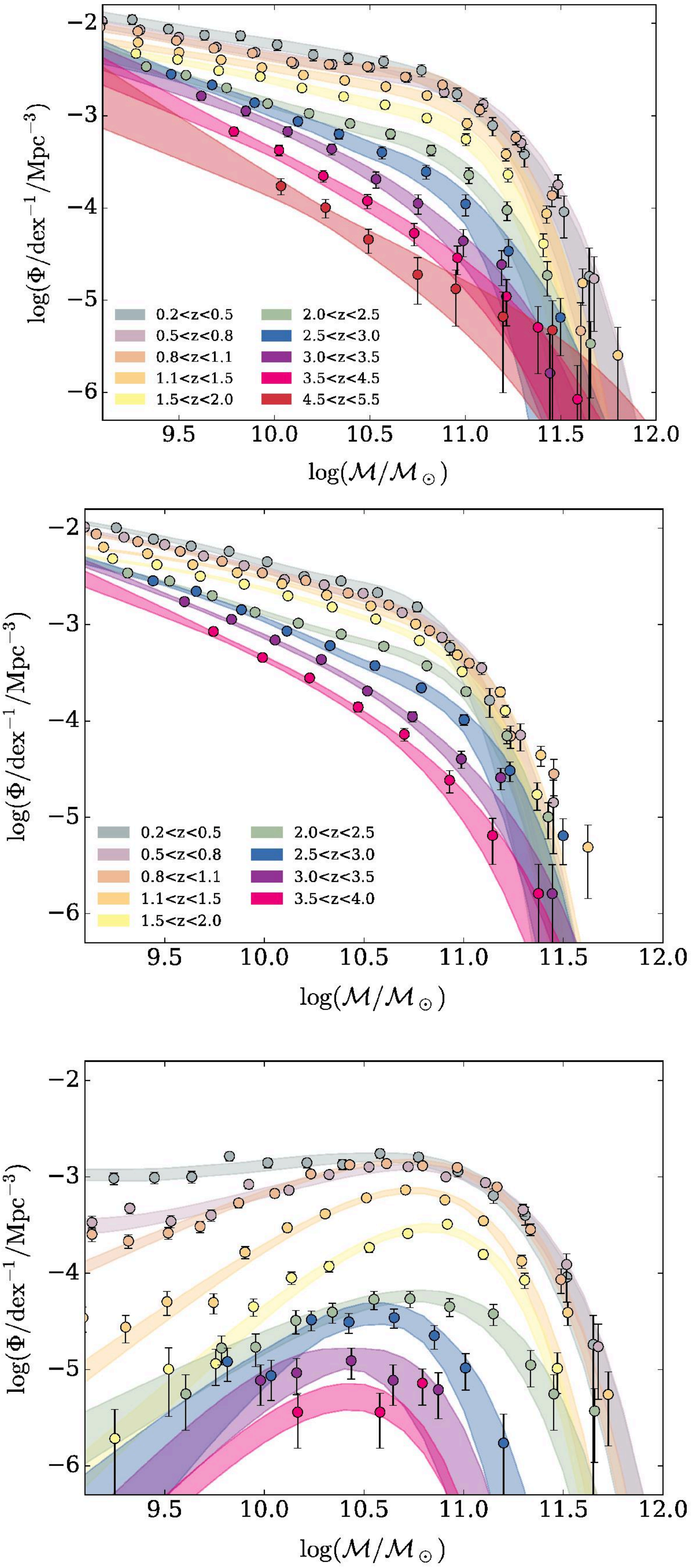

Figure 17: *Evolution of the SMF of the full sample of galaxies in the* $0.2 \leqslant z < 5.5$ *range (top), and active (middle) and passive (bottom) galaxies in the* $0.2 \leqslant z < 4$ *range. Filled circles are 1/Vmax estimates and shaded areas are the best Schechter fits with* 1σ *dispersion. Figures are from the work of Davidzon et al., (2017).*

EUCLID PIPELINE

Stellar mass function with 1/Vmax method

We develop and test the `Python` pipeline using the *Euclid* Flagship mock galaxy catalog (Section 2.2.2; Carretero et al., 2017) and COSMOS2015 photometric redshift catalog (Section 2.2.3; Laigle et al., 2016; Davidzon et al., 2017). The work on obtaining the SMF of galaxies, using a subsample of galaxies inside a 1 deg^2 area from the Flagship simulation (Section 2.2.2; Carretero et al., 2017) was started by the LERMA IT team and completed as part of this PhD Thesis. In order to improve the code efficiency, we replace some functions by simpler or already existing functions from the standard Python packages. For instance, we compute the minimum and maximum of stellar mass in a more efficient way, by using simple functions (min $(\log(M_*))$ and (max $(\log(M_*))$ and avoiding loops over each galaxy.

In order to adapt the existing *Euclid* pipeline to be able to read the different data format and derive the SMF and SMF fit of the COSMOS2015 galaxies, I implement some modifications in the main program and in some modules and I develop additional modules, functions and `class` objects. Furthermore, there are several differences in working with the Flagship mock and COSMOS2015 catalogs: galaxy parameter names in the data fits files, the selection criteria for galaxies, the binning of galaxies, computing the maximum comoving volume, the weights, etc. First, when using the COSMOS2015 catalog, we read the necessary galaxy parameters (photometric redshift, stellar mass, K_s magnitude, object type, etc.) from the COSMOS2015 data file according to the same selection criteria as in Davidzon et al., (2017), in order to select the same sample of galaxies and reproduce their work: $15.0 < \text{Mag\_K}_s < 24.7$, type $\geqslant 0$, $0.2 < z < 2.5$ and deep $= 1$ (in order to use the COSMOS2015 deep field data). Since there are galaxies with negative stellar mass values $\log(M_*) = -99$, I set an additional condition: $\log(M_*) > 0$, in order to exclude them from the SMF. Number of these galaxies is very low ($\sim 0.01\%$) and it does not affect the results.

Stellar mass bins

In order to derive the SMF using the 1/Vmax method, we sort galaxies into stellar mass bins. First, we need to define the bin structure: the number of bins, the bin width, and their limits.

First, we replace the complicated system of modules, classes and functions that were used for defining the stellar mass bin structure and counting the galaxies with a simple `numpy` function. Next, for the Flagship data, we set the bin number and bin width as constant for all the galaxy samples and redshift bins (Figure 18).

For the COSMOS2015 data, as a first step, we simply use the values from Davidzon et al., (2017), in order to reproduce their work. In the final pipeline version, we set the bin_width as optional parameter set by the user, and

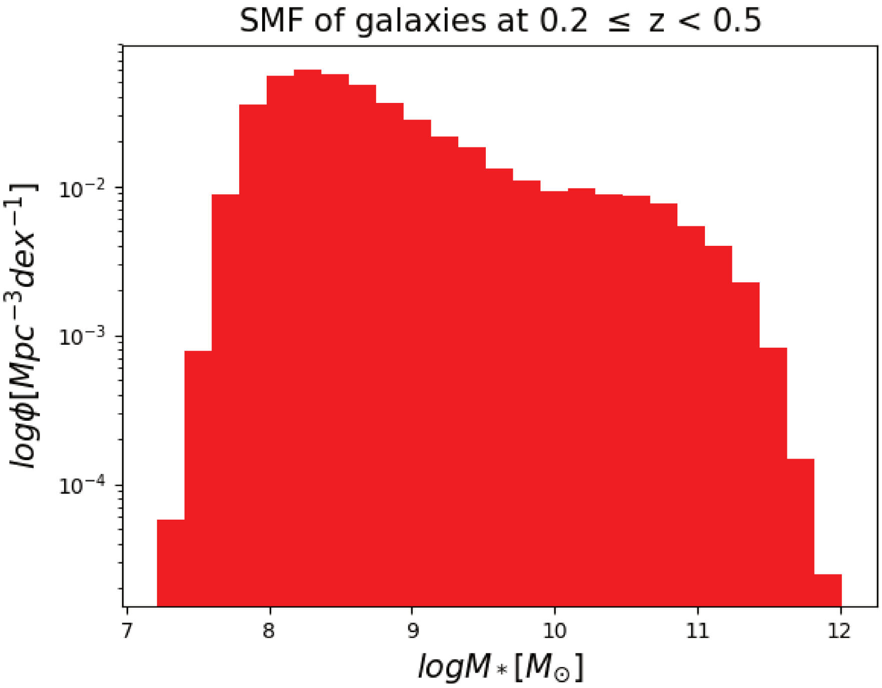

Figure 18: *An example of a SMF of Flagship mock galaxies (Section 2.2.2; Carretero et al., 2017) at* $0.2 \leqslant z < 0.5$.

the $\log(M_*^{\min})$ and $\log(M_*^{\max})$ parameters are computed with the following equations:

$$\log(M_*^{\min}) = \max\left(\log(M_*^{\text{complete}}), \min(\log(M_*))\right) \tag{37}$$

$$\log(M_*^{\max}) = \max\left(\log(M_*)\right) \tag{38}$$

where $\log(M_*^{\text{complete}})$ is the stellar mass completeness limit. The number of stellar mass bins is:

$$n_{\text{bin}} = \frac{\log(M_*^{\max}) - \log(M_*^{\min})}{\text{bin\_width}} \tag{39}$$

We set a constant number of bins $n_{\text{bin}}^{\max}$ for all the galaxy samples and redshift bins. In case the maximum number of bins is larger than the actual number of bins $n_{\text{bin}}^{\max} > n_{\text{bin}}$, in a certain redshift bin, I add extra bins at the low-mass end of the SMF. Galaxies inside these extra bins are not used for fitting the SMF with the Schechter model, since their masses are lower than the stellar mass completeness limit $\log(M_*^{\text{complete}})$, and they have no effect on the end result of the SMF fit. In case $n_{\text{bin}}^{\max} < n_{\text{bin}}$, the pipeline raises a value error.

Finally, for the COSMOS2015 data, we compute the median stellar mass $\log(M_*^{\text{median}})$ and use it instead of the mean stellar mass $\log(M_*^{\text{mean}})$ for each stellar mass bin, in order to reproduce the work of Davidzon et al., (2017).

Stellar mass completeness limit

When deriving the SMF using the 1/Vmax estimator, the 1/Vmax underestimates the low-mass end of the SMF below a certain stellar mass, called the stellar mass completeness limit $\log(M_*^{\text{complete}})$ (Pozzetti et al., 2010). Estimating this parameter is important in order to have an idea on the range of the stellar masses within which we can trust the 1/Vmax method when deriving the SMF.

As a starting point, we simply take the stellar mass completeness limits from Davidzon et al., (2017). Next, we follow the works of Pozzetti et al., (2010), Ilbert et al., (2013), and Davidzon et al., (2017) in order to compute the limiting stellar mass $\log(M_*^{\text{lim}})$ and finally stellar mass completeness limit $\log(M_*^{\text{complete}})$.

The limiting stellar mass $\log(M_*^{\text{lim}})$ is a stellar mass of a galaxy with a magnitude equal to a limiting magnitude of a given survey at the redshift z. We compute the limiting stellar mass using the following equation:

$$\log(M_*^{\text{lim}}) = \log(M_*) + 0.4(\text{mag\_Ks} - \text{mag\_Ks}_{\text{faint}}) \tag{40}$$

where $\text{mag\_Ks}_{\text{faint}} = 24.7$ is the apparent magnitude limit of the COSMOS2015 deep survey. First, in a given redshift bin, we select 20% of the faintest galaxies inside a given redshift range. Next, we select 15% of these faintest galaxies with the lowest redshifts for each redshift bin (Figure 19, red points). In this way we obtain a representative sample of $\sim 250 - 550$ galaxies per redshift bin, for which we compute the $\log(M_*^{\text{lim}})$. Next, we define the stellar mass completeness limit $\log(M_*^{\text{complete}})$ as the 90^{th} percentile of the $\log(M_*^{\text{lim}})$ distribution, i.e. it is the stellar mass below which 90% of stellar mass limits ($\log(M_*^{\text{lim}})$) lie. Note that these percentile values are set as optional parameters and can be modified in case there is a redshift bin with not enough galaxies to compute the $\log(M_*^{\text{complete}})$ parameter.

In Table 1 I compare values of the $\log(M_*^{\text{complete}})$ with those from Davidzon et al., (2017). Our values are slightly higher at high-z. These differences might originate from a slightly different galaxy sample and/or a different percentiles used in the two works.

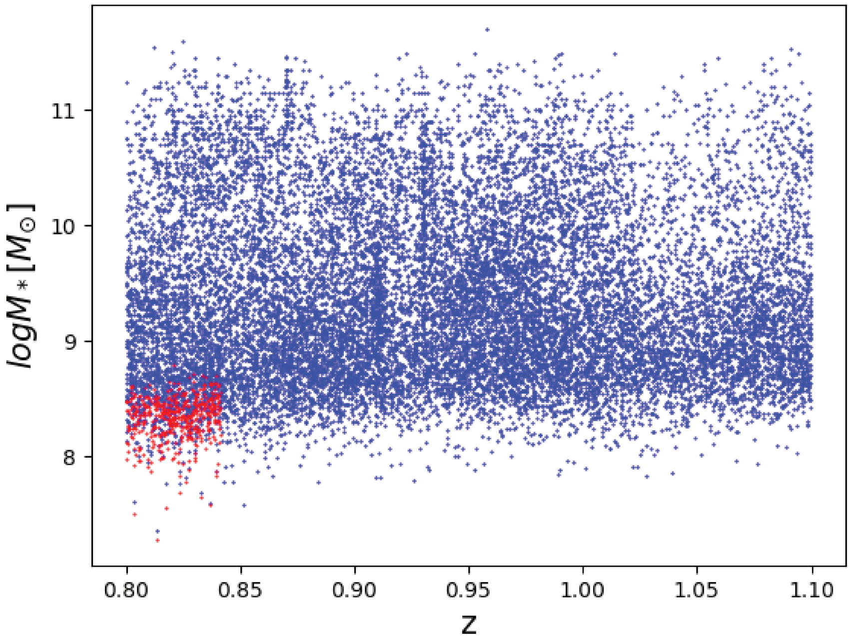

Figure 19: *Stellar mass (blue points) and limiting stellar mass (red points) for the* 20% *of the faintest and* 15% *of the low-z galaxies, as a function of redshift for all galaxies at* $0.8 \leqslant z < 1.1$.

Table 1: Stellar mass completeness limits M_*^{complete} from this work and $M_{*,\text{D17}}^{\text{complete}}$ from Davidzon et al., (2017), for a full sample, star-forming and quiescent galaxies

z-bin	$\log(M_*^{\text{complete}})$	$\log(M_{*,\text{D17}}^{\text{complete}})$
	Full sample	
$0.2 - 0.5$	7.58	7.53
$0.5 - 0.8$	8.22	8.40
$0.8 - 1.1$	8.58	8.79
$1.1 - 1.5$	8.83	8.75
$1.5 - 2.0$	9.09	8.95
$2.0 - 2.5$	9.40	9.22
	Star-forming sample	
$0.2 - 0.5$	7.55	7.51
$0.5 - 0.8$	8.22	8.31
$0.8 - 1.1$	8.58	8.63
$1.1 - 1.5$	8.83	8.64
$1.5 - 2.0$	9.09	8.91
$2.0 - 2.5$	9.40	9.21
	Quiescent sample	
$0.2 - 0.5$	8.02	8.00
$0.5 - 0.8$	8.65	8.64
$0.8 - 1.1$	9.00	9.03
$1.1 - 1.5$	9.19	9.01
$1.5 - 2.0$	9.57	9.23
$2.0 - 2.5$	9.81	9.47

1/Vmax estimator and Poissonian uncertainties

In order to obtain the galaxy SMF using the 1/Vmax estimator, we need to normalize the number of galaxies by the stellar mass bin width and the maximum comoving volume $V_{\mathrm{max},i}$ in which we are still able to observe a galaxy i of a given brightness (Equation 14; Section 2.1.2).

Maximum comoving volume of a galaxy i, in the $z_{\mathrm{min},i} \leqslant z < z_{\mathrm{max},i}$ range, is defined with Equation 14 and can be estimated with the `astropy` `comoving_volume` function (Astropy Collaboration et al., 2013). The redshift limits are:

$$z_{\mathrm{min},i} = \max(z_{\mathrm{min}}, z_{\mathrm{min,Ks}}) \tag{41}$$

$$z_{\mathrm{max},i} = \min(z_{\mathrm{max}}, z_{\mathrm{max,Ks}}) \tag{42}$$

where z_{min} and z_{max} are the redshift bin limits of a given subsample of galaxies, i.e. $z_{\mathrm{min}} \in$ (0.2, 0.5, 0.8, 1.1, 1.5, 2.0) and $z_{\mathrm{max}} \in$ (0.5, 0.8, 1.1, 1.5, 2.0, 2.5), and $z_{min,Ks}$ and $z_{max,Ks}$ are the redshift limits of a galaxy of an apparent magnitude Ks. However, since the $z_{min,Ks}$ and $z_{max,Ks}$ parameters are missing in the Flagship mock galaxy catalog, we implement the 1/Vmax estimator by normalizing the number of galaxies by the bin width and the total maximum comoving volume V_{tot} inside a given redshift bin ($z_{\mathrm{min}} \leqslant z < z_{\mathrm{max}}$). Therefore, current limitations in the Flagship mock galaxy catalog do not allow the estimation of the maximum comoving volume for each galaxy, and deriving the correct SMF.

Moreover, we add statistical weights w_i for each galaxy i in the SMF estimate, for which we set arbitrary values of $w_i = 1$. These weights will be required when taking into account sample incompleteness and sources with uncertain or failed redshift measurements.

On the other hand, the COSMOS2015 catalog contains the $z_{min,Ks}$ and $z_{max,Ks}$ parameters which allows us to compute the maximum comoving volume ($V_{\mathrm{max},i}$) for each galaxy i inside the redshift range: $\max(z_{\mathrm{min}}, z_{\mathrm{min,Ks}})$ and $\min(z_{\mathrm{max}}, z_{\mathrm{min,Ks}})$. Since some values of $z_{\mathrm{min,Ks}}$ and $z_{\mathrm{max,Ks}}$ are negative (e.g. $z_{\mathrm{min,Ks}} = -99$), we set the values of these parameters as $z_{\mathrm{max,Ks}} = z_{\mathrm{max}} + 0.1$, and $z_{\mathrm{min,Ks}} = z_{\mathrm{min}} - 0.1$. The number of these objects is $< 2\%$ and it does not affect the end results. Computing the $V_{\mathrm{max},i}$ for each galaxy i significantly increases the computational time of the pipeline.

For the COSMOS2015 data, we implement the 1/Vmax estimator (Section 2.1.2) by normalizing the number of galaxies per stellar mass bin by the bin width and multiplying it with the ratio of the total comoving volume V_{total} in a given redshift range and the maximum comoving volume of the galaxy i, which is the equivalent of normalizing the histogram values by the sum of all individual maximum comoving volumes $V_{\mathrm{max},i}$ in a given stellar mass and redshift bin (Ilbert et al., 2004). We set this ratio as a weight in the `numpy` histogram function:

$$w_i = \frac{V_{\mathrm{total}}}{V_{\mathrm{max},i}} \tag{43}$$

and we compute both volumes with the `astropy` `comoving_volume` function (Astropy Collaboration et al., 2013).

Finally, we implement the Poissonian uncertainties (Equation 27), normalized by the bin width and the total maximum comoving volume, in order to have the SMF values and their uncertainties in the same units.

SMF fit with Schechter models using the maximum likelihood method

We extend the pipeline for deriving the SMF with a new algorithm that fits the derived SMF with a chosen model.

First, we define the models to be used for fitting the SMF: a single Schechter function (Equation 10, Schechter, 1976), a double Schechter function (Equation 11, Pozzetti et al., 2010), and a double Schechter function with the α_2 parameter fixed, following Ilbert et al., (2013). However, it is more convenient to define the Schechter functions in the $\log M$ space. Therefore, a single Schechter function is:

$$\Phi(\log M) = \ln 10 \times \Phi^* * 10^{(\log M - \log M^*)^{(\alpha+1)}} \times e^{-10^{(\log M - \log M^*)}} \tag{44}$$

and a double Schechter function is:

$$\begin{aligned}\Phi(\log M) = \ln 10 \times e^{(-10^{\log M - \log M^*})} \times (\Phi_1^* * 10^{(\log M - \log M^*)^{(\alpha_1+1)}} \\ + \Phi_2^* * 10^{(\log M - \log M^*)^{(\alpha_2+1)}})\end{aligned} \tag{45}$$

Davidzon et al., (2017) use different Schechter models depending on the galaxy type and redshift range. For instance, for the full sample and star-forming galaxies they use a double Schechter function at $0.2 \leqslant z < 3.0$, whereas they use a single Schechter function at the $z > 3.0$. Moreover, for quiescent galaxies they use a double Schechter function in the $0.2 \leqslant z < 0.8$ and a single Schechter function for higher redshifts. We follow their work in order to reproduce their results over the redshift range $0.2 \leqslant z < 2.5$.

Next, we use the `scipy.optimize.minimize` function and the maximum likelihood method in order to fit the SMF of galaxies with the chosen Schechter function and obtain the best-fit parameters of the model. The `scipy.optimize.minimize` function takes the given observations and its uncertainties (x, y, dy), the model (e.g. a single Schechter function) and its unknown parameters (e.g. $\log(M^*)$, Φ^* and α) as arguments, and returns the values of the best-fit parameters of the model without the uncertainty estimates.

The `scipy.optimize.minimize` function is based on maximizing the likelihood of $\mathcal{L}$ of obtaining certain values of the data y_i^{obs} with a given set of parameters of the model. The maximum likelihood function $\mathcal{L}$ and its logarithm are given as $\mathcal{L}$:

$$\mathcal{L} \propto e^{-\chi^2/2} \tag{46}$$

$$\ln(\mathcal{L}) \propto -\frac{\chi^2}{2} \tag{47}$$

where χ^2 is the total squared offset between the observed values y_i^{obs} and the values obtained by the model $y^{model}(x_i)$, scaled by the uncertainties σ^2:

$$\chi^2 = \sum_i \frac{(y_i^{obs} - y^{model}(x_i))^2}{\sigma_i^2} \tag{48}$$

Thus, maximizing the (negative) likelihood is equivalent to minimizing the χ^2 function (e.g. Hogg, Bovy, and Lang, 2010).

Eddington bias

In order to take into account the Eddington bias, we fit the SMF with the Schechter function convolved by stellar mass uncertainties and obtain the best-fit parameters of the model deconvolved by the stellar mass uncertainties (Ilbert et al., 2013). The stellar mass uncertainties can be modeled by a Gaussian function (as in e.g. Kitzbichler and White, 2007; Caputi et al., 2011, 2015; Bower, Benson, and Crain, 2012; Davidzon et al., 2017):

$$G(x) = \frac{1}{\sqrt{2\pi\sigma^2}} e^{-\frac{(\log(M_*) - \log(M_*^{mean})^2}{2\sigma^2}} \tag{49}$$

a Lorentzian function:

$$L(x) = \frac{\tau}{2\pi} \frac{1}{(\frac{\tau}{2})^2 + (\log(M_*) - \log(M_*^{mean})^2} \tag{50}$$

or the product of a Gaussian and Lorentzian functions (Ilbert et al., 2013; Davidzon et al., 2017):

$$L(x) \times G(x) = \frac{\tau}{2\pi\sqrt{2\pi\sigma^2}} \frac{1}{(\frac{\tau}{2})^2 + (\log(M_*) - \log(M_*^{mean})^2} \times e^{-\frac{(\log(M_*) - \log(M_*^{mean})^2}{2\sigma^2}} \tag{51}$$

where σ is the standard deviation, τ is a parameter of the Lorentzian function defining the width of the distribution. In general, both σ and τ are functions of redshift z and stellar mass M_*.

Inside the pipeline, I define the three kernel functions (the Gaussian (Equation 49), the Lorentzian (Equation 50) and their product (Equation 51) to be used for the convolution. Next, I define the σ and τ parameters of the Gaussian and Lorentzian function, respectively, as redshift dependent:

$$\sigma = \text{sig\_par} \times (1 + z_{mean}) \tag{52}$$

$$\tau = \text{tau\_par} \times (1 + z_{mean}) \tag{53}$$

where z_{mean} is the mean redshift within a given redshift bin, and sig_par and tau_par are constants. For comparison, in Davidzon et al., (2017) and

Ilbert et al., (2013) σ is set as a constant (0.35, and 05 dex, respectively) and τ as a function of redshift. Therefore, I set the same value of $\sigma = 0.35$ when working with the COSMOS2015 catalog and reproducing the work of Davidzon et al., (2017).

Finally, I define a Schechter function convolved by a kernel function, (e.g. the product of a Gaussian and Lorentzian functions; Ilbert et al., 2013) as a model, i.e. a likelihood function:

$$\begin{gathered}\Phi_{\text{conv}}(\log M) = (\Phi * (L \times G))(\log M) = \\ \int_{-\infty}^{\infty} \Phi(x) * L(\log M - x, \tau) \times G(\log M - x, \sigma) dx\end{gathered} \tag{54}$$

Several Python convolution functions from different libraries are available (`numpy`, `astropy`). I decide to use `astropy.convolve` (Astropy Collaboration et al., 2013), since it provides a better fit for all the different values of σ and τ taken into account.

MCMC PYTHON CODE

This part of the script was developed outside of the *Euclid* environment and it is not included in the *Euclid* pipeline.

MCMC algorithm

First, I introduce some statistical terms that will be used with the maximum likelihood method and the MCMC. If we have a model (e.g. a Schechter function) with some unknown parameters θ (Φ^*, α and M^*) that depend on a given data D (e.g. the SMF values and the Poissonian uncertainties), we can introduce likelihood, prior and probability functions (Gilks, Richardson, and Spiegelhalter, 1996):

- prior $P(\theta)$ is a probability distribution over parameters of a model θ before we have any information on data (D). In practice we assume a range of values for parameters we want to determine, for example, using values computed from an independent study, experiments, simulations, or a range of values that are physical, etc. For instance, the parameters we want to compute are the Schechter function parameters Φ^*, α and M^*.

- posterior $P(\theta|D)$ is a probability distribution over parameters of the model that best fit the given data. In practice, it is a set of unknown parameters of a function we want to compute (in this case it is the Schechter function parameters).

- likelihood $P(D|\theta)$ is a probability distribution over datasets with a given model. In practice it is the probability of obtaining certain values of the data with a given set of parameters of the model.

- marginal likelihood P(D), is a probability over data D for any given model. In practice it is a normalization constant. It is unknown and usually very hard to compute (Hou, Goodman, and Hogg, 2014).

The goal of the MCMC is to draw a sample from posterior function $P(\theta|D)$, which is proportional to the likelihood function and the prior:

$$P(\theta|D) = \frac{1}{P(D)} P(D|\theta) P(\theta) \tag{55}$$

We can reconstruct the posterior $P(\theta|D)$ distribution function (PDF) $f(\theta)$ up to a constant $P(D)$. Therefore, we sample a non-normalized posterior function $f(\theta) \sim P(\theta|D)$. However, instead of using $f(\theta)$, it is advisable (Hogg and Foreman-Mackey, 2018) to use the natural logarithm of the probability function which will be a sum of the likelihood and prior functions:

$$\ln f(\theta) = \ln(P(D|\theta)) + \ln(P(\theta)) \tag{56}$$

In practice, if we have a set of data D and we want to fit a model $P(D|\theta)$ (likelihood function) to this data, and we do not know the exact values of the parameters θ, but we have some vague idea about the range of values of these parameters $P(\theta)$(prior), we run the MCMC and obtain a posterior distribution in parameter space that is consistent with data ($f(\theta) \sim P(\theta|D)$).

The MCMC generates a random walk in a N-dimensional small *ball* in N-dimensional parameter space, around the initial position defined by the maximum likelihood probability value. The *walkers* or *chains* start in small distributions around the maximum likelihood values and then they quickly branch-out and start exploring the full posterior distribution. In order to confine the *walkers* to a finite volume of the parameter space we set the parameter limits in the prior function. We draw samples (X_0, X_1, X_2, ..., X_n) from the Markov chain so that X_{i+1} step depends only on the X_i step and not on the previous ones. If the proposed step X_{i+1} is accepted it becomes a part of the samples, and if not, the previous step X_i is repeated. This algorithm is called the Metropolis-Hastings MCMC method (Metropolis et al., 1953). After a certain number of steps (m), the *chain* will converge, so we can discard all the first m values, which usually make about 10% of the total *chain* length n, and are called *burning*.

Ideally, the MCMC chains converge and we obtain the best-fit parameters of the model and their uncertainties. We can either use the mean or median of the posterior PDF or the maximum likelihood value as the best-fit parameters of the model. Moreover, by taking the quantiles of the posterior distribution we take into account the whole shape of the posterior distribution, and we have access to uncertainties. For instance, if we take the 16^{th}, the 50^{th} (the median) and the 84^{th} quantiles of the posterior distribution (q_{16}, q_{50} and q_{84}, respectively), we exclude the first and the last 16% of samples and we have 1σ error bars that contain 68% of samples:

$$q_{low} = q_{50} - q_{16} \qquad q_{up} = q_{84} - q_{50} \tag{57}$$

where q_{low} and q_{up} are lower and upper 1σ error. Furthermore, if we take the 2.5^{th}, the 50^{th} and the 97.5^{th}, we have 95% of all samples and 2σ error bars.

emcee package

We use the `emcee` software package (Foreman-Mackey et al., 2013), a MIT licensed pure-Python implementation of affine invariant MCMC ensemble sampler (Goodman and Weare, 2010). It is based on ensemble methods that use many independent *walkers* to determine the best sizes and directions of the following steps. As a result, we get a properly tuned posterior distribution in the parameter space. However, this tuning improvement comes with a price of a relatively large *burning* phase in the beginning of each run of the MCMC, of at least a few autocorrelation times.

We make use of the functions from this package and modify them to fit our project. We use the maximum-likelihood method (Section 2.3.2) and the MCMC Metropolis-Hastings method (Mackay, 2003; Hogg, Bovy, and Lang, 2010; Foreman-Mackey et al., 2013; Hogg and Foreman-Mackey, 2018), in order to fit the COSMOS2015 galaxy SMF (Davidzon et al., 2017) with different Schechter functions as models and obtain the best-fit parameters of the Schechter model and their uncertainties.

Testing the MCMC code

In order to develop and test the MCMC algorithm and the `Python` code we start with a simple example of a linear function model (Section 2.4.2.1). Next we use the COSMOS2015 generated data, produced by fitting the SMF with Schechter functions deconvolved by the stellar mass uncertainties (Section 2.4.2.2; Davidzon et al., 2017). Finally, I run the MCMC code on the SMF of COSMOS2015 galaxies, obtained with the 1/Vmax method from the work of Davidzon et al., (2017) in order to reproduce their work.

We also test the MCMC code in a similar way on the UltraVISTA generated data and the SMF of UltraVISTA galaxies (McCracken et al., 2012) and reproduce the work of Ilbert et al., (2013) (Appendix B).

Fitting the linear function model

We start with the simple example of a linear model in order to test the MCMC algorithm. We use a linear function:

$$y = ax + b \tag{58}$$

where a and b are the *unknown* parameters that I give some random values, e.g. $a = -0.9594$ and $b = 4.294$. I generate the data by using Equation 58 and computing the $y = f(x)$ over a range of $x \in [0, 1000]$ values. Next, I generate the noise δy by adding a random Gaussian scattering around the (x_i, y_i) points. I define the prior function by setting a range of values around the true values of parameters, $-3 < a < 2$ and $-10 < b < 10$. Next, I define the likelihood function using the Equation 58 as the model. Thus, the χ^2 of the likelihood function is:

$$\chi^2 = \sum_i \frac{(y_i - (ax_i + b))^2}{\delta y_i^2} \tag{59}$$

In order to minimize χ^2 and to maximize the likelihood I use the `scipy.optimize.minimize` function. I give some initial values of parameters close to their real values. Since the parameter values are already known, I simply give them their true values. The function returns the best-fit parameter values: $a = -0.95916397$ and $b = 4.08880422$, which are close to their true values. Note that using this minimization function is optional and we can simply put some initial values ourselves. Next, I scatter the maximum likelihood results in order to obtain random starting values close to the true parameter values for each *walker*. I set the number of parallel *walkers*, the number of steps and the *burning* as $n_{\text{chain}} = 50$, $l_{\text{chain}} = 10000$, $n_{\text{burn}} = 1000$. Since I have a simple linear model with a small number of unknown parameters, I do not need a large number of *walkers*, and steps for the *walkers* to converge.

I set up the sampler and run the MCMC. I discard the first 10% of the steps, i.e. the *burning*. Finally, I obtain the posterior distribution with best-fit parameters and their 1σ uncertainties (Figure 20, top panel). I plot the real linear function with the known values of the parameters set beforehand, the generated scattered data around this function, and the best-fit model to this data for comparison (Figure 20, bottom panel).

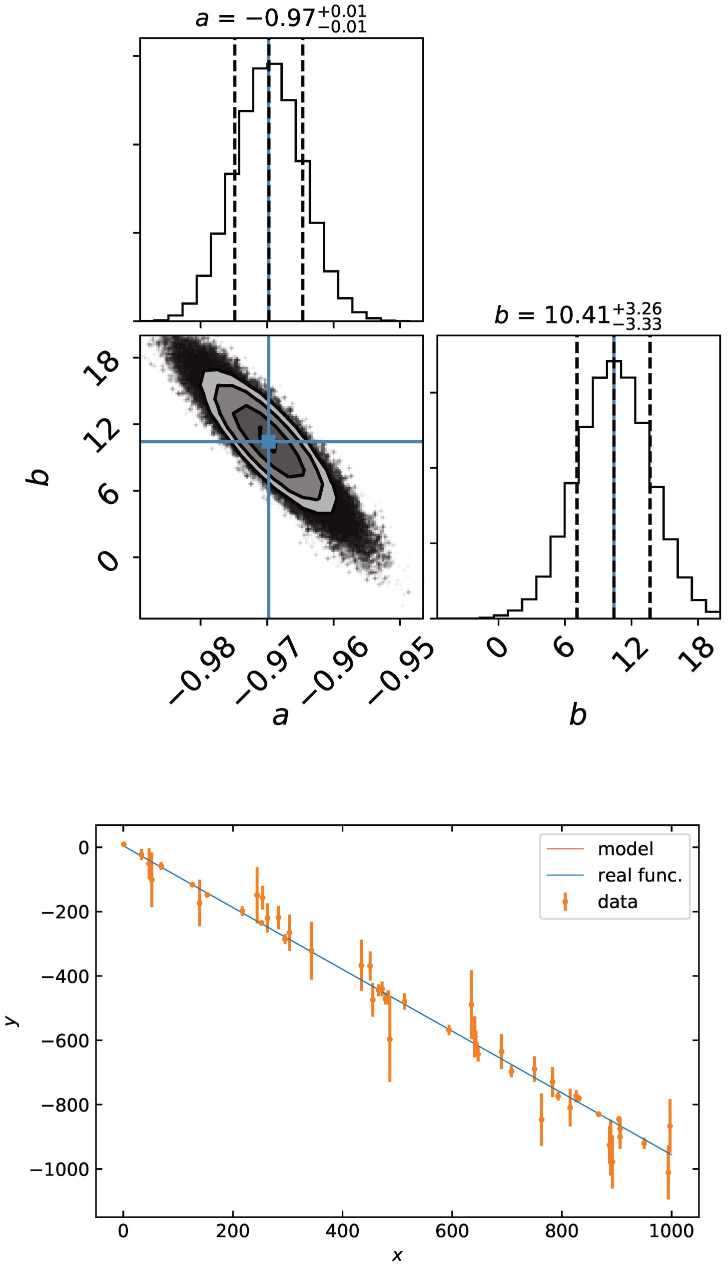

Figure 20: *Corner plot representation (Foreman-Mackey, 2016) of the posterior distribution of linear function parameters (top) and the linear function, generated scattered data points for the same function and a model obtained with MCMC (bottom).*

Fitting the SMF fit of COSMOS2015 generated data

This is another simple test on the MCMC code, since we are using a Schechter model and the MCMC algorithm to fit the data produced by that same model. COSMOS2015 generated data are produced by fitting the SMF (derived with the 1/Vmax method) with a deconvolved single and double Schechter functions (depending on the galaxy type and redshift), with parameter values from Table 1 of Davidzon et al., 2017, for a full sample, active and passive galaxies at $0.2 \leqslant z < 4.0$. I run the MCMC in order to fit these data and obtain the best-fit parameters of the Schechter models and their uncertainties.

These generated data contain values of the $\log M_*$, $\log\Phi$, $\log\Phi_{\mathrm{min}}$ and $\log\Phi_{\mathrm{max}}$ in the mass range $7.0 < \log M_* < 13.0$. First, I compute mean uncertainty that is used for the minimization function:

$$\log\Phi_{\mathrm{err}} = \frac{1}{2}(\log\Phi_{\mathrm{max}} - \log\Phi_{\mathrm{min}}) \tag{60}$$

I discard the stellar mass bins with $\log\Phi < -6$ and those below the stellar mass completeness limits derived by Davidzon et al., (2017), in order to reproduce their results.

I set the single and double Schechter functions as the models, i.e. likelihood functions. For the prior function, I set limits for parameters of the model in the range of physical values known in astrophysics and close to the values obtained in Davidzon et al., (2017).

Next, in order to minimize the χ^2 function and maximize the likelihood, we use the `optimize.minimize` function (Section 2.3.2). This function requires some initial values of the parameters, so I set the best-fit parameter values from Table 1 of Davidzon et al., (2017) as initial values and obtain the preliminary best-fit parameters of the model.

I scatter the preliminary minimization function results to get random starting values for each *walker*, in order to initialize the *walkers* at different positions around the maximum likelihood result. I set the number of parallel *walkers* i.e. *chains* $n_{\mathrm{chain}} = 50$, with the number of steps (i.e. *chain* length) $l_{\mathrm{chain}} = 25000$ and the *burning* phase $n_{\mathrm{burn}} = 2500$. In general, it is recommended to use hundreds of steps, but since the Schechter models are relatively complicated with three to five unknown parameters, I set a higher number of steps, in order to allow enough steps for the *walkers* to converge.

Finally, I set up a sampler and run the MCMC. Graphical representation of the progression of each chain at first 2500 steps for the $\log M^*$ parameter is shown on Figure 21.

I discard the first 10% of the steps (i.e. the *burning* phase) and obtain the posterior distribution and the best-fit parameters of the Schechter models and their uncertainties. We use the recommended values of the quantiles of the posterior distribution (Foreman-Mackey et al., 2013) and have access to 1σ uncertainties with Equation 57 and have access to the best-fit parameter values and their 1σ uncertainties (Figure 22, top panels). I show an example of a `corner` plot (Foreman-Mackey, 2016), i.e. a graphical representation of the posterior probability distribution of parameters of a double Schechter function fit, the parameters' relations (Figure 22, bottom panels).

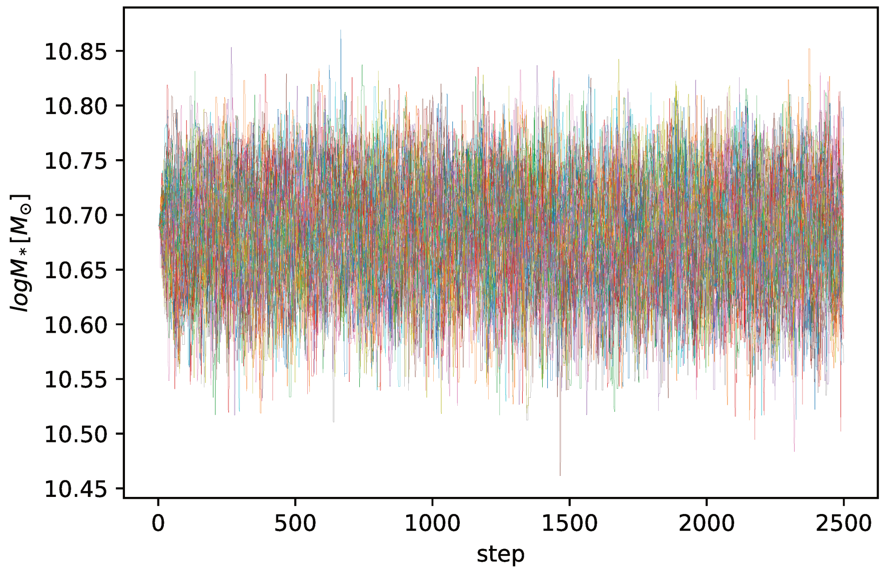

Figure 21: *Trace plot representation of the progression of each MCMC chain in the first 2500 steps for the parameter* $\log M^*$ *of the single Schechter function.*

I show an example of the SMF of COSMOS2015 generated data, for a full sample of galaxies in the $0.5 \leqslant z < 0.8$ range, with the double Schechter function fits from this work and from Davidzon et al., (2017) for comparison (Figure 23, bottom panel). I conclude that there is almost a perfect match (within 1σ) between the results from this work and from Davidzon et al., (2017).

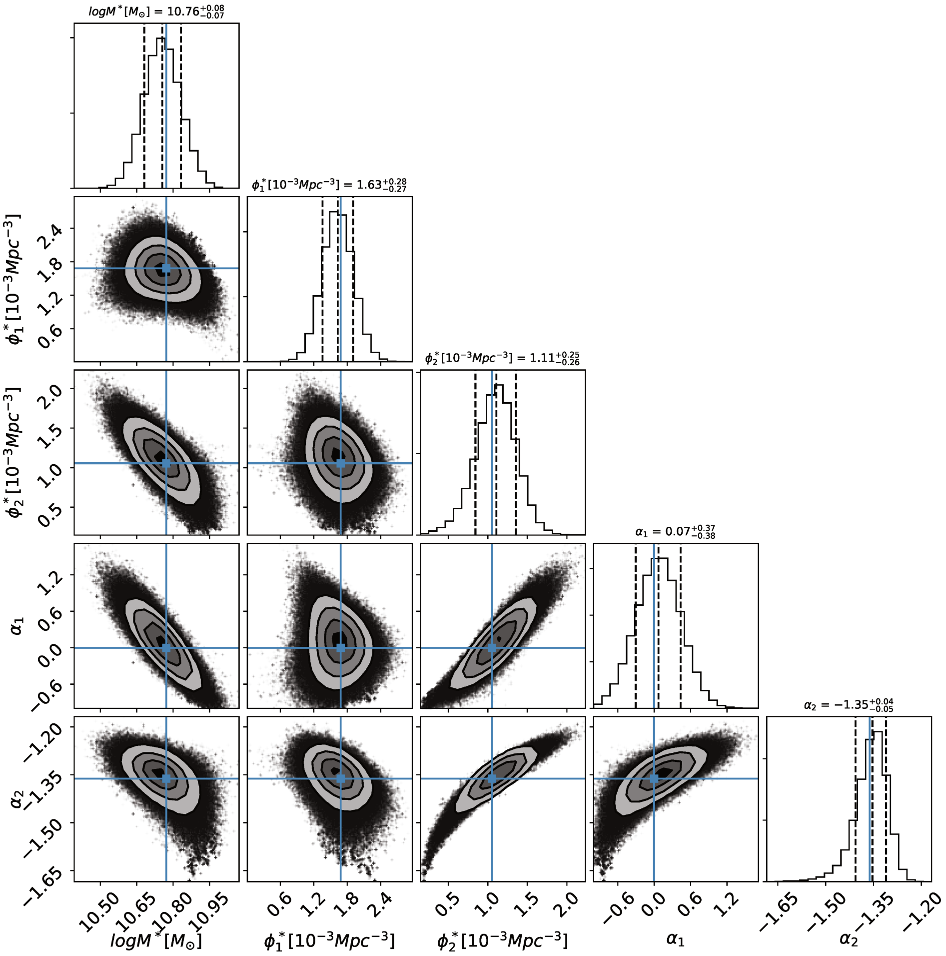

Figure 22: *Corner plot representation of the posterior distribution of parameters of a double Schechter function fitted on the COSMOS2015 generated data for the full sample of galaxies at* $0.5 \leqslant z < 0.8$*. The plots show the 1D and 2D projections of the posterior distribution of parameter samples. The* 16th*, the* 50th *and the* 84th *quantiles (the median and* 1σ *uncertainties) cut and divide the datasets and they are represented as dashed lines while the maximum likelihood value is represented as blue line.*

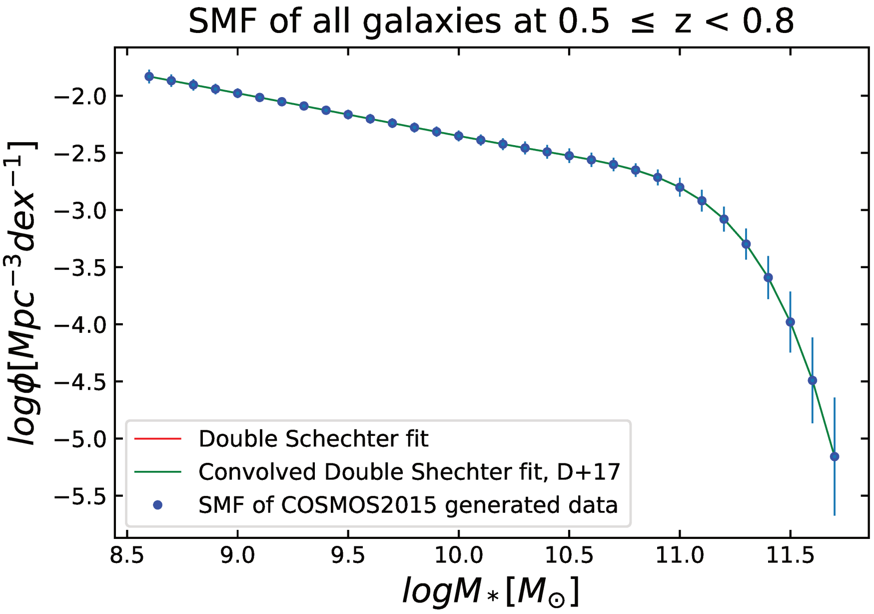

Figure 23: *The SMF of COSMOS2015 generated data at* $0.5 \leqslant z < 0.8$ *(blue points), with a double Schechter function fit from this work (red line) and a deconvolved double Schechter fit from Davidzon et al., (2017) (green line).*

Fitting the SMF of COSMOS2015 data

We test the MCMC algorithm by fitting the SMF of COSMOS2015 galaxies derived with the 1/Vmax method by Davidzon et al., (2017), in order to reproduce their work. These data contain $\log M$, $\log\Phi$, $\log\Phi^{+}_{\mathrm{err}}$ and $\log\Phi^{-}_{\mathrm{err}}$ for a full sample, active and passive galaxies at $0.2 \leqslant z < 4.0$. I compute the errors by using the following equation:

$$\log\Phi_{\mathrm{err}} = \frac{1}{2}(\log\Phi^{+}_{\mathrm{err}} + \log\Phi^{-}_{\mathrm{err}}) \tag{61}$$

We take into account the Eddington bias by convolving the Schechter function with the stellar mass uncertainties, modeled by the product of a Lorentzian and Gaussian function with $\sigma = 0.35$ (Section 2.3.2.1), in order to reproduce the work of Davidzon et al., (2017).

I define the Schechter and deconvolved Schechter models as the likelihood functions. The rest of the algorithm is exactly the same as in Section 2.4.2.2. I run the MCMC and obtain the posterior distribution of parameters of a deconvolved double (Figure 24, top panel) and single Schechter models (Figure 25, top panel). Furthermore, we have access to the best-fit parameters deconvolved by the stellar mass uncertainties, and their 1σ uncertainties.

I show an example of a SMF of COSMOS2015 full sample of galaxies at $2.0 \leqslant z < 2.5$, and the double Schechter fit from this work and the deconvolved double Schechter fit from this work and from Davidzon et al., (2017) (Figure 24, (bottom panel). Next, I show a SMF of COSMOS2015 quiescent galaxies at $2.0 \leqslant z < 2.5$, and the single Schechter fit from this work and the deconvolved single Schechter fit from this work and from Davidzon et al., (2017) (Figure 25, (bottom panel)

In most of the cases there is an overlap between non-convolved and deconvolved fits. The difference between the two fits starts to be obvious at higher redshifts and at high-mass end of the SMF since the uncertainties increase with redshift and stellar mass.

In some cases, mostly for galaxies at high-z ($3.0 \leqslant< z < 4.0$) the `scipy.optimize.minimize` function with the *Nelder-Mead* method (Nelder and Mead, 1965) fails to find the correct values of the preliminary best-fit parameters within the constraints given in the prior function, and MCMC run does not converge. For those cases, I use methods that allow constraints on parameters, such as the *TNC* (Nocedal and Wright, 2006), and set parameter bounds with the same values as in a prior.

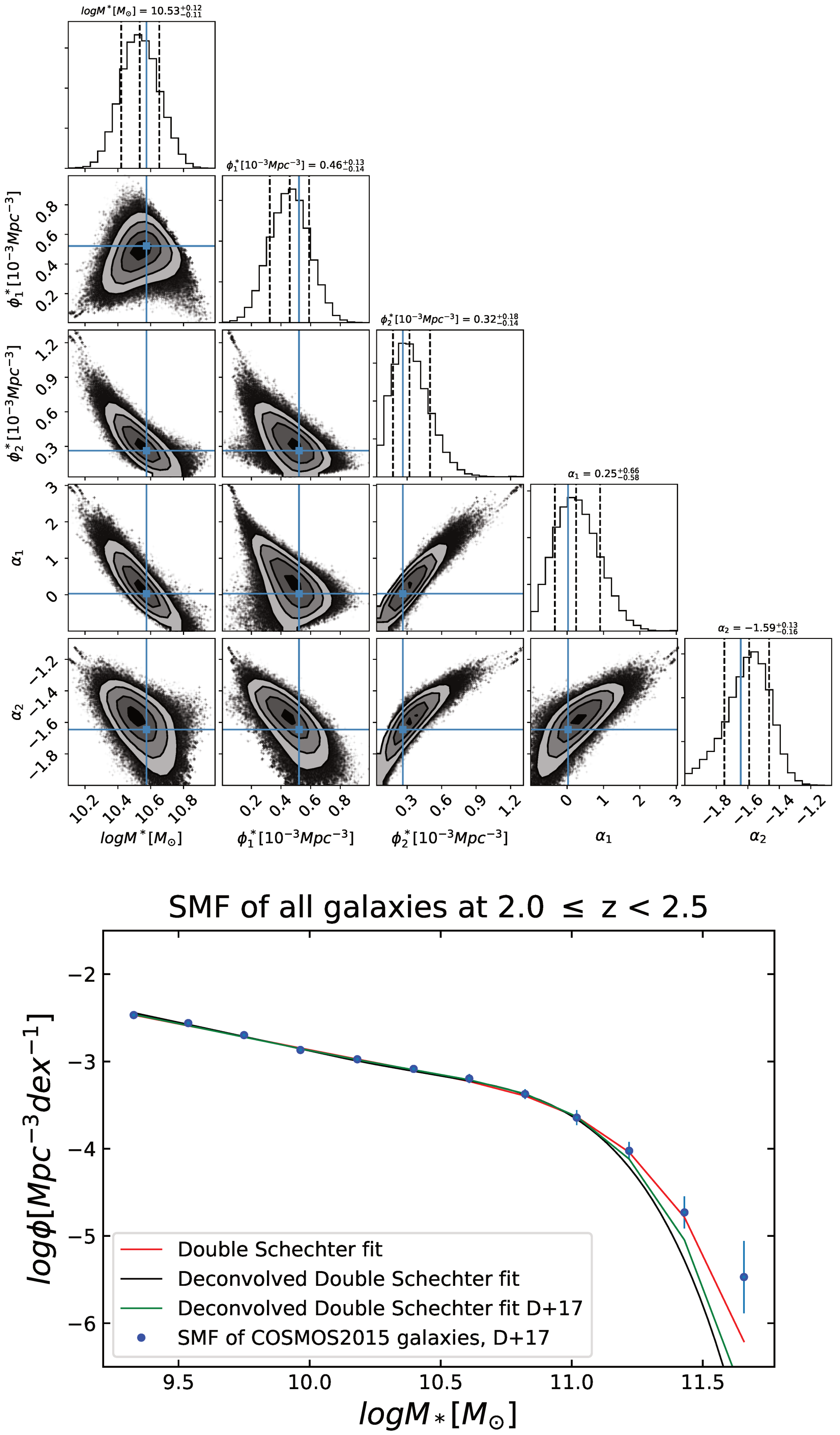

Figure 24: *Top: Corner plot representation of the posterior distribution of parameters of a deconvolved double Schechter function fit on the COSMOS2015 data for the full sample of galaxies at* $2.0 \leqslant z < 2.5$. *Bottom: The SMF of COSMOS2015 galaxies at* $2.0 \leqslant z < 2.5$ *from Davidzon et al., (2017) (blue points), with a double Schechter function fit from this work (red line) and a deconvolved double Schechter fits from this work (black line) and Davidzon et al., (2017) (green line).*

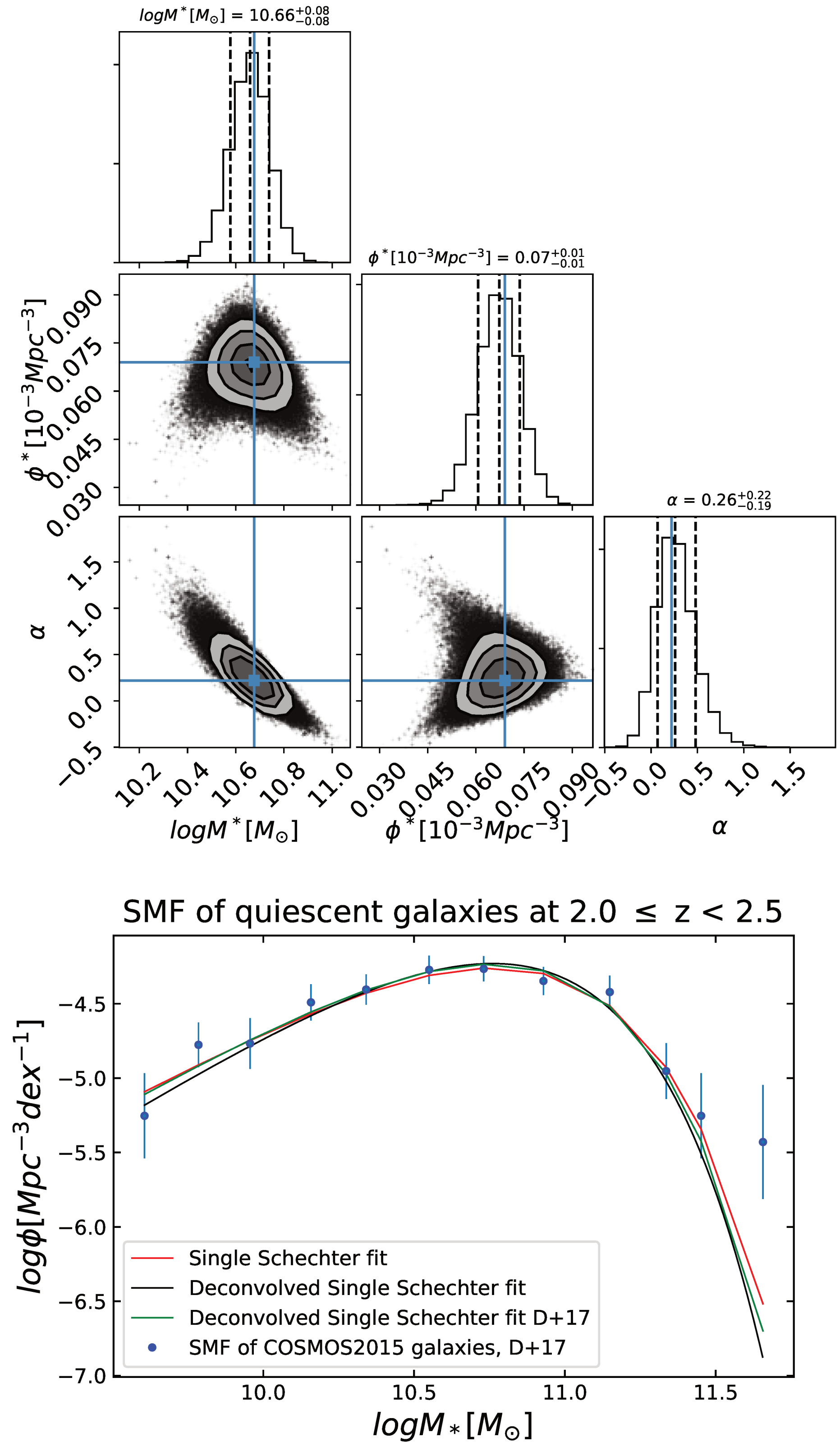

Figure 25: *Top: Corner plot representation of the posterior distribution of parameters of a deconvolved single Schechter function fitted on the SMF of COSMOS2015 quiescent galaxies at* $2.0 \leqslant z < 2.5$*. Bottom: The SMF of COSMOS2015 quiescent galaxies at* $2.0 \leqslant z < 2.5$ *from Davidzon et al., (2017) (blue points), with a single Schechter function fit from this work (red line) and a deconvolved single Schechter fits from this work (black line) and Davidzon et al., (2017) (green line).*

Convergence tests for the MCMC

How do we know if the MCMC sampled the entire parameter space and converged to best-fit values and we have reliable results? In practice we can never be completely sure if we have sampled the entire parameter space, and there is always a possibility that there are two or more high-probability regions which are separated and we sampled only one of them.

There is a number of standard performance and convergence tests for the MCMC.

Visualization of samples

A simple way to check the MCMC performance is visualization. For instance, I use trace plots (Figure 21) to visually represent the progression of each *walker* for an unknown parameter of the Schechter model, in order to make sure that the *walkers* sample the entire parameter space many times during the MCMC run. Next, I use corner plots (Foreman-Mackey, 2016) to visually represent the posterior distribution of all the unknown parameters, with best-fit values and their 1σ uncertainties (e.g. Figure 22), in order to check the shape of the posterior distribution. In general, the shape of the posterior distribution of each parameter should be oval, not too elongated, and without multiple peaks. I check the shape of the posterior distribution in corner plots for all galaxy samples at all redshift ranges, and I conclude that the MCMC did a good job in finding values of the posterior distribution. However, there are a few cases at higher redshift $z > 3.0$ where the posterior distribution is sometimes elongated, but this is expected since statistical uncertainties are larger.

Testing the consistency of the posterior PDF

A standard way to check for the MCMC convergence is simply to increase the number of steps of each *walker* and check if there are substantial variations in the shape of the posterior PDF and the final results. However, increasing the number of steps is limited by the available time and computer memory.

Moreover, the posterior distribution should be independent on the initialization of the *walkers*. If it is not the case, it indicates a problem with the MCMC. Therefore, I change the initial positions of the *walkers* and I obtain quite similar posterior PDF and the best-fit parameters and their uncertainties.

Autocorrelation time

Autocorrelation time is a measurement of the number of steps required in each *chain* in order to draw a representative independent samples. The shorter it is, the fewer steps the *chains* need for the MCMC to converge. Therefore, τ is can be used to estimate the MCMC performance.

I use `sampler.get_autocorr_time()` and `sampler.acor` modules for computing the autocorrelation time, and `emcee.autocorr.integrated_time()` for computing the integrated autocorrelation time (Goodman and Weare, 2010; Foreman-Mackey et al., 2013). The integrated autocorrelation time is estimated using more than one sample. The idea is that the samples are not always independent and we need to use more than one in order to estimate the correct value of τ.

In order to make sure that the *chains* converge, it is recommended that the chain length should be at least several autocorrelation times e.g. $l_{chain} \sim c \times \tau$ (Foreman-Mackey et al., 2013), where c is the minimum number of autocorrelation times needed to trust the drawn samples. c is a parameter in the `emcee.autocorr.integrated_time()` function and is set by default to $c = 10$. Therefore, I increase the number of steps in order to run the sampler for at least $10 \times \tau$.

Acceptance fraction

Since estimating the autocorrelation time can be time consuming and difficult, the simplest autocorrelation time proxy is acceptance fraction. It is a fraction of steps that are accepted in a chain. Although there is no absolute agreement about the values, in general it should be in the $0.2 - 0.5$ range (Foreman-Mackey et al., 2013) and the ideal value for a model with multiple parameters is 0.234 (Hogg, Bovy, and Lang, 2010).

In order to compute the acceptance fraction I use a Python module `sampler.acceptance_fraction`. I find that the acceptance fraction is within the recommended values when running the MCMC on different galaxy samples at certain redshifts. But, sometimes the acceptance fraction is higher than recommended (> 0.5). In those cases, I improve the acceptance fraction by increasing the number of steps, but the acceptance fraction does not change significantly (~ 0.05).

Next, I change the value of the a argument of the `emcee.EnsembleSampler` function. The a parameter is the proposal scale factor, which controls the step size of the walkers. It is by default set as $a = 2.0$. Increasing the a parameter results in a decrease of the acceptance fraction, and vice-versa.

However, if step size is too large, the *chain* jumps from one low-probability region to another, and all of the steps are rejected. On the other hand, if step size is too small all of them are accepted, but the *chain* gets stuck in a small region and will not probe the entire parameters space. In both cases, the chain will not produce representative samples.

RESULTS

SMF of Flagship mock galaxies

We test the *Euclid* pipeline first by producing the SMF of galaxies and the SMF fit of Flagship mock galaxies (Section 2.2.2; Carretero et al., 2017), at $0.2 \leqslant z < 2.5$. There are 479864 mock galaxies inside an area of 1 deg^2.

I plot the SMF obtained with the 1/Vmax estimator and the SMF fit by the double Schechter model and the double Schechter model deconvolved by the stellar mass uncertainties (which is modeled by the product of a Gaussian and Lorentzian functions), over the entire redshift range ($0.2 \leqslant z < 2.5$) (Figure 26 and Figure 27). Difference between the SMF fits by the non-convolved and deconvolved models becomes apparent only at high-mass end of the SMF, when the stellar uncertainties become significant.

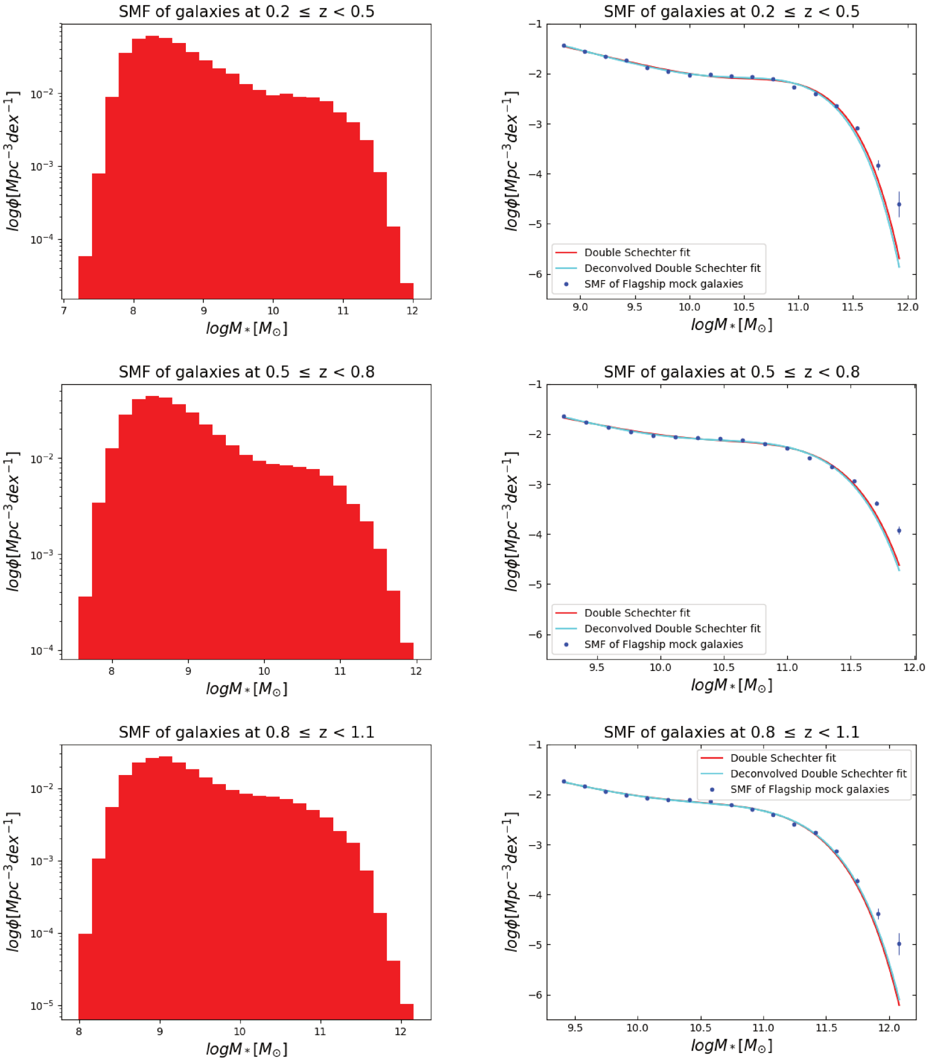

Figure 26: *Left: Three examples of the SMF of Flagship mock galaxies (Section 2.2.2; Carretero et al., 2017), at $0.2 \leqslant z < 0.5$ (top panel), $0.5 \leqslant z < 0.8$ (middle) and $0.8 \leqslant z < 1.1$ (bottom). SMF are derived with 1/Vmax method. Right: SMF of Flagship mock galaxies (blue points) and the SMF fit with a double Schechter function (red line) and a double Schechter function deconvolved by the stellar mass uncertainties (cyan line). Vertical error bars show the Poissonian errors.*

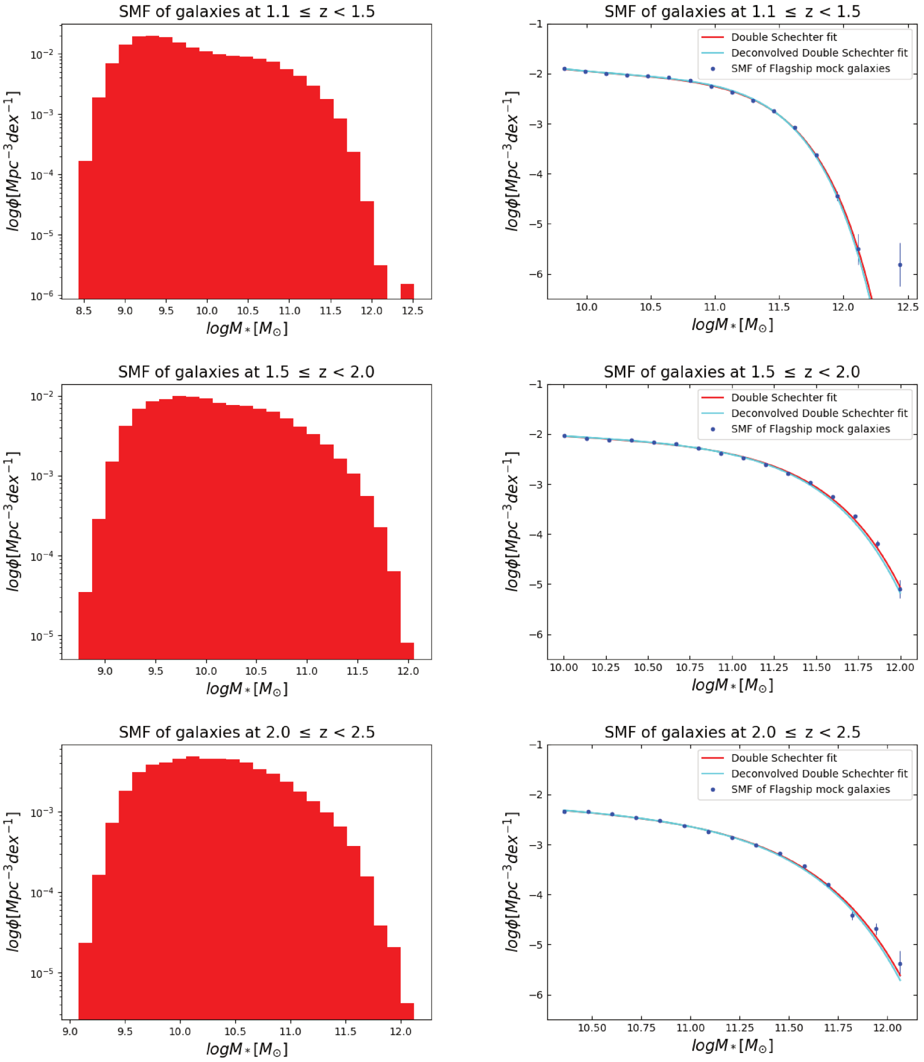

Figure 27: *Left: Three examples of the SMF of Flagship mock galaxies (Section 2.2.2; Carretero et al., 2017), at* $1.1 \leqslant z < 1.5$ *(top panel),* $1.5 \leqslant z < 2.0$ *(middle) and* $2.0 \leqslant z < 2.5$ *(bottom). SMF are derived with 1/Vmax method. Right: SMF of Flagship mock galaxies (blue points) and the SMF fit with a double Schechter function (red line) and a double Schechter function deconvolved by the stellar mass uncertainties (cyan line). Vertical error bars show the Poissonian errors.*

SMF of COSMOS2015 galaxies

We test the *Euclid* pipeline by reproducing the SMF of galaxies and the SMF fit using the COSMOS2015 data (Section 2.2.3; Davidzon et al., 2017), over the redshift range $0.2 \leqslant z < 2.5$, in order to cover the redshift range of the *Euclid Mission*. There are 536 077 objects inside an area of 1.38 $\deg^2$ and 190 650 objects inside the *Deep* area of 0.46 $\deg^2$ of which 85453 are galaxies.

I plot the SMF values from this work and from Davidzon et al., (2017), the double Schechter fit, the double Schechter fit deconvolved by the stellar mass uncertainties (Figure 28, Figure 29). Stellar mass uncertainties are modeled by the product of a Lorentzian and Gaussian with a $\sigma = 0.35$ in order to reproduce the work of Davidzon et al., (2017). In order to have smoother kernel function and more accurate estimate of the convolved Schechter model, I define these functions on an array with many points (~ 1000), instead of using only the SMF points which are sparse, especially at the high mass end (cyan lines in Figure 26 Figure 27, Figure 28, Figure 29). As with the SMF fit on the Flagship mock galaxy catalog, the difference between the non-convolved and deconvolved model starts to be obvious only at high-mass end of the SMF fit.

There are differences in the SMF values of this work and those of Davidzon et al., (2017), possibly coming from using slightly different selection criteria and therefore, a slightly different galaxy sample. For example, there are approximately twice as much galaxies in some redshift bins compared to Davidzon et al., (2017), so there might be some additional selection criteria that are missing.

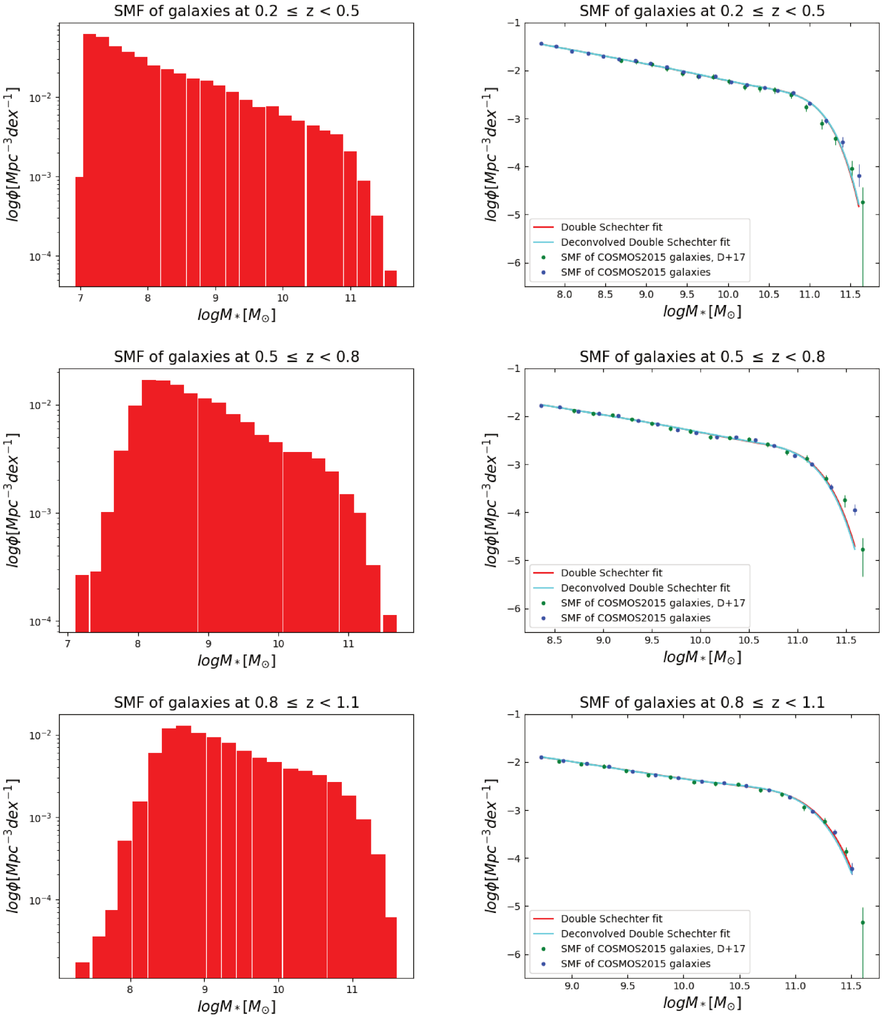

Figure 28: *Left: Three examples of the SMF of COSMOS2015 galaxies (Section 2.2.3; Laigle et al., 2016), at $0.2 \leqslant z < 0.5$ (top panel), $0.5 \leqslant z < 0.8$ (middle) and $0.8 \leqslant z < 1.1$ (bottom). SMF are derived with 1/Vmax method. Right: SMF of COSMOS2015 galaxies from this work (blue points) and from Davidzon et al., (2017) (green points) and the SMF fit with a double Schechter function (red line) and a double Schechter function deconvolved by the stellar mass uncertainties (cyan line). Vertical error bars show the Poissonian errors.*

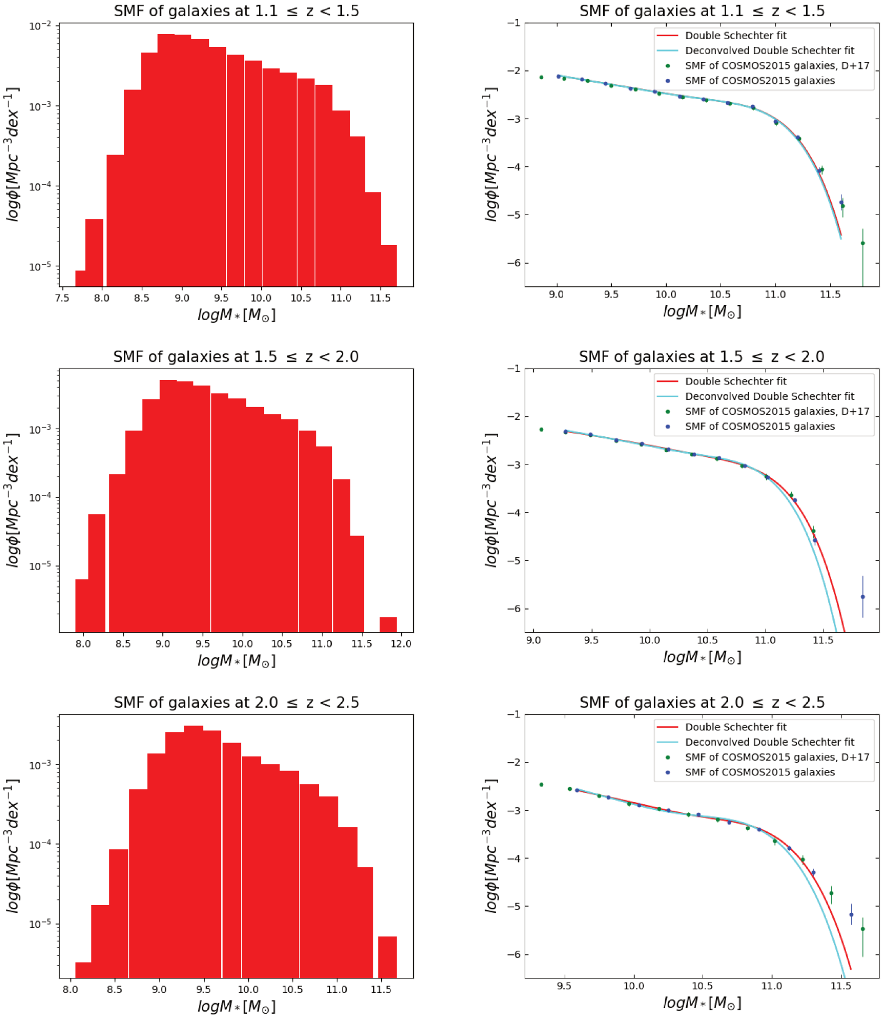

Figure 29: *Left: Three examples of the SMF of COSMOS2015 galaxies (Section 2.2.3; Laigle et al., 2016), at* $1.1 \leqslant z < 1.5$ *(top panel),* $1.5 \leqslant z < 2.0$ *(middle) and* $2.0 \leqslant z < 2.5$ *(bottom). SMF are derived with 1/Vmax method. Right: SMF of COSMOS2015 galaxies from this work (blue points) and from Davidzon et al., (2017) (green points) and the SMF fit with a double Schechter function (red line) and a double Schechter function deconvolved by the stellar mass uncertainties (cyan line). Vertical error bars show the Poissonian errors.*

We report the best-fit parameters of a double Schechter function deconvolved by the stellar mass uncertainties for the COSMOS2015 full sample and star-forming galaxies in the $0.2 \leqslant z < 2.5$ range and quiescent galaxies in the $0.2 \leqslant z < 0.8$ range, whereas for quiescent galaxies in the $0.8 \leqslant z < 2.5$ range we use a deconvolved single Schechter function, following the work of Davidzon et al., (2017) (Table 2). At $0.2 \leqslant z < 2.5$, the values obtained in Davidzon et al., (2017) are fiducial values obtained without constraining the parameter space i.e. with flat priors, while we set bounds for each parameter in the `optimize.minimize` function. Thus, the best-fit parameters change depending on these values.

Table 2: Best-fit parameters of a Schechter function deconvolved by the stellar mass uncertainties for a COSMOS2015 full galaxy sample, star-forming and quiescent galaxies. The parameters are derived using the `optimize.minimize` function and the *Euclid* pipeline.

z-bin	$\log M^{*}[M_\odot]$	$\Phi_1^{*}[10^{-3}\mathrm{Mpc}^{-3}]$	α_1	$\Phi_2^{*}[10^{-3}\mathrm{Mpc}^{-3}]$	α_2
		Full sample			
0.2 – 0.5	10.66	2.50	0.27	1.82	−1.31
0.5 – 0.8	10.67	1.69	0.37	1.41	−1.32
0.8 – 1.1	10.66	2.26	0.15	1.12	−1.35
1.1 – 1.5	10.63	1.55	0.05	0.85	−1.38
1.5 – 2.0	10.52	0.92	0.43	0.79	−1.37
2.0 – 2.5	10.44	0.55	0.57	0.36	−1.67
		Star-forming sample			
0.2 – 0.5	10.63	0.46	0.83	1.54	−1.34
0.5 – 0.8	10.59	0.63	−0.05	1.34	−1.34
0.8 – 1.1	10.57	1.20	−0.10	1.21	−1.36
1.1 – 1.5	10.66	0.65	0.03	0.91	−1.34
1.5 – 2.0	10.64	0.44	−0.06	0.75	−1.34
2.0 – 2.5	10.61	0.44	−0.26	0.25	−1.65
		Quiescent sample			
0.2 – 0.5	10.93	1.53	−0.54	0.16	−1.00
0.5 – 0.8	10.86	1.27	−0.14	0.03	−1.00
0.8 – 1.1	10.69	1.51	0.23		
1.1 – 1.5	10.55	0.55	0.73		
1.5 – 2.0	10.36	0.06	2.23		
2.0 – 2.5	10.36	0.01	2.23		

Fitting the SMF of COSMOS2015 galaxies with the MCMC

We test the MCMC code by fitting the SMF of COSMOS2015 galaxies derived with the 1/Vmax method. Advantage of using the MCMC algorithm compared to the minimization function is that we have access to 1σ uncertainties.

I plot the SMF of a full sample of galaxies at $0.2 \leqslant z < 2.5$, the double Schechter fit, and deconvolved double Schechter fit using the MCMC code. Moreover, I plot the deconvolved double Schechter fits from the *Euclid* pipeline and from Davidzon et al., (2017) for comparison (Figure 30).

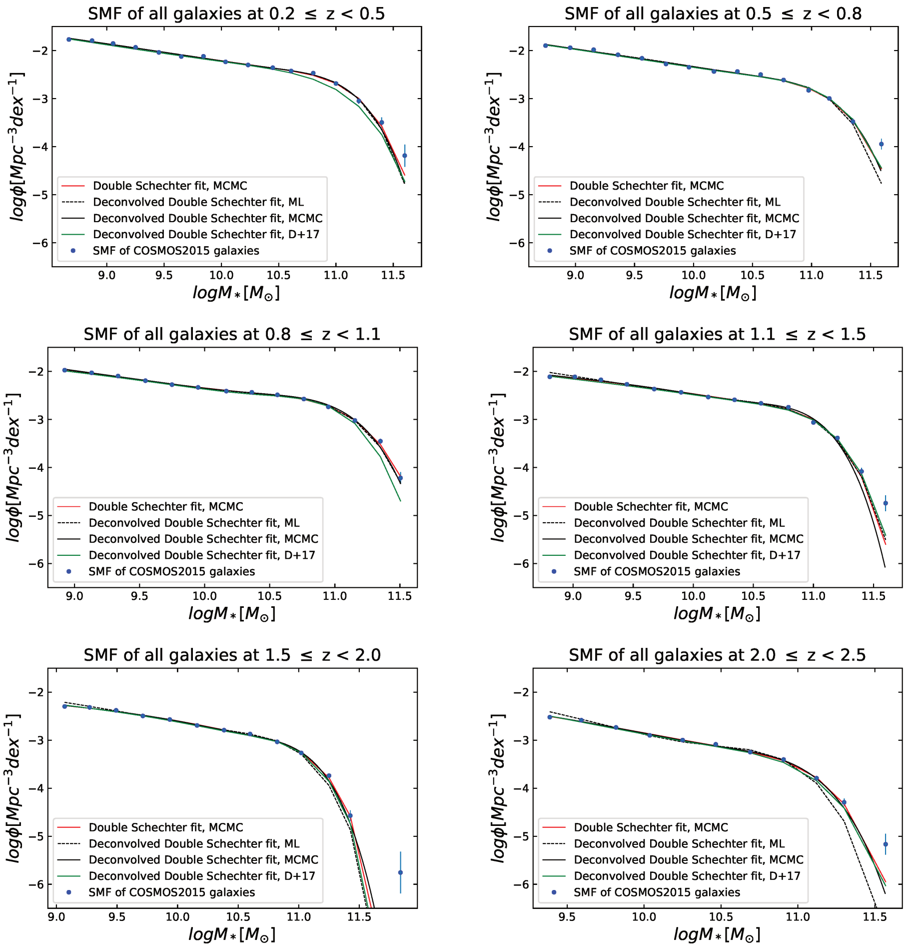

Figure 30: *SMF of COSMOS2015 galaxies from this work (blue points), a double Schechter function fit using the MCMC (red line), and deconvolved double Schechter using the maximum likelihood and MCMC (black dashed and solid lines, respectively). Vertical error bars show the Poissonian errors.*

We report the best-fit parameters and their uncertainties of a deconvolved double Schechter model for a full sample and star-forming galaxies at $0.2 \leqslant z < 2.5$, and quiescent galaxies at $0.2 \leqslant z < 0.8$ range, and a deconvolved single Schechter function for quiescent galaxies at $0.8 \leqslant z < 2.5$, following the work of Davidzon et al., (2017) (Table 3). Unlike Davidzon et al., (2017), I constrain the parameter space by setting bounds for each parameter in the prior function.

Table 3: Best-fit parameters and their uncertainties of a deconvolved Schechter model for a full galaxy sample, star-forming and quiescent galaxies. The parameters are derived using the MCMC.

z-bin	$\log M^*[M_\odot]$	$\Phi_1^*[10^{-3}\text{Mpc}^{-3}]$	α_1	$\Phi_2^*[10^{-3}\text{Mpc}^{-3}]$	α_2
			Full sample		
$0.2-0.5$	$10.67^{+0.08}_{-0.07}$	$2.54^{+0.29}_{-0.32}$	$0.18^{+0.28}_{-0.30}$	$1.69^{+0.26}_{-0.28}$	$-1.33^{+0.03}_{-0.03}$
$0.5-0.8$	$10.75^{+0.07}_{-0.06}$	$1.68^{+0.20}_{-0.22}$	$0.03^{+0.21}_{-0.22}$	$1.13^{+0.14}_{-0.15}$	$-1.36^{+0.02}_{-0.02}$
$0.8-1.1$	$10.65^{+0.03}_{-0.03}$	$2.40^{+0.15}_{-0.14}$	$0.17^{+0.15}_{-0.16}$	$1.17^{+0.14}_{-0.14}$	$-1.36^{+0.03}_{-0.03}$
$1.1-1.5$	$10.50^{+0.04}_{-0.04}$	$1.30^{+0.10}_{-0.10}$	$0.75^{+0.17}_{-.17}$	$1.38^{+0.10}_{-0.10}$	$-1.25^{+0.02}_{-0.02}$
$1.5-2.0$	$10.50^{+0.03}_{-0.03}$	$0.57^{+0.06}_{-0.06}$	$0.95^{+0.18}_{-0.19}$	$1.10^{+0.08}_{-0.08}$	$-1.24^{+0.02}_{-0.02}$
$2.0-2.5$	$10.53^{+0.07}_{-0.06}$	$0.41^{+0.06}_{-0.06}$	$0.50^{+0.32}_{-0.34}$	$0.42^{+0.09}_{-0.09}$	$-1.47^{+0.05}_{-0.06}$
			Star-forming sample		
$0.2-0.5$	$10.52^{+0.22}_{-0.12}$	$0.68^{+0.26}_{-0.38}$	$0.87^{+0.41}_{-0.45}$	$1.71^{+0.37}_{-0.45}$	$-1.34^{+0.03}_{-0.03}$
$0.5-0.8$	$10.36^{+0.07}_{-0.07}$	$1.16^{+0.16}_{-0.16}$	$0.67^{+0.28}_{-0.29}$	$1.79^{+0.24}_{-0.23}$	$-1.32^{+0.02}_{-0.02}$
$0.8-1.1$	$10.51^{+0.08}_{-0.07}$	$1.32^{+0.17}_{-0.19}$	$0.15^{+0.27}_{-0.30}$	$1.36^{+0.19}_{-0.20}$	$-1.35^{+0.02}_{-0.03}$
$1.1-1.5$	$10.41^{+0.04}_{-0.04}$	$0.49^{+0.07}_{-0.06}$	$1.32^{+0.18}_{-0.18}$	$1.67^{+0.10}_{-0.10}$	$-1.19^{+0.01}_{-0.01}$
$1.5-2.0$	$10.57^{+0.07}_{-0.05}$	$0.34^{+0.07}_{-0.07}$	$0.61^{+0.25}_{-0.32}$	$1.00^{+0.10}_{-0.11}$	$-1.25^{+0.02}_{-0.02}$
$2.0-2.5$	$10.49^{+0.07}_{-0.06}$	$0.40^{+0.06}_{-0.06}$	$0.49^{+0.34}_{-0.36}$	$0.46^{+0.10}_{-0.10}$	$-1.46^{+0.06}_{-0.06}$
			Quiescent sample		
$0.2-0.5$	$10.81^{+0.06}_{-0.06}$	$1.87^{+0.16}_{-0.17}$	$-0.16^{+0.20}_{-0.18}$	$0.25^{+0.10}_{-0.13}$	$-1.08^{+0.06}_{-0.13}$
$0.5-0.8$	$10.82^{+0.04}_{-0.04}$	$1.34^{+0.06}_{-0.07}$	$-0.05^{+0.10}_{-0.09}$	$0.03^{+0.02}_{-0.01}$	$-1.10^{+0.08}_{-0.16}$
$0.8-1.1$	$10.68^{+0.02}_{-0.02}$	$1.50^{+0.05}_{-0.05}$	$0.24^{+0.05}_{-0.04}$		
$1.1-1.5$	$10.45^{+0.03}_{-0.03}$	$0.47^{+0.03}_{-0.03}$	$1.11^{+0.11}_{-0.10}$		
$1.5-2.0$	$10.27^{+0.05}_{-0.05}$	$0.02^{+0.01}_{-0.01}$	$3.11^{+0.41}_{-0.37}$		
$2.0-2.5$	$10.51^{+0.14}_{-0.13}$	$0.02^{+0.01}_{-0.01}$	$1.79^{+0.89}_{-0.77}$		

DISCUSSION

Stellar mass assembly of Flagship mock galaxies

I overplot the SMF and SMF fit with a deconvolved double Schechter function, over the entire redshift range ($0.2 \leqslant z < 2.5$), in order to show the evolution of the SMF for the full sample of galaxies (Figure 31, top panel). Next, I split the Flagship mock galaxies into star-forming and quiescent galaxies, in order to quantify the evolution of the SMF of different subsamples of galaxies. I define star-forming galaxies as those with a $\log(\text{sSFR}) \geqslant -11$, and those with $\log(\text{sSFR}) < -11$ as quiescent. The population of quiescent galaxies is roughly constant at the high-mass end, while it increases at the low mass end over the entire redshift range (Figure 31, bottom panel). Moreover, the population of a full and star-forming samples of galaxies increase from $2.0 < z \leqslant 2.5$ to $1.1 < z \leqslant 1.5$, while they decrease between $1.1 < z \leqslant 1.5$ and $0.2 < z \leqslant 0.5$ (Figure 31, top and middle panels). There might be some problems, but there was not enough time to go deeper in this issue. Thus, it is not possible to draw any conclusions on the stellar mass assembly of Flagship mock galaxy sample.

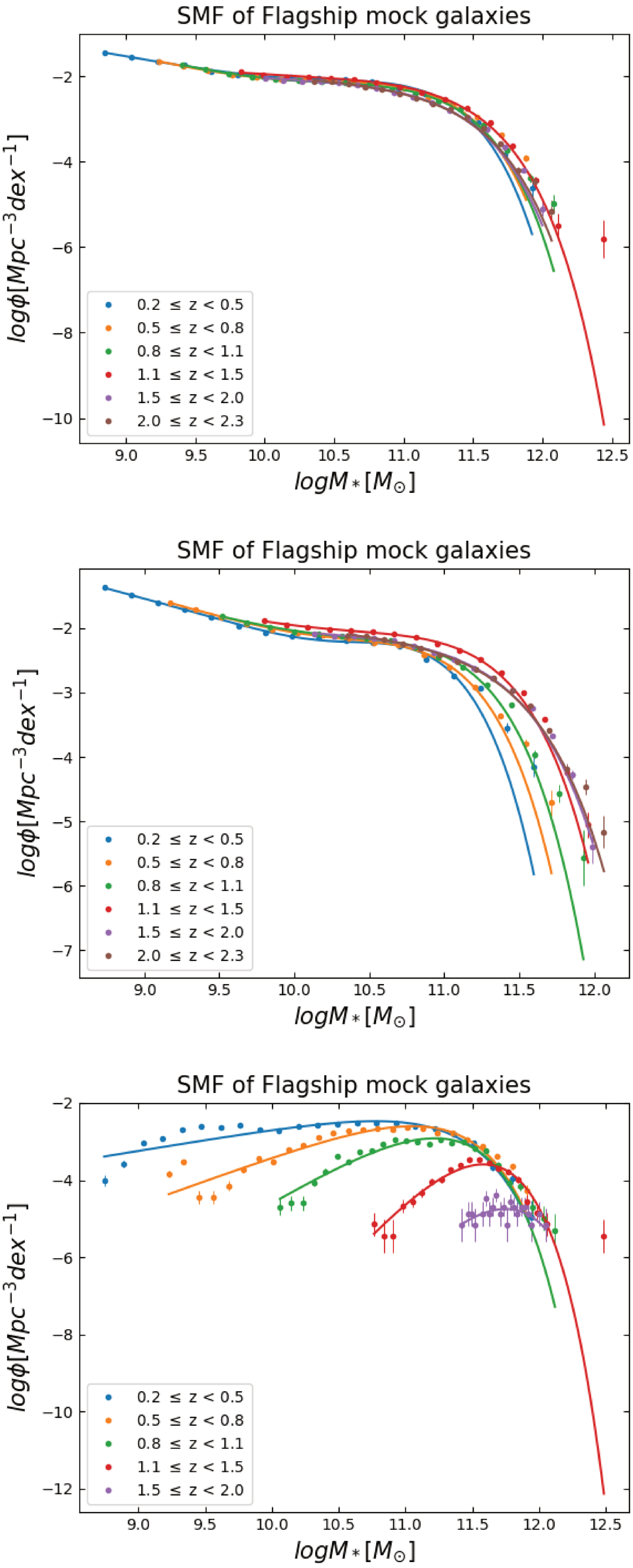

Figure 31: *SMF and SMF fit with a deconvolved double Schechter function on Flagship mock galaxies (Section 2.2.2; Carretero et al., 2017), over the entire redshift range* ($0.2 \leqslant z < 2.5$) *for a full sample (top), blue* ($\log(\text{sSFR}) \geqslant -11$) *(middle) and red (bottom)* ($\log(\text{sSFR}) < -11$) *galaxies. Vertical error bars show the Poissonian errors.*

Stellar mass assembly of COSMOS2015 galaxies

I overplot the SMF and SMF fit with a double Schechter function deconvolved by the stellar mass uncertainties over the entire redshift range ($0.2 \leqslant z < 2.5$) for a full sample, star-forming ($\log(\mathrm{sSFR}) \geqslant -11$) and quiescent ($\log(\mathrm{sSFR}) < -11$) galaxies (Figure 32, top, middle and bottom panels, respectively). Unlike the SMF evolution for the Flagship data (Figure 31), there is a consistent SMF evolution for the COSMOS2015 data, with galaxy populations increasing steadily from $2.0 < z < 2.5$ to $0.2 < z < 0.5$, i.e. in the redshift range covered by the future *Euclid Mission* ($0.2 < z < 2.5$). For the full sample, there is a number density increase over the entire stellar mass range. However, the evolution is slightly faster at the high-mass end of the SMF (Figure 32, top panel; Davidzon et al., 2017). For instance, the stellar mass number density of the full sample of $M_* \sim 10^{9.5} M_\odot$ galaxies increases by $\sim 0.52 \pm 0.16$ dex between $2.0 < z < 2.5$ and $0.2 < z < 0.5$ (of which $\sim 0.39 \pm 0.15$ dex between $2.0 < z < 2.5$ and $0.8 < z < 1.1$), while for $M_* \sim 10^{10.5} M_\odot$ galaxies it grows by $\sim 0.75 \pm 0.11$ dex ($\sim 0.66 \pm 0.09$ dex), and for $M_* \sim 10^{11.5} M_\odot$ galaxies it increases by $\sim 1.47 \pm 0.78$ dex ($\sim 1.26 \pm 0.66$ dex), over the same redshift ranges. Thus, the evolution of the full sample of galaxies is mass-dependent, with intermediate and high-mass galaxies evolving faster than the low-mass end of the SMF over the redshift range taken into account, in agreement with the result of Davidzon et al., (2017), that observed flattening of the SMF and sharpening of the *knee* of the function over a wider redshift range ($0.2 \leqslant z < 5.5$ and $0.2 \leqslant z < 4.0$ for the full and star-forming samples, respectively). However, this is not consistent with some results from the literature, with some works showing no significant evolution of the shape of the SMF (Tomczak et al., 2014), or a faster mass build-up of the low-mass end of the global SMF at lower z (*downsizing*; e.g. Pozzetti et al., 2010; Ilbert et al., 2013).

Next, the stellar mass number density of a subsample of $M_* \sim 10^{9.5} M_\odot$ star-forming galaxies grows by $\sim 0.47 \pm 0.18$ dex between $2.0 < z < 2.5$ and $0.2 < z < 0.5$ ($\sim 0.38 \pm 0.14$ dex between $2.0 < z < 2.5$ and $0.8 < z < 1.1$), for $\log(M_*) \sim 10^{10.5} M_\odot$ galaxies it increases by $\sim 0.46 \pm 0.23$ dex ($\sim 0.51 \pm 0.11$ dex) and for $(M_*) \sim 10^{11.1} M_\odot$ galaxies it does not show statistically significant evolution $\sim 0.53 \pm 0.53$ ($\sim 0.38 \pm 0.35$) over the same redshift range. A population of massive $(M_*) \sim 10^{11.5}$ star-forming galaxies is not detected at lower redshift $z < 1.1$, probably since they are already in the process of quenching. Therefore, the mass build-up of the star-forming subsample is in general mass independent, the shape of the SMF is roughly the same, and the overall evolution is weak over the redshift range taken into account (e.g. Arnouts et al., 2007; Pozzetti et al., 2010; Tomczak et al., 2014).

A population of low-mass $M_* \sim 10^{9.5} M_\odot$ quiescent galaxies is not observed at the highest redshift range $2.5 < z < 2.0$, and it first appears at $z \sim 1.5$. The stellar mass number density of low-mass quiescent galaxies $M_* \sim 10^{9.5} M_\odot$ grows by $\sim 2.04 \pm 0.24$ dex between $1.1 < z < 1.5$ and $0.2 < z < 0.5$ (of which $\sim 1.06 \pm 0.15$ dex between $1.1 < z < 1.5$ and $0.8 < z < 1.1$). Next, the stellar mass number density of the $\log(M_*) \sim 10^{10.5} M_\odot$ quiescent galaxies increases by $\sim 2.13 \pm 0.48$ dex between $2.5 < z < 2.0$

and $0.2 < z < 0.5$ (of which $\sim 1.90 \pm 0.47$ dex between $2.5 < z < 2.0$ and $0.8 < z < 1.1$), and finally, for $\log(M_*) \sim 10^{11.4} M_\odot$ quiescent galaxies it increases by $\sim 1.88 \pm 1.28$ dex ($\sim 1.60 \pm 1.53$ dex) over the same redshift ranges. Therefore, the evolution of the quiescent sample is mass dependent. A clear flattening of the low-mass end of the SMF of quiescent subsample at lower redshifts suggests that populations of low and intermediate-mass quiescent galaxies have assembled their stellar mass at a later epoch $z < 1$, compared to their high-mass counterparts which emerged at earlier epoch $1 < z < 2$ (Figure 32, bottom panel) (Pozzetti et al., 2010; Ilbert et al., 2010, 2013; Davidzon et al., 2017). This confirms the so called *downsizing effect* (Cowie et al., 1996; Brinchmann and Ellis, 2000; Heavens et al., 2004; Juneau et al., 2005; Bundy et al., 2006; Panter et al., 2007; Vergani et al., 2008; Pérez-González et al., 2008; Ilbert et al., 2010; Muzzin et al., 2012; Pacifici et al., 2016).

There is a build-up of all galaxies around the M^*, over the entire redshift range taken into account ($0.2 < z < 2.5$), and beyond ($z > 3$; e.g. Davidzon et al., 2017), indicating that, when galaxies reach a certain stellar mass M^* (i.e. the mass that defines the change in the slope of the SMF), they start quenching, mass growth of galaxies through star formation slows down, and galaxies start to accumulate at $\sim M^*$ (i.e. *mass quenching*; Thomas et al., 2005; Bundy et al., 2006; Vergani et al., 2008; Peng et al., 2010, 2012; Ilbert et al., 2010, 2013; Guglielmo et al., 2015; Tomczak et al., 2016; Sklias et al., 2017). Next, low and intermediate-mass quiescent galaxies quench at a later epoch, possibly through *environmental quenching* of satellite galaxies and galaxy merging (Kauffmann et al., 2004; Peng et al., 2010, 2012; Strazzullo et al., 2013; Delaye et al., 2014; Guglielmo et al., 2015; Foltz et al., 2018).

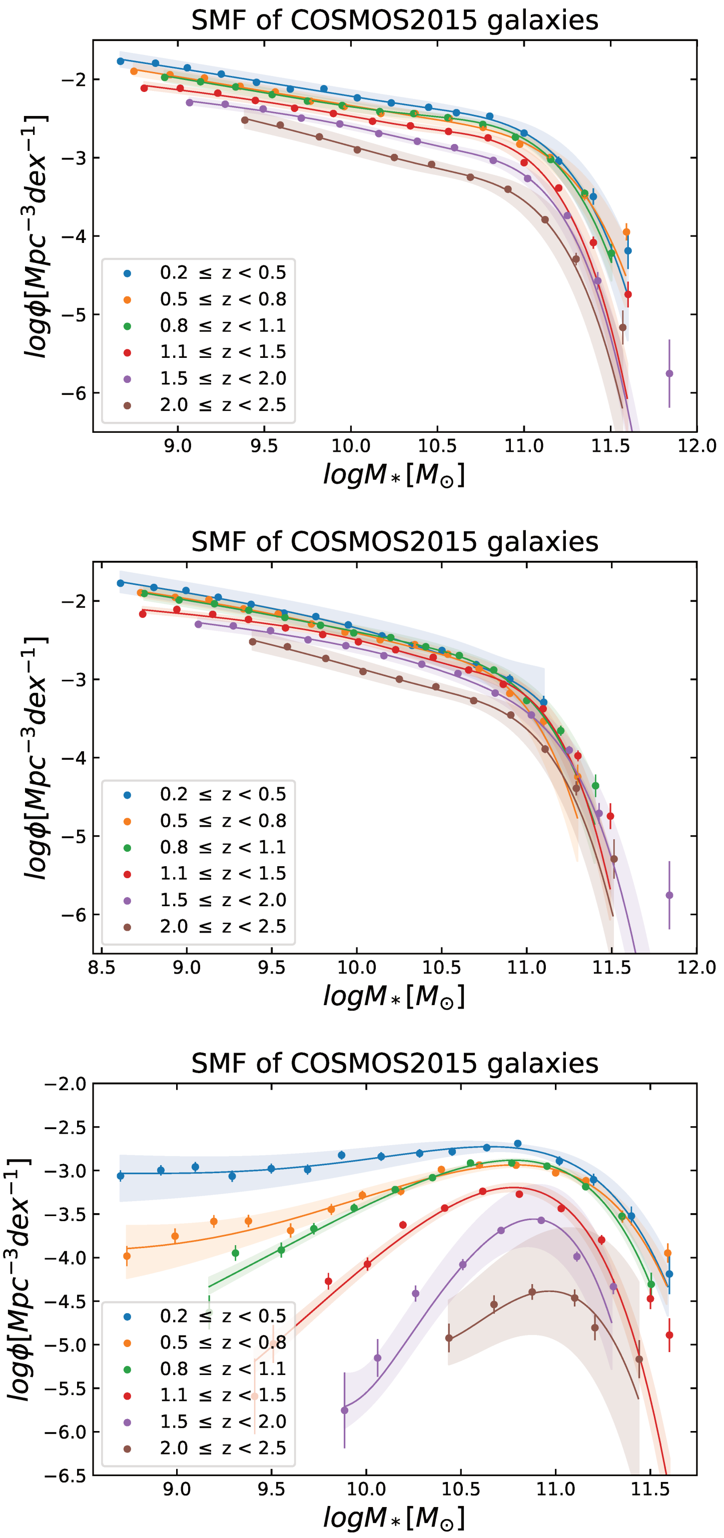

Figure 32: *SMF estimate with the 1/Vmax method (filled circles), and fit of the SMF with a deconvolved double Schechter function (solid lines) on COSMOS2015 galaxies (Section 2.2.3; Laigle et al., 2016), over the entire redshift range* $(0.2 \leqslant z < 2.5)$ *for a full sample (top), blue* $(\log(\text{sSFR}) \geqslant -11)$ *(middle) and red (bottom)* $(\log(\text{sSFR}) < -11)$ *galaxies. Vertical error bars show the Poissonian errors. Shaded areas are* 1σ *uncertainty of the Schechter function fit.*

Following the work of Ilbert et al., (2010), I split the star-forming sample of galaxies into *high activity* ($\log(\text{sSFR}) \geqslant -9.5$) and *intermediate activity* galaxies ($-9.5 > \log(\text{sSFR}) \geqslant -11$), and I overplot the SMF and SMF fit of the two subsamples for all the redshift bins (Figure 33, top and bottom panels, respectively). The evolution of the SMF of both subsamples is mass dependent. The $M_* \sim 10^{9.5} M_\odot$ *high activity* star-forming galaxies do not show significant evolution $\sim 0.1 \pm 0.2$ dex between $2.5 < z < 2.0$ and $0.2 < z < 0.5$. Next, there is an increase in the number density of the $M_* \sim 10^{10.5} M_\odot$ intermediate-mass *high activity* galaxies by $\sim 0.3 \pm 0.1$ dex, between $2.5 < z < 2.0$ and $0.8 < z < 1.1$, followed by a significant drop of $\sim 1.25 \pm 0.65$ dex, between $0.8 < z < 1.1$ and $0.2 < z < 0.5$. Moreover, the $M_* \sim 10^{11} M_\odot$ *high activity* star-forming galaxies shows a hint of a decrease in the number density by 0.52 ± 0.43, between $2.5 < z < 2.0$ and $0.8 < z < 1.1$, whereas the most massive galaxies are not observed ($M > 10^{11} M_\odot$) at lower redshift $z < 1$. These galaxies have probably already evolved to *intermediate activity* or quiescent galaxies at earlier epoch $z > 1$ (Pozzetti et al., 2010; Ilbert et al., 2010). Besides, there is a gradual shift of the *high activity* star-forming population to lower masses with cosmic time (Figure 33, top panel), indicating a relocation of the high star-formation activity from high-mass galaxies to intermediate and low-mass galaxies over cosmic time (i.e. *downsizing effect*; Bundy et al., 2006; Ilbert et al., 2010).

Furthermore, the evolution of the *intermediate activity* star-forming galaxies is strongly mass dependent, with a population of low-mass galaxies growing much faster than their high-mass counterparts (Figure 33, bottom panel), in a similar way as for the quiescent sample. The stellar mass number density of the low-mass $M \sim 10^{9.5} M_\odot$ galaxies grows by $\sim 3.4 \pm 0.7$ dex, between $2.5 < z < 2.0$ and $0.2 < z < 0.5$, whereas for intermediate-mass $M \sim 10^{10.5} M_\odot$ galaxies it increases by $\sim 2.2 \pm 0.3$ dex over the same redshift range. Finally, the number density of massive $M \sim 10^{11.3} M_\odot$ galaxies increases by $\sim 0.9 \pm 0.7$ between $2.5 < z < 2.0$ and $0.8 < z < 1.1$. At lower redshifts, their number density remains roughly constant, probably since the rate of which these massive galaxies migrate to the *red sequence* is similar to the rate of which the *high activity* galaxies move to the *intermediate activity* subsample.

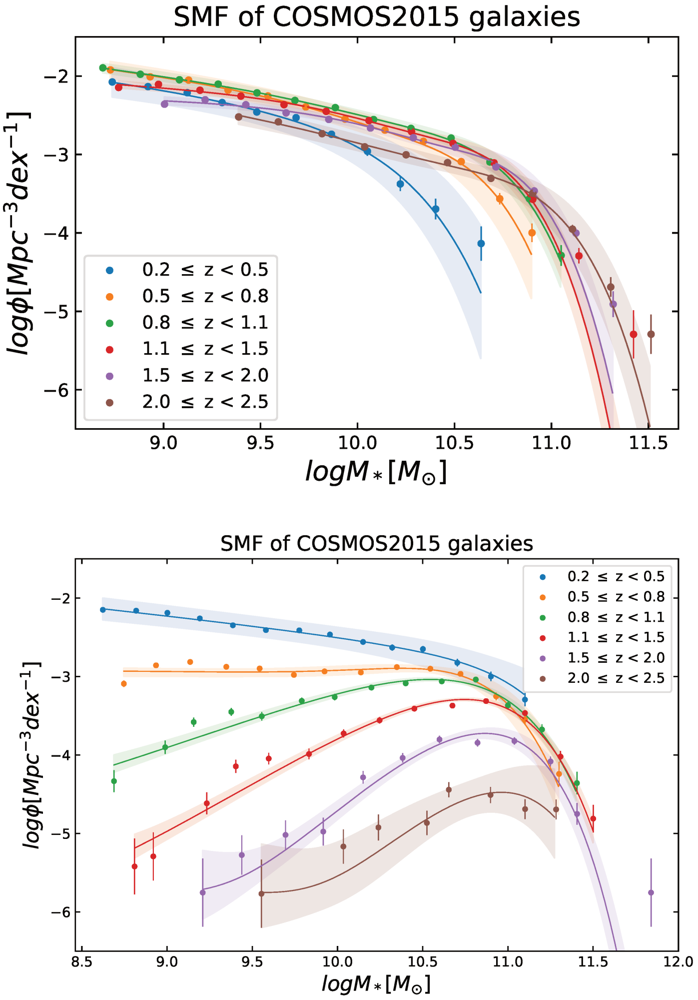

Figure 33: *SMF estimate with the 1/Vmax method (filled circles), and fit of the SMF with a deconvolved double Schechter function (solid lines), on COSMOS2015 star-forming galaxies (Section 2.2.3; Laigle et al., 2016) over the entire redshift range ($0.2 \leqslant z < 2.5$) for high activity ($\log(\mathrm{sSFR}) \geqslant -9.5$) (top panel) and intermediate activity star-forming galaxies ($-9.5 > \log(\mathrm{sSFR}) \geqslant -11$) (bottom). Vertical error bars show the Poissonian errors. Shaded areas are 1σ uncertainty of the Schechter function fit.*

Evolution of Schechter parameters

I plot the best-fit parameters of the Schechter models deconvolved by the stellar mass uncertainties as a function of redshift, derived using the maximum likelihood method with the *Euclid* pipeline (Table 2), the MCMC algorithm (Table 3) and from the work of Davidzon et al., (2017) (Figure 34, Figure 35, Figure 36, dashed-dotted black, solid black and dashed gray lines). The best-fit parameters for the full sample of galaxies (derived using the MCMC) from this work are mostly within 1σ of the best-fit parameters from the work of Davidzon et al., (2017) (Figure 34), gray area). However, the difference between the best-fit parameters of star-forming and quiescent galaxies from this work and from Davidzon et al., (2017) is mostly $< 3\sigma$ (Figure 35, and Figure 36, respectively), probably since the two populations are not entirely the same, due to a different selection method used to split the full sample into star-forming and quiescent subsamples.

The characteristic stellar mass parameter $\log(M^*)$ is roughly constant $\Delta\log(M^*) \sim 0.15 \pm 0.11$ dex for the full sample (Figure 34, top panel; see Muzzin et al., 2013b; Tomczak et al., 2014; Mortlock et al., 2015; Davidzon et al., 2017) and $\Delta\log(M^*) \sim 0.03 \pm 0.23$ dex for star-forming galaxies (Figure 35, top panel; see Peng et al., 2010; Davidzon et al., 2017). However, the $\log(M^*)$ parameter increases by $\Delta\log(M^*) \sim 0.4 \pm 0.1$ dex for quiescent galaxies (Figure 36, top panel; see Ilbert et al., 2010), which is a consequence of the mass build-up of quiescent galaxies, probably due to post-quenching *dry* merging at the high-mass end, where quiescent galaxies dominate the galaxy population (Peng et al., 2010).

The normalization factor Φ_1^* parameter increases by $\Delta\Phi_1 \sim 2.0 \pm 0.2 \times 10^{-3}$ Mpc^{-3} for the full (Figure 34 middle left panel), by $\Delta\Phi_1 \sim 0.9 \pm 0.2 \times 10^{-3}$ Mpc^{-3} for star-forming (Figure 35, middle left panel), and by $\Delta\Phi_1 \sim 1.5 \pm 0.05 \times 10^{-3}$ Mpc^{-3} for quiescent sample (Figure 36, middle left panel) over the redshift range $1.0 < z < 2.5$. After reaching a peak at $z \sim 1$, it does not show statistically significant evolution (see Ilbert et al., 2010; Ilbert et al., 2013; Davidzon et al., 2017). The Φ_2^* parameter shows a similar evolution, increasing by $\Delta\Phi_2 \sim 1.3 \pm 0.3 \times 10^{-3}$ Mpc^{-3} for the full sample (Figure 34, middle panels) and by $\Delta\Phi_2 \sim 1.3 \pm 0.5 \times 10^{-3}$ Mpc^{-3} for star-forming sample over the redshift range $0.2 < z < 2.5$ (Figure 35, middle panels).

Finally, there is a significant decrease of the α_1 parameter $\Delta\alpha_1 \sim 2.5 \pm 0.9$ for quiescent galaxies (Figure 36, bottom left panel), which is a consequence of the stellar mass build-up of low-mass quiescent galaxies (Ilbert et al., 2010; Ilbert et al., 2013), possibly driven by the *environmental quenching* (Peng et al., 2010). On the other hand, the α_1 parameter does not show statistically significant evolution $\Delta\alpha_1 \sim 0.33 \pm 0.45$ for the full sample Figure 34 bottom left panel) and $\Delta\alpha_1 \sim 0.41 \pm 0.57$ for star-forming galaxies (Figure 35 bottom left panels) (Peng et al., 2010; Ilbert et al., 2013; Davidzon et al., 2017). Next, there is a slight decrease of the slope parameter α_2 with redshift, $\Delta\alpha_2 \sim 0.14 \pm 0.06$ and $\Delta\alpha_2 \sim 0.12 \pm 0.07$, for the full (Figure 34; bottom right panel) and star-forming sample (Figure 35; bottom right panel), respectively.

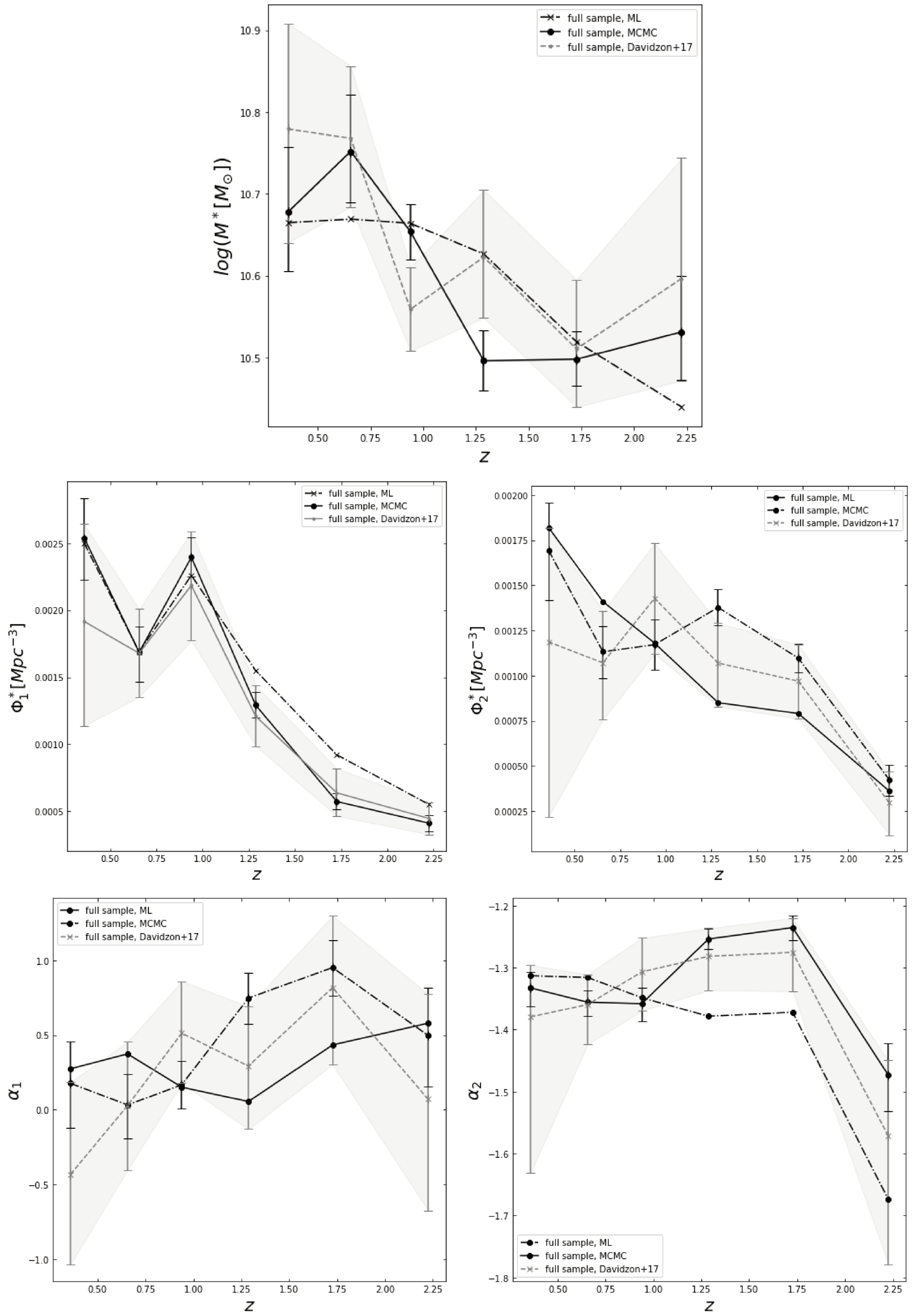

Figure 34: *Deconvolved Schechter function parameters for a full sample of galaxies: the characteristic stellar mass* M^* *(top), normalization factors* Φ_1 *and* Φ_2 *(middle) and slope parameters* α_1 *and* α_2 *(bottom). The best-fit parameters (and their uncertainties) from the Euclid pipeline are shown as dashed-dotted black lines, the MCMC code as solid black lines, and from Davidzon et al., (2017) as dashed gray lines.* 1σ *uncertainties from Davidzon et al., (2017) are shown as shaded areas.*

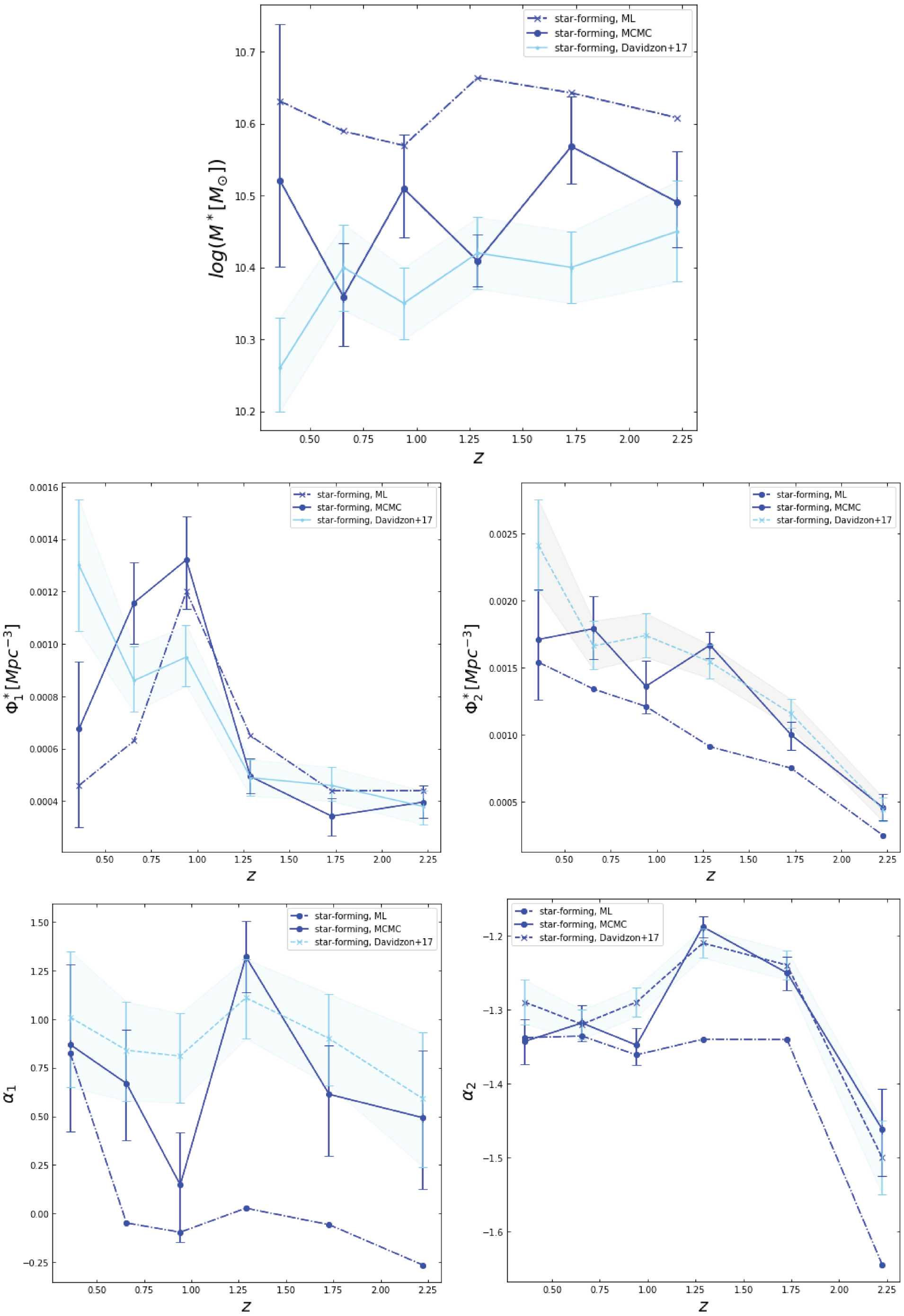

Figure 35: *Deconvolved Schechter function parameters for star-forming galaxies: the characteristic stellar mass* M^* *(top), normalization factors* Φ_1 *and* Φ_2 *(middle) and slope parameters* α_1 *and* α_2 *(bottom). The best-fit parameters (and their uncertainties) from the Euclid pipeline are shown as dashed-dotted blue lines, the MCMC code as solid blue lines, and from Davidzon et al., (2017) as dashed sky-blue lines.* 1σ *uncertainties from Davidzon et al., (2017) are shown as shaded areas.*

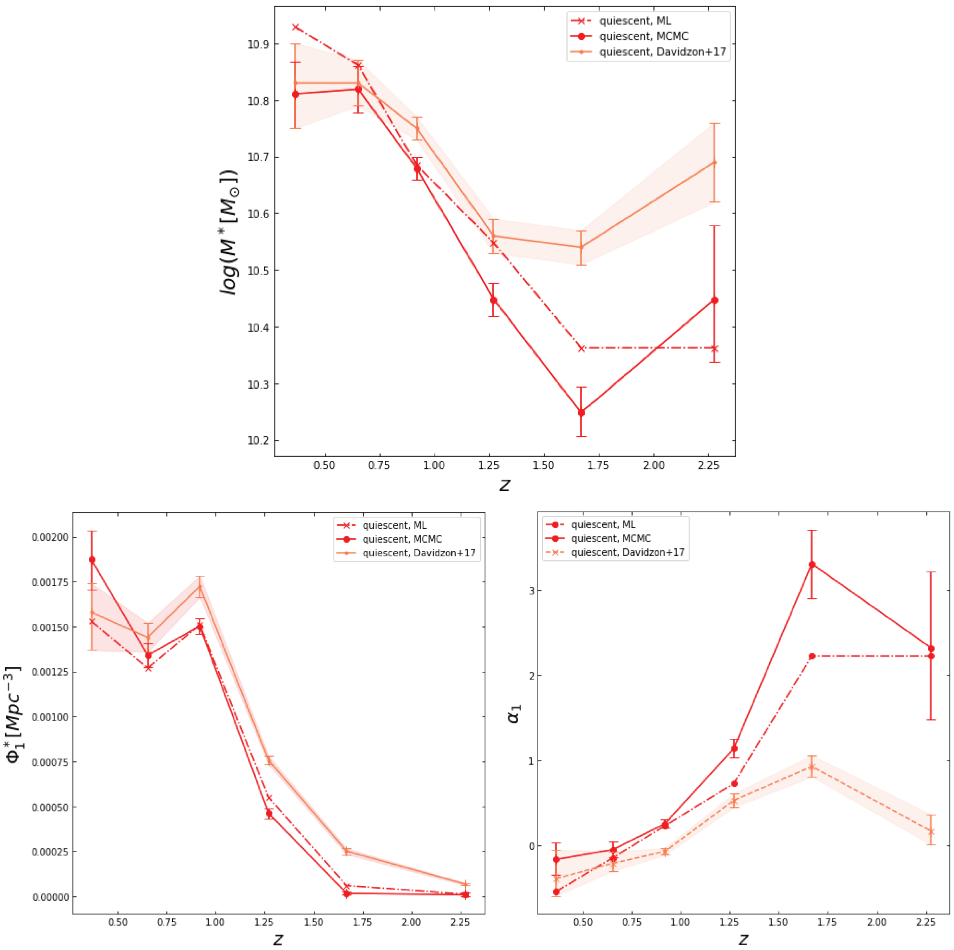

Figure 36: *Deconvolved Schechter function parameters for quiescent galaxies: the characteristic stellar mass* M^* *(top), normalization factors* Φ_1 *and* Φ_2 *(middle) and slope parameters* α_1 *and* α_2 *(bottom). The best-fit parameters (and their uncertainties) from the Euclid pipeline are shown as dashed-dotted red lines, the MCMC code as solid red lines and from Davidzon et al., (2017) as dashed coral lines.* 1σ *uncertainties from Davidzon et al., (2017) are shown as shaded areas.*

Stellar mass density

I derive the stellar mass density ρ_*, by integrating the Schechter function between $10^8 - 10^{13} M_\odot$ (Equation 7) for the full, star-forming and quiescent galaxy samples (Figure 37, black, blue and red solid lines, respectively). Following the work of Davidzon et al., (2017), I use the double Schechter function as a model to fit the SMF, with the best-fit parameters of the deconvolved double Schechter model (Table 2 and Table 3), derived with the maximum likelihood and the MCMC methods (Figure 37, dashed-dotted and solid lines, respectively). I plot the stellar mass densities of the full sample, and compute and plot the stellar mass densities of star-forming and quiescent galaxies from the work of Davidzon et al., (2017) (Figure 37, gray, sky-blue and coral dashed lines, respectively).

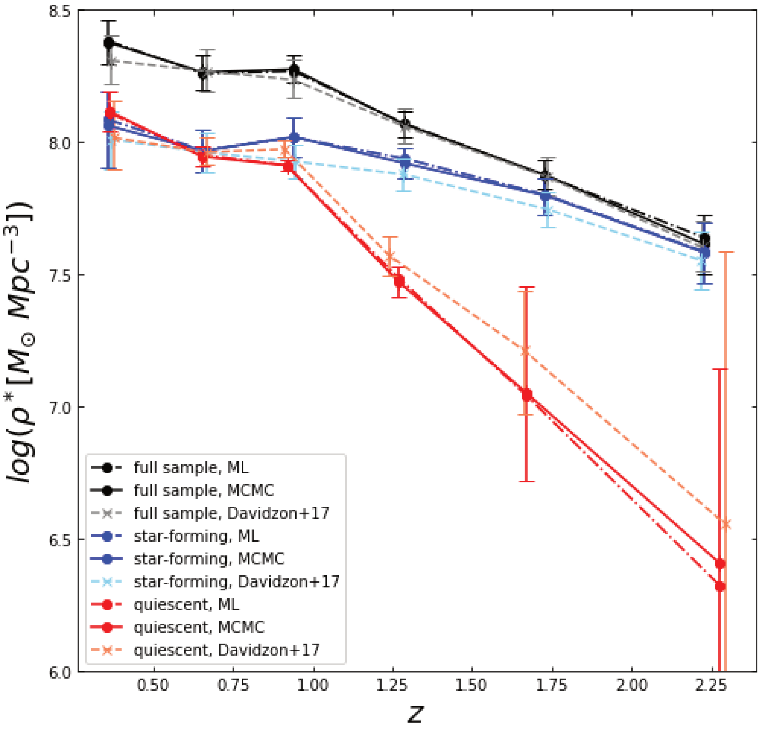

Figure 37: *Stellar mass density as a function of median redshift, for the full sample, star-forming and quiescent galaxies (black, blue and red solid lines, respectively), derived using the maximum likelihood (dashed-dotted lines) and the MCMC method (solid lines). Stellar mass density values from the work of Davidzon et al., 2017 for full, active and passive samples are shown for comparison (gray, sky-blue and coral lines, respectively).*

The stellar mass densities from this work are in a good agreement and within 1σ of the values from Davidzon et al., (2017). The two estimates agree well for the full sample, while the ρ_* estimates from this work are up to ~ 0.1 dex higher for the star-forming sample, and up to ~ 0.2 dex lower for the quiescent sample, than the values from Davidzon et al., (2017). This is probably due to the fact that the sSFR method is more restrictive in classifying the population of quiescent galaxies compared to the color-color method used to select the population of passive galaxies in Davidzon et al., (2017). At higher redshifts, the difference between the two methods increases and there are less quiescent galaxies compared to the passive galaxies (see e.g. Ilbert et al., 2013 for more details).

The global stellar mass density increases by $\sim 0.76 \pm 0.14$ dex between $2.0 < z < 2.5$ and $0.2 < z < 0.5$, of which $\sim 0.66 \pm 0.12$ dex between $2.0 < z < 2.5$ and $0.8 < z < 1.1$. The stellar mass density of the star-forming sample shows an increase of $\sim 0.48 \pm 0.19$ dex, i.e. $\sim 0.44 \pm 0.14$ dex, over the same redshift ranges. Finally, the stellar mass density of quiescent galaxies increases by $\sim 1.71 \pm 0.74$ dex between $2.0 < z < 2.5$ and $0.2 < z < 0.5$, of which $\sim 1.50 \pm 0.74$ dex between $2.0 < z < 2.5$ and $0.8 < z < 1.1$. This is in agreement with previous works that show a modest evolution of the ρ_* at low redshift $z < 1$ (e.g. Brinchmann and Ellis, 2000; Fontana et al., 2004; Moustakas et al., 2013), preceded by a stronger evolution during the *cosmic noon epoch* (e.g. Ilbert et al., 2010, 2013).

Furthermore, there is a moderate evolution of the ρ_* of star-forming galaxies compared to the ρ_* of quiescent galaxies over the redshift range $0 < z < 2-3$, consistent with similar works from the literature (e.g. Arnouts et al., 2007; Ilbert et al., 2010; Muzzin et al., 2013b; Tomczak et al., 2014; Mortlock et al., 2015). Moreover, the stellar mass density ρ_* of quiescent galaxies significantly grows during the epoch of $1 < z < 2.5$ (Ilbert et al., 2010, 2013), and surpasses the ρ_* of star-forming galaxies at $z \sim 0.75 - 1$ (Pozzetti et al., 2003; Fontana et al., 2004, 2009; Williams et al., 2009; Ilbert et al., 2010; Buitrago et al., 2013; Muzzin et al., 2013b; Tomczak et al., 2014; Davidzon et al., 2017). This reproduces similar published results from Ilbert et al., (2013) and Davidzon et al., (2017).

I split the star-forming sample into high activity and intermediate activity star-forming galaxies following Ilbert et al., (2010), and derive the stellar mass densities of each subsample (Figure 33, blue, navy blue and green, respectively). The stellar mass density of the high activity star-forming sample is slightly increasing $\sim 0.23 \pm 0.13 \pm$ dex between $2.0 < z < 2.5$ and $0.8 < z < 1.1$, while it decreases by $\sim 0.52 \pm 0.22$ dex between $0.8 < z < 1.1$ and $0.2 < z < 0.5$. On the other hand, the stellar mass density of the intermediate activity star-forming sample grows by $\sim 1.27 \pm 0.36$ dex between $2.0 < z < 2.5$ and $0.8 < z < 1.1$, while it grows by $\sim 0.38 \pm 0.19$ dex between $0.8 < z < 1.1$ and $0.2 < z < 0.5$. Therefore, at lower redshift $z < 1$, there is a drop in the stellar mass density ρ_* of the high activity star-forming galaxies, which roughly balances the ρ_* increase of the intermediate activity subsample, and the stellar mass density of the entire star-forming sample shows virtually no evolution over the given redshift range (Ilbert et al., 2010). Furthermore, at $z \sim 1$ the intermediate activity subsample starts to dominate over the star-forming galaxies. This can be interpreted as a gradual evolution of the mean star formation in galaxies, from high activity star formation at higher redshift, to intermediate activity star formation at lower redshift.

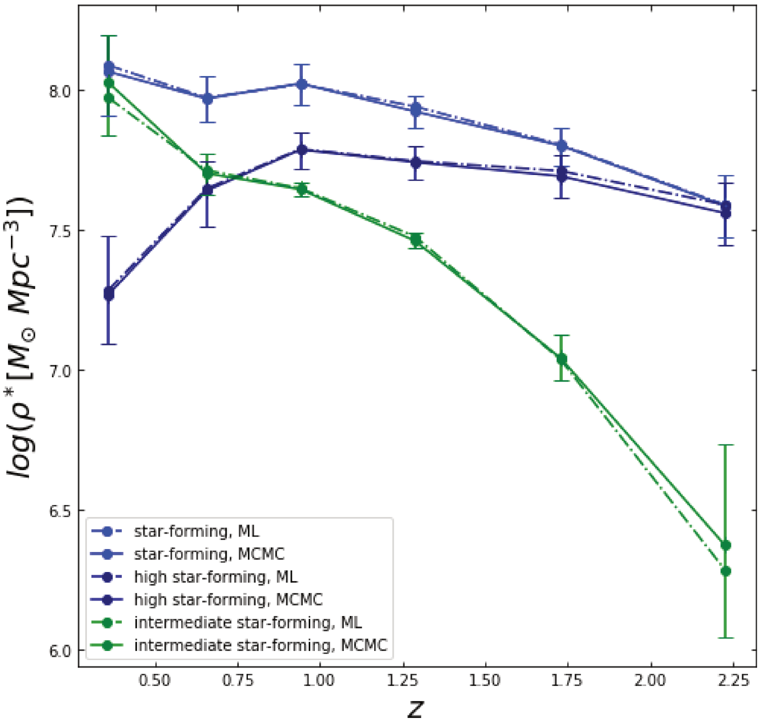

Figure 38: *Stellar mass density as a function of median redshift, for total, high activity, and intermediate activity star-forming galaxies (blue, navy blue and green lines, respectively), derived using the maximum likelihood (dashed-dotted lines) and the MCMC method (solid lines).*

SUMMARY

The goal of the project of my Thesis is to develop a pipeline that derives the SMF of cluster galaxies and fits the SMF with a chosen model, for the upcoming *Euclid Mission* (Laureijs et al., 2011).

Main results of this Thesis project are:

- I develop a `Python` pipeline for deriving the SMF of cluster galaxies, using the 1/Vmax estimator (Figure 28 and Figure 29, left panels). Since the 1/Vmax is a non-parametric estimator, I define the stellar mass bin structure and sort galaxies in these bins. Moreover, I estimate the limiting stellar masses $M_* < M_*^{\mathrm{lim}}$ and stellar mass completeness limits $M_* < M_*^{\mathrm{complete}}$ (Pozzetti et al., 2010) for each galaxy type and redshift epoch. Next, I normalize the number of galaxies by the stellar mass bin width and the total maximum comoving volume (for the Flagship mock galaxies) and the sum of the maximum comoving volume $V_{\mathrm{max,i}}$ of all galaxies in a given bin (for the COSMOS2015 galaxies). Next, I take into account the Poissonian uncertainties, normalized by the bin width and the maximum comoving volume, in order to estimate the statistical uncertainties.

- I fit the SMF using different Schechter models, such as a single Schechter model (Schechter, 1976), a double Schechter model (Pozzetti et al., 2010) and a double Schechter model with the α_2 parameter fixed (Ilbert et al., 2013). Moreover, in order to take into account the Eddington bias, I convolve the Schechter function by the stellar mass uncertainties, following the work of Ilbert et al., (2013) (Figure 26, Figure 27, Figure 28, Figure 29, right panels). I use the `scipy.optimize.minimize` function and the maximum likelihood method in order to fit the SMF with a chosen model and obtain the best-fit parameters of the model (Table 2). Moreover, I use the MCMC algorithm in order to fit the SMF and obtain the best-fit parameters of the fitting model and their uncertainties (Table 3).

- I test the *Euclid* pipeline using the *Flagship* mock galaxy sample (Carretero et al., 2017) and the *COSMOS2015* photometric redshift catalog (Davidzon et al., 2017), over the redshift range $0.2 \leqslant z < 2.5$, i.e. the redshift range expected to be covered by the future *Euclid Mission*.

- I plot the SMF of Flagship mock galaxies and COSMOS2015 galaxies, for the full sample, star-forming and quiescent galaxies, over the redshift range taken into account $0.2 < z < 2.5$ (Figure 31 and Figure 32, respectively). The evolution of the SMF of the Flagship mock galaxies is not consistent since the population of the full sample of Flagship mock galaxies starts to decrease at $z < 1.1 - 1.5$ (Figure 31, top panel).However, there was not enough time to go deeper in this issue, and it is not possible to draw any conclusions on the stellar mass assembly of Flagship mock galaxy sample.

  On the other hand, there is a consistent, mass-dependent evolution of the SMF of COSMOS2015 full sample, flattening of the SMF and sharpening of the *knee* of the SMF at the high-mass end. The mass build-up around the characteristic stellar mass M^* is probably a consequence of *mass quenching* (Figure 32, top panel). Moreover, the SMF of COSMOS2015 star-forming subsample does not show any significant evolution (Figure 32, middle panel). Finally, the SMF of COSMOS2015 quiescent subsample is strongly mass-dependent, with a clear flattening of the low-mass end of the SMF at $z < 1$ (Figure 32, bottom panel). The stellar mass assembly of low and intermediate-mass quiescent galaxies occurs at $z < 1$, possibly through *environmental quenching* (Peng et al., 2010, 2012). The evolution of low-mass quiescent galaxies at a later epoch is consistent with the *downsizing effect* (Cowie et al., 1996).

Moreover, I split the COSMOS2015 star-forming galaxies according to their sSFR, into *high activity* ($\log(\text{sSFR}) \geqslant -9.5$) and *intermediate activity* galaxies ($-9.5 > \log(\text{sSFR}) \geqslant -11$), following the work of Ilbert et al., (2010). The sites of *high activity* star-formation progressively transfers to low and intermediate-mass galaxies (Figure 33, top panel), which is again in agreement with the *downsizing effect* (Cowie et al., 1996). Finally, the *intermediate activity* star-forming galaxies show a similar mass-dependent evolution as the quiescent galaxies, and the stellar mass build-up of low and intermediate mass galaxies at a later epoch (Figure 33, bottom panel).

- I show the evolution of the best-fit parameters of the Schechter models deconvolved by the stellar mass uncertainties, for the COSMOS2015 full sample, star-forming and quiescent galaxies (Figure 34, Figure 35 and Figure 36, respectively). The characteristic stellar mass $\log(M^*)$ and the slope parameters α_1 and α_2 are roughly constant for the full sample (Figure 34, top and bottom panels) and star-forming galaxies (Figure 35, top and bottom panels). Next, the normalization parameters Φ_1 and Φ_2 of all three galaxy samples show an increase at higher redshift $1.0 < z < 2.5$, that slows down at lower redshift $z < 1$. For the quiescent sample, the $\log(M^*)$ parameter increases by $\Delta\log(M^*) \sim 0.4 \pm 0.1$ dex for quiescent galaxies, probably due to *dry* merging of massive quiescent galaxies (Figure 36, top panel; see Peng et al., 2010). Finally, the slope parameter α_1 decreases for quiescent galaxies (Figure 36, bottom left panel), possibly due to the *environmental quenching*.

- I integrate the Schechter fit to the SMF in order to derive the stellar mass density ρ_*, for the COSMOS2015 full, star-forming and quiescent galaxies (Figure 37, black, blue and red solid lines, respectively). The ρ_* values from this work are within 1σ of the values from Davidzon et al., (2017) for the full sample, while ρ_* estimates are up to ~ 0.1 dex higher for the star-forming, and up to ~ 0.2 dex lower for the quiescent sample. This is probably due to the fact that the we use the sSFR to split the galaxy sample, while Davidzon et al., (2017) use a color-color selection. The two methods are consistent at lower redshifts, but at higher z, the sSFR method is more restrictive in selecting the quiescent galaxies (Ilbert et al., 2013).

The redshift evolution of the ρ_* of the COSMOS2015 star-forming galaxies is modest (Pozzetti et al., 2010), compared to the ρ_* of the COSMOS2015 quiescent galaxies. Furthermore, the stellar mass density ρ_* of quiescent galaxies grows substantially during the epoch of $1 < z < 2.5$ (Ilbert et al., 2010, 2013), and surpasses the ρ_* of star-forming galaxies at $z \sim 1$ (Pozzetti et al., 2003).

I derive the stellar mass densities of the high activity and intermediate activity COSMOS2015 star-forming galaxies (Figure 33, blue, navy blue and green, respectively). There is a decrease in the stellar mass density ρ_* of the high activity star-forming galaxies, roughly balances the ρ_* increase of the intermediate activity subsample, and the stellar mass density of the entire star-forming sample shows almost no evolution over the entire redshift range (Ilbert et al., 2010). Furthermore, at $z \sim 1$ the intermediate activity subsample starts to dominate the star-forming galaxies. This can be interpreted as suppression of the high activity star-formation at lower redshifts, which progressively evolves to intermediate activity star-formation.

This part of the thesis reproduces published results from Ilbert et al., (2013) and Davidzon et al., (2017).

3

MOLECULAR GAS IN THE CARLA J1103+3449 CLUSTER

INTRODUCTION

In the previous chapter, I presented my work on developing a `Python` tool for deriving the SMF and fitting the SMF with a chosen model. Next, I derive the SMF and stellar mass density of galaxies over a broad redshift range, extending from the nearby Universe out to the *cosmic noon epoch* (i.e. $0.2 \leqslant z < 2.5$), in order to reproduce the statistical study of Davidzon et al., 2017 on the stellar mass assembly of different galaxy subsamples. In this chapter, the focus of my work was on other two important galaxy parameters, i.e. on estimating the molecular gas mass and SFR of individual cluster galaxies at the *cosmic noon* epoch. I present the work on detecting the molecular gas reservoir in the CARLA J1103+3449 cluster center and the molecular gas mass upper limits, star formation and other properties of the cluster confirmed member galaxies, including the RLAGN host galaxy in the cluster core. Finally, I compare these results with similar works for cluster and field galaxies at similar redshifts from the literature (Markov et al., 2020b).

Molecular gas reservoir around galaxies

Cosmic molecular gas is distributed both inside and around galaxies in the InterGalactic Medium (IGM). The cold gas residing in the IGM might trace the molecular gas originating from various sources: from an extended cold molecular gas rotating around the central galaxy in shape of a disk or torus, cold gas of gas-rich, but faint galaxies that are undetected in the optical and IR, tidal tails of two or more interacting and merging galaxies, gas outflows and/or inflows connected to the AGN jets, etc., or a combination of some of the above mentioned cases.

For instance, molecular gas can be in the form of an extended (up to ~tens of kpc) rotating disk or torus of molecular gas around the central galaxy, with one part of the disk approaching and it is blueshifted, whereas the opposite part of the disk is receding and it is redshifted (Gaspari, Ruszkowski, and Sharma, 2012; Hamer et al., 2014; McNamara et al., 2014; Li and Bryan, 2014; Russell et al., 2014, 2017a; Emonts et al., 2015; Costa, Sijacki, and Haehnelt, 2015; Li et al., 2015; Morganti et al., 2015; Prasad, Sharma, and Babul, 2015; Dannerbauer et al., 2017; Noble et al., 2018; Olivares et al., 2019).

Next, the origin of the extended molecular gas might be from tidal tails of two or more interacting and merging galaxies with disturbed morphologies (Bell et al., 2006; Dasyra et al., 2012; Emonts et al., 2013, 2015; Vantyghem et al., 2016, Cicone et al., 2018; Davis et al., 2018). Furthermore, the molecular gas might originate from two or more gas-rich galaxies, that are detectable in the mm wavelength range, but are too faint and remain undetectable in the accessible optical and/or IR images (Nesvadba et al., 2009; Emonts et al., 2014; Franco et al., 2018; Castignani, Combes, and Salomé, 2020).

Extended molecular gas outflows and/or inflows connected to the AGN feedback have been observed (Salomé et al., 2006; Lim, Ao, and Dinh-V-Trung, 2008; McNamara et al., 2014; Cicone et al., 2014, 2018; Russell et al., 2014, 2016, 2017a,b, 2019; Morganti et al., 2015; Vantyghem et al., 2016; Tremblay et al., 2018; Olivares et al., 2019) and predicted from simulations (Revaz, Combes, and Salomé, 2008; Wagner, Bicknell, and Umemura, 2012; Gaspari, Ruszkowski, and Sharma, 2012; Li and Bryan, 2014; Li et al., 2015; Costa, Sijacki, and Haehnelt, 2015; Prasad, Sharma, and Babul, 2015; McNamara et al., 2016; Voit et al., 2017; Gaspari and Sądowski, 2017; Richings and Faucher-Giguère, 2018). In local galaxies, the central AGN jets can lift significant amounts of molecular gas, usually entrained with the ionized and neutral gas, at ~kpc, or even ~tens of kpc from the AGN (Wagner, Bicknell, and Umemura, 2012; McNamara et al., 2014; Cicone et al., 2014, 2018; Morganti et al., 2015; Prasad, Sharma, and Babul, 2015; Gaspari and Sądowski, 2017; Tremblay et al., 2018; Olivares et al., 2019). The cold gas has also been observed to fall back onto the AGN, in complex gas dynamics resembling a fountain mechanism (e.g., Salomé et al., 2006; Tremblay et al., 2018). It is difficult to distinguish an inflow from an outflow, since the molecular can be in front or behind the host galaxy. In case of an inflow, the molecular gas falls towards the galaxy, and is expected to reach the maximum velocity close to the galaxy, while in case of an outflow the velocity should increase towards the outer regions (Lim, Ao, and Dinh-V-Trung, 2008; McNamara et al., 2014, Russell et al., 2014, 2016; Vantyghem et al., 2016; Tremblay et al., 2018).

Molecular gas cooling from the hot IGM or ICM, usually occurs during the interaction of the hot gas and the AGN jets, at a distance of up to tens of kpc from the central galaxy. In this case, the hot gas around the host galaxy is disturbed, pushed and compressed by the expanding radio jets. AGN feedback boosts the radiative cooling of the hot gas, molecular gas filaments form on the edges of the X-ray cavities or radio lobes (Salomé et al., 2006, 2011; Revaz, Combes, and Salomé, 2008; Lim, Ao, and Dinh-V-Trung, 2008; Gaspari, Ruszkowski, and Sharma, 2012; Emonts et al., 2014; Emonts et al., 2019; Li and Bryan, 2014; Li et al., 2015; Gaspari and Sądowski, 2017 Voit et al., 2017; Tremblay et al., 2018; Olivares et al., 2019).

An alternative mechanism of gas cooling is cooling of the hot, low-entropy gas uplifted by the AGN jets. In this case, the hot gas is uplifted by the rising buoyant bubbles to large distances of up to tens of kpc, where the AGN heating is less efficient and the displaced low-entropy gas is denser and cooler than its surroundings. The low-entropy hot gas becomes thermally unstable, cools radiatively and condensates into molecular gas that usually wraps around or is trailing behind the X-ray cavities or radio jets (Revaz, Combes, and Salomé, 2008; Li and Bryan, 2014; Costa, Sijacki, and Haehnelt, 2015; McNamara et al., 2016; Vantyghem et al., 2016; Russell et al., 2014, 2016, 2017a,b, 2019; Voit et al., 2017; Tremblay et al., 2018; Olivares et al., 2019).

The AGN feedback plays an important role in gas cooling and can have a positive feedback, by compressing the gas and boosting gas cooling, which is both predicted by simulations (Croton et al., 2006; Revaz, Combes, and Salomé, 2008; Li and Bryan, 2014; Li et al., 2015; McNamara et al., 2016; Gaspari and Sądowski, 2017), and observed (Nesvadba et al., 2009; Emonts et al., 2014; Emonts et al., 2019; Russell et al., 2014, 2016, 2017a,b; Vantyghem et al., 2016; Olivares et al., 2019). For instance, Emonts et al., (2014) found a radio-CO emission alignment in three out of five CO sources, with CO components located beyond the brighter radio jet, tens of kpc away from any optical and/or IR source. This is similar to what is simulated in Li and Bryan, (2014), where the molecular gas clumps are formed along the direction of the AGN jets.

Simulations show that gas cooling occurs when the gas thermal instability (i.e. cooling) time is sufficiently short $t_{ti} \sim 10^8$yr (Li and Bryan, 2014; Li et al., 2015; Prasad, Sharma, and Babul, 2015; McNamara et al., 2016) or when the cooling time to free-fall time ratio is sufficiently low $t_{ti}/t_{ff} \sim 1-20$ (Sharma et al., 2012; Gaspari, Ruszkowski, and Sharma, 2012; Li and Bryan, 2014; Li et al., 2015; Costa, Sijacki, and Haehnelt, 2015; Prasad, Sharma, and Babul, 2015; Voit et al., 2017) or when the cooling time to infall time ratio is $t_{ti}/t_i < 1$ (McNamara et al., 2016). For example, Li and Bryan, (2014) show that during the gas uplift, the cooling time remains roughly constant while the free-fall time increases quickly. When the t_{ti}/t_{ff} falls below a value of ~ 10, the gas starts cooling and forming molecular gas clumps.

The cold gas observed outside of the AGN host galaxy can either escape or be accreted by the host galaxy. Either condensed or lifted by the AGN jets, part of the molecular gas with velocities higher than the escape velocity of the system would manage to escape the galaxy. However, it is expected to be a small fraction of the total molecular gas reservoir (Morganti et al., 2015; Russell et al., 2016, 2017a; McNamara et al., 2016; Tremblay et al., 2018; Olivares et al., 2019), especially in the case of a molecular gas around the massive galaxy in the cluster center. Some of the molecular gas would also be lost by heating or gas stripping through stellar, supernovae (SNe) or the AGN feedback, shock heating and ram-pressure stripping (Li et al., 2015). The remaining molecular gas content would remain inside the potential well of the galaxy or galaxy group/cluster. Some of it will fall back to the RLAGN, feeding its emission, in the form of a gas inflow (Salomé et al., 2006; Lim, Ao, and Dinh-V-Trung, 2008; Revaz, Combes, and Salomé, 2008; Gaspari, Ruszkowski, and Sharma, 2012; Li and Bryan, 2014; Li et al., 2015; Prasad, Sharma, and Babul, 2015; Costa, Sijacki, and Haehnelt, 2015; Vantyghem et al., 2016; McNamara et al., 2016; Gaspari and Sądowski, 2017; Russell et al., 2017a; Tremblay et al., 2018; Olivares et al., 2019). Eventually, this gas could go through several cycles of rising in the form of an outflow and falling back to the AGN in the form of an inflow (Salomé et al., 2006, 2011; McNamara et al., 2014, 2016; Li et al., 2015; Prasad, Sharma, and Babul, 2015; Gaspari and Sądowski, 2017). Finally, part of this molecular gas will fuel star formation (Salomé et al., 2006; McNamara et al., 2014, 2016; Russell et al., 2017a,b). However, it is not clear which fraction of the total molecular gas reservoir will be used as star formation fuel, but Li et al., (2015) argue it is the main part of the total molecular gas.

Star formation of cluster galaxies

Galaxy clusters are the largest known virialized structures in the universe, with total mass up to $\sim 10^{15} M_{\odot}$ (Arnaud, 2009). At redshifts $z < 1.5$ galaxy cluster cores are dominated by red, quenched, early-type galaxies, while blue, star-forming, late-type galaxies are mostly found in the field (e.g., Dressler, 1980; Balogh et al., 1998; Balogh et al., 2004; Postman et al., 2005; Mei et al., 2009; Rettura et al., 2011; Lemaux et al., 2012, 2018; Wagner et al., 2015; Tomczak et al., 2018). This points to a crucial role of environment in galaxy evolution at lower redshifts.

At higher redshifts, results are somewhat conflicting. Some results show that at $z > 1.5$ the star formation is already quenched in cluster cores (Kodama et al., 2007; Strazzullo et al., 2010; Papovich et al., 2010; Snyder et al., 2012; Grützbauch et al., 2012; Stanford et al., 2012; Zeimann et al., 2012; Gobat et al., 2013; Muzzin et al., 2013a; Newman et al., 2014; Mantz et al., 2014; Hayashi et al., 2017). Other observations show a reversal of the star formation-density relation and ongoing star formation in cluster cores at $z > 1.5$, with a much more varied galaxy population compared to clusters at lower redshifts (Elbaz et al., 2007; Cooper et al., 2008; Tran et al., 2010; Brodwin et al., 2013; Santos et al., 2015; Mei et al., 2015; Alberts et al., 2016; Wang et al., 2016a; Noirot et al., 2016, 2018; Oteo et al., 2018; Martinache et al., 2018; Shimakawa et al., 2018). A reversal of the star formation at $z \gtrsim 1$ is also predicted from hydrodynamical and semi-analytical simulations (Tonnesen and Cen, 2014; Chiang et al., 2017). Other cluster cores at $z \gtrsim 1.5$ present equal percentages of quiescent and star-forming galaxies (Fassbender et al., 2011; Tadaki et al., 2012; Zeimann et al., 2012; Mei et al., 2012; Noirot et al., 2016). A large presence of star-forming galaxies in cluster cores at $z \approx 1.5 - 2$ indicates that most of the star formation quenching observed at lower redshift has not yet occurred, and that this is the key epoch of transformation of cluster galaxies from star-forming to quiescent.

Few galaxy clusters are confirmed at $z \gtrapprox 1.5$. Current observations of the CO emission line in clusters at these epochs show that cluster galaxies still have cold gas to fuel their star formation. However, these results are not yet statistically significant, and some results point towards higher molecular gas content in cluster galaxies with respect to the field and others to lower (Casasola et al., 2013; Rudnick et al., 2017; Noble et al., 2017; Hayashi et al., 2018; Coogan et al., 2018; Castignani et al., 2018). Molecular gas has been detected in two protoclusters at $z \sim 2.5$ (Chapman et al., 2015; Wang et al., 2016b). Both protoclusters are dominated by star-forming (with a high starburst fraction), massive galaxies, with a substantial amount of molecular gas, and a small percentage of passive galaxies, which probably quenched after their accretion onto the cluster. Furthermore, Lewis et al., (2018) found 86 dusty star-forming galaxies (DSFGs) around overdensities over the redshift range $2.8 < z < 3.6$. Next, Oteo et al., (2018) found ten molecular gas-rich DSFGs within a cold core of a protocluster at $z \sim 4$, and follow-up observations by Ivison et al., (2020) detected additional six DSFGs. Miller et al., (2018) found 14 gas-rich, star-forming galaxies in a protocluster core and Hill et al., (2020) confirmed their detection and identified another 15 galaxies in a protocluster at $z \sim 4.3$.

Molecular gas and SFR tracers

Molecular gas mainly consists of the most dominant interstellar molecule, i.e. molecular hydrogen H_2. However, this molecule is practically invisible to observations due to its lack of a permanent dipole moment and the fact that its rotational dipole transitions require high temperatures $T > 100$ K. In order to assess the molecular gas content of galaxies, there are several tracers that can be used. However, the rotational transitions of CO molecules are predominantly used for multiple reasons. The CO molecule has a weak permanent dipole moment and it is easily excited even inside cold molecular clouds due to the low energy rotational transitions. CO is also the second most abundant molecule after H_2. CO rotational levels are excited by collisions with H_2 molecules. Finally, CO rotational transitions lie in a relatively transparent millimeter window (Solomon and Vanden Bout, 2005; Kennicutt and Evans, 2012; Carilli and Walter, 2013; Bolatto, Wolfire, and Leroy, 2013). Furthermore, low-level CO rotational transitions are used as direct tracers of the cold ($T < 100$ K) and diffuse molecular gas, and the overall molecular gas content, whereas higher CO rotational transitions trace gradually warmer, denser and more perturbed molecular gas, related to processes such as star formation or AGN feedback (Papadopoulos et al., 2001; Carilli et al., 2010; see Solomon and Vanden Bout, 2005; Bolatto, Wolfire, and Leroy, 2013; Carilli and Walter, 2013 for reviews).

One of the drawbacks of tracing the molecular gas with the CO line emission is that CO is a poor tracer of the so-called *CO-dark* molecular gas, that usually makes a significant fraction ($\sim 30\%$) of the total molecular gas mass (Wolfire, Hollenbach, and McKee, 2010; Abdo et al., 2010; Pineda et al., 2013). The *CO-dark* diffuse molecular gas is in an outer region of a molecular cloud, where CO is photodissociated, but H_2 is not, and it encompasses the CO emitting central regions of the molecular cloud (Wolfire, Hollenbach, and McKee, 2010). The *CO-dark* can be traced by [CII] or dust thermal continuum emission (Abdo et al., 2010; Planck Collaboration et al., 2011; Pineda et al., 2013; Langer et al., 2014; Tang et al., 2016; Lebouteiller et al., 2019).

The [CII] fine-structure emission at 158 μm is mostly tracing the PhotoDissociation Regions (PDR) associated with star formation, but a fraction of it traces the *CO-dark* molecular gas, along with the cool atomic and ionized gas (Wolfire, Hollenbach, and McKee, 2010; Pineda et al., 2013; Langer et al., 2014). Moreover, the [CII] is a good tracer of outflowing molecular gas in galaxies and quasars at high-redshift ($z > 6$), (Maiolino et al., 2012; Cicone et al., 2015), etc. Dust thermal continuum emission in the FIR can be used as a molecular gas tracer (Genzel et al., 2015; Scoville et al., 2016; Tacconi et al., 2018). Rotational transitions of molecules such as CS, HCN, HCO^+ etc., are used as tracers of the densest molecular gas associated with star formation (Solomon et al., 2003; Wu et al., 2010; Riechers et al., 2011). Finally, molecular gas mass can be constrained by dynamical mass measurements (see e.g. Solomon and Vanden Bout, 2005; Bolatto, Wolfire, and Leroy, 2013; Carilli and Walter, 2013 for reviews).

Gas fraction $f_{gas} = M_{gas}/(M_* + M_{gas})$ (or gas-to-stellar mass ratio M_{gas}/M_*) characterizes the efficiency of transforming the cold molecular gas into stars. It depends on redshift, galaxy stellar mass and environment. For galaxies at a given stellar mass, the gas fraction increases with redshift (Sargent et al., 2014; Genzel et al., 2015; Scoville et al., 2017; Silverman et al., 2018; Darvish et al., 2018a; Tacconi et al., 2018). For galaxies at the same redshift, the gas fraction increases with decreasing stellar mass (Tacconi et al., 2013, 2018; Sargent et al., 2014; Lee et al., 2017). Finally, at $z < 1.5$, for galaxies of the same mass and at the same redshift, cluster galaxies show lower amounts of molecular gas and thus, lower gas fractions (Jablonka et al., 2013; Rudnick et al., 2017; Lee et al., 2017; Castignani et al., 2018; Hayashi et al., 2018). Finally, some works have shown that at higher redshifts ($z > 2$), there is no difference in the gas fraction of cluster and field galaxies (Husband et al., 2016; Dannerbauer et al., 2017).

SFR can be derived using various methods (see e.g. Kennicutt, 1998b; Kennicutt and Evans, 2012; Madau and Dickinson, 2014 for reviews). Stellar Population Synthesis models can provide an approximate SFR estimate, based on a relation between the SFR and the *U*-*V* color (Kennicutt, Tamblyn, and Congdon, 1994). One of the best methods for directly estimating the SFR is using the Hα recombination line emission, originating from the HII regions ionized by young, blue, massive and short-lived stars (Hunter et al., 1986; Madau, Pozzetti, and Dickinson, 1998; Moustakas, Kennicutt, and Tremonti, 2006). Next, the [OII] forbidden line doublet can be calibrated through Hα emission and used as a SFR tracer at higher redshifts (Gallagher, Bushouse, and Hunter, 1989; Kennicutt, 1992; Moustakas, Kennicutt, and Tremonti, 2006;). Another way of directly tracing the emission of young stellar populations is through the far-UV (FUV) luminosity (Donas and Deharveng, 1984; Madau, Pozzetti, and Dickinson, 1998; Schiminovich et al., 2005; Treyer et al., 2007). However, part of the FUV emission will be absorbed and re-emitted by the dust in form of a thermal continuum emission in the mid-IR (MIR) and far-IR (FIR). Thus, we can use the MIR and FIR continuum emission (Hunter et al., 1986; Devereux and Hameed, 1997) or emission at $\lambda = 24\ \mu$m and $\lambda = 70\ \mu$m, i.e. *Spitzer* and *Herschel* bands (Calzetti et al., 2007, 2010; Rieke et al., 2009), to estimate the SFR. Moreover, tight radio-IR correlation provides the extinction-free SFR estimate, using the free-free radio emission at $\nu = 1.4$ GHz (Condon, 1992; Yun, Reddy, and Condon, 2001). Finally, multiwavelength surveys allow the SFR estimates using a combination of several tracers (Buat et al., 2005; Schruba et al., 2011; Hao et al., 2011).

With the measurements of the molecular gas mass, SFR and stellar mass, we can derive other important properties, such as the specific star formation rate sSFR, depletion time and star formation efficiency SFE.

Goal of the project

In this chapter, I present IRAM (Institut de Radio Astronomie Millimetrique) NOEMA (NOrthern Extended Millimeter Array) observations, data reduction and analysis of the core of a confirmed cluster from the CARLA (Clusters Around Radio-Loud AGNs; Wylezalek et al., 2013) survey at $z = 1.44$, CARLA J1103+3449 (Noirot et al., 2018). CARLA J1103+3449 was selected for observations (PI: S. Mei, A. Galametz) as one of the highest CARLA IRAC color-selected overdensities ($\sim 6.5\sigma$, from Wylezalek et al., 2014), and shows a $\sim 3.5\sigma$ overdensity of spectroscopically confirmed sources (Figure 41, Noirot et al., 2018).

The most frequent way to study the molecular gas content of high redshift galaxies are the CO millimeter observations (see Kennicutt and Evans, 2012, Carilli and Walter, 2013, Bolatto, Wolfire, and Leroy, 2013, for reviews). Therefore, we use the CO(2-1) rotational transition emission line as a molecular gas tracer in the central region of the CARLA J1103+3449 cluster. We find synchrotron emission (Section 3.3.1) and a substantial molecular gas reservoir around the central RLAGN (Section 3.3.2) and discuss on the possible origin of this gas (Section 3.4.1). Next, we estimate the molecular gas content (Section 3.3.3) and SFR using the Hα emission from Noirot et al., (2018) (Section 3.3.6) of the confirmed cluster members within the NOEMA field of view, and we compare it with similar observations in clusters and in the field (Section 3.4.2; Markov et al., 2020b). While working on this Thesis project, I was a part of an international team of scientists, including S. Mei, P. Salomé, F. Combes, D. Stern, A. Galametz, C. De Breuck, D. Wylezalek, S. Amodeo, E. A. Cooke, A. H. Gonzalez, N. A. Hatch, G. Noirot, A. Rettura, N. Seymour, S. A. Stanford, J. Vernet and myself. As part of this PhD Thesis, I participated in data reduction, imaging and analysis of the NOEMA observations of the CARLA J1103+3449 cluster at $z \sim 1.44$.

This chapter is organized as follows. Observations, data reduction and mapping are described in Section 3.2, the results are given in Section 3.3, the discussion and analysis of the results is given in Section 3.4 and finally, the summary of the main results is given in Section 3.5. Throughout this chapter, we adopt a ΛCDM cosmology, with of $\Omega_m = 0.3$, $\Omega_\Lambda = 0.7$, $\Omega_k = 0$ and $h = 0.7$, and assume a Chabrier initial mass function (IMF) (Chabrier, 2003).

DATA

The CARLA survey

The CARLA survey (Wylezalek et al., 2013) is a substantial contribution to the subject of high-redshift galaxy clusters at $z > 1.5$. CARLA is a 408h Warm *Spitzer*/IRAC survey of galaxy overdensities around 420 radio-loud AGNs (RLAGNs). The RLAGNs were selected across the full sky, approximately half of the RLAGNs are radio loud quasars (RLQs) and half high-z radio galaxies (HzRGs), over the redshift range of $1.3 < z < 3.2$. Wylezalek et al., (2013) identified galaxies at $z > 1.3$ around the RLAGNs in each field, using a color selection in the IRAC channel 1 ($\lambda = 3.6$ μm; IRAC1, hereafter) and channel 2 ($\lambda = 4.5$ μm; IRAC2, hereafter). They find that 92% of all RLAGNs reside in denser environments, with the majority (55%) of them being overdense at a $> 2\sigma$ level, and 10% of them at a $> 5\sigma$ level, with respect to the field surface density of sources in the Spitzer UKIDSS Ultra Deep Survey (SpUDS, Rieke et al., 2004), selected in the same way.

A *Hubble Space Telescope* Wide Field Camera 3 (*HST*/WFC3) follow-up (Program ID: 13740; P.I.: D. Stern) of the twenty highest CARLA *Spitzer* overdensities (consisting of 10 HzRGs and 10 RLQs) spectroscopically confirmed sixteen of these overdensities over the redshift range $1.4 < z < 2.8$

and seven serendipitous structures at $0.9 < z < 2.1$ (Noirot et al., 2018). The structure members are confirmed through line-emission (in Hα, Hβ, [OII], and/or [OIII], depending on the redshift) and have star formation estimates from the line fluxes (Noirot et al., 2018). They found that the star-formation of $M_* > 10^{10}$ M$\odot$ galaxies is below the star-forming *main sequence* (MS) of field galaxies at similar redshift. Moreover, active, star-forming galaxies are mostly found within the central regions of these overdensities (Noirot et al., 2018). This program also provided WFC3/F140W imaging from which our collaborator S. Mei obtained galaxy visual morphologies.

From their IRAC luminosity function, Wylezalek et al., (2014) showed that CARLA overdensities have probably quenched faster and earlier compared to field galaxies. Next, some of the CARLA Northern overdensities were observed in either deep z-band or deep i-band, with Gemini/GMOS and WHT/ACAM by Cooke et al., (2015), which permitted them to estimate their galaxy star formation rate histories.

Spitzer IRAC and HST/WFC3 Observations

As a target of the *Spitzer* CARLA survey, CARLA J1103+3449 was observed with *Spitzer* IRAC1 and IRAC2 (Cycle 7 and 8 snapshot program, P.I. D. Stern), for a total exposure of 800s and 2000s, respectively. The IRAC cameras have 256×256 InSb detector arrays with a pixel size of 1.22 arcsec and a field of view of 5.2×5.2 arcmin. Wylezalek et al., (2013) performed the data calibration and mapping with the `MOPEX` package (Makovoz and Khan, 2005) and extracted sources with SExtractor (Bertin and Arnouts, 1996), using the IRAC-optimized SExtractor parameters from the work of Lacy et al., (2005). The final *Spitzer* IRAC1 and IRAC2 resolution was 0.61 arcsec, after taking into account dithering.

The *HST*/WFC3 imaging and grism spectroscopy were obtained with the *HST* follow-up program (Noirot et al., 2018). They obtained F140W imaging (with a field of view of 2×2.3 arcmin^2 at a sampling of 0.13 arsec pix^{-1}) and G141 grism spectroscopy (with the wavelength range of $1.08\ \mu m < \lambda < 1.70\ \mu m$ and a spectral resolution $R = \lambda/\Delta\lambda = 130$). This grism was chosen in order to permit the identification of strong emission lines at the target redshift, such as Hα, Hβ, and [OII]. Noirot et al., (2016, 2018) performed the data reduction with the `aXe` (Kümmel et al., 2009) pipeline, by combining the individual exposures, and removing cosmic ray and sky signal. Noirot et al., (2018) performed source detection with SExtractor (Bertin and Arnouts, 1996) and extracted two-dimensional spectra for each field, based on the positions and sizes of the sources. The redshifts and emission line fluxes were determined using the python version of `mpfit` and are published in Noirot et al., (2018).

Our collaborators N. Hatch and E. Cooke followed-up CARLA J1103+3449 with *i*-band imaging with WHT/ACAM (Cooke et al., 2015). S. Amodeo and S. Mei obtained a psf-matched photometric catalog in the *i*-band, WFC3/F140W (detection image), IRAC1 and IRAC2. The *i*-band, WFC3/F140W, and IRAC1 correspond to the UVJ rest-frame bandpasses at its redshift. I used this catalog for the analysis I performed in the context of this PhD thesis.

More details on the *Spitzer* IRAC, *HST*/WFC3 and WHT/ACAM observations, data reduction and results can be found in Wylezalek et al., (2013, 2014), Noirot et al., (2016, 2018), and Cooke et al., (2015), respectively.

S. Mei and S. Amodeo performed a morphological and photometric analysis of the central sources, and found the RLAGN host to be an elliptical galaxy (Figure 39, blue square), the spiral galaxy close to the RLAGN is a spectroscopically confirmed member (Noirot et al., 2018), but is not detected as an independent galaxy in the IRAC images because of their poor spatial resolution. The bright central source south of the RLAGN is a star (Figure 39, magenta star), with a spectral energy distribution consistent with a black body and not consistent with an early-type galaxy (ETG) spectrum.

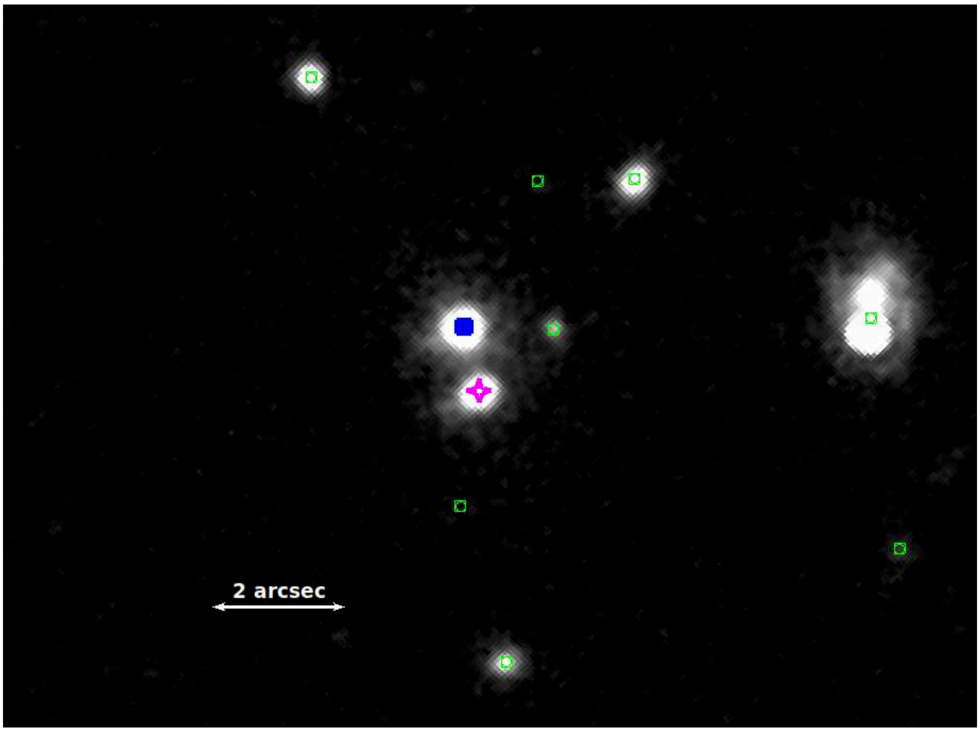

Figure 39: *HST/WFC3 F140W image of the central region of the cluster. North is up and East is to the left. The blue square marks the position of the RLAGN. The object south of the RLAGN is a star (magenta star). The green squares are the positions of IRAC color-selected galaxies in the cluster central region.*

Keck AGN Spectrum Observations

The redshift for the radio source B2 1100+35, associated with WISE was first reported in Eales et al., (1997) as $z = 1.44$, but with no spectrum presented. With no spectrum available from the Sloan Digital Sky Survey of the faint, red ($g = 23.9$ mag, $i = 21.4$ mag) optical counterpart to the radio source, our collaborator Daniel Stern observed B2 1100+35 with the dual-beam Low Resolution Imaging Spectrometer (LRIS; Oke et al., 1995) at Keck Observatory on UT 2019 March 10. The night suffered strongly from variable, often thick cloud cover.

The data were obtained through the 1."00 slit with the 5600 dichroic. The blue arm of the spectrograph used the 600 ↕ mm^{-1} grism ($\lambda_{\mathrm{blaze}} = 4000$ Å;

resolving power $R \equiv \lambda/\Delta\lambda \sim 1600$ for objects filling the slit), while the red arm used the 400 $\updownarrow \mathrm{mm}^{-1}$ grating ($\lambda_{\mathrm{blaze}} = 8500$ Å; $R \sim 1300$). Three 600 s exposures were attempted, though ultimately only one proved useful. D. Stern processed the spectra using standard techniques, and flux calibrated the spectrum using observations of the standard stars Hilter 600 and HZ44 from Massey and Gronwall, (1990), obtained the same night with the same instrument configuration. Figure 40 presents the processed spectrum. Multiple redshifted emission lines are detected, including broadened CIV ($\lambda = 1549$ Å), narrow CIII] ($\lambda = 1909$ Å), narrow [NeV ($\lambda = 3426$ Å), and strong, narrow [OII] ($\lambda = 3727$ Å). Based on the latter feature, D. Stern reports a redshift of $z = 1.4427 \pm 0.0005$, where the uncertainty reflects both statistical uncertainties in the line fitting, as well as an estimate of systematic uncertainties in the wavelength calibration, and a comparison with other well-detected emission lines in this source. This measurement is consistent with the Noirot et al., (2018) AGN redshift measurement of $z = 1.444 \pm 0.006$, from the HST/WFC3 grism observations.

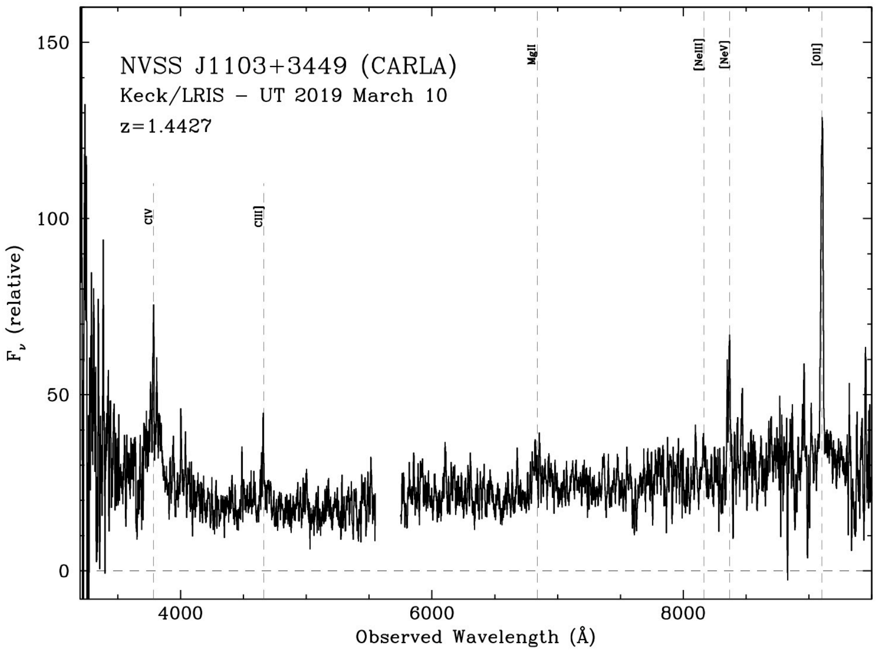

Figure 40: *The Keck/LRIS spectrum of B2 1100+35, the radio galaxy at the center of CARLA J1103+3449. Since the night was not photometric, the y-axis only provides relative flux calibration.*

IRAM observations and data reduction

As part of this PhD Thesis, I was responsible for the reduction and analysis of the IRAM observations, and performed this data reduction and analysis with the help of P. Salomé, and with scientific guidance by F. Combes and S. Mei. The observation strategy was established by A. Galametz, S. Mei, P. Salomé, F. Combes and C. de Breuck.

CARLA J1103+3449 was observed with the NOEMA, with 8 antennas over a five day period (28–30 July, 3–4 August 2017), for a total exposure time of ~29 h (including overheads) (PI: S. Mei, A. Galametz). CARLA J1103+3449 was observed with average weather conditions (PWV $\sim 10-20$ mm). The average system temperature was of $T_{sys} \sim 100-200$ K, and reached maximum values of 300 K.

The target was the CO(2-1) emission line at the rest-frame frequency $\nu_{rest} = 230.538$ GHz, which is redshifted to $\nu_{obs} = 94.48$ GHz at $z \sim 1.44$, observed with NOEMA's 3 mm wavelength. The target was covered with three pointings to map the RLAGN and central cluster region. The pointings were positioned in order to cover as many IRAC-selected members as possible (~ 40) along with the 7 (out of 8) *HST*/WFC3 spectroscopically confirmed members (green circles and a red star in Figure 41, based on Noirot et al., 2018). Moreover, the three pointings cover the central cluster region with a sensitivity of ~ 1.5 times the depth at the center of the individual pointings. The angular resolution was chosen to separate the minimal distance between two cluster members, which is ~ 3 arcsec in cluster core, for which antenna configuration C with the 2.7 arcsec separation was used. The beam size is 4.1×3.5 arcsec, the PA is $-171°$ is and the velocity resolution is 50 km s^{-1} (smoothed to 100 km s^{-1}).

With the help of the IRAM support astronomers in Grenoble, C. Herrera and M. Krips, I performed the data calibration of the NOEMA data by running the pipeline in the `clic` package in the IRAM/GILDAS software[1]. It is an open software, which can be used for data reduction, mapping, and analysis, by running different pipelines and commands in the terminal or by choosing different options in the widget menu.

The initial data reduction was performed by the Astronomer On Duty (AOD), by running the pipeline. This pipeline automatically checks the data for errors in phase, amplitude, pointing, focus and tracking due to bad conditions during observations (e.g. bad weather conditions, instrumentation problems, etc.) and automatically flags the data if the errors are outside of the initially set constraints. These constraints are set by astronomers after years of working with a large amount of data, and they are set to be the best compromise between the quality and the quantity of the data obtained after reduction. However, these constraints are just a recommendation and they can be modified, depending on the project.

Next, following instructions and recommendations of the AOD, I performed further data reduction: additional data flagging, modifying antenna positions, modifying the RF (receiver bandpass), flux and amplitude/phase calibrators, etc. Additional data flagging is sometimes necessary due to bad

---

[1] http://www.iram.fr/IRAMFR/GILDAS/

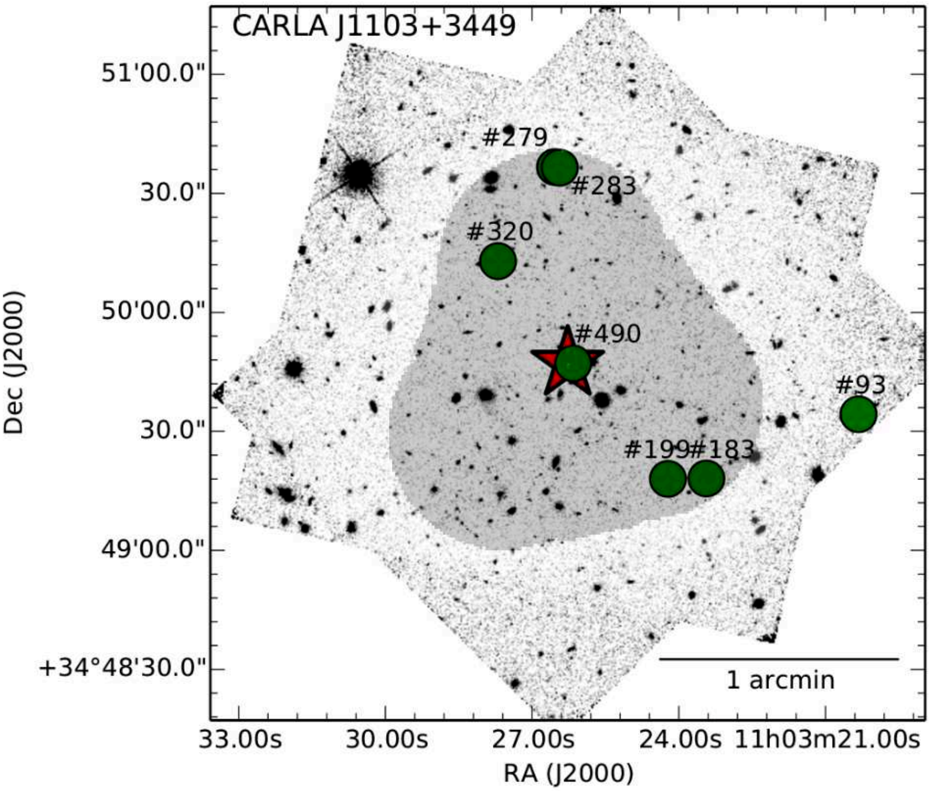

Figure 41: *HST/WFC3 F140W image of the central region of the CARLA J1103+3449 cluster. The distribution of spectroscopically confirmed members (green circles) with the central RLAGN (red star) are taken from Noirot et al., (2018). The shaded area indicates the NOEMA mosaic map area.*

weather, problems with instruments, pointing, tracking, inaccurate amplitude, etc. For instance, data flagging was performed on the data from July 28, because of problems with electrical power and bad weather conditions during observations, on August 3 due to incorrect values of the amplitude, and finally, on August 4, flagging was necessary due to wrong values on both total power and the amplitude. Modifying antenna positions is sometimes necessary, because a good baseline model is not available during observations. Therefore, we modify the baseline by applying a good baseline model that was available after the observations, but within hours or days of the observational date. For example, for the observations of July 28 a baseline solution for July 29 was applied, whereas for August 3, a baseline from August 4 was used.

RF, flux and amplitude/phase calibrators are standard bright, point sources, usually radio stars or quasars with a well-known flux, that are used for calibrating the source. Sometimes the standard calibrators are not observable during certain observational days, so other available calibrators need to be used. Sources used as the RF calibrator, flux calibrator and amplitude/phase calibrators were the 3C84 and LKHA101 radio stars, and the 1128+385 quasar, except on July 30, when quasars 3C273, 1128+385 (measured on July 28) and 1156+295 were used.

After making all the necessary modifications, I rerun the pipeline and reduce the data again. While pointing and focus were excellent, amplitude and phase were of average quality, because of the weather conditions during observations (e.g. passing of clouds affects the amplitude and hot/cold air fronts affect the phase). Since a large percentage of our data is flagged, even up to 62% for some observational days, and since the largest percentage of the entire data loss is due to bad *seeing* (i.e. phase normalized by the distance between antennas), more relaxed constraints on the *seeing* parameter, i.e. < 2.0 arcsec are put instead of the default value of < 1.5 arcsec, and we rerun the `clic` pipeline and reduce the data again. However, putting more relaxed constraints just adds more noise to the data and the signal is becoming weaker. Therefore, we decide to use the data with the default seeing constrains of < 1.5 arcsec to produce the final map.

I stacked the data from the entire run for each of the three beams, and obtained three uv-tables, that contain the total emission including the CO(2-1) line and continuum emission. Next, I use the `mapping` package of the GILDAS software to create the continuum uv-tables and we subtract the continuum from the total emission in order to obtain the continuum subtracted, CO(2-1) line uv-tables. We use these uv-tables to create the *dirty* maps, deconvolve the *dirty* maps by the beam and obtain *clean* maps. We obtain the continuum mosaic map by averaging the flux over a velocity range of 2450 km s^{-1}, excluding the emission line velocity range. The rms noise level is $\sigma \sim 0.18$ mJy beam^{-1} (Figure 42).

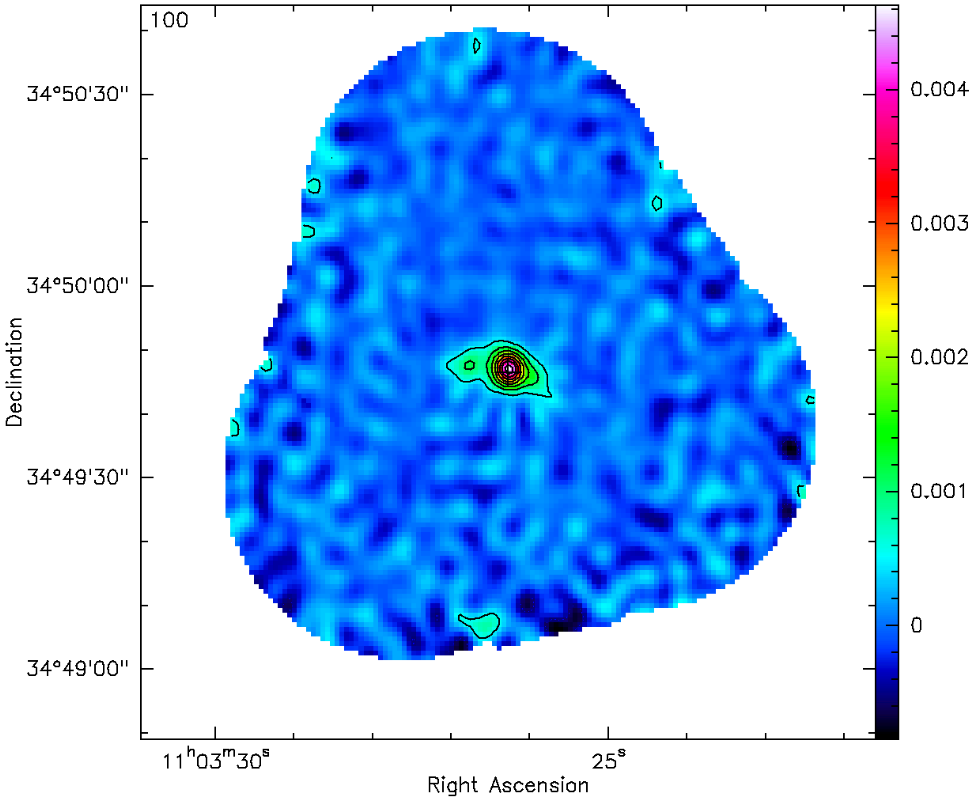

Figure 42: *Continuum emission map at* $\nu_{\rm obs} \sim 94.48$ GHz *of the CARLA J1103+3449 cluster. The map was obtained by averaging the flux over a velocity range of* 2450 km s^{-1}*, outside of the emission lines, the rms noise level is* $\sigma \sim 0.18$ mJy beam^{-1}. *The contours run as* 3σ, 6σ, 9σ, *etc. up to* 24σ. *The color scale of the intensity maps is in* Jy beam^{-1}.

The original velocity resolution of the datacube is 50 km s^{-1} and the rms noise level is $\sigma \sim 1.0$ mJy $beam^{-1}$. In order to improve the SNR, the data was smoothed to a final velocity resolution of 100 km s^{-1} and a rms noise level of $\sigma \sim 0.7$ mJy $beam^{-1}$. We create the CO(2-1) intensity map, by averaging the flux over a velocity range of 1200 km s^{-1}, in the approximate range of velocities where the emission line is, with the rms noise level of $\sigma \sim 0.28$ mJy $beam^{-1}$ (Figure 43).

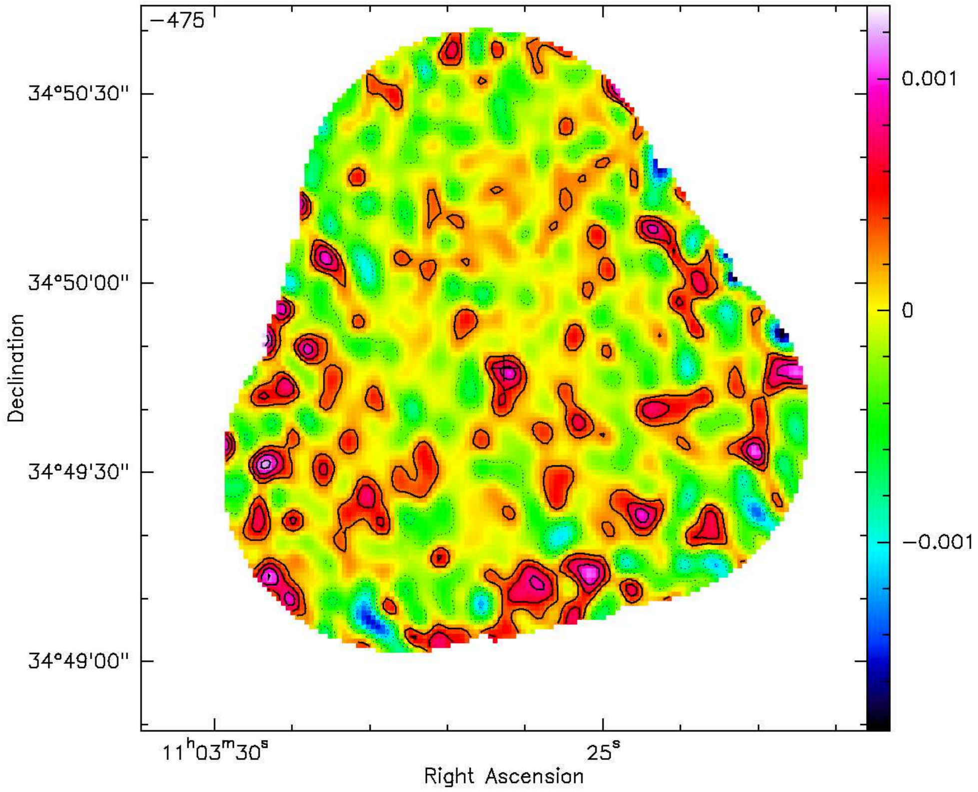

Figure 43: *Continuum subtracted CO(2-1) line emission mosaic map of the CARLA J1103+3449 cluster, which shows an extended source in the cluster center. The map was obtained by averaging the flux over a velocity range of* 1200 km s^{-1}, *covering both emission lines, and has a rms noise level of* $\sigma \sim 0.28$ mJy $beam^{-1}$. *The continuous lines show positive* σ *contours and the dotted lines show negative* σ. *The contours run as* 1σ, 2σ *and* 3σ. *The cross marks the center of the mosaic. The color scale of the intensity maps is in* Jy $beam^{-1}$.

The noise increases towards the edges of the continuum-subtracted CO(2-1) line emission map because of the primary beam correction (Figure 44).

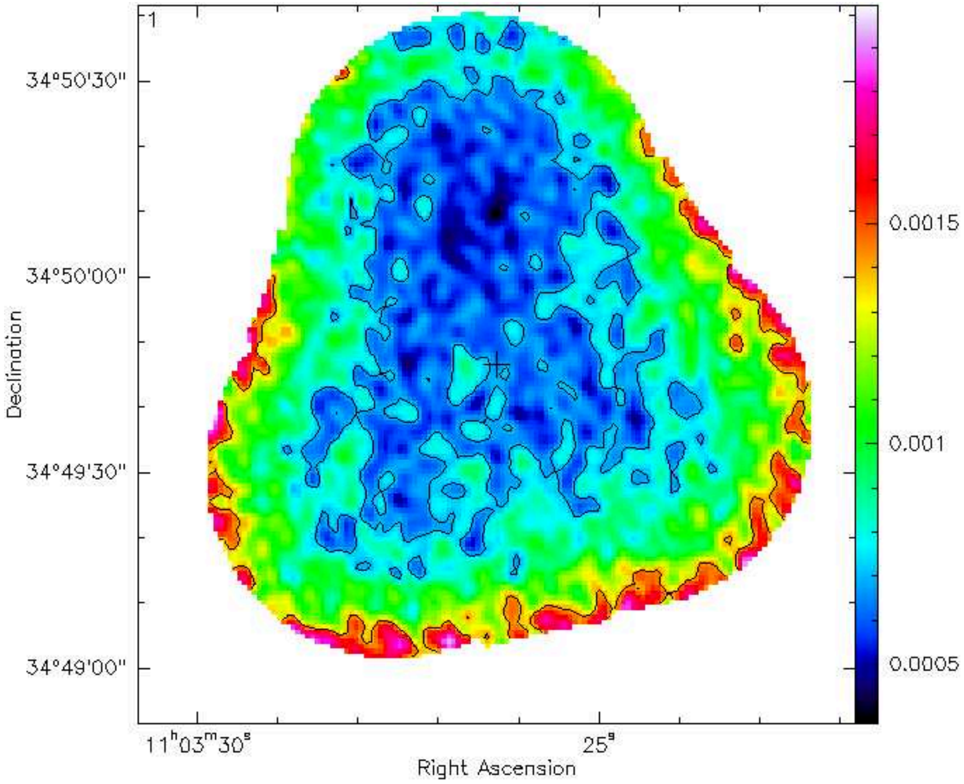

Figure 44: *Noise map of the continuum subtracted CO(2-1) line emission of the CARLA J1103+3449 cluster. The contours run as* 1σ *and* 2σ*, where* σ ∼ 0.7 mJy beam^{-1} *is the rms noise level of our data. The cross marks the center of the mosaic. The color scale of the intensity maps is in* Jy beam^{-1}.

RESULTS

The RLAGN Continuum Emission

On the continuum emission map at the observed frequency of $\nu_{\rm obs} \sim 94.48$ GHz, we detect an extended source in the cluster central region (Figure 45, white contours). Comparing the NOEMA continuum emission with radio observations from Best et al., (1999) (Figure 45, blue contours), the NOEMA continuum emission traces the two radio jets. Both the NOEMA continuum emission peak and the central radio emission correspond to the RLAGN position. The brighter continuum component is centered on the RLAGN core and extends towards the western radio lobe (>26σ, Figure 45, white contours). We also detect a significant (>6σ) continuum emission at the position of the eastern radio lobe and a part of the radio jet (Figure 45). The position and the scale of this continuum emission detection follows the emission from the radio lobes, which is consistent with the same or a connected physical origin of the two emissions.

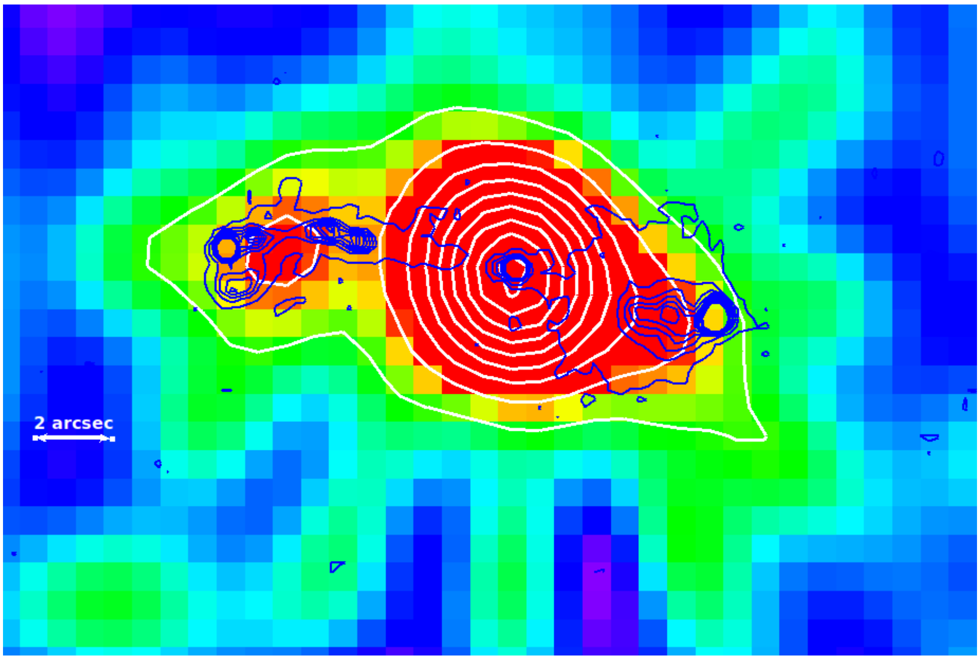

Figure 45: *A zoom-in on the continuum emission map at* $\nu_{\rm obs} \sim 94.48$ GHz *on the extended source in the CARLA J1103+3449 cluster center. North is up and East is to the left. The continuum emission contours (white) run as* 3σ, 6σ, 9σ, *etc. up to* 24σ. *The radio emission contours at 4.71* GHz *from the work of Best et al., (1999) are overlaid on the image (blue). The brightest continuum emission peak and one of the radio peaks are both centered on the RLAGN. The white line indicates the NOEMA effective resolution of* ~ 2 *arcsec. The continuum emissions seems consistent with the two radio jets, suggesting the same or a connected physical origin between the two emissions.*

Thermal emission of the interstellar dust peaks at frequencies $\nu \sim 3000$ GHz ($\lambda \sim 0.1$ mm), and continues to dominate at submillimeter wavelengths $\lambda <$ 1 mm (> 300 GHz), whereas the RLAGN synchrotron emission dominates at lower frequencies, therefore, at the rest-frame frequency $\nu \sim 230$ GHz/$\lambda \sim$ 1.3 mm, and in the radio domain (Bregman, 1990; Haas et al., 1998; Hönig, Prieto, and Beckert, 2008, Nyland et al., 2017), and originates from the non-thermal, synchrotron radiation emitted by the relativistic charged particles from the AGN jets (Gómez et al., 1995, 1997; Mioduszewski, Hughes, and Duncan, 1997; Aloy et al., 2000; Porth et al., 2011; Fuentes et al., 2018). These particles are trapped, and are spiraling around the magnetic field lines with relativistic velocities, and their emitting radiation at different frequencies is detected as continuum, non-thermal emission (Blumenthal and Gould, 1970).

I measure the flux centered at the RLAGN core, at the eastern lobe + the jet and the western lobe within the effective NOEMA resolution (~ 2 arcsec). With the NOEMA resolution it is not possible to distinguish the eastern lobe emission from the jet. I obtain $S_{\rm cont}^{\rm RLAGN} = 4.6 \pm 0.2$ mJy, $S_{\rm cont}^{\rm east\_lobe} = 1.1 \pm 0.2$ mJy and $S_{\rm cont}^{\rm west\_lobe} = 0.8 \pm 0.2$ mJy for the flux centered at the RLAGN core, at the eastern lobe + the jet, and the western lobe, respectively. Best et al., (1999) measured total fluxes of the RLAGN at two radio frequencies, $\nu = 8.21$ GHz and $\nu = 4.71$ GHz. They separate the radio emission into four different components: core, jet, eastern and western lobe, and measure the flux of each of these components. The flux of our brighter continuum component makes ~ 83% of the total continuum emission flux, while the corresponding flux in the radio (core and western lobe) makes ~ 65% at $\nu = 8210$ MHz and 66% at $\nu = 4710$ MHz of the total flux (Table 4). However, most (~ 71%) of the continuum emission at 94.48 GHz is coming from the core, while more than half of the total radio emission (52 – 59%) originates from the western lobe.

Table 4: Continuum flux measurements from our work at 94.5 GHz, and those from Best et al., (1999) at 4.71 GHz and 8.21 GHz. α is the spectral index measured over this wavelength range, and $\alpha^{\rm B99}$ are the spectral indexes from Best et al., (1999).

Component	RA (J2000) (h:m:s)	DEC (J2000) (d:m:s)	$F_{4.71\ \rm GHz}$ (mJy)	$F_{8.21\ \rm GHz}$ (mJy)	$F_{94.5\ \rm GHz}$ (mJy)	$\alpha^{\rm B99}$	α
total	/	/	96.6	55.7	6.5 ± 0.3	/	0.94 ± 0.01
core	11:03:26.26	+34:49:47.2	6.8	6.9	4.6 ± 0.2	-0.04	0.14 ± 0.03
west	11:03:25.83	+34:49:45.9	57.0	29.1	0.8 ± 0.2	1.21	1.43 ± 0.04
east+jet	11:03:26.77	+34:49:47.7	32.8	19.7	1.1 ± 0.2	/	1.15 ± 0.04
east	11:03:26:89	+34:49:47.8	21.7	12.7	/	0.96	/
jet	11:03:26.64	+34:49:48.2	11.1	7.0	/	0.82	/

Table 4 shows continuum flux measurements of the RLAGN core and its components at 94.48 GHz from Markov et al., (2020b) and at 4.71 GHz and 8.21 GHz from Best et al., (1999). I measure the spectral index α from a linear fit of these measurements (Figure 46). Next, in Table 4 I compare spectral indexes with the $\alpha^{\rm B99}$ values from Best et al., (1999). Spectra of the lobes can be modeled by a steep power law ($S_{\rm synch} \propto \nu^{-\alpha}$), consistent with optically thin synchrotron emission of the AGN jets, which is typically in the range of $0.5 < \alpha < 1.2$ locally (Laing and Bridle, 2013; Nyland et al., 2017; Ruffa et al., 2019; Grossová et al., 2019), while it is $1.0 < \alpha < 2.0$ and up to $\alpha \sim 3$, for high-redshift ($z > 2$) galaxies (Carilli et al., 1997; Best et al., 1999). Moreover, the spectra of the AGN core is flatter, which is consistent with the optically thicker (self-absorbed) synchrotron emission, which is in the range of $-0.5 < \alpha < 0.5$ locally (Ruffa et al., 2019; Grossová et al., 2019), while it is $-1.0 < \alpha < 1.0$ for high-redshift ($z > 2$) galaxies (Carilli et al., 1997; Athreya et al., 1997; Best et al., 1999). Furthermore, Best et al., (1999) shows a spectral index map of the RLAGN calculated between the range of frequencies of 4.71 GHz and 8.21 GHz (Figure 47).

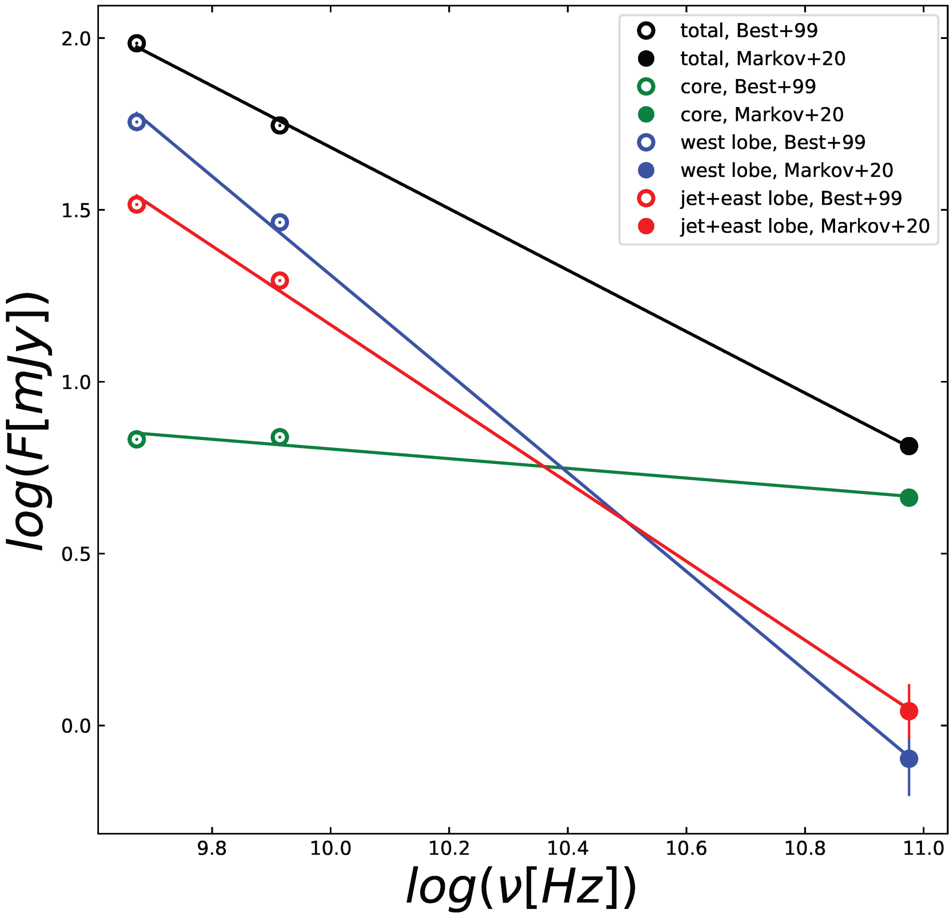

Figure 46: *SED plot of the RLAGN core and its components in the radio and mm wavelengths from our work (filled circles) and Best et al., (1999) (open circles).*

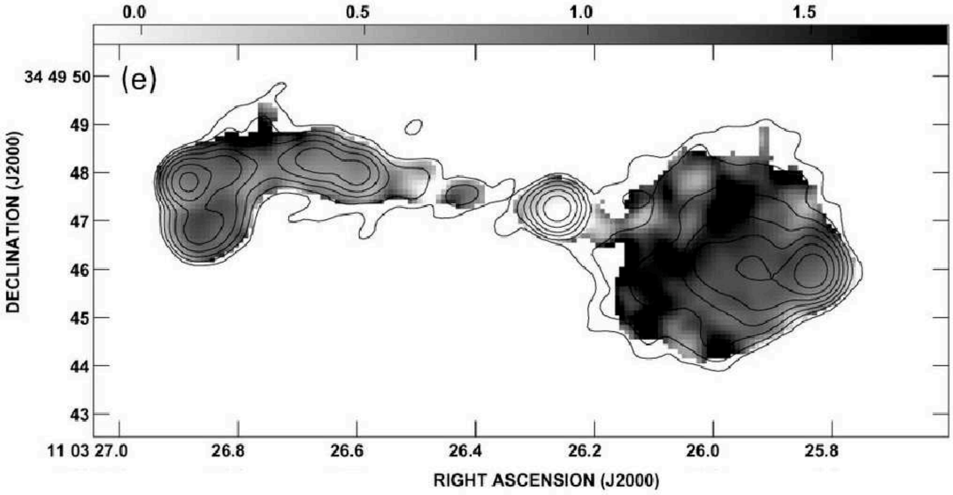

Figure 47: *Spectral index map of the RLAGN, calculated between the 4.71 GHz and 8.21 GHz. Figure is from the work of Best et al., (1999).*

In Figure 48 I show the spectral energy distribution (SED) of the RLAGN at radio wavelengths from the literature and mm observations from our work. The spectral index determined over the range of frequencies that spans over three orders of magnitude is $\alpha = 0.92 \pm 0.02$. The spectra shows no flattening at high-frequency ($\nu > 10$ GHz), which means that the radio source is still active.

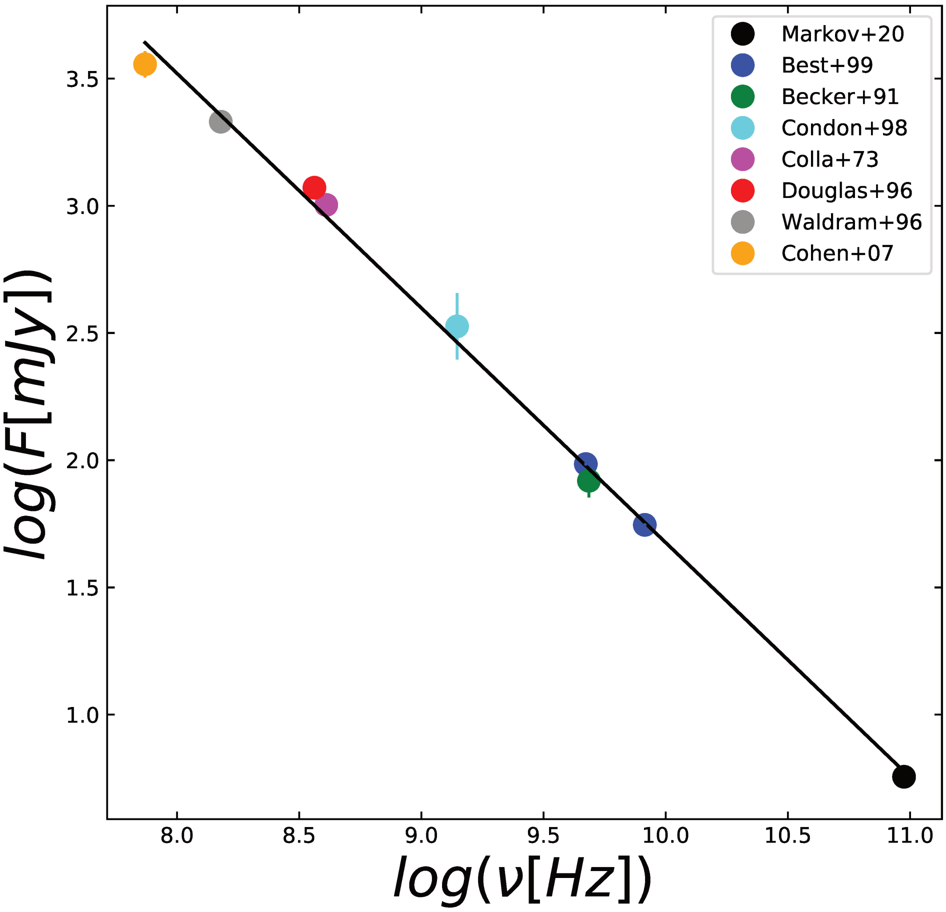

Figure 48: *SED plot of the RLAGN in the radio and mm wavelengths from our work (black), Best et al., 1999 (blue), Becker, White, and Edwards, 1991 (green), Condon et al., 1998 (cyan), Colla et al., 1973 (magenta), Douglas et al., 1996 (red), Waldram et al., 1996 (gray) and Cohen et al., 2007 (orange).*

The molecular gas content around the RLAGN

In this subsection I present the molecular gas mass content in the central region of the cluster around the RLAGN. Furthermore, I present the molecular gas upper limits, SFR estimates and other parameters of the RLAGN and other spectroscopically confirmed cluster members.

The CO(2-1) line emission around the RLAGN

SYSTEM VELOCITY AND FWHM. With the help of P. Salomé and F. Combes, I use the `class` package from the GILDAS software, in order to estimate the system velocity and the FWHM (Full Width Half Maximum) velocity dispersion from the CO(2-1) line emission. I extract the CO(2-1) line profile from a region enclosing all $> 1\sigma$ CO(2-1) emission in the cluster center (Figure 49), and mask out the pixels outside of this region. Next, I set equal weights and average the spectra. Moreover, I convert the flux units from Kelvin K to Jansky Jy, since in the `class` package the default flux unit is K.

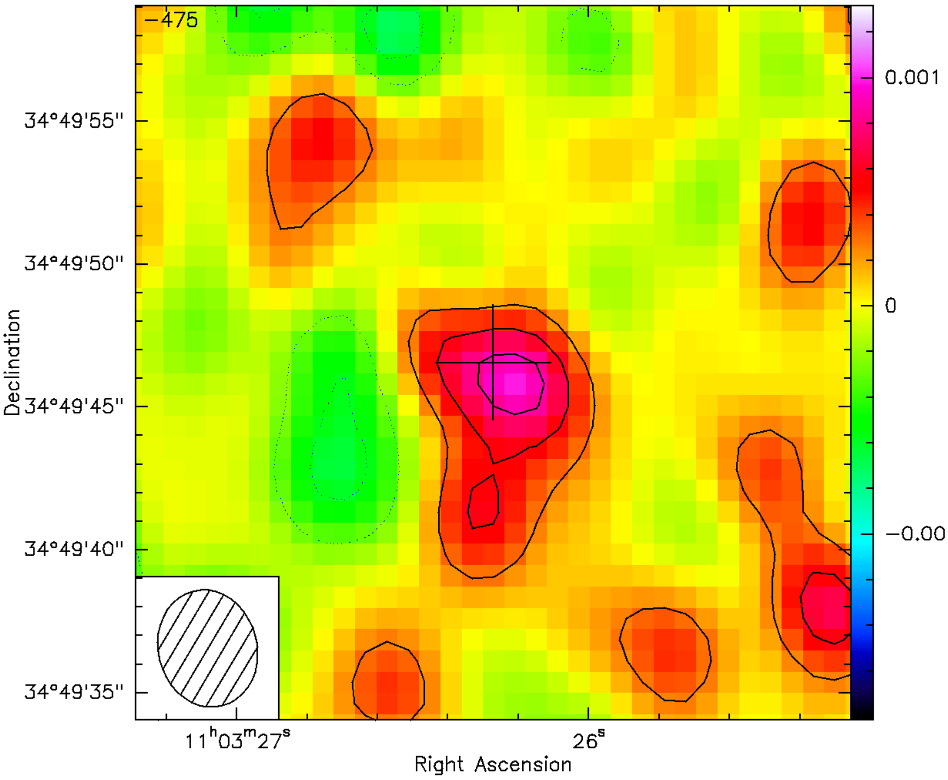

Figure 49: *A zoom-in on the CO(2-1) line emission, continuum-subtracted mosaic map on the extended source in the cluster center. The black cross marks the center of observations. The beam size* (4.14 × 3.45 *arcsec) is plotted at the lower left. The color scale of the intensity map is in* Jy beam^{-1}. *The rms noise level is of* $\sigma \sim 0.28$ mJy beam^{-1}. *The contours correspond to the* 1σ, 2σ *and* 3σ *levels.*

Finally, I plot the spectrum and identify two emission lines, which I fit with Gaussians (Figure 50). The two Gaussian emission peaks are at $V_{\rm sys} = -623.0 \pm 29.8$ km s^{-1} with velocity dispersion FWHM $= 178.7 \pm 71.3$ km s^{-1}, and $V_{\rm sys} = -115.5 \pm 40.1$ km s^{-1} with velocity dispersion FWHM $= 346.0 \pm 87.2$ km s^{-1}. These fits are shown as the blue and red

Gaussians, respectively, in Figure 50. The zero point $V_{sys} = 0$ km s^{-1} in the spectrum corresponds to a redshift $z \sim 1.44$, the mean confirmed cluster member redshift from Noirot et al., (2018).

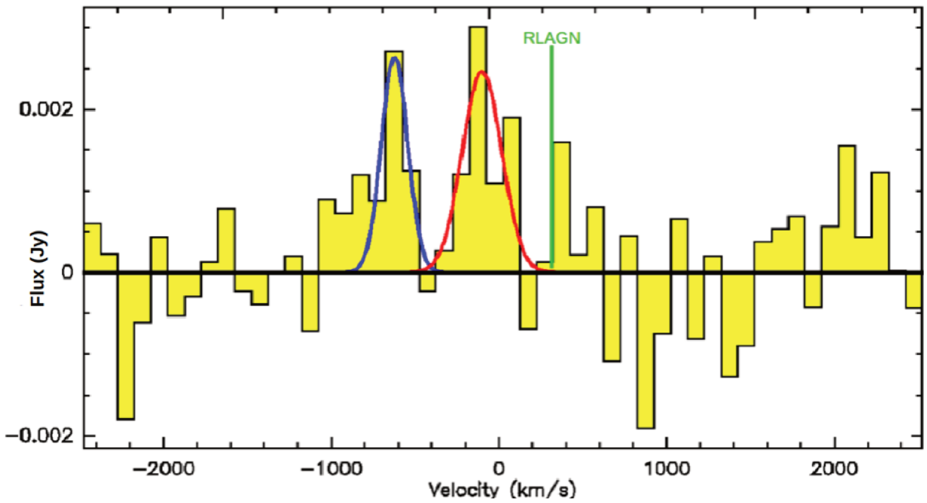

Figure 50: *Right: CO(2-1) line emission integrated spectrum. The two Gaussians fits correspond to system velocities of* Vsys ~ -623.0 km s^{-1} *(blue), and* Vsys ~ -115.5 km s^{-1} *(red). The RLAGN spectroscopic redshift corresponds to a velocity of* $v \sim 331.6$km s^{-1} *(vertical green line).*

In Figure 51, Figure 52 and Figure 53, P. Salomé and I identify the emission regions of the two CO(2-1) emission peaks by mapping the position of each component using the GILDAS software. We kinematically resolve the two components of the two CO(2-1) emission lines, by selecting a different range of channels (velocities or frequencies) in the CO(2-1) spectrum and creating the corresponding CO(2-1) emission line intensity maps, averaged over a chosen range of velocities. We select a range of velocities so that we include both emissions (-1075km s^{-1} $< v < +125$ km s^{-1}, Figure 51), only the blue peak emission (-1075km s^{-1} $< v < -475$ km s^{-1}, Figure 52) and only the red peak emission (-375km s^{-1} $< v < +125$ km s^{-1} Figure 53). Although both the blue and red emission peaks are superposed in some regions of the cluster core, they can be kinematically separated.

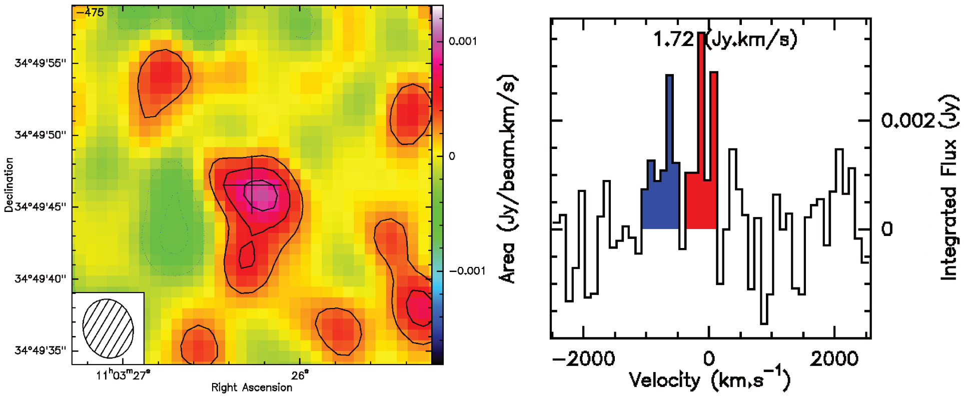

Figure 51: *CO(2-1) line emission intensity map of the central cluster region with NOEMA (left panel) created by selecting the channel ranges that include both the blue and the red emission peaks (right panel). The contour levels are* 1σ, 2σ *and* 3σ.

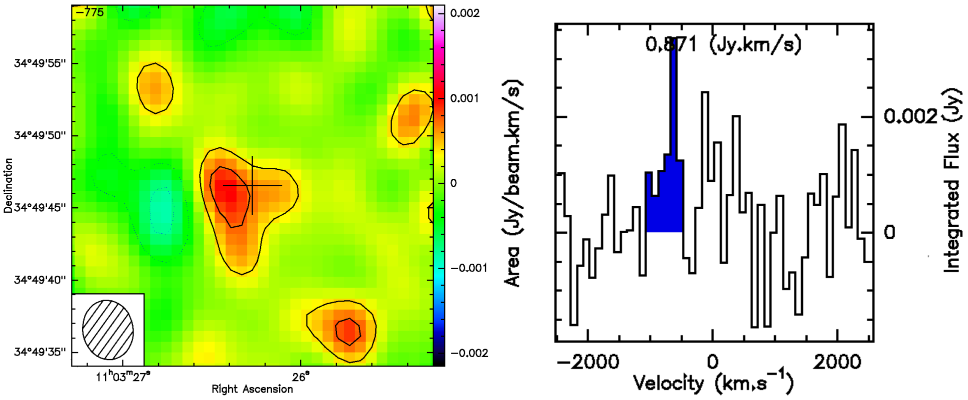

Figure 52: *CO(2-1) line emission intensity map of the central cluster region with NOEMA (left panel) created by selecting the channel ranges that include only the blue emission component (right panel). The contour levels are* 1σ *and* 2σ*.*

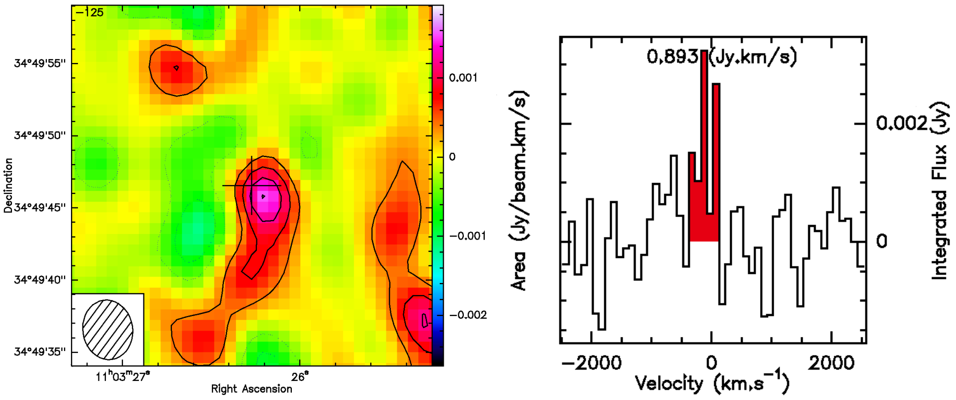

Figure 53: *CO(2-1) line emission intensity map of the central cluster region with NOEMA (left panel) created by selecting the channel ranges that include only the red emission component (right panel). The contour levels are* 1σ*,* 2σ*,* 3σ *and* 4σ*.*

In Figure 54, we compare the emission regions from NOEMA observations to the positions of the CARLA IRAC color-selected galaxies in the HST/F140W image. The spatial extension that corresponds to the red emission peak (red contours in Figure 54) is close to, but not centered on, the central RLAGN and the companion galaxy west of the RLAGN. The 2σ spatial extension of the blue peak emission (blue contours in Figure 54) does not correspond to any source in the optical (*HST*/WFC3) or infrared (*Spitzer*/IRAC). Neither the red nor the blue emission peaks correspond to the spatial position or to the spectroscopic redshift of the RLAGN (blue square in Figure 54).

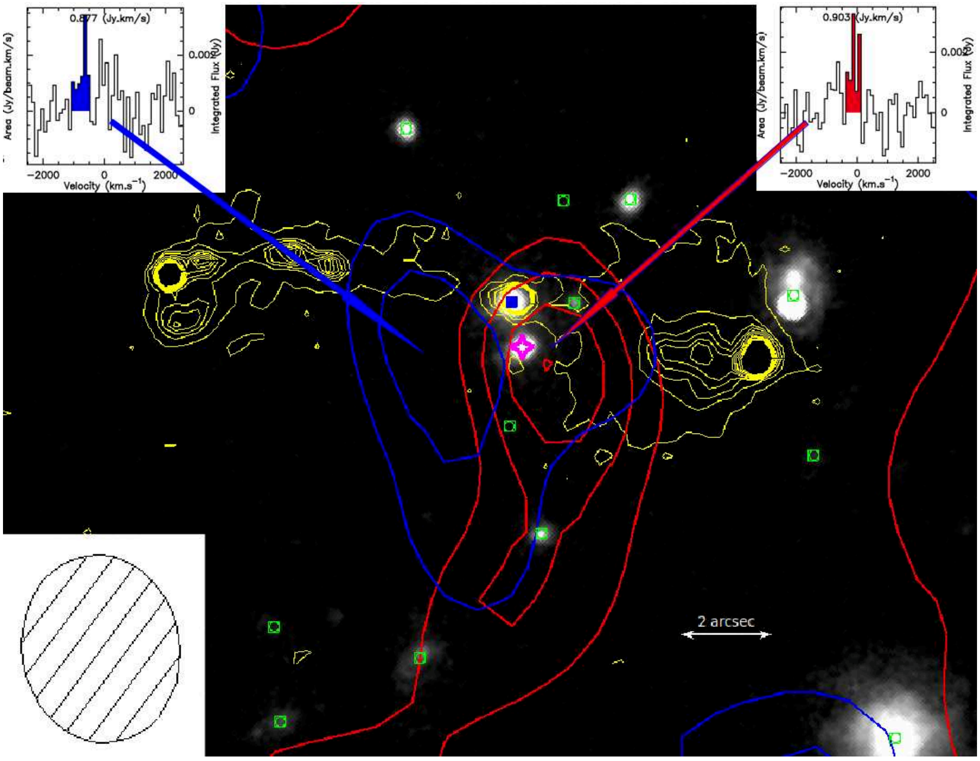

Figure 54: *HST/WFC3 F140W image of the central region of the cluster, with the contours of CO(2-1) emission of the blue and red emission peaks (shown as contours of their respective colors), and the radio emission at* 4.71 *GHz (yellow) from the work of Best et al., (1999). North is up and East is to the left. The central peak of the radio emission corresponds to the position of the RLAGN (blue square). The object south of the RLAGN is a star (magenta star). The green squares are the positions of IRAC color-selected galaxies in the cluster central region. The contours are derived by averaging the CO(2-1) emission across the velocities marked by their corresponding color on the CO(2-1) emission line spectra (top left and right insets). The contour levels of the blue and the red emission peaks are* $1-2\sigma$ *and* $1-4\sigma$*, respectively. The red emission peak is close to, but not centered on, the RLAGN. The blue emission peak does not correspond to any galaxy detected on the HST and Spitzer images. The beam size* (4.14×3.45 *arcsec) is plotted at the lower left.*

In Figure 55 I compare the spatial extension of the blue and the red emission peak with the extended continuum emission. The continuum emission is in the same direction (east-west) as the two CO(2-1) components, but spatially offset from the two CO(2-1) components and spread over larger distances.

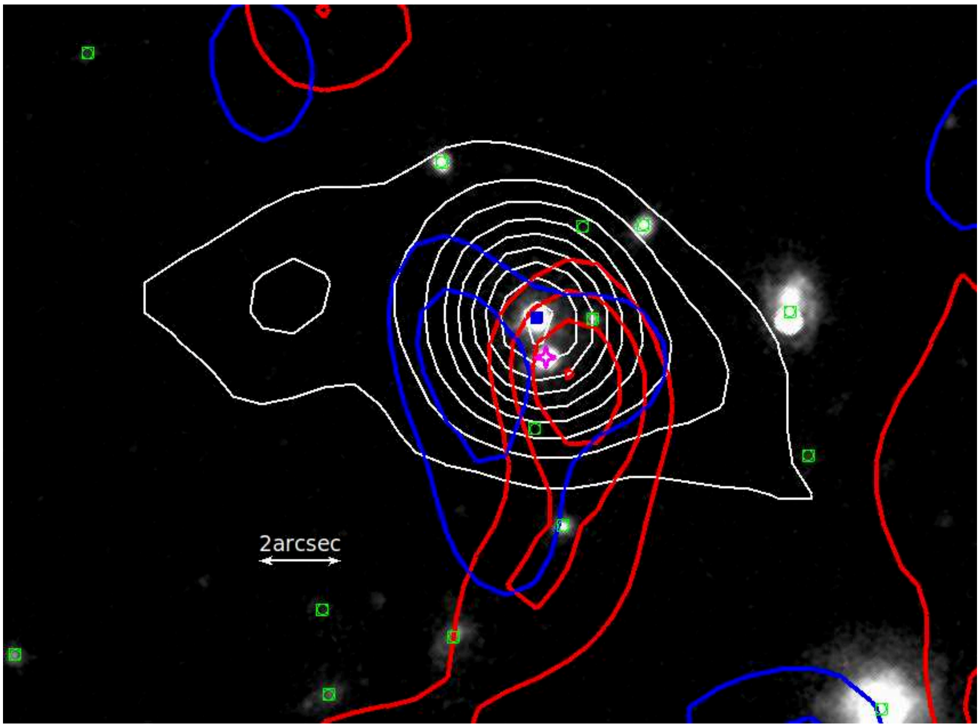

Figure 55: *HST/WFC3 F140W image of the central region of the cluster, with the contours of CO(2-1) emission of the blue and red emission peaks (shown as contours of their respective colors), and the continuum emission at 94.5 GHz (white). North is up and East is to the left. The contour levels of the blue, the red emission peaks and the continuum emission are* $1-2\sigma$ *and* $1-4\sigma$, $3-24\sigma$ *respectively. The green squares are the positions of IRAC color selected galaxies in the cluster central region.*

Other overdensities at the center of the NOEMA CO(2-1) line emission mosaic map (Figure 43) are at SNR $\leqslant$ 2. Their velocity peak is at the same spectral position as that of the blue and red peak emission velocity, but galaxies are not detected at their position in the *HST*/WFC3 or *Spitzer*/IRAC images. The detections at $> 3\sigma$ at the edges of the mosaic are not to be trusted, since the noise is higher (Figure 44).

Furthermore, I cross-correlate the two catalogs of the positions of cluster galaxies in the *HST* image and the positions of the overdensities on the NOEMA mosaic map, and found that only two overdensities (including the central overdensity) are correlated to the positions of the galaxies from the *HST*/WFC3 image. Therefore, all the overdensities might be due to the side lobes, and only the central source is detected.

VELOCITY INTEGRATED FLUX When fitting the spectral lines with the Gaussian fits, all parameters are left free to vary. From the Gaussian fit, the velocity integrated flux for the blue and red emission peaks are $S_{\mathrm{CO(2-1)}}\Delta v = 0.56 \pm 0.19$ Jy km s^{-1} (SNR $\sim$ 3), and $S_{\mathrm{CO(2-1)}}\Delta v = 0.90 \pm 0.21$ Jy km s^{-1} (SNR $\sim$ 4.4), respectively. Next, the Gaussian fit of both emission lines is $S_{\mathrm{CO(2-1)}}\Delta v = 1.71 \pm 0.35$ Jy km s^{-1}. The uncertainty on the measurements includes the uncertainties in the Gaussian fit and the noise in the region in which the fit is performed. In Table 5, I summarize the values, i.e. the systemic velocity, its FWHM, the velocity integrated flux, derived from the Gaussian fits of the two CO(2-1) emission lines.

Table 5: Velocity V_{sys}, velocity dispersion FWHM and the velocity integrated CO(2-1) flux $S_{CO}\Delta v$ of two CO(2-1) components estimated from the Gaussian fits to the CO(2-1) line emission.

peak	V_{sys}[km s^{-1}]	FWHM [km s^{-1}]	$S_{CO}\Delta v$[Jy km s^{-1}]
blue	$-623. \pm 30$	179 ± 71	0.56 ± 0.19
red	-116 ± 40	346 ± 87	0.90 ± 0.21
both	-334 ± 116	1043 ± 192	1.71 ± 0.35

The total flux of the blue and red emission peaks, obtained by integrating over the entire range of velocities are $S_{CO(2-1)}\Delta v = 0.88 \pm 0.16$ Jy km s^{-1} (SNR ~ 5.5; Figure 52) and $S_{CO(2-1)}\Delta v = 0.90 \pm 0.15$ Jy km s^{-1} (SNR ~ 6.0; Figure 53), respectively. The flux of the blue peak is larger then the flux obtained with the Gaussian fit, since part of the emission is missing when it is fitted by the Gaussian (Figure 50, blue line). However, the difference between these flux measurements is consistent with zero given the large uncertainty. The integrated flux from the blue and red emission peaks over the velocity range [-1075km s^{-1} $< v <$ $+125$ km s^{-1}] is $S_{CO(2-1)}\Delta v = 1.73 \pm 0.22$ Jy km s^{-1} (SNR ~ 8.0; Figure 51). Hereafter, the velocity integrated fluxes for both the blue and red emission peaks is used, since the SNR is higher.

Most of the red emission peak flux (~ 70%) corresponds to the circular region close to the RLAGN (Figure 56, middle panels), while the rest (~ 30%) corresponds to the region that extends to the south (Figure 56, bottom panels). However, this is emission of only one channel, and therefore, at the noise level. There is not enough signal to resolve possible different components of the red emission peak.

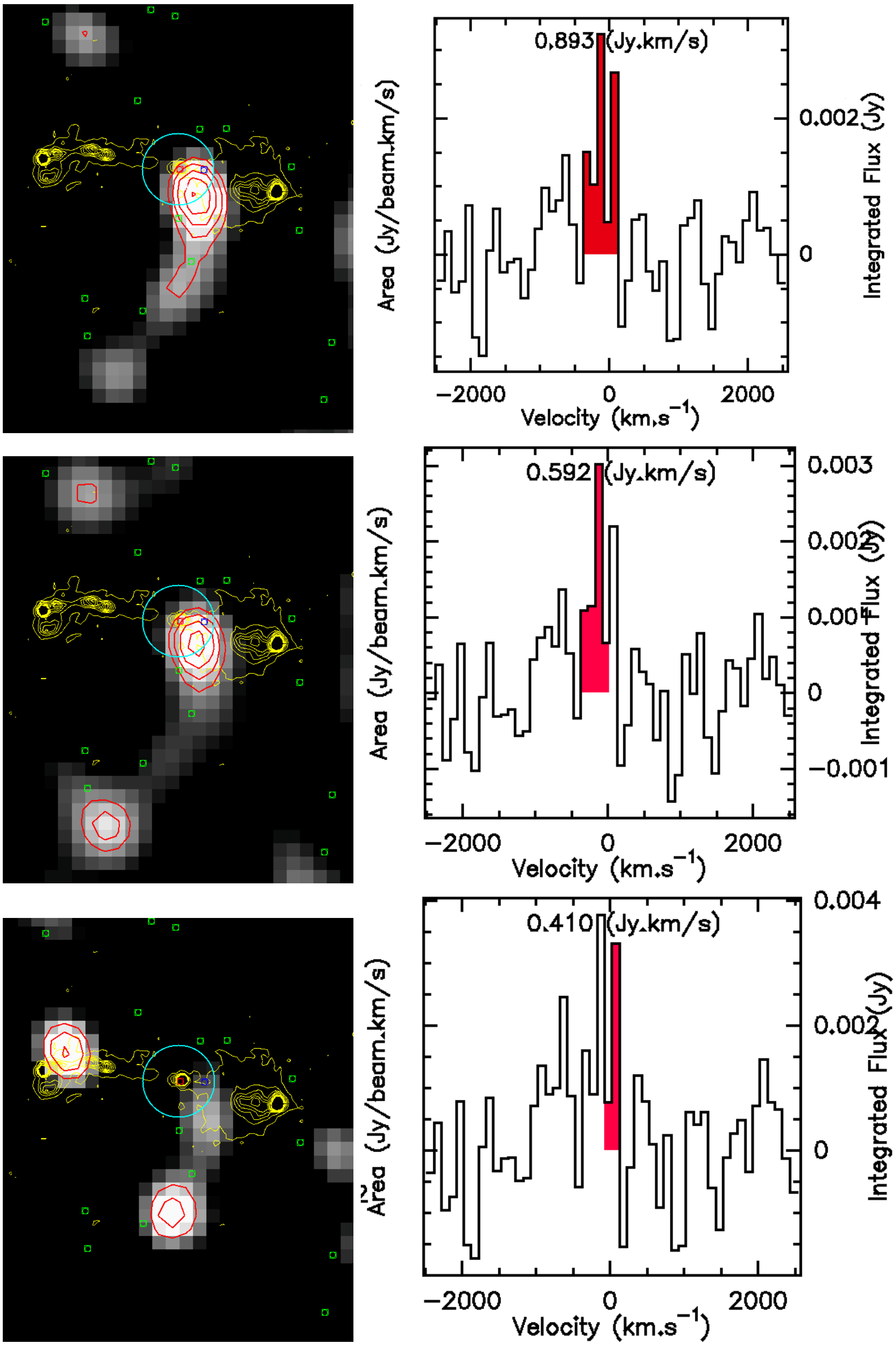

Figure 56: *CO(2-1) line emission intensity map of the central cluster region with NOEMA (left panels) with contours from the velocity range of the red emission component (right panels). The contour levels are 2σ, 2.5σ, 3σ, 3.5σ and 4σ. The yellow contours represent the radio emission from Best et al., (1999). The CO(2-1) emission is mapped by selecting the channel ranges that include the entire red emission (top right), channels 22-25 (middle right), and channel 26 (bottom right). The positions of the RLAGN, the companion spiral galaxy and other IRAC color-selected galaxies are shown as the blue, red and green squares. The NOEMA effective resolution ($\sim$ 2 arcsec) is shown as a cyan circle.*

Both the red and blue emission peaks do not correspond to the spectroscopic redshift of the RLAGN $z = 1.4427 \pm 0.0005$ (Figure 50). Therefore, S. Mei and I investigate the CO(2-1) line emission around the spectral position of the RLAGN (Figure 57).

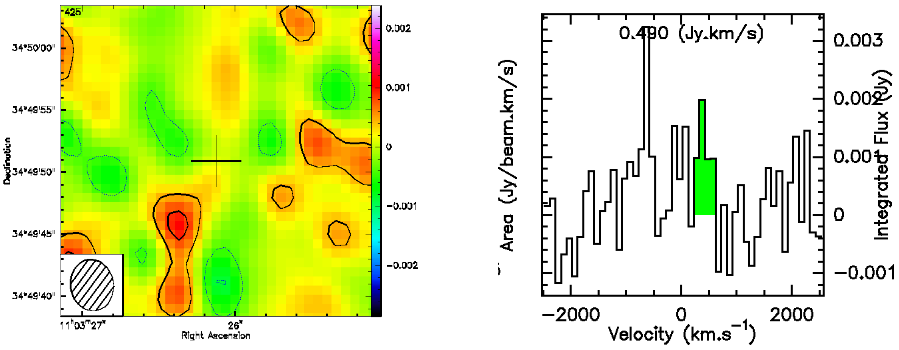

Figure 57: *CO(2-1) line emission intensity map of the central cluster region with NOEMA (left panel), created by selecting the channel ranges that include only the signal around the RLAGN redshift (right panel). The contour levels are* 1σ *and* 2σ*.*

I compare the spatial positions of this emission around the RLAGN redshift to the positions of the blue and the red emission peak and the RLAGN and the IRAC color-selected galaxies (Figure 58). The component around the RLAGN redshift spatially corresponds to the blue emission, it is spatially offset from the RLAGN by ~ one synthesized beam and does not have any optical/IR counterpart.

I measure the CO(2-1) line emission at the RLAGN redshift $z = 1.4427 \pm 0.0005$, which corresponds to a velocity position of $v \sim 331.6$ km s^{-1}, shown as a vertical green line in Figure 50. From a Gaussian fit around this velocity, the velocity integrated flux is $S_{CO(2-1)}\Delta v = 0.51 \pm 0.23$ Jy km s^{-1} (SNR ~ 2.2). Moreover, the Gaussian fit overestimates the velocity integrated flux (Figure 59).

Therefore, since this emission is spatially offset from the RLAGN, has no significant SNR nor an optical/IR counterpart, it cannot be trusted and it is not considered further.

LUMINOSITY AND MOLECULAR GAS MASS. I estimate the CO(2-1) luminosity, using the following relation from Equation (3) of Solomon and Vanden Bout, (2005):

$$L'_{CO(2-1)} = 3.25 \times 10^7 \frac{S_{CO(2-1)}\Delta v D_L^2}{\nu_{rest}^2 (1+z)} \tag{62}$$

where $L'_{CO(2-1)}$ is the CO(2-1) line luminosity in K km s^{-1} pc^2, $S_{CO(2-1)}\Delta v$ is the CO(2-1) velocity integrated flux in Jy km s^{-1}, $D_L = 10397.4$ Mpc is the RLAGN luminosity distance (calculated using the Ned Wright's cosmology calculator (Wright, 2006)), $\nu_{rest} = 230.538$ GHz is the rest frequency of the

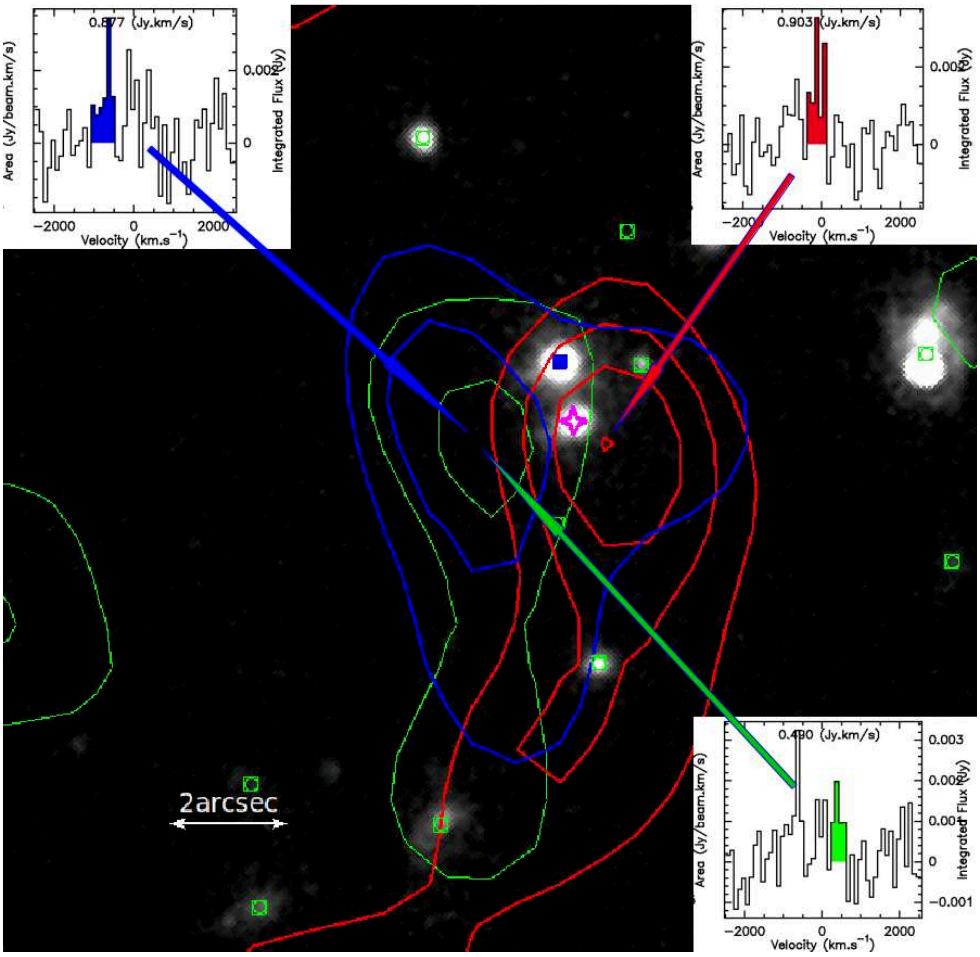

Figure 58: *CO(2-1) line emission contours from the blue, red and RLAGN-z emission components overlaid on the HST/F140W image. The object south of the RLAGN (blue square) is a star (magenta star). The green squares are the cluster IRAC color-selected galaxies from Wylezalek et al., (2013).*

CO(2-1) rotational transition, and 1.4427 ± 0.0005 is the RLAGN redshift (see Section 3.2.3). The CO(2-1) luminosity uncertainty is calculated as:

$$\delta L'_{CO(2-1)} = L'_{CO(2-1)} \sqrt{\left(\frac{\delta(S_{CO(2-1)})}{S_{CO(2-1)}}\right)^2 + \left(\frac{\delta z}{1+z}\right)^2} \tag{63}$$

I find $L'_{CO(2-1)} = 2.38 \pm 0.43 \times 10^{10}$ K km s^{-1}pc^2 and $L'_{CO(2-1)} = 2.44 \pm 0.41 \times 10^{10}$ K km s^{-1}pc^2, for the blue and red emission peaks, respectively.

In order to estimate the molecular gas mass, I use the mass-to-luminosity relation:

$$M_{gas} = \alpha_{CO} \frac{L'_{CO(2-1)}}{r_{21}} \tag{64}$$

where M_{gas} is the molecular gas mass, α_{CO} is the CO-to-H_2 conversion factor (e.g., see a review by Bolatto, Wolfire, and Leroy, 2013), r_{21} is the $L'_{CO(2-1)}/L'_{CO(1-0)}$ luminosity ratio, and $L'_{CO(2-1)}$ and $L'_{CO(1-0)}$ are the lumi-

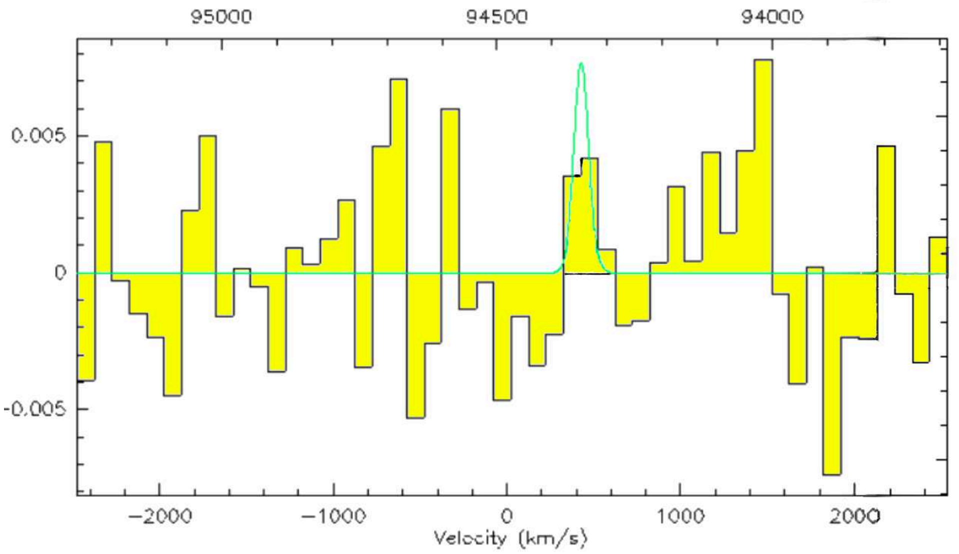

Figure 59: *The Gaussian fit of the CO(2-1) line emission integrated spectrum around the RLAGN redshift.*

nosities of the CO(2-1) and CO(1-0) emission lines, respectively. The mass uncertainty is calculated as:

$$\delta M_{\mathrm{gas}} = \alpha_{\mathrm{CO}} \frac{\delta L'_{\mathrm{CO}(2-1)}}{r_{21}} \tag{65}$$

I assume thermalized, optically thick CO emission for which the CO luminosities are independent of the rotational transitions, thus, $L'_{\mathrm{CO}(2-1)} = L'_{\mathrm{CO}(1-0)} \equiv L'_{\mathrm{CO}}$ and $r_{21} = 1$ (Solomon and Vanden Bout, 2005). This is a standard value used for the local galaxy M82 (Weiß, Walter, and Scoville, 2005) and for color-selected star-forming galaxies (CSGs, Dannerbauer et al., 2009). However other works use different values of r_{21}, an example is $r_{21} = 0.5$ for the Milky Way (Weiß, Walter, and Scoville, 2005). The reader should take into account these differences when comparing our results to other works in the literature (e.g. Casasola et al., 2013; Noble et al., 2017; Rudnick et al., 2017; Hayashi et al., 2018; Coogan et al., 2018; Castignani et al., 2018).

The CO-to-H$_2$ conversion factor α_{CO} is a large uncertainty in this calculation. Its value is not universal and depends on galaxy type, metallicity and CO gas excitation temperature and density (Bolatto, Wolfire, and Leroy, 2013; Carilli and Walter, 2013; Combes, 2018). For different kinds of galaxies and environments, its average range of values is $0.8 < \alpha_{\mathrm{CO}} < 4.36\ M_{\odot}(\mathrm{K\ km\ s^{-1}pc^{2}})^{-1}$ (Bolatto, Wolfire, and Leroy, 2013). The Galactic value $\alpha_{\mathrm{CO}} = 4.36\ M_{\odot}(\mathrm{K\ km\ s^{-1}pc^{2}})^{-1}$ is usually used when the molecular gas is associated to a standard galaxy, and, in fact, this is the value adopted in the majority of the literature, including the brightest cluster galaxies (BCGs) with extended molecular gas filaments of up to tens of kpc (McNamara et al., 2014; Russell et al., 2014, 2016; Vantyghem et al., 2016; Tremblay et al., 2018). Genzel et al., (2012, 2015) also gives α_{CO} as a function of metallicity. The lower value used for Ultra Luminous Infra-Red Galaxies (ULIRG), starburst and radio-galaxies, quasars, and in general for a warmer, unbound molecular gas, and/or molecular gas outflows/inflows is $\alpha_{CO} = 0.8\ M_\odot(\text{K km s}^{-1}\text{pc}^2)^{-1}$ (Bolatto, Wolfire, and Leroy, 2013; Carilli and Walter, 2013).

Since both the blue and red emission peaks are diffuse and are not associated with galaxies detected in the optical and near-infrared images, their emission might be associated with an inflow or outflow from the RLAGN. In that case, the observed molecular gas is expected to be partially transparent, more excited and with more chaotic, non-virial motions. This might lead to different values of r_{21} and α_{CO} than expected, i.e. $r_{21} > 1$, and $\alpha_{CO} < 4.36\ M_\odot(\text{K km s}^{-1}\text{pc}^2)^{-1}$ (Bolatto, Wolfire, and Leroy, 2013; Carilli and Walter, 2013; Cicone et al., 2018). For these reasons, I use the lower end of the standard α_{CO} values, and this will give the lower limits to the molecular gas mass estimates.

Therefore, with the assumed conversion factor $\alpha_{CO} = 0.8\ M_\odot(\text{K km s}^{-1}\text{pc}^2)^{-1}$, the molecular gas masses of the blue and the red emission peaks are $M_{gas}^{blue} = 1.91 \pm 0.34 \times 10^{10} M_\odot$ and $M_{gas}^{red} = 1.95 \pm 0.32 \times 10^{10} M_\odot$, respectively. The total molecular gas mass from the blue and the red emission peaks is of $M_{gas}^{tot,br} = 3.75 \pm 0.48 \times 10^{10} M_\odot$. Even when assuming the lowest α_{CO}, there is a large molecular gas reservoir that corresponds to the blue and red emission peaks.

As a comparison, when using the Galactic conversion factor $\alpha_{CO} = 4.36\ M_\odot(\text{K km s}^{-1}\text{pc}^2)^{-1}$, the molecular gas mass is ≈ 5 times larger $M_{gas}^{blue} = 1.0 \pm 0.2 \times 10^{11} M_\odot$, $M_{gas}^{red} = 1.1 \pm 0.2 \times 10^{11} M_\odot$, and total molecular gas mass from the sum of the blue and red emission peaks is $M_{gas}^{tot} = 2.1 \pm 0.3 \times 10^{11} M_\odot$, in the cluster central region. This shows that the value of the conversion factor is the largest uncertainty in the calculation of the molecular mass.

In Table 6, I give the velocity integrated flux, the CO luminosity and the molecular gas mass of the two components, assuming $\alpha_{CO} = 0.8\ M_\odot(\text{K km s}^{-1}\text{pc}^2)^{-1}$.

Table 6: Total velocity integrated CO(2-1) flux $S_{CO}\Delta v$, luminosity L'_{CO} and molecular gas mass M_{gas} of two CO(2-1) components.

peak	$S_{CO}\Delta v$[Jy km s^{-1}]	L'_{CO} [10^{10} K pc^2 km s^{-1}]	$M_{gas}[10^{10} M_\odot]$
blue	0.88 ± 0.14	2.4 ± 0.4	1.9 ± 0.3
red	0.90 ± 0.14	2.4 ± 0.4	2.0 ± 0.3
both	1.7 ± 0.2	4.7 ± 0.6	3.9 ± 0.4

Molecular gas content of cluster core members

In this section I report upper limits on the molecular gas content of the cluster members that were spectroscopically confirmed in the region covered by the NOEMA observations.

Besides the RLAGN, there are seven other spectroscopically confirmed CARLA J1103+3449 cluster members (Noirot et al., 2018), of which six are within the NOEMA beam (Figure 41), and three of them have stellar masses estimated by S. Mei. Furthermore, S. Mei morphologically classified all seven members as late-type galaxies. The NOEMA observations do not show CO(2-1) emission with SNR > 3 at the positions of the spectroscopically confirmed members. However, I use the 3σ values of the flux rms noise level at the position of each confirmed cluster member to derive an upper limit to the velocity integrated flux:

$$S_{CO(2-1)}\Delta v = (3\sigma_{rms})\Delta v \tag{66}$$

where Δv is a typical line width. The uncertainty on the velocity integrated flux is calculated as:

$$\delta(S_{CO(2-1)}\Delta v) = S_{CO(2-1)}\Delta v \times \sqrt{\left(\frac{\delta S_{CO(2-1)}}{S_{CO(2-1)}}\right)^2 + \left(\frac{\delta(\Delta v)}{\Delta v}\right)^2} \tag{67}$$

An average value of Δv, usually taken in the literature is $\Delta v = 300$ km s^{-1} for local galaxies from the SDSS survey (Saintonge et al., 2017). Since the velocity resolution of our CO(2-1) map of uncertainty is $\sigma_{\Delta v} = 100$ km s^{-1}, the velocity range within $300 \pm 3\sigma_{\Delta v}$ km s^{-1} includes most of the published Δv for star-forming cluster galaxies at these redshifts (e.g. Noble et al., 2017; Lee et al., 2017; Castignani et al., 2018; Hayashi et al., 2018).

With the help of P. Salomé, I estimate the rms noise level σ_{rms} using a CO(2-1) map averaged over the velocity width taken into account, i.e. 300 km s^{-1} (Figure 60). Next, I measure the average σ_{rms} at the position of each galaxy, from a large region $\sim 40\times$ beam size, in order to accurately measure σ_{rms}. Furthermore, for the RLAGN (id: 491) and the companion spiral galaxy (id: 490) at the cluster core, I measure the σ_{rms} from the entire region at the intersection of the three pointings, but excluding the signal from the detected source, since the signal has its own intrinsic noise that will add up to the total σ_{rms} (Figure 60).

I use the upper limits to the velocity integrated flux in order to estimate the upper limits of luminosity and molecular gas mass. For the molecular gas measurement, I use the Galactic conversion factor $\alpha_{CO} = 4.36\ M_\odot (\mathrm{K\ km\ s^{-1} pc^2})^{-1}$, typical for star-forming, late-type galaxies (Bolatto, Wolfire, and Leroy, 2013; Carilli and Walter, 2013; Combes, 2018). The estimated physical properties of the spectroscopically confirmed members are given in Table 7.

With the guidance of S. Mei, I also tried stacking the CO(2-1) line emission of all the confirmed members, except the RLAGN. I performed a *jackknife* analysis by stacking the emission of the confirmed members, but each time excluding one, two, three, etc. random galaxies from the sample, in order to identify if any of the galaxies stands out and gives rise to the signal. Finally, I concluded that this type of analysis is not possible with the available data, since four out of six confirmed members are at the very edges of the NOEMA map where the noise is high (Figure 44), and the question is if their emission can be trusted (Figure 61). Moreover, the emission of the companion spiral galaxy (id 490) is contaminated by the emission of both the red and blue emission peaks (Figure 54). Therefore, the emission of five out of six galaxies is questionable, and there is no visible CO(2-1) line emission at the position of the sixth galaxy on the CO(2-1) map (Figure 61).

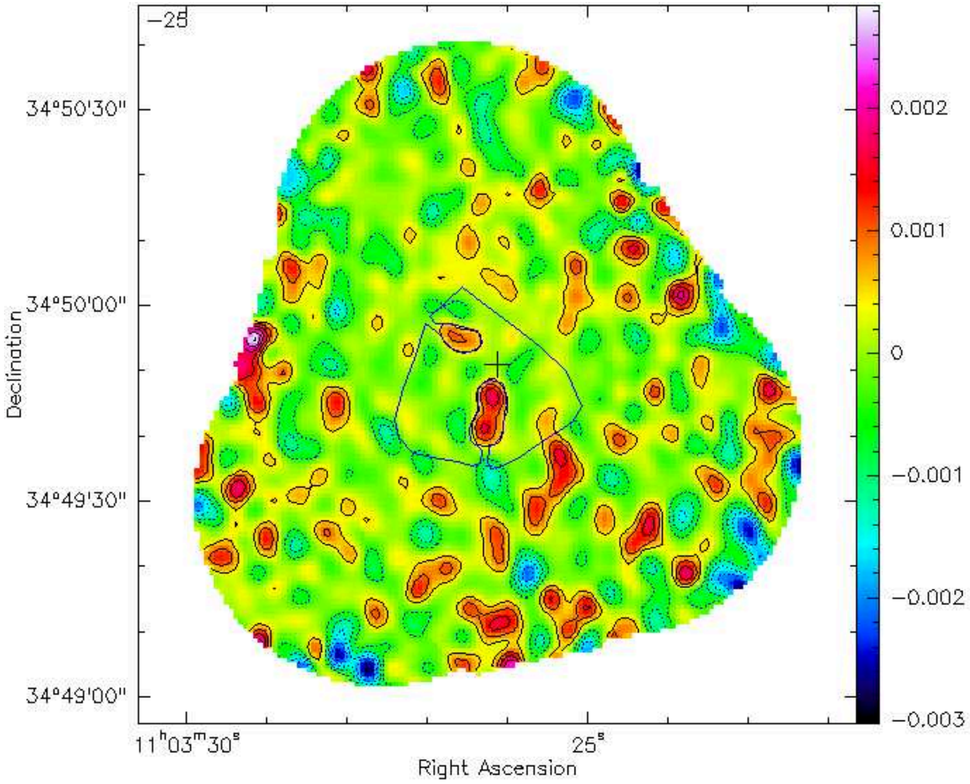

Figure 60: *CO(2-1) line emission intensity map of the central cluster region with NOEMA averaged over* 300 $\mathrm{km\,s^{-1}}$*, created by selecting the channel ranges between* $-150\ \mathrm{km\,s^{-1}} < v < +150\ \mathrm{km\,s^{-1}}$*. The blue line marks the region in the cluster core used for measuring the* σ_{rms} *for the RLAGN and the companion spiral galaxy. The color scale is in* $\mathrm{Jy\ beam^{-1}}$*. The contour levels are* 1σ*,* 2σ*,* 3σ*.*

Galaxy stellar mass

Our collaborators S. Amodeo and S. Mei measured galaxy stellar masses of the CARLA confirmed members by calibrating the psf-matched *Spitzer*/IRAC1 magnitudes with galaxy stellar masses from Santini et al., (2015) derived from the Guo et al., (2013) multi-wavelength catalog in the Cosmic Assembly Near-infrared Deep Extragalactic Legacy Survey (CANDELS; PI: S. Faber, H. Ferguson; Koekemoer et al., 2011; Grogin et al., 2011) WIDE GOODS-S field.

The *Spitzer* IRAC1 magnitudes correspond to the rest-frame near-infrared in the redshift range of the CARLA sample, and are expected not to be biased by extinction. S. Amodeo and S. Mei find a very good correlation between these magnitudes and the Santini et al., (2015) mass measurements, with scatters of ≈ 0.12 dex at the redshift of the cluster. Adding in quadrature the scatter of the relation and uncertainties from Santini et al., (2015), the obtained mass uncertainties are in the range $\sim 0.4 - 0.5$ dex, and $\approx 0.2 - 0.3$ dex for masses larger than $\log_{10}(\frac{M}{M_\odot}) > 10.5$.

Table 8 shows the stellar masses of the cluster spectroscopically confirmed members. The masses derived from this calibration are on average ≈ 0.5 dex smaller that those derived from stellar populations models by Noirot et al., (2018) (Table 9), and the difference is larger at fainter mag-

Table 7: Velocity integrated CO(2-1) flux $S_{CO}\Delta v$, luminosity L'_{CO} and molecular gas mass M_{gas} of the CARLA J1103+3449 spectroscopically confirmed cluster members. None of the spectroscopically confirmed members were detected with NOEMA and I report their $3\sigma_{rms}$ upper limits.

id*	$S_{CO}\Delta v$[Jy km s^{-1}]	L'_{CO} [10^9 K pc^2 km s^{-1}]	$M_{gas}[10^{10}M_\odot]$
491**	< 0.27	< 7.2	< 3.1
490	< 0.27	< 7.2	< 3.1
320	< 0.35	< 9.5	< 4.1
283	< 0.45	< 12.1	< 5.3
279	< 0.45	< 12.1	< 5.3
199	< 0.62	< 16.7	< 7.3
183	< 0.62	< 16.6	< 7.2

*

The identification numbers are the same as in the Noirot et al., (2018). ** The RLAGN.

nitudes. In Noirot et al., (2018) the stellar masses were determined using the Spitzer/IRAC fluxes, scaled to stellar population synthesis models using Chabrier initial mass function (IMF, Chabrier, 2003). For instance, the reported stellar mass of the RLAGN is by an order of magnitude higher (Table 9). This difference in mass estimates does not significantly change results from Noirot et al., (2018), in particular the conclusions from the SFR vs. stellar mass analysis (Fig. 7 in Noirot et al., 2018).

Gas-to-stellar mass ratio and gas fraction.

From our molecular gas mass upper limits, combined with the stellar masses estimated by S. Amodeo and S. Mei, I compute the gas-to-stellar mass ratio as M_{gas}/M_* and the molecular gas fraction as $f_{gas} = M_{gas}/(M_{gas} + M_*)$. The results are shown in Table 8.

Table 8: Stellar mass M_*, molecular gas-to-stellar mass M_{gas}/M_* ratio and molecular gas fraction f_{gas} of the CARLA J1103+3449 spectroscopically confirmed cluster members.

id*	$M_*[10^{10}M_\odot]$	M_{gas}/M_*	$f_{gas}[\%]$
491**	4.7 ± 2.3	< 0.7	< 40
320	0.7 ± 0.7	< 5.8	< 85
199	3.8 ± 1.9	< 1.9	< 66
183	0.3 ± 0.3	< 27.0	< 96

* The identification numbers are the same as in the Noirot et al., (2018). ** The RLAGN.

Method for deriving the SFR

In this subsection, I present the system of equations used for estimating the SFR of the spectroscopically confirmed CARLA J1103+3449 cluster mem-

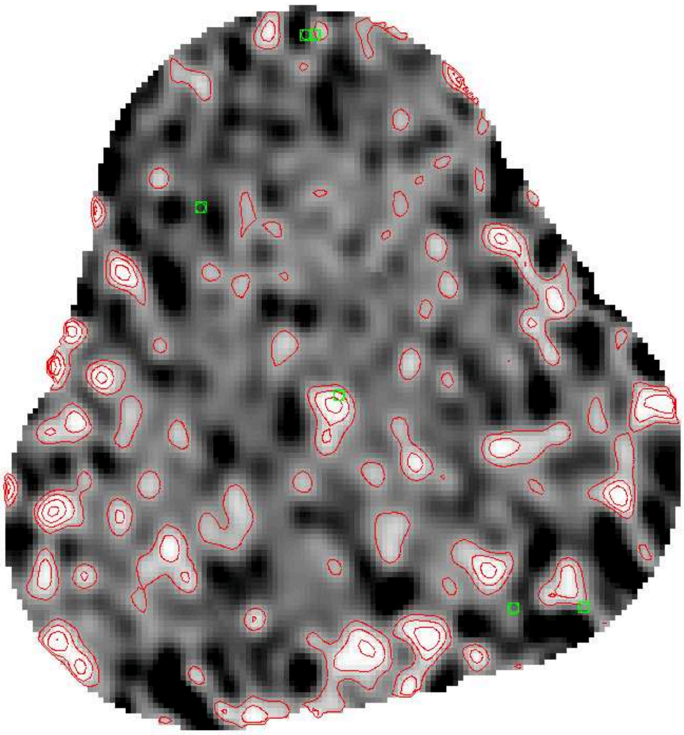

Figure 61: *CO(2-1) line emission mosaic map of the CARLA J1103+3449 cluster, obtained by averaging the flux over a velocity range of* 1200km s^{-1}. *The green squares are the spectroscopically confirmed cluster members from Noirot et al., (2018), excluding the RLAGN.*

bers. This method is based on a system of equations from Zeimann et al., (2013) and Curti et al., (2020).

The Kennicut law (Kennicutt, 1998b) shows a direct proportionality between the SFR and Hα flux:

$$\mathrm{SFR}_{H\alpha}[M_\odot \mathrm{yr}^{-1}] = 5 \times 10^{-42} L_{H\alpha} \times 10^{0.4 \times A_{H\alpha}} \tag{68}$$

where $\mathrm{SFR}_{H\alpha}$ is the estimated SFR including the contributions from the [NII] line and corrected for the dust attenuation $A_{H\alpha}$. I estimate $A_{H\alpha}$ using the Garn and Best, (2010) empirical law and the Calzetti et al., (2000) extinction law:

$$A_{H\alpha} = 0.91 + 0.77M + 0.11M^2 - 0.09M^3 \tag{69}$$

where $M = \log_{10} \frac{M_*}{10^{10} M_\odot}$ and M_* is the stellar mass. $L_{H\alpha}$ is the luminosity in erg s^{-1}, and it is calculated with the following equation:

$$L_{H\alpha} = 4\pi D_L^2 F_{H\alpha} \tag{70}$$

where $F_{H\alpha}$ is the Hα flux given in erg cm^{-2} s^{-1}, computed as:

$$F_{H\alpha} = F_{H\alpha+[NII]\lambda6548,6584} \frac{1}{1+\frac{[NII]\lambda6548,6584}{H\alpha}} \tag{71}$$

where $F_{H\alpha+[NII]\lambda6548,6584}$ is the total observed Hα flux plus the [NII]λ6548, 6584 flux. In fact, the WFC3/G141 grism resolution does not permit us to deblend the three lines (Noirot et al., 2018). Following Curti et al., (2020) (equations (2) and (5) and Table 6), I calculate the metallicity $12 + \log(O/H)$, expressed as a function of stellar mass and SFR:

$$12 + \log(O/H) = Z_0 - \gamma/\beta \times \log \left[1 + \left(\frac{M_*}{M_0(SFR)} \right)^{-\beta} \right] \tag{72}$$

where $Z_0 = 8.779 \pm 0.005$, $\log(M_0(SFR)) = m_0 + m_1 \times \log(SFR)$, $m_0 = 10.11 \pm 0.03$, $m_1 = 0.56 \pm 0.01$, $\gamma = 0.31 \pm 0.01$, and $\beta = 2.1 \pm 0.4$. Curti et al., (2020) also provide a new calibration for the relation between metallicity and $\frac{[NII]\lambda6584}{H\alpha}$:

$$\log \left(\frac{[NII]\lambda6584}{H\alpha} \right) = \sum_{n=1}^{4} c_n x^n \tag{73}$$

where x =12 + log(O/H) - 8.69, $c_0 = -0.489$, $c_1 = 1.513$, $c_2 = -2.554$, $c_3 = -5.293$, and $c_4 = -2.867$. Assuming a constant ratio $[NII]_{\lambda6584}$:$[NII]_{\lambda6548}$ of 3:1 (Osterbrock and Ferland, 2006), I derive $\frac{[NII]\lambda6548,6584}{H\alpha}$.

In order to calculate SFR we need the $\frac{[NII]\lambda6548,6584}{H\alpha}$ (Equation 68), and to measure $\frac{[NII]\lambda6548,6584}{H\alpha}$ we need the SFR (Equation 73). I follow a combined system of equations from the works of Zeimann et al., (2013) and Curti et al., (2020), and set an initial value of $\frac{[NII]\lambda6548,6584}{H\alpha} = 0.2$ and iterate on a system of equations Equation 68-Equation 73 till convergence. Zeimann et al., (2013) estimated a ~ 50% error on the SFR estimated by using a similar system of equations, and the uncertainty is dominated by the uncertainty on the attenuation.

Star formation rate, specific star formation rate, depletion time and star formation efficiency.

In this subsection, I report galaxy star formation rates using the Hα emission line flux from Noirot et al., (2018). Next, I combine them with our measurements of the molecular gas mass upper limits from the CO(2-1) line emission, and the galaxy stellar mass estimates performed by S. Mei, in order to estimate the molecular gas fraction, metallicity, SFR, sSFR, depletion time and SFE.

In Table 9, I show measurements of the Hα flux, SFR and stellar mass for the spectroscopically confirmed galaxies in the CARLA J1103+3449 cluster from the work of Noirot et al., (2018).

Following a system of equations described in Section 3.3.5, and using the Hα line fluxes from Noirot et al., (2018) and the stellar mass estimates from S. Mei and S. Amodeo, I re-compute the $SFR_{H\alpha}$ and calculate the Hα-[NII] ratio, attenuation $A_{H\alpha}$ and metallicity $12 + \log(O/H)$. I present the results in Table 10. For the RLAGN, the SFR is overestimated since the Hα emission line flux is contaminated by the emission coming from the central AGN. Since we cannot separate the Hα line emission stellar contribution from the

Table 9: H_α flux $F_{H\alpha}$, $SFR_{H\alpha}$ and stellar mass M_* of the CARLA J1103+3449 cluster confirmed members from the work of Noirot et al., 2018.

id*	$F_{H\alpha}[10^{-17}\text{erg s}^{-1}\text{cm}^{-2}]$	$SFR_{H\alpha}[M_\odot \text{yr}^{-1}]$	$M_*[10^{10} M_\odot]$ **
491***	73.8 ± 6.6	<140	<31.6
490	13.4 ± 2.4	25 ± 5	<1.0
320	5.5 ± 2.8	10 ± 5	7.6 ± 0.1
283	8.6 ± 3.6	16 ± 7	< 1.0
279	5.6 ± 3.1	11 ± 6	<1.0
199	5.8 ± 2.0	11 ± 4	13.6 ± 0.1
183	6.9 ± 2.6	13 ± 5	1.6 ± 0.1
93	10.2 ± 2.1	19 ± 4	<1.0

* The identification numbers are the same as in the Noirot et al., (2018). ** Stellar mass uncertainties cited here are only the IRAC flux uncertainties, without the 20% systematics towards lower masses (Noirot et al., 2018). *** RLAGN

contribution due to the AGN, I estimate the SFR upper limit (see a review by Tadhunter, 2016). The stellar contribution to the total Hα emission varies in the range of $20 - 100\%$ and I compute the SFR within this range (see Table 10).

In Table 10, I compare our SFR estimates with those from Noirot et al., 2018. The difference between our SFR and those from Noirot et al., 2018 is typically within 1σ. For some cluster galaxies, stellar mass measurements are not available, because they are not detected in the IRAC images by S. Mei and S. Amodeo. For those galaxies I cannot re-compute the SFR. Hereafter, I will use our SFR measurements when I could derive them, and Noirot et al., (2018) SFR measurements for other galaxies.

For the RLAGN, the obtained range of values $H\alpha/[NII] = 2.3 - 3.7$ (depending on the assumed AGN contribution) is in agreement to the assumed value $H\alpha/[NII] = 3.33$ from Noirot et al., (2018). However, our attenuation estimate $A_{H\alpha} = 1.4 - 1.5$ is lower compared to the assumed value $A_{H\alpha} = 2.0$ from Noirot et al., 2018. Our values of the Hα/[NII] ratio and metallicity $12 + \log(O/H) = 8.58 - 8.69$ are in agreement with the expected values from the works of Shapley et al., (2005), Queyrel et al., (2009) and Wuyts et al., (2012), for galaxies at intermediate redshifts ($1.0 < z < 2.0$). The Hα-[NII] ratio is uncertain since it is not universal and varies with redshift and stellar mass (mass-metallicity relation; Tremonti et al., 2004; Erb et al., 2006; Maiolino et al., 2008; Queyrel et al., 2009; Wuyts et al., 2012).

Combining our measured SFR with the stellar masses estimates from S. Mei and S. Amodeo, I compute the sSFR:

$$sSFR = \frac{SFR_{H\alpha}}{M_*} \tag{74}$$

Results are shown in Table 10.

Table 10: Attenuation $A_{H\alpha}$, metallicity 12 + log(O/H), $SFR_{H\alpha}$, and sSFR for the CARLA J1103+3449 cluster confirmed members.

id*	$A_{H\alpha}$	12 + log(O/H)	$SFR_{H\alpha}[M_{\odot} yr^{-1}]$	sSFR [Gyr^{-1}]
491^{**} 100%	1.4	8.58	143.3 ± 45.4	3.1 ± 1.8
491 80%	1.4	8.59	112.7 ± 35.7	2.4 ± 1.4
491 60%	1.4	8.61	82.7 ± 26.2	1.8 ± 1.0
491 40%	1.5	8.64	53.5 ± 17.0	1.1 ± 0.7
491 20%	1.5	8.69	25.5 ± 8.1	0.5 ± 0.3
320	0.8	8.56	5.9 ± 3.4	0.8 ± 0.9
199	1.4	8.72	9.0 ± 3.8	0.2 ± 0.1
183	0.5	8.43	6.2 ± 3.8	2.3 ± 2.6

The identification numbers are the same as in the Noirot et al., (2018). ** In case of the RLAGN (id 491), since we cannot separate the AGN and stellar contributions, the stellar contribution to the total Hα emission flux in the range $20-100\%$.

I use the $SFR_{H\alpha}$ estimates and the upper limits of the molecular gas mass to compute the depletion time:

$$\tau_{dep} = \frac{M_{gas}}{SFR_{H\alpha}} \tag{75}$$

and the SFE:

$$SFE = \frac{SFR_{H\alpha}}{M_{gas}} \tag{76}$$

Results are shown in Table 11. Here I note that the rms noise of the CO(2-1) line emission map used for the molecular gas mass limit estimate does not coincide spatially with the Hα emission. The CO(2-1) line emission flux limit is measured by taking an average $3\sigma_{rms}$ over a much broader area than the Hα emission, in order to avoid local fluctuations of the rms noise (e.g. Figure 60).

Table 11: Depletion time τ_{dep} and SFE for the CARLA J1103+3449 spectroscopically confirmed cluster galaxies.

id*	τ_{dep}[Gyr]	SFE[Gyr^{-1}]
491** 100%	< 0.2	> 4.5
491 80%	< 0.3	> 3.6
491 60%	< 0.4	> 2.6
491 40%	< 0.6	> 1.7
491 20%	< 1.2	> 0.8
490+	< 1.2	> 0.8
320	< 7.0	> 0.1
283+	< 3.3	> 0.3
279+	< 5.0	> 0.2
199	< 8.1	> 0.1
183	< 11.6	> 0.1

* The identification numbers are the same as in the Noirot et al., (2018). ** In case of the RLAGN (id 491), the stellar contribution to the total Hα emission flux is in the range $20 - 100\%$. + Cluster members for which the values of the SFR are reported in Noirot et al., 2018 that are used for estimating the depletion time and SFE.

DISCUSSION

Origin of the molecular gas in the cluster core

In the central region of the CARLA J1103+3449 cluster, we observe two CO(2-1) emission components that do not correspond to any galaxy detected in the *HST* or *Spitzer* images (Figure 54, blue and red contours). Radio observations of the CARLA J1103+3449 cluster from the work of Best et al., (1999) reveal two radio lobes, which are roughly in the same direction (east and west) as our CO(2-1) molecular gas components, but spread over larger distances (Figure 54, yellow contours). The two radio lobes are asymmetrical, the eastern being more compact, while the western is more diffuse. Both CO(2-1) emission peaks are blueshifted with respect to the central velocity of 0 km s^{-1} (which corresponds to the cluster redshift of $z = 1.44$) and to the RLAGN redshift (Figure 50), and their spatial position is very close to the position of the radio lobes, which indicates that the molecular gas might be associated with the RLAGN jets (Figure 54).

The two CO(2-1) emission lines might trace the molecular gas originating from various sources. We discuss several hypotheses in order to compare our results to the literature and understand the most probable origin of the detected molecular gas.

Rotating disk or torus

First, I consider the hypothesis that the two CO(2-1) emission lines might trace molecular gas originating from an extended (up to tens of kpc) rotating disk or torus of molecular gas around the central galaxy. In case the blue and red CO(2-1) components are part of a rotating disk or torus, I estimate the dynamical mass of the interior region of the orbits of the two CO(2-1) components (see e.g. Solomon and Vanden Bout, 2005):

$$M_{\rm dyn} = \frac{dv^2}{G} \tag{77}$$

where d is the projected distance between the CO(2-1) component and the RLAGN, v is the orbital velocity and $G = 6.67 \times 10^{-11}$ m^3 kg^{-1} s^{-2}. The mass of the interior region of the blue and red components are $M_{\rm dyn}^{\rm blue} = 3.7 \times 10^{12}$ $M_\odot$ and $M_{\rm dyn}^{\rm red} = 6.3 \times 10^{11}$ $M_\odot$, which is not unreasonable. Stellar masses and the upper limit to the molecular gas masses of the RLAGN are $M_* = 4.7 \times 10^{10}$ $M_\odot$ and $M_{\rm gas} < 3.3 \times 10^{10}$ $M_\odot$, respectively. Thus the total baryonic mass excluding the dust mass is $M_{\rm baryon} \sim 8 \times 10^{10}$ $M_\odot$, which is $2 - 13\%$ of the total dynamical mass of the internal region encompassing the RLAGN.

However, I find no evidence to support this hypothesis. In our case, both CO(2-1) components are blueshifted with respect to the RLAGN redshift of $z = 1.4427 \pm 0.0005$. Next, the two CO(2-1) components are spatially located south of the RLAGN position (Figure 54). Finally, the preferred orientation of the central rotational disk should be perpendicular to the AGN jets (Hamer et al., 2014; Li et al., 2015; Costa, Sijacki, and Haehnelt, 2015;

Russell et al., 2017a), even if the AGN jets are originally lying in the disk plane (Morganti et al., 2015; Cielo et al., 2018). In our case, the orientation of the AGN jets is roughly in the same plane of the assumed rotational disk (Figure 54).

Tidal tails

The CO(2-1) line emission is quite extended (tens of kpc) and encloses the RLAGN, the spectroscopically confirmed spiral galaxy west of the RLAGN, a couple of IRAC color-selected galaxies and possible other undetected galaxies in the dense region of the cluster center (Figure 54, blue and green squares, respectively). The peaks of emissions of both components are positioned kpcs away from the RLAGN and they could be broad, low surface brightness tidal tails of two or more interacting galaxies (Bell et al., 2006). However, the molecular gas and stars are decoupled (Figure 54), which is not consistent with the tidal stripping, since it is a gravitational effect and affects all matter equally. Therefore, I argue that although there probably are some galaxies interacting in the dense region of the cluster core, tidal effects cannot explain the extended molecular gas components (Vantyghem et al., 2016; Cicone et al., 2018).

Undetected galaxies

Next, the two CO(2-1) line emission components might originate from two or more gas-rich galaxies that are detected in the mm wavelengths, but are too faint to be detected at the detection limit of the optical or IR images. I estimate the properties of these hypothetical galaxies by making reasonable assumptions.

Since the *HST*/WFC3 F140W images have a depth similar to the CANDELS WIDE survey, I use the CANDELS/WIDE survey mass limit (Grogin et al., 2011) as an upper limit to the stellar mass of each of these two hypothetical galaxies, $M_* < 5 \times 10^9 M_\odot$. I assume that these hypothetical galaxies are at the cluster redshift. Next, I assume the 3σ Hα emission line flux limit of $F_{H\alpha} = 2.1 \times 10^{-17}$ erg cm^{-2} s^{-1} for the HST/WFC3 G141 grism spectra (Momcheva et al., 2016; Noirot et al., 2018) as an upper limit of the undetected Hα flux and with the stellar mass upper limits, I estimate the SFR upper limit of the two hypothetical galaxies $\mathrm{SFR}_{H\alpha} < 2\ M_\odot\ \mathrm{yr}^{-1}$, using the system of equations described in Section 3.3.5. $\mathrm{SFR}_{H\alpha}$ is calculated using the galaxy intrinsic luminosity and does not depend on redshift, but it does depend on attenuation. Therefore, there is a possibility that these hypothetical galaxies are dust-obscured and that the true intrinsic SFR is higher.

Molecular gas masses of the blue and the red emissions are $M_{\mathrm{gas}}^{\mathrm{blue}} = 1.0 \pm 0.2 \times 10^{11} M_\odot$, $M_{\mathrm{gas}}^{\mathrm{red}} = 1.1 \pm 0.2 \times 10^{10} M_\odot$, respectively, assuming the Galactic conversion factor $\alpha_{\mathrm{CO}} = 4.36\ M_\odot(\mathrm{K\ km\ s^{-1} pc^2})^{-1}$ (Section 3.3.2.1). I use a Galactic conversion factor because it is very improbable that these hypothetical galaxies are star-burst galaxies since they are not detected in the *HST*/WFC3 G141 grism observations. They could be only if the attenuation is anomalously high, i.e. $A_{H\alpha} > 5$. Next, I estimate the gas fractions lower limits that correspond to the blue and the red components $f_{gas}^{blue} \gtrsim 95\%$ and $f_{gas}^{red} \gtrsim 96\%$, respectively. The estimated lower limit of depletion time for the blue and the red emissions are $\tau_{dep}^{blue} \gtrsim 52$ Gyr and $\tau_{dep}^{red} \gtrsim 54$ Gyr, much longer than the typical depletion times observed for standard star-forming galaxies up to $z \sim 4$, $\tau_{dep} \sim 1-3$ Gyr (e.g., Tacconi et al., 2013, 2018).

All these calculations are based on the assumption that the hypothetical galaxies are at the cluster redshift, but there is also a possibility that they are background galaxies. It is known that some massive galaxies at $z > 2$ can be detected in millimeter wavelength but not in the *HST* optical and near-infrared bands (e.g. Franco et al., 2018). However, these galaxies are rare (0.1 galaxy/arcmin^2), massive and usually detected with *Spitzer*/IRAC.

All these results mean that these two hypothetical galaxies would be unusually gas-rich, with low SFR (or anomalously high attenuation), high gas fractions and very long depletion times. Furthermore, given the number densities of high redshift galaxies (Davidzon et al., 2018; Franco et al., 2018), having two galaxies of this kind so spatially close is possible but very improbable.

Gas outflows/inflows

The origin of the two CO(2-1) line emission components might be from the molecular gas outflows or inflows associated with the radio jets. If the two components are due to gas outflow from the RLAGN, we can estimate the outflow rate of the two components:

$$\dot{M}_{out} = \frac{M_{out}}{t_{dyn}} \tag{78}$$

where M_{out} is the molecular gas mass of the outflow, t_{dyn} is the dynamical timescale $t_{dyn} = d/v$, where d and v are the projected distance and the velocity of the outflow with respect to the RLAGN, respectively. Next, I take the distance uncertainty to be half of the beam size ~ 8.6 kpc. The obtained outflow rates of the blue and red emissions are $\dot{M}_{out} = 1073 \pm 573\ M_{\odot}yr^{-1}$ and $\dot{M}_{out} = 654 \pm 446\ M_{\odot}yr^{-1}$, and their corresponding dynamical timescales $t_{dyn} \sim 1.8 \times 10^7$ yr and $t_{dyn} \sim 3.0 \times 10^7$ yr, respectively. This is in agreement with the typical radiative ages of radio galaxies which are in the range of $10^7 - 10^8$ yr.

The total kinetic power of the outflows is given by the following equation:

$$P_k = \frac{1}{2} v^2 \dot{M}_{out} \tag{79}$$

and I obtain $P_k = 3.2 \times 10^{45} \mathrm{erg\ s^{-1}}$ for the total kinetic power of both hypothetical outflows. To understand if the mechanical jet power is sufficient to drive the molecular gas outflow, I use the monochromatic radio power of the RLAGN at 1.4 GHz $P_{1.4\ GHz} = 10^{27.06}$ W Hz^{-1} from the work of Fan and Zhang, (2003) and the scaling relation between the mechanical jet power and radio synchrotron power from Bîrzan et al., (2008):

$$\log(P_{jet}) = (0.35 \pm 0.07)\log(P_{1.4\ GHz}) + (1.85 \pm 0.10) \tag{80}$$

and I obtain $P_{jet} \sim 8.9 \times 10^{44}$erg s^{-1} for the total mechanical jet power of the RLAGN. Finally, I conclude that the mechanical jet power is not sufficient to drive a molecular gas outflow.

Furthermore, the molecular gas outflows entrained by the radio jets are usually only a fraction of the total molecular gas reservoir centered on the AGN host (McNamara et al., 2014; Cicone et al., 2014; Morganti et al., 2015; Prasad, Sharma, and Babul, 2015; Tremblay et al., 2018). Furthermore, these molecular gas outflows are detected as broad symmetrical wings around the central peak emission in the CO line emission spectra (Cicone et al., 2014). However, we detect substantial amount of molecular gas mass in two blueshifted structures, offset and detached from the RLAGN host galaxy, while we do not detect any molecular gas in the RLAGN host. Next, if the molecular gas mass upper limit of the RLAGN host is taken into account, the molecular gas content is in the best case $\sim 45\%$ of the total molecular gas in and around the RLAGN host galaxy.

Gas cooling

When the amount of molecular gas outside the host galaxy is comparable or higher than the host galaxy molecular gas reservoir, this suggests gas cooling (e.g., Klamer et al., 2004; Nesvadba et al., 2009; Emonts et al., 2014; Emonts et al., 2019; Russell et al., 2019). For instance, Russell et al., (2019) studied a local sample of cluster central galaxies, and found that the molecular gas morphology goes from gas disk-dominated to filament-dominated galaxies. In the first type, most of the molecular gas is concentrated in a disk around the central galaxy, while in the second type, the molecular gas is mostly ($> 70\%$) in filaments around the central galaxy (the most known example being the Perseus cluster; Salomé et al., 2006). The filaments that they observed extend from a few kpc in length up to $10-20$ kpc, and the molecular gas emission is offset with respect to the central AGN by projected distances of a few kpc. For the central galaxy of the cluster A1795, some molecular gas clumps are associated with the lobes of the radio jets. In filament-dominated galaxies, the filaments trace radio bubbles, and are associated with both gas outflow and inflow. We observe a molecular gas mass distribution similar to the filament-dominated galaxies from Russell et al., (2019). The total molecular gas mass in structures around the RLAGN is $M_{gas}^{tot} = 3.9 \pm 0.5 \times 10^{10} M_{\odot}$ (from the sum of the blue and red emission components) and the molecular gas mass upper limit of the RLAGN is $< 3.3 \times 10^{10} M_{\odot}$ (Section 3.3.2.1). This means that the total molecular gas mass of the two structures is $> 55\%$ of the total molecular gas within and around the RLAGN host galaxy. The blue and red emission peaks are offset from the RLAGN, with the offsets being comparable to the beam size of ~ 17 kpc, but centered south-east and south-west of the RLAGN, respectively (Figure 54; Figure 55).

For the CARLA J1103+3449 cluster, a reservoir of hot intracluster medium (ICM) that surrounds the host RLAGN is expected, with gas accretion at the center of the cluster potential well. Massive molecular gas components outside of the RLAGN host galaxy and the bipolar radio emission roughly corresponding to the two CO(2-1) emission components, favor the hypotheses of the AGN induced molecular gas cooling from the uplifted low-entropy hot gas or from enhanced gas cooling of the hot ICM due to interaction of the ICM and AGN jets (Salomé et al., 2006; Nesvadba et al., 2009; Emonts et al., 2014; Morganti et al., 2015; Russell et al., 2017b; Tremblay et al., 2018). Therefore, our results, compared to the predictions and observations from the literature, imply that the most probable origin of the molecular gas in our cluster central region is gas cooling, most probably boosted by interaction of the AGN jets and the hot atmospheres.

Cluster core members properties

In this section, I compare the measured physical properties (Section 3.3) of the cluster confirmed galaxies to cluster and field galaxies over a similar redshift range ($1 < z < 2.6$).

Molecular gas mass and gas fraction upper limits

Galaxy properties such as velocity integrated CO(2-1) flux, luminosity and molecular gas mass upper limits, stellar masses (from S. Mei and S. Amodeo) of the RLAGN and other cluster confirmed members (Table 7, Table 8) is comparable to other cluster and field galaxies at similar redshifts from the literature: e.g. Casasola et al., (2013) for an AGN at $z \sim 1.4$, Rudnick et al., (2017) for an AGN and a disk galaxy at $z \sim 1.6$, Noble et al., (2017) for gas-rich galaxies at $z \sim 1.6$, Castignani et al., (2018) for two spiral galaxies at $z \sim 1.2$, Coogan et al., (2018) for cluster core galaxies at $z \sim 2.0$, and finally, Tacconi et al., (2013) for field galaxies at $z \sim 1 - 1.5$ and $z \sim 2 - 2.5$.

When comparing the molecular gas mass upper limits from our work and the literature, differences in the way the results are obtained need to be taken into account. For instance, most of the authors cited here used the same rotational transition emission line as we do, i.e. the CO(2-1) (Wagg et al., 2012; Casasola et al., 2013; Dannerbauer et al., 2017; Noble et al., 2017; Castignani et al., 2018; Hayashi et al., 2018), but some of them used the CO(1-0) (Rudnick et al., 2017; Dannerbauer et al., 2017; Coogan et al., 2018), the CO(3-2) (Tacconi et al., 2013), or a combination of several rotational transitions (Coogan et al., 2018; Perna et al., 2018). Next, when estimating the molecular gas mass, I assume $L'_{CO(2-1)}/L'_{CO(1-0)} = 1$ (Section 3.3; Solomon and Vanden Bout, 2005), while Noble et al., (2017) used $L'_{CO(2-1)}/L'_{CO(1-0)} = 0.77$, Hayashi et al., (2018) used $L'_{CO(2-1)}/L'_{CO(1-0)} \sim 0.83$, and finally Tacconi et al., (2013) assumed $L'_{CO(3-2)}/L'_{CO(1-0)} \sim 0.5$. Moreover, Wagg et al., (2012) and Casasola et al., (2013), used a lower value of the conversion factor $\alpha = 0.8$, while in our and most of other cited works (Tacconi et al., 2013, Rudnick et al., 2017, Noble et al., 2017 , Hayashi et al., 2018 and Castignani et al., 2018) a standard Galactic value $\alpha = 4.36$ is used. In Coogan et al., (2018) the values of the conversion factor are $3.9 < \alpha < 4.5$ and in Dannerbauer et al., (2017) $\alpha = 4$.

Stellar mass estimations can differ up to a factor of $\sim 1.5 - 6$ ($\sim 0.1 - 0.8$ dex) when using different techniques or different stellar population models (Van der Wel et al., 2006; Lee et al., 2009; Maraston et al., 2010; Raichoor et al., 2011; Pforr, Maraston, and Tonini, 2012; Sorba and Sawicki, 2018). In the following figures, I show the original published values from the literature, without rescaling them to the values used in this work.

In Figure 62, I show upper limits to the molecular gas mass as a function of stellar mass of the spectroscopically confirmed cluster members. The upper limits to the molecular gas mass and stellar masses of the RLAGN and most of the other confirmed members agree (within $\sim 1\sigma$) with the molecular gas masses and stellar masses of field galaxies from the PHIBBS survey (Tacconi et al., 2013). The RLAGN gas fraction upper limit $f_{gas} < 40\%$ is comparable to the reported gas fraction of the field main-sequence galaxies from the PHIBBS survey, i.e. 33% and 47% in the $z \sim 1 - 1.5$ and $z \sim 2 - 2.5$ redshift ranges, respectively (Tacconi et al., 2013). However, average gas fraction upper limits of the other confirmed cluster members from out work are higher $f_{gas} < 82\%$.

Most of the works from the literature show comparable but lower gas fractions for cluster galaxies compared to the expected values for their field counterparts at intermediate redshifts. For instance, Wagg et al., (2012) reports $f_{gas} \sim 14\%$ for an AGN host and $f_{gas} < 13\%$ and two dust-obscured galaxies (DOGs), Rudnick et al., (2017) found $f_{gas} \sim 17\%$, and $f_{gas} \sim 45\%$ for an AGN and a disk galaxy at $z \sim 1.6$, Castignani et al., (2018) reports $f_{gas} \sim 15\%$ for two spiral galaxies at $z \sim 1.2$, Coogan et al., (2018) $f_{gas} \sim 30\%$ for cluster core galaxies at $z \sim 2.0$, etc. This suggests possible ongoing mechanisms which are stripping and/or heating the cold molecular gas and suppressing star formation inside cluster galaxies. However, Noble et al., (2017) and Hayashi et al., (2018) report the opposite results, i.e. $f_{gas} \sim 62\%$ for gas-rich galaxies at $z \sim 1.6$ and $f_{gas} \sim 55\%$ for cluster galaxies at $z \sim 1.5$ respectively). Since I only estimate molecular gas upper limits, it is difficult to make conclusions about the possible environmental effects.

Star formation

In Figure 63 I show SFR as a function of stellar mass. Compared to the field galaxies, the SFR of the RLAGN, with different contributions of the Hα stellar emission to the total flux (20% 40%, 60%, 80% and 100%; Table 10), is almost always within $\sim 1\sigma$ of the MS from Tacconi et al., (2013), and the SFR of the other spectroscopically confirmed cluster members is $> 2\sigma$ below the MS (Figure 63), consistent with results of Noirot et al., (2018), which suggests an impact of the environment as early as $z \sim 2$.

In Figure 64 I show sSFR as a function of stellar mass. The sSFR on average declines with increasing stellar mass (Brinchmann et al., 2004; Elbaz et al., 2007; Karim et al., 2011; Muzzin et al., 2012; Hatch et al., 2017). The sSFR of the RLAGN (assuming stellar contribution to the total Hα emission line flux in the range of $20\% - 100\%$) (Table 10) is comparable to the average sSFR of field galaxies from Tacconi et al., (2013), whereas the sSFR of other confirmed cluster galaxies is on average lower, which again indicates possible environmental quenching (Figure 64). Furthermore, the sSFR of the RLAGN is comparable to the sSFR of cluster galaxies, mostly hosting AGN from the literature: e.g. sSFR of an AGN host galaxy at $z \sim 1.2$ from Wagg et al., (2012), gas-rich galaxies at $z \sim 1.6$ from Noble et al., (2017) , an AGN host at $z \sim 1.6$ from Rudnick et al., (2017), cluster galaxies at $z \sim 1.5$ from

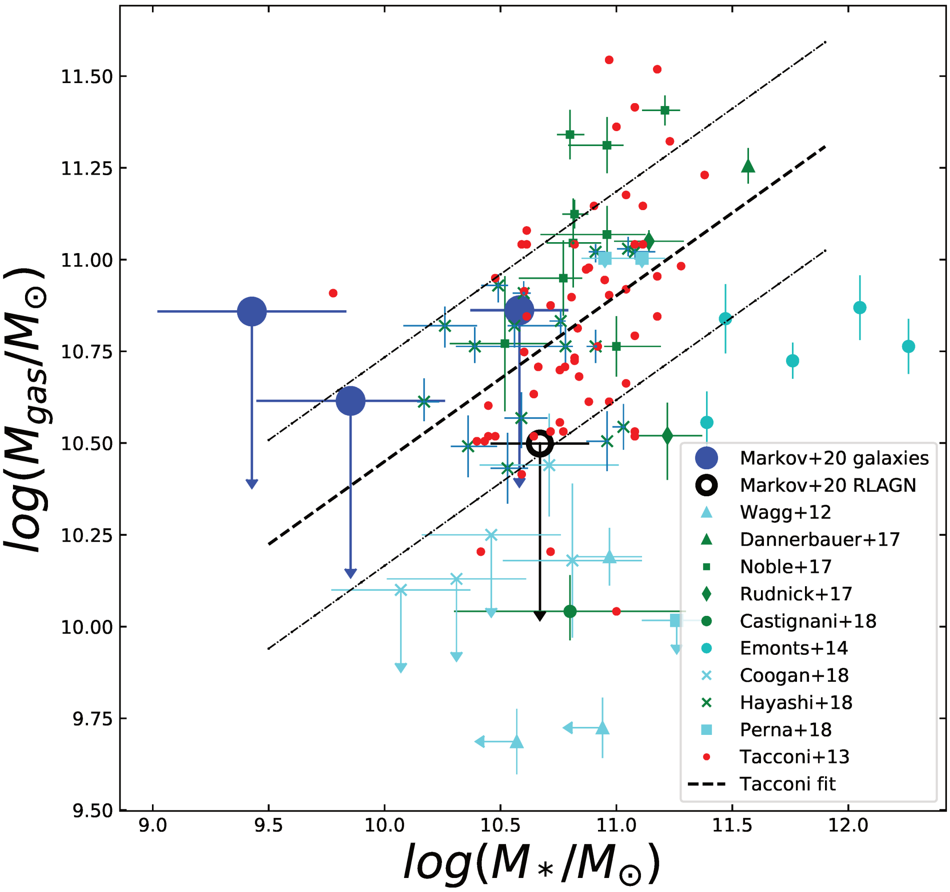

Figure 62: *Molecular gas mass as a function of stellar mass. I compare the RLAGN (empty black circle) and other CARLA J1103+3449 spectroscopically confirmed cluster members from Markov et al., (2020a) (filled blue circles) with other cluster (green and cyan) and field galaxies (red) from the literature. Arrows indicate upper and lower limits. Green markers are results for cluster galaxies for which gas masses were estimated using the Galactic conversion factor. Cyan markers are estimations with different values of the conversion factor. Dashed and dashed-dotted lines represent the Tacconi et al., (2013) relation for field star-forming galaxies and its 1σ scatter.*

Hayashi et al., (2018) and cluster core galaxies at $z \sim 2.0$ from Coogan et al., (2018). Moreover, the sSFR of other confirmed cluster galaxies from Markov et al., (2020a) (Table 10) is comparable to the sSFR of cluster disk galaxies from the literature: e.g. sSFR of a disk galaxy at $z \sim 1.6$ from Rudnick et al., (2017), of a starburst disk galaxy at $z \sim 2.2$ from Dannerbauer et al., (2017) and of two disk galaxies at $z \sim 1.2$ from Castignani et al., (2018).

In Figure 65, I show SFR as a function of molecular gas mass. The RLAGN SFR is within $\sim 1.5\sigma$ of field galaxies with similar molecular gas masses. This shows that its SFR is comparable to the average SFR of the field galaxies with a similar molecular gas reservoir. The other spectroscopically confirmed members show lower SFR than the field galaxies with similar molecular gas masses. This is in agreement with Figure 63). However, since I can only calculate molecular gas mass upper limits, these results are not conclusive.

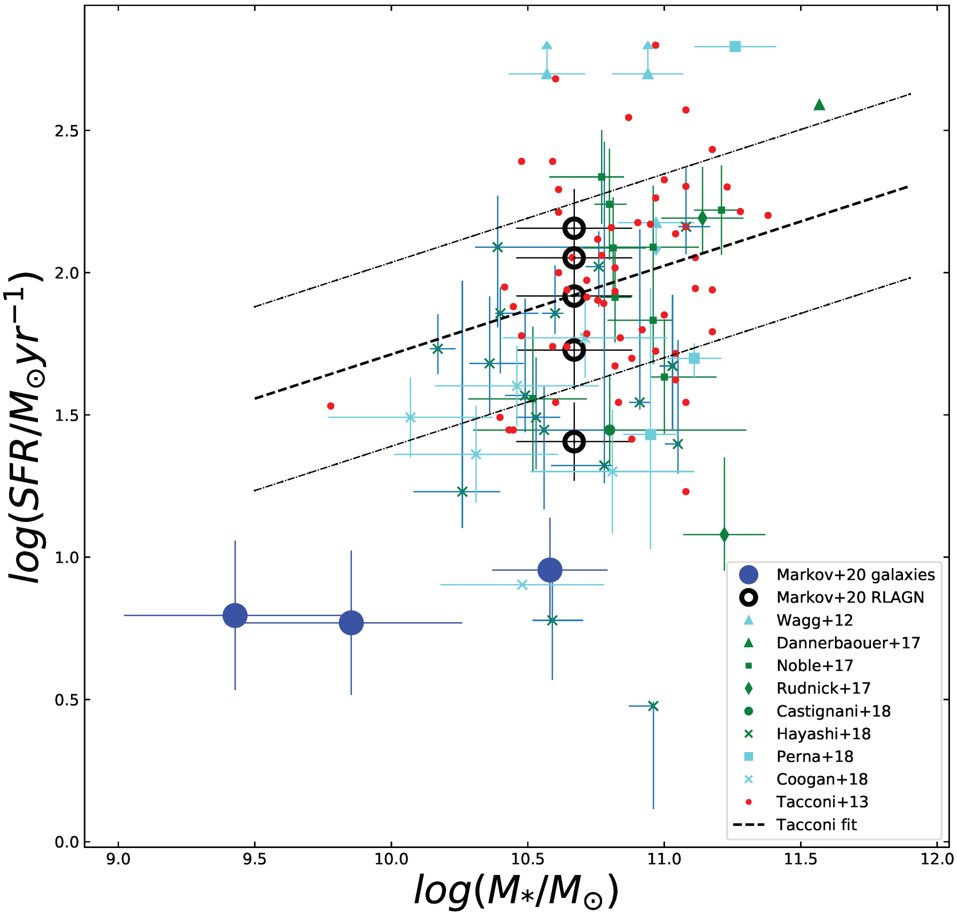

Figure 63: *SFR as a function of stellar mass. The RLAGN SFR is shown with different contributions of the Hα stellar emission to the total flux (20% 40%, 60%, 80% and 100%) by empty black circles. Other symbols are the same as in Figure 62. The dashed and the dashed-dotted lines represent the best fit with 1σ scatter around MS for the field galaxies from Tacconi et al., (2013).*

Depletion times of most of the cluster galaxies at intermediate redshifts from the literature are $\tau \sim 10^9$ yr (Casasola et al., 2013; Noble et al., 2017; Rudnick et al., 2017; Hayashi et al., 2018; Coogan et al., 2018). These values are about an order of magnitude longer than the average depletion time $\tau \sim 10^8$ yr of the field galaxies from Tacconi et al., (2013). Exceptions are mostly disk, gas-rich, cluster galaxies that show comparable τ as their field counterparts (Dannerbauer et al., 2017; Castignani et al., 2018). Upper limits to the depletion time τ of the RLAGN are comparable to the average depletion time of mostly disk, gas-rich cluster galaxies and star-forming field galaxies from the literature, whereas other confirmed cluster members show on average an order of magnitude longer τ upper limits. Similar comparison can be performed with the SFE lower limits, since it is equal to the inverse of the depletion time.

The RLAGN SFR is comparable to the MS of star-forming field galaxies, and its star formation has not yet quenched. This is consistent with the large molecular gas reservoir in the center of the cluster. As a massive early-type central cluster galaxy, the RLAGN is predicted to have gone through at least one major merger, which might have triggered a starburst phase (Sec-

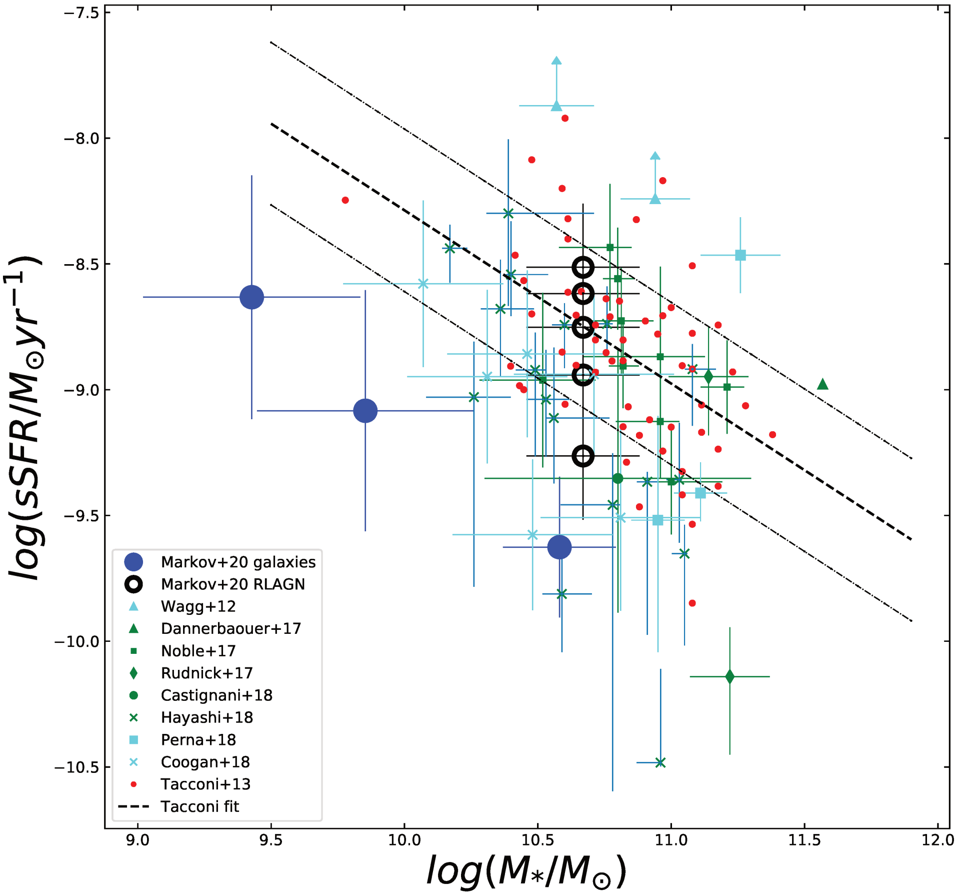

Figure 64: *sSFR as a function of stellar mass. The RLAGN sSFR is shown with different contributions of the Hα stellar emission to the total flux (20% 40%, 60%, 80% and 100%) by empty black circles. Other symbols are the same as in Figure 62.*

tion 1.4.1; Hopkins et al., 2006a, 2008; Yesuf et al., 2014). During this phase, the galaxy is predicted to lie above the MS in the SFR − M_* and SFR − M_{gas} diagrams (Figure 63, Figure 65), and the galaxy molecular gas is converted into stars. Afterwards, the remaining molecular gas content is expected to be consumed by the combination of star-formation and feedback (Snyder et al., 2011; Yesuf et al., 2014). The RLAGN is observed on the star-forming galaxy MS with a SFR $\sim 70 - 140 M_{\odot} yr^{-1}$, and it is expect to evolve toward quenching when the molecular gas reservoir is depleted, becoming a passive ETG similar to those observed in lower redshift cluster centers (Norton et al., 2001; Hopkins et al., 2008; Snyder et al., 2011; Yesuf et al., 2014).

SUMMARY

CARLA J1103+3449 was observed with the NOEMA interferometer (PI: S. Mei, A. Galametz). The target was the CO(2-1) emission line at the redshifted frequency $\nu_{obs} = 94.48$ GHz, observed with NOEMA's 3 mm wavelength. The central region of the cluster was covered with three pointings, in order to map most of the *HST*/WFC3 spectroscopically confirmed cluster members, including the central RLAGN. I use GILDAS software for data re-

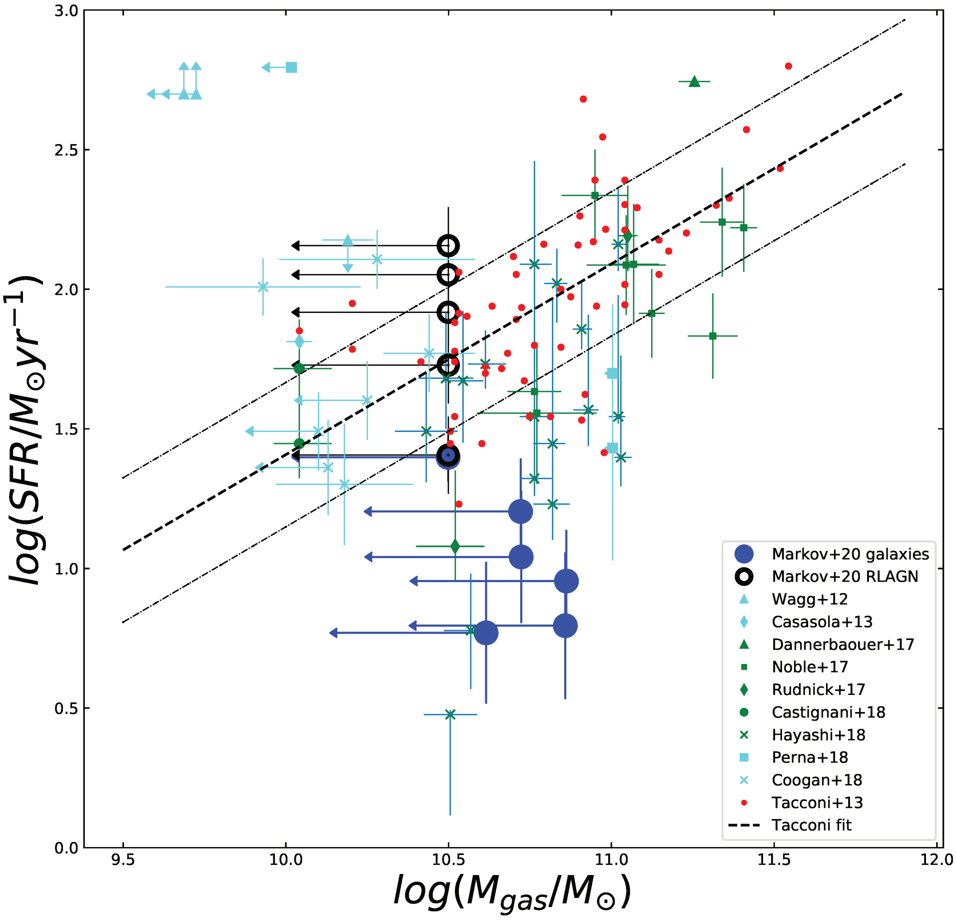

Figure 65: *SFR as a function of molecular gas mass. The black and blue leftward triangles show the upper limits for the AGN and the spectroscopically confirmed cluster members, respectively. Other symbols are the same as in Figure 62 and Figure 63. Dashed and dashed-dotted lines represent the Tacconi et al., (2013) relation for field star-forming galaxies and its 1σ scatter.*

duction, mapping the continuum (Figure 42) and the continuum-subtracted CO(2-1) line emissions (Figure 43) and for most of the data analysis.

Our main results are:

- I detect an extended continuum emission at $\nu_{\rm obs} \sim 94.48$ GHz in the cluster core, with the brightest peak at the position of the RLAGN, that extends towards the western radio lobe, while the fainter component is at the position of the eastern radio lobe and radio jet (Figure 45, white contours). The two continuum emission components visually correspond to the two radio jets observed by Best et al., (1999) (Figure 45, blue contours). The brightest peak is at the position of the RLAGN host galaxy, that extends towards the western radio lobe, while the fainter component is at the position between the eastern radio lobe and the radio jet (Figure 45, white contours). This is consistent with the same or a connected physical origin of the two emissions. At the rest frequency of $\nu_{\rm rest} = 230.5$ GHz the dominant source of the continuum emission is non-thermal synchrotron emission. I measure the continuum flux associated with the RLAGN, the eastern lobe and the jet, and the western radio lobe to be $S_{cont} = 4.6 \pm 0.2$ mJy, $S_{cont} = 1.1 \pm 0.2$ mJy and $S_{cont} = 0.8 \pm 0.2$ mJy, respectively.

I fit the flux measurements from our work and Best et al., (1999) (Figure 46) and obtain the total spectral index $\alpha = 0.94 \pm 0.01$ from a linear fit of measurements from our work and Best et al., (1999) (Figure 46). The spectral index is consistent with optically thin synchrotron emission of the AGN jets, while the spectra of the AGN core is flatter, with $\alpha = 0.14 \pm 0.03$, which is consistent with the optically thicker (self-absorbed) synchrotron emission (Figure 46). Finally, I combine the radio observations from the literature and mm observations from our work and calculate the total spectral index $\alpha = 0.92 \pm 0.02$, determined over the range of frequencies that spans over three orders of magnitude.

- I detect two CO(2-1) emission lines in the center of the CARLA J1103+3449 cluster (Figure 49), which correspond to two extended regions. The position of the red emission peak is south-west of the RLAGN, and it encompasses the RLAGN and companion disk galaxy, while the blue emission peak is south-east of the RLAGN and it does not have an optical counterpart (Figure 54). The two CO(2-1) emissions are in the same direction (east-west) as the two continuum emission components and the two radio lobes, but spatially offset and less extended (Figure 55).

  I obtain the velocity integrated flux $S\Delta v = 0.88 \pm 0.14$ Jykm s^{-1} and $S\Delta v = 0.90 \pm 0.14$ Jykm s^{-1}. I estimate the CO luminosities, and molecular gas masses of the blue and red component $M_{gas} = 1.9 \pm 0.3 \times 10^{10} M_{\odot}$ and $M_{gas} = 2.0 \pm 0.3 \times 10^{10} M_{\odot}$, respectively. I find a substantial molecular gas reservoir in the cluster center around the RLAGN, with a total molecular gas mass of $M_{gas} = 3.9 \pm 0.4 \times 10^{10} M_{\odot}$.

  We discuss several hypotheses on the most probable origin of the detected molecular gas around the RLAGN, ranging from the two molecular gas-rich, cluster galaxies, that are not observed in the optical and IR, the molecular outflows pushed by the AGN jets tens of kpc from the host galaxy, etc. However, the hypothesis that we favor the most is gas inflows/outflows, either due to cluster gas accretion or, most probably, driven by the jets, as is observed in filament-dominated central galaxies in the local Universe. The gas might be cooled by the interaction of the ICM and AGN jets or can be due to condensation of low entropy hot gas uplifted by the AGN jet away from the host galaxy.

- I estimate the molecular gas mass upper limits of the RLAGN and other spectroscopically confirmed cluster members which are within the NOEMA beam. Next, I use the stellar mass measurements from S. Mei and S. Amodeo to estimate their gas fraction upper limits. The molecular gas mass upper limits and stellar masses are comparable to the expected average values of field galaxies at similar redshift (Figure 62). Therefore, it is difficult to make any conclusions on the possible ongoing environmental mechanisms.

I use the Hα flux measurements from Noirot et al., (2018), the stellar masses from S. Mei and S. Amodeo, and a method described in Section 3.3.5, in order to estimate the SFR. For the RLAGN host galaxy, I assume a stellar contribution to the total Hα flux in the $20-100\%$ range, and find $\mathrm{SFR}_{\mathrm{H}\alpha} = 30-140\ \mathrm{M}_{\odot}\mathrm{yr}^{-1}$, consistent with the MS star-forming galaxies, while the SFR of the other cluster confirmed members are below the MS, which suggests an impact of the environment (Figure 63). I estimate the sSFR, the depletion time and SFE of the cluster confirmed members.

4

SUMMARY, CONCLUSIONS AND PROSPECTIVES

The goal of my Thesis is to try answer some of the open questions in the theory of galaxy formation and evolution, such as: *How and when did galaxies assemble most of their mass? What is the molecular gas content, star formation rate, and other properties of cluster galaxies at intermediate-redshifts? How are galaxy properties affected by the environment?* In order to answer some of these questions, the main focus of my PhD Thesis research was on developing a `Python` code for deriving the SMF of cluster galaxies for the upcoming *Euclid Space Mission*, and on the study on the stellar mass assembly of galaxies at $0 < z < 2.5$ (Chapter 2). Furthermore, molecular gas acts as star formation fuel and therefore, regulates the stellar mass build-up of galaxies. Information on the galaxy molecular gas content and star formation provide complementary information on the mass assembly and galaxy evolution. Therefore, the focus of my work was on investigating the molecular gas content and star formation of cluster galaxies at the *cosmic noon* epoch at $z \sim 1.5$ (Chapter 3, Appendix A).

EUCLID PIPELINE FOR THE SMF OF CLUSTER GALAXIES

Within the *Euclid* collaboration (S. Mei, M. Bolzonella, E. Zucca, O. Ilbert, I. Davidzon, G. Zamorani, L.Tresse, L. Pozzetti, G. Girelli and myself), I participated in developing a `Python` pipeline for deriving the SMF of cluster galaxies, using the 1/Vmax estimator (Figure 26, Figure 27, Figure 28, Figure 29, left panels). However, it is preferable to use more than one estimator in deriving the SMF, in order to check for consistency between different estimators and to estimate the bias. Therefore, besides the 1/Vmax, other standard statistical estimators can be implemented, such as the STY, SWML, etc (Section 2.1.2).

I implemented the Poissonian uncertainties in order to estimate the statistical uncertainties. Besides the Poissonian uncertainties, other relevant statistical uncertainties need to be implemented in the calculations of the total statistical uncertainty, such as the cosmic variance, the photometric redshift uncertainties, and of course the cluster membership uncertainty (Section 2.1.3).

I fitted the SMF with a chosen model (variation of Schechter functions), deconvolved by the stellar mass uncertainties, in order to take into account the Eddington bias (Ilbert et al., 2013). Besides the Schechter functions, there are other fitting models that have been used in the literature and that can be added in the pipeline, for example, different power laws, Gaussian function, a combination of Schechter and Gaussian functions, etc (Section 2.1.1).

I tested the pipeline using the *Flagship* mock galaxy sample (Carretero et al., 2017) and the *COSMOS2015* photometric redshift catalog (Davidzon et al., 2017. However, the *Euclid* pipeline is expected to be tested on more diverse data and galaxy samples, including cluster galaxies. Deriving the

SMF of cluster galaxies is important since the shape of the SMF depends on the environment, and there is an additional uncertainty that needs to be taken into account. The final version of the *Euclid* pipeline should be adapted for reading the upcoming *Euclid* data, and deriving the SMF and SMF fit of the *Euclid* cluster galaxies.

I showed the evolution of the SMF of Flagship mock galaxies (Figure 31). Moreover, I reproduced the work of Davidzon et al., (2017) and showed the evolution of the SMF and stellar mass density ρ_* of COSMOS2015 galaxies, over the redshift range taken into account ($0.2 \leqslant z < 2.5$). Finally, I showed the evolution of the best-fit parameters of the Schechter models deconvolved by the stellar mass uncertainties, for the COSMOS2015 galaxies (Figure 34, Figure 35 and Figure 36). For instance, I showed the evolution of the $\log(M^*)$ parameter, which is probably a consequence of *dry* merging of massive quiescent galaxies (Figure 36, top panel; see Peng et al., 2010).

In order to answer the question of my Thesis on how did galaxies assemble their stellar mass and at which epoch, I analyzed the evolution plots of the SMF and ρ_* of different COSMOS2015 galaxy samples, including the full sample, star-forming, high and intermediate activity star-forming and quiescent galaxies. I showed that the key epoch of the stellar mass assembly of galaxies, occurs during the stellar mass assembly and star formation epoch, i.e. the *cosmic noon* epoch $1 < z < 2.5$. Next, I showed that after this very active phase in cosmic history, the stellar mass build-up of galaxies slows down, which is consistent with a drop of the cosmic SFR and molecular gas content of galaxies during the last cosmic epoch $z < 1$. Moreover, I showed that quiescent galaxies have assembled their mass substantially over the redshift range $1 < z < 2.5$, which implies that the star formation quenching mechanisms were very efficient during the *cosmic noon* epoch. This part of the thesis reproduces published results from Ilbert et al., (2013) and Davidzon et al., (2017).

I showed the stellar mass build-up of massive galaxies around the characteristic stellar mass M^*, that is probably a consequence of internal quenching mechanisms i.e. the so-called *mass quenching* of galaxies after reaching a stellar mass $M \sim M^*$. Next, the stellar mass assembly of the quiescent sample is mass dependent, with low and intermediate-mass quiescent galaxies assembling most of their mass at a later epoch $z < 1$, possibly through *environmental mechanisms*, since large-scale structures are better differentiated at lower redshifts. Finally, the mass dependent stellar mass build-up of quiescent galaxies is in agreement with the *downsizing scenario*, according to which star formation activity, stellar mass assembly, quenching and the overall evolution of massive galaxies is faster and ends at earlier times, whereas intermediate and low-mass galaxies assemble their mass at later cosmic epochs.

The *Euclid Mission* will observe a substantial sample of ~ billions of galaxies, and it will be possible to study the evolution of the SMF and ρ_* of different galaxy samples, including rare objects, and to probe the evolution of diverse galaxy populations across cosmic time, covering the last ~ 11 Gyrs of the history of the Universe. Besides the *Euclid*, the next generation facilities such as the *JWST*, the *WFIRST* space missions, and the E-ELT ground facility will focus on providing a consistent picture on the formation and evolution of galaxies out to reionization epoch, and put constraints on the galaxy formation and evolution models.

MOLECULAR GAS IN THE CARLA J1103+3449 CLUSTER

While working on this Thesis project, I was a part of an international team of scientists, including S. Mei, P. Salomé, F. Combes, D. Stern, A. Galametz, C. De Breuck, D. Wylezalek, S. Amodeo, E. A. Cooke, A. H. Gonzalez, A. Hatch, G. Noirot, A. Rettura, N. Seymour, S. A. Stanford, J. Vernet and myself. As part of this PhD Thesis, I participated in data reduction, imaging and analysis of the NOEMA observations of the CARLA J1103+3449 cluster at $z \sim 1.44$.

I detected an extended continuum emission at $\nu_{\text{obs}} \sim 94.48$ GHz, originating from the non-thermal synchrotron emission of the SMBH at the center of the RLAGN host galaxy. Moreover, the total spectral index $\alpha = 0.94 \pm 0.01$ is consistent with optically thin synchrotron emission of the AGN jets, while the RLAGN core shows a flatter spectra, with $\alpha = 0.14 \pm 0.03$ (Figure 48).

In order to answer the question of my Thesis on the molecular gas content and star formation of cluster galaxies at intermediate redshifts, first, I used the CO(2-1) rotational transition emission line as a molecular gas tracer, and I measured the molecular gas content in the central region of the CARLA J1103+3449 cluster at $z = 1.44$ (Markov et al., 2020a). I detected a substantial molecular gas reservoir ($M_{\text{gas}} = 3.9 \pm 0.4 \times 10^{10} M_{\odot}$) in the core of the CARLA J1103+3449 cluster at $z \sim 1.44$ with NOEMA (Markov et al., 2020a) in two extended regions offset from the RLAGN host and other galaxies (Figure 54). The most reasonable hypothesis on the origin of this extended massive molecular gas structure is the hypothesis of the gas inflows/outflows, either due to cluster gas accretion or, most probably, driven by the jets, as is observed in filament-dominated central galaxies in the local Universe. The cold gas might have cooled either from the ICM due to its interaction with AGN jets, or from low-entropy hot gas that is uplifted by the AGN jets from the host galaxy to a large distance from the AGN host galaxy, where it can cool more efficiently. The molecular gas reservoir is expected to feed the star formation and the AGN jets of the RLAGN host galaxy in the cluster center.

Next, I estimated the molecular gas mass upper limits, and using the stellar mass estimates of S. Mei and Hα flux measurements of Noirot et al., (2018), I estimated the SFR, and other properties such as the gas fraction, SFR, sSFR, SFE, etc., of the CARLA J1103+3449 cluster member galaxies. I compared the properties of the CARLA J1103+3449 cluster galaxies with the values of cluster and field galaxies at intermediate redshifts from the literature, in order to answer the question on the impact of the environment on galaxy properties. I showed that the SFR of the central RLAGN host galaxy is consistent with the *MS* field galaxies at similar redshift, whereas other cluster members show on average lower SFR, which implies environmental effects on these satellite galaxies.

In order to probe the molecular gas content of the CARLA J1103+3449 cluster confirmed members with a better resolution, we need a follow-up program with the NOEMA interferometer. Furthermore, the following work might include a follow-up with NOEMA observations targeting higher CO rotational transitions, in order to trace warmer, denser and more disturbed molecular gas connected with different types of high-energy processes, such as star formation, different types of feedback, and cooling flows. Furthermore, follow-up observations using the X-ray telescopes is necessary to test the gas cooling hypothesis on the origin of the molecular gas (see e.g. Fabian, 1994). Hα line emission follow-up is important for tracing the warm ionized and cold molecular gas at the core of the Hα nebulae, related to the cooling flows (e.g. Edge, 2001).

Finally, I presented the preliminary results of the CO(2-1) detections in several sources of two other CARLA clusters at $z \sim 1.5$ with ALMA (Appendix A).

These results imply that galaxy cluster cores are rich in cold molecular gas reservoirs, and that cluster galaxies are commonly star-forming at intermediate redshifts, which is in agreement with the reversal of the star formation-density relation at earlier cosmic epochs. I showed studies on individual clusters with a about a dozen confirmed member galaxies. Cold gas surveys of statistically large samples of cluster galaxies are necessary in order to fill in the many gaps in our knowledge on the molecular gas content of intermediate and high-redshift galaxies. This will be possible with significant improvements of the existing ground facilities such as NOEMA, ALMA, the next-generation VLA (ngVLA), etc., in the submm and radio wavelengths (more antennas, multi-beam receivers, etc.; see e.g. Walter et al., 2019).

A

MOLECULAR GAS OF TWO CARLA CLUSTERS AT $z \sim 1.5$ WITH ALMA

I extend the study on molecular gas content of the CARLA cluster galaxies at intermediate redshifts, by analyzing the ALMA observations of a CO(2-1) rotational emission line in the CARLA J0116-211 cluster at $z \sim 1.42$ and CARLA J1052-0806 cluster at $z \sim 1.65$ (PI: A. Galametz). Both of these clusters are a part of the CARLA survey (Wylezalek et al., 2013) and the *HST* follow-up program by Noirot et al., (2018). Noirot et al., (2018) found 12 spectroscopically confirmed cluster members in the CARLA J0116-211 cluster, mostly located north of the RLAGN host galaxy, which suggests that the radio galaxy is not at the cluster center. Furthermore, they confirmed 6 cluster members in the CARLA J1052-0806 cluster, while most of the other member galaxies emit only in the continuum.

Data reduction was performed using the Common Astronomy Software Applications (`CASA`) software[1]. This software contains tasks and tools used for data processing, mapping, and data analysis of radio telescopes such as ALMA, VLA, NOEMA, etc. The original data reduction was performed by one of our collaborators, and the reduced data contained noise in one of the channels. As part of this Thesis, I re-reduce the data by running a `Python` script in the CASA software.

Mapping and preliminary data analysis were performed mainly using a combination of the `CASA` and `GILDAS` software[2]. First, I produce the preliminary continuum and continuum subtracted CO(2-1) line emission maps in order to check for any sources. The preliminary mapping and data analysis show multiple continuum and CO(2-1) line emission sources.

First, I detect two continuum sources at the positions of the two RLAGN (*HST* id 437 and 338 in the CARLA J0116-211 and J1052-0806 clusters, respectively) in the continuum emission maps. As discussed previously in Section 3.3.1, the origin of the continuum emission at the rest frequency of $\nu_{\rm rest} = 230.538$ GHz is non-thermal synchrotron emission of the SMBH at the center of radio galaxies.

Next, I find a $\sim 4\sigma$ detection of a CO(2-1) emission with a broad line profile (FWHM ~ 1100 km/s), close to the position of the RLAGN, but slightly south-west. This cluster was also observed by Emonts et al., (2014). They detected CO(1-0) emission line with a similar FWHM ~ 1130 km/s and slightly offset from the radio galaxy in the same direction. On the other hand, we do not detect CO(2-1) line emission at the position of the RLAGN for the CARLA J1052-0806 cluster.

Finally, I run the `uvcontsub` script in order to derive the continuum subtracted calibrated data, and use these data to produce the CO(2-1) line emission map. Moreover, these data can be exported in GILDAS to produce the UV-tables, maps, and continue with further mapping and data analysis. The

---

[1] https://casa.nrao.edu/

[2] http://www.iram.fr/IRAMFR/GILDAS/

`uvcontsub` script fits the continuum emission by a simple model, e.g. a constant or linear model, removes the modeled continuum from the total emission and leaves the line emission. Therefore, following work should include modeling and subtracting the continuum emission in order to obtain the calibrated data containing the continuum-subtracted CO(2-1) line emission that can be exported to GILDAS and continue with further data analysis and estimating the molecular gas mass and other galaxy properties.

Early results of ALMA observations of the two CARLA clusters are quite promising, with a better resolution and SNR than the NOEMA observations from my previous work (Markov et al., 2020b). Besides the ALMA observations of the CO(2-1) line emission, there are more multi-wavelength observations of the two CARLA clusters available in the literature, including the *Spitzer* observations from Wylezalek et al., 2013, *HST* imaging and spectroscopy from Noirot et al., (2018) and CO(1-0) emission from Emonts et al., (2014), that will allow building a complete picture on the stage of evolution of these cluster galaxies.

B

FITTING THE SMF OF ULTRAVISTA GALAXIES

We test the MCMC algorithm by fitting the SMF of UltraVISTA galaxies (McCracken et al., 2012), derived by Ilbert et al., (2013). We use a single, a double and a double Schechter function with α_2 parameter fixed. Moreover, we convolve the Schechter by the Gaussian function with $\sigma = 0.04(1+z)$, and a product of the Gaussian and Lorentzian (G × L) function, defining the Gaussian function with $\sigma = 0.5$ and $\sigma = 1.0$) and the Lorentzian function with $\tau = 0.04(1+z)$, following Ilbert et al., (2013).

We define the Schechter and the convolved Schechter function as our models, we minimize the likelihood, we run the MCMC, and obtain the best-fit parameters and errors of the Schechter model deconvolved by the product of the Gaussian (with $\sigma = 0.5$) and Lorentzian function (G × L) (Table 12). Our results are in agreement with the results of Ilbert et al., (2013) (Table 2 from their work).

We plot the SMF and the SMF fit of the full galaxy sample (Figure 66 and Figure 67), quiescent (Figure 68 and Figure 69) and star-forming galaxies (Figure 70 and Figure 71). We fit the SMF using before mentioned Schechter, convolved Schechter functions, and a deconvolved Schechter functions from Ilbert et al., (2013) for comparison.

We argue that for lower redshifts ($\sim z < 2.5$) the model from the work of Ilbert et al., (2013), convolved with the G × L, with $\sigma = 0.5$, best fits our model convolved with a Gaussian function, while for higher redshifts ($\sim z > 2.5$) best fits our model convolved with the G × L, with $\sigma = 0.5$. This is possibly due to a difference in the way we define z in the $\tau = 0.04(1+z)$ function. While in Ilbert et al., (2013) they calculate the mean value of z for the galaxies inside a certain morphology and redshift bin (each Vmax file), we simply use a value within the given redshift range (for example $z = 0.2$ for the galaxies in the $0.2 < z < 0.5$ range, $z = 0.5$ for $0.5 < z < 0.8$, etc.).

Table 12: Best-fit parameters of different Schechter function deconvolved by the expected stellar mass uncertainties for a full galaxy sample, star-forming and quiescent galaxies.

z-bin	$\log M^*[M_\odot]$	$\Phi_1^*[10^{-3}\mathrm{Mpc}^{-3}]$	α_1	$\Phi_2^*[10^{-3}\mathrm{Mpc}^{-3}]$	α_2
			Full sample		
$0.2-0.5$	$10.82^{+0.10}_{-0.11}$	$1.79^{+0.64}_{-0.67}$	$-0.45^{+0.39}_{-0.32}$	$1.04^{+0.32}_{-0.33}$	$-1.39^{+0.05}_{-0.06}$
$0.5-0.8$	$10.93^{+0.08}_{-0.09}$	$1.27^{+0.37}_{-0.44}$	$-0.59^{+0.36}_{-0.26}$	$0.55^{+0.28}_{-0.26}$	$-1.46^{+0.09}_{-0.12}$
$0.8-1.1$	$10.75^{+0.06}_{-0.07}$	$2.11^{+0.34}_{-0.37}$	$-0.08^{+0.38}_{-0.32}$	$0.63^{+0.35}_{-0.30}$	$-1.47^{+0.12}_{-0.16}$
$1.1-1.5$	$10.59^{+0.08}_{-0.07}$	$1.29^{+0.37}_{-0.37}$	$0.45^{+0.52}_{-0.50}$	$1.01^{+0.40}_{-0.40}$	$-1.38^{+0.13}_{-0.17}$
$1.5-2.0$	$10.59^{+0.06}_{-0.06}$	$0.96^{+0.09}_{-0.09}$	$0.27^{+0.29}_{-0.29}$	$0.48^{+0.08}_{-0.07}$	-1.6
$2.0-2.5$	$10.63^{+0.08}_{-0.09}$	$0.68^{+0.10}_{-0.10}$	$0.04^{+0.48}_{-0.44}$	$0.19^{+0.10}_{-0.10}$	-1.6
$2.5-3.0$	$10.62^{+0.14}_{-0.14}$	$0.23^{+0.11}_{-0.10}$	$0.37^{+0.97}_{-0.81}$	$0.22^{+0.17}_{-0.11}$	-1.6
$3.0-4.0$	$10.66^{+0.25}_{-0.19}$	$0.02^{+0.02}_{-0.01}$	$1.23^{+1.08}_{-1.11}$	$0.12^{+0.10}_{-0.05}$	-1.6
			Star-forming sample		
$0.2-0.5$	$10.59^{+0.14}_{-0.10}$	$1.06^{+0.33}_{-0.36}$	$0.18^{+0.52}_{-0.54}$	$1.09^{+0.27}_{-0.25}$	$-1.40^{+0.03}_{-0.04}$
$0.5-0.8$	$10.61^{+0.13}_{-0.10}$	$0.72^{+0.23}_{-0.25}$	$0.02^{+0.54}_{-0.56}$	$0.84^{+0.26}_{-0.23}$	$-1.43^{+0.05}_{-0.06}$
$0.8-1.1$	$10.67^{+0.09}_{-0.10}$	$0.65^{+0.24}_{-0.25}$	$-0.21^{+0.56}_{-0.49}$	$0.66^{+0.25}_{-0.25}$	$-1.47^{+0.08}_{-0.11}$
$1.1-1.5$	$10.51^{+0.10}_{-0.08}$	$0.63^{+0.26}_{-0.21}$	$0.62^{+0.59}_{-0.64}$	$1.16^{+0.35}_{-0.36}$	$-1.33^{+0.09}_{-0.12}$
$1.5-2.0$	$10.65^{+0.07}_{-0.06}$	$0.73^{+0.08}_{-0.09}$	$-0.02^{+0.28}_{-0.31}$	$0.41^{+0.07}_{-0.07}$	-1.6
$2.0-2.5$	$10.74^{+0.07}_{-0.08}$	$0.50^{+0.08}_{-0.07}$	$-0.41^{+0.42}_{-0.35}$	$0.14^{+0.07}_{-0.07}$	-1.6
$2.5-3.0$	$10.79^{+0.14}_{-0.15}$	$0.15^{+0.07}_{-0.06}$	$-0.08^{+0.77}_{-0.62}$	$0.16^{+0.09}_{-0.05}$	-1.6
$3.0-4.0$	$10.68^{+0.20}_{-0.16}$	$0.01^{+0.01}_{-0.01}$	$1.38^{+0.83}_{-0.93}$	$0.11^{+0.07}_{-0.04}$	-1.6
			Quiescent sample		
$0.2-0.5$	$10.83^{+0.08}_{-0.09}$	$1.25^{+0.27}_{-0.28}$	$-0.42^{+0.27}_{-0.20}$	$0.21^{+0.20}_{-0.14}$	$-1.22^{+0.12}_{-0.17}$
$0.5-0.8$	$10.91^{+0.04}_{-0.04}$	$1.13^{+0.10}_{-0.09}$	$-0.45^{+0.05}_{-0.05}$		
$0.8-1.1$	$10.76^{+0.03}_{-0.03}$	$1.66^{+0.09}_{-0.09}$	$-0.03^{+0.05}_{-0.05}$		
$1.1-1.5$	$10.68^{+0.03}_{-0.03}$	$0.72^{+0.03}_{-0.03}$	$0.16^{+0.07}_{-0.07}$		
$1.5-2.0$	$10.66^{+0.04}_{-0.04}$	$0.23^{+0.01}_{-0.01}$	$0.27^{+0.11}_{-0.10}$		
$2.0-2.5$	$10.50^{+0.06}_{-0.06}$	$0.08^{+0.01}_{-0.01}$	$1.26^{+0.29}_{-0.26}$		
$2.5-3.0$	$10.32^{+0.09}_{-0.08}$	$0.006^{+0.007}_{-0.004}$	$2.76^{+0.71}_{-0.74}$		

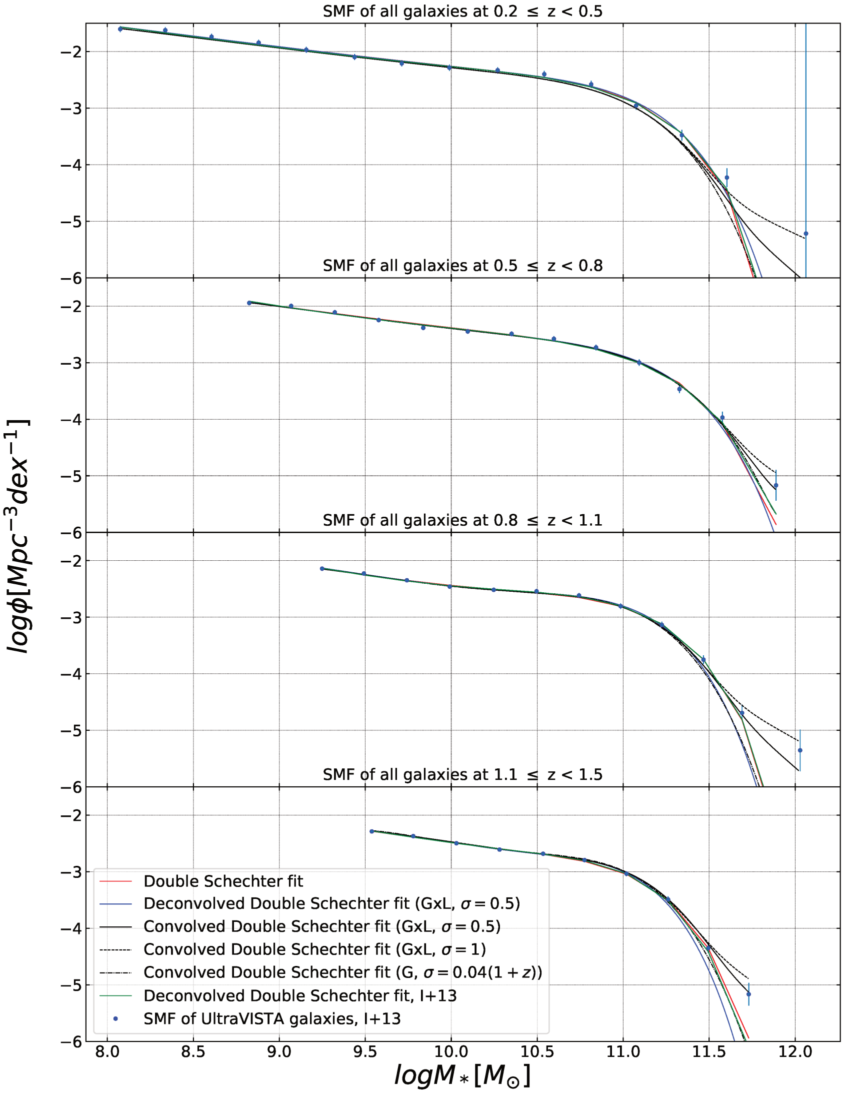

Figure 66: *SMF of UltraVISTA galaxies from Ilbert et al., (2013) at* $0.2 < z < 1.5$ *(blue points) and fits of SMF with the double Schechter model (red lines), double Schechter model deconvolved by the product of the Gaussian and Lorentzian from this work (blue lines) and from Ilbert et al., (2013) (green lines), and convolved double Schechter models (solid, dashed and dashed-dotted black lines).*

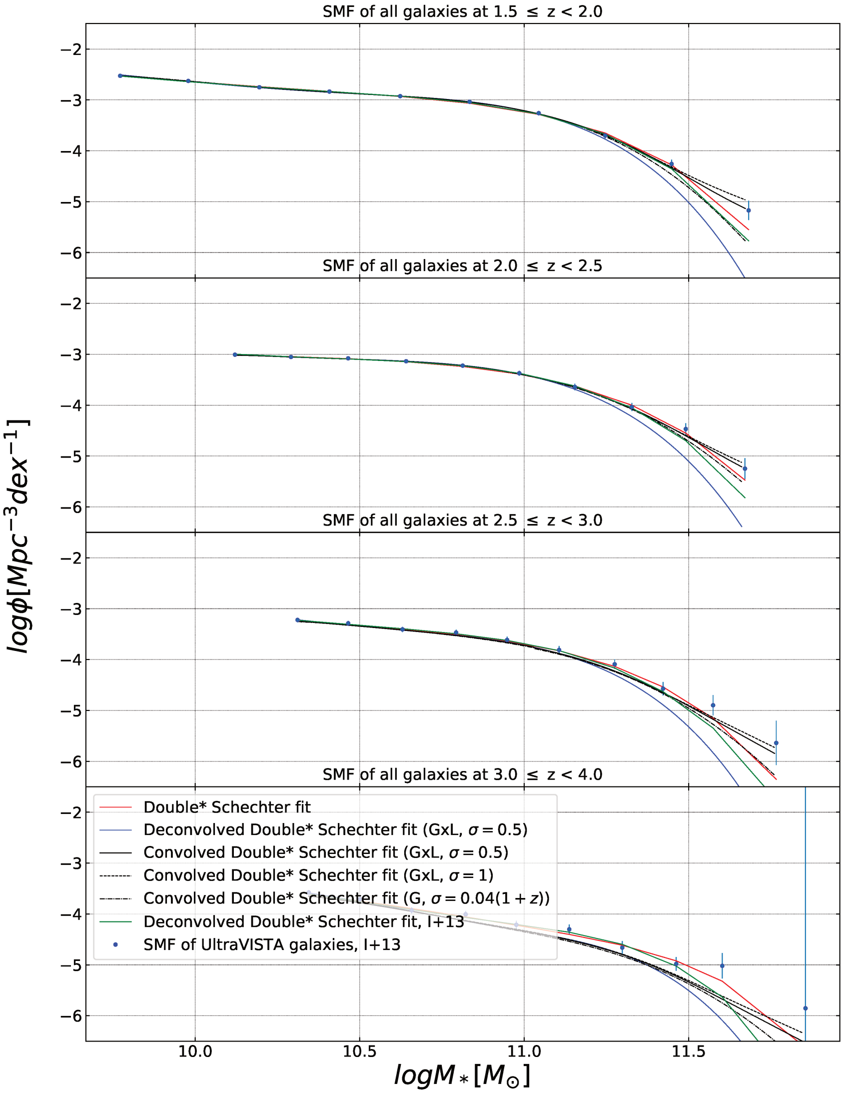

Figure 67: *SMF of UltraVISTA galaxies from Ilbert et al., (2013) at* $1.5 < z < 4.0$ *(blue points) and fits of SMF with the double* Schechter model (*α_2 *parameter fixed) (red lines), double* Schechter model deconvolved by the product of the Gaussian and Lorentzian from this work (blue lines) and from Ilbert et al., (2013) (green lines), and convolved double* Schechter models (solid, dashed and dashed-dotted black lines, respectively).*

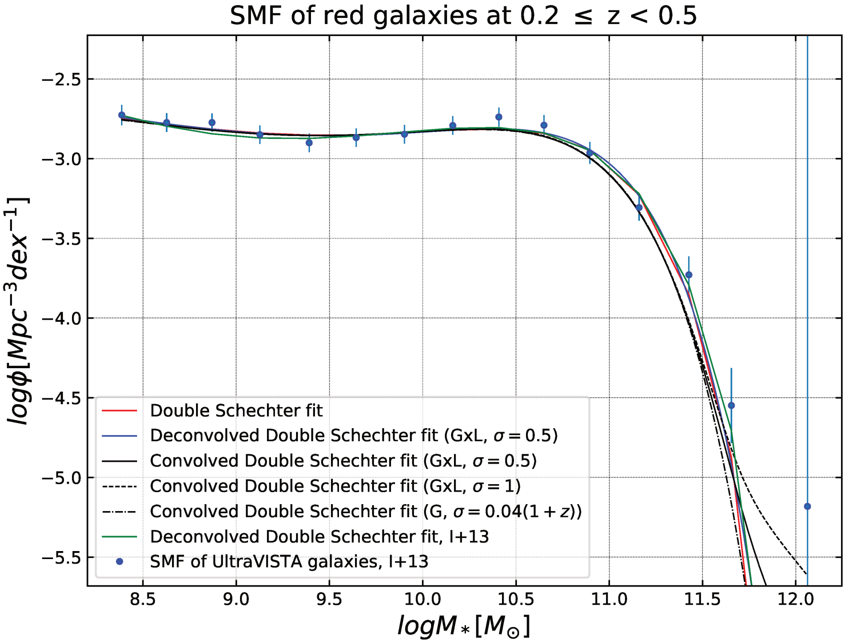

Figure 68: *SMF of UltraVISTA quiescent galaxies from Ilbert et al., (2013) at* $0.2 < z < 0.5$ *(blue points) and fits of SMF with the double Schechter model (red lines), double Schechter model deconvolved by the product of the Gaussian and Lorentzian from this work (blue lines) and from Ilbert et al., (2013) (green lines), and convolved double Schechter models (solid, dashed and dashed-dotted black lines, respectively).*

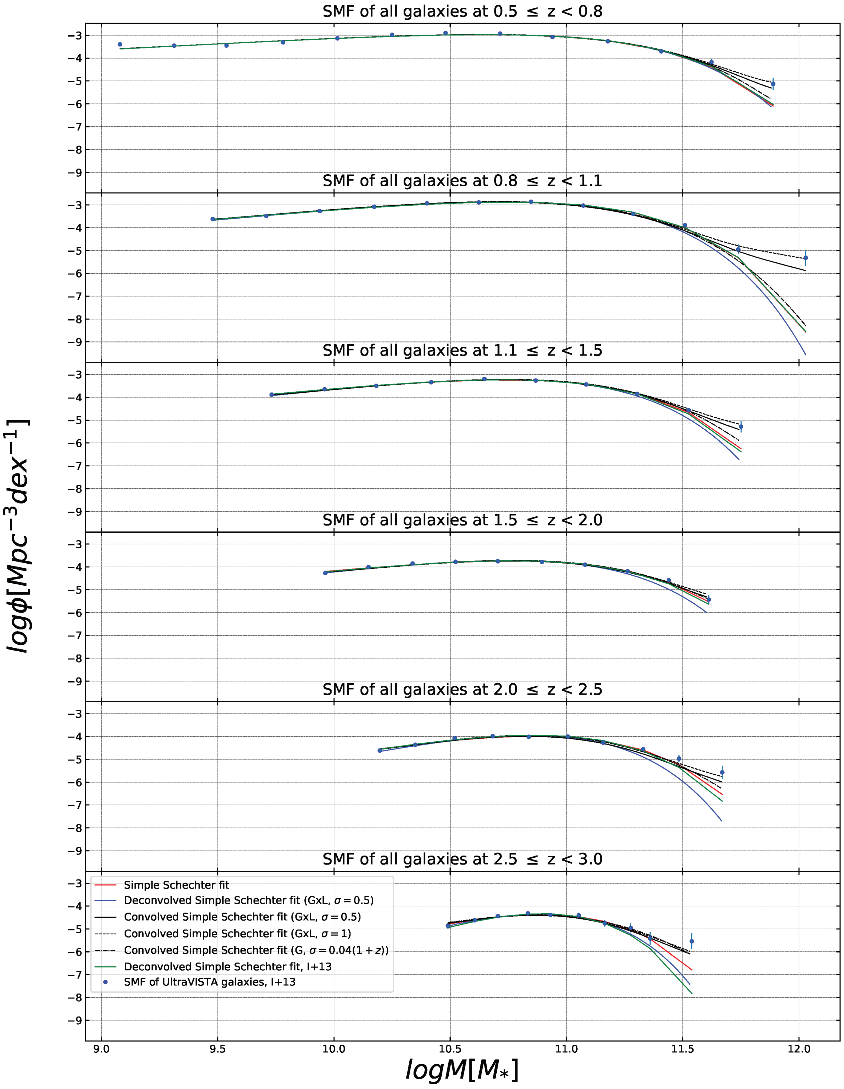

Figure 69: *SMF of UltraVISTA quiescent galaxies from Ilbert et al., (2013) at* $0.5 < z < 3.0$ *(blue points) and fits of SMF with the single Schechter model (red lines), single Schechter model deconvolved by the product of the Gaussian and Lorentzian from this work (blue lines) and from Ilbert et al., (2013) (green lines), and convolved single Schechter models (solid, dashed and dashed-dotted black lines, respectively).*

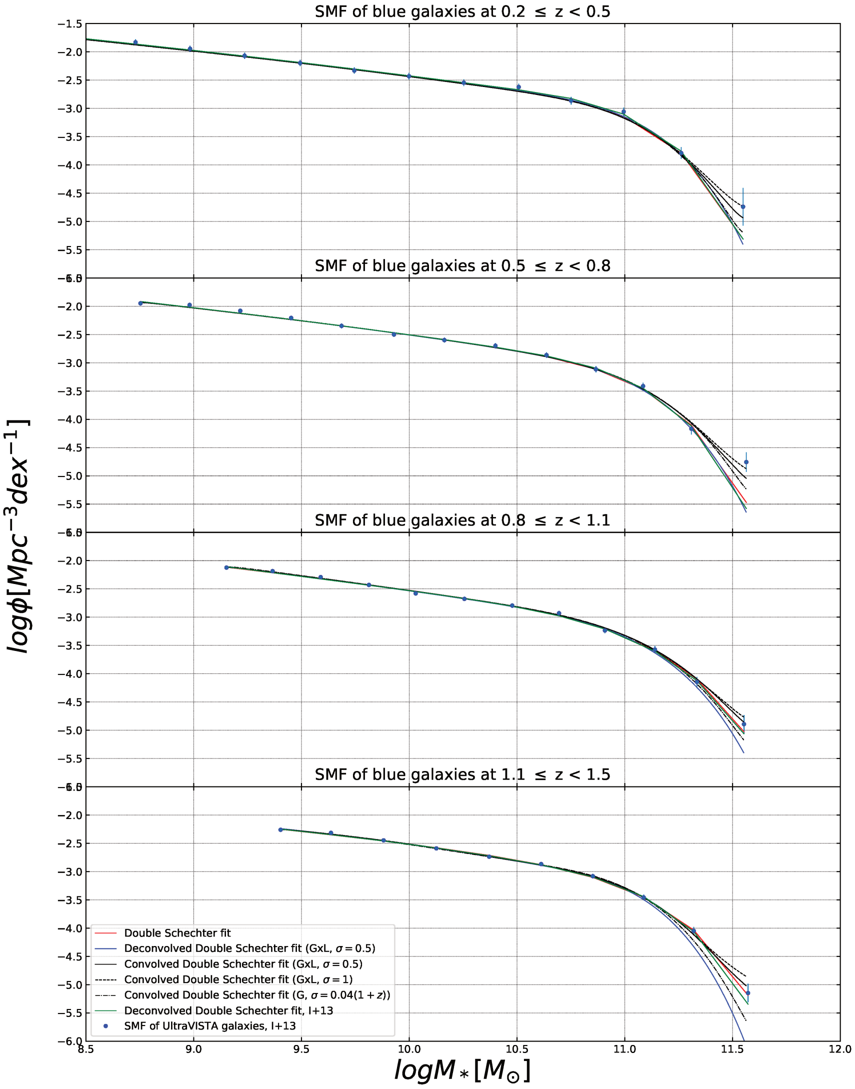

Figure 70: *SMF of UltraVISTA star-forming galaxies from Ilbert et al., (2013) at* $0.2 < z < 1.5$ *(blue points) and fits of SMF with the double Schechter model (red lines), double Schechter model deconvolved by the product of the Gaussian and Lorentzian from this work (blue lines) and from Ilbert et al., (2013) (green lines), and convolved double Schechter models (solid, dashed and dashed-dotted black lines).*

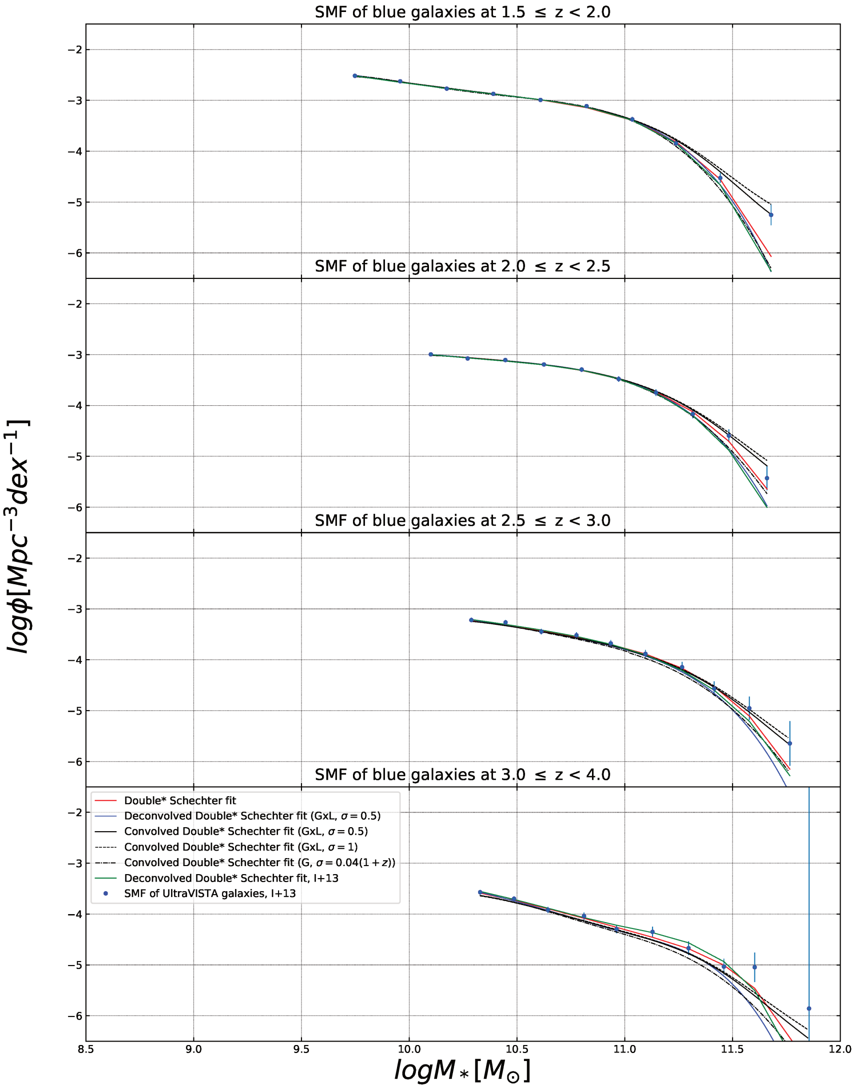

Figure 71: *SMF of UltraVISTA star-forming galaxies from Ilbert et al., (2013) at* $1.5 < z < 4.0$ *(blue points) and fits of SMF with the double* Schechter model (*α_2 *parameter fixed) (red lines), double* Schechter model deconvolved by the product of the Gaussian and Lorentzian from this work (blue lines) and from Ilbert et al., (2013) (green lines), and convolved double* Schechter models (solid, dashed and dashed-dotted black lines, respectively).*

A&A 641, A22 (2020)
https://doi.org/10.1051/0004-6361/202038673

Astronomy & Astrophysics

Massive molecular gas reservoir around the central AGN in the CARLA J1103 + 3449 cluster at $z = 1.44$[⋆]

Vladan Markov[1], Simona Mei[2,1,3], Philippe Salomé[1], Françoise Combes[1,4], Daniel Stern[3], Audrey Galametz[5], Carlos De Breuck[6], Dominika Wylezalek[6], Stefania Amodeo[1,7], Elizabeth A. Cooke[8], Anthony H. Gonzalez[9], Nina A. Hatch[10], Gaël Noirot[11], Alessandro Rettura[3], Nick Seymour[12], Spencer A. Stanford[13], and Joël Vernet[6]

[1] LERMA, Observatoire de Paris, PSL university, Sorbonne Université, CNRS, LERMA, 75014, Paris, France
e-mail: `vladan.markov@obspm.fr`
[2] Université de Paris, 75013, Paris, France
e-mail: `simona.mei@obspm.fr`
[3] Jet Propulsion Laboratory, Cahill Center for Astronomy & Astrophysics, California Institute of Technology, 4800 Oak Grove Drive, Pasadena, CA, USA
[4] Collège de France, 11 Place Marcelin Berthelot, 75231 Paris, France
[5] Department of Astronomy, University of Geneva, 1205 Versoix, Switzerland
[6] European Southern Observatory, Karl-Schwarzschildstrasse 2, 85748 Garching, Germany
[7] Cornell Center for Astrophysics and Planetary Science, Cornell University, Ithaca, NY 14853, USA
[8] National Physical Laboratory, Hampton Road, Teddington, Middlesex, TW11 0LW, UK
[9] Department of Astronomy, University of Florida, Gainesville, FL 32611-2055, USA
[10] School of Physics and Astronomy, University of Nottingham, University Park, Nottingham NG7 2RD, UK
[11] Department of Astronomy & Physics, Saint Mary's University, 923 Robie Street, Halifax, NS B3H 3C3, Canada
[12] International Center for Radio Astronomy Research, Curtin University, GPO Box U1987, 6102 Perth, Australia
[13] Department of Physics, University of California, One Shields Avenue, Davis, CA 95616, USA

Received 16 June 2020 / Accepted 2 July 2020

ABSTRACT

Passive early-type galaxies dominate cluster cores at $z \lesssim 1.5$. At higher redshift, cluster core galaxies are observed to have on-going star-formation, which is fueled by cold molecular gas. We measured the molecular gas reservoir of the central region around the radio-loud active galactic nucleus (AGN) in the cluster CARLA J1103 + 3449 at $z = 1.44$ using NOEMA. The AGN synchrotron emission dominates the continuum emission at 94.48 GHz, and we measured its flux at the AGN position and at the position of two radio jets. Combining our measurements with published results over the range 4.71–94.5 GHz, and assuming $S_{\rm synch} \propto \nu^{-\alpha}$, we obtain a flat spectral index of $\alpha = 0.14 \pm 0.03$ for the AGN core emission, and a steeper index of $\alpha = 1.43 \pm 0.04$ and $\alpha = 1.15 \pm 0.04$ at positions close to the western and eastern lobes, respectively. The total spectral index is $\alpha = 0.92 \pm 0.02$ over the range 73.8 MHz–94.5 GHz. We detect two CO(2–1) emission lines, both blueshifted with respect to the AGN. Their emission corresponds to two regions, ~17 kpc southeast and ~14 kpc southwest of the AGN, not associated with galaxies. In these two regions, we find a total massive molecular gas reservoir of $M_{\rm gas}^{\rm tot} = 3.9 \pm 0.4 \times 10^{10}\,M_\odot$, which dominates ($\gtrsim$60%) the central total molecular gas reservoir. These results can be explained by massive cool gas flows in the center of the cluster. The AGN early-type host is not yet quenched; its star formation rate is consistent with being on the main sequence of star-forming galaxies in the field (star formation rate ~30–140 $M_\odot\,{\rm yr}^{-1}$), and the cluster core molecular gas reservoir is expected to feed the AGN and the host star formation before quiescence. The other confirmed cluster members show star formation rates at ~2σ below the field main sequence at similar redshifts and do not have molecular gas masses larger than galaxies of similar stellar mass in the field.

Key words. galaxies: clusters: individual: CARLA J1103 + 3449 – galaxies: evolution – galaxies: star formation – galaxies: jets – radio continuum: galaxies

1. Introduction

At redshifts $z < 1.5$ galaxy cluster cores are dominated by red, quenched, early-type galaxies, while blue, star-forming, late-type galaxies are mostly found in the field (e.g., Dressler 1980; Balogh et al. 1998, 2004; Postman et al. 2005; Mei et al. 2009; Rettura et al. 2011; Lemaux et al. 2012, 2019; Wagner et al. 2015; Tomczak et al. 2019). At higher redshifts, the results are somewhat conflicting, as it also becomes more difficult to define clusters of galaxies using measurements of their mass. Some results show that at $z > 1.5$ the star formation is already quenched in cluster cores (Kodama et al. 2007; Strazzullo et al. 2010; Papovich et al. 2010; Snyder et al. 2012; Grützbauch et al. 2012; Stanford et al. 2012; Zeimann et al. 2012; Gobat et al. 2013; Muzzin et al. 2013a; Newman et al. 2014; Mantz et al. 2014; Hayashi et al. 2017). Other observations show a reversal of the star formation–density relation and of ongoing star formation in cluster cores at $z > 1.5$, with a much more varied galaxy population compared to clusters at lower redshifts (Elbaz et al. 2007; Cooper et al. 2008; Tran et al. 2010; Brodwin et al. 2013; Santos et al. 2015; Mei et al. 2015; Alberts et al. 2016; Wang et al. 2016a;

[⋆] The reduced images and datacubes are only available at the CDS via anonymous ftp to `cdsarc.u-strasbg.fr` (`130.79.128.5`) or via `http://cdsarc.u-strasbg.fr/viz-bin/cat/J/A+A/641/A22`

Noirot et al. 2016, 2018; Cucciati et al. 2018; Martinache et al. 2018; Shimakawa et al. 2018a,b; Tadaki et al. 2019). A reversal of the star formation at $z \gtrsim 1$ is also predicted from hydrodynamical and semi-analytical simulations (Tonnesen & Cen 2014; Chiang et al. 2017). Other cluster cores at $z \gtrsim 1.5$ present equal percentages of quiescent and star-forming galaxies (Fassbender et al. 2011; Tadaki et al. 2012; Zeimann et al. 2012; Mei et al. 2012; Noirot et al. 2016). A large presence of star-forming galaxies in cluster cores at $z \sim 1.5$–2 indicates that most of the star formation quenching observed at lower redshifts has not yet occurred, and that this is the key epoch of transformation of cluster galaxies from star forming to passive. At higher redshifts ($z \sim 3$–4), protoclusters show high star formation and star-burst activity (Umehata et al. 2015; Lewis et al. 2018; Miller et al. 2018; Oteo et al. 2018; Kubo et al. 2019; Hill et al. 2020; Ivison et al. 2020; Long et al. 2020; Toshikawa et al. 2020).

Galaxy star formation is fueled by cold and dense molecular gas (McKee & Ostriker 2007; Kennicutt & Evans 2012; Krumholz 2014). Therefore, galaxies rich in cold molecular gas are mostly star forming (bluish, mostly late-type spiral and irregular galaxies). Once the molecular gas is heated or stripped through different mechanisms, the star formation is quenched, and galaxies stop forming new, young, blue stars, which explode relatively fast due to their short life cycle. These galaxies will slowly become dominated by long-lived red stars, and galaxies will evolve into red, mostly elliptical, quenched galaxies (Binney & Tremaine 1987; Kennicutt 1998; Kennicutt & Evans 2012). There are several possible processes that can be responsible for star formation quenching, and each plays a different role in cold molecular gas removal, at different epochs and with different timescales (Boselli & Gavazzi 2006). Quenching depends on both galaxy stellar mass and environment (Kauffmann et al. 2004; Baldry et al. 2006; Cucciati et al. 2010; Peng et al. 2010, 2012, 2014; Scoville et al. 2013; Darvish et al. 2015, 2016; Paccagnella et al. 2019). More massive galaxy stellar populations are quenched at earlier epochs (Thomas et al. 2005; Ilbert et al. 2013; Muzzin et al. 2013b; Tanaka et al. 2013; Guglielmo et al. 2015; Pacifici et al. 2016; Tomczak et al. 2016; Sklias et al. 2017; Davidzon et al. 2017; Morishita et al. 2019; Falkendal et al. 2019). Moreover, observations of galaxies of the same stellar mass at $z < 1.5$ show that the evolution from star forming to quiescent is more rapid for cluster galaxies than for their field counterparts (Raichoor et al. 2011; Muzzin et al. 2012; Papovich et al. 2012; Bassett et al. 2013; Shankar et al. 2013, 2014; Strazzullo et al. 2013; Scoville et al. 2013; Delaye et al. 2014; Guglielmo et al. 2015; Hatch et al. 2017; Tomczak et al. 2017; Foltz et al. 2018). This is due to additional environmental mechanisms, such as tidal stripping (Farouki & Shapiro 1981; Moore et al. 1999; Carleton et al. 2019), ram-pressure stripping (Abadi et al. 1999: McCarthy et al. 2008; Merluzzi et al. 2013; Jaffé et al. 2018), strangulation (Larson et al. 1980; Balogh & Morris 2000; Peng et al. 2012, 2015; Maier et al. 2016), and galaxy merging in the first epochs of cluster formation (Hopkins et al. 2006a; Dubois et al. 2016).

In the literature, the fraction of cold gas available for star formation is quantified as $f_{\mathrm{gas}} = M_{\mathrm{gas}}/(M_* + M_{\mathrm{gas}})$, or as a gas-to-stellar mass ratio M_{gas}/M_*. These quantities depend on redshift, galaxy stellar mass, and environment. Observations have shown that for galaxies at a given stellar mass, the gas fraction and gas-to-stellar mass ratio increase with redshift (Sargent et al. 2014; Genzel et al. 2015; Scoville et al. 2017; Silverman et al. 2018; Darvish et al. 2018; Tacconi et al. 2018). For galaxies at the same redshift, the gas fraction increases with decreasing stellar mass (Tacconi et al. 2013, 2018; Sargent et al. 2014; Lee et al. 2017). Finally, at $z < 1.5$, for galaxies of the same mass and at the same redshift, cluster galaxies show lower amounts of molecular gas and thus, lower gas fractions (Jablonka et al. 2013; Rudnick et al. 2017; Lee et al. 2017; Castignani et al. 2018; Hayashi et al. 2018). Some works have shown that at higher redshifts ($z > 2$), there is no difference in the gas fraction of cluster and field galaxies (Husband et al. 2016; Dannerbauer et al. 2017).

In order to assess the molecular gas mass, we can estimate the mass of the most dominant interstellar molecule – H_2, which is also the star formation fuel. However, this molecule is practically invisible to observations due to its lack of a permanent dipole moment and the fact that its rotational dipole transitions require high temperatures, $T > 100$ K. In order to trace molecular hydrogen, rotational transitions of CO molecules are generally used for multiple reasons (Kennicutt & Evans 2012; Carilli & Walter 2013; Bolatto et al. 2013). The CO molecule has a weak permanent dipole moment and it is easily excited even inside cold molecular clouds due to its low energy rotational transitions (Kennicutt & Evans 2012; Bolatto et al. 2013). CO is also the second most abundant molecule after H_2. CO rotational levels are excited by collisions with H_2 molecules. Finally, CO rotational transitions lie in a relatively transparent millimeter window (Solomon & Vanden Bout 2005; Kennicutt & Evans 2012). The main drawback of tracing molecular gas with CO line emission is that CO is a poor tracer of the so-called CO-dark molecular gas, which usually accounts for a significant fraction (~30 to ~100%) of the total molecular gas mass in galaxies (Grenier et al. 2005; Wolfire et al. 2010; Abdo et al. 2010; Planck Collaboration XIX 2011; Pineda et al. 2013; Bisbas et al. 2017; Hall et al. 2020). In this paper, we focus on the molecular gas that can be detected by CO emission and molecular gas upper limits that can be inferred from the CO emission, with the caveat that this might not trace all the molecular gas in the galaxies that we study.

Few galaxy clusters are confirmed at $z \gtrsim 1.5$. Current observations of the CO emission line in clusters at these epochs show that cluster galaxies still have cold gas to fuel their star formation. However, these results are not yet statistically significant, and some results point toward higher molecular gas content in cluster galaxies with respect to the field and others to lower (Casasola et al. 2013; Rudnick et al. 2017; Noble et al. 2017; Hayashi et al. 2018; Coogan et al. 2018; Castignani et al. 2018). Molecular gas has also been detected in two protoclusters at $z \sim 2.5$ (Chapman et al. 2015; Wang et al. 2016b). Both protoclusters are dominated by star-forming (with a high starburst fraction), massive galaxies, with a substantial amount of molecular gas, and a small percentage of passive galaxies, which probably quenched after their accretion onto the cluster.

In this paper, we present IRAM (Institut de Radio Astronomie Millimetrique) NOEMA (NOrthern Extended Millimeter Array) observations of the core of a confirmed cluster from the CARLA (Clusters Around Radio-Loud AGNs; Wylezalek et al. 2013) survey at $z = 1.44$, CARLA J1103 + 3449 (Noirot et al. 2018). CARLA J1103 + 3449 was selected as one of the highest CARLA IRAC color-selected overdensities (~6.5σ, from Wylezalek et al. 2014), and shows a ~3.5σ overdensity of spectroscopically confirmed sources (our Fig. 2, and Table 4 from Noirot et al. 2018). We found a large molecular gas reservoir south of the central AGN, consistent with gas inflows and outflows. We measured galaxy star formation rates and other properties for confirmed cluster members. We compared our results with similar observations in clusters and in the field.

Our observations, data reduction, and mapping are described in Sect. 2, the results are given in Sect. 3, the discussion is in Sect. 4, and finally, the summary of our results is given in Sect. 5. Throughout this paper, we adopt a ΛCDM cosmology, with of $\Omega_M = 0.3$, $\Omega_\Lambda = 0.7$, $\Omega_k = 0$, and $h = 0.7$, and assume a Chabrier initial mass function (IMF; Chabrier 2003).

2. Data

In this section, we describe the CARLA survey. Then, we present our observations and our available data.

2.1. CARLA survey

The CARLA survey (Wylezalek et al. 2013) is a substantial contribution to the field of high-redshift galaxy clusters at $z > 1.5$. CARLA is a 408h Warm *Spitzer*/IRAC survey of galaxy overdensities around 420 radio-loud AGN (RLAGN). The AGNs were selected across the full sky, approximately half radio loud quasars (RLQs) and half radio galaxies (HzRGs), and in the redshift range of $1.3 < z < 3.2$. Wylezalek et al. (2013) identified galaxies at $z > 1.3$ around the AGNs in each field, using a color selection in IRAC channel 1 ($\lambda = 3.6\,\mu$m; IRAC1, hereafter) and channel 2 ($\lambda = 4.5\,\mu$m; IRAC2, hereafter). They found that 92% of the selected RLAGN reside in dense environments, with the majority (55%) of them being overdense at a $>2\sigma$ level, and 10% of them at a $>5\sigma$ level, with respect to the field surface density of sources in the *Spitzer* UKIRT Infrared Deep Sky Survey Ultra Deep Survey (SpUDS; Galametz et al. 2013), selected in the same way.

A *Hubble* Space Telescope Wide Field Camera 3 (HST/WFC3) follow-up of the twenty highest CARLA *Spitzer* overdensities (consisting of ten HzRGs and ten RLQs) spectroscopically confirmed sixteen of these at $1.4 < z < 2.8$, and also discovered and spectroscopically confirmed seven serendipitous structures at $0.9 < z < 2.1$ (Noirot et al. 2018). The structure members were confirmed as line emitters (in Hα, Hβ, [O II], and/or [O III], depending on the redshift) and have star formation estimates from the line fluxes (Noirot et al. 2018). The star formation of galaxies with a stellar mass $\gtrsim 10^{10} M_\odot$ is below the star-forming main sequence (MS) of field galaxies at similar redshift, and star-forming galaxies are mostly found within the central regions (Noirot et al. 2018). This program also provided WFC3 imaging in the F140W filter (WFC3/F140W) from which we obtained point-spread-function (PSF)-matched photometric catalogs (Amodeo et al., in prep.), and galaxy visual morphologies (Mei et al., in prep.).

From their IRAC luminosity function, Wylezalek et al. (2014) showed that CARLA overdensity galaxies have probably quenched faster and earlier compared to field galaxies. Some of the CARLA northern overdensities were also observed in either deep z-band or deep i-band, with the Gemini Multi-Object Spectrographs (GMOS) at the Gemini telescope (hereafter Gemini/GMOS), ISAAC at the European Southern Observatory Very Large Telescope (VLT/ISAAC) and ACAM at the WHT (*William Herschel* Telescope) telescope (WHT/ACAM). This permitted us to estimate their galaxy star formation rate histories, and we deduced that, on average, the star formation of galaxies in these targets had been rapidly quenched, producing the observed colors and luminosities (Cooke et al. 2015).

2.2. Optical and near-infrared multi-wavelength observations of CARLA J1103 + 3449

As a target of the *Spitzer* CARLA survey, CARLA J1103 + 3449 was observed with *Spitzer* IRAC1 and IRAC2 (Cycle 7 and 8 snapshot program; PI: D. Stern), for a total exposure of 800 s and 2000 s, respectively. The IRAC cameras have 256 × 256 InSb detector arrays with a pixel size of 1.22 arcsec and a field of view of 5.2 × 5.2 arcmin. Wylezalek et al. (2013) performed the data calibration and mapping with the `MOPEX` package (Makovoz & Khan 2005) and detected sources with SExtractor (Bertin & Arnouts 1996), using the IRAC-optimized SExtractor parameters from the work of Lacy et al. (2005). The final *Spitzer* IRAC1 and IRAC2 mosaic has a pixel size of 0.61 arcsec, after taking into account dithering and sub-pixelation.

The HST/WFC3 imaging and grism spectroscopy were obtained with a dedicated HST follow-up program (Program ID: 13 740; PI: D. Stern). We obtained F140W imaging (with a field of view of 2 × 2.3 arcmin^2 at a resolution of 0.06 arcsec pix^{-1}, obtained after taking into account dithering), and G141 grism spectroscopy (with a throughput >10% in the wavelength range of $1.08\,\mathrm{m} < \lambda < 1.70\,\mathrm{m}$ and a spectral resolution of $R = \lambda/\Delta\lambda = 130$). This grism was chosen in order to permit the identification of strong emission lines at our target redshift, such as Hα, Hβ, [O II], and [O III]. Noirot et al. (2016, 2018) performed the data reduction using the `aXe` (Kümmel et al. 2009) pipeline, by combining the individual exposures, and removing cosmic ray and sky signal. Noirot et al. (2018) performed the source detection with SExtractor (Bertin & Arnouts 1996) and extracted 2D spectra for each field, based on the positions and sizes of the sources. The redshifts and emission line fluxes were determined using the python version of `mpfit` and are published in Noirot et al. (2018).

CARLA J1103 + 3449 was followed-up with i-band imaging using WHT/ACAM (PI: N. Hatch; Cooke et al. 2015), and we obtained a PSF-matched photometric catalog in the WHT/ACAM i-band, WFC3/F140W (detection image), IRAC1, and IRAC2. The i-band, WFC3/F140W, and IRAC1 filters correspond to the *UVJ* rest-frame bandpasses at the redshift of CARLA J1103 + 3449. More details on the *Spitzer* IRAC, HST/WFC3, and WHT/ACAM observations, data reduction, and results can be found in Wylezalek et al. (2013, 2014), Noirot et al. (2016, 2018), and Cooke et al. (2015), respectively.

From a morphological (from the HST/F140W images) and photometric analysis of the central sources (Amodeo et al., in prep.; Mei et al., in prep.), the host galaxy of the AGN is an elliptical galaxy. The spiral galaxy close to the AGN is a spectroscopically confirmed member (Noirot et al. 2018), but is not detected as an independent galaxy in the IRAC images because of their poor spatial resolution. The bright central source south of the AGN is a star, with a spectral energy distribution consistent with a black body and not consistent with an early-type galaxy (ETG) spectrum.

2.3. Keck AGN spectrum observations

The redshift for the radio source B2 1100 + 35, associated with WISE J110326.19 + 344947.2 at the center of CARLA J1103 + 3449, was first reported in Eales et al. (1997) as $z = 1.44$, but with no spectrum presented. With no spectrum available from the Sloan Digital Sky Survey of the faint, red ($g = 23.9$ mag, $i = 21.4$ mag) optical counterpart to the radio source, we observed B2 1100 + 35 with the dual-beam Low Resolution Imaging Spectrometer (LRIS; Oke et al. 1995) at the Keck Observatory on UT 10 March 2019. The night suffered strongly from variable, often thick cloud cover.

The data were obtained through the 1.″0 slit with the 5600 Å dichroic. The blue arm of the spectrograph used the 600 $\ell\,\mathrm{mm}^{-1}$ grism ($\lambda_{\mathrm{blaze}} = 400$ Å; resolving power $R \equiv \lambda/\Delta\lambda \sim 1600$ for

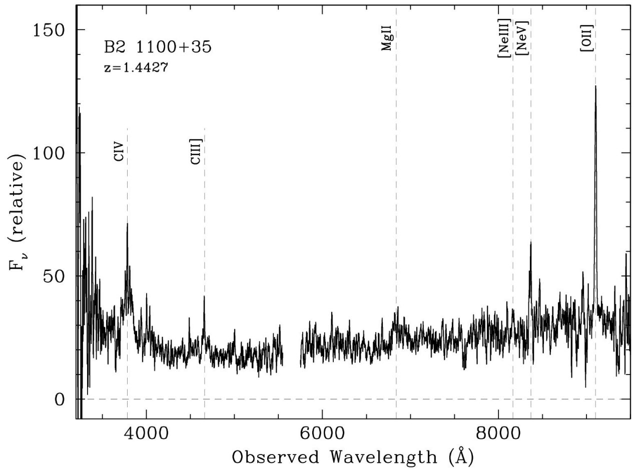

Fig. 1. Keck/LRIS spectrum of B2 1100 + 35, the radio galaxy at the center of CARLA J1103 + 3449. Since the night was not photometric, the y-axis only provides relative flux calibration.

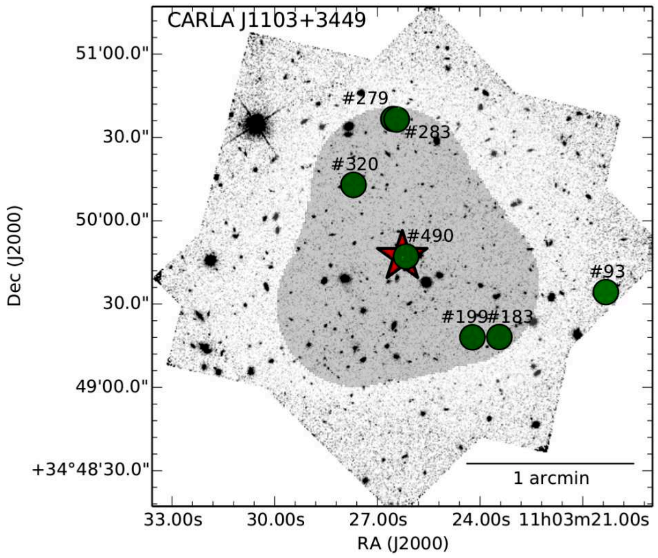

Fig. 2. Distribution of spectroscopically confirmed members of CARLA J1103 + 3449 (green circles) with the central AGN (red star) (Noirot et al. 2018). The background images are the two orientation HST/WFC3 F140W frames. The shaded area indicates the NOEMA mosaic map area.

objects filling the slit), while the red arm used the 4000 ℓ mm^{-1} grating ($\lambda_{\rm blaze}$ = 8500 Å; $R \sim 1300$). Three 600 s exposures were attempted, though ultimately only one proved useful. We processed the spectrum using standard techniques, and flux calibrated the spectrum using observations of the standard stars Hilter 600 and HZ44 from Massey & Gronwall (1990) obtained the same night with the same instrument configuration. Figure 1 presents the processed spectrum. Multiple redshifted emission lines are detected, including broadened C IV λ1549 Å, narrow C III] λ1909 Å, narrow [Ne V] λ3426 Å, and strong, narrow [O II] λ3727 Å. Based on the latter feature, we report a redshift of $z = 1.4427 \pm 0.0005$, where the uncertainty reflects both statistical uncertainties in the line fitting, as well as an estimate of systematic uncertainties in the wavelength calibration, and a comparison with other well-detected emission lines in this source. This measurement is consistent with the Noirot et al. (2018) AGN redshift measurement of $z = 1.444 \pm 0.006$, from the HST/WFC3 grism observations (see above).

2.4. IRAM observations

For this work, we observe CARLA J1103 + 3449 with the IRAM/NOEMA (PI: A. Galametz, S. Mei), with eight antennas over a five-day period (28–30 Jul., 3–4 Aug. 2017), for a total exposure time of ~29 h (including overheads). The weather conditions were within the average precipitable water vapor (PWV~10–20 mm). The average system temperature was $T_{\rm sys} \sim$ 100–200 K, and reached maximum values of 300 K. The sources used as RF (receiver bandpass) calibrator, the flux calibrator, and amplitude/phase calibrators were the 3C84 radio galaxy, the LKHA101 radio star, and the 1128 + 385 quasar, except on the 30 Jul., when we used the quasars 3C273, 1128 + 385 (measured on the 28 Jul.) and 1156 + 295.

We targeted the CO(2–1) emission line at the rest-frame frequency $\nu_{\rm rest}$ = 230.538 GHz, which is redshifted to $\nu_{\rm obs}$ = 94.48 GHz at $z = 1.44$ (approximately the mean confirmed cluster member redshift from Noirot et al. 2018), observed in the NOEMA 3 mm band. We covered our target with three pointings to map the AGN and the central cluster region. The pointings were positioned so that we could cover as many IRAC color-selected members as possible (~40) along with the seven (out of eight) HST/WFC3 spectroscopically confirmed members (green circles and a red star, for the AGN, in Fig. 2, based on Noirot et al. 2018). We chose the antenna configuration C to be able to separate cluster members in the cluster core. The beam size is 4.14 × 3.46 arcsec^2, the PA = −171.01°, and the velocity resolution is 50 km s^{-1} (smoothed to 100 km s^{-1}; see below).

We performed the entire NOEMA data calibration by running the pipeline in the `clic` package of the IRAM/GILDAS software[1]. We flagged additional data, modified antenna positions, and calibrated the flux again. While the pointing and the focus were excellent, the amplitude, and phase were of average quality because of the weather conditions.

With the reduced data, we created a CO(2–1) continuum emission mosaic map, by using the `mapping` package of the GILDAS software (Fig. 3, left). The map was obtained by averaging the flux over a velocity range of 2450 km s^{-1}, excluding emission lines, with a background root mean square (rms) noise level of $\sigma \sim 0.2$ mJy beam^{-1}. Then, we subtracted the continuum from the CO(2–1) emission in the uv-data set in order to obtain a clean, continuum-subtracted CO(2–1) map.

We calculated the rms noise level in the three pointing intersection regions of the CO(2–1) map (see Fig. 2). In this region, the original velocity resolution is 50 km s^{-1} and the rms noise level is $\sigma \sim 0.8 \times$ mJy beam^{-1}. In order to improve the signal-to-noise ratio (S/N), we smoothed the CO(2–1) map to a final velocity resolution of 100 km s^{-1} by averaging two consecutive channels, and obtained a rms noise level of $\sigma \sim 0.5 \times$ mJy beam^{-1} after smoothing. We created the CO(2–1) intensity map by averaging the flux over a velocity range of 1200 km s^{-1} with the background rms noise level of $\sigma \sim 0.2$ mJy beam^{-1}, and applied a primary beam correction (Fig. 3, right). On the mosaic edges, the rms noise level approximately doubles.

3. Results

In this section, we describe our results. First, we present the active galactic nucleus continuum emission. Then, we derive the

---

[1] http://www.iram.fr/IRAMFR/GILDAS/

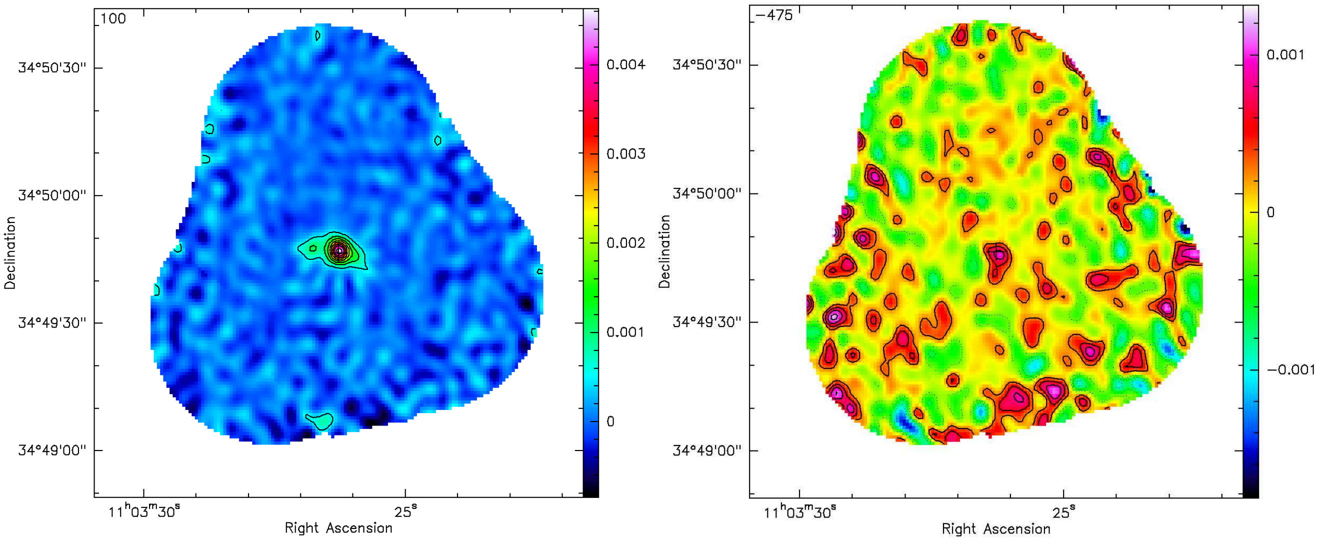

Fig. 3. *Left*: continuum emission map of the CARLA J1103 + 3449 cluster at 94.48 GHz. The map was obtained by averaging the flux over a velocity range of 2450 km s^{-1}, outside of the emission lines. The rms noise level is $\sigma \sim 0.2$ mJy beam^{-1} in the central pointing intersection region, and the contours show the 3σ, 6σ, 9σ, etc. levels up to 24σ. *Right*: continuum subtracted CO(2–1) line emission mosaic map. The color wedge of the intensity maps is in Jy beam^{-1}. The map was obtained by averaging the flux over a velocity range of 1200 km s^{-1}, and has an average rms noise level of $\sigma \sim 0.2$ mJy beam^{-1} in the central pointing intersection region. The continuous lines show positive σ contours and the dotted lines show negative σ contours. The contours show the 1σ, 2σ, and 3σ levels. The cross marks the phase center of the mosaic. The noise approximately doubles toward the map edges because of the primary beam correction. Both maps show an extended source in the cluster center.

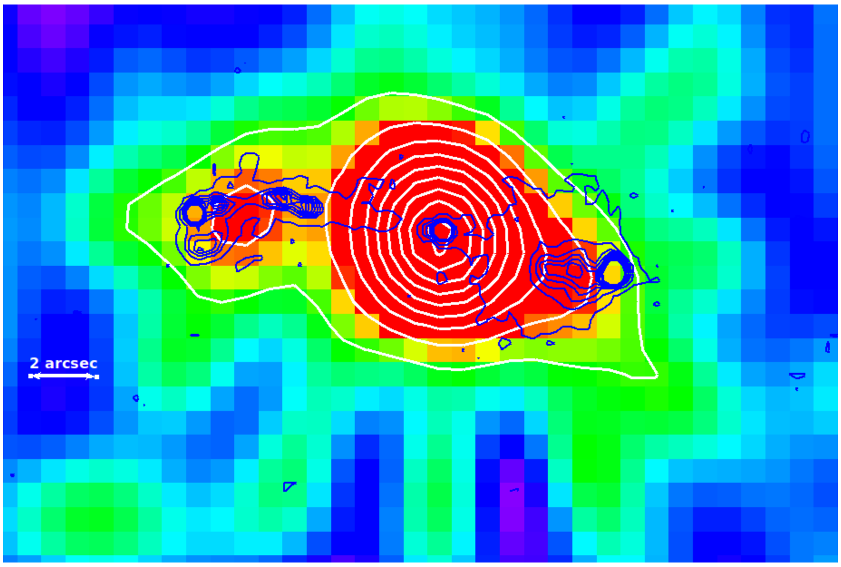

Fig. 4. Zoom-in on the continuum emission map of the extended source in the cluster center. The continuum emission contours (white) run as 3σ, 6σ, 9σ, etc. up to 24σ. The radio emission contours at 4.71 GHz from the work of Best et al. (1999) are overlaid on the image (in blue). The brightest continuum emission peak and one of the radio peaks are both centered on the AGN. The continuum emissions visually correspond to the position of the radio jets, suggesting the same or a connected physical origin. North is up and east is to the left.

molecular gas content in the cluster central region using CO(1-2) emission flux measurements.

3.1. Active galactic nucleus continuum emission

On the continuum emission map at the observed frequency of $\nu_{\rm obs} = 94.48$ GHz, we detect an extended source in the cluster central region, with the brightest peak at the position of the AGN (>26σ, Fig. 4, white contours). Comparing the NOEMA continuum emission with radio observations at 4.71 GHz from Best et al. (1999) (Fig. 4, blue contours), the NOEMA continuum emission visually corresponds to the radio jets. Both the NOEMA extended continuum emission peak, and the central radio emission, correspond to the AGN position. We also detect significant (>6σ) continuum emission at the position of the tip of the eastern radio lobe (Fig. 4).

The position and the scale of this continuum emission detection follow the emission from the radio lobes, with the brighter and the fainter continuum components corresponding to the western and eastern radio lobe, respectively. This is consistent with the same or a connected physical origin of the two emissions. In fact, the AGN synchrotron emission dominates at both our NOEMA observed frequency (rest-frame $\nu \sim 230$ GHz/$\lambda \sim 1.3$ mm), and in the radio observation frequency range (Bregman 1990; Haas et al. 1998; Hönig et al. 2008; Nyland et al. 2017; Ruffa et al. 2019). At both frequency ranges, the signal corresponds to the non-thermal synchrotron radiation emitted by the relativistic charged particles from the AGN jets (Gómez et al. 1995, 1997; Mioduszewski et al. 1997; Aloy et al. 2000; Porth et al. 2011; Fuentes et al. 2018).

We measured the continuum within a region the size of the NOEMA beam centered on the AGN and the two lobes. We

Table 1. Continuum flux measurements.

Component	RA (J2000) (h:m:s)	Dec (J2000) (d:m:s)	$F_{4.71\,\mathrm{GHz}}$ (mJy)	$F_{8.21\,\mathrm{GHz}}$ (mJy)	$F_{94.5\,\mathrm{GHz}}$ (mJy)	α^{B99}	α
Total	...	...	96.6	55.7	6.5 ± 0.3	...	0.94 ± 0.01
Core	11:03:26.26	+34:49:47.2	6.8	6.9	4.6 ± 0.2	−0.04	0.14 ± 0.03
West	11:03:25.83	+34:49:45.9	57.0	29.1	0.8 ± 0.2	1.21	1.43 ± 0.04
East + jet	11:03:26.77	+34:49:47.7	32.8	19.7	1.1 ± 0.2	...	1.15 ± 0.04
East	11:03:26:89	+34:49:47.8	21.7	12.7	...	0.96	...
Jet	11:03:26.64	+34:49:48.2	11.1	7.0	...	0.82	...

Notes. Continuum flux measurements from our work at 94.5 GHz, and those from Best et al. (1999) at 4.71 and 8.21 GHz. We measure the spectral index α over this wavelength range, while α^{B99} are the spectral indexes from Best et al. (1999).

obtain $S^{\mathrm{AGN}}_{\mathrm{cont}} = 4.6 \pm 0.2$ mJy, $S^{\mathrm{east\_lobe}}_{\mathrm{cont}} = 1.1 \pm 0.2$ mJy, and $S^{\mathrm{west\_lobe}}_{\mathrm{cont}} = 0.8 \pm 0.2$ mJy. For the eastern lobe, we centered our measurement on the peak of the emission in our observations, while for the western lobe, where we do not have a clear peak, we centered on the radio peak.

Comparing the continuum emission from this work and the radio emission from Best et al. (1999) (white and blue contours in Fig. 4, respectively), we note that our brighter continuum component (~83% of the total continuum emission flux) roughly corresponds to the radio emission of the core and the western lobe (~65% at $\nu = 8210$ MHz and 66% at $\nu = 4710$ MHz of the total flux), and also includes the fainter part of the eastern jet. The peak of the continuum emission at 94.48 GHz is centered on the AGN (~71% of the total continuum emission flux), while most of the radio emission from Best et al. (1999) is from the western lobe (~52% at $\nu = 8210$ MHz and 59% at $\nu = 4710$ MHz of the total flux). Our fainter continuum component (~17% of the total flux) corresponds to the radio emission of the eastern lobe and a brighter part of the eastern jet (~35% at $\nu = 8210$ MHz and 34% at $\nu = 4710$ MHz of the total flux).

Table 1 shows our continuum flux measurements at 94.48 GHz, and those from Best et al. (1999) at 4.71 and 8.21 GHz. The total flux in the table is the sum of the three components, the core and the two lobes. The total flux measured in an area with the signal exceeding 3σ of the background is $S^{3\sigma}_{\mathrm{cont}} = 8.2 \pm 0.2$ mJy. We modeled the AGN and lobe spectral energy distribution (SED) as a power law ($S_{\mathrm{synch}} \propto \nu^{-\alpha}$), and obtained the spectral index α for the different components from a linear fit in logarithmic scale, using all three frequencies. The uncertainty on α is the statistical uncertainty from the linear fit. The systematic uncertainty on α^{B99} of 0.07 from Best et al. (1999) is much larger than the statistical uncertainty and is calculated by assuming 3% uncertainties in the absolute calibration at each Best et al. (1999) frequency. Our indexes are consistent (1–1.5σ) with those from Best et al. (1999) (also shown in Table 1). The lobes present a steep SED, consistent with the optically thin synchrotron emission of the jets (Best et al. 1999; Laing & Bridle 2013; Nyland et al. 2017; Ruffa et al. 2019; Grossová et al. 2019), while the AGN core SED is flatter, which is consistent with optically thicker (self-absorbed) synchrotron emission (Best et al. 1999; Ruffa et al. 2019; Grossová et al. 2019).

In Fig. 5, we show the total AGN SED at radio and millimeter wavelengths from our work (total AGN emission) and the literature. Over this larger range of frequencies, we obtain $\alpha = 0.92 \pm 0.02$, consistent with the optically thin synchrotron emission of AGN jets that dominate the total continuum emission. The SED does not show a flattening or steepening at high-frequency ($\nu > 10$ GHz) either, in agreement with previous results (Klamer et al. 2006; Emonts et al. 2011; Falkendal et al. 2019).

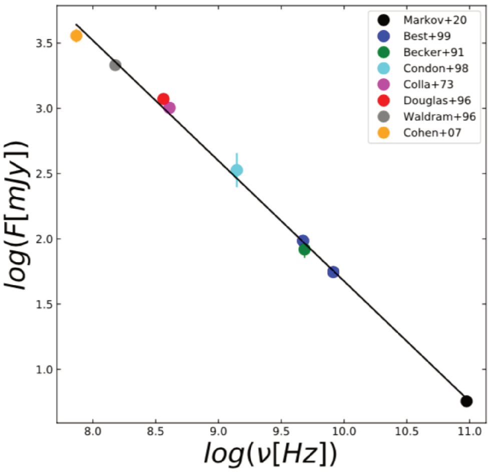

Fig. 5. Total SED plot of the AGN in the radio and millimeter wavebands from our work (black), Best et al. (1999) (blue), Becker et al. (1991) (green), Condon et al. (1998) (cyan), Colla et al. (1973) (magenta), Douglas et al. (1996) (red), Waldram et al. (1996) (gray), and Cohen et al. (2007) (orange). Over this range of frequencies, we obtain an AGN spectral index of $\alpha = 0.92 \pm 0.02$.

Our results are within the range of spectral indexes found in previous work. The typical spectral index of optically thin synchrotron emission (which corresponds to jets) is in the range of $0.5 \lesssim \alpha \lesssim 1.5$ in the local Universe (Laing & Bridle 2013; Nyland et al. 2017; Ruffa et al. 2019; Grossová et al. 2019) and $1 \lesssim \alpha \lesssim 2$ for galaxies at $z > 2$, with higher values being rarer (Carilli et al. 1997; Best et al. 1999; Falkendal et al. 2019). For the optically thick emission (which corresponds to the core), $-0.5 \lesssim \alpha \lesssim 0.5$ is found in the local Universe (Ruffa et al. 2019; Grossová et al. 2019) and $-1 \lesssim \alpha \lesssim 1$ is found at $z > 2$, with most of the measurements being $\alpha > 0.5$ (Carilli et al. 1997; Athreya et al. 1997; Best et al. 1999; Falkendal et al. 2019).

3.2. Molecular gas content around the active galactic nucleus

System velocity and FWHM. In order to estimate the system velocity and the velocity full width at half maximum (FWHM) from the CO(2–1) line emission, we use the `class` package from the GILDAS software. We extract the CO(2–1) line profile from a polygon enclosing all >1σ CO(2–1) emission in the central region of the cluster.

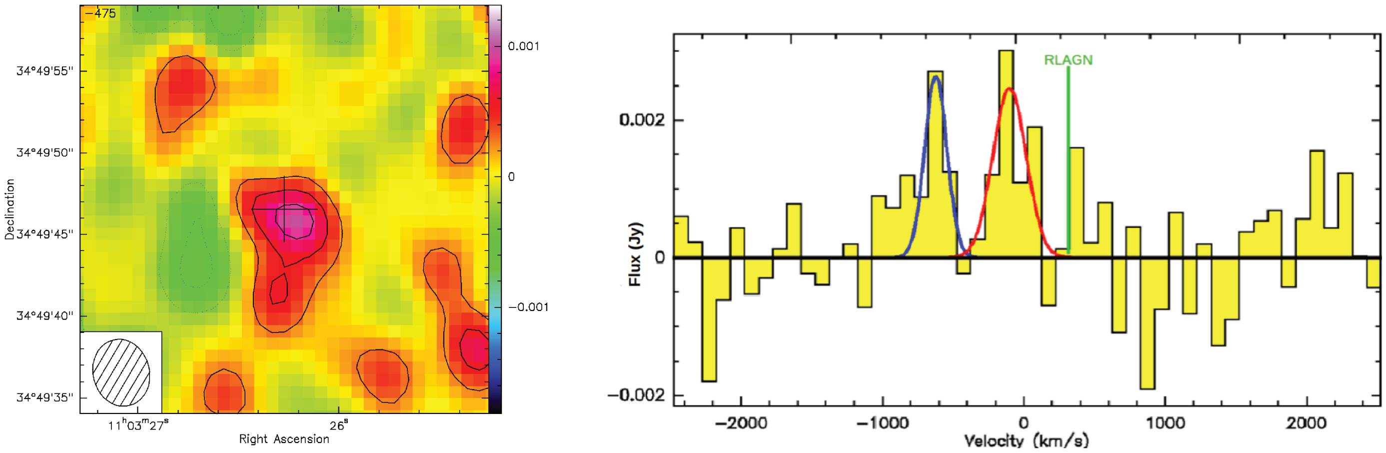

Fig. 6. *Left*: zoom-in on the CO(2–1) line emission, continuum-subtracted mosaic map of the extended source in the cluster center. The black cross marks the center of our observations. The beam size (4.14×3.45 arcsec^2) is plotted at the lower left. The color scale of the intensity map is in Jy beam^{-1}. The rms noise level is $\sigma \sim 0.2$ mJy beam^{-1} in the central pointing intersection region. The contours correspond to the 1σ, 2σ, and 3σ levels. *Right*: CO(2–1) line emission integrated spectrum. The two Gaussian fits correspond to system velocities of $V_{\rm sys} = -623.0$ km s^{-1} (blue) and $V_{\rm sys} = -115.5$ km s^{-1} (red). The AGN spectroscopic redshift corresponds to a velocity of $v = 331.6$ km s^{-1} (vertical green line).

In the integrated spectrum, we identify two emission lines, which we fit as Gaussians (Fig. 6, right). The two Gaussian emission peaks are at $V_{\rm sys} = -623 \pm 30$ km s^{-1} with a velocity of $FWHM = 179 \pm 71$ km s^{-1}, and $V_{\rm sys} = -116 \pm 40$ km s^{-1} with a velocity of $FWHM = 346 \pm 87$ km s^{-1}. We show these fits as the blue and the red Gaussians, respectively, in Fig. 6. The zero point $V_{\rm sys} = 0$ km s^{-1} in the spectrum corresponds to a redshift of $z = 1.44$, approximately the mean confirmed cluster member redshift from Noirot et al. (2018), as explained in the observation section. In Appendix A, we identify the emission regions of the two CO(2–1) emission peaks by mapping the position of each component using the GILDAS software and we find that the two peaks correspond to two separate regions, one southeast and the other southwest of the AGN. Hereafter we identify the two peaks as the eastern and western emission peaks.

In Fig. 7, we compare the emission regions that we find from this analysis to the position of the CARLA IRAC color-selected galaxies in our HST/F140W image. We find that the spatial extension that corresponds to the eastern and western emission peaks is south of central AGN. Neither the eastern nor the western emission peaks correspond to the spatial position or to the spectroscopic redshift of the AGN (Fig. 6). The peaks do not correspond to any optical (HST/WFC3) or infrared (*Spitzer*/IRAC) counterpart. We remind the reader that the bright central source south of the AGN is a star and not a galaxy (see Sect. 2.2).

The other detections at the center of the NOEMA CO(2–1) line emission mosaic map (Fig. 3, right) are at $S/N \leq 2$. Their velocity peak is at the same spectral position as the western peak, and we again do not detect galaxies at their position in the HST/WFC3 or *Spitzer*/IRAC images. We conclude that those overdensities might be due to the side lobes, and neglect them. We do not have detections at $>3\sigma$ at the edges of the mosaic, where the noise is higher.

Flux and luminosity. From the Gaussian fit, the velocity-integrated flux for the eastern and western emission peaks are $S_{\rm CO(2-1)}\Delta v = 0.6 \pm 0.2$ Jy km s^{-1} ($S/N \sim 3$; here and hereafter the S/N is calculated as the signal divided by its uncertainty, before approximating to one significant figure), and $S_{\rm CO(2-1)}\Delta v = 0.9 \pm 0.2$ Jy km s^{-1} ($S/N \sim 4$), respectively. In the Gaussian fit, we leave all parameters free to vary. The uncertainty on the measurements includes the uncertainties in the Gaussian fit and the noise in the region in which the fit is performed. The total flux for the eastern emission peak, obtained by integrating over the velocity range -1075 km s^{-1} $< v <$ -475 km s^{-1}, is $S_{\rm CO(2-1)}\Delta v = 0.88 \pm 0.16$ Jy km s^{-1} ($S/N \sim 6$; Figs. 7 and A.2). The difference between this flux measurement and that obtained from the Gaussian fit is consistent with zero. The total flux for the western emission peak, obtained by integrating over the velocity range -375 km s^{-1} $< v <$ $+125$ km s^{-1}, is $S_{\rm CO(2-1)}\Delta v = 0.90 \pm 0.15$ Jy km s^{-1} ($S/N \sim 6$; Figs. 7 and A.3), and very similar to the value obtained from the Gaussian fit. The integrated flux from the eastern and western emission peaks over the velocity range -1075 km s^{-1} $< v <$ 125 km s^{-1} is $S_{\rm CO(2-1)}\Delta v = 1.7 \pm 0.2$ Jy km s^{-1} ($S/N \sim 10$). We do not measure any CO(2–1) line emission at the spectral position of the AGN, $z = 1.4427 \pm 0.0005$, which corresponds to a velocity of $v = 331.6$ km s^{-1}, shown as a vertical green line in Fig. 6. Hereafter, we use the velocity integrated fluxes for both the eastern and western emission peaks, for which we have the higher S/N. We calculate the CO(2–1) luminosity using the following relation from Eq. (3) of Solomon & Vanden Bout (2005):

$$L'_{\rm CO(2-1)} = 3.25 \times 10^7 \frac{S_{\rm CO(2-1)}\Delta v D_L^2}{\nu_{\rm rest}^2 (1+z)}, \tag{1}$$

where $L'_{\rm CO(2-1)}$ is the CO(2–1) line luminosity in K km s^{-1} pc^2, $S_{\rm CO(2-1)}\Delta v$ is the CO(2–1) velocity integrated flux in Jy km s^{-1}, $D_L = 10\,397.4$ Mpc is the AGN luminosity distance, $\nu_{\rm rest} = 230.538$ GHz is the rest frequency of the CO(2–1) rotational transition, and $z = 1.4427 \pm 0.0005$ is the AGN redshift (see Sect. 2.2). We find $L'_{\rm CO(2-1)} = 2.4 \pm 0.4 \times 10^{10}$ K km s^{-1}pc^2 and $L'_{\rm CO(2-1)} = 2.4 \pm 0.4 \times 10^{10}$ K km s^{-1}pc^2, for the eastern and western emission peaks, respectively.

Molecular gas mass. In order to estimate the molecular gas mass, we use the mass-to-luminosity relation

$$M_{\rm gas} = \alpha_{\rm CO} \frac{L'_{\rm CO(2-1)}}{r_{21}}, \tag{2}$$

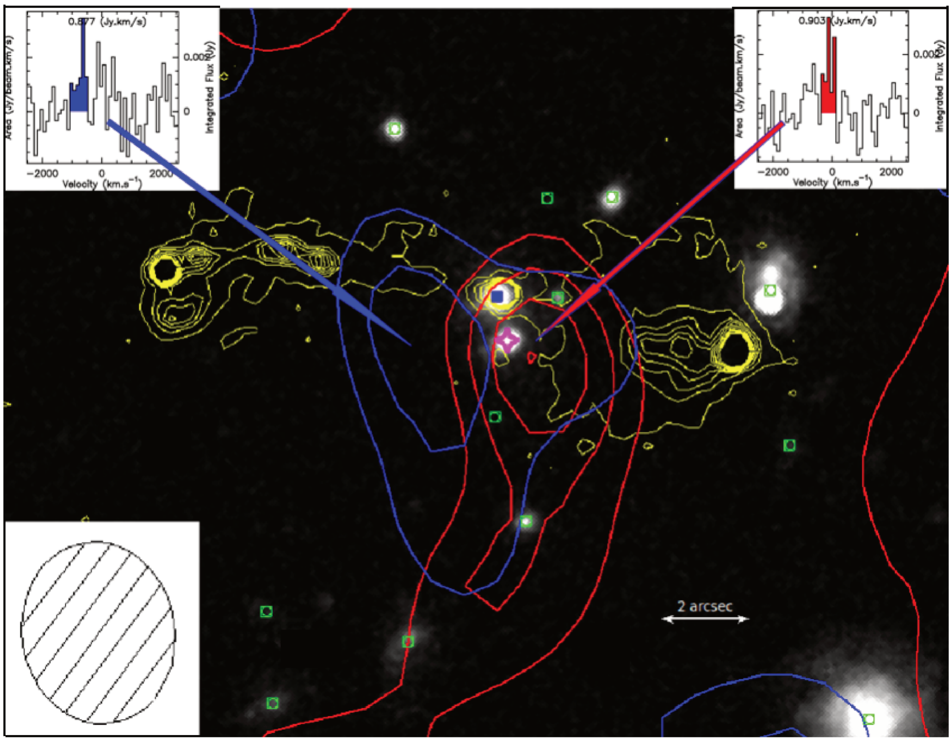

Fig. 7. HST/WFC3 F140W image of the central region of the cluster, with contours of CO(2–1) emission of the eastern and western emission peaks (shown as blue and red contours, respectively), and the radio emission at 4.71 GHz (yellow) from the work of Best et al. (1999). The central peak of the radio emission corresponds to the position of the AGN. The two radio lobes are asymmetrical, with the one to the east (left of the AGN) being more compact and the one to the west more diffuse. The central blue square and the pink star with four spikes show the position of the AGN and of the star, respectively. The green squares are the positions of IRAC color-selected galaxies in the cluster's central region. The contours are derived by integrating the CO(2–1) emission across the velocities marked by their corresponding color on the CO(2–1) emission line spectra. The spectra are shown in the top left and right insets (see Appendix A for more details). The contour levels of the eastern and western emission peaks are 1–2σ and 1–4σ, respectively. The eastern and western emission peaks are south of the AGN, and do not correspond to any galaxy detected on the HST or *Spitzer* images. North is up and east is to the left. The beam scale is shown on the bottom left.

where $M_{\rm gas}$ is the molecular gas mass, $\alpha_{\rm CO}$ is the CO-to-H$_2$ conversion factor (e.g., see review by Bolatto et al. 2013), r_{21} is the $L'_{\rm CO(2-1)}/L'_{\rm CO(1-0)}$ luminosity ratio, and $L'_{\rm CO(2-1)}$ and $L'_{\rm CO(1-0)}$ are the luminosities of the CO(2–1) and CO(1–0) emission lines, respectively.

We assume thermalized, optically thick CO emission for which the CO luminosities are independent of the rotational transitions, thus, $L'_{\rm CO(2-1)} = L'_{\rm CO(1-0)} \equiv L'_{\rm CO}$ and $r_{21} = 1$ (Solomon & Vanden Bout 2005). This is a standard value used for the local galaxy M82 (Weiß et al. 2005) and for color-selected star-forming galaxies (CSGs, Dannerbauer et al. 2009). However other works use different values of r_{21}, such as $r_{21} = 0.5$ for the Milky Way (Weiß et al. 2005). The reader should take into account these differences when comparing with other works in the literature (e.g., Casasola et al. 2013; Noble et al. 2017; Rudnick et al. 2017; Hayashi et al. 2018; Coogan et al. 2018; Castignani et al. 2018).

The CO-to-H$_2$ conversion factor $\alpha_{\rm CO}$ is a large uncertainty in this calculation. Its value is not universal and depends on galaxy type, metallicity, and CO gas excitation temperature and density (Bolatto et al. 2013; Carilli & Walter 2013; Combes 2018). For different kinds of galaxies and environments, its average range of values is $0.8 < \alpha_{\rm CO} < 4.36$ $M_\odot$ (K km s^{-1}pc^2)$^{-1}$ (Bolatto et al. 2013). Since neither the eastern nor the western emission peaks are associated with galaxies detected in our optical and near-infrared images, they might be associated with extended emission around the AGN. In that case, we expect that the molecular gas might be more excited and have more chaotic motions, and this might lead to an expected value of $r_{21} > 1$, and to $\alpha_{\rm CO} < 4.36$ $M_\odot$ (K km s^{-1} pc^2)$^{-1}$ (Bolatto et al. 2013; Carilli & Walter 2013; Cicone et al. 2018). For these reasons, we use the lower end of standard $\alpha_{\rm CO}$ values, and this will give us lower limits to the molecular gas mass. When using $\alpha_{\rm CO} = 0.8$ $M_\odot$ (K km s^{-1} pc^2)$^{-1}$, we obtain $M_{\rm gas}^{\rm eastern} = 1.9 \pm 0.3 \times 10^{10} M_\odot$ and $M_{\rm gas}^{\rm western} = 2.0 \pm 0.3 \times 10^{10} M_\odot$, for the eastern and western peak components, respectively. When using the Galactic conversion factor $\alpha_{\rm CO} = 4.36$ $M_\odot$ (K km s^{-1}pc^2)$^{-1}$, the molecular gas masses are approximately five times larger. Summing the two components, the total molecular gas mass is $M_{\rm gas}^{\rm tot} = 3.9 \pm 0.4 \times 10^{10}$ $M_\odot$ ($S/N \sim 8$), and this mass is not spatially associated with galaxies detected in our optical or near-infrared images. Table 2 shows the integrated flux measurements, the CO luminosity, and the molecular gas mass.

3.3. Molecular gas content and star formation in cluster core members

We present the star formation properties of spectroscopically confirmed cluster members that are in the region covered by the NOEMA observations. We measure the upper limits on the molecular gas content of the confirmed cluster members and their star formation rates. We derive the galaxy gas fraction, and specific star formation rate (sSFR), and gas depletion time and star formation efficiency (SFE) upper limits.

Table 2. Integrated flux measurements, the CO luminosity, and the gas mass from the integrated CO(2–1) line emission.

Peak	$S_{\rm CO}\Delta v$ (Jy km s^{-1})	$L'_{\rm CO}$ (10^{10} Kpc^{2}km s^{-1})	$M_{\rm gas}$ ($10^{10} M_\odot$)
Eastern	0.88 ± 0.14	2.4 ± 0.4	1.9 ± 0.3
Western	0.90 ± 0.14	2.4 ± 0.4	2.0 ± 0.3

Notes. Since we used the lower end of standard $\alpha_{\rm CO}$ values, we show lower limits to the molecular gas.

3.3.1. Upper limits on the molecular gas content of the confirmed cluster members

Besides the AGN, there are seven other spectroscopically confirmed CARLA J1103 + 3449 cluster members (Noirot et al. 2018), of which six are within the NOEMA beam, and three have stellar mass estimates (Fig. 2). Our NOEMA observations do not show CO(2–1) emission with $S/N > 3$ at the positions of the spectroscopically confirmed members. However, we can use the 3σ values of the flux rms noise level around the position of each confirmed cluster member to derive an upper limit on the velocity integrated flux $S_{\rm CO(2-1)}\Delta v = (3\sigma_{\rm rms})\Delta v$. As Δv, we used an average $\Delta v = 300\,{\rm km\,s^{-1}}$, following Saintonge et al. (2017). Since the velocity resolution of our CO(2–1) map has an uncertainty of $\sigma_{\Delta \rm v} = 100\,{\rm km\,s^{-1}}$, the velocity range within $300 \pm 3\sigma_{\Delta \rm v}$ km s^{-1} includes most of the published Δv for star-forming cluster galaxies at these redshifts (e.g., Noble et al. 2017; Lee et al. 2017; Castignani et al. 2018; Hayashi et al. 2018). For the molecular gas measurement, we use the Galactic conversion factor $\alpha_{\rm CO} = 4.36\,M_\odot$ (K km s^{-1}pc^2)$^{-1}$, as typical for normal galaxies (Bolatto et al. 2013; Carilli & Walter 2013; Combes 2018). The estimated physical properties of the spectroscopically confirmed members are given in Table 3.

3.3.2. Star formation rates

We calculate galaxy star formation rates using the Hα emission line flux from Noirot et al. (2018). We then combine them with our measurements of the molecular gas mass from the CO(2–1) line emission, and the galaxy stellar masses from Mei et al. (in prep.), in order to estimate the galaxy gas fraction, and sSFR, and depletion time and SFE upper limits.

Galaxy stellar masses and gas fractions. Mei et al. (in prep.) describe the details of our stellar mass measurements. We measure our CARLA galaxy stellar masses by calibrating our PSF-matched *Spitzer* IRAC1 magnitudes (Amodeo et al., in prep.) with galaxy stellar masses from Santini et al. (2015) derived from the Guo et al. (2013) multiwavelength catalog in the Cosmic Assembly Near-infrared Deep Extragalactic Legacy Survey (CANDELS; PI: S. Faber, H. Ferguson; Koekemoer et al. 2011; Grogin et al. 2011) WIDE GOODS-S field.

The *Spitzer* IRAC1 magnitudes correspond to the rest-frame near infrared in the redshift range of the CARLA sample, and we expect them not to be biased by extinction. We find a very good correlation between these magnitudes and the Santini et al. (2015) mass measurements, with scatters of ~0.12 dex at the redshift of the cluster studied in this paper. Adding in quadrature the scatter of the relation and uncertainties from Santini et al. (2015), we obtain mass uncertainties in the range ~0.4–0.5 dex, and ~0.2–0.3 dex for masses larger than $\log_{10}\left(\frac{M}{M_\odot}\right) > 10.5$.

Table 3 shows the stellar masses of the spectroscopically confirmed cluster members. The masses derived from this calibration are on average ~0.5 dex smaller to those derived from stellar population models by Noirot et al. (2018), and the difference is larger at fainter magnitudes. This difference in mass estimates does not significantly change results from Noirot et al. (2018), in particular the conclusions from the SFR versus stellar mass analysis (Fig. 7 in Noirot et al. 2018). From our molecular gas mass upper limits, combined with our stellar masses, we compute the gas-to-stellar mass ratio as $M_{\rm gas}/M_*$ and the molecular gas fraction as $f_{\rm gas} = M_{\rm gas}/(M_{\rm gas} + M_*)$. The results are shown in Table 3.

Star formation rates, specific star formation rates, depletion times and star formation efficiencies. We re-compute SFR$_{\rm H\alpha}$, using the Hα line fluxes from Noirot et al. (2018) and our stellar masses from Mei et al. (in prep.). The Kennicut law (Kennicutt 1998) shows a direct proportionality between SFR and Hα flux,

$$\mathrm{SFR}_{\rm H\alpha}[M_\odot {\rm yr}^{-1}] = 5 \times 10^{-42} L_{\rm H\alpha} \times 10^{0.4 \times A_{\rm H\alpha}}, \tag{3}$$

where SFR$_{\rm H\alpha}$ is the estimated SFR corrected for the contribution from the [NII] line and $A_{\rm H\alpha}$ is the dust attenuation.

We estimate $A_{\rm H\alpha}$ using the Garn & Best (2010) empirical law (which used the Calzetti et al. 2000 extinction law),

$$A_{\rm H\alpha} = 0.91 + 0.77M + 0.11M^2 - 0.09M^3, \tag{4}$$

where $M = \log_{10}\frac{M_*}{10^{10}M_\odot}$ and M_* is the stellar mass.
The symbol $L_{\rm H\alpha}$ represents the Hα luminosity in erg s^{-1}, and it is calculated from $F_{\rm H\alpha}$, the Hα flux given in erg cm^{-2} s^{-1}, which is computed as

$$F_{\rm H\alpha} = F_{\rm H\alpha+[NII]\lambda6548,6584}\frac{1}{1+\frac{F_{\rm [NII]\lambda6548,6584}}{F_{\rm H\alpha}}}, \tag{5}$$

where $F_{\rm H\alpha+[NII]\lambda6548,6584}$ is the total observed Hα flux plus the [NII]λ6548, 6584 flux. In fact, the WFC3/G141 grism resolution does not permit us to deblend the three lines (Noirot et al. 2018). To measure $\frac{F_{\rm [NII]\lambda6548,6584}}{F_{\rm H\alpha}}$, we use the relation between this ratio and metallicity, and the fundamental relation between stellar mass, SFR, and metallicity. Following Curti et al. (2020) (Eqs. (2) and (5) and Table 6), we calculate the metallicity 12 + log(O/H), expressed as a function of stellar mass and SFR:

$$12 + \log({\rm O/H}) = {\rm Z}_0 - \gamma/\beta \times \log\left[1 + \left(\frac{M_*}{M_0({\rm SFR})}\right)^{-\beta}\right], \tag{6}$$

where $Z_0 = 8.779 \pm 0.005$, $\log(M_0({\rm SFR})) = m_0 + m_1 \times \log({\rm SFR})$, $m_0 = 10.11 \pm 0.03$, $m_1 = 0.56 \pm 0.01$, $\gamma = 0.31 \pm 0.01$, and $\beta = 2.1 \pm 0.4$.

Curti et al. (2020) also provide a new calibration for the relation between metallicity and $\frac{F_{\rm [NII]\lambda6584}}{F_{\rm H\alpha}}$:

$$\log\left(\frac{F_{\rm [NII]\lambda6584}}{F_{\rm H\alpha}}\right) = \sum_{n=1}^{4} c_n x^n, \tag{7}$$

where $x = 12 + \log({\rm O/H}) - 8.69$, $c_0 = -0.489$, $c_1 = 1.513$, $c_2 = -2.554$, $c_3 = -5.293$, and $c_4 = -2.867$. Assuming a constant ratio $F_{\rm [NII]\lambda6584}$:$F_{\rm [NII]\lambda6548}$ of 3:1 (Osterbrock & Ferland 2006), we derive $\frac{F_{\rm [NII]\lambda6548,6584}}{F_{\rm H\alpha}}$.

Table 3. Velocity integrated CO(2–1) flux, luminosity, molecular gas mass, stellar mass, molecular gas-to-stellar mass ratio, and molecular gas fraction for the CARLA J1103 + 3449 cluster confirmed members.

id	$S_{\rm CO}\Delta v$ (Jy km s^{-1})	$L_{\rm CO}$ (10^9 Kpc^{2}km s^{-1})	$M_{\rm gas}$ ($10^{10} M_\odot$)	M_* ($10^{10} M_\odot$)	$M_{\rm gas}/M_*$	$f_{\rm gas}$ (%)
AGN/491	<0.3	<7	<3	5 ± 2	<0.6	<40
490	<0.3	<7	<3	...	...	...
320	<0.4	<10	<4	0.7 ± 0.7	<6	<85
283	<0.5	<12	<5	...	...	...
279	<0.5	<12	<5	...	...	...
199	<0.6	<17	<7	4 ± 2	<2	<66
183	<0.6	<17	<7	0.3 ± 0.3	<23	<96

Notes. The identification numbers in the column "id" are the same as in the catalog published by Noirot et al. (2018). The other columns show the velocity integrated CO(2–1) flux, luminosity, molecular gas mass, stellar mass, molecular gas-to-stellar mass ratio, and molecular gas fraction of the CARLA J1103 + 3449 spectroscopically confirmed cluster members in the cluster core. The spectroscopically confirmed members were not detected with NOEMA and we report their $3\sigma_{\rm rms}$ upper limits.

Table 4. CARLA J1103 + 3449 cluster confirmed member $\rm SFR^{N18}_{H\alpha}$, attenuation, metallicity, SFR, sSFR, depletion time, and SFE.

id	$\rm SFR^{N18}_{H\alpha}$ ($M_\odot$ yr^{-1})	$A_{\rm H\alpha}$	12 + log(O/H)	$\rm SFR_{H\alpha}$ ($M_\odot$ yr^{-1})	sSFR (Gyr^{-1})	$\tau_{\rm dep}$ (Gyr)	SFE (Gyr^{-1})
AGN/491 100%	<140	1.4	8.6	140 ± 50	3 ± 2	<0.2	>5
AGN/491 80%	...	1.4	8.6	110 ± 40	2 ± 1	<0.3	>4
AGN/491 60%	...	1.4	8.6	80 ± 30	2 ± 1	<0.4	>3
AGN/491 40%	...	1.5	8.6	50 ± 20	1.1 ± 0.7	<0.6	>2
AGN/491 20%	...	1.5	8.7	30 ± 8	0.5 ± 0.3	<1	>0.8
490$^{(+)}$	25 ± 5	...	...	...	...	<1	> 0.8
320	10 ± 5	0.8	8.6	6 ± 3	1 ± 1	<7	>0.1
283$^{(+)}$	16 ± 7	...	...	...	...	<3	>0.3
279$^{(+)}$	11 ± 6	...	... .	...	...	<5	>0.2
199	11 ± 4	1.4	8.7	9 ± 4	0.2 ± 0.1	<8	>0.1
183	13 ± 5	0.5	8.4	6 ± 4	2 ± 3	<12	>0.1
93	10 ± 2	...	...	...	...	...	...

Notes. The identification numbers in the column "id" are the same as in the catalog published by Noirot et al. (2018). The column $\rm SFR^{N18}_{H\alpha}$ shows the SFR calculated in Noirot et al. (2018). The other columns show our measurements of attenuation, metallicity, SFR, sSFR, depletion time, and SFE for the confirmed members of the CARLA J1103 + 3449 cluster. In the case of the AGN (id 491), since we cannot separate the AGN and stellar contributions, we vary the stellar contribution to the total Hα+[NII] emission flux in the range 20−100%. The plus symbol (+) shows the cluster members for which we use the values of SFR reported in Noirot et al. (2018) to estimate depletion time and SFE.

Since to calculate SFR in Eq. (3) we need to know $\frac{F_{[\rm NII]\lambda6548,6584}}{F_{\rm H\alpha}}$, and to measure $\frac{F_{[\rm NII]\lambda6548,6584}}{F_{\rm H\alpha}}$ in Eq. (7) we need to know the SFR, we follow Zeimann et al. (2013) and start with an initial value of $\frac{F_{[\rm NII]\lambda6548,6584}}{F_{\rm H\alpha}} = 0.2$ and iterate Eqs. (3)–(7) until convergence.

Our results are shown in Table 4. For the AGN, we cannot separate the stellar contribution to the Hα+[NII] line emission from the AGN contribution (Tadhunter 2016). Since we know that the hosts of powerful AGNs present young stellar populations (e.g., Heckman & Kauffmann 2006), we consider that the stellar contribution to the total Hα+[NII] emission varies in the range of 20–100%. In Table 4, we compare our SFR measurements with those from Noirot et al. (2018), and we are consistent within 1.5–2σ. For some cluster galaxies we could not measure stellar masses, because they are not detected in the IRAC images, and we cannot re-compute the SFR. Hereafter, we will use our SFR measurements when we could derive them, and Noirot et al. (2018) SFR measurements for the other galaxies. Combining our measured SFR with the stellar masses from Mei et al. (in prep.), we compute the specific star formation rate $\rm sSFR = \frac{SFR_{H\alpha}}{M_*}$, the depletion time $\tau_{\rm dep} = \frac{M_{\rm gas}}{\rm SFR_{H\alpha}}$, and the star formation efficiency $\rm SFE = \frac{SFR_{H\alpha}}{M_{gas}}$. Our results are shown in Table 4.

4. Discussion

In this section, we discuss our results. We focus on understanding the origin of the molecular gas in the cluster central region and on the physical properties and scaling relations of the confirmed cluster members.

4.1. *Origin of the molecular gas in the cluster core*

In the core of the cluster, we observe two CO(2–1) emission peaks that correspond to a region spatially offset from the center of the AGN continuum emission and that does not correspond to any galaxy detected in our HST or *Spitzer* images. Radio observations of the CARLA J1103 + 3449 cluster from the work of Best et al. (1999) reveal two radio lobes, which are roughly in the same directions (east and west) as our CO(2–1) molecular gas

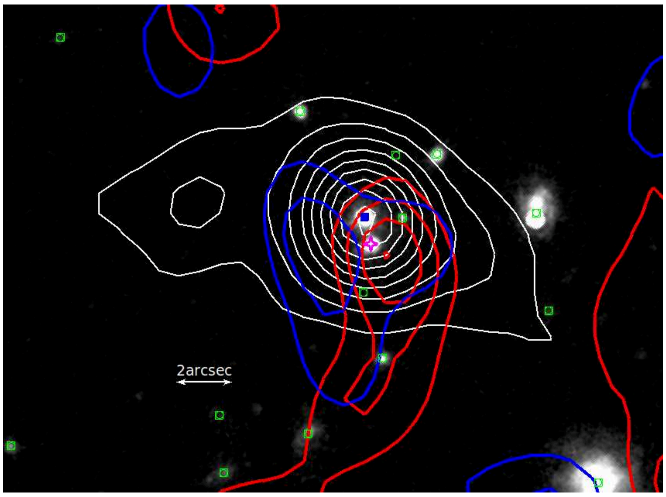

Fig. 8. HST/WFC3 F140W image of the central region of the cluster, with the contours of CO(2–1) emission of the eastern (1–2σ) and western (1–4σ) emission peaks (shown as blue and red contours, respectively), and the continuum emission at 94.5 GHz (white contours; 3–24σ). The central blue square and the pink star with four spikes show the position of the AGN and of the star, respectively. The green squares are the positions of IRAC color-selected galaxies in the cluster's central region. North is up and east is to the left.

components and our data extended continuum emission (Figs. 4, 7, and 8). The two radio lobes are asymmetrical, the western being more compact, while the eastern is more diffuse. The asymmetry of their widths may be due to their expansion in an ICM (intracluster medium) with a density gradient, in which the more diffuse lobe, the western lobe, would be expanding in a less dense environment (e.g., Seymour et al. 2020). Both CO(2–1) emission peaks are blueshifted compared to the NOEMA observation central velocity of 0 km s^{-1} (which corresponds to the cluster redshift of z = 1.44) and to the AGN redshift, and their spatial position is close to, but south of the AGN and the radio lobes.

4.1.1. Undetected galaxies

To exclude the hypothesis that the two CO(2–1) line emission components might originate from two or more galaxies that are not detected at the detection limit of our optical or near infrared images, we measure their hypothetical properties by making reasonable assumptions. Since our HST/WFC3 F140W images have a depth similar to the CANDELS WIDE survey, we use the CANDELS/WIDE survey mass limit $M_* = 5 \times 10^9\ M_\odot$ (Grogin et al. 2011; similar to our *Spitzer* mass limit) as an upper limit to the stellar mass of each of these two hypothetical galaxies.

Assuming the 3σ Hα emission line flux limit of $F_{\mathrm{H}\alpha} = 2.1 \times 10^{-17}$ erg cm^{-2} s^{-1} for the HST/WFC3 G141 grism spectra (Momcheva et al. 2016; Noirot et al. 2018) as an upper limit of the undetected Hα flux, and using the upper limit of the stellar mass, we estimate an upper limit to the SFR of the two emission peak components as $\mathrm{SFR}_{\mathrm{H}\alpha} < 2\ M_\odot$ yr^{-1}, using the same system of equations in Sect. 3.3.2 and the cluster redshift[2]. We then estimate lower limits to the molecular gas-to-stellar mass ratios and gas fractions that correspond to the eastern and western peak emission. We obtain molecular gas masses of $M_{\mathrm{gas}}^{\mathrm{blue}} = 10 \pm 3 \times 10^{10}\ M_\odot$, and $M_{\mathrm{gas}}^{\mathrm{red}} = 11 \pm 3 \times 10^{10}\ M_\odot$. We use the Galactic conversion factor because it is very improbable that these hypothetical galaxies are star-burst galaxies since they are not detected in our HST/WFC3 G141 grism observations. They could be only if the attenuation has an anomalously high values, of $A_{\mathrm{H}\alpha} > 5$. Those gas masses lead to estimated gas fraction lower limits of $f_{\mathrm{gas}} \gtrsim 95\%$, and a lower limit on the depletion times of $\tau_{\mathrm{dep}} \gtrsim 55$ Gyr. This is much longer than the depletion times observed for standard star-forming galaxies up to $z \sim 4$, which are closer to ~1–3 Gyr (e.g., Tacconi et al. 2013, 2018). The probability that the line that we are observing is not CO(2–1) is very small, given that it is very close to the CO(2–1) emission expected at the cluster redshift.

Some massive galaxies at $z > 2$ can be detected in millimeter wavelengths but not in the HST optical and near-infrared bands (e.g., Franco et al. 2018). However, these galaxies are rare (0.1 galaxy arcmin^{-2}), massive, and usually detected with *Spitzer*/IRAC. Given the number densities of high redshift galaxies (e.g., Davidzon et al. 2018; Franco et al. 2018), having two galaxies of this kind so spatially close is possible but very improbable. These results mean that these two hypothetical galaxies would be unusually gas rich, with low SFR (or anomalously high attenuation), high gas fractions, and very long depletion times, independent of the conversion factor that we use. It is then very unlikely that our signal is due to undetected galaxies.

4.1.2. Extended emission

Excluding the hypothesis that the two CO(2–1) emission lines are due to undetected galaxies, they might trace molecular gas originating from an extended disk or torus, or emission components of molecular gas outflows or inflows associated with the AGN and its two radio jet lobes. We find no evidence to support the hypothesis of CO emission from an extended (up to tens of kiloparsecs) rotating disk or torus of molecular gas around the AGN. In fact, the CO(2–1) eastern and western peak emissions are not spatially located at the AGN position, they are located southeast and southwest of the AGN and the radio jets. The total molecular gas mass in the southern structures around the AGN is ≳60% of the total molecular gas, from $M_{\mathrm{gas}}^{\mathrm{tot}} = 3.9 \pm 0.4 \times 10^{10}\ M_\odot$, and the upper limit on the AGN molecular gas mass (<$3 \times 10^{10}\ M_\odot$; Sect. 3.2; Table 3).

In the local Universe, both disk-dominated and filament-dominated central cluster galaxies have been observed with the Atacama Large Millimeter/submillimeter Array (ALMA; Russell et al. 2019; Olivares et al. 2019). In the first type, most of the molecular gas is concentrated in a disk around the central galaxy, while in the second type the molecular gas is mostly (>70%) in filaments around the central galaxy (the most known example being the Perseus cluster; Salomé et al. 2006). The filaments typically extend from a few kiloparsecs in length up to 10–20 kpc, and the molecular gas emission is offset with respect to the central AGN by projected distances of a few kiloparsecs. For the central galaxy of the cluster A1795, some molecular gas clumps are associated with the lobes of the radio jets. In filament-dominated galaxies, the filaments trace radio bubbles, and are associated with both gas outflow and inflow.

The molecular gas that we detect south of our central AGN also dominates the cluster central molecular gas reservoir and our observations are consistent with the filament-dominated

---

[2] We assume that these hypothetical galaxies are at the cluster redshift because it would be very improbable to have two galaxies at another redshift so close to the cluster center and with spectral peaks so close to the cluster redshift.

local central galaxies. This suggests that the eastern and western emission peaks can be associated with gas outflow and inflow from the AGN. In fact, the AGN jets can drive a large amount of molecular gas, but this is not always expelled from the galaxy surroundings (e.g., Costa et al. 2015; Prasad et al. 2015), and can be re-accreted. As a consequence, the signal that we observe can be due to both inflows and outflows. When the amount of molecular gas outside the host galaxy is comparable to or higher than the host galaxy molecular gas reservoir, this also suggests that the gas has been cooled (e.g., Klamer et al. 2004; Nesvadba et al. 2009; Emonts et al. 2014; Russell et al. 2019). For the CARLA J1103 + 3449 cluster, we expect a reservoir of hot ICM that surrounds the host AGN, with accretion at the center of the cluster potential well. The detection of cool molecular gas around a central cluster AGN can indicate cooling due to the interaction of the ICM and AGN jets or can be due to condensation of low entropy hot gas uplifted by the AGN jet away from the host galaxy (Salomé et al. 2006; Lim et al. 2008; Gaspari et al. 2012; McNamara et al. 2014; Russell et al. 2014; Emonts et al. 2014; Li et al. 2015; Prasad et al. 2015; Gaspari & Sądowski 2017; Voit et al. 2017; Tremblay et al. 2018; Olivares et al. 2019). With our observations, we cannot distinguish between these two scenarios.

4.2. Confirmed cluster member physical properties and scaling relations

In this section, we compare the physical properties of our measured cluster confirmed members to both cluster and field galaxies at similar redshifts ($1 < z < 2.6$). Our CO(2–1) luminosity, estimated upper limits to the velocity integrated CO(2–1) flux, and depletion times are similar to the literature for other cluster galaxies, AGN, and spiral galaxies at $1 < z < 2.5$ (Wagg et al. 2012; Casasola et al. 2013; Emonts et al. 2014; Rudnick et al. 2017; Noble et al. 2017; Castignani et al. 2018, 2020; Hayashi et al. 2018), and galaxies in the field in the same redshift range (Tacconi et al. 2013). To compare our molecular gas upper limits to the literature, we have to take into account that we assume $L'_{\rm CO(2-1)}/L'_{\rm CO(1-0)} = 1$ (Sect. 3; Solomon & Vanden Bout 2005), and in several works a lower ratio of ∼20−50% is assumed. For example, Noble et al. (2017) use a ratio of $L'_{\rm CO(2-1)}/L'_{\rm CO(1-0)} = 0.77$, Hayashi et al. (2018) use $L'_{\rm CO(2-1)}/L'_{\rm CO(1-0)} \sim 0.83$, and Tacconi et al. (2013) assume $L'_{\rm CO(3-2)}/L'_{\rm CO(1-0)} \sim 0.5$. In Figs. 9–11, we show the original published values, without scaling. In fact, our results do not significantly change when using other values of $L'_{\rm CO(2-1)}/L'_{\rm CO(1-0)}$. We also know that stellar mass estimations can differ by up to a factor of ∼1.5−6 (∼0.1−0.8 dex) when using different techniques or different stellar population models (van der Wel et al. 2006; Lee et al. 2009; Maraston et al. 2010; Raichoor et al. 2011; Pforr et al. 2012; Sorba & Sawicki 2018).

In Fig. 9, we compare our molecular gas mass versus stellar mass relation to other works. Our upper limits agree with the field molecular gas mass-to-stellar mass ratio from the Plateau de Bure high-z Blue Sequence Survey (PHIBBS) survey (Tacconi et al. 2013). This result also holds when considering the uncertainties in the $L'_{\rm CO(2-1)}/L'_{\rm CO(1-0)}$ conversion, conversion factor $\alpha_{\rm CO}$, and stellar masses. Our galaxies show upper limits that are higher than the molecular gas mass-to-stellar mass ratio in some of the other clusters. However, since they are only upper limits, we cannot make conclusions on environmental effects, apart from the fact that our cluster galaxies do not show evidence for larger gas reservoirs than field galaxies with similar stellar masses.

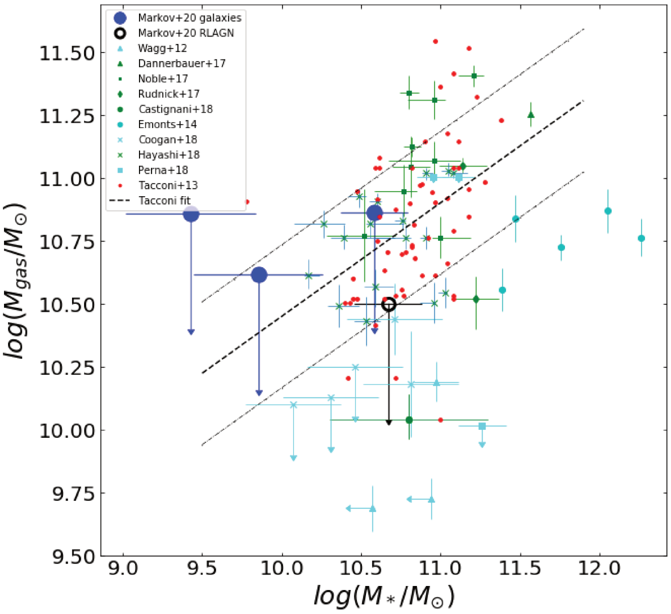

Fig. 9. Molecular gas mass vs. stellar mass relation for the AGN (empty black circles) and for other CARLA J1103 + 3449 spectroscopically confirmed cluster members (blue filled circles) compared to other cluster (green and cyan) and field galaxies (red) from the literature. The arrows show lower and upper limits. Green markers are the results for cluster galaxies for which gas masses were estimated using the Galactic conversion factor. Cyan markers are estimations with different values of the conversion factor. Dashed and dashed-dotted lines represent the Tacconi et al. (2013) relation for field star-forming galaxies and its 1σ scatter.

In Figs. 10 and 11, we show SFR as a function of stellar and molecular gas mass, respectively. Figure 10 only shows results for galaxies for which we can measure the stellar mass. Compared to field galaxies, the SFR of the AGN host is within ∼1−1.5σ of the MS from Tacconi et al. (2013), and the SFR of the other spectroscopically confirmed cluster members is ∼2σ lower than the MS (Fig. 10), consistent with results from Noirot et al. (2018), which concluded that star-forming galaxies with stellar mass $>10^{10}\,M_{\odot}$ in the CARLA HST cluster sample have lower SFR than field galaxies with similar masses at the same redshifts. In Fig. 11, the AGN SFR (for all the Hα stellar emission percentages considered in this paper) is also within ∼1σ of field galaxies with gas masses similar to its molecular gas mass upper limit. This shows that its SFR is typical of galaxies in the field with the same molecular gas reservoir.

The AGN SFR is comparable to the main sequence of star-forming field galaxies, and its star formation has not yet been quenched. This is consistent with the large molecular gas reservoir in the center of the cluster. As a massive early-type central cluster galaxy, the AGN is predicted to have gone through at least one major merger, which might have triggered a starburst phase (Hopkins et al. 2006b, 2008; Snyder et al. 2011; Yesuf et al. 2014), which we do not observe as on-going in our data. During this phase, the galaxy is predicted to lie above the MS in the SFR−M_* and SFR−$M_{\rm gas}$ diagrams (Figs. 10 and 11), and the galaxy molecular gas is converted into stars. Afterwards, the remaining molecular gas content is expected to be consumed by the combination of star formation and feedback (Snyder et al. 2011; Yesuf et al. 2014). Our AGN is observed on the star-forming galaxy MS (with a SFR of ∼30–140 $M_{\odot}\,{\rm yr}^{-1}$), and we

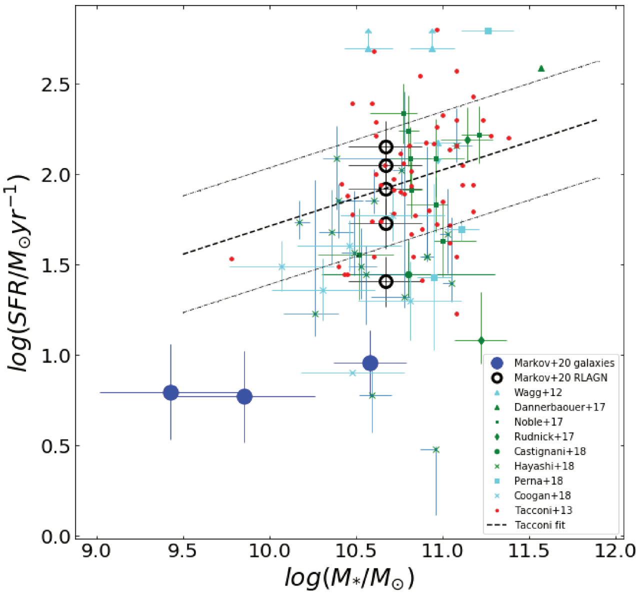

Fig. 10. Star formation rate as a function of stellar mass. Symbols are the same as in Fig. 9. The AGN SFR is shown with different contributions of the Hα+[NII] stellar emission to the total flux. We compare our results with those from other works. The dashed and the dashed-dotted lines represent the best fit with 1σ scatter for the MS of field galaxies from Tacconi et al. (2013).

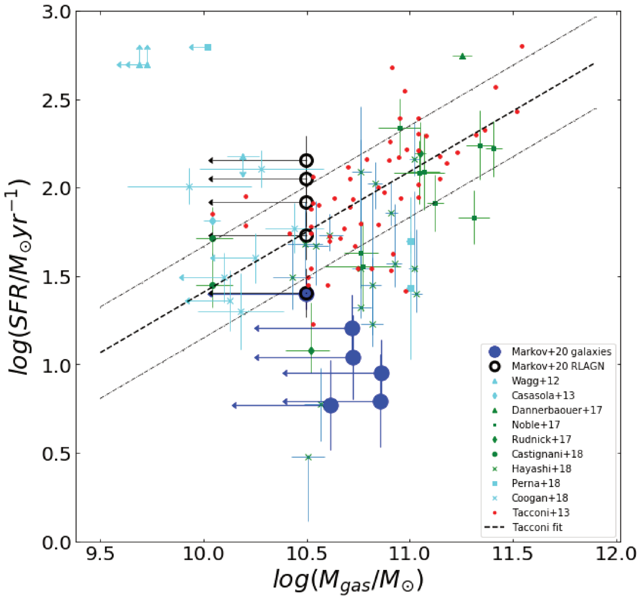

Fig. 11. Star formation rate as a function of gas mass. Symbols are the same as in Fig. 9. The arrows show upper limits. Dashed and dashed-dotted lines represent the Tacconi et al. (2013) relation for field star-forming galaxies and its 1σ scatter.

expect that it will evolve toward quenching when the molecular gas reservoir is depleted, becoming a passive ETG similar to those observed in lower redshift cluster centers (Norton et al. 2001; Hopkins et al. 2008; Snyder et al. 2011; Yesuf et al. 2014).

5. Summary

We report on observations of the central region of the galaxy cluster CARLA J1103 + 3449 at $z = 1.44$ with NOEMA, and measure the molecular gas content in the center of the cluster. We also obtain SFR, sSFR, molecular gas mass, and SFE, and gas depletion time upper limits for the spectroscopically confirmed cluster members.

Our main results are:

- At the rest frequency of $\nu_{\rm rest} = 230.5$ GHz, the dominant source of our NOEMA extended continuum emission is the non-thermal synchrotron radio emission from the AGN. We measured its flux at the AGN position and at the position of two radio jets. The central AGN in CARLA J1103 + 3449 has been already observed at 4.71 and 8.21 GHz by Best et al. (1999), who found two asymmetrical radio lobes, one oriented toward the east and the other toward the west. We measured the continuum within a region the size of the NOEMA beam centered on the AGN and the two lobes, and obtained $S^{\rm AGN}_{\rm cont} = 4.6 \pm 0.2$ mJy, $S^{\rm east\_lobe}_{\rm cont} = 1.1 \pm 0.2$ mJy, and $S^{\rm west\_lobe}_{\rm cont} = 0.8 \pm 0.2$ mJy. Combining our measurements with published results over the range 4.71–94.5 GHz, and assuming $S_{\rm synch} \propto \nu^{-\alpha}$, we obtained a flat spectral index $\alpha = 0.14 \pm 0.03$ for the AGN core emission, and a steeper index $\alpha = 1.43 \pm 0.04$ and $\alpha = 1.15 \pm 0.04$ at positions close to the western and eastern lobe, respectively, which is consistent with optically thicker synchrotron emission. The total spectral index is $\alpha = 0.92 \pm 0.02$ over the range 73.8 MHz–94.5 GHz.
- We detected two CO(2–1) emission line peaks with $S/N \sim 6$, blueshifted with respect to the AGN redshift. One of the two detected emission peaks is situated at a projected distance of ~17 kpc southeast of the AGN, and the second one is ~14 kpc southwest of the AGN. These regions are roughly aligned with the radio jets (east-west), and south of them. These two emissions do not correspond to the position of any galaxy that we detect in our optical or near-infrared images, and it is very unlikely that they are due to undetected galaxies (see Sect. 4).
- We found a massive reservoir of cool molecular gas in the center of the cluster, distributed south of the AGN. From the CO(2–1) total velocity integrated flux, the total cluster core molecular gas mass is $M^{\rm tot}_{\rm gas} = 3.9 \pm 0.4 \times 10^{10}\,M_{\odot}$. The two CO(2–1) emission line peaks correspond to molecular gas masses of $M_{\rm gas} = 1.9 \pm 0.3 \times 10^{10}\,M_{\odot}$ for the eastern component, and of $M_{\rm gas} = 2.0 \pm 0.3 \times 10^{10}\,M_{\odot}$ for the western component. Considering the upper limit of $3 \times 10^{10}\,M_{\odot}$ on the AGN molecular mass (see below), the southern emission molecular gas mass is $\gtrsim 60\%$ of the cluster total central molecular mass reservoir. Our observations can be explained by gas inflows and outflows, either due to cluster gas accretion or, most probably, driven by the jets, as is observed in filament-dominated central galaxies in the local Universe. The gas might be cooled by the interaction of the ICM and AGN jets or could be due to condensation of low entropy hot gas uplifted by the AGN jet away from the host galaxy.
- The central AGN host is an ETG with a SFR of $\sim 30-140\ M_{\odot}\,{\rm yr}^{-1}$, depending on the assumed percentage of AGN contribution to its Hα+[NII] flux (20–100%). The upper limit on its gas reservoir is of $M_{\rm gas} < 3 \times 10^{10}\,M_{\odot}$. This means that the AGN molecular gas reservoir amounts to $\lesssim 40\%$ of the total molecular gas reservoir in the center of the cluster. The AGN host SFR lies on the MS of star-forming galaxies at a similar redshift, and it has not yet been quenched. We expect that its star formation will be also fed by the larger southern molecular gas reservoir.
- We measured SFR and sSFR, and estimated upper limits on the molecular gas masses, gas fractions, SFE, and depletion

times for the other spectroscopically confirmed cluster members. Our spectroscopically confirmed cluster member SFR is at ∼2σ below the field star-forming MS (Fig. 10), consistent with results from Noirot et al. (2018), who concluded that star-forming galaxies with stellar mass $>10^{10}\,M_{\odot}$ in the CARLA HST cluster sample have a lower SFR than field galaxies at a similar redshift, and of similar stellar mass. We find that the molecular gas mass upper limits are in the range of average values for field galaxies at similar redshifts and of similar stellar mass, and we cannot make conclusions on environmental effects apart from the fact that our cluster galaxies do not show evidence for larger gas reservoir than field galaxies with similar stellar mass.

Acknowledgments. We thank the PI: of the Keck observations, Fiona Harrison, for providing these observations and Thomas Connor for assisting with the Keck observing. We thank Philip Best and Katherine Inskip for useful discussion and their kind sharing of their radio, optical and infrared observations of the central radio sources and lobes. The data reduction and mapping and most of data analysis was done by using IRAM/GILDAS free software (`http://www.iram.fr/IRAMFR/GILDAS/`), and with the assistance of the IRAM support astronomers in Grenoble, Cynthya Herrera and Melanie Krips, which we warmly thank. We would like to thank the GILDAS support team for their help and guidance for the data analysis, Sébastien Bardeau and Vincent Pietu. V.M. would like to thank Anelise Audibert, Benoit Tabone, Valeria Olivares and Gianluca Castignani for their help with the data mapping and analysis. The work of D.S. was carried out at the Jet Propulsion Laboratory, California Institute of Technology, under a contract with NASA. This work was supported by the CNES.

References

Abadi, M. G., Moore, B., & Bower, R. G. 1999, MNRAS, 308, 947
Abdo, A. A., Ackermann, M., Ajello, M., et al. 2010, ApJ, 710, 133
Alberts, S., Pope, A., Brodwin, M., et al. 2016, ApJ, 825, 72
Aloy, M.-A., Gómez, J.-L., Ibáñez, J.-M., Martí, J.-M., & Müller, E. 2000, ApJ, 528, L85
Athreya, R. M., Kapahi, V. K., McCarthy, P. J., & van Breugel, W. 1997, MNRAS, 289, 525
Baldry, I. K., Balogh, M. L., Bower, R. G., et al. 2006, MNRAS, 373, 469
Balogh, M. L., & Morris, S. L. 2000, MNRAS, 318, 703
Balogh, M. L., Schade, D., Morris, S. L., et al. 1998, ApJ, 504, L75
Balogh, M., Eke, V., Miller, C., et al. 2004, MNRAS, 348, 1355
Bassett, R., Papovich, C., Lotz, J. M., et al. 2013, ApJ, 770, 58
Becker, R. H., White, R. L., & Edwards, A. L. 1991, ApJS, 75, 1
Bertin, E., & Arnouts, S. 1996, A&AS, 117, 393
Best, P. N., Eales, S. A., Longair, M. S., Rawlings, S., & Rottgering, H. J. A. 1999, MNRAS, 303, 616
Binney, J., & Tremaine, S. 1987, Galactic dynamics (Princeton: Princeton University Press)
Bisbas, T. G., van Dishoeck, E. F., Papadopoulos, P. P., et al. 2017, ApJ, 839, 90
Bolatto, A. D., Wolfire, M., & Leroy, A. K. 2013, ARA&A, 51, 207
Boselli, A., & Gavazzi, G. 2006, PASP, 118, 517
Bregman, J. N. 1990, A&ARv, 2, 125
Brodwin, M., Stanford, S. A., Gonzalez, A. H., et al. 2013, ApJ, 779, 138
Calzetti, D., Armus, L., Bohlin, R. C., et al. 2000, ApJ, 533, 682
Carilli, C. L., & Walter, F. 2013, ARA&A, 51, 105
Carilli, C. L., Röttgering, H. J. A., van Ojik, R., Miley, G. K., & van Breugel, W. J. M. 1997, ApJS, 109, 1
Carleton, T., Errani, R., Cooper, M., Kaplinghat, M., & Peñarrubia, J. 2019, MNRAS, 485, 382
Casasola, V., Magrini, L., Combes, F., et al. 2013, A&A, 558, A60
Castignani, G., Combes, F., Salomé, P., et al. 2018, A&A 617, A103
Castignani, G., Pandey-Pommier, M., Hamer, S. L., et al. 2020, A&A, 640, A65
Chabrier, G. 2003, PASP, 115, 763
Chapman, S. C., Bertoldi, F., Smail, I., et al. 2015, MNRAS, 449, L68
Chiang, Y.-K., Overzier, R. A., Gebhardt, K., & Henriques, B. 2017, ApJ, 844, L23
Cicone, C., Severgnini, P., Papadopoulos, P. P., et al. 2018, ApJ, 863, 143
Cohen, A. S., Lane, W. M., Cotton, W. D., et al. 2007, AJ, 134, 1245
Colla, G., Fanti, C., Fanti, R., et al. 1973, A&AS, 11, 291
Combes, F. 2018, A&ARv, 26, 5
Condon, J. J., Cotton, W. D., Greisen, E. W., et al. 1998, AJ, 115, 1693
Coogan, R. T., Daddi, E., Sargent, M. T., et al. 2018, MNRAS, 479, 703
Cooke, E. A., Hatch, N. A., Rettura, A., et al. 2015, MNRAS, 452, 2318
Cooper, M. C., Newman, J. A., Weiner, B. J., et al. 2008, MNRAS, 383, 1058
Costa, T., Sijacki, D., & Haehnelt, M. G. 2015, MNRAS, 448, L30
Cucciati, O., Iovino, A., Kovač, K., et al. 2010, A&A, 524, A2
Cucciati, O., Lemaux, B. C., Zamorani, G., et al. 2018, A&A, 619, A49
Curti, M., Mannucci, F., Cresci, G., & Maiolino, R. 2020, MNRAS, 491, 944
Dannerbauer, H., Daddi, E., Riechers, D. A., et al. 2009, ApJ, 698, L178
Dannerbauer, H., Lehnert, M. D., Emonts, B., et al. 2017, A&A, 608, A48
Darvish, B., Mobasher, B., Sobral, D., Scoville, N., & Aragon-Calvo, M. 2015, ApJ, 805, 121
Darvish, B., Mobasher, B., Sobral, D., et al. 2016, ApJ, 825, 113
Darvish, B., Scoville, N. Z., Martin, C., et al. 2018, ApJ, 860, 111
Davidzon, I., Ilbert, O., Laigle, C., et al. 2017, A&A, 605, A70
Davidzon, I., Ilbert, O., Faisst, A. L., Sparre, M., & Capak, P. L. 2018, ApJ, 852, 107
Delaye, L., Huertas-Company, M., Mei, S., et al. 2014, MNRAS, 441, 203
Douglas, J. N., Bash, F. N., Bozyan, F. A., Torrence, G. W., & Wolfe, C. 1996, AJ, 111, 1945
Dressler, A. 1980, ApJ, 236, 351
Dubois, Y., Peirani, S., Pichon, C., et al. 2016, MNRAS, 463, 3948
Eales, S., Rawlings, S., Law-Green, D., Cotter, G., & Lacy, M. 1997, MNRAS, 291, 593
Elbaz, D., Daddi, E., Le Borgne, D., et al. 2007, A&A, 468, 33
Emonts, B. H. C., Feain, I., Mao, M. Y., et al. 2011, ApJ, 734, L25
Emonts, B. H. C., Norris, R. P., Feain, I., et al. 2014, MNRAS, 438, 2898
Falkendal, T., De Breuck, C., Lehnert, M. D., et al. 2019, A&A, 621, A27
Farouki, R., & Shapiro, S. L. 1981, ApJ, 243, 32
Fassbender, R., Nastasi, A., Böhringer, H., et al. 2011, A&A, 527, L10
Foltz, R., Wilson, G., Muzzin, A., et al. 2018, ApJ, 866, 136
Franco, M., Elbaz, D., Béthermin, M., et al. 2018, A&A, 620, A152
Fuentes, A., Gómez, J. L., Martí, J. M., & Perucho, M. 2018, ApJ, 860, 121
Galametz, A., Grazian, A., Fontana, A., et al. 2013, ApJS, 206, 10
Garn, T., & Best, P. N. 2010, MNRAS, 409, 421
Gaspari, M., & Sądowski, A. 2017, ApJ, 837, 149
Gaspari, M., Ruszkowski, M., & Sharma, P. 2012, ApJ, 746, 94
Genzel, R., Tacconi, L. J., Lutz, D., et al. 2015, ApJ, 800, 20
Gobat, R., Strazzullo, V., Daddi, E., et al. 2013, ApJ, 776, 9
Gómez, J. L., Marti, J. M. A., Marscher, A. P., Ibañez, J. M. A., & Marcaide, J. M. 1995, ApJ, 449, L19
Gómez, J. L., Martí, J. M., Marscher, A. P., Ibáñez, J. M., & Alberdi, A. 1997, ApJ, 482, L33
Grenier, I. A., Casandjian, J.-M., & Terrier, R. 2005, Science, 307, 1292
Grogin, N. A., Kocevski, D. D., Faber, S. M., et al. 2011, ApJS, 197, 35
Grossová, R., Werner, N., Rajpurohit, K., et al. 2019, MNRAS, 488, 1917
Grützbauch, R., Bauer, A. E., Jørgensen, I., & Varela, J. 2012, MNRAS, 423, 3652
Guglielmo, V., Poggianti, B. M., Moretti, A., et al. 2015, MNRAS, 450, 2749
Guo, Y., Ferguson, H. C., Giavalisco, M., et al. 2013, ApJS, 207, 24
Haas, M., Chini, R., Meisenheimer, K., et al. 1998, ApJ, 503, L109
Hall, K. P., Stanimirović, S., Lee, M.-Y., Wolfire, M., & Goldsmith, P. 2020, ApJ, 899, 23
Hatch, N. A., Cooke, E. A., Muldrew, S. I., et al. 2017, MNRAS, 464, 876
Hayashi, M., Kodama, T., Kohno, K., et al. 2017, ApJ, 841, L21
Hayashi, M., Tadaki, K.-i., Kodama, T., et al. 2018, ApJ, 856, 118
Heckman, T. M., & Kauffmann, G. 2006, New Astron. Rev., 50, 677
Hill, R., Chapman, S., Scott, D., et al. 2020, MNRAS, 495, 3124
Hönig, S. F., Prieto, M. A., & Beckert, T. 2008, A&A, 485, 33
Hopkins, P. F., Somerville, R. S., Hernquist, L., et al. 2006a, ApJ, 652, 864
Hopkins, P. F., Hernquist, L., Cox, T. J., et al. 2006b, ApJS, 163, 1
Hopkins, P. F., Hernquist, L., Cox, T. J., & Kereš, D. 2008, ApJS, 175, 356
Husband, K., Bremer, M. N., Stott, J. P., & Murphy, D. N. A. 2016, MNRAS, 462, 421
Ilbert, O., McCracken, H. J., Le Fèvre, O., et al. 2013, A&A, 556, A55
Ivison, R. J., Biggs, A. D., Bremer, M., Arumugam, V., & Dunne, L. 2020, MNRAS, 496, 4358
Jablonka, P., Combes, F., Rines, K., Finn, R., & Welch, T. 2013, A&A, 557, A103
Jaffé, Y. L., Poggianti, B. M., Moretti, A., et al. 2018, MNRAS, 476, 4753
Kauffmann, G., White, S. D. M., Heckman, T. M., et al. 2004, MNRAS, 353, 713
Kennicutt, Jr. R. C. 1998, ARA&A, 36, 189
Kennicutt, R. C., & Evans, N. J. 2012, ARA&A, 50, 531
Klamer, I. J., Ekers, R. D., Sadler, E. M., & Hunstead, R. W. 2004, ApJ, 612, L97
Klamer, I. J., Ekers, R. D., Bryant, J. J., et al. 2006, MNRAS, 371, 852
Kodama, T., Tanaka, I., Kajisawa, M., et al. 2007, MNRAS, 377, 1717
Koekemoer, A. M., Faber, S. M., Ferguson, H. C., et al. 2011, ApJS, 197, 36
Krumholz, M. R. 2014, Phys. Rep., 539, 49
Kubo, M., Toshikawa, J., Kashikawa, N., et al. 2019, ApJ, 887, 214

Kümmel, M., Walsh, J. R., Pirzkal, N., Kuntschner, H., & Pasquali, A. 2009, PASP, 121, 59

Lacy, M., Wilson, G., Masci, F., et al. 2005, ApJS, 161, 41

Laing, R. A., & Bridle, A. H. 2013, MNRAS, 432, 1114

Larson, R. B., Tinsley, B. M., & Caldwell, C. N. 1980, ApJ, 237, 692

Lee, S.-K., Idzi, R., Ferguson, H. C., et al. 2009, ApJS, 184, 100

Lee, M. M., Tanaka, I., Kawabe, R., et al. 2017, ApJ, 842, 55

Lemaux, B. C., Gal, R. R., Lubin, L. M., et al. 2012, ApJ, 745, 106

Lemaux, B. C., Tomczak, A. R., Lubin, L. M., et al. 2019, MNRAS, 490, 1231

Lewis, A. J. R., Ivison, R. J., Best, P. N., et al. 2018, ApJ, 862, 96

Li, Y., Bryan, G. L., Ruszkowski, M., et al. 2015, ApJ, 811, 73

Lim, J., Ao, Y., & Dinh-V-Trung. 2008, ApJ, 672, 252

Long, A. S., Cooray, A., Ma, J., et al. 2020, ApJ, 898, 133

Maier, C., Kuchner, U., Ziegler, B. L., et al. 2016, A&A, 590, A108

Makovoz, D., & Khan, I. 2005, ASP Conf. Ser., 347, 81

Mantz, A. B., Abdulla, Z., Carlstrom, J. E., et al. 2014, ApJ, 794, 157

Maraston, C., Pforr, J., Renzini, A., et al. 2010, MNRAS, 407, 830

Martinache, C., Rettura, A., Dole, H., et al. 2018, A&A, 620, A198

Massey, P., & Gronwall, C. 1990, ApJ, 358, 344

McCarthy, I. G., Frenk, C. S., Font, A. S., et al. 2008, MNRAS, 383, 593

McKee, C. F., & Ostriker, E. C. 2007, ARA&A, 45, 565

McNamara, B. R., Russell, H. R., Nulsen, P. E. J., et al. 2014, ApJ, 785, 44

Mei, S., Holden, B. P., Blakeslee, J. P., et al. 2009, ApJ, 690, 42

Mei, S., Stanford, S. A., Holden, B. P., et al. 2012, ApJ, 754, 141

Mei, S., Scarlata, C., Pentericci, L., et al. 2015, ApJ, 804, 117

Merluzzi, P., Busarello, G., Dopita, M. A., et al. 2013, MNRAS, 429, 1747

Miller, T. B., Chapman, S. C., Aravena, M., et al. 2018, Nature, 556, 469

Mioduszewski, A. J., Hughes, P. A., & Duncan, G. C. 1997, ApJ, 476, 649

Momcheva, I. G., Brammer, G. B., van Dokkum, P. G., et al. 2016, ApJS, 225, 27

Moore, B., Lake, G., Quinn, T., & Stadel, J. 1999, MNRAS, 304, 465

Morishita, T., Abramson, L. E., Treu, T., et al. 2019, ApJ, 877, 141

Muzzin, A., Wilson, G., Yee, H. K. C., et al. 2012, ApJ, 746, 188

Muzzin, A., Wilson, G., Demarco, R., et al. 2013a, ApJ, 767, 39

Muzzin, A., Marchesini, D., Stefanon, M., et al. 2013b, ApJ, 777, 18

Nesvadba, N. P. H., Neri, R., De Breuck, C., et al. 2009, MNRAS, 395, L16

Newman, A. B., Ellis, R. S., Andreon, S., et al. 2014, ApJ, 788, 51

Noble, A. G., McDonald, M., Muzzin, A., et al. 2017, ApJ, 842, L21

Noirot, G., Vernet, J., De Breuck, C., et al. 2016, ApJ, 830, 90

Noirot, G., Stern, D., Mei, S., et al. 2018, ApJ, 859, 38

Norton, S. A., Gebhardt, K., Zabludoff, A. I., & Zaritsky, D. 2001, ApJ, 557, 150

Nyland, K., Davis, T. A., Nguyen, D. D., et al. 2017, ApJ, 845, 50

Oke, J. B., Cohen, J. G., Carr, M., et al. 1995, PASP, 107, 375

Olivares, V., Salome, P., Combes, F., et al. 2019, A&A, 631, A22

Osterbrock, D. E., & Ferland, G. J. 2006, Astrophysics of Gaseous Nebulae and Active Galactic Nuclei (Sausalito, CA: University Science Books)

Oteo, I., Ivison, R. J., Dunne, L., et al. 2018, ApJ, 856, 72

Paccagnella, A., Vulcani, B., Poggianti, B. M., et al. 2019, MNRAS, 482, 881

Pacifici, C., Kassin, S. A., Weiner, B. J., et al. 2016, ApJ, 832, 79

Papovich, C., Momcheva, I., Willmer, C. N. A., et al. 2010, ApJ, 716, 1503

Papovich, C., Bassett, R., Lotz, J. M., et al. 2012, ApJ, 750, 93

Peng, Y.-j., Lilly, S. J., Kovač, K., et al. 2010, ApJ, 721, 193

Peng, Y.-j., Lilly, S. J., Renzini, A., & Carollo, M. 2012, ApJ, 757, 4

Peng, Y.-j., Lilly, S. J., Renzini, A., & Carollo, M. 2014, ApJ, 790, 95

Peng, Y., Maiolino, R., & Cochrane, R. 2015, Nature, 521, 192

Pforr, J., Maraston, C., & Tonini, C. 2012, MNRAS, 422, 3285

Pineda, J. L., Langer, W. D., Velusamy, T., & Goldsmith, P. F. 2013, A&A, 554, A103

Planck Collaboration XIX. 2011, A&A, 536, A19

Porth, O., Fendt, C., Meliani, Z., & Vaidya, B. 2011, ApJ, 737, 42

Postman, M., Franx, M., Cross, N. J. G., et al. 2005, ApJ, 623, 721

Prasad, D., Sharma, P., & Babul, A. 2015, ApJ, 811, 108

Raichoor, A., Mei, S., Nakata, F., et al. 2011, ApJ, 732, 12

Rettura, A., Mei, S., Stanford, S. A., et al. 2011, ApJ, 732, 94

Rudnick, G., Hodge, J., Walter, F., et al. 2017, ApJ, 849, 27

Ruffa, I., Prandoni, I., Laing, R. A., et al. 2019, MNRAS, 484, 4239

Russell, H. R., McNamara, B. R., Edge, A. C., et al. 2014, ApJ, 784, 78

Russell, H. R., McNamara, B. R., Fabian, A. C., et al. 2019, MNRAS, 490, 3025

Saintonge, A., Catinella, B., Tacconi, L. J., et al. 2017, ApJS, 233, 22

Salomé, P., Combes, F., Edge, A. C., et al. 2006, A&A, 454, 437

Santini, P., Ferguson, H. C., Fontana, A., et al. 2015, ApJ, 801, 97

Santos, J. S., Altieri, B., Valtchanov, I., et al. 2015, MNRAS, 447, L65

Sargent, M. T., Daddi, E., Béthermin, M., et al. 2014, ApJ, 793, 19

Scoville, N., Arnouts, S., Aussel, H., et al. 2013, ApJS, 206, 3

Scoville, N., Lee, N., Vanden Bout, P., et al. 2017, ApJ, 837, 150

Seymour, N., Huynh, M., Shabala, S. S., et al. 2020, PASA, 37, e013

Shankar, F., Marulli, F., Bernardi, M., et al. 2013, MNRAS, 428, 109

Shankar, F., Mei, S., Huertas-Company, M., et al. 2014, MNRAS, 439, 3189

Shimakawa, R., Kodama, T., Hayashi, M., et al. 2018a, MNRAS, 473, 1977

Shimakawa, R., Koyama, Y., Röttgering, H. J. A., et al. 2018b, MNRAS, 481, 5630

Silverman, J. D., Rujopakarn, W., Daddi, E., et al. 2018, ApJ, 867, 92

Sklias, P., Schaerer, D., Elbaz, D., et al. 2017, A&A, 605, A29

Snyder, G. F., Cox, T. J., Hayward, C. C., Hernquist, L., & Jonsson, P. 2011, ApJ, 741, 77

Snyder, G. F., Brodwin, M., Mancone, C. M., et al. 2012, ApJ, 756, 114

Solomon, P. M., & Vanden Bout, P. A. 2005, ARA&A, 43, 677

Sorba, R., & Sawicki, M. 2018, MNRAS, 476, 1532

Stanford, S. A., Brodwin, M., Gonzalez, A. H., et al. 2012, ApJ, 753, 164

Strazzullo, V., Rosati, P., Pannella, M., et al. 2010, A&A, 524, A17

Strazzullo, V., Gobat, R., Daddi, E., et al. 2013, ApJ, 772, 118

Tacconi, L. J., Neri, R., Genzel, R., et al. 2013, ApJ, 768, 74

Tacconi, L. J., Genzel, R., Saintonge, A., et al. 2018, ApJ, 853, 179

Tadaki, K.-i., Kodama, T., Ota, K., et al. 2012, MNRAS, 423, 2617

Tadaki, K.-i., Kodama, T., Hayashi, M., et al. 2019, PASJ, 71, 40

Tadhunter, C. 2016, A&ARv, 24, 10

Tanaka, M., Toft, S., Marchesini, D., et al. 2013, ApJ, 772, 113

Thomas, D., Maraston, C., Bender, R., & Mendes de Oliveira, C. 2005, ApJ, 621, 673

Tomczak, A. R., Quadri, R. F., Tran, K.-V. H., et al. 2016, ApJ, 817, 118

Tomczak, A. R., Lemaux, B. C., Lubin, L. M., et al. 2017, MNRAS, 472, 3512

Tomczak, A. R., Lemaux, B. C., Lubin, L. M., et al. 2019, MNRAS, 484, 4695

Tonnesen, S., & Cen, R. 2014, ApJ, 788, 133

Toshikawa, J., Malkan, M. A., Kashikawa, N., et al. 2020, ApJ, 888, 89

Tran, K.-V. H., Papovich, C., Saintonge, A., et al. 2010, ApJ, 719, L126

Tremblay, G. R., Combes, F., Oonk, J. B. R., et al. 2018, ApJ, 865, 13

Umehata, H., Tamura, Y., Kohno, K., et al. 2015, ApJ, 815, L8

van der Wel, A., Franx, M., Wuyts, S., et al. 2006, ApJ, 652, 97

Voit, G. M., Meece, G., Li, Y., et al. 2017, ApJ, 845, 80

Wagg, J., Pope, A., Alberts, S., et al. 2012, ApJ, 752, 91

Wagner, C. R., Brodwin, M., Snyder, G. F., et al. 2015, ApJ, 800, 107

Waldram, E. M., Yates, J. A., Riley, J. M., & Warner, P. J. 1996, MNRAS, 282, 779

Wang, T., Elbaz, D., Daddi, E., et al. 2016a, ApJ, 828, 56

Wang, Z.-Y., Haase, J. F., Casanova, J., & Plenio, M. B. 2016b, Phys. Rev. B, 93, 174104

Weiß, A., Walter, F., & Scoville, N. Z. 2005, A&A, 438, 533

Wolfire, M. G., Hollenbach, D., & McKee, C. F. 2010, ApJ, 716, 1191

Wylezalek, D., Galametz, A., Stern, D., et al. 2013, ApJ, 769, 79

Wylezalek, D., Vernet, J., De Breuck, C., et al. 2014, ApJ, 786, 17

Yesuf, H. M., Faber, S. M., Trump, J. R., et al. 2014, ApJ, 792, 84

Zeimann, G. R., Stanford, S. A., Brodwin, M., et al. 2012, ApJ, 756, 115

Zeimann, G. R., Stanford, S. A., Brodwin, M., et al. 2013, ApJ, 779, 137

Appendix A: Positions of the two CO(2–1) emission peaks

In order to kinematically resolve the two components of the CO(2–1) emission line, we performed an analysis of different ranges of channels (velocities or frequencies) in the CO(2–1) spectrum and created the corresponding CO(2–1) emission line intensity maps, averaged over the chosen range of velocities. In Fig. A.1, we select a range of velocities so that we include both the eastern and western emission peaks ($-1075\,\mathrm{km\,s^{-1}} < v < +125\,\mathrm{km\,s^{-1}}$). In Fig. A.2, we select only the range of velocities that correspond to the eastern peak ($-1075\,\mathrm{km\,s^{-1}} < v < -475\,\mathrm{km\,s^{-1}}$). In Fig. A.3, we select only the range of velocities that correspond to the western peak ($-375\,\mathrm{km\,s^{-1}} < v < +125\,\mathrm{km\,s^{-1}}$). We can see that, although both the eastern and western emission peaks are superposed in some regions of the cluster core, we can kinematically separate them.

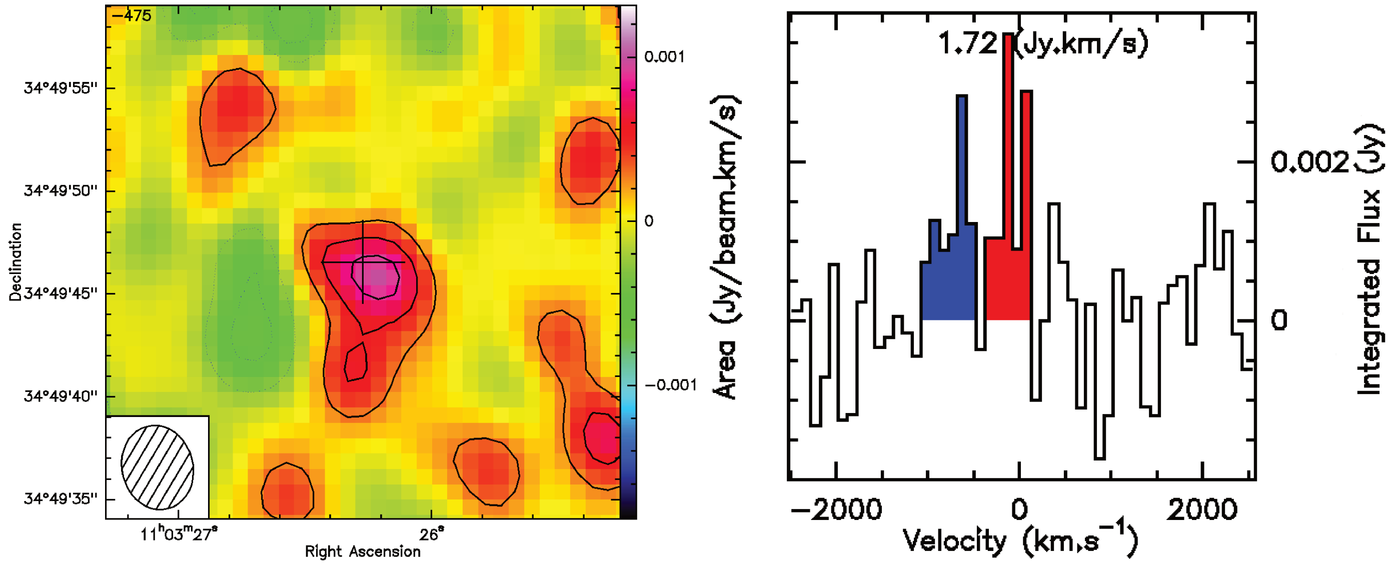

Fig. A.1. *Left*: CO(2–1) line emission intensity map of the central cluster region with NOEMA created by selecting the channel ranges that include both the eastern and western emission peaks (on the *right*). The spectra are binned in channels of 100 km s^{-1}. The contour levels are 1σ, 2σ, and 3σ.

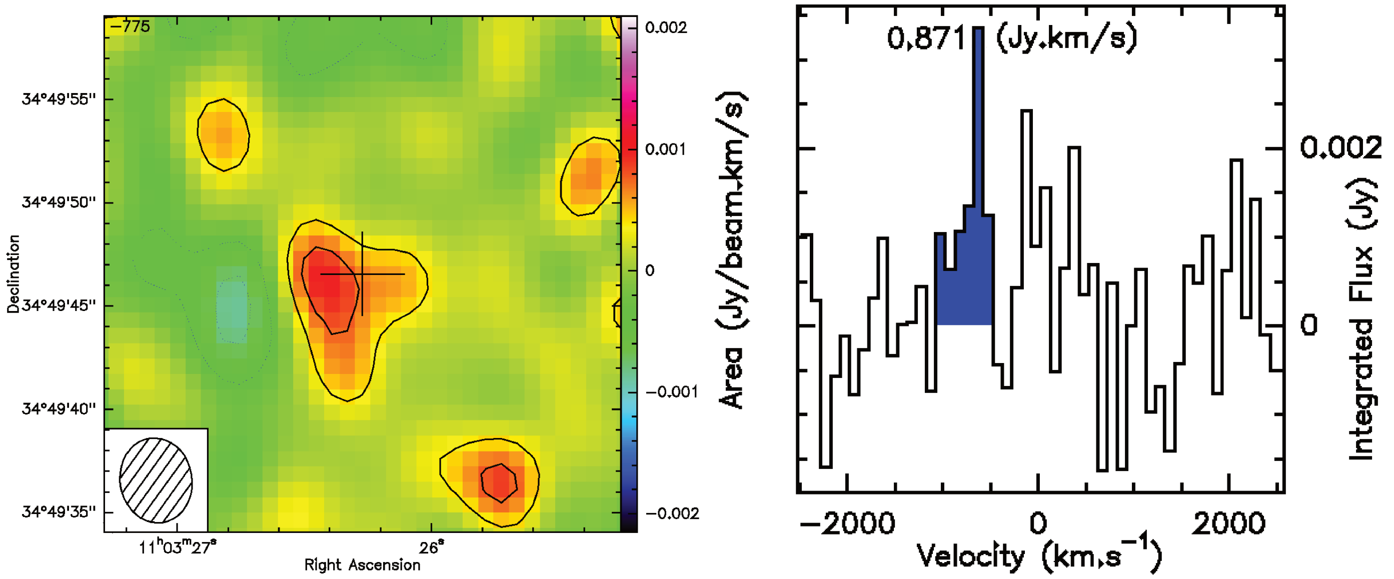

Fig. A.2. *Left*: CO(2–1) line emission intensity map of the central cluster region with NOEMA created by selecting the channel ranges that include only the eastern emission peak (on the *right*). The spectra are binned in channels of 100 km s^{-1}. The contour levels are 1σ and 2σ.

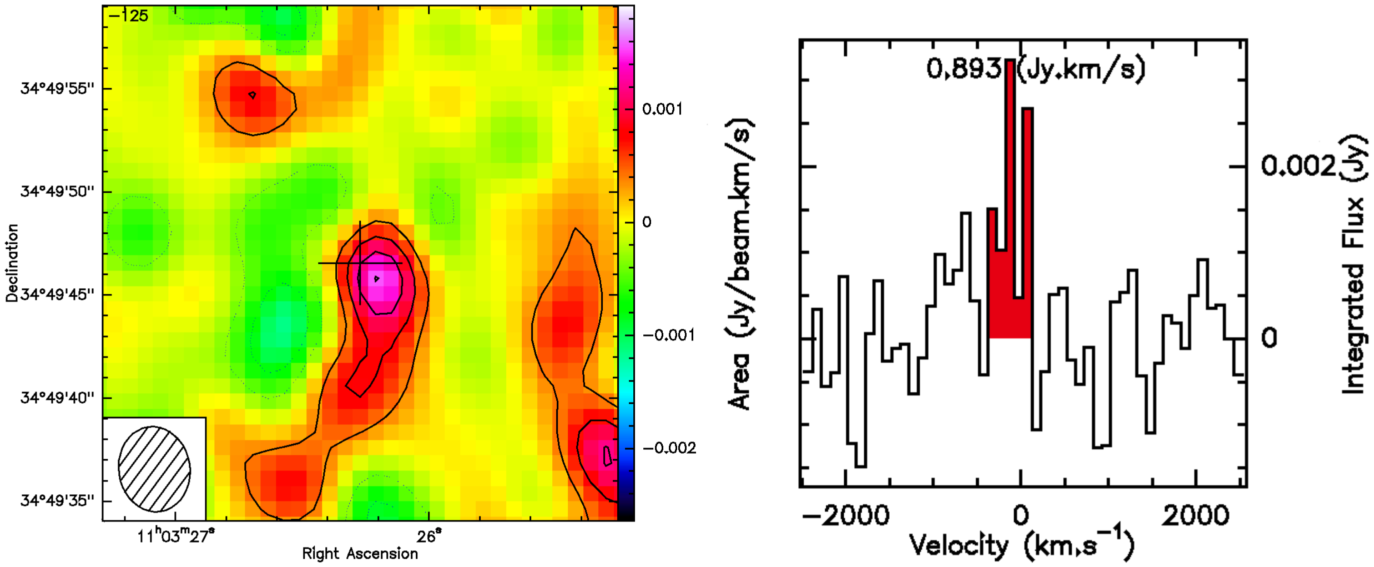

Fig. A.3. *Left*: CO(2–1) line emission intensity map of the central cluster region with NOEMA created by selecting the channel ranges that include only the western emission peak (on the *right*). The spectra are binned in channels of 100 km s^{-1}. The contour levels are 1σ, 2σ, 3σ, and 4σ.

BIBLIOGRAPHY

Abadi, M. G., B. Moore, and R. G. Bower (1999). "Ram pressure stripping of spiral galaxies in clusters." In: *MNRAS* 308, pp. 947–954. doi: `10.1046/j.1365-8711.1999.02715.x`. eprint: `astro-ph/9903436` (cit. on p. 21).

Abdo, A. A. et al. (2010). "Fermi Observations of Cassiopeia and Cepheus: Diffuse Gamma-ray Emission in the Outer Galaxy." In: *ApJ* 710.1, pp. 133–149. doi: `10.1088/0004-637X/710/1/133`. arXiv: `0912.3618 [astro-ph.HE]` (cit. on p. 99).

Abraham, R. G. (1998). "Perspectives in Physical Morphology." In: *arXiv e-prints*, astro-ph/9809131, astro–ph/9809131. arXiv: `astro-ph/9809131 [astro-ph]` (cit. on p. 6).

Adam, Planck Collaboration R. et al. (2015). "Planck 2015 results. I. Overview of products and scientific results." In: (cit. on p. 40).

Alberts, S. et al. (2016). "Star Formation and AGN Activity in Galaxy Clusters from z=1-2: a Multi-Wavelength Analysis Featuring Herschel/PACS." In: *ApJ* 825, 72, p. 72. doi: `10.3847/0004-637X/825/1/72`. arXiv: `1604.03564` (cit. on p. 98).

Allen, S. W., A. C. Fabian, R. M. Johnstone, K. A. Arnaud, and P. E. J. Nulsen (2001). "ASCA and ROSAT observations of nearby cluster cooling flows." In: *MNRAS* 322.3, pp. 589–613. doi: `10.1046/j.1365-8711.2001.04135.x`. arXiv: `astro-ph/9910188 [astro-ph]` (cit. on p. 17).

Allgood, Brandon, Ricardo A. Flores, Joel R. Primack, Andrey V. Kravtsov, Risa H. Wechsler, Andreas Faltenbacher, and James S. Bullock (2006). "The shape of dark matter haloes: dependence on mass, redshift, radius and formation." In: *MNRAS* 367.4, pp. 1781–1796. doi: `10.1111/j.1365-2966.2006.10094.x`. arXiv: `astro-ph/0508497 [astro-ph]` (cit. on p. 4).

Aloy, M.-A., J.-L. Gómez, J.-M. Ibáñez, J.-M. Martí, and E. Müller (2000). "Radio Emission from Three-dimensional Relativistic Hydrodynamic Jets: Observational Evidence of Jet Stratification." In: *ApJ* 528, pp. L85–L88. doi: `10.1086/312436`. eprint: `astro-ph/9911153` (cit. on p. 111).

Alpher, R. A., H. Bethe, and G. Gamow (1948). "The Origin of Chemical Elements." In: *Physical Review* 73.7, pp. 803–804. doi: `10.1103/PhysRev.73.803` (cit. on p. 2).

Angulo, R. E., V. Springel, S. D. M. White, A. Jenkins, C. M. Baugh, and C. S. Frenk (2012). "Scaling relations for galaxy clusters in the Millennium-XXL simulation." In: *MNRAS* 426.3, pp. 2046–2062. doi: `10.1111/j.1365-2966.2012.21830.x`. arXiv: `1203.3216 [astro-ph.CO]` (cit. on p. 7).

Arnaud, M. (2009). "The β-model of the intracluster medium. Commentary on: Cavaliere A. and Fusco-Femiano R., 1976, AA, 49, 137." In: *A&A* 500, pp. 103–104. doi: `10.1051/0004-6361/200912150` (cit. on p. 98).

Arnouts, S., S. Cristiani, L. Moscardini, S. Matarrese, F. Lucchin, A. Fontana, and E. Giallongo (1999). "Measuring and modelling the redshift evolution of clustering: the Hubble Deep Field North." In: *MNRAS* 310, pp. 540–556. doi: `10.1046/j.1365-8711.1999.02978.x`. eprint: `astro-ph/9902290` (cit. on pp. 11, 32).

Arnouts, S., L. Moscardini, E. Vanzella, S. Colombi, S. Cristiani, A. Fontana, E. Giallongo, S. Matarrese, and P. Saracco (2002). "Measuring the redshift evolution of clustering: the Hubble Deep Field South." In: *MNRAS* 329, pp. 355–366. DOI: `10.1046/j.1365-8711.2002.04988.x`. eprint: `astro-ph/0109453` (cit. on pp. 11, 32, 36).

Arnouts, S. et al. (2007). "The SWIRE-VVDS-CFHTLS surveys: stellar mass assembly over the last 10 Gyr. Evidence for a major build up of the red sequence between z = 2 and z = 1." In: *A&A* 476, pp. 137–150. DOI: `10.1051/0004-6361:20077632`. arXiv: `0705.2438` (cit. on pp. 11, 22, 23, 25, 26, 80, 90).

Arnouts, S. et al. (2013). "Encoding of the infrared excess in the NUVrK color diagram for star-forming galaxies." In: *A&A* 558, A67, A67. DOI: `10.1051/0004-6361/201321768`. arXiv: `1309.0008 [astro-ph.CO]` (cit. on p. 45).

Ascaso, B., S. Mei, and N. Benítez (2015). "Apples to apples A^2 - I. Realistic galaxy simulated catalogues and photometric redshift predictions for next-generation surveys." In: *MNRAS* 453, pp. 2515–2532. DOI: `10.1093/mnras/stv1597`. arXiv: `1503.01113` (cit. on p. 36).

Astropy Collaboration et al. (2013). "Astropy: A community Python package for astronomy." In: *A&A* 558, A33, A33. DOI: `10.1051/0004-6361/201322068`. arXiv: `1307.6212 [astro-ph.IM]` (cit. on pp. 52, 53, 55).

Athreya, R. M., V. K. Kapahi, P. J. McCarthy, and W. van Breugel (1997). "Steep- spectrum radio cores in high-redshift galaxies." In: *MNRAS* 289.3, pp. 525–534. DOI: `10.1093/mnras/289.3.525` (cit. on p. 112).

Bailin, Jeremy and Matthias Steinmetz (2005). "Internal and External Alignment of the Shapes and Angular Momenta of ΛCDM Halos." In: *ApJ* 627.2, pp. 647–665. DOI: `10.1086/430397`. arXiv: `astro-ph/0408163 [astro-ph]` (cit. on p. 4).

Baldry, I. K., K. Glazebrook, and S. P. Driver (2008). "On the galaxy stellar mass function, the mass-metallicity relation and the implied baryonic mass function." In: *MNRAS* 388, pp. 945–959. DOI: `10.1111/j.1365-2966.2008.13348.x`. arXiv: `0804.2892` (cit. on p. 38).

Baldry, I. K., M. L. Balogh, R. G. Bower, K. Glazebrook, R. C. Nichol, S. P. Bamford, and T. Budavari (2006). "Galaxy bimodality versus stellar mass and environment." In: *MNRAS* 373, pp. 469–483. DOI: `10.1111/j.1365-2966.2006.11081.x`. eprint: `astro-ph/0607648` (cit. on p. 6).

Baldry, Ivan K., Karl Glazebrook, Jon Brinkmann, Željko Ivezić, Robert H. Lupton, Robert C. Nichol, and Alexander S. Szalay (2004). "Quantifying the Bimodal Color-Magnitude Distribution of Galaxies." In: *ApJ* 600.2, pp. 681–694. DOI: `10.1086/380092`. arXiv: `astro-ph/0309710 [astro-ph]` (cit. on p. 18).

Balogh, M. L. and S. L. Morris (2000). "Hα photometry of Abell 2390." In: *MNRAS* 318, pp. 703–714. DOI: `10.1046/j.1365-8711.2000.03826.x`. eprint: `astro-ph/0007111` (cit. on p. 21).

Balogh, M. L., D. Schade, S. L. Morris, H. K. C. Yee, R. G. Carlberg, and E. Ellingson (1998). "The Dependence of Cluster Galaxy Star Formation Rates on the Global Environment." In: *ApJ* 504, pp. L75–L78. DOI: `10.1086/311576`. eprint: `astro-ph/9806146` (cit. on p. 98).

Balogh, M. et al. (2004). “Galaxy ecology: groups and low-density environments in the SDSS and 2dFGRS.” In: *MNRAS* 348, pp. 1355–1372. doi: 10.1111/j.1365-2966.2004.07453.x. eprint: astro-ph/0311379 (cit. on p. 98).

Barlow, R. J. (1989). *Statistics: A Guide to the Use of Statistical Methods in the Physical Sciences (Manchester Physics Series)*. Reprint. WileyBlackwell. isbn: 0471922951. url: http://www.amazon.co.uk/Statistics-Statistical-Physical-Sciences-Manchester/dp/0471922951%3FSubscriptionId%3D13CT5CVB80YFWJEPWS02%26tag%3Dws%26linkCode%3Dxm2%26camp%3D2025%26creative%3D165953%26creativeASIN%3D0471922951 (cit. on pp. 34, 37).

Barnes, Joshua E. and Lars E. Hernquist (1991). “Fueling Starburst Galaxies with Gas-rich Mergers.” In: *ApJ* 370, p. L65. doi: 10.1086/185978 (cit. on pp. 13, 14).

Barnes, Joshua E. and Lars Hernquist (1996). “Transformations of Galaxies. II. Gasdynamics in Merging Disk Galaxies.” In: *ApJ* 471, p. 115. doi: 10.1086/177957 (cit. on pp. 13, 14).

Baum, W. A. (1962). “Photoelectric Magnitudes and Red-Shifts.” In: *Problems of Extra-Galactic Research*. Ed. by G. C. McVittie. Vol. 15. IAU Symposium, p. 390 (cit. on p. 11).

Becker, Robert H., Richard L. White, and Alan L. Edwards (1991). “A New Catalog of 53,522 4.85 GHz Sources.” In: *ApJS* 75, p. 1. doi: 10.1086/191529 (cit. on p. 114).

Becker, Robert H. et al. (2001). “Evidence for Reionization at z∼6: Detection of a Gunn-Peterson Trough in a z=6.28 Quasar.” In: *AJ* 122.6, pp. 2850–2857. doi: 10.1086/324231. arXiv: astro-ph/0108097 [astro-ph] (cit. on pp. 2, 5).

Beckwith, S. V. W. et al. (2006). “The Hubble Ultra Deep Field.” In: *AJ* 132, pp. 1729–1755. doi: 10.1086/507302. eprint: astro-ph/0607632 (cit. on p. 9).

Begelman, Mitchell, Martijn de Kool, and Marek Sikora (1991). “Outflows Driven by Cosmic-Ray Pressure in Broad Absorption Line QSOs.” In: *ApJ* 382, p. 416. doi: 10.1086/170731 (cit. on p. 19).

Behroozi, Peter S., Risa H. Wechsler, and Charlie Conroy (2013). “The Average Star Formation Histories of Galaxies in Dark Matter Halos from z = 0-8.” In: *ApJ* 770.1, 57, p. 57. doi: 10.1088/0004-637X/770/1/57. arXiv: 1207.6105 [astro-ph.CO] (cit. on pp. 18, 22).

Bell, E. F., D. H. McIntosh, N. Katz, and M. D. Weinberg (2003). “The Optical and Near-Infrared Properties of Galaxies. I. Luminosity and Stellar Mass Functions.” In: *ApJS* 149, pp. 289–312. doi: 10.1086/378847. eprint: astro-ph/0302543 (cit. on p. 25).

Bell, E. F. et al. (2006). “Dry Mergers in GEMS: The Dynamical Evolution of Massive Early-Type Galaxies.” In: *ApJ* 640, pp. 241–251. doi: 10.1086/499931. eprint: astro-ph/0506425 (cit. on pp. 95, 135).

Bell, Eric F., Christian Wolf, Klaus Meisenheimer, Hans-Walter Rix, Andrea Borch, Simon Dye, Martina Kleinheinrich, Lutz Wisotzki, and Daniel H. McIntosh (2004). “Nearly 5000 Distant Early-Type Galaxies in COMBO-17: A Red Sequence and Its Evolution since z∼1.” In: *ApJ* 608.2, pp. 752–767. doi: 10.1086/420778. arXiv: astro-ph/0303394 [astro-ph] (cit. on pp. 23, 25).

Benítez, N. et al. (2004). "Faint Galaxies in Deep Advanced Camera for Surveys Observations." In: *ApJS* 150, pp. 1–18. doi: `10.1086/380120`. eprint: `astro-ph/0309077` (cit. on p. 12).

Bennett, C. L. et al. (2003). "First-Year Wilkinson Microwave Anisotropy Probe (WMAP) Observations: Preliminary Maps and Basic Results." In: *ApJS* 148.1, pp. 1–27. doi: `10.1086/377253`. arXiv: `astro-ph/0302207 [astro-ph]` (cit. on p. 2).

Benson, A. J., S. Cole, C. S. Frenk, C. M. Baugh, and C. G. Lacey (2000). "The nature of galaxy bias and clustering." In: *MNRAS* 311.4, pp. 793–808. doi: `10.1046/j.1365-8711.2000.03101.x`. arXiv: `astro-ph/9903343 [astro-ph]` (cit. on p. 7).

Benson, A. J., R. G. Bower, C. S. Frenk, C. G. Lacey, C. M. Baugh, and S. Cole (2003). "What Shapes the Luminosity Function of Galaxies?" In: *ApJ* 599, pp. 38–49. doi: `10.1086/379160`. eprint: `astro-ph/0302450` (cit. on pp. 13, 20).

Bernardi, M. et al. (2003). "Early-type Galaxies in the Sloan Digital Sky Survey. II. Correlations between Observables." In: *AJ* 125, pp. 1849–1865. doi: `10.1086/374256`. eprint: `astro-ph/0301624` (cit. on p. 27).

Bertin, E. and S. Arnouts (1996). "SExtractor: Software for source extraction." In: *A&AS* 117, pp. 393–404. doi: `10.1051/aas:1996164` (cit. on p. 102).

Best, P. N., S. A. Eales, M. S. Longair, S. Rawlings, and H. J. A. Rottgering (1999). "Studies of a sample of 6C radio galaxies at a redshift of 1 - I. Deep multifrequency radio observations." In: *MNRAS* 303, pp. 616–640. doi: `10.1046/j.1365-8711.1999.02267.x`. eprint: `astro-ph/9811145` (cit. on pp. 110–114, 118, 121, 134, 143, 144).

Bevington, Philip R and D Keith Robinson (2003). *Data reduction and error analysis for the physical sciences; 3rd ed.* New York, NY: McGraw-Hill. url: `https://cds.cern.ch/record/1305448` (cit. on pp. 34, 35, 37, 39).

Beyer, William H. and Chemical Rubber Company (1968). *CRC handbook of tables for probability and statistics*. CRC handbook series. Chemical Rubber Co. url: `https://books.google.fr/books?id=Y2VqAAAAMAAJ` (cit. on p. 34).

Bezanson, R. et al. (2016). "Leveraging 3D-HST Grism Redshifts to Quantify Photometric Redshift Performance." In: *ApJ* 822, 30, p. 30. doi: `10.3847/0004-637X/822/1/30`. arXiv: `1510.07049` (cit. on p. 36).

Binney, J. and S. Tremaine (1987). *Galactic dynamics* (cit. on p. 18).

Binney, James (2004). "On the origin of the galaxy luminosity function." In: *MNRAS* 347.4, pp. 1093–1096. doi: `10.1111/j.1365-2966.2004.07277.x`. arXiv: `astro-ph/0308172 [astro-ph]` (cit. on p. 13).

Birnboim, Yuval and Avishai Dekel (2003). "Virial shocks in galactic haloes?" In: *MNRAS* 345.1, pp. 349–364. doi: `10.1046/j.1365-8711.2003.06955.x`. arXiv: `astro-ph/0302161 [astro-ph]` (cit. on pp. 13, 15).

Bîrzan, L., B. R. McNamara, P. E. J. Nulsen, C. L. Carilli, and M. W. Wise (2008). "Radiative Efficiency and Content of Extragalactic Radio Sources: Toward a Universal Scaling Relation between Jet Power and Radio Power." In: *ApJ* 686.2, pp. 859–880. doi: `10.1086/591416`. arXiv: `0806.1929 [astro-ph]` (cit. on p. 136).

Blanton, M. R. et al. (2017). "Sloan Digital Sky Survey IV: Mapping the Milky Way, Nearby Galaxies, and the Distant Universe." In: *AJ* 154, 28, p. 28. doi: `10.3847/1538-3881/aa7567`. arXiv: `1703.00052` (cit. on p. 9).

Blumenthal, G. R. and R. J. Gould (1970). "Bremsstrahlung, Synchrotron Radiation, and Compton Scattering of High-Energy Electrons Traversing Dilute Gases." In: *Reviews of Modern Physics* 42, pp. 237–271. doi: `10.1103/RevModPhys.42.237` (cit. on p. 111).

Bolatto, A. D., M. Wolfire, and A. K. Leroy (2013). "The CO-to-H_2 Conversion Factor." In: *ARA&A* 51, pp. 207–268. doi: `10.1146/annurev-astro-082812-140944`. arXiv: `1301.3498` (cit. on pp. 99, 101, 123–126).

Bolzonella, M., J.-M. Miralles, and R. Pelló (2000). "Photometric redshifts based on standard SED fitting procedures." In: *A&A* 363, pp. 476–492. eprint: `astro-ph/0003380` (cit. on pp. 11, 35, 36).

Bolzonella, M. et al. (2010). "Tracking the impact of environment on the galaxy stellar mass function up to z 1 in the 10 k zCOSMOS sample." In: *A&A* 524, A76, A76. doi: `10.1051/0004-6361/200912801`. arXiv: `0907.0013 [astro-ph.CO]` (cit. on pp. 25, 27).

Bond, J. R. and A. S. Szalay (1983). "The collisionless damping of density fluctuations in an expanding universe." In: *ApJ* 274, pp. 443–468. doi: `10.1086/161460` (cit. on p. 2).

Borne, Kirk D., Howard Bushouse, Ray A. Lucas, and Luis Colina (2000). "Evidence for Multiple Mergers among Ultraluminous Infrared Galaxies: Remnants of Compact Groups?" In: *ApJ* 529.2, pp. L77–L80. doi: `10.1086/312461`. arXiv: `astro-ph/9912151 [astro-ph]` (cit. on p. 13).

Boselli, A. and G. Gavazzi (2006). "Environmental Effects on Late-Type Galaxies in Nearby Clusters." In: *PASP* 118, pp. 517–559. doi: `10.1086/500691`. eprint: `astro-ph/0601108` (cit. on p. 19).

Bouché, N., M. T. Murphy, G. G. Kacprzak, C. Péroux, T. Contini, C. L. Martin, and M. Dessauges-Zavadsky (2013). "Signatures of Cool Gas Fueling a Star-Forming Galaxy at Redshift 2.3." In: *Science* 341.6141, pp. 50–53. doi: `10.1126/science.1234209`. arXiv: `1306.0134 [astro-ph.CO]` (cit. on p. 15).

Bouwens, R. J. et al. (2015). "UV Luminosity Functions at Redshifts z 4 to z 10: 10,000 Galaxies from HST Legacy Fields." In: *ApJ* 803, 34, p. 34. doi: `10.1088/0004-637X/803/1/34`. arXiv: `1403.4295` (cit. on p. 19).

Bower, R. G., A. J. Benson, and R. A. Crain (2012). "What shapes the galaxy mass function? Exploring the roles of supernova-driven winds and active galactic nuclei." In: *MNRAS* 422, pp. 2816–2840. doi: `10.1111/j.1365-2966.2012.20516.x`. arXiv: `1112.2712` (cit. on p. 54).

Bowler, R. A. A. et al. (2014). "The bright end of the galaxy luminosity function at z 7: before the onset of mass quenching?" In: *MNRAS* 440, pp. 2810–2842. doi: `10.1093/mnras/stu449`. arXiv: `1312.5643` (cit. on p. 35).

Boylan-Kolchin, Michael, James S. Bullock, and Manoj Kaplinghat (2012). "The Milky Way's bright satellites as an apparent failure of ΛCDM." In: *MNRAS* 422.2, pp. 1203–1218. doi: `10.1111/j.1365-2966.2012.20695.x`. arXiv: `1111.2048 [astro-ph.CO]` (cit. on p. 9).

Boylan-Kolchin, Michael, Volker Springel, Simon D. M. White, Adrian Jenkins, and Gerard Lemson (2009). "Resolving cosmic structure formation with the Millennium-II Simulation." In: *MNRAS* 398.3, pp. 1150–1164. DOI: `10.1111/j.1365-2966.2009.15191.x`. arXiv: `0903.3041 [astro-ph.CO]` (cit. on p. 7).

Bregman, J. N. (1990). "Continuum radiation from active galactic nuclei." In: *A&A Rev.* 2, pp. 125–166. DOI: `10.1007/BF00872765` (cit. on p. 110).

Brinchmann, J., S. Charlot, S. D. M. White, C. Tremonti, G. Kauffmann, T. Heckman, and J. Brinkmann (2004). "The physical properties of star-forming galaxies in the low-redshift Universe." In: *MNRAS* 351.4, pp. 1151–1179. DOI: `10.1111/j.1365-2966.2004.07881.x`. arXiv: `astro-ph/0311060 [astro-ph]` (cit. on pp. 18, 139).

Brinchmann, Jarle and Richard S. Ellis (2000). "The Mass Assembly and Star Formation Characteristics of Field Galaxies of Known Morphology." In: *ApJ* 536.2, pp. L77–L80. DOI: `10.1086/312738`. arXiv: `astro-ph/0005120 [astro-ph]` (cit. on pp. 18, 22, 23, 81, 90).

Brodwin, M. et al. (2013). "The Era of Star Formation in Galaxy Clusters." In: *ApJ* 779, 138, p. 138. DOI: `10.1088/0004-637X/779/2/138`. arXiv: `1310.6039` (cit. on p. 98).

Brunner, R. J. and L. M. Lubin (2000). "A Probabilistic Quantification of Galaxy Cluster Membership." In: *AJ* 120, pp. 2851–2858. DOI: `10.1086/316849`. eprint: `astro-ph/0008462` (cit. on p. 37).

Brunner, R. J., A. J. Connolly, A. S. Szalay, and M. A. Bershady (1997). "Toward More Precise Photometric Redshifts: Calibration Via CCD Photometry." In: *ApJ* 482, pp. L21–L24. DOI: `10.1086/310674`. eprint: `astro-ph/9703058` (cit. on pp. 11, 12).

Bruzual, G. and S. Charlot (2003). "Stellar population synthesis at the resolution of 2003." In: *MNRAS* 344.4, pp. 1000–1028. DOI: `10.1046/j.1365-8711.2003.06897.x`. arXiv: `astro-ph/0309134 [astro-ph]` (cit. on p. 12).

Bryan, G. L. and M. L. Norman (1995). "Simulating X-ray Clusters with Adaptive Mesh Refinement." In: *American Astronomical Society Meeting Abstracts*. Vol. 187. American Astronomical Society Meeting Abstracts, p. 95.04 (cit. on p. 7).

Buat, V. et al. (2005). "Dust Attenuation in the Nearby Universe: A Comparison between Galaxies Selected in the Ultraviolet and in the Far-Infrared." In: *ApJ* 619.1, pp. L51–L54. DOI: `10.1086/423241`. arXiv: `astro-ph/0411343 [astro-ph]` (cit. on p. 100).

Budavári, T., A. S. Szalay, A. J. Connolly, I. Csabai, and M. Dickinson (2000). "Creating Spectral Templates from Multicolor Redshift Surveys." In: *AJ* 120, pp. 1588–1598. DOI: `10.1086/301514`. eprint: `astro-ph/9908008` (cit. on p. 12).

Buitrago, Fernando, Ignacio Trujillo, Christopher J. Conselice, and Boris Häußler (2013). "Early-type galaxies have been the predominant morphological class for massive galaxies since only $z \sim 1$." In: *MNRAS* 428.2, pp. 1460–1478. DOI: `10.1093/mnras/sts124`. arXiv: `1111.6993 [astro-ph.CO]` (cit. on pp. 23, 90).

Bundy, Kevin, Richard S. Ellis, Christopher J. Conselice, James E. Taylor, Michael C. Cooper, Christopher N. A. Willmer, Benjamin J. Weiner, Alison L. Coil, Kai G. Noeske, and Peter R. M. Eisenhardt (2006). "The Mass Assembly History of Field Galaxies: Detection of an Evolving Mass Limit for Star-Forming Galaxies." In: *ApJ* 651.1, pp. 120–141. DOI: `10.1086/`

507456. arXiv: astro-ph/0512465 [astro-ph] (cit. on pp. 18, 19, 21, 23, 81, 83).

Calzetti, D. et al. (2007). “The Calibration of Mid-Infrared Star Formation Rate Indicators.” In: *ApJ* 666.2, pp. 870–895. DOI: 10.1086/520082. arXiv: 0705.3377 [astro-ph] (cit. on p. 100).

Calzetti, D. et al. (2010). “The Calibration of Monochromatic Far-Infrared Star Formation Rate Indicators.” In: *ApJ* 714.2, pp. 1256–1279. DOI: 10.1088/0004-637X/714/2/1256. arXiv: 1003.0961 [astro-ph.CO] (cit. on p. 100).

Calzetti, Daniela, Lee Armus, Ralph C. Bohlin, Anne L. Kinney, Jan Koornneef, and Thaisa Storchi-Bergmann (2000). “The Dust Content and Opacity of Actively Star-forming Galaxies.” In: *ApJ* 533.2, pp. 682–695. DOI: 10.1086/308692. arXiv: astro-ph/9911459 [astro-ph] (cit. on p. 129).

Capak, P. et al. (2007). “The First Release COSMOS Optical and Near-IR Data and Catalog.” In: *ApJS* 172, pp. 99–116. DOI: 10.1086/519081. arXiv: 0704.2430 (cit. on p. 10).

Capak, P. et al. (2012). *SPLASH: Spitzer Large Area Survey with Hyper-Suprime-Cam*. Spitzer Proposal (cit. on p. 43).

Caputi, K. I., M. Cirasuolo, J. S. Dunlop, R. J. McLure, D. Farrah, and O. Almaini (2011). “The stellar mass function of the most-massive galaxies at $3 < z < 5$ in the UKIDSS Ultra Deep Survey.” In: *MNRAS* 413, pp. 162–176. DOI: 10.1111/j.1365-2966.2010.18118.x. arXiv: 1008.5244 (cit. on pp. 12, 22, 36–38, 54).

Caputi, K. I., O. Ilbert, C. Laigle, H. J. McCracken, O. Le Fèvre, J. Fynbo, B. Milvang-Jensen, P. Capak, M. Salvato, and Y. Taniguchi (2015). “Spitzer Bright, UltraVISTA Faint Sources in COSMOS: The Contribution to the Overall Population of Massive Galaxies at z = 3-7.” In: *ApJ* 810, 73, p. 73. DOI: 10.1088/0004-637X/810/1/73. arXiv: 1505.05721 (cit. on pp. 22, 54).

Carilli, C. L. and F. Walter (2013). “Cool Gas in High-Redshift Galaxies.” In: *ARA&A* 51, pp. 105–161. DOI: 10.1146/annurev-astro-082812-140953. arXiv: 1301.0371 (cit. on pp. 99, 101, 124–126).

Carilli, C. L., H. J. A. Röttgering, R. van Ojik, G. K. Miley, and W. J. M. van Breugel (1997). “Radio Continuum Imaging of High-Redshift Radio Galaxies.” In: *ApJS* 109.1, pp. 1–44. DOI: 10.1086/312973. arXiv: astro-ph/9610157 [astro-ph] (cit. on p. 112).

Carilli, C. L. et al. (2010). “Imaging the Molecular Gas in a Submillimeter Galaxy at z = 4.05: Cold Mode Accretion or a Major Merger?” In: *ApJ* 714.2, pp. 1407–1417. DOI: 10.1088/0004-637X/714/2/1407. arXiv: 1002.3838 [astro-ph.CO] (cit. on p. 99).

Carleton, T., R. Errani, M. Cooper, M. Kaplinghat, and J. Peñarrubia (2018). “The Formation of Ultra Diffuse Galaxies in Cored Dark Matter Halos Through Tidal Stripping and Heating.” In: *ArXiv e-prints*. arXiv: 1805.06896 (cit. on p. 21).

Carollo, C. M., A. Cibinel, S. J. Lilly, A. Pipino, S. Bonoli, A. Finoguenov, F. Miniati, P. Norberg, and J. D. Silverman (2016). “ZENS. IV. Similar Morphological Changes Associated with Mass Quenching and Environment Quenching and the Relative Importance of Bulge Growth versus the Fading of Disks*.” In: *ApJ* 818, 180, p. 180. DOI: 10.3847/0004-637X/818/2/180. arXiv: 1402.1172 (cit. on p. 19).

Carr, B. J., W. D. Arnett, and J. R. Bond (1982). "Pregalactic very massive objects and their cosmological consequences." In: *NATO Advanced Science Institutes (ASI) Series C*. Ed. by M. J. Rees and R. J. Stoneham. Vol. 90. NATO Advanced Science Institutes (ASI) Series C, pp. 313–318 (cit. on p. 1).

Carretero, Jorge et al. (2017). "CosmoHub and SciPIC: Massive cosmological data analysis, distribution and generation using a Big Data platform." In: *PoS* EPS-HEP2017, p. 488. DOI: `10.22323/1.314.0488` (cit. on pp. 7, 8, 39, 42, 43, 47, 48, 69–71, 79, 92, 147).

Casasola, V., L. Magrini, F. Combes, A. Mignano, E. Sani, R. Paladino, and F. Fontani (2013). "A gas-rich AGN near the centre of a galaxy cluster at z ˜ 1.4." In: *A&A* 558, A60, A60. DOI: `10.1051/0004-6361/201321599`. arXiv: `1307.4576` (cit. on pp. 98, 124, 138, 141).

Castignani, G. and C. Benoist (2016). "A new method to assign galaxy cluster membership using photometric redshifts." In: *A&A* 595, A111, A111. DOI: `10.1051/0004-6361/201528009`. arXiv: `1606.08744` (cit. on pp. 36, 37, 39).

Castignani, G., F. Combes, and P. Salomé (2020). "Environmental processing in cluster core galaxies at z = 1.7." In: *A&A* 635, L10, p. L10. DOI: `10.1051/0004-6361/201937155`. arXiv: `2001.05776 [astro-ph.GA]` (cit. on p. 96).

Castignani, G. et al. (2018). "Molecular gas in two companion cluster galaxies at z=1.2." In: *ArXiv e-prints*. arXiv: `1806.01826` (cit. on pp. 98, 100, 124, 126, 138–141).

Cattaneo, A., A. Dekel, J. Devriendt, B. Guiderdoni, and J. Blaizot (2006). "Modelling the galaxy bimodality: shutdown above a critical halo mass." In: *MNRAS* 370.4, pp. 1651–1665. DOI: `10.1111/j.1365-2966.2006.10608.x`. arXiv: `astro-ph/0601295 [astro-ph]` (cit. on pp. 13, 15, 17, 23).

Cattaneo, A., G. A. Mamon, K. Warnick, and A. Knebe (2011). "How do galaxies acquire their mass?" In: *A&A* 533, A5, A5. DOI: `10.1051/0004-6361/201015780`. arXiv: `1002.3257 [astro-ph.CO]` (cit. on pp. 13, 15).

Chabrier, G. (2003). "Galactic Stellar and Substellar Initial Mass Function." In: *PASP* 115, pp. 763–795. DOI: `10.1086/376392`. eprint: `astro-ph/0304382` (cit. on pp. 5, 101, 128).

Chapman, S. C., F. Bertoldi, I. Smail, A. W. Blain, J. E. Geach, M. Gurwell, R. J. Ivison, G. R. Petitpas, N. Reddy, and C. C. Steidel (2015). "A blind CO detection of a distant red galaxy in the HS1700+64 protocluster." In: *MNRAS* 449, pp. L68–L72. DOI: `10.1093/mnrasl/slv010`. arXiv: `1501.02839` (cit. on p. 98).

Chiang, Y.-K., R. A. Overzier, K. Gebhardt, and B. Henriques (2017). "Galaxy Protoclusters as Drivers of Cosmic Star Formation History in the First 2 Gyr." In: *ApJ* 844, L23, p. L23. DOI: `10.3847/2041-8213/aa7e7b`. arXiv: `1705.01634` (cit. on p. 98).

Choloniewski, J. (1986). "New method for the determination of the luminosity function of galaxies." In: *MNRAS* 223, pp. 1–9. DOI: `10.1093/mnras/223.1.1` (cit. on p. 32).

Cicone, C. et al. (2014). "Massive molecular outflows and evidence for AGN feedback from CO observations." In: *A&A* 562, A21, A21. DOI: `10.1051/0004-6361/201322464`. arXiv: `1311.2595` (cit. on pp. 6, 96, 137).

Cicone, C., R. Maiolino, S. Gallerani, R. Neri, A. Ferrara, E. Sturm, F. Fiore, E. Piconcelli, and C. Feruglio (2015). "Very extended cold gas, star formation and outflows in the halo of a bright quasar at z > 6." In: *A&A* 574, A14, A14. DOI: `10.1051/0004-6361/201424980`. arXiv: `1409.4418 [astro-ph.GA]` (cit. on p. 99).

Cicone, C. et al. (2018). "ALMA [C I]^3 P $_1$–^{3} P $_0$ Observations of NGC 6240: A Puzzling Molecular Outflow, and the Role of Outflows in the Global α $_{\rm CO}$ Factor of (U)LIRGs." In: *ApJ* 863, 143, p. 143. DOI: `10.3847/1538-4357/aad32a`. arXiv: `1807.06015` (cit. on pp. 95, 96, 125, 135).

Cielo, S., R. Bieri, M. Volonteri, A. Y. Wagner, and Y. Dubois (2018). "AGN feedback compared: jets versus radiation." In: *MNRAS* 477, pp. 1336–1355. DOI: `10.1093/mnras/sty708`. arXiv: `1712.03955` (cit. on p. 135).

Cohen, A. S., W. M. Lane, W. D. Cotton, N. E. Kassim, T. J. W. Lazio, R. A. Perley, J. J. Condon, and W. C. Erickson (2007). "The VLA Low-Frequency Sky Survey." In: *AJ* 134.3, pp. 1245–1262. DOI: `10.1086/520719`. arXiv: `0706.1191 [astro-ph]` (cit. on p. 114).

Cole, S. (2011). "Maximum likelihood random galaxy catalogues and luminosity function estimation." In: *MNRAS* 416, pp. 739–746. DOI: `10.1111/j.1365-2966.2011.19093.x`. arXiv: `1104.0009` (cit. on p. 29).

Cole, S., A. Aragon-Salamanca, C. S. Frenk, J. F. Navarro, and S. E. Zepf (1994). "A recipe for galaxy formation." In: *MNRAS* 271, pp. 781–806. DOI: `10.1093/mnras/271.4.781`. arXiv: `astro-ph/9402001 [astro-ph]` (cit. on p. 4).

Cole, Shaun, Cedric G. Lacey, Carlton M. Baugh, and Carlos S. Frenk (2000). "Hierarchical galaxy formation." In: *MNRAS* 319.1, pp. 168–204. DOI: `10.1046/j.1365-8711.2000.03879.x`. arXiv: `astro-ph/0007281 [astro-ph]` (cit. on p. 4).

Colla, G. et al. (1973). "The B2 catalogue of radio sources - third part." In: *A&AS* 11, p. 291 (cit. on p. 114).

Collister, A. et al. (2007). "MegaZ-LRG: a photometric redshift catalogue of one million SDSS luminous red galaxies." In: *MNRAS* 375, pp. 68–76. DOI: `10.1111/j.1365-2966.2006.11305.x`. eprint: `astro-ph/0607630` (cit. on p. 12).

Combes, Françoise (2018). "Molecular gas in distant galaxies from ALMA studies." In: *A&A Rev.* 26.1, 5, p. 5. DOI: `10.1007/s00159-018-0110-4`. arXiv: `1806.06712 [astro-ph.GA]` (cit. on pp. 124, 126).

Condon, J. J. (1989). "The 1.4 gigahertz luminosity function and its evolution." In: *ApJ* 338, pp. 13–23. DOI: `10.1086/167176` (cit. on p. 29).

Condon, J. J. (1992). "Radio emission from normal galaxies." In: *ARA&A* 30, pp. 575–611. DOI: `10.1146/annurev.aa.30.090192.003043` (cit. on p. 100).

Condon, J. J., W. D. Cotton, E. W. Greisen, Q. F. Yin, R. A. Perley, G. B. Taylor, and J. J. Broderick (1998). "The NRAO VLA Sky Survey." In: *AJ* 115.5, pp. 1693–1716. DOI: `10.1086/300337` (cit. on p. 114).

Connolly, A. J., I. Csabai, A. S. Szalay, D. C. Koo, R. G. Kron, and J. A. Munn (1995). "Slicing Through Multicolor Space: Galaxy Redshifts from Broadband Photometry." In: *AJ* 110, p. 2655. DOI: `10.1086/117720`. eprint: `astro-ph/9508100` (cit. on pp. 11, 12, 35, 36).

Connolly, A. J., A. S. Szalay, M. Dickinson, M. U. SubbaRao, and R. J. Brunner (1997). "The Evolution of the Global Star Formation History as Measured from the Hubble Deep Field." In: *ApJ* 486, pp. L11–L14. DOI: `10.1086/310829`. eprint: `astro-ph/9706255` (cit. on p. 12).

Conroy, Charlie (2013). "Modeling the Panchromatic Spectral Energy Distributions of Galaxies." In: *ARA&A* 51.1, pp. 393–455. DOI: `10.1146/annurev-astro-082812-141017`. arXiv: `1301.7095 [astro-ph.CO]` (cit. on p. 12).

Conroy, Charlie, James E. Gunn, and Martin White (2009). "The Propagation of Uncertainties in Stellar Population Synthesis Modeling. I. The Relevance of Uncertain Aspects of Stellar Evolution and the Initial Mass Function to the Derived Physical Properties of Galaxies." In: *ApJ* 699.1, pp. 486–506. DOI: `10.1088/0004-637X/699/1/486`. arXiv: `0809.4261 [astro-ph]` (cit. on p. 12).

Coogan, R. T. et al. (2018). "Merger driven star-formation activity in Cl J1449+0856 at z=1.99 as seen by ALMA and JVLA." In: *ArXiv e-prints*. arXiv: `1805.09789` (cit. on pp. 98, 124, 138–141).

Cooke, E. A. et al. (2015). "The formation history of massive cluster galaxies as revealed by CARLA." In: *MNRAS* 452, pp. 2318–2336. DOI: `10.1093/mnras/stv1413`. arXiv: `1507.00350` (cit. on pp. 102, 103).

Cooper, A. P. et al. (2010). "Galactic stellar haloes in the CDM model." In: *MNRAS* 406.2, pp. 744–766. DOI: `10.1111/j.1365-2966.2010.16740.x`. arXiv: `0910.3211 [astro-ph.GA]` (cit. on p. 21).

Cooper, M. C. et al. (2008). "The DEEP2 Galaxy Redshift Survey: the role of galaxy environment in the cosmic star formation history." In: *MNRAS* 383, pp. 1058–1078. DOI: `10.1111/j.1365-2966.2007.12613.x`. arXiv: `0706.4089` (cit. on p. 98).

Cora, S. A., T. Hough, C. A. Vega-Martínez, and Á. Orsi (2018). "Semi-Analytic Galaxies - II. Revealing the role of environmental and mass quenching in galaxy formation." In: *ArXiv e-prints*. arXiv: `1801.03884` (cit. on p. 19).

Costa, T., D. Sijacki, and M. G. Haehnelt (2015). "Fast cold gas in hot AGN outflows." In: *MNRAS* 448, pp. L30–L34. DOI: `10.1093/mnrasl/slu193`. arXiv: `1411.0678` (cit. on pp. 95–97, 134).

Cowie, L. L. and J. Binney (1977). "Radiative regulation of gas flow within clusters of galaxies: a model for cluster X-ray sources." In: *ApJ* 215, pp. 723–732. DOI: `10.1086/155406` (cit. on p. 16).

Cowie, Lennox L., Antoinette Songaila, Esther M. Hu, and J. G. Cohen (1996). "New Insight on Galaxy Formation and Evolution From Keck Spectroscopy of the Hawaii Deep Fields." In: *AJ* 112, p. 839. DOI: `10.1086/118058`. arXiv: `astro-ph/9606079 [astro-ph]` (cit. on pp. 18, 81, 93).

Croom, S. M. et al. (2009). "The 2dF-SDSS LRG and QSO survey: the QSO luminosity function at $0.4 < z < 2.6$." In: *MNRAS* 399, pp. 1755–1772. DOI: `10.1111/j.1365-2966.2009.15398.x`. arXiv: `0907.2727` (cit. on p. 29).

Cropper, M. et al. (2016). "VIS: the visible imager for Euclid." In: *Space Telescopes and Instrumentation 2016: Optical, Infrared, and Millimeter Wave*. Vol. 9904. *Proc. SPIE*, 99040Q. DOI: `10.1117/12.2234739`. arXiv: `1608.08603 [astro-ph.IM]` (cit. on p. 40).

Croton, D. J. et al. (2005). "The 2dF Galaxy Redshift Survey: luminosity functions by density environment and galaxy type." In: *MNRAS* 356, pp. 1155–1167. doi: 10.1111/j.1365-2966.2004.08546.x. eprint: astro-ph/0407537 (cit. on p. 25).

Croton, D. J., V. Springel, S. D. M. White, G. De Lucia, C. S. Frenk, L. Gao, A. Jenkins, G. Kauffmann, J. F. Navarro, and N. Yoshida (2006). “The many lives of active galactic nuclei: cooling flows, black holes and the luminosities and colours of galaxies.” In: *MNRAS* 365, pp. 11–28. doi: 10.1111/j.1365-2966.2005.09675.x. eprint: astro-ph/0508046 (cit. on pp. 19, 97).

Cucciati, O. et al. (2012). “The star formation rate density and dust attenuation evolution over 12 Gyr with the VVDS surveys.” In: *A&A* 539, A31, A31. doi: 10.1051/0004-6361/201118010. arXiv: 1109.1005 [astro-ph.CO] (cit. on p. 19).

Curti, Mirko, Filippo Mannucci, Giovanni Cresci, and Roberto Maiolino (2020). “The mass-metallicity and the fundamental metallicity relation revisited on a fully T_e-based abundance scale for galaxies.” In: *MNRAS* 491.1, pp. 944–964. doi: 10.1093/mnras/stz2910. arXiv: 1910.00597 [astro-ph.GA] (cit. on pp. 129, 130).

Dahlen, Tomas et al. (2013). “A Critical Assessment of Photometric Redshift Methods: A CANDELS Investigation.” In: *ApJ* 775.2, 93, p. 93. doi: 10.1088/0004-637X/775/2/93. arXiv: 1308.5353 [astro-ph.CO] (cit. on pp. 12, 36, 37).

Dalgarno, A. and R. A. McCray (1972). “Heating and Ionization of HI Regions.” In: *ARA&A* 10, p. 375. doi: 10.1146/annurev.aa.10.090172.002111 (cit. on p. 5).

Dannerbauer, H., E. Daddi, D. A. Riechers, F. Walter, C. L. Carilli, M. Dickinson, D. Elbaz, and G. E. Morrison (2009). “Low Milky-Way-Like Molecular Gas Excitation of Massive Disk Galaxies at z ˜ 1.5.” In: *ApJ* 698, pp. L178–L182. doi: 10.1088/0004-637X/698/2/L178. arXiv: 0905.3637 [astro-ph.CO] (cit. on p. 124).

Dannerbauer, H. et al. (2017). “The implications of the surprising existence of a large, massive CO disk in a distant protocluster.” In: *A&A* 608, A48, A48. doi: 10.1051/0004-6361/201730449. arXiv: 1701.05250 (cit. on pp. 95, 100, 138, 140, 141).

Darvish, B., B. Mobasher, D. Sobral, A. Rettura, N. Scoville, A. Faisst, and P. Capak (2016). “The Effects of the Local Environment and Stellar Mass on Galaxy Quenching to $z \sim 3$.” In: *ApJ* 825, 113, p. 113. doi: 10.3847/0004-637X/825/2/113. arXiv: 1605.03182 (cit. on pp. 18, 19).

Darvish, B., N. Z. Scoville, C. Martin, B. Mobasher, T. Diaz-Santos, and L. Shen (2018a). “Similar Scaling Relations for the Gas Content of Galaxies Across Environments to $z \sim 3.5$.” In: *ApJ* 860, 111, p. 111. doi: 10.3847/1538-4357/aac836. arXiv: 1805.10291 (cit. on p. 100).

Darvish, Behnam, Christopher Martin, Thiago S. Gonçalves, Bahram Mobasher, Nick Z. Scoville, and David Sobral (2018b). “Quenching or Bursting: The Role of Stellar Mass, Environment, and Specific Star Formation Rate to z 1.” In: *ApJ* 853.2, 155, p. 155. doi: 10.3847/1538-4357/aaa5a4. arXiv: 1801.02618 [astro-ph.GA] (cit. on p. 19).

Dasyra, K. M., F. Combes, P. Salomé, and J. Braine (2012). “Survival of molecular gas in Virgo’s hot intracluster medium: CO near M 86.” In: *A&A* 540, A112, A112. DOI: 10.1051/0004-6361/201218775. arXiv: 1202.1763 (cit. on p. 95).

Davidzon, I. et al. (2016). "The VIMOS Public Extragalactic Redshift Survey (VIPERS). Environmental effects shaping the galaxy stellar mass function." In: *A&A* 586, A23, A23. DOI: 10.1051/0004-6361/201527129. arXiv: 1511.01145 [astro-ph.GA] (cit. on p. 25).

Davidzon, I. et al. (2017). "The COSMOS2015 galaxy stellar mass function . Thirteen billion years of stellar mass assembly in ten snapshots." In: *A&A* 605, A70, A70. DOI: 10.1051/0004-6361/201730419. arXiv: 1701.02734 (cit. on pp. iii, 10–13, 20, 22, 23, 25, 27, 35, 38, 39, 43, 45–49, 51, 53–55, 57, 60, 61, 63–66, 72–77, 80, 81, 85–90, 92–95, 147, 148).

Davidzon, Iary, Olivier Ilbert, Andreas L. Faisst, Martin Sparre, and Peter L. Capak (2018). "An Alternate Approach to Measure Specific Star Formation Rates at 2< z< 7." In: *ApJ* 852.2, 107, p. 107. DOI: 10.3847/1538-4357/aaa19e. arXiv: 1712.03959 [astro-ph.GA] (cit. on p. 136).

Davis, M. and J. Huchra (1982). "A survey of galaxy redshifts. III - The density field and the induced gravity field." In: *ApJ* 254, pp. 437–450. DOI: 10.1086/159751 (cit. on p. 30).

Davis, M., G. Efstathiou, C. S. Frenk, and S. D. M. White (1985). "The evolution of large-scale structure in a universe dominated by cold dark matter." In: *ApJ* 292, pp. 371–394. DOI: 10.1086/163168 (cit. on pp. 2, 7).

Davis, Marc et al. (2003). "Science Objectives and Early Results of the DEEP2 Redshift Survey." In: *Proc. SPIE*. Ed. by Puragra Guhathakurta. Vol. 4834. Society of Photo-Optical Instrumentation Engineers (SPIE) Conference Series, pp. 161–172. DOI: 10.1117/12.457897. arXiv: astro-ph/0209419 [astro-ph] (cit. on p. 9).

Davis, T. A., F. van de Voort, K. Rowlands, S. McAlpine, V. Wild, and R. A. Crain (2018). "Evolution of the cold gas properties of simulated post-starburst galaxies." In: *arXiv e-prints*. arXiv: 1810.00882 (cit. on p. 95).

De Lucia, Gabriella and Jérémy Blaizot (2007). "The hierarchical formation of the brightest cluster galaxies." In: *MNRAS* 375.1, pp. 2–14. DOI: 10.1111/j.1365-2966.2006.11287.x. arXiv: astro-ph/0606519 [astro-ph] (cit. on p. 7).

De Lucia, Gabriella, Guinevere Kauffmann, and Simon D. M. White (2004). "Chemical enrichment of the intracluster and intergalactic medium in a hierarchical galaxy formation model." In: *MNRAS* 349.3, pp. 1101–1116. DOI: 10.1111/j.1365-2966.2004.07584.x. arXiv: astro-ph/0310268 [astro-ph] (cit. on pp. 6, 17).

Decarli, Roberto et al. (2019). "The ALMA Spectroscopic Survey in the HUDF: CO Luminosity Functions and the Molecular Gas Content of Galaxies through Cosmic History." In: *ApJ* 882.2, 138, p. 138. DOI: 10.3847/1538-4357/ab30fe. arXiv: 1903.09164 [astro-ph.GA] (cit. on p. 19).

Dekel, A. and Y. Birnboim (2006). "Galaxy bimodality due to cold flows and shock heating." In: *MNRAS* 368, pp. 2–20. DOI: 10.1111/j.1365-2966.2006.10145.x. eprint: astro-ph/0412300 (cit. on pp. 13, 15–18).

Dekel, A., Y. Birnboim, G. Engel, J. Freundlich, T. Goerdt, M. Mumcuoglu, E. Neistein, C. Pichon, R. Teyssier, and E. Zinger (2009). "Cold streams in early massive hot haloes as the main mode of galaxy formation." In:

Nature 457.7228, pp. 451–454. DOI: 10.1038/nature07648. arXiv: 0808.0553 [astro-ph] (cit. on pp. 15, 16).

Delaye, L. et al. (2014). “Larger sizes of massive quiescent early-type galaxies in clusters than in the field at $0.8 < z < 1.5$.” In: *MNRAS* 441, pp. 203–223. DOI: 10.1093/mnras/stu496. arXiv: 1307.0003 (cit. on pp. 21, 81).

Devereux, Nicholas A. and Salman Hameed (1997). “Massive Star Formation Along the Hubble Sequence.” In: *AJ* 113, p. 599. DOI: 10.1086/118279 (cit. on p. 100).

Di Matteo, Tiziana, Volker Springel, and Lars Hernquist (2005). “Energy input from quasars regulates the growth and activity of black holes and their host galaxies.” In: *Nature* 433.7026, pp. 604–607. DOI: 10.1038/nature03335. arXiv: astro-ph/0502199 [astro-ph] (cit. on p. 14).

Domínguez Sánchez, H. et al. (2011). “The evolution of quiescent galaxies at high redshifts ($z \geqslant 1.4$).” In: *MNRAS* 417.2, pp. 900–915. DOI: 10.1111/j.1365-2966.2011.19263.x. arXiv: 1106.3194 [astro-ph.CO] (cit. on p. 25).

Donas, J. and J. M. Deharveng (1984). “Ultraviolet luminosities and colors of spiral and irregular galaxies. The present-day star formation rate.” In: *A&A* 140, pp. 325–333 (cit. on p. 100).

Douglas, James N., Frank N. Bash, F. Arakel Bozyan, Geoffrey W. Torrence, and Chip Wolfe (1996). “The Texas Survey of Radio Sources Covering -35.5 degrees < declination < 71.5 degrees at 365 MHz.” In: *AJ* 111, p. 1945. DOI: 10.1086/117932 (cit. on p. 114).

Dressler, A. (1980). “Galaxy morphology in rich clusters - Implications for the formation and evolution of galaxies.” In: *ApJ* 236, pp. 351–365. DOI: 10.1086/157753 (cit. on p. 98).

Driver, S. P. and A. S. G. Robotham (2010). “Quantifying cosmic variance.” In: *MNRAS* 407, pp. 2131–2140. DOI: 10.1111/j.1365-2966.2010.17028.x. arXiv: 1005.2538 (cit. on p. 35).

Dubois, Y., S. Peirani, C. Pichon, J. Devriendt, R. Gavazzi, C. Welker, and M. Volonteri (2016). “The HORIZON-AGN simulation: morphological diversity of galaxies promoted by AGN feedback.” In: *MNRAS* 463, pp. 3948–3964. DOI: 10.1093/mnras/stw2265. arXiv: 1606.03086 (cit. on pp. 8, 13, 14, 21).

Eales, S. (1993). “Direct construction of the galaxy luminosity function as a function of redshift.” In: *ApJ* 404, pp. 51–62. DOI: 10.1086/172257 (cit. on p. 29).

Eales, Stephen, Steve Rawlings, Duncan Law-Green, Garret Cotter, and Mark Lacy (1997). “A first sample of faint radio sources with virtually complete redshifts - I. Infrared images, the Hubble diagram and the alignment effect.” In: *MNRAS* 291.4, pp. 593–615. DOI: 10.1093/mnras/291.4.593. arXiv: astro-ph/9701023 [astro-ph] (cit. on p. 103).

Eddington, A. S. (1913). “On a formula for correcting statistics for the effects of a known error of observation.” In: *MNRAS* 73, pp. 359–360. DOI: 10.1093/mnras/73.5.359 (cit. on p. 37).

Edge, A. C. (2001). “The detection of molecular gas in the central galaxies of cooling flow clusters.” In: *MNRAS* 328.3, pp. 762–782. DOI: 10.1046/j.1365-8711.2001.04802.x. arXiv: astro-ph/0106225 [astro-ph] (cit. on pp. 16, 150).

Edge, A. C., G. C. Stewart, and A. C. Fabian (1992). "Properties of cooling flows in a flux-limited sample of clusters of galaxies." In: *MNRAS* 258, pp. 177–188. DOI: `10.1093/mnras/258.1.177` (cit. on p. 16).

Edge, A. C., R. J. Wilman, R. M. Johnstone, C. S. Crawford, A. C. Fabian, and S. W. Allen (2002). "A survey of molecular hydrogen in the central galaxies of cooling flows." In: *MNRAS* 337.1, pp. 49–62. DOI: `10.1046/j.1365-8711.2002.05790.x`. arXiv: `astro-ph/0206379 [astro-ph]` (cit. on p. 16).

Edge, Alastair C. and David T. Frayer (2003). "Resolving Molecular gas in the Central Galaxies of Cooling Flow Clusters." In: *ApJ* 594.1, pp. L13–L17. DOI: `10.1086/378386` (cit. on p. 16).

Edwards, Louise O. V., Michael J. Hudson, Michael L. Balogh, and Russell J. Smith (2007). "Line emission in the brightest cluster galaxies of the NOAO Fundamental Plane and Sloan Digital Sky Surveys." In: *MNRAS* 379.1, pp. 100–110. DOI: `10.1111/j.1365-2966.2007.11910.x`. arXiv: `0704.3242 [astro-ph]` (cit. on p. 16).

Efstathiou, G., R. S. Ellis, and B. A. Peterson (1988). "Analysis of a complete galaxy redshift survey. II - The field-galaxy luminosity function." In: *MNRAS* 232, pp. 431–461. DOI: `10.1093/mnras/232.2.431` (cit. on pp. 30, 31, 39).

Efstathiou, G. and J. Silk (1983). "The Formation of Galaxies." In: *Fund. Cosmic Phys.* 9, pp. 1–138 (cit. on p. 4).

Einstein, A. (1916). "Die Grundlage der allgemeinen Relativitätstheorie." In: *Annalen der Physik* 354.7, pp. 769–822. DOI: `10.1002/andp.19163540702` (cit. on p. 1).

Eisenstein, Daniel J. et al. (2005). "Detection of the Baryon Acoustic Peak in the Large-Scale Correlation Function of SDSS Luminous Red Galaxies." In: *ApJ* 633.2, pp. 560–574. DOI: `10.1086/466512`. arXiv: `astro-ph/0501171 [astro-ph]` (cit. on p. 2).

Elbaz, D. et al. (2007). "The reversal of the star formation-density relation in the distant universe." In: *A&A* 468, pp. 33–48. DOI: `10.1051/0004-6361:20077525`. eprint: `astro-ph/0703653` (cit. on pp. 18, 98, 139).

Ellis, Richard S., Matthew Colless, Tom Broadhurst, Jeremy Heyl, and Karl Glazebrook (1996). "Autofib Redshift Survey - I. Evolution of the galaxy luminosity function." In: *MNRAS* 280.1, pp. 235–251. DOI: `10.1093/mnras/280.1.235`. arXiv: `astro-ph/9512057 [astro-ph]` (cit. on p. 9).

Ellis, Richard S. et al. (2013). "The Abundance of Star-forming Galaxies in the Redshift Range 8.5-12: New Results from the 2012 Hubble Ultra Deep Field Campaign." In: *ApJ* 763.1, L7, p. L7. DOI: `10.1088/2041-8205/763/1/L7`. arXiv: `1211.6804 [astro-ph.CO]` (cit. on p. 5).

Emonts, B. H. C. et al. (2013). "CO(1-0) detection of molecular gas in the massive Spiderweb Galaxy (z = 2)." In: *MNRAS* 430, pp. 3465–3471. DOI: `10.1093/mnras/stt147`. arXiv: `1301.6012` (cit. on p. 95).

Emonts, B. H. C. et al. (2014). "CO(1-0) survey of high-z radio galaxies: alignment of molecular halo gas with distant radio sources." In: *MNRAS* 438, pp. 2898–2915. DOI: `10.1093/mnras/stt2398`. arXiv: `1312.4785` (cit. on pp. 96, 97, 137, 138, 151, 152).

Emonts, B. H. C. et al. (2015). "The Dragonfly Galaxy. II. ALMA unveils a triple merger and gas exchange in a hyper-luminous radio galaxy at z =

2." In: *A&A* 584, A99, A99. DOI: 10.1051/0004-6361/201526090. arXiv: 1510.02381 (cit. on p. 95).

Emonts, Bjorn, Zheng Cai, Xavier Prochaska, Qiong Li, and Matthew Lehnert (2019). "The cold circumgalactic environment of MAMMOTH-I: dynamically cold gas in the core of an Enormous Ly-alpha Nebula." In: *arXiv e-prints*, arXiv:1911.05053, arXiv:1911.05053. arXiv: 1911.05053 [astro-ph.GA] (cit. on pp. 96, 97, 137).

Erb, D. K., A. E. Shapley, M. Pettini, C. C. Steidel, N. A. Reddy, and K. L. Adelberger (2006). "The Mass-Metallicity Relation at z>~2." In: *ApJ* 644, pp. 813–828. DOI: 10.1086/503623. eprint: astro-ph/0602473 (cit. on p. 131).

Euclid Collaboration et al. (2019). "Euclid preparation. IV. Impact of undetected galaxies on weak-lensing shear measurements." In: *A&A* 627, A59, A59. DOI: 10.1051/0004-6361/201935187. arXiv: 1902.00044 (cit. on p. 41).

Evrard, August E. (1988). "Beyond N-body: 3D cosmological gas dynamics." In: *MNRAS* 235, pp. 911–934. DOI: 10.1093/mnras/235.3.911 (cit. on p. 7).

Evrard, August E. (1990). "Formation and Evolution of X-Ray Clusters: A Hydrodynamic Simulation of the Intracluster Medium." In: *ApJ* 363, p. 349. DOI: 10.1086/169350 (cit. on p. 4).

Faber, S. M. et al. (2007). "Galaxy Luminosity Functions to z~1 from DEEP2 and COMBO-17: Implications for Red Galaxy Formation." In: *ApJ* 665.1, pp. 265–294. DOI: 10.1086/519294. arXiv: astro-ph/0506044 [astro-ph] (cit. on pp. 15, 18, 23, 25, 26).

Fabian, A. C. (1994). "Cooling Flows in Clusters of Galaxies." In: *ARA&A* 32, pp. 277–318. DOI: 10.1146/annurev.aa.32.090194.001425 (cit. on pp. 6, 15, 16, 150).

Fabian, A. C. (2012). "Observational Evidence of Active Galactic Nuclei Feedback." In: *ARA&A* 50, pp. 455–489. DOI: 10.1146/annurev-astro-081811-125521. arXiv: 1204.4114 (cit. on pp. 17, 19).

Fan, J. H. and J. S. Zhang (2003). "The core dominance parameter of extragalactic radio sources." In: *A&A* 407, pp. 899–904. DOI: 10.1051/0004-6361:20030896 (cit. on p. 136).

Fan, Xiaohui, C. L. Carilli, and B. Keating (2006). "Observational Constraints on Cosmic Reionization." In: *ARA&A* 44.1, pp. 415–462. DOI: 10.1146/annurev.astro.44.051905.092514. arXiv: astro-ph/0602375 [astro-ph] (cit. on pp. 2, 5).

Farouki, R. and S. L. Shapiro (1981). "Computer simulations of environmental influences on galaxy evolution in dense clusters. II - Rapid tidal encounters." In: *ApJ* 243, pp. 32–41. DOI: 10.1086/158563 (cit. on p. 21).

Fassbender, R. et al. (2011). "The X-ray luminous galaxy cluster XMMU J1007.4+1237 at z = 1.56. The dawn of starburst activity in cluster cores." In: *A&A* 527, L10, p. L10. DOI: 10.1051/0004-6361/201016169. arXiv: 1101.3313 (cit. on p. 98).

Felten, J. E. (1976). "On Schmidt's Vm estimator and other estimators of luminosity functions." In: *ApJ* 207, pp. 700–709. DOI: 10.1086/154538 (cit. on p. 28).

Fernández-Soto, Alberto, Kenneth M. Lanzetta, and Amos Yahil (1999). "A New Catalog of Photometric Redshifts in the Hubble Deep Field." In:

ApJ 513.1, pp. 34–50. DOI: 10.1086/306847. arXiv: astro-ph/9809126 [astro-ph] (cit. on p. 9).

Finkelstein, S. L. et al. (2013). “A galaxy rapidly forming stars 700 million years after the Big Bang at redshift 7.51.” In: *Nature* 502.7472, pp. 524–527. DOI: 10.1038/nature12657. arXiv: 1310.6031 [astro-ph.CO] (cit. on p. 5).

Firth, A. E., O. Lahav, and R. S. Somerville (2003). “Estimating photometric redshifts with artificial neural networks.” In: *MNRAS* 339, pp. 1195–1202. DOI: 10.1046/j.1365-8711.2003.06271.x. eprint: astro-ph/0203250 (cit. on p. 12).

Folkes, S. et al. (1999). “The 2dF Galaxy Redshift Survey: spectral types and luminosity functions.” In: *MNRAS* 308, pp. 459–472. DOI: 10.1046/j.1365-8711.1999.02721.x. eprint: astro-ph/9903456 (cit. on p. 9).

Foltz, R. et al. (2018). “The Evolution of Environmental Quenching Timescales to z~1.6: Evidence for Dynamically Driven Quenching of the Cluster Galaxy Population.” In: *ApJ* 866, 136, p. 136. DOI: 10.3847/1538-4357/aad80d (cit. on pp. 21, 81).

Fontana, A. et al. (2004). “The K20 survey. VI. The distribution of the stellar masses in galaxies up to z = 2.” In: *A&A* 424, pp. 23–42. DOI: 10.1051/0004-6361:20035626. arXiv: astro-ph/0405055 [astro-ph] (cit. on pp. 22, 23, 90).

Fontana, A. et al. (2009). “The fraction of quiescent massive galaxies in the early Universe.” In: *A&A* 501.1, pp. 15–20. DOI: 10.1051/0004-6361/200911650. arXiv: 0901.2898 [astro-ph.GA] (cit. on pp. 23, 90).

Foreman-Mackey, D., D. W. Hogg, D. Lang, and J. Goodman (2013). “emcee: The MCMC Hammer.” In: *PASP* 125, p. 306. DOI: 10.1086/670067. arXiv: 1202.3665 [astro-ph.IM] (cit. on pp. 57, 60, 68).

Foreman-Mackey, Daniel (2016). “corner.py: Scatterplot matrices in Python.” In: *The Journal of Open Source Software* 24. DOI: 10.21105/joss.00024. URL: http://dx.doi.org/10.5281/zenodo.45906 (cit. on pp. 59, 60, 67).

Franco, M. et al. (2018). “GOODS-ALMA: 1.1 mm galaxy survey. I. Source catalog and optically dark galaxies.” In: *A&A* 620, A152, A152. DOI: 10.1051/0004-6361/201832928. arXiv: 1803.00157 [astro-ph.GA] (cit. on pp. 96, 136).

Fraternali, Filippo (2017). “Gas Accretion via Condensation and Fountains.” In: *Gas Accretion onto Galaxies*. Ed. by Andrew Fox and Romeel Davé. Vol. 430. Astrophysics and Space Science Library, p. 323. DOI: 10.1007/978-3-319-52512-9_14 (cit. on p. 17).

Fuentes, A., J. L. Gómez, J. M. Martí, and M. Perucho (2018). “Total and Linearly Polarized Synchrotron Emission from Overpressured Magnetized Relativistic Jets.” In: *ApJ* 860, 121, p. 121. DOI: 10.3847/1538-4357/aac091. arXiv: 1804.01928 [astro-ph.HE] (cit. on p. 111).

Gabasch, A. et al. (2004). “The evolution of the luminosity functions in the FORS Deep Field from low to high redshift. I. The blue bands.” In: *A&A* 421, pp. 41–58. DOI: 10.1051/0004-6361:20035909. eprint: astro-ph/0403535 (cit. on p. 11).

Gallagher, J. S., H. Bushouse, and D. A. Hunter (1989). “Star Formation Rates and [O II] Emission in Blue Galaxies.” In: *AJ* 97, p. 700. DOI: 10.1086/115015 (cit. on p. 100).

Gamow, G. (1946). "Expanding Universe and the Origin of Elements." In: *Physical Review* 70.7-8, pp. 572–573. DOI: `10.1103/PhysRev.70.572.2` (cit. on p. 2).

Gamow, G. and E. Teller (1939). "On the Origin of Great Nebulae." In: *Physical Review* 55.7, pp. 654–657. DOI: `10.1103/PhysRev.55.654` (cit. on pp. 1, 5).

Gardner, J. P. et al. (2006). "The James Webb Space Telescope." In: *Space Sci. Rev.* 123, pp. 485–606. DOI: `10.1007/s11214-006-8315-7`. eprint: `astro-ph/0606175` (cit. on pp. 5, 10).

Garn, T. and P. N. Best (2010). "Predicting dust extinction from the stellar mass of a galaxy." In: *MNRAS* 409, pp. 421–432. DOI: `10.1111/j.1365-2966.2010.17321.x`. arXiv: `1007.1145` (cit. on p. 129).

Garrison-Kimmel, Shea, Michael Boylan-Kolchin, James S. Bullock, and Kyle Lee (2014). "ELVIS: Exploring the Local Volume in Simulations." In: *MNRAS* 438.3, pp. 2578–2596. DOI: `10.1093/mnras/stt2377`. arXiv: `1310.6746 [astro-ph.CO]` (cit. on p. 8).

Gaspari, M., M. Ruszkowski, and P. Sharma (2012). "Cause and Effect of Feedback: Multiphase Gas in Cluster Cores Heated by AGN Jets." In: *ApJ* 746, 94, p. 94. DOI: `10.1088/0004-637X/746/1/94`. arXiv: `1110.6063` (cit. on pp. 16, 95–97).

Gaspari, M. and A. Sądowski (2017). "Unifying the Micro and Macro Properties of AGN Feeding and Feedback." In: *ApJ* 837, 149, p. 149. DOI: `10.3847/1538-4357/aa61a3`. arXiv: `1701.07030 [astro-ph.HE]` (cit. on pp. 96, 97).

Geller, Margaret J. and John P. Huchra (1989). "Mapping the Universe." In: *Science* 246.4932, pp. 897–903. DOI: `10.1126/science.246.4932.897` (cit. on p. 9).

Genzel, R. et al. (2010). "A study of the gas-star formation relation over cosmic time." In: *MNRAS* 407.4, pp. 2091–2108. DOI: `10.1111/j.1365-2966.2010.16969.x`. arXiv: `1003.5180 [astro-ph.CO]` (cit. on p. 18).

Genzel, R. et al. (2012). "The Metallicity Dependence of the CO H_2 Conversion Factor in z >= 1 Star-forming Galaxies." In: *ApJ* 746, 69, p. 69. DOI: `10.1088/0004-637X/746/1/69`. arXiv: `1106.2098` (cit. on p. 124).

Genzel, R. et al. (2015). "Combined CO and Dust Scaling Relations of Depletion Time and Molecular Gas Fractions with Cosmic Time, Specific Star-formation Rate, and Stellar Mass." In: *ApJ* 800, 20, p. 20. DOI: `10.1088/0004-637X/800/1/20`. arXiv: `1409.1171` (cit. on pp. 99, 100, 124).

George, M. R. et al. (2011). "Galaxies in X-Ray Groups. I. Robust Membership Assignment and the Impact of Group Environments on Quenching." In: *ApJ* 742, 125, p. 125. DOI: `10.1088/0004-637X/742/2/125`. arXiv: `1109.6040` (cit. on pp. 36, 37).

Gershtein, S. S. and Ya. B. Zel'dovich (1966). "Rest Mass of Muonic Neutrino and Cosmology." In: *ZhETF Pisma Redaktsiiu* 4, p. 174 (cit. on p. 1).

Giannantonio, Tommaso, Yong-Seon Song, and Kazuya Koyama (2008). "Detectability of a phantom-like braneworld model with the integrated Sachs-Wolfe effect." In: *Phys. Rev. D* 78.4, 044017, p. 044017. DOI: `10.1103/PhysRevD.78.044017`. arXiv: `0803.2238 [astro-ph]` (cit. on p. 2).

Gilks, W., Sylvia Richardson, and D. Spiegelhalter (1996). "Introducing Markov Chain Monte Carlo." In: *Markov Chain Monte Carlo in Practice* (cit. on p. 55).

Gilmozzi, R. and J. Spyromilio (2007). "The European Extremely Large Telescope (E-ELT)." In: *The Messenger* 127, p. 11 (cit. on p. 5).

Gobat, R., V. Strazzullo, E. Daddi, M. Onodera, M. Carollo, A. Renzini, A. Finoguenov, A. Cimatti, C. Scarlata, and N. Arimoto (2013). "WFC3 GRISM Confirmation of the Distant Cluster Cl J1449+0856 at langzrang = 2.00: Quiescent and Star-forming Galaxy Populations." In: *ApJ* 776, 9, p. 9. DOI: `10.1088/0004-637X/776/1/9`. arXiv: `1305.3576` (cit. on p. 98).

Gómez, J. L., J. M. A. Marti, A. P. Marscher, J. M. A. Ibanez, and J. M. Marcaide (1995). "Parsec-Scale Synchrotron Emission from Hydrodynamic Relativistic Jets in Active Galactic Nuclei." In: *ApJ* 449, p. L19. DOI: `10.1086/309623` (cit. on p. 111).

Gómez, J. L., J. M. Martí, A. P. Marscher, J. M. Ibáñez, and A. Alberdi (1997). "Hydrodynamical Models of Superluminal Sources." In: *ApJ* 482, pp. L33–L36. DOI: `10.1086/310671` (cit. on p. 111).

Goodman, J. and J. Weare (2010). "Ensemble samplers with affine invariance." In: *Communications in Applied Mathematics and Computational Science, Vol. 5, No. 1, p. 65-80, 2010* 5, pp. 65–80. DOI: `10.2140/camcos.2010.5.65` (cit. on pp. 57, 67).

Grand, Robert J. J., Facundo A. Gómez, Federico Marinacci, Rüdiger Pakmor, Volker Springel, David J. R. Campbell, Carlos S. Frenk, Adrian Jenkins, and Simon D. M. White (2017). "The Auriga Project: the properties and formation mechanisms of disc galaxies across cosmic time." In: *MNRAS* 467.1, pp. 179–207. DOI: `10.1093/mnras/stx071`. arXiv: `1610.01159 [astro-ph.GA]` (cit. on p. 8).

Grazian, A. et al. (2015). "The galaxy stellar mass function at $3.5 \leqslant z \leqslant 7.5$ in the CANDELS/UDS, GOODS-South, and HUDF fields." In: *A&A* 575, A96, A96. DOI: `10.1051/0004-6361/201424750`. arXiv: `1412.0532` (cit. on pp. 11, 12, 22, 37, 38).

Grogin, N. A. et al. (2011). "CANDELS: The Cosmic Assembly Near-infrared Deep Extragalactic Legacy Survey." In: *ApJS* 197, 35, p. 35. DOI: `10.1088/0067-0049/197/2/35`. arXiv: `1105.3753` (cit. on pp. 10, 35, 127, 135).

Grossová, R. et al. (2019). "Powerful AGN jets and unbalanced cooling in the hot atmosphere of IC 4296." In: *MNRAS* 488.2, pp. 1917–1925. DOI: `10.1093/mnras/stz1728`. arXiv: `1903.03198 [astro-ph.GA]` (cit. on p. 112).

Grützbauch, R., A. E. Bauer, I. Jørgensen, and J. Varela (2012). "Suppression of star formation in the central 200 kpc of a z= 1.4 galaxy cluster." In: *MNRAS* 423, pp. 3652–3662. DOI: `10.1111/j.1365-2966.2012.21161.x`. arXiv: `1204.4417` (cit. on p. 98).

Guglielmo, V., B. M. Poggianti, A. Moretti, J. Fritz, R. Calvi, B. Vulcani, G. Fasano, and A. Paccagnella (2015). "The star formation history of galaxies: the role of galaxy mass, morphology and environment." In: *MNRAS* 450, pp. 2749–2763. DOI: `10.1093/mnras/stv757`. arXiv: `1504.01594` (cit. on pp. 19, 21, 81).

Guo, Qi, Simon White, Michael Boylan-Kolchin, Gabriella De Lucia, Guinevere Kauffmann, Gerard Lemson, Cheng Li, Volker Springel, and Simone Weinmann (2011). "From dwarf spheroidals to cD galaxies: simulating the galaxy population in a ΛCDM cosmology." In: *MNRAS* 413.1, pp. 101–131. DOI: 10.1111/j.1365-2966.2010.18114.x. arXiv: 1006.0106 [astro-ph.CO] (cit. on p. 7).

Guo, Yicheng et al. (2013). "CANDELS Multi-wavelength Catalogs: Source Detection and Photometry in the GOODS-South Field." In: *ApJS* 207.2, 24, p. 24. DOI: 10.1088/0067-0049/207/2/24. arXiv: 1308.4405 [astro-ph.CO] (cit. on p. 127).

Guth, Alan H. (1981). "Inflationary universe: A possible solution to the horizon and flatness problems." In: *Phys. Rev. D* 23.2, pp. 347–356. DOI: 10.1103/PhysRevD.23.347 (cit. on pp. 2, 3).

Guzzo, L. and VIPERS Team (2013). "VIPERS: An Unprecedented View of Galaxies and Large-scale Structure Halfway Back in the Life of the Universe." In: *The Messenger* 151, pp. 41–46. arXiv: 1303.3930 [astro-ph.CO] (cit. on pp. 3, 9, 10).

Haas, M., R. Chini, K. Meisenheimer, M. Stickel, D. Lemke, U. Klaas, and E. Kreysa (1998). "On the Far-Infrared Emission of Quasars." In: *ApJ* 503, pp. L109–L113. DOI: 10.1086/311543 (cit. on p. 110).

Hamer, S. L. et al. (2014). "Cold gas dynamics in Hydra-A: evidence for a rotating disc." In: *MNRAS* 437, pp. 862–878. DOI: 10.1093/mnras/stt1949. arXiv: 1310.4501 (cit. on pp. 95, 134).

Hao, Cai-Na, Robert C. Kennicutt, Benjamin D. Johnson, Daniela Calzetti, Daniel A. Dale, and John Moustakas (2011). "Dust-corrected Star Formation Rates of Galaxies. II. Combinations of Ultraviolet and Infrared Tracers." In: *ApJ* 741.2, 124, p. 124. DOI: 10.1088/0004-637X/741/2/124. arXiv: 1108.2837 [astro-ph.CO] (cit. on p. 100).

Hatch, N. A., E. A. Cooke, S. I. Muldrew, W. G. Hartley, O. Almaini, C. J. Conselice, and C. J. Simpson (2017). "The impact of protocluster environments at z = 1.6." In: *MNRAS* 464, pp. 876–884. DOI: 10.1093/mnras/stw2359. arXiv: 1609.08629 (cit. on pp. 18, 21, 139).

Hayashi, M., T. Kodama, K. Kohno, Y. Yamaguchi, K.-i. Tadaki, B. Hatsukade, Y. Koyama, R. Shimakawa, Y. Tamura, and T. L. Suzuki (2017). "Evolutionary Phases of Gas-rich Galaxies in a Galaxy Cluster at z = 1.46." In: *ApJ* 841, L21, p. L21. DOI: 10.3847/2041-8213/aa71ad. arXiv: 1705.02567 (cit. on p. 98).

Hayashi, M., K.-i. Tadaki, T. Kodama, K. Kohno, Y. Yamaguchi, B. Hatsukade, Y. Koyama, R. Shimakawa, Y. Tamura, and T. L. Suzuki (2018). "Molecular Gas Reservoirs in Cluster Galaxies at z=1.46." In: *ApJ* 856, 118, p. 118. DOI: 10.3847/1538-4357/aab3e7. arXiv: 1803.00298 (cit. on pp. 98, 100, 124, 126, 138–141).

Heavens, Alan, Benjamin Panter, Raul Jimenez, and James Dunlop (2004). "The star-formation history of the Universe from the stellar populations of nearby galaxies." In: *Nature* 428.6983, pp. 625–627. DOI: 10.1038/nature02474. arXiv: astro-ph/0403293 [astro-ph] (cit. on pp. 18, 81).

Heckman, T. M., L. Armus, and G. K. Miley (1990). "On the nature and implications of starburst-driven galactic superwinds." In: *ApJS* 74, pp. 833–868. DOI: 10.1086/191522 (cit. on p. 20).

Heyl, J., M. Colless, R. S. Ellis, and T. Broadhurst (1997). "Autofib Redshift Survey - II. Evolution of the galaxy luminosity function by spectral type."

In: *MNRAS* 285, pp. 613–634. DOI: 10.1093/mnras/285.3.613. eprint: astro-ph/9610036 (cit. on p. 9).

Hill, Ryley et al. (2020). "Megaparsec-scale structure around the protocluster core SPT2349-56 at z = 4.3." In: *MNRAS* 495.3, pp. 3124–3159. DOI: 10.1093/mnras/staa1275. arXiv: 2002.11600 [astro-ph.GA] (cit. on p. 98).

Hinshaw, G. et al. (2007). "Three-Year Wilkinson Microwave Anisotropy Probe (WMAP) Observations: Temperature Analysis." In: *ApJS* 170.2, pp. 288–334. DOI: 10.1086/513698. arXiv: astro-ph/0603451 [astro-ph] (cit. on p. 2).

Hogg, D. W., J. Bovy, and D. Lang (2010). "Data analysis recipes: Fitting a model to data." In: *ArXiv e-prints*. arXiv: 1008.4686 [astro-ph.IM] (cit. on pp. 54, 57, 68).

Hogg, David W. and Daniel Foreman-Mackey (2018). "Data Analysis Recipes: Using Markov Chain Monte Carlo." In: *The Astrophysical Journal Supplement Series* 236.1, p. 11. ISSN: 1538-4365. DOI: 10.3847/1538-4365/aab76e. URL: http://dx.doi.org/10.3847/1538-4365/aab76e (cit. on pp. 56, 57).

Hönig, S. F., M. A. Prieto, and T. Beckert (2008). "High-spatial resolution SED of NGC 1068 from near-IR to radio. Disentangling the thermal and non-thermal contributions." In: *A&A* 485, pp. 33–39. DOI: 10.1051/0004-6361:200809606. arXiv: 0804.0236 (cit. on p. 110).

Hopkins, P. F., L. Hernquist, T. J. Cox, T. Di Matteo, B. Robertson, and V. Springel (2006a). "A Unified, Merger-driven Model of the Origin of Starbursts, Quasars, the Cosmic X-Ray Background, Supermassive Black Holes, and Galaxy Spheroids." In: *ApJS* 163, pp. 1–49. DOI: 10.1086/499298. eprint: astro-ph/0506398 (cit. on pp. 13, 14, 142).

Hopkins, P. F., R. S. Somerville, L. Hernquist, T. J. Cox, B. Robertson, and Y. Li (2006b). "The Relation between Quasar and Merging Galaxy Luminosity Functions and the Merger-driven Star Formation History of the Universe." In: *ApJ* 652, pp. 864–888. DOI: 10.1086/508503. eprint: astro-ph/0602290 (cit. on pp. 13, 14, 21).

Hopkins, P. F., L. Hernquist, T. J. Cox, and D. Kereš (2008). "A Cosmological Framework for the Co-Evolution of Quasars, Supermassive Black Holes, and Elliptical Galaxies. I. Galaxy Mergers and Quasar Activity." In: *ApJS* 175, pp. 356–389. DOI: 10.1086/524362. arXiv: 0706.1243 (cit. on pp. 13, 14, 18, 21, 142).

Hopkins, P. F., D. Kereš, J. Oñorbe, C.-A. Faucher-Giguère, E. Quataert, N. Murray, and J. S. Bullock (2014). "Galaxies on FIRE (Feedback In Realistic Environments): stellar feedback explains cosmologically inefficient star formation." In: *MNRAS* 445, pp. 581–603. DOI: 10.1093/mnras/stu1738. arXiv: 1311.2073 (cit. on p. 20).

Hou, Fengji, Jonathan Goodman, and David W. Hogg (2014). *The Probabilities of Orbital-Companion Models for Stellar Radial Velocity Data*. arXiv: 1401.6128 [astro-ph.IM] (cit. on p. 55).

Hoyle, F., R. R. Rojas, M. S. Vogeley, and J. Brinkmann (2005). "The Luminosity Function of Void Galaxies in the Sloan Digital Sky Survey." In: *ApJ* 620, pp. 618–628. DOI: 10.1086/427176. eprint: astro-ph/0309728 (cit. on p. 35).

Hubble, E. P. (1926). “Extragalactic nebulae.” In: *ApJ* 64, pp. 321–369. DOI: 10.1086/143018 (cit. on p. 5).

Hubble, Edwin (1929). “A Relation between Distance and Radial Velocity among Extra-Galactic Nebulae.” In: *Proceedings of the National Academy of Science* 15.3, pp. 168–173. DOI: 10.1073/pnas.15.3.168 (cit. on pp. 2, 5).

Hubble, Edwin and Milton L. Humason (1931). “The Velocity-Distance Relation among Extra-Galactic Nebulae.” In: *ApJ* 74, p. 43. DOI: 10.1086/143323 (cit. on pp. 2, 5).

Huchra, J., M. Davis, D. Latham, and J. Tonry (1983). “A survey of galaxy redshifts. IV - The data.” In: *ApJS* 52, pp. 89–119. DOI: 10.1086/190860 (cit. on p. 9).

Hudson, D. S., R. Mittal, T. H. Reiprich, P. E. J. Nulsen, H. Andernach, and C. L. Sarazin (2010). “What is a cool-core cluster? a detailed analysis of the cores of the X-ray flux-limited HIFLUGCS cluster sample.” In: *A&A* 513, A37, A37. DOI: 10.1051/0004-6361/200912377. arXiv: 0911.0409 [astro-ph.CO] (cit. on p. 17).

Hunter, D. A., F. C. Gillett, III Gallagher J. S., W. L. Rice, and F. J. Low (1986). “IRAS Observations of a Small Sample of Blue Irregular Galaxies.” In: *ApJ* 303, p. 171. DOI: 10.1086/164064 (cit. on p. 100).

Husband, K., M. N. Bremer, J. P. Stott, and D. N. A. Murphy (2016). “Early quenching of massive protocluster galaxies around z = 2.2 radio galaxies.” In: *MNRAS* 462, pp. 421–428. DOI: 10.1093/mnras/stw1520. arXiv: 1606.07452 (cit. on p. 100).

Ilbert, O. et al. (2004). “Bias in the estimation of global luminosity functions.” In: *MNRAS* 351, pp. 541–551. DOI: 10.1111/j.1365-2966.2004.07796.x. eprint: astro-ph/0402202 (cit. on pp. 27–30, 32, 33, 35, 39, 52).

Ilbert, O. et al. (2005). “The VIMOS-VLT deep survey. Evolution of the galaxy luminosity function up to z = 2 in first epoch data.” In: *A&A* 439, pp. 863–876. DOI: 10.1051/0004-6361:20041961. eprint: astro-ph/0409134 (cit. on pp. 9, 30, 35, 45).

Ilbert, O. et al. (2006). “Accurate photometric redshifts for the CFHT legacy survey calibrated using the VIMOS VLT deep survey.” In: *A&A* 457, pp. 841–856. DOI: 10.1051/0004-6361:20065138. eprint: astro-ph/0603217 (cit. on pp. 11, 36, 37).

Ilbert, O. et al. (2009). “Cosmos Photometric Redshifts with 30-Bands for 2-deg^2.” In: *ApJ* 690, pp. 1236–1249. DOI: 10.1088/0004-637X/690/2/1236. arXiv: 0809.2101 (cit. on pp. 11, 12, 36, 37).

Ilbert, O. et al. (2010). “Galaxy Stellar Mass Assembly Between 0.2 < z < 2 from the S-COSMOS Survey.” In: *ApJ* 709.2, pp. 644–663. DOI: 10.1088/0004-637X/709/2/644. arXiv: 0903.0102 [astro-ph.CO] (cit. on pp. 12, 18, 19, 22, 23, 25, 27, 81, 83, 85, 90, 93, 94).

Ilbert, O. et al. (2013). “Mass assembly in quiescent and star-forming galaxies since z ∼ 4 from UltraVISTA.” In: *A&A* 556, A55, A55. DOI: 10.1051/0004-6361/201321100. arXiv: 1301.3157 (cit. on pp. iii, 11, 12, 18, 19, 22, 23, 25, 27, 35, 36, 38, 39, 49, 53–55, 57, 80, 81, 85, 90, 92–94, 147, 148, 153, 155–160).

Ivezić, Ž. et al. (2019). “LSST: From Science Drivers to Reference Design and Anticipated Data Products.” In: *ApJ* 873, 111, p. 111. DOI: 10.3847/1538-4357/ab042c. arXiv: 0805.2366 (cit. on p. 10).

Ivison, R. J., A. D. Biggs, M. Bremer, V. Arumugam, and L. Dunne (2020). "ALMA unveils wider environment of distant red protocluster core." In: *arXiv e-prints*, arXiv:2006.10753, arXiv:2006.10753. arXiv: `2006.10753 [astro-ph.GA]` (cit. on p. 98).

Jablonka, P., F. Combes, K. Rines, R. Finn, and T. Welch (2013). "Cold gas in the inner regions of intermediate redshift clusters." In: *A&A* 557, A103, A103. DOI: `10.1051/0004-6361/201321104`. arXiv: `1303.6396` (cit. on p. 100).

Jaffe, W. and M. N. Bremer (1997). "Molecular hydrogen emission in cooling flows." In: *MNRAS* 284.1, pp. L1–L5. DOI: `10.1093/mnras/284.1.L1` (cit. on p. 16).

Jaffe, W., M. N. Bremer, and K. Baker (2005). "HII and H_2 in the envelopes of cooling flow central galaxies." In: *MNRAS* 360.2, pp. 748–762. DOI: `10.1111/j.1365-2966.2005.09073.x`. arXiv: `astro-ph/0504413 [astro-ph]` (cit. on p. 16).

Jaffé, Y. L. et al. (2018). "GASP. IX. Jellyfish galaxies in phase-space: an orbital study of intense ram-pressure stripping in clusters." In: *MNRAS* 476, pp. 4753–4764. DOI: `10.1093/mnras/sty500`. arXiv: `1802.07297` (cit. on p. 21).

Jing, Y. P. and Yasushi Suto (2002). "Triaxial Modeling of Halo Density Profiles with High-Resolution N-Body Simulations." In: *ApJ* 574.2, pp. 538–553. DOI: `10.1086/341065`. arXiv: `astro-ph/0202064 [astro-ph]` (cit. on p. 4).

Johnston, R. (2011). "Shedding light on the galaxy luminosity function." In: *A&A Rev.* 19, 41, p. 41. DOI: `10.1007/s00159-011-0041-9`. arXiv: `1106.2039 [astro-ph.CO]` (cit. on pp. 9, 25, 27).

Juneau, Stéphanie et al. (2005). "Cosmic Star Formation History and Its Dependence on Galaxy Stellar Mass." In: *ApJ* 619.2, pp. L135–L138. DOI: `10.1086/427937`. arXiv: `astro-ph/0411775 [astro-ph]` (cit. on pp. 18, 23, 81).

Karim, A. et al. (2011). "The Star Formation History of Mass-selected Galaxies in the COSMOS Field." In: *ApJ* 730.2, 61, p. 61. DOI: `10.1088/0004-637X/730/2/61`. arXiv: `1011.6370 [astro-ph.CO]` (cit. on pp. 18, 139).

Katz, Neal and James E. Gunn (1991). "Dissipational Galaxy Formation. I. Effects of Gasdynamics." In: *ApJ* 377, p. 365. DOI: `10.1086/170367` (cit. on p. 7).

Katz, Neal and Simon D. M. White (1993). "Hierarchical Galaxy Formation: Overmerging and the Formation of an X-Ray Cluster." In: *ApJ* 412, p. 455. DOI: `10.1086/172935` (cit. on p. 7).

Kauffmann, G., S. D. M. White, and B. Guiderdoni (1993). "The formation and evolution of galaxies within merging dark matter haloes." In: *MNRAS* 264, pp. 201–218. DOI: `10.1093/mnras/264.1.201` (cit. on pp. 4, 7).

Kauffmann, G., S. D. M. White, T. M. Heckman, B. Ménard, J. Brinchmann, S. Charlot, C. Tremonti, and J. Brinkmann (2004). "The environmental dependence of the relations between stellar mass, structure, star formation and nuclear activity in galaxies." In: *MNRAS* 353, pp. 713–731. DOI: `10.1111/j.1365-2966.2004.08117.x`. eprint: `astro-ph/0402030` (cit. on pp. 6, 21, 81).

Kauffmann, Guinevere, Jorg M. Colberg, Antonaldo Diaferio, and Simon D. M. White (1999). "Clustering of galaxies in a hierarchical universe - I. Methods and results at z=0." In: *MNRAS* 303.1, pp. 188–206. DOI: `10.1046/j.1365-8711.1999.02202.x`. arXiv: `astro-ph/9805283 [astro-ph]` (cit. on p. 13).

Kauffmann, Guinevere et al. (2003). "The dependence of star formation history and internal structure on stellar mass for 10^5 low-redshift galaxies." In: *MNRAS* 341.1, pp. 54–69. DOI: `10.1046/j.1365-8711.2003.06292.x`. arXiv: `astro-ph/0205070 [astro-ph]` (cit. on p. 17).

Kazantzidis, Stelios, James S. Bullock, Andrew R. Zentner, Andrey V. Kravtsov, and Leonidas A. Moustakas (2008). "Cold Dark Matter Substructure and Galactic Disks. I. Morphological Signatures of Hierarchical Satellite Accretion." In: *ApJ* 688.1, pp. 254–276. DOI: `10.1086/591958`. arXiv: `0708.1949 [astro-ph]` (cit. on pp. 13, 15).

Kelly, B. C., X. Fan, and M. Vestergaard (2008). "A Flexible Method of Estimating Luminosity Functions." In: *ApJ* 682, pp. 874–895. DOI: `10.1086/589501`. arXiv: `0805.2946` (cit. on p. 31).

Kennicutt Robert C., Jr. (1998a). "The Global Schmidt Law in Star-forming Galaxies." In: *ApJ* 498.2, pp. 541–552. DOI: `10.1086/305588`. arXiv: `astro-ph/9712213 [astro-ph]` (cit. on p. 18).

Kennicutt Robert C., Jr., Peter Tamblyn, and Charles E. Congdon (1994). "Past and Future Star Formation in Disk Galaxies." In: *ApJ* 435, p. 22. DOI: `10.1086/174790` (cit. on p. 100).

Kennicutt Robert C., Jr. et al. (2007). "Star Formation in NGC 5194 (M51a). II. The Spatially Resolved Star Formation Law." In: *ApJ* 671.1, pp. 333–348. DOI: `10.1086/522300`. arXiv: `0708.0922 [astro-ph]` (cit. on p. 18).

Kennicutt, R. C. and N. J. Evans (2012). "Star Formation in the Milky Way and Nearby Galaxies." In: *ARA&A* 50, pp. 531–608. DOI: `10.1146/annurev-astro-081811-125610`. arXiv: `1204.3552` (cit. on pp. 17, 18, 99–101).

Kennicutt Jr., R. C. (1992). "The integrated spectra of nearby galaxies - General properties and emission-line spectra." In: *ApJ* 388, pp. 310–327. DOI: `10.1086/171154` (cit. on p. 100).

Kennicutt Jr., R. C. (1998b). "Star Formation in Galaxies Along the Hubble Sequence." In: *ARA&A* 36, pp. 189–232. DOI: `10.1146/annurev.astro.36.1.189`. eprint: `astro-ph/9807187` (cit. on pp. 17, 18, 100, 129).

Kereš, D., N. Katz, D. H. Weinberg, and R. Davé (2005). "How do galaxies get their gas?" In: *MNRAS* 363, pp. 2–28. DOI: `10.1111/j.1365-2966.2005.09451.x`. eprint: `astro-ph/0407095` (cit. on pp. 4, 13, 15).

Kereš, Dušan and Lars Hernquist (2009). "Seeding the Formation of Cold Gaseous Clouds in Milky Way-Size Halos." In: *ApJ* 700.1, pp. L1–L5. DOI: `10.1088/0004-637X/700/1/L1`. arXiv: `0905.2186 [astro-ph.CO]` (cit. on p. 15).

Kereš, Dušan, Neal Katz, Mark Fardal, Romeel Davé, and David H. Weinberg (2009). "Galaxies in a simulated ΛCDM Universe - I. Cold mode and hot cores." In: *MNRAS* 395.1, pp. 160–179. DOI: `10.1111/j.1365-2966.2009.14541.x`. arXiv: `0809.1430 [astro-ph]` (cit. on p. 15).

Kitzbichler, M. G. and S. D. M. White (2007). "The high-redshift galaxy population in hierarchical galaxy formation models." In: *MNRAS* 376, pp. 2–

12. DOI: 10.1111/j.1365-2966.2007.11458.x. eprint: astro-ph/0609636 (cit. on p. 54).

Klamer, I. J., R. D. Ekers, E. M. Sadler, and R. W. Hunstead (2004). "Molecular Gas at High Redshift: Jet-induced Star Formation?" In: *ApJ* 612.2, pp. L97–L100. DOI: 10.1086/424843. arXiv: astro-ph/0408015 [astro-ph] (cit. on p. 137).

Klinkhamer, F. R. and C. A. Norman (1981). "Massive neutrinos and galaxy formation." In: *ApJ* 243, pp. L1–L4. DOI: 10.1086/183430 (cit. on p. 1).

Klypin, Anatoly A., Sebastian Trujillo-Gomez, and Joel Primack (2011). "Dark Matter Halos in the Standard Cosmological Model: Results from the Bolshoi Simulation." In: *ApJ* 740.2, 102, p. 102. DOI: 10.1088/0004-637X/740/2/102. arXiv: 1002.3660 [astro-ph.CO] (cit. on p. 7).

Knobel, C., S. J. Lilly, J. Woo, and K. Kovač (2015). "Quenching of Star Formation in Sloan Digital Sky Survey Groups: Centrals, Satellites, and Galactic Conformity." In: *ApJ* 800, 24, p. 24. DOI: 10.1088/0004-637X/800/1/24. arXiv: 1408.2553 (cit. on p. 19).

Kodama, T., E. F. Bell, and R. G. Bower (1999). "A Bayesian classifier for photometric redshifts: identification of high-redshift clusters." In: *MNRAS* 302, pp. 152–166. DOI: 10.1046/j.1365-8711.1999.02184.x. eprint: astro-ph/9806120 (cit. on p. 12).

Kodama, T., I. Tanaka, M. Kajisawa, J. Kurk, B. Venemans, C. De Breuck, J. Vernet, and C. Lidman (2007). "The first appearance of the red sequence of galaxies in proto-clusters at $2 <\tilde{} z <\tilde{} 3$." In: *MNRAS* 377, pp. 1717–1725. DOI: 10.1111/j.1365-2966.2007.11739.x. eprint: astro-ph/0703382 (cit. on p. 98).

Koekemoer, Anton M. et al. (2011). "CANDELS: The Cosmic Assembly Near-infrared Deep Extragalactic Legacy Survey—The Hubble Space Telescope Observations, Imaging Data Products, and Mosaics." In: *ApJS* 197.2, 36, p. 36. DOI: 10.1088/0067-0049/197/2/36. arXiv: 1105.3754 [astro-ph.CO] (cit. on p. 127).

Kolb, Edward W. and Michael S. Turner (1990). *The early universe*. Vol. 69 (cit. on p. 2).

Komatsu, E. et al. (2009). "Five-Year Wilkinson Microwave Anisotropy Probe Observations: Cosmological Interpretation." In: *ApJS* 180.2, pp. 330–376. DOI: 10.1088/0067-0049/180/2/330. arXiv: 0803.0547 [astro-ph] (cit. on p. 2).

Koo, D. C. (1985). "Optical multicolors - A poor person's Z machine for galaxies." In: *AJ* 90, pp. 418–440. DOI: 10.1086/113748 (cit. on pp. 11, 36).

Koo, D. C. (1999). "Overview - Photometric Redshifts: A Perspective from an Old-Timer[!] on their Past, Present, and Potential." In: *Photometric Redshifts and the Detection of High Redshift Galaxies*. Ed. by R. Weymann, L. Storrie-Lombardi, M. Sawicki, and R. Brunner. Vol. 191. Astronomical Society of the Pacific Conference Series, p. 3. eprint: astro-ph/9907273 (cit. on p. 11).

Kroupa, Pavel (2002). "The Initial Mass Function of Stars: Evidence for Uniformity in Variable Systems." In: *Science* 295.5552, pp. 82–91. DOI: 10.1126/science.1067524. arXiv: astro-ph/0201098 [astro-ph] (cit. on p. 5).

Krumholz, M. R. (2014). “The big problems in star formation: The star formation rate, stellar clustering, and the initial mass function.” In: *Phys. Rep.* 539, pp. 49–134. DOI: `10.1016/j.physrep.2014.02.001`. arXiv: `1402.0867` (cit. on p. 17).

Kümmel, M., J. R. Walsh, N. Pirzkal, H. Kuntschner, and A. Pasquali (2009). “The Slitless Spectroscopy Data Extraction Software aXe.” In: *PASP* 121, p. 59. DOI: `10.1086/596715`. arXiv: `0812.1434` (cit. on p. 102).

LSST Science Collaboration et al. (2009). “LSST Science Book, Version 2.0.” In: *arXiv e-prints*. arXiv: `0912.0201 [astro-ph.IM]` (cit. on p. 10).

Lacey, Cedric and Shaun Cole (1993). “Merger rates in hierarchical models of galaxy formation.” In: *MNRAS* 262.3, pp. 627–649. DOI: `10.1093/mnras/262.3.627` (cit. on p. 4).

Lacy, M. et al. (2005). “The Infrared Array Camera Component of the Spitzer Space Telescope Extragalactic First Look Survey.” In: *ApJS* 161, pp. 41–52. DOI: `10.1086/432894`. eprint: `astro-ph/0507143` (cit. on p. 102).

Lada, Charles J., Marco Lombardi, and João F. Alves (2010). “On the Star Formation Rates in Molecular Clouds.” In: *ApJ* 724.1, pp. 687–693. DOI: `10.1088/0004-637X/724/1/687`. arXiv: `1009.2985 [astro-ph.GA]` (cit. on p. 18).

Laigle, C. et al. (2016). “The COSMOS2015 Catalog: Exploring the $1 < z < 6$ Universe with Half a Million Galaxies.” In: *ApJS* 224, 24, p. 24. DOI: `10.3847/0067-0049/224/2/24`. arXiv: `1604.02350` (cit. on pp. 10, 39, 43–45, 47, 73, 74, 82, 84).

Laing, R. A. and A. H. Bridle (2013). “The spectra of jet bases in FR I radio galaxies: implications for particle acceleration.” In: *Monthly Notices of the Royal Astronomical Society* 432.2, pp. 1114–1132. ISSN: 0035-8711. DOI: `10.1093/mnras/stt531`. eprint: `https://academic.oup.com/mnras/article-pdf/432/2/1114/18455870/stt531.pdf`. URL: `https://doi.org/10.1093/mnras/stt531` (cit. on p. 111).

Langer, W. D., T. Velusamy, J. L. Pineda, K. Willacy, and P. F. Goldsmith (2014). “A Herschel [C ii] Galactic plane survey. II. CO-dark H_2 in clouds.” In: *A&A* 561, A122, A122. DOI: `10.1051/0004-6361/201322406`. arXiv: `1312.3320 [astro-ph.GA]` (cit. on p. 99).

Lanzetta, Kenneth M., Amos Yahil, and Alberto Fernández-Soto (1996). “Star-forming galaxies at very high redshifts.” In: *Nature* 381.6585, pp. 759–763. DOI: `10.1038/381759a0`. arXiv: `astro-ph/9606171 [astro-ph]` (cit. on p. 11).

Larson, R. B., B. M. Tinsley, and C. N. Caldwell (1980). “The evolution of disk galaxies and the origin of S0 galaxies.” In: *ApJ* 237, pp. 692–707. DOI: `10.1086/157917` (cit. on p. 21).

Laureijs, R. et al. (2011). “Euclid Definition Study Report.” In: *arXiv e-prints*. arXiv: `1110.3193 [astro-ph.CO]` (cit. on pp. 5, 10, 38, 40, 42, 92).

Le Fèvre, O. et al. (2015). “The VIMOS Ultra-Deep Survey: 10 000 galaxies with spectroscopic redshifts to study galaxy assembly at early epochs $2 < z < 6$.” In: *A&A* 576, A79, A79. DOI: `10.1051/0004-6361/201423829`. arXiv: `1403.3938 [astro-ph.CO]` (cit. on p. 10).

Lebouteiller, V. et al. (2019). “Physical conditions in the gas phases of the giant H II region LMC-N 11. II. Origin of [C II] and fraction of CO-dark gas." In: *A&A* 632, A106, A106. DOI: 10.1051/0004-6361/201936303. arXiv: 1911.03280 [astro-ph.GA] (cit. on p. 99).

Lee, Jaehyun and Sukyoung K. Yi (2013). "On the Assembly History of Stellar Components in Massive Galaxies." In: *ApJ* 766.1, 38, p. 38. DOI: 10.1088/0004-637X/766/1/38. arXiv: 1302.1588 [astro-ph.CO] (cit. on p. 13).

Lee, Minju M. et al. (2017). "A Radio-to-mm Census of Star-forming Galaxies in Protocluster 4C23.56 at Z = 2.5: Gas Mass and Its Fraction Revealed with ALMA." In: *The Astrophysical Journal* 842.1, p. 55. URL: http://stacks.iop.org/0004-637X/842/i=1/a=55 (cit. on pp. 100, 126).

Lee, Seong-Kook, Rafal Idzi, Henry C. Ferguson, Rachel S. Somerville, Tommy Wiklind, and Mauro Giavalisco (2009). "Biases and Uncertainties in Physical Parameter Estimates of Lyman Break Galaxies from Broadband Photometry." In: *ApJS* 184.1, pp. 100–132. DOI: 10.1088/0067-0049/184/1/100. arXiv: 0812.5111 [astro-ph] (cit. on p. 138).

Lemaître, G. (1931). "Expansion of the universe, A homogeneous universe of constant mass and increasing radius accounting for the radial velocity of extra-galactic nebulae." In: *MNRAS* 91, pp. 483–490. DOI: 10.1093/mnras/91.5.483 (cit. on p. 1).

Lemaux, B. C., R. R. Gal, L. M. Lubin, D. D. Kocevski, C. D. Fassnacht, E. J. McGrath, G. K. Squires, J. A. Surace, and M. Lacy (2012). "The Assembly of the Red Sequence at z ˜ 1: The Color and Spectral Properties of Galaxies in the Cl1604 Supercluster." In: *ApJ* 745, 106, p. 106. DOI: 10.1088/0004-637X/745/2/106. arXiv: 1108.5799 (cit. on p. 98).

Lemaux, B. C. et al. (2018). "Persistence of the Color-Density Relation and Efficient Environmental Quenching to $z \sim 1.4$." In: *arXiv e-prints*. arXiv: 1812.04624 (cit. on p. 98).

Lewis, A. J. R. et al. (2018). "Ultra-red Galaxies Signpost Candidate Protoclusters at High Redshift." In: *ApJ* 862.2, 96, p. 96. DOI: 10.3847/1538-4357/aacc25. arXiv: 1711.08803 [astro-ph.GA] (cit. on p. 98).

Li, Y. and G. L. Bryan (2014). "Modeling Active Galactic Nucleus Feedback in Cool-core Clusters: The Formation of Cold Clumps." In: *ApJ* 789, 153, p. 153. DOI: 10.1088/0004-637X/789/2/153. arXiv: 1310.7580 (cit. on pp. 17, 95–97).

Li, Y., G. L. Bryan, M. Ruszkowski, G. M. Voit, B. W. O'Shea, and M. Donahue (2015). "Cooling, AGN Feedback, and Star Formation in Simulated Cool-core Galaxy Clusters." In: *ApJ* 811, 73, p. 73. DOI: 10.1088/0004-637X/811/2/73. arXiv: 1503.02660 (cit. on pp. 7, 95–97, 134).

Liddle, Andrew R. and David H. Lyth (2000). *Cosmological Inflation and Large-Scale Structure* (cit. on p. 2).

Lifshitz, E. M. (1946). "On the gravitational stability of the expanding universe." In: *Zhurnal Eksperimentalnoi i Teoreticheskoi Fiziki* 16, pp. 587–602 (cit. on p. 5).

Lilly, S. J., L. Tresse, F. Hammer, D. Crampton, and O. Le Fevre (1995). "The Canada-France Redshift Survey. VI. Evolution of the Galaxy Luminosity Function to Z approximately 1." In: *ApJ* 455, p. 108. DOI: 10.1086/176560. eprint: astro-ph/9507079 (cit. on pp. 9, 25).

Lilly, S. J. et al. (2007). "zCOSMOS: A Large VLT/VIMOS Redshift Survey Covering $0 < z < 3$ in the COSMOS Field." In: *ApJS* 172, pp. 70–85. DOI: 10.1086/516589. eprint: astro-ph/0612291 (cit. on p. 10).

Lim, J., Y. Ao, and Dinh-V-Trung (2008). "Radially Inflowing Molecular Gas in NGC 1275 Deposited by an X-Ray Cooling Flow in the Perseus Cluster." In: *ApJ* 672, pp. 252–265. DOI: 10.1086/523664. arXiv: 0712.2979 (cit. on pp. 96, 97).

Lim, Jeremy, Youichi Ohyama, Yan Chi-Hung, Dinh-V-Trung, and Wang Shiang-Yu (2012). "A Molecular Hydrogen Nebula in the Central cD Galaxy of the Perseus Cluster." In: *ApJ* 744.2, 112, p. 112. DOI: 10.1088/0004-637X/744/2/112 (cit. on p. 16).

Lin, H., H. K. C. Yee, R. G. Carlberg, S. L. Morris, M. Sawicki, D. R. Patton, G. Wirth, and C. W. Shepherd (1999). "The CNOC2 Field Galaxy Luminosity Function. I. A Description of Luminosity Function Evolution." In: *ApJ* 518, pp. 533–561. DOI: 10.1086/307297. eprint: astro-ph/9902249 (cit. on p. 25).

Linde, A. D. (1982). "Scalar field fluctuations in the expanding universe and the new inflationary universe scenario." In: *Physics Letters B* 116.5, pp. 335–339. DOI: 10.1016/0370-2693(82)90293-3 (cit. on pp. 2, 3).

Loh, E. D. and E. J. Spillar (1986). "Photometric redshifts of galaxies." In: *ApJ* 303, pp. 154–161. DOI: 10.1086/164062 (cit. on pp. 11, 36, 37).

López-Sanjuan, C. et al. (2012). "The dominant role of mergers in the size evolution of massive early-type galaxies since $z \sim 1$." In: *A&A* 548, A7, A7. DOI: 10.1051/0004-6361/201219085. arXiv: 1202.4674 [astro-ph.CO] (cit. on pp. 13, 14).

López-Sanjuan, C. et al. (2013). "MASSIV: Mass Assembly Survey with SINFONI in VVDS. V. The major merger rate of star-forming galaxies at 0.9 < z < 1.8 from IFS-based close pairs." In: *A&A* 553, A78, A78. DOI: 10.1051/0004-6361/201220286. arXiv: 1208.5020 [astro-ph.CO] (cit. on pp. 13–15).

Lupton, R. (1993). *Statistics in theory and practice* (cit. on p. 34).

Lynden-Bell, D. (1971). "A method of allowing for known observational selection in small samples applied to 3CR quasars." In: *MNRAS* 155, p. 95. DOI: 10.1093/mnras/155.1.95 (cit. on p. 30).

Maciaszek, T. et al. (2016). "Euclid Near Infrared Spectrometer and Photometer instrument concept and first test results obtained for different breadboards models at the end of phase C." In: *Space Telescopes and Instrumentation 2016: Optical, Infrared, and Millimeter Wave*. Vol. 9904. *Proc. SPIE*, 99040T. DOI: 10.1117/12.2232941 (cit. on p. 42).

Mackay, David J. C. (2003). *Information Theory, Inference and Learning Algorithms* (cit. on p. 57).

Madau, Piero and Mark Dickinson (2014). "Cosmic Star-Formation History." In: *ARA&A* 52, pp. 415–486. DOI: 10.1146/annurev-astro-081811-125615. arXiv: 1403.0007 [astro-ph.CO] (cit. on pp. 19, 20, 22, 26, 100).

Madau, Piero, Lucia Pozzetti, and Mark Dickinson (1998). "The Star Formation History of Field Galaxies." In: *ApJ* 498.1, pp. 106–116. DOI: 10.1086/305523. arXiv: astro-ph/9708220 [astro-ph] (cit. on pp. 19, 100).

Madau, Piero, Henry C. Ferguson, Mark E. Dickinson, Mauro Giavalisco, Charles C. Steidel, and Andrew Fruchter (1996). "High-redshift galaxies in the Hubble Deep Field: colour selection and star formation history to z∼4." In: *MNRAS* 283.4, pp. 1388–1404. doi: `10.1093/mnras/283.4.1388`. arXiv: `astro-ph/9607172 [astro-ph]` (cit. on p. 19).

Magnelli, B., D. Elbaz, R. R. Chary, M. Dickinson, D. Le Borgne, D. T. Frayer, and C. N. A. Willmer (2009). "The $0.4 < z < 1.3$ star formation history of the Universe as viewed in the far-infrared." In: *A&A* 496, pp. 57–75. doi: `10.1051/0004-6361:200811443`. arXiv: `0901.1543 [astro-ph.CO]` (cit. on p. 27).

Magnelli, B., D. Elbaz, R. R. Chary, M. Dickinson, D. Le Borgne, D. T. Frayer, and C. N. A. Willmer (2011). "Evolution of the dusty infrared luminosity function from $z = 0$ to $z = 2.3$ using observations from Spitzer." In: *A&A* 528, A35, A35. doi: `10.1051/0004-6361/200913941`. arXiv: `1101.2467` (cit. on p. 27).

Maier, C. et al. (2016). "CLASH-VLT: Strangulation of cluster galaxies in MACS J0416.1-2403 as seen from their chemical enrichment." In: *A&A* 590, A108, A108. doi: `10.1051/0004-6361/201628223`. arXiv: `1602.00686` (cit. on p. 21).

Maiolino, R. et al. (2008). "AMAZE. I. The evolution of the mass-metallicity relation at $z > 3$." In: *A&A* 488, pp. 463–479. doi: `10.1051/0004-6361:200809678`. arXiv: `0806.2410` (cit. on p. 131).

Maiolino, R. et al. (2012). "Evidence of strong quasar feedback in the early Universe." In: *MNRAS* 425.1, pp. L66–L70. doi: `10.1111/j.1745-3933.2012.01303.x`. arXiv: `1204.2904 [astro-ph.CO]` (cit. on p. 99).

Makovoz, D. and I. Khan (2005). "Mosaicking with MOPEX." In: *Astronomical Data Analysis Software and Systems XIV*. Ed. by P. Shopbell, M. Britton, and R. Ebert. Vol. 347. Astronomical Society of the Pacific Conference Series, p. 81 (cit. on p. 102).

Malmquist, G. K. (1920). "A study of the stars of spectral type A." In: *Meddelanden fran Lunds Astronomiska Observatorium Serie II* 22, pp. 3–69 (cit. on p. 27).

Mantz, A. B. et al. (2014). "The XXL Survey. V. Detection of the Sunyaev-Zel'dovich Effect of the Redshift 1.9 Galaxy Cluster XLSSU J021744.1-034536 with CARMA." In: *ApJ* 794, 157, p. 157. doi: `10.1088/0004-637X/794/2/157`. arXiv: `1401.2087` (cit. on p. 98).

Maraston, Claudia, Janine Pforr, Alvio Renzini, Emanuele Daddi, Mark Dickinson, Andrea Cimatti, and Chiara Tonini (2010). "Star formation rates and masses of z ∼2 galaxies from multicolour photometry." In: *MNRAS* 407.2, pp. 830–845. doi: `10.1111/j.1365-2966.2010.16973.x`. arXiv: `1004.4546 [astro-ph.CO]` (cit. on p. 138).

Marchesini, Danilo, Pieter G. van Dokkum, Natascha M. Förster Schreiber, Marijn Franx, Ivo Labbé, and Stijn Wuyts (2009). "The Evolution of the Stellar Mass Function of Galaxies from $z = 4.0$ and the First Comprehensive Analysis of its Uncertainties: Evidence for Mass-Dependent Evolution." In: *ApJ* 701.2, pp. 1765–1796. doi: `10.1088/0004-637X/701/2/1765`. arXiv: `0811.1773 [astro-ph]` (cit. on p. 23).

Markov, Vladan et al. (2020a). "Massive molecular gas reservoir around the central AGN in the CARLA J1103 + 3449 cluster at $z = 1.44$." In: *A&A* 641, A22, A22. doi: `10.1051/0004-6361/202038673`. arXiv: `2007.03706 [astro-ph.GA]` (cit. on pp. iii, vi, ix, 17, 24, 140, 149).

Markov, Vladan et al. (2020b). "Massive molecular gas reservoir around the central AGN in the CARLA J1103+3449 cluster at z=1.44." In: *arXiv e-prints*, arXiv:2007.03706, arXiv:2007.03706. arXiv: `2007.03706 [astro-ph.GA]` (cit. on pp. 95, 101, 111, 152).

Martin, Crystal L. (1999). "Properties of Galactic Outflows: Measurements of the Feedback from Star Formation." In: *ApJ* 513.1, pp. 156–160. DOI: `10.1086/306863`. arXiv: `astro-ph/9810233 [astro-ph]` (cit. on p. 20).

Martinache, C. et al. (2018). "Spitzer Planck Herschel Infrared Cluster (SPHerIC) survey: Candidate galaxy clusters at $1.3 < z < 3$ selected by high star-formation rate." In: *A&A* 620, A198, A198. DOI: `10.1051/0004-6361/201833198`. arXiv: `1810.07330` (cit. on p. 98).

Marzke, R. O., L. N. da Costa, P. S. Pellegrini, C. N. A. Willmer, and M. J. Geller (1998). "The Galaxy Luminosity Function at Z <= 0.05: Dependence on Morphology." In: *ApJ* 503, pp. 617–631. DOI: `10.1086/306011`. eprint: `astro-ph/9805218` (cit. on p. 25).

Massey, Philip and Caryl Gronwall (1990). "The Kitt Peak Spectrophotometric Standards: Extension to 1 Micron." In: *ApJ* 358, p. 344. DOI: `10.1086/168991` (cit. on p. 104).

Mazure, A. et al. (2007). "Structure detection in the D1 CFHTLS deep field using accurate photometric redshifts: a benchmark." In: *A&A* 467, pp. 49–62. DOI: `10.1051/0004-6361:20066379`. eprint: `astro-ph/0702430` (cit. on p. 11).

McCarthy, I. G., C. S. Frenk, A. S. Font, C. G. Lacey, R. G. Bower, N. L. Mitchell, M. L. Balogh, and T. Theuns (2008). "Ram pressure stripping the hot gaseous haloes of galaxies in groups and clusters." In: *MNRAS* 383, pp. 593–605. DOI: `10.1111/j.1365-2966.2007.12577.x`. arXiv: `0710.0964` (cit. on p. 21).

McCarthy, Patrick J. et al. (2004). "Evolved Galaxies at z>1.5 from the Gemini Deep Deep Survey: The Formation Epoch of Massive Stellar Systems." In: *ApJ* 614.1, pp. L9–L12. DOI: `10.1086/425306`. arXiv: `astro-ph/0408367 [astro-ph]` (cit. on p. 23).

McCracken, H. J. et al. (2010). "The COSMOS-WIRCam Near-Infrared Imaging Survey. I. BzK-Selected Passive and Star-Forming Galaxy Candidates at z gsim 1.4." In: *ApJ* 708, pp. 202–217. DOI: `10.1088/0004-637X/708/1/202`. arXiv: `0910.2705` (cit. on p. 44).

McCracken, H. J. et al. (2012). "UltraVISTA: a new ultra-deep near-infrared survey in COSMOS." In: *A&A* 544, A156, A156. DOI: `10.1051/0004-6361/201219507`. arXiv: `1204.6586 [astro-ph.CO]` (cit. on pp. 43, 57, 153).

McDonald, Michael, Sylvain Veilleux, David S. N. Rupke, and Richard Mushotzky (2010). "On the Origin of the Extended Hα Filaments in Cooling Flow Clusters." In: *ApJ* 721.2, pp. 1262–1283. DOI: `10.1088/0004-637X/721/2/1262`. arXiv: `1008.0392 [astro-ph.HE]` (cit. on p. 16).

McKee, C. F. and E. C. Ostriker (2007). "Theory of Star Formation." In: *ARA&A* 45, pp. 565–687. DOI: `10.1146/annurev.astro.45.051806.110602`. arXiv: `0707.3514` (cit. on pp. 13, 17).

McNamara, B. R. and P. E. J. Nulsen (2007). "Heating Hot Atmospheres with Active Galactic Nuclei." In: *ARA&A* 45.1, pp. 117–175. DOI: `10.1146/annurev.astro.45.051806.110625`. arXiv: `0709.2152 [astro-ph]` (cit. on pp. 6, 17, 19).

McNamara, B. R. et al. (2000). “Chandra X-Ray Observations of the Hydra A Cluster: An Interaction between the Radio Source and the X-Ray-emitting Gas.” In: *ApJ* 534.2, pp. L135–L138. DOI: `10.1086/312662`. arXiv: `astro-ph/0001402 [astro-ph]` (cit. on pp. 16, 19).

McNamara, B. R. et al. (2014). “A 10^{10} Solar Mass Flow of Molecular Gas in the A1835 Brightest Cluster Galaxy.” In: *ApJ* 785, 44, p. 44. DOI: `10.1088/0004-637X/785/1/44`. arXiv: `1309.0013` (cit. on pp. 95–97, 124, 137).

McNamara, B. R., H. R. Russell, P. E. J. Nulsen, M. T. Hogan, A. C. Fabian, F. Pulido, and A. C. Edge (2016). “A Mechanism for Stimulating AGN Feedback by Lifting Gas in Massive Galaxies.” In: *ApJ* 830, 79, p. 79. DOI: `10.3847/0004-637X/830/2/79`. arXiv: `1604.04629` (cit. on pp. 17, 96, 97).

McNamara, Brian R., Buell T. Jannuzi, Richard Elston, Craig L. Sarazin, and Michael Wise (1996). “U-Band Polarimetry of the Radio-aligned Optical Continuum in the Abell 1795 Cluster Central Galaxy.” In: *ApJ* 469, p. 66. DOI: `10.1086/177758` (cit. on p. 16).

McNaught-Roberts, T. et al. (2014). “Galaxy And Mass Assembly (GAMA): the dependence of the galaxy luminosity function on environment, redshift and colour.” In: *MNRAS* 445, pp. 2125–2145. DOI: `10.1093/mnras/stu1886`. arXiv: `1409.4681` (cit. on p. 25).

Mei, S. et al. (2009). “Evolution of the Color-Magnitude Relation in Galaxy Clusters at z ˜ 1 from the ACS Intermediate Redshift Cluster Survey.” In: *ApJ* 690, pp. 42–68. DOI: `10.1088/0004-637X/690/1/42`. arXiv: `0810.1917` (cit. on p. 98).

Mei, S. et al. (2012). “Early-type Galaxies at z = 1.3. I. The Lynx Supercluster: Cluster and Groups at z = 1.3. Morphology and Color-Magnitude Relation.” In: *ApJ* 754, 141, p. 141. DOI: `10.1088/0004-637X/754/2/141`. arXiv: `1205.1785` (cit. on p. 98).

Mei, S. et al. (2015). “Star-forming Blue ETGs in Two Newly Discovered Galaxy Overdensities in the HUDF at z=1.84 and 1.9: Unveiling the Progenitors of Passive ETGs in Cluster Cores.” In: *ApJ* 804, 117, p. 117. DOI: `10.1088/0004-637X/804/2/117`. arXiv: `1403.7524` (cit. on p. 98).

Mellema, Garrelt, Ilian T. Iliev, Ue-Li Pen, and Paul R. Shapiro (2006). “Simulating cosmic reionization at large scales - II. The 21-cm emission features and statistical signals.” In: *MNRAS* 372.2, pp. 679–692. DOI: `10.1111/j.1365-2966.2006.10919.x`. arXiv: `astro-ph/0603518 [astro-ph]` (cit. on pp. 2, 5).

Mellier, Yannick (1999). “Probing the Universe with Weak Lensing.” In: *ARA&A* 37, pp. 127–189. DOI: `10.1146/annurev.astro.37.1.127`. arXiv: `astro-ph/9812172 [astro-ph]` (cit. on pp. 1, 2).

Merluzzi, P., G. Busarello, M. A. Dopita, C. P. Haines, D. Steinhauser, A. Mercurio, A. Rifatto, R. J. Smith, and S. Schindler (2013). “ACCESS - V. Dissecting ram-pressure stripping through integral-field spectroscopy and multiband imaging.” In: *MNRAS* 429, pp. 1747–1773. DOI: `10.1093/mnras/sts466`. arXiv: `1211.6532` (cit. on p. 21).

Metropolis, Nicholas, Arianna W. Rosenbluth, Marshall N. Rosenbluth, Augusta H. Teller, and Edward Teller (1953). “Equation of State Calculations by Fast Computing Machines.” In: *J. Chem. Phys.* 21.6, pp. 1087–1092. DOI: `10.1063/1.1699114` (cit. on p. 56).

Mihos, J. Christopher and Lars Hernquist (1994). "Merger-Induced Starbursts and Ultraluminous Infrared Galaxies." In: *American Astronomical Society Meeting Abstracts*. Vol. 185. American Astronomical Society Meeting Abstracts, p. 68.02 (cit. on p. 14).

Mihos, J. Christopher and Lars Hernquist (1996). "Gasdynamics and Starbursts in Major Mergers." In: *ApJ* 464, p. 641. DOI: `10.1086/177353`. arXiv: `astro-ph/9512099 [astro-ph]` (cit. on p. 14).

Miley, George and Carlos De Breuck (2008). "Distant radio galaxies and their environments." In: *A&A Rev.* 15.2, pp. 67–144. DOI: `10.1007/s00159-007-0008-z`. arXiv: `0802.2770 [astro-ph]` (cit. on p. 15).

Miller, G. E. and J. M. Scalo (1979). "The Initial Mass Function and Stellar Birthrate in the Solar Neighborhood." In: *ApJS* 41, p. 513. DOI: `10.1086/190629` (cit. on p. 5).

Miller, T. B. et al. (2018). "A massive core for a cluster of galaxies at a redshift of 4.3." In: *Nature* 556.7702, pp. 469–472. DOI: `10.1038/s41586-018-0025-2`. arXiv: `1804.09231 [astro-ph.GA]` (cit. on p. 98).

Mioduszewski, A. J., P. A. Hughes, and G. C. Duncan (1997). "Simulated VLBI Images from Relativistic Hydrodynamic Jet Models." In: *ApJ* 476, pp. 649–665. DOI: `10.1086/303652`. eprint: `astro-ph/9606004` (cit. on p. 111).

Miyazaki, S. et al. (2012). "Hyper Suprime-Cam." In: *Ground-based and Airborne Instrumentation for Astronomy IV*. Vol. 8446. *Proc. SPIE*, 84460Z. DOI: `10.1117/12.926844` (cit. on pp. 43, 44).

Mo, Houjun, Frank C. van den Bosch, and Simon White (2010). *Galaxy Formation and Evolution* (cit. on pp. 4–6, 15).

Mobasher, B. et al. (2015). "A Critical Assessment of Stellar Mass Measurement Methods." In: *ApJ* 808, 101, p. 101. DOI: `10.1088/0004-637X/808/1/101`. arXiv: `1505.01501` (cit. on p. 12).

Momcheva, Ivelina G. et al. (2016). "The 3D-HST Survey: Hubble Space Telescope WFC3/G141 Grism Spectra, Redshifts, and Emission Line Measurements for ~100,000 Galaxies." In: *ApJS* 225.2, 27, p. 27. DOI: `10.3847/0067-0049/225/2/27`. arXiv: `1510.02106 [astro-ph.GA]` (cit. on p. 135).

Moore, B., G. Lake, T. Quinn, and J. Stadel (1999a). "On the survival and destruction of spiral galaxies in clusters." In: *MNRAS* 304, pp. 465–474. DOI: `10.1046/j.1365-8711.1999.02345.x`. eprint: `astro-ph/9811127` (cit. on p. 21).

Moore, Ben, Sebastiano Ghigna, Fabio Governato, George Lake, Thomas Quinn, Joachim Stadel, and Paolo Tozzi (1999b). "Dark Matter Substructure within Galactic Halos." In: *ApJ* 524.1, pp. L19–L22. DOI: `10.1086/312287`. arXiv: `astro-ph/9907411 [astro-ph]` (cit. on p. 9).

Morganti, R., T. Oosterloo, J. B. R. Oonk, W. Frieswijk, and C. Tadhunter (2015). "The fast molecular outflow in the Seyfert galaxy IC 5063 as seen by ALMA." In: *A&A* 580, A1, A1. DOI: `10.1051/0004-6361/201525860`. arXiv: `1505.07190` (cit. on pp. 95–97, 135, 137, 138).

Mortlock, Alice et al. (2015). "Deconstructing the galaxy stellar mass function with UKIDSS and CANDELS: the impact of colour, structure and environment." In: *MNRAS* 447.1, pp. 2–24. DOI: `10.1093/mnras/stu2403`. arXiv: `1411.3339 [astro-ph.GA]` (cit. on pp. 25, 26, 85, 90).

Moster, B. P., R. S. Somerville, J. A. Newman, and H.-W. Rix (2011). "A Cosmic Variance Cookbook." In: *ApJ* 731, 113, p. 113. DOI: `10.1088/0004-637X/731/2/113`. arXiv: `1001.1737` (cit. on pp. 35, 39).

Moustakas, J., A. L. Coil, J. Aird, M. R. Blanton, R. J. Cool, D. J. Eisenstein, A. J. Mendez, K. C. Wong, G. Zhu, and S. Arnouts (2013). "PRIMUS: Constraints on Star Formation Quenching and Galaxy Merging, and the Evolution of the Stellar Mass Function from z = 0-1." In: *ApJ* 767, 50, p. 50. DOI: `10.1088/0004-637X/767/1/50`. arXiv: `1301.1688 [astro-ph.CO]` (cit. on pp. 22, 90).

Moustakas, John, Jr. Kennicutt Robert C., and Christy A. Tremonti (2006). "Optical Star Formation Rate Indicators." In: *ApJ* 642.2, pp. 775–796. DOI: `10.1086/500964`. arXiv: `astro-ph/0511730 [astro-ph]` (cit. on p. 100).

Mushotzky, Richard (1993). "Cooling Flows in Clusters of Galaxies." In: *The Environment and Evolution of Galaxies*. Ed. by J. Michael Shull and Harley A. Thronson. Vol. 188. Astrophysics and Space Science Library, p. 383. DOI: `10.1007/978-94-011-1882-8_22` (cit. on pp. 6, 15).

Mutch, S. J., D. J. Croton, and G. B. Poole (2013). "The simplest model of galaxy formation - I. A formation history model of galaxy stellar mass growth." In: *MNRAS* 435, pp. 2445–2459. DOI: `10.1093/mnras/stt1453`. arXiv: `1304.2774` (cit. on pp. 20, 21).

Muzzin, A. et al. (2012). "The Gemini Cluster Astrophysics Spectroscopic Survey (GCLASS): The Role of Environment and Self-regulation in Galaxy Evolution at z ~ 1." In: *ApJ* 746, 188, p. 188. DOI: `10.1088/0004-637X/746/2/188`. arXiv: `1112.3655` (cit. on pp. 18, 19, 81, 139).

Muzzin, A., G. Wilson, R. Demarco, C. Lidman, J. Nantais, H. Hoekstra, H. K. C. Yee, and A. Rettura (2013a). "Discovery of a Rich Cluster at z = 1.63 Using the Rest-frame 1.6 μm "Stellar Bump Sequence" Method." In: *ApJ* 767, 39, p. 39. DOI: `10.1088/0004-637X/767/1/39`. arXiv: `1301.5905` (cit. on p. 98).

Muzzin, A. et al. (2013b). "The Evolution of the Stellar Mass Functions of Star-forming and Quiescent Galaxies to z = 4 from the COSMOS/UltraVISTA Survey." In: *ApJ* 777, 18, p. 18. DOI: `10.1088/0004-637X/777/1/18`. arXiv: `1303.4409` (cit. on pp. 23, 85, 90).

Naab, Thorsten, Sadegh Khochfar, and Andreas Burkert (2006). "Properties of Early-Type, Dry Galaxy Mergers and the Origin of Massive Elliptical Galaxies." In: *ApJ* 636.2, pp. L81–L84. DOI: `10.1086/500205`. arXiv: `astro-ph/0509667 [astro-ph]` (cit. on p. 15).

Navarro, J. F., C. S. Frenk, and S. D. M. White (1994). "Accretion of satellite galaxies and the density of the universe." In: *MNRAS* 267, pp. L1–L3. DOI: `10.1093/mnras/267.1.L1` (cit. on p. 7).

Navarro, Julio F., Carlos S. Frenk, and Simon D. M. White (1996). "The Structure of Cold Dark Matter Halos." In: *ApJ* 462, p. 563. DOI: `10.1086/177173`. arXiv: `astro-ph/9508025 [astro-ph]` (cit. on p. 4).

Navarro, Julio F., Carlos S. Frenk, and Simon D. M. White (1997). "A Universal Density Profile from Hierarchical Clustering." In: *ApJ* 490.2, pp. 493–508. DOI: `10.1086/304888`. arXiv: `astro-ph/9611107 [astro-ph]` (cit. on p. 4).

Nelder, J.A. and RA Mead (1965). "A Simplex Method for Function Minimization Comput." In: 7 (cit. on p. 64).

Nelson, Dylan, Mark Vogelsberger, Shy Genel, Debora Sijacki, Dušan Kereš, Volker Springel, and Lars Hernquist (2013). "Moving mesh cosmology: tracing cosmological gas accretion." In: *MNRAS* 429.4, pp. 3353–3370. DOI: `10.1093/mnras/sts595`. arXiv: `1301.6753 [astro-ph.CO]` (cit. on p. 15).

Nesvadba, N. P. H., R. Neri, C. De Breuck, M. D. Lehnert, D. Downes, F. Walter, A. Omont, F. Boulanger, and N. Seymour (2009). "CO line emission in the halo of a radio galaxy at z = 2.6." In: *MNRAS* 395.1, pp. L16–L20. DOI: `10.1111/j.1745-3933.2009.00631.x`. arXiv: `0903.0862 [astro-ph.CO]` (cit. on pp. 96, 97, 137, 138).

Newman, A. B., R. S. Ellis, S. Andreon, T. Treu, A. Raichoor, and G. Trinchieri (2014). "Spectroscopic Confirmation of the Rich z = 1.80 Galaxy Cluster JKCS 041 using the WFC3 Grism: Environmental Trends in the Ages and Structure of Quiescent Galaxies." In: *ApJ* 788, 51, p. 51. DOI: `10.1088/0004-637X/788/1/51`. arXiv: `1310.6754` (cit. on p. 98).

Newman, J. A. and M. Davis (2002). "Measuring the Cosmic Equation of State with Counts of Galaxies. II. Error Budget for the DEEP2 Redshift Survey." In: *ApJ* 564, pp. 567–575. DOI: `10.1086/324148`. eprint: `astro-ph/0109130` (cit. on p. 35).

Noble, A. G. et al. (2017). "ALMA Observations of Gas-rich Galaxies in z ~ 1.6 Galaxy Clusters: Evidence for Higher Gas Fractions in High-density Environments." In: *ApJ* 842, L21, p. L21. DOI: `10.3847/2041-8213/aa77f3`. arXiv: `1705.03062` (cit. on pp. 98, 124, 126, 138, 139, 141).

Noble, A. G. et al. (2018). "Resolving CO (2-1) in zĩ.6 Gas-Rich Cluster Galaxies with ALMA: Rotating Molecular Gas Disks with Possible Signatures of Gas Stripping." In: *arXiv e-prints*. arXiv: `1809.03514` (cit. on p. 95).

Nocedal, Jorge and Stephen J. Wright (2006). *Numerical Optimization*. second. New York, NY, USA: Springer (cit. on p. 64).

Noirot, G. et al. (2016). "HST Grism Confirmation of Two z ~ 2 Structures from the Clusters around Radio-loud AGN (CARLA) Survey." In: *ApJ* 830, 90, p. 90. DOI: `10.3847/0004-637X/830/2/90`. arXiv: `1609.04162` (cit. on pp. 98, 102, 103).

Noirot, G. et al. (2018). "HST Grism Confirmation of 16 Structures at 1.4<z<2.8 from the Clusters Around Radio-Loud AGN (CARLA) Survey." In: *ApJ* 859, 38, p. 38. DOI: `10.3847/1538-4357/aabadb`. arXiv: `1804.01500` (cit. on pp. 98, 100–106, 116, 125, 127–133, 135, 139, 145, 149, 151, 152).

Norton, S. A., K. Gebhardt, A. I. Zabludoff, and D. Zaritsky (2001). "The Spatial Distribution and Kinematics of Stellar Populations in E+A Galaxies." In: *ApJ* 557, pp. 150–164. DOI: `10.1086/321668`. eprint: `astro-ph/0104433` (cit. on p. 142).

Nyland, K. et al. (2017). "A Multi-wavelength Study of the Turbulent Central Engine of the Low-mass AGN Hosted by NGC 404." In: *ApJ* 845, 50, p. 50. DOI: `10.3847/1538-4357/aa7ecf`. arXiv: `1707.02303` (cit. on p. 111).

Ocvirk, P., C. Pichon, and R. Teyssier (2008). "Bimodal gas accretion in the Horizon-MareNostrum galaxy formation simulation." In: *MNRAS* 390.4, pp. 1326–1338. DOI: `10.1111/j.1365-2966.2008.13763.x`. arXiv: `0803.4506 [astro-ph]` (cit. on p. 15).

Oesch, P. A. et al. (2016). "A Remarkably Luminous Galaxy at z=11.1 Measured with Hubble Space Telescope Grism Spectroscopy." In: *ApJ* 819.2, 129, p. 129. doi: 10.3847/0004-637X/819/2/129. arXiv: 1603.00461 [astro-ph.GA] (cit. on p. 5).

Oke, J. B. et al. (1995). "The Keck Low-Resolution Imaging Spectrometer." In: *PASP* 107, p. 375. doi: 10.1086/133562 (cit. on p. 103).

Olivares, V. et al. (2019). "Ubiquitous cold and massive filaments in cool core clusters." In: *A&A* 631, A22, A22. doi: 10.1051/0004-6361/201935350. arXiv: 1902.09164 [astro-ph.GA] (cit. on pp. 17, 95–97).

Olive, K. A., G. Steigman, and T. P. Walker (2000). "Primordial nucleosynthesis: theory and observations." In: *Phys. Rep.* 333, pp. 389–407. doi: 10.1016/S0370-1573(00)00031-4. arXiv: astro-ph/9905320 [astro-ph] (cit. on p. 2).

Oser, Ludwig, Jeremiah P. Ostriker, Thorsten Naab, Peter H. Johansson, and Andreas Burkert (2010). "The Two Phases of Galaxy Formation." In: *ApJ* 725.2, pp. 2312–2323. doi: 10.1088/0004-637X/725/2/2312. arXiv: 1010.1381 [astro-ph.CO] (cit. on p. 13).

Osterbrock, D. E. and G. J. Ferland (2006). *Astrophysics of gaseous nebulae and active galactic nuclei* (cit. on p. 130).

Oteo, I. et al. (2018). "An Extreme Protocluster of Luminous Dusty Starbursts in the Early Universe." In: *ApJ* 856, 72, p. 72. doi: 10.3847/1538-4357/aaa1f1. arXiv: 1709.02809 (cit. on p. 98).

Pacifici, C. et al. (2016). "The Evolution of Star Formation Histories of Quiescent Galaxies." In: *ApJ* 832, 79, p. 79. doi: 10.3847/0004-637X/832/1/79. arXiv: 1609.03572 (cit. on pp. 18, 19, 81).

Panter, Benjamin, Raul Jimenez, Alan F. Heavens, and Stephane Charlot (2007). "The star formation histories of galaxies in the Sloan Digital Sky Survey." In: *MNRAS* 378.4, pp. 1550–1564. doi: 10.1111/j.1365-2966.2007.11909.x. arXiv: astro-ph/0608531 [astro-ph] (cit. on pp. 18, 81).

Papadopoulos, Padeli, Rob Ivison, Chris Carilli, and Geraint Lewis (2001). "A massive reservoir of low-excitation molecular gas at high redshift." In: *Nature* 409.6816, pp. 58–60. doi: 10.1038/35051029. arXiv: astro-ph/0101028 [astro-ph] (cit. on p. 99).

Papovich, C. et al. (2010). "A Spitzer-selected Galaxy Cluster at $z = 1.62$." In: *ApJ* 716, pp. 1503–1513. doi: 10.1088/0004-637X/716/2/1503. arXiv: 1002.3158 (cit. on p. 98).

Peacock, John A. et al. (2002). "Studying Large-scale Structure with the 2dF Galaxy Redshift Survey." In: *A New Era in Cosmology*. Ed. by Nigel Metcalfe and Tom Shanks. Vol. 283. Astronomical Society of the Pacific Conference Series, p. 19. arXiv: astro-ph/0204239 [astro-ph] (cit. on pp. 2, 6, 10).

Peebles, P. J. E. (1968). "Recombination of the Primeval Plasma." In: *ApJ* 153, p. 1. doi: 10.1086/149628 (cit. on p. 2).

Peebles, P. J. E. (1980). *The large-scale structure of the universe* (cit. on pp. 4, 35).

Peebles, P. J. E. (1982). "Large-scale background temperature and mass fluctuations due to scale-invariant primeval perturbations." In: *ApJ* 263, pp. L1–L5. doi: 10.1086/183911 (cit. on p. 1).

Peebles, P. J. E. (1993). *Principles of Physical Cosmology* (cit. on p. 2).

Peebles, P. J. E. and B. Ratra (1988). "Cosmology with a time-variable cosmological 'constant'." In: *ApJ* 325, pp. L17–L20. DOI: `10.1086/185100` (cit. on p. 1).

Peng, Y.-j. et al. (2010). "Mass and Environment as Drivers of Galaxy Evolution in SDSS and zCOSMOS and the Origin of the Schechter Function." In: *ApJ* 721, pp. 193–221. DOI: `10.1088/0004-637X/721/1/193`. arXiv: `1003.4747 [astro-ph.CO]` (cit. on pp. 15, 18–20, 23, 27, 81, 85, 93, 148).

Peng, Y.-j., S. J. Lilly, A. Renzini, and M. Carollo (2012). "Mass and Environment as Drivers of Galaxy Evolution. II. The Quenching of Satellite Galaxies as the Origin of Environmental Effects." In: *ApJ* 757, 4, p. 4. DOI: `10.1088/0004-637X/757/1/4`. arXiv: `1106.2546 [astro-ph.CO]` (cit. on pp. 19, 20, 23, 81, 93).

Peng, Y.-j., S. J. Lilly, A. Renzini, and M. Carollo (2014). "Mass and Environment as Drivers of Galaxy Evolution. III. The Constancy of the Faint-end Slope and the Merging of Galaxies." In: *ApJ* 790, 95, p. 95. DOI: `10.1088/0004-637X/790/2/95`. arXiv: `1406.7291` (cit. on p. 19).

Peng, Y., R. Maiolino, and R. Cochrane (2015). "Strangulation as the primary mechanism for shutting down star formation in galaxies." In: *Nature* 521, pp. 192–195. DOI: `10.1038/nature14439`. arXiv: `1505.03143` (cit. on p. 21).

Penzias, A. A. and R. W. Wilson (1965). "A Measurement of Excess Antenna Temperature at 4080 Mc/s." In: *ApJ* 142, pp. 419–421. DOI: `10.1086/148307` (cit. on p. 2).

Pérez-González, Pablo G. et al. (2008). "The Stellar Mass Assembly of Galaxies from $z = 0$ to $z = 4$: Analysis of a Sample Selected in the Rest-Frame Near-Infrared with Spitzer." In: *ApJ* 675.1, pp. 234–261. DOI: `10.1086/523690`. arXiv: `0709.1354 [astro-ph]` (cit. on pp. 18, 23, 81).

Perlmutter, S. et al. (1999). "Measurements of Ω and Λ from 42 High-Redshift Supernovae." In: *ApJ* 517, pp. 565–586. DOI: `10.1086/307221`. eprint: `astro-ph/9812133` (cit. on p. 1).

Perna, M. et al. (2018). "The molecular gas content in obscured AGN at $z > 1$." In: *ArXiv e-prints*. arXiv: `1807.03378` (cit. on p. 138).

Persic, Massimo, Paolo Salucci, and Fulvio Stel (1996). "The universal rotation curve of spiral galaxies — I. The dark matter connection." In: *MNRAS* 281.1, pp. 27–47. DOI: `10.1093/mnras/278.1.27`. arXiv: `astro-ph/9506004 [astro-ph]` (cit. on p. 1).

Peterson, J. R. and A. C. Fabian (2006). "X-ray spectroscopy of cooling clusters." In: *Phys. Rep.* 427.1, pp. 1–39. DOI: `10.1016/j.physrep.2005.12.007`. arXiv: `astro-ph/0512549 [astro-ph]` (cit. on p. 16).

Peterson, J. R., F. B. S. Paerels, J. S. Kaastra, M. Arnaud, T. H. Reiprich, A. C. Fabian, R. F. Mushotzky, J. G. Jernigan, and I. Sakelliou (2001). "X-ray imaging-spectroscopy of Abell 1835." In: *A&A* 365, pp. L104–L109. DOI: `10.1051/0004-6361:20000021`. arXiv: `astro-ph/0010658 [astro-ph]` (cit. on p. 16).

Pforr, Janine, Claudia Maraston, and Chiara Tonini (2012). "Recovering galaxy stellar population properties from broad-band spectral energy distribution fitting." In: *MNRAS* 422.4, pp. 3285–3326. DOI: `10.1111/j.1365-2966.2012.20848.x`. arXiv: `1203.3548 [astro-ph.CO]` (cit. on p. 138).

Pineda, J. L., W. D. Langer, T. Velusamy, and P. F. Goldsmith (2013). "A Herschel [C ii] Galactic plane survey. I. The global distribution of ISM gas components." In: *A&A* 554, A103, A103. DOI: `10.1051/0004-6361/201321188`. arXiv: `1304.7770 [astro-ph.GA]` (cit. on p. 99).

Planck Collaboration et al. (2011). "Planck early results. XIX. All-sky temperature and dust optical depth from Planck and IRAS. Constraints on the "dark gas" in our Galaxy." In: *A&A* 536, A19, A19. DOI: `10.1051/0004-6361/201116479`. arXiv: `1101.2029 [astro-ph.GA]` (cit. on p. 99).

Planck Collaboration et al. (2016). "Planck 2015 results. XIII. Cosmological parameters." In: *A&A* 594, A13, A13. DOI: `10.1051/0004-6361/201525830`. arXiv: `1502.01589 [astro-ph.CO]` (cit. on p. 2).

Planck Collaboration et al. (2018a). "Planck 2018 results. I. Overview and the cosmological legacy of Planck." In: *arXiv e-prints*, arXiv:1807.06205, arXiv:1807.06205. arXiv: `1807.06205 [astro-ph.CO]` (cit. on p. 2).

Planck Collaboration et al. (2018b). "Planck 2018 results. VI. Cosmological parameters." In: *arXiv e-prints*, arXiv:1807.06209, arXiv:1807.06209. arXiv: `1807.06209 [astro-ph.CO]` (cit. on p. 2).

Porth, O., C. Fendt, Z. Meliani, and B. Vaidya (2011). "Synchrotron Radiation of Self-collimating Relativistic Magnetohydrodynamic Jets." In: *ApJ* 737, 42, p. 42. DOI: `10.1088/0004-637X/737/1/42`. arXiv: `1105.4258 [astro-ph.HE]` (cit. on p. 111).

Postman, M. et al. (2005). "The Morphology-Density Relation in z ˜ 1 Clusters." In: *ApJ* 623, pp. 721–741. DOI: `10.1086/428881`. eprint: `astro-ph/0501224` (cit. on p. 98).

Potter, D., J. Stadel, and R. Teyssier (2017). "PKDGRAV3: beyond trillion particle cosmological simulations for the next era of galaxy surveys." In: *Computational Astrophysics and Cosmology* 4, 2, p. 2. DOI: `10.1186/s40668-017-0021-1`. arXiv: `1609.08621 [astro-ph.IM]` (cit. on pp. 7, 8, 42).

Pozzetti, L. et al. (2003). "The K20 survey. V. The evolution of the near-IR Luminosity Function." In: *A&A* 402, pp. 837–848. DOI: `10.1051/0004-6361:20030292`. arXiv: `astro-ph/0302599 [astro-ph]` (cit. on pp. 23, 90, 94).

Pozzetti, L. et al. (2010). "zCOSMOS - 10k-bright spectroscopic sample. The bimodality in the galaxy stellar mass function: exploring its evolution with redshift." In: *A&A* 523, A13, A13. DOI: `10.1051/0004-6361/200913020`. arXiv: `0907.5416` (cit. on pp. 20, 23, 25, 26, 38, 39, 49, 53, 80, 81, 83, 92, 94).

Prasad, D., P. Sharma, and A. Babul (2015). "Cool Core Cycles: Cold Gas and AGN Jet Feedback in Cluster Cores." In: *ApJ* 811, 108, p. 108. DOI: `10.1088/0004-637X/811/2/108`. arXiv: `1504.02215` (cit. on pp. 95–97, 137).

Press, William H. and Paul Schechter (1974). "Formation of Galaxies and Clusters of Galaxies by Self-Similar Gravitational Condensation." In: *ApJ* 187, pp. 425–438. DOI: `10.1086/152650` (cit. on p. 4).

Qin, Y. P. and G. Z. Xie (1997). "A Generalization of the V/V_{max} Test." In: *ApJ* 486, pp. 100–101. DOI: `10.1086/304525` (cit. on p. 29).

Qin, Y.-P. and G.-Z. Xie (1999). "A proposal for a sufficient test of luminosity functions." In: *A&A* 341, pp. 693–696 (cit. on p. 29).

Queyrel, J. et al. (2009). "Integral field spectroscopy with SINFONI of VVDS galaxies. II. The mass-metallicity relation at $1.2 < z < 1.6$." In: *A&A* 506, pp. 681–687. doi: 10.1051/0004-6361/200911994. arXiv: 0903.1211 (cit. on p. 131).

Racca, G. D. et al. (2016). "The Euclid mission design." In: *Space Telescopes and Instrumentation 2016: Optical, Infrared, and Millimeter Wave*. Vol. 9904. *Proc. SPIE*, 99040O. doi: 10.1117/12.2230762. arXiv: 1610.05508 [astro-ph.IM] (cit. on p. 40).

Raichoor, A. et al. (2011). "Early-type Galaxies at z ˜ 1.3. II. Masses and Ages of Early-type Galaxies in Different Environments and Their Dependence on Stellar Population Model Assumptions." In: *ApJ* 732, 12, p. 12. doi: 10.1088/0004-637X/732/1/12. arXiv: 1103.0259 (cit. on p. 138).

Refregier, Alexandre (2003). "Weak Gravitational Lensing by Large-Scale Structure." In: *ARA&A* 41, pp. 645–668. doi: 10.1146/annurev.astro.41.111302.102207. arXiv: astro-ph/0307212 [astro-ph] (cit. on pp. 1, 2).

Rettura, A. et al. (2011). "Early-type Galaxies at z ˜ 1.3. III. On the Dependence of Formation Epochs and Star Formation Histories on Stellar Mass and Environment." In: *ApJ* 732, 94, p. 94. doi: 10.1088/0004-637X/732/2/94. arXiv: 1103.0265 (cit. on p. 98).

Revaz, Y., F. Combes, and P. Salomé (2008). "Formation of cold filaments in cooling flow clusters." In: *A&A* 477, pp. L33–L36. doi: 10.1051/0004-6361:20078915. arXiv: 0711.4051 (cit. on pp. 96, 97).

Richings, A. J. and C.-A. Faucher-Giguère (2018). "Radiative cooling of swept-up gas in AGN-driven galactic winds and its implications for molecular outflows." In: *MNRAS* 478, pp. 3100–3119. doi: 10.1093/mnras/sty1285. arXiv: 1710.09433 (cit. on p. 96).

Riechers, Dominik A., Fabian Walter, Christopher L. Carilli, Pierre Cox, Axel Weiss, Frank Bertoldi, and Karl M. Menten (2011). "Dense Molecular Gas Excitation at High Redshift: Detection of $HCO^+(J = 4 \rightarrow 3)$ Emission in the Cloverleaf Quasar." In: *ApJ* 726.1, 50, p. 50. doi: 10.1088/0004-637X/726/1/50. arXiv: 1011.0991 [astro-ph.CO] (cit. on p. 99).

Rieke, G. H. et al. (2004). "The Multiband Imaging Photometer for Spitzer (MIPS)." In: *ApJS* 154.1, pp. 25–29. doi: 10.1086/422717 (cit. on p. 101).

Rieke, G. H., A. Alonso-Herrero, B. J. Weiner, P. G. Pérez-González, M. Blaylock, J. L. Donley, and D. Marcillac (2009). "Determining Star Formation Rates for Infrared Galaxies." In: *ApJ* 692.1, pp. 556–573. doi: 10.1088/0004-637X/692/1/556. arXiv: 0810.4150 [astro-ph] (cit. on p. 100).

Riess, A. G. et al. (1998). "Observational Evidence from Supernovae for an Accelerating Universe and a Cosmological Constant." In: *AJ* 116, pp. 1009–1038. doi: 10.1086/300499. eprint: astro-ph/9805201 (cit. on p. 1).

Rindler, Wolfgang (1977). *Essential relativity. Special, general and cosmological* (cit. on p. 1).

Robertson, Brant E., Richard S. Ellis, James S. Dunlop, Ross J. McLure, and Daniel P. Stark (2010). "Early star-forming galaxies and the reionization of the Universe." In: *Nature* 468.7320, pp. 49–55. doi: 10.1038/nature09527. arXiv: 1011.0727 [astro-ph.CO] (cit. on pp. 2, 5).

Robertson, Brant E. et al. (2013). "New Constraints on Cosmic Reionization from the 2012 Hubble Ultra Deep Field Campaign." In: *ApJ* 768.1, 71, p. 71. doi: 10.1088/0004-637X/768/1/71. arXiv: 1301.1228 [astro-ph.CO] (cit. on pp. 2, 5).

Robertson, Brant E., Richard S. Ellis, Steven R. Furlanetto, and James S. Dunlop (2015). "Cosmic Reionization and Early Star-forming Galaxies: A Joint Analysis of New Constraints from Planck and the Hubble Space Telescope." In: *ApJ* 802.2, L19, p. L19. DOI: `10.1088/2041-8205/802/2/L19`. arXiv: `1502.02024 [astro-ph.CO]` (cit. on pp. 2, 5).

Rodighiero, G. et al. (2011). "The Lesser Role of Starbursts in Star Formation at z = 2." In: *ApJ* 739.2, L40, p. L40. DOI: `10.1088/2041-8205/739/2/L40`. arXiv: `1108.0933 [astro-ph.CO]` (cit. on p. 18).

Rodriguez-Gomez, Vicente et al. (2016). "The stellar mass assembly of galaxies in the Illustris simulation: growth by mergers and the spatial distribution of accreted stars." In: *MNRAS* 458.3, pp. 2371–2390. DOI: `10.1093/mnras/stw456`. arXiv: `1511.08804 [astro-ph.GA]` (cit. on pp. 13, 15, 21).

Rozo, E., E. S. Rykoff, M. Becker, R. M. Reddick, and R. H. Wechsler (2015). "redMaPPer - IV. Photometric membership identification of red cluster galaxies with 1 per cent precision." In: *MNRAS* 453, pp. 38–52. DOI: `10.1093/mnras/stv1560`. arXiv: `1410.1193` (cit. on p. 37).

Rubin, V. C., Jr. Ford W. K., and N. Thonnard (1980). "Rotational properties of 21 SC galaxies with a large range of luminosities and radii, from NGC 4605 (R=4kpc) to UGC 2885 (R=122kpc)." In: *ApJ* 238, pp. 471–487. DOI: `10.1086/158003` (cit. on p. 1).

Rudnick, G. et al. (2017). "Deep CO(1-0) Observations of z = 1.62 Cluster Galaxies with Substantial Molecular Gas Reservoirs and Normal Star Formation Efficiencies." In: *ApJ* 849, 27, p. 27. DOI: `10.3847/1538-4357/aa87b2`. arXiv: `1709.06963` (cit. on pp. 98, 100, 124, 138–141).

Ruffa, Ilaria, Isabella Prandoni, Robert A. Laing, Rosita Paladino, Paola Parma, Hans de Ruiter, Arturo Mignano, Timothy A. Davis, Martin Bureau, and Joshua Warren (2019). "The AGN fuelling/feedback cycle in nearby radio galaxies I. ALMA observations and early results." In: *MNRAS* 484.3, pp. 4239–4259. DOI: `10.1093/mnras/stz255`. arXiv: `1901.07513 [astro-ph.GA]` (cit. on p. 112).

Russell, H. R. et al. (2014). "Massive Molecular Gas Flows in the A1664 Brightest Cluster Galaxy." In: *ApJ* 784, 78, p. 78. DOI: `10.1088/0004-637X/784/1/78`. arXiv: `1309.0014` (cit. on pp. 95–97, 124).

Russell, H. R. et al. (2016). "ALMA observations of cold molecular gas filaments trailing rising radio bubbles in PKS 0745-191." In: *MNRAS* 458, pp. 3134–3149. DOI: `10.1093/mnras/stw409`. arXiv: `1602.05962` (cit. on pp. 96, 97, 124).

Russell, H. R. et al. (2017a). "Alma Observations of Massive Molecular Gas Filaments Encasing Radio Bubbles in the Phoenix Cluster." In: *ApJ* 836, 130, p. 130. DOI: `10.3847/1538-4357/836/1/130`. arXiv: `1611.00017` (cit. on pp. 95–97, 135).

Russell, H. R. et al. (2017b). "Close entrainment of massive molecular gas flows by radio bubbles in the central galaxy of Abell 1795." In: *MNRAS* 472.4, pp. 4024–4037. DOI: `10.1093/mnras/stx2255`. arXiv: `1708.08935 [astro-ph.GA]` (cit. on pp. 96, 97, 138).

Russell, H. R., B. R. McNamara, A. C. Fabian, P. E. J. Nulsen, F. Combes, A. C. Edge, M. Madar, V. Olivares, P. Salomé, and A. N. Vantyghem (2019). "Driving massive molecular gas flows in central cluster galaxies with AGN feedback.” In: *MNRAS* 490.3, pp. 3025–3045. doi: 10.1093/mnras/stz2719. arXiv: 1902.09227 [astro-ph.GA] (cit. on pp. 96, 137).

Saintonge, Amélie et al. (2017). “xCOLD GASS: The Complete IRAM 30 m Legacy Survey of Molecular Gas for Galaxy Evolution Studies.” In: *ApJS* 233.2, 22, p. 22. doi: 10.3847/1538-4365/aa97e0. arXiv: 1710.02157 [astro-ph.GA] (cit. on p. 126).

Salomé, P., F. Combes, A. C. Edge, C. Crawford, M. Erlund, A. C. Fabian, N. A. Hatch, R. M. Johnstone, J. S. Sanders, and R. J. Wilman (2006). “Cold molecular gas in the Perseus cluster core. Association with X-ray cavity, Hα filaments and cooling flow.” In: *A&A* 454, pp. 437–445. doi: 10.1051/0004-6361:20054745. eprint: astro-ph/0603350 (cit. on pp. 17, 96, 97, 137, 138).

Salomé, P., F. Combes, Y. Revaz, D. Downes, A. C. Edge, and A. C. Fabian (2011). “A very extended molecular web around NGC 1275.” In: *A&A* 531, A85, A85. doi: 10.1051/0004-6361/200811333. arXiv: 1105.3108 (cit. on pp. 96, 97).

Salpeter, Edwin E. (1955). “The Luminosity Function and Stellar Evolution.” In: *ApJ* 121, p. 161. doi: 10.1086/145971 (cit. on p. 5).

Sandage, A., G. A. Tammann, and A. Yahil (1979). “The velocity field of bright nearby galaxies. I - The variation of mean absolute magnitude with redshift for galaxies in a magnitude-limited sample.” In: *ApJ* 232, pp. 352–364. doi: 10.1086/157295 (cit. on pp. 30, 39).

Sanders, D. B., J. M. Mazzarella, D.-C. Kim, J. A. Surace, and B. T. Soifer (2003). “The IRAS Revised Bright Galaxy Sample.” In: *AJ* 126, pp. 1607–1664. doi: 10.1086/376841. eprint: astro-ph/0306263 (cit. on p. 27).

Santini, P. et al. (2015). “Stellar Masses from the CANDELS Survey: The GOODS-South and UDS Fields.” In: *ApJ* 801.2, 97, p. 97. doi: 10.1088/0004-637X/801/2/97. arXiv: 1412.5180 [astro-ph.GA] (cit. on p. 127).

Santos, J. S. et al. (2015). “The reversal of the SF-density relation in a massive, X-ray-selected galaxy cluster at $z = 1.58$: results from Herschel.” In: *MNRAS* 447, pp. L65–L69. doi: 10.1093/mnrasl/slu180. arXiv: 1412.5188 (cit. on p. 98).

Sargent, M. T., M. Béthermin, E. Daddi, and D. Elbaz (2012). “The Contribution of Starbursts and Normal Galaxies to Infrared Luminosity Functions at z < 2.” In: *ApJ* 747.2, L31, p. L31. doi: 10.1088/2041-8205/747/2/L31. arXiv: 1202.0290 [astro-ph.CO] (cit. on p. 18).

Sargent, M. T., E. Daddi, M. Béthermin, H. Aussel, G. Magdis, H. S. Hwang, S. Juneau, D. Elbaz, and E. da Cunha (2014). “Regularity Underlying Complexity: A Redshift-independent Description of the Continuous Variation of Galaxy-scale Molecular Gas Properties in the Mass-star Formation Rate Plane.” In: *ApJ* 793, 19, p. 19. doi: 10.1088/0004-637X/793/1/19. arXiv: 1303.4392 (cit. on pp. 18, 100).

Saunders, W., M. Rowan-Robinson, A. Lawrence, G. Efstathiou, N. Kaiser, R. S. Ellis, and C. S. Frenk (1990). “The 60-micron and far-infrared luminosity functions of IRAS galaxies.” In: *MNRAS* 242, pp. 318–337. doi: 10.1093/mnras/242.3.318 (cit. on p. 27).

Saunders, W. et al. (2000). “The PSCz catalogue.” In: *MNRAS* 317, pp. 55–63. doi: 10.1046/j.1365-8711.2000.03528.x. eprint: astro-ph/0001117 (cit. on p. 9).

Sawala, Till et al. (2016). “The APOSTLE simulations: solutions to the Local Group’s cosmic puzzles.” In: *MNRAS* 457.2, pp. 1931–1943. DOI: `10.1093/mnras/stw145`. arXiv: `1511.01098 [astro-ph.GA]` (cit. on p. 8).

Scalo, J. M. (1986). “The Stellar Initial Mass Function.” In: *Fund. Cosmic Phys.* 11, pp. 1–278 (cit. on p. 5).

Schafer, C. M. (2007). “A Statistical Method for Estimating Luminosity Functions Using Truncated Data.” In: *ApJ* 661, pp. 703–713. DOI: `10.1086/515390`. eprint: `astro-ph/0702401` (cit. on p. 31).

Schaye, Joop et al. (2015). “The EAGLE project: simulating the evolution and assembly of galaxies and their environments.” In: *MNRAS* 446.1, pp. 521–554. DOI: `10.1093/mnras/stu2058`. arXiv: `1407.7040 [astro-ph.GA]` (cit. on p. 7).

Schechter, P. (1976). “An analytic expression for the luminosity function for galaxies.” In: *ApJ* 203, pp. 297–306. DOI: `10.1086/154079` (cit. on pp. 26, 38, 39, 53, 92).

Schiminovich, D. et al. (2005). “The GALEX-VVDS Measurement of the Evolution of the Far-Ultraviolet Luminosity Density and the Cosmic Star Formation Rate.” In: *ApJ* 619.1, pp. L47–L50. DOI: `10.1086/427077`. arXiv: `astro-ph/0411424 [astro-ph]` (cit. on pp. 26, 100).

Schmidt, M. (1968). “Space Distribution and Luminosity Functions of Quasi-Stellar Radio Sources.” In: *ApJ* 151, p. 393. DOI: `10.1086/149446` (cit. on pp. 28, 39).

Schmidt, Maarten (1959). “The Rate of Star Formation.” In: *ApJ* 129, p. 243. DOI: `10.1086/146614` (cit. on p. 18).

Schrabback, T. et al. (2010). “Evidence of the accelerated expansion of the Universe from weak lensing tomography with COSMOS.” In: *A&A* 516, A63, A63. DOI: `10.1051/0004-6361/200913577`. arXiv: `0911.0053 [astro-ph.CO]` (cit. on p. 2).

Schreiber, C. et al. (2015). “The Herschel view of the dominant mode of galaxy growth from z = 4 to the present day.” In: *A&A* 575, A74, A74. DOI: `10.1051/0004-6361/201425017`. arXiv: `1409.5433 [astro-ph.GA]` (cit. on p. 18).

Schruba, Andreas et al. (2011). “A Molecular Star Formation Law in the Atomic-gas-dominated Regime in Nearby Galaxies.” In: *AJ* 142.2, 37, p. 37. DOI: `10.1088/0004-6256/142/2/37`. arXiv: `1105.4605 [astro-ph.CO]` (cit. on pp. 18, 100).

Schweizer, Francois (1996). “Colliding and Merging Galaxies. III. The Dynamically Young Merger Remnant NGC 3921.” In: *AJ* 111, p. 109. DOI: `10.1086/117765` (cit. on p. 13).

Schweizer, Francois and Patrick Seitzer (1992). “Correlation Between UBV Colors and Fine Structure in E and SO.” In: *AJ* 104, p. 1039. DOI: `10.1086/116296` (cit. on p. 13).

Scoville, N. et al. (2007). “The Cosmic Evolution Survey (COSMOS): Overview.” In: *ApJS* 172, pp. 1–8. DOI: `10.1086/516585`. eprint: `astro-ph/0612305` (cit. on p. 43).

Scoville, N. et al. (2013). “Evolution of Galaxies and Their Environments at z = 0.1-3 in COSMOS.” In: *ApJS* 206, 3, p. 3. DOI: `10.1088/0067-0049/206/1/3`. arXiv: `1303.6689` (cit. on pp. 18, 19, 21).

Scoville, N. et al. (2016). "ISM Masses and the Star formation Law at Z = 1 to 6: ALMA Observations of Dust Continuum in 145 Galaxies in the COSMOS Survey Field." In: *ApJ* 820, 83, p. 83. DOI: 10.3847/0004-637X/820/2/83. arXiv: 1511.05149 (cit. on p. 99).

Scoville, N. et al. (2017). "Evolution of Interstellar Medium, Star Formation, and Accretion at High Redshift." In: *ApJ* 837, 150, p. 150. DOI: 10.3847/1538-4357/aa61a0. arXiv: 1702.04729 (cit. on p. 100).

Shapley, A. E., A. L. Coil, C.-P. Ma, and K. Bundy (2005). "Chemical Abundances of DEEP2 Star-forming Galaxies at z˜1.0-1.5." In: *ApJ* 635, pp. 1006–1021. DOI: 10.1086/497630. eprint: astro-ph/0509102 (cit. on p. 131).

Sharma, Prateek, Michael McCourt, Eliot Quataert, and Ian J. Parrish (2012). "Thermal instability and the feedback regulation of hot haloes in clusters, groups and galaxies." In: *MNRAS* 420.4, pp. 3174–3194. DOI: 10.1111/j.1365-2966.2011.20246.x. arXiv: 1106.4816 [astro-ph.CO] (cit. on p. 97).

Shimakawa, R., T. Kodama, M. Hayashi, J. X. Prochaska, I. Tanaka, Z. Cai, T. L. Suzuki, K.-i. Tadaki, and Y. Koyama (2018). "MAHALO Deep Cluster Survey I. Accelerated and enhanced galaxy formation in the densest regions of a protocluster at z = 2.5." In: *MNRAS* 473, pp. 1977–1999. DOI: 10.1093/mnras/stx2494. arXiv: 1708.06369 (cit. on p. 98).

Silk, Joseph (2011). "Feedback in Galaxy Formation." In: *Tracing the Ancestry of Galaxies*. Ed. by Claude Carignan, Françoise Combes, and Ken C. Freeman. Vol. 277. IAU Symposium, pp. 273–281. DOI: 10.1017/S1743921311022939. arXiv: 1102.0283 [astro-ph.CO] (cit. on p. 20).

Silk, Joseph and Gary A. Mamon (2012). "The current status of galaxy formation." In: *Research in Astronomy and Astrophysics* 12.8, pp. 917–946. DOI: 10.1088/1674-4527/12/8/004. arXiv: 1207.3080 [astro-ph.CO] (cit. on p. 20).

Silverman, J. D. et al. (2018). "The Molecular Gas Content and Fuel Efficiency of Starbursts at z~1.6 with ALMA." In: *ApJ* 867, 92, p. 92. DOI: 10.3847/1538-4357/aae25e. arXiv: 1810.01596 (cit. on p. 100).

Skelton, R. E. et al. (2014). "3D-HST WFC3-selected Photometric Catalogs in the Five CANDELS/3D-HST Fields: Photometry, Photometric Redshifts, and Stellar Masses." In: *ApJS* 214, 24, p. 24. DOI: 10.1088/0067-0049/214/2/24. arXiv: 1403.3689 (cit. on p. 12).

Skillman, Samuel W., Michael S. Warren, Matthew J. Turk, Risa H. Wechsler, Daniel E. Holz, and P. M. Sutter (2014). "Dark Sky Simulations: Early Data Release." In: *arXiv e-prints*, arXiv:1407.2600, arXiv:1407.2600. arXiv: 1407.2600 [astro-ph.CO] (cit. on p. 7).

Sklias, P., D. Schaerer, D. Elbaz, M. Pannella, C. Schreiber, and A. Cava (2017). "Insights on star-formation histories and physical properties of $1.2 \leqslant z < 4$ Herschel-detected galaxies." In: *A&A* 605, A29, A29. DOI: 10.1051/0004-6361/201628330. arXiv: 1705.01174 (cit. on pp. 19, 81).

Smoot, G. F. et al. (1992). "Structure in the COBE Differential Microwave Radiometer First-Year Maps." In: *ApJ* 396, p. L1. DOI: 10.1086/186504 (cit. on p. 2).

Snyder, G. F., T. J. Cox, C. C. Hayward, L. Hernquist, and P. Jonsson (2011). "K+A Galaxies as the Aftermath of Gas-rich Mergers: Simulating the Evolution of Galaxies as Seen by Spectroscopic Surveys." In: *ApJ* 741, 77, p. 77.

doi: 10.1088/0004-637X/741/2/77. arXiv: 1102.3689 [astro-ph.CO] (cit. on pp. 14, 142).

Snyder, G. F. et al. (2012). "Assembly of the Red Sequence in Infrared-selected Galaxy Clusters from the IRAC Shallow Cluster Survey." In: *ApJ* 756, 114, p. 114. doi: 10.1088/0004-637X/756/2/114. arXiv: 1207.4790 [astro-ph.CO] (cit. on p. 98).

Sofue, Y. and V. Rubin (2001). "Rotation Curves of Spiral Galaxies." In: *ARA&A* 39, pp. 137–174. doi: 10.1146/annurev.astro.39.1.137. eprint: astro-ph/0010594 (cit. on p. 1).

Solomon, P. M. and P. A. Vanden Bout (2005). "Molecular Gas at High Redshift." In: *ARA&A* 43, pp. 677–725. doi: 10.1146/annurev.astro.43.051804.102221. eprint: astro-ph/0508481 (cit. on pp. 99, 122, 124, 134, 138).

Solomon, P., P. Vanden Bout, C. Carilli, and M. Guelin (2003). "The essential signature of a massive starburst in a distant quasar." In: *Nature* 426.6967, pp. 636–638. doi: 10.1038/nature02149. arXiv: astro-ph/0312436 [astro-ph] (cit. on p. 99).

Somerville, R. S., K. Lee, H. C. Ferguson, J. P. Gardner, L. A. Moustakas, and M. Giavalisco (2004). "Cosmic Variance in the Great Observatories Origins Deep Survey." In: *ApJ* 600, pp. L171–L174. doi: 10.1086/378628. eprint: astro-ph/0309071 (cit. on p. 35).

Somerville, Rachel S. and Joel R. Primack (1999). "Semi-analytic modelling of galaxy formation: the local Universe." In: *MNRAS* 310.4, pp. 1087–1110. doi: 10.1046/j.1365-8711.1999.03032.x. arXiv: astro-ph/9802268 [astro-ph] (cit. on pp. 7, 8).

Sorba, Robert and Marcin Sawicki (2018). "Spatially unresolved SED fitting can underestimate galaxy masses: a solution to the missing mass problem." In: *MNRAS* 476.2, pp. 1532–1547. doi: 10.1093/mnras/sty186. arXiv: 1801.07368 [astro-ph.GA] (cit. on p. 138).

Spergel, D. N. et al. (2003). "First-Year Wilkinson Microwave Anisotropy Probe (WMAP) Observations: Determination of Cosmological Parameters." In: *ApJS* 148.1, pp. 175–194. doi: 10.1086/377226. arXiv: astro-ph/0302209 [astro-ph] (cit. on p. 2).

Spergel, D. et al. (2015). "Wide-Field InfrarRed Survey Telescope-Astrophysics Focused Telescope Assets WFIRST-AFTA 2015 Report." In: *arXiv e-prints*, arXiv:1503.03757, arXiv:1503.03757. arXiv: 1503.03757 [astro-ph.IM] (cit. on p. 5).

Spitler, Lee R. et al. (2014). "Exploring the z = 3-4 Massive Galaxy Population with ZFOURGE: The Prevalence of Dusty and Quiescent Galaxies." In: *ApJ* 787.2, L36, p. L36. doi: 10.1088/2041-8205/787/2/L36. arXiv: 1405.1048 [astro-ph.GA] (cit. on p. 23).

Spitzer, Lyman (1978). *Physical processes in the interstellar medium*. doi: 10.1002/9783527617722 (cit. on p. 5).

Springel, V., T. Di Matteo, and L. Hernquist (2005). "Black Holes in Galaxy Mergers: The Formation of Red Elliptical Galaxies." In: *ApJ* 620, pp. L79–L82. doi: 10.1086/428772. eprint: astro-ph/0409436 (cit. on pp. 14, 17–19).

Springel, V., J. Wang, M. Vogelsberger, A. Ludlow, A. Jenkins, A. Helmi, J. F. Navarro, C. S. Frenk, and S. D. M. White (2008). "The Aquarius Project:

the subhaloes of galactic haloes." In: *MNRAS* 391.4, pp. 1685–1711. DOI: `10.1111/j.1365-2966.2008.14066.x`. arXiv: `0809.0898 [astro-ph]` (cit. on p. 8).

Springel, Volker (2005). "The cosmological simulation code GADGET-2." In: *MNRAS* 364.4, pp. 1105–1134. DOI: `10.1111/j.1365-2966.2005.09655.x`. arXiv: `astro-ph/0505010 [astro-ph]` (cit. on p. 7).

Springel, Volker and Lars Hernquist (2003). "Cosmological smoothed particle hydrodynamics simulations: a hybrid multiphase model for star formation." In: *MNRAS* 339.2, pp. 289–311. DOI: `10.1046/j.1365-8711.2003.06206.x`. arXiv: `astro-ph/0206393 [astro-ph]` (cit. on p. 8).

Springel, Volker et al. (2005). "Simulations of the formation, evolution and clustering of galaxies and quasars." In: *Nature* 435.7042, pp. 629–636. DOI: `10.1038/nature03597`. arXiv: `astro-ph/0504097 [astro-ph]` (cit. on p. 7).

Squires, G. L. (2001). *Practical Physics*, p. 224 (cit. on pp. 34, 37).

Stadel, J., D. Potter, B. Moore, J. Diemand, P. Madau, M. Zemp, M. Kuhlen, and V. Quilis (2009). "Quantifying the heart of darkness with GHALO - a multibillion particle simulation of a galactic halo." In: *MNRAS* 398.1, pp. L21–L25. DOI: `10.1111/j.1745-3933.2009.00699.x`. arXiv: `0808.2981 [astro-ph]` (cit. on p. 8).

Stanford, S. A., M. Brodwin, A. H. Gonzalez, G. Zeimann, D. Stern, A. Dey, P. R. Eisenhardt, G. F. Snyder, and C. Mancone (2012). "IDCS J1426.5+3508: Discovery of a Massive, Infrared-selected Galaxy Cluster at z = 1.75." In: *ApJ* 753, 164, p. 164. DOI: `10.1088/0004-637X/753/2/164`. arXiv: `1205.3786` (cit. on p. 98).

Stark, Daniel P., Matthew A. Schenker, Richard Ellis, Brant Robertson, Ross McLure, and James Dunlop (2013). "Keck Spectroscopy of 3 < z < 7 Faint Lyman Break Galaxies: The Importance of Nebular Emission in Understanding the Specific Star Formation Rate and Stellar Mass Density." In: *ApJ* 763.2, 129, p. 129. DOI: `10.1088/0004-637X/763/2/129`. arXiv: `1208.3529 [astro-ph.CO]` (cit. on p. 22).

Steinhardt, P. J., L. Wang, and I. Zlatev (1999). "Cosmological tracking solutions." In: *Phys. Rev. D* 59.12, 123504, p. 123504. DOI: `10.1103/PhysRevD.59.123504`. eprint: `astro-ph/9812313` (cit. on p. 1).

Stewart, Kyle R., James S. Bullock, Risa H. Wechsler, Ariyeh H. Maller, and Andrew R. Zentner (2008). "Merger Histories of Galaxy Halos and Implications for Disk Survival." In: *ApJ* 683.2, pp. 597–610. DOI: `10.1086/588579`. arXiv: `0711.5027 [astro-ph]` (cit. on p. 4).

Stewart, Kyle R., Tobias Kaufmann, James S. Bullock, Elizabeth J. Barton, Ariyeh H. Maller, Jürg Diemand, and James Wadsley (2011). "Observing the End of Cold Flow Accretion Using Halo Absorption Systems." In: *ApJ* 735.1, L1, p. L1. DOI: `10.1088/2041-8205/735/1/L1`. arXiv: `1012.2128 [astro-ph.CO]` (cit. on p. 15).

Straatman, Caroline M. S. et al. (2014). "A Substantial Population of Massive Quiescent Galaxies at z ~4 from ZFOURGE." In: *ApJ* 783.1, L14, p. L14. DOI: `10.1088/2041-8205/783/1/L14`. arXiv: `1312.4952 [astro-ph.GA]` (cit. on p. 23).

Strazzullo, V. et al. (2010). "Cluster galaxies in XMMU J2235-2557: galaxy population properties in most massive environments at z ˜ 1.4." In: *A&A*

524, A17, A17. DOI: 10.1051/0004-6361/201015251. arXiv: 1009.1423 (cit. on p. 98).

Strazzullo, V. et al. (2013). “Galaxy Evolution in Overdense Environments at High Redshift: Passive Early-type Galaxies in a Cluster at z ˜ 2.” In: *ApJ* 772, 118, p. 118. DOI: 10.1088/0004-637X/772/2/118. arXiv: 1305.3577 (cit. on pp. 21, 23, 81).

Strickland, D. K. and T. M. Heckman (2009). “Supernova Feedback Efficiency and Mass Loading in the Starburst and Galactic Superwind Exemplar M82.” In: *ApJ* 697, pp. 2030–2056. DOI: 10.1088/0004-637X/697/2/2030. arXiv: 0903.4175 [astro-ph.CO] (cit. on p. 20).

Struve, C., T. Oosterloo, R. Sancisi, R. Morganti, and B. H. C. Emonts (2010). “Cold gas in massive early-type galaxies: the case of NGC 1167.” In: *A&A* 523, A75, A75. DOI: 10.1051/0004-6361/201015311. arXiv: 1009.0658 (cit. on pp. 13, 15, 21).

Subbarao, M. U., A. J. Connolly, A. S. Szalay, and D. C. Koo (1996). “Luminosity Functions From Photometric Redshifts. I. Techniques.” In: *AJ* 112, p. 929. DOI: 10.1086/118066. eprint: astro-ph/9606075 (cit. on pp. 11, 35).

Tacconi, L. J. et al. (2013). “Phibss: Molecular Gas Content and Scaling Relations in z ˜ 1-3 Massive, Main-sequence Star-forming Galaxies.” In: *ApJ* 768, 74, p. 74. DOI: 10.1088/0004-637X/768/1/74. arXiv: 1211.5743 (cit. on pp. 19, 100, 136, 138–141, 143).

Tacconi, L. J. et al. (2018). “PHIBSS: Unified Scaling Relations of Gas Depletion Time and Molecular Gas Fractions.” In: *ApJ* 853, 179, p. 179. DOI: 10.3847/1538-4357/aaa4b4. arXiv: 1702.01140 (cit. on pp. 19, 99, 100, 136).

Tadaki, K.-i., T. Kodama, K. Ota, M. Hayashi, Y. Koyama, C. Papovich, M. Brodwin, M. Tanaka, and M. Iye (2012). “A large-scale structure traced by [O II] emitters hosting a distant cluster at z= 1.62.” In: *MNRAS* 423, pp. 2617–2626. DOI: 10.1111/j.1365-2966.2012.21063.x. arXiv: 1204.1165 (cit. on p. 98).

Tadhunter, Clive (2016). “Radio AGN in the local universe: unification, triggering and evolution.” In: *A&A Rev.* 24.1, 10, p. 10. DOI: 10.1007/s00159-016-0094-x. arXiv: 1605.08773 [astro-ph.GA] (cit. on p. 131).

Takeuchi, T. T. (2010). “Constructing a bivariate distribution function with given marginals and correlation: application to the galaxy luminosity function.” In: *MNRAS* 406, pp. 1830–1840. DOI: 10.1111/j.1365-2966.2010.16778.x. arXiv: 1004.0439 (cit. on p. 31).

Takeuchi, T. T., K. Yoshikawa, and T. T. Ishii (2000). “Tests of Statistical Methods for Estimating Galaxy Luminosity Function and Applications to the Hubble Deep Field.” In: *ApJS* 129, pp. 1–31. DOI: 10.1086/313409. eprint: astro-ph/0003127 (cit. on pp. 29, 32).

Tanaka, M., S. Toft, D. Marchesini, A. Zirm, C. De Breuck, T. Kodama, Y. Koyama, J. Kurk, and I. Tanaka (2013). “On the Formation Timescale of Massive Cluster Ellipticals Based on Deep Near-infrared Spectroscopy at z ˜ 2.” In: *ApJ* 772, 113, p. 113. DOI: 10.1088/0004-637X/772/2/113. arXiv: 1306.4406 (cit. on pp. 18, 23).

Tang, Ningyu, Di Li, Carl Heiles, Shen Wang, Zhichen Pan, and Jun-Jie Wang (2016). “Physical properties of CO-dark molecular gas traced by

C^+." In: *A&A* 593, A42, A42. doi: 10.1051/0004-6361/201528055. arXiv: 1606.00949 [astro-ph.GA] (cit. on p. 99).

Taniguchi, Y. et al. (2007). "The Cosmic Evolution Survey (COSMOS): Subaru Observations of the HST Cosmos Field." In: *ApJS* 172, pp. 9–28. doi: 10.1086/516596. eprint: astro-ph/0612295 (cit. on p. 44).

Taniguchi, Y. et al. (2015). "The Subaru COSMOS 20: Subaru optical imaging of the HST COSMOS field with 20 filters*." In: *PASJ* 67, 104, p. 104. doi: 10.1093/pasj/psv106. arXiv: 1510.00550 (cit. on p. 44).

Tasca, L. A. M. et al. (2014). "Evidence for major mergers of galaxies at 2 $\lesssim$ z < 4 in the VVDS and VUDS surveys." In: *A&A* 565, A10, A10. doi: 10.1051/0004-6361/201321507. arXiv: 1303.4400 [astro-ph.CO] (cit. on p. 13).

Tasca, L. A. M. et al. (2015). "The evolving star formation rate: M_* relation and sSFR since $z = 5$ from the VUDS spectroscopic survey." In: *A&A* 581, A54, A54. doi: 10.1051/0004-6361/201425379. arXiv: 1411.5687 [astro-ph.GA] (cit. on p. 18).

Taylor, John (1997). *An introduction to error analysis : the study of uncertainties in physical measurements*. Sausalito, Calif: University Science Books. isbn: 093570275X (cit. on pp. 34, 37).

Teyssier, R. (2002). "Cosmological hydrodynamics with adaptive mesh refinement. A new high resolution code called RAMSES." In: *A&A* 385, pp. 337–364. doi: 10.1051/0004-6361:20011817. arXiv: astro-ph/0111367 [astro-ph] (cit. on p. 7).

Thomas, D., C. Maraston, R. Bender, and C. Mendes de Oliveira (2005). "The Epochs of Early-Type Galaxy Formation as a Function of Environment." In: *ApJ* 621, pp. 673–694. doi: 10.1086/426932. eprint: astro-ph/0410209 (cit. on pp. 19, 81).

Tielens, A. G. G. M. (2010). *The Physics and Chemistry of the Interstellar Medium* (cit. on pp. 5, 6).

Tomczak, A. R. et al. (2016). "The SFR-M* Relation and Empirical Star-Formation Histories from ZFOURGE* at $0.5 < z < 4$." In: *ApJ* 817, 118, p. 118. doi: 10.3847/0004-637X/817/2/118. arXiv: 1510.06072 (cit. on pp. 18, 19, 23, 81).

Tomczak, A. R. et al. (2018). "Conditional Quenching: A detailed look at the SFR-Density Relation at z ~ 0.9 from ORELSE." In: *arXiv e-prints*. arXiv: 1812.04633 (cit. on p. 98).

Tomczak, Adam R. et al. (2014). "Galaxy Stellar Mass Functions from ZFOURGE/-CANDELS: An Excess of Low-mass Galaxies since $z = 2$ and the Rapid Buildup of Quiescent Galaxies." In: *ApJ* 783.2, 85, p. 85. doi: 10.1088/0004-637X/783/2/85. arXiv: 1309.5972 [astro-ph.CO] (cit. on pp. 23, 27, 80, 85, 90).

Tonnesen, S. and R. Cen (2014). "On the Reversal of Star formation Rate-Density Relation at $z = 1$: Insights from Simulations." In: *ApJ* 788, 133, p. 133. doi: 10.1088/0004-637X/788/2/133. arXiv: 1405.1049 (cit. on p. 98).

Toomre, Alar and Juri Toomre (1972). "Galactic Bridges and Tails." In: *ApJ* 178, pp. 623–666. doi: 10.1086/151823 (cit. on pp. 13, 14).

Tran, K.-V. H. et al. (2010). "Reversal of Fortune: Confirmation of an Increasing Star Formation-Density Relation in a Cluster at $z = 1.62$." In: *ApJ* 719, pp. L126–L129. doi: `10.1088/2041-8205/719/2/L126`. arXiv: `1005.5126` (cit. on p. 98).

Tremblay, G. R. et al. (2018). "A Galaxy-scale Fountain of Cold Molecular Gas Pumped by a Black Hole." In: *ApJ* 865, 13, p. 13. doi: `10.3847/1538-4357/aad6dd`. arXiv: `1808.00473` (cit. on pp. 96, 97, 124, 137, 138).

Tremblay, Grant R. et al. (2016). "Cold, clumpy accretion onto an active supermassive black hole." In: *Nature* 534.7606, pp. 218–221. doi: `10.1038/nature17969`. arXiv: `1606.02304 [astro-ph.GA]` (cit. on p. 16).

Tremonti, C. A. et al. (2004). "The Origin of the Mass-Metallicity Relation: Insights from 53,000 Star-forming Galaxies in the Sloan Digital Sky Survey." In: *ApJ* 613, pp. 898–913. doi: `10.1086/423264`. eprint: `astro-ph/0405537` (cit. on p. 131).

Trenti, M. and M. Stiavelli (2008). "Cosmic Variance and Its Effect on the Luminosity Function Determination in Deep High-z Surveys." In: *ApJ* 676, pp. 767–780. doi: `10.1086/528674`. arXiv: `0712.0398` (cit. on pp. 34, 35).

Treyer, Marie et al. (2007). "Extinction-corrected Star Formation Rates Empirically Derived from Ultraviolet-Optical Colors." In: *ApJS* 173.2, pp. 256–266. doi: `10.1086/521794`. arXiv: `0707.3165 [astro-ph]` (cit. on p. 100).

Van Waerbeke, Ludovic, Takashi Hamana, Román Scoccimarro, Stephane Colombi, and Francis Bernardeau (2001). "Weak lensing predictions at intermediate scales." In: *MNRAS* 322.4, pp. 918–926. doi: `10.1046/j.1365-8711.2001.04241.x`. arXiv: `astro-ph/0009426 [astro-ph]` (cit. on pp. 1, 2).

Van den Bosch, Frank C., Daniel Aquino, Xiaohu Yang, H. J. Mo, Anna Pasquali, Daniel H. McIntosh, Simone M. Weinmann, and Xi Kang (2008). "The importance of satellite quenching for the build-up of the red sequence of present-day galaxies." In: *MNRAS* 387.1, pp. 79–91. doi: `10.1111/j.1365-2966.2008.13230.x`. arXiv: `0710.3164 [astro-ph]` (cit. on p. 21).

Van der Wel, A., M. Franx, S. Wuyts, P. G. van Dokkum, J. Huang, H. W. Rix, and G. D. Illingworth (2006). "Comparing Dynamical and Photometric Mass Estimates of Low- and High-Redshift Galaxies: Random and Systematic Uncertainties." In: *ApJ* 652.1, pp. 97–106. doi: `10.1086/508128`. arXiv: `astro-ph/0607649 [astro-ph]` (cit. on p. 138).

Vantyghem, A. N. et al. (2016). "Molecular Gas Along a Bright Hα Filament in 2A 0335+096 Revealed by ALMA." In: *ApJ* 832, 148, p. 148. doi: `10.3847/0004-637X/832/2/148`. arXiv: `1610.00716` (cit. on pp. 95–97, 124, 135).

Velazquez, Hector and Simon D. M. White (1999). "Sinking satellites and the heating of galaxy discs." In: *MNRAS* 304.2, pp. 254–270. doi: `10.1046/j.1365-8711.1999.02354.x`. arXiv: `astro-ph/9809412 [astro-ph]` (cit. on p. 15).

Vergani, D. et al. (2008). "The VIMOS VLT Deep Survey. Tracing the galaxy stellar mass assembly history over the last 8 Gyr." In: *A&A* 487.1, pp. 89–101. doi: `10.1051/0004-6361:20077910`. arXiv: `0705.3018 [astro-ph]` (cit. on pp. 18, 19, 23, 81).

Vogelsberger, Mark, Shy Genel, Debora Sijacki, Paul Torrey, Volker Springel, and Lars Hernquist (2013). "A model for cosmological simulations of galaxy formation physics." In: *MNRAS* 436.4, pp. 3031–3067. DOI: 10.1093/mnras/stt1789. arXiv: 1305.2913 [astro-ph.CO] (cit. on p. 6).

Vogelsberger, Mark, Shy Genel, Volker Springel, Paul Torrey, Debora Sijacki, Dandan Xu, Greg Snyder, Dylan Nelson, and Lars Hernquist (2014). "Introducing the Illustris Project: simulating the coevolution of dark and visible matter in the Universe." In: *MNRAS* 444.2, pp. 1518–1547. DOI: 10.1093/mnras/stu1536. arXiv: 1405.2921 [astro-ph.CO] (cit. on p. 7).

Vogelsberger, Mark, Federico Marinacci, Paul Torrey, and Ewald Puchwein (2020). "Cosmological simulations of galaxy formation." In: *Nature Reviews Physics* 2.1, pp. 42–66. DOI: 10.1038/s42254-019-0127-2. arXiv: 1909.07976 [astro-ph.GA] (cit. on pp. 7, 8).

Voit, G. M., G. Meece, Y. Li, B. W. O'Shea, G. L. Bryan, and M. Donahue (2017). "A Global Model for Circumgalactic and Cluster-core Precipitation." In: *ApJ* 845, 80, p. 80. DOI: 10.3847/1538-4357/aa7d04. arXiv: 1607.02212 (cit. on pp. 96, 97).

Wagg, J. et al. (2012). "CO J = 2-1 Line Emission in Cluster Galaxies at z ˜ 1: Fueling Star Formation in Dense Environments." In: *ApJ* 752, 91, p. 91. DOI: 10.1088/0004-637X/752/2/91. arXiv: 1204.3897 (cit. on pp. 138, 139).

Wagner, A. Y., G. V. Bicknell, and M. Umemura (2012). "Driving Outflows with Relativistic Jets and the Dependence of Active Galactic Nucleus Feedback Efficiency on Interstellar Medium Inhomogeneity." In: *ApJ* 757, 136, p. 136. DOI: 10.1088/0004-637X/757/2/136. arXiv: 1205.0542 (cit. on p. 96).

Wagner, C. R. et al. (2015). "Star Formation in High-redshift Cluster Ellipticals." In: *ApJ* 800, 107, p. 107. DOI: 10.1088/0004-637X/800/2/107. arXiv: 1412.6717 (cit. on p. 98).

Wagoner, Robert V., William A. Fowler, and F. Hoyle (1967). "On the Synthesis of Elements at Very High Temperatures." In: *ApJ* 148, p. 3. DOI: 10.1086/149126 (cit. on p. 2).

Waldram, E. M., J. A. Yates, J. M. Riley, and P. J. Warner (1996). "The 7C survey of radio sources at 151 MHz - a region covering RA 9ĥ to 16ĥ and Dec. 20 deg to 35 deg." In: *MNRAS* 282.3, pp. 779–787. DOI: 10.1093/mnras/282.3.779 (cit. on p. 114).

Walker, Terry P., Gary Steigman, David N. Schramm, Keith A. Olive, and Ho-Shik Kang (1991). "Primordial Nucleosynthesis Redux." In: *ApJ* 376, p. 51. DOI: 10.1086/170255 (cit. on p. 2).

Wall, J. V. and C. R. Jenkins (2003). *Practical Statistics for Astronomers*. Ed. by R. Ellis, J. Huchra, S. Kahn, G. Rieke, and P. B. Stetson (cit. on p. 27).

Walter, F. et al. (2014). "A Molecular Line Scan in the Hubble Deep Field North: Constraints on the CO Luminosity Function and the Cosmic H_2 Density." In: *ApJ* 782.2, 79, p. 79. DOI: 10.1088/0004-637X/782/2/79. arXiv: 1312.6365 [astro-ph.CO] (cit. on p. 19).

Walter, Fabian et al. (2019). "The evolution of the cosmic molecular gas density." In: *BAAS* 51.3, 442, p. 442. arXiv: 1903.08659 [astro-ph.GA] (cit. on pp. 19, 20, 150).

Wang, T. et al. (2016a). "Discovery of a Galaxy Cluster with a Violently Starbursting Core at z = 2.506." In: *ApJ* 828, 56, p. 56. DOI: 10.3847/0004-637X/828/1/56. arXiv: 1604.07404 (cit. on p. 98).

Wang, Z.-Y., J. F. Haase, J. Casanova, and M. B. Plenio (2016b). “Positioning nuclear spins in interacting clusters for quantum technologies and bioimaging.” In: *Phys. Rev. B* 93.17, 174104, p. 174104. DOI: `10.1103/PhysRevB.93.174104`. arXiv: `1510.02811 [quant-ph]` (cit. on p. 98).

Weigel, A. K., K. Schawinski, and C. Bruderer (2016). “Stellar mass functions: methods, systematics and results for the local Universe.” In: *MNRAS* 459, pp. 2150–2187. DOI: `10.1093/mnras/stw756`. arXiv: `1604.00008` (cit. on pp. 25, 32).

Weinberg, David H., Romeel Davé, Neal Katz, and Lars Hernquist (2004). “Galaxy Clustering and Galaxy Bias in a ΛCDM Universe.” In: *ApJ* 601.1, pp. 1–21. DOI: `10.1086/380481`. arXiv: `astro-ph/0212356 [astro-ph]` (cit. on p. 7).

Weinberg, Steven (1972). *Gravitation and Cosmology: Principles and Applications of the General Theory of Relativity* (cit. on p. 1).

Weiß, A., F. Walter, and N. Z. Scoville (2005). “The spectral energy distribution of CO lines in M 82.” In: *A&A* 438, pp. 533–544. DOI: `10.1051/0004-6361:20052667`. eprint: `astro-ph/0504377` (cit. on p. 124).

Werner, N., M. Sun, J. Bagchi, S. W. Allen, G. B. Taylor, S. K. Sirothia, A. Simionescu, E. T. Million, J. Jacob, and M. Donahue (2011). “Violent interaction between the active galactic nucleus and the hot gas in the core of the galaxy cluster Sérsic 159-03.” In: *MNRAS* 415.4, pp. 3369–3379. DOI: `10.1111/j.1365-2966.2011.18957.x`. arXiv: `1102.5080 [astro-ph.CO]` (cit. on p. 17).

Wetzel, Andrew R., Philip F. Hopkins, Ji-hoon Kim, Claude-André Faucher-Giguère, Dušan Kereš, and Eliot Quataert (2016). “Reconciling Dwarf Galaxies with ΛCDM Cosmology: Simulating a Realistic Population of Satellites around a Milky Way-mass Galaxy.” In: *ApJ* 827.2, L23, p. L23. DOI: `10.3847/2041-8205/827/2/L23`. arXiv: `1602.05957 [astro-ph.GA]` (cit. on p. 8).

White, Martin (2002). “The Mass Function.” In: *ApJS* 143.2, pp. 241–255. DOI: `10.1086/342752`. arXiv: `astro-ph/0207185 [astro-ph]` (cit. on p. 8).

White, S. D. M. and M. J. Rees (1978). “Core condensation in heavy halos: a two-stage theory for galaxy formation and clustering.” In: *MNRAS* 183, pp. 341–358. DOI: `10.1093/mnras/183.3.341` (cit. on pp. 1, 4, 13).

White, Simon D. M. and Carlos S. Frenk (1991). “Galaxy Formation through Hierarchical Clustering.” In: *ApJ* 379, p. 52. DOI: `10.1086/170483` (cit. on pp. 4, 7, 8).

White, Simon D. M., Marc Davis, George Efstathiou, and Carlos S. Frenk (1987). “Galaxy distribution in a cold dark matter universe.” In: *Nature* 330.6147, pp. 451–453. DOI: `10.1038/330451a0` (cit. on p. 7).

Wiersma, Robert P. C., Joop Schaye, Tom Theuns, Claudio Dalla Vecchia, and Luca Tornatore (2009). “Chemical enrichment in cosmological, smoothed particle hydrodynamics simulations.” In: *MNRAS* 399.2, pp. 574–600. DOI: `10.1111/j.1365-2966.2009.15331.x`. arXiv: `0902.1535 [astro-ph.CO]` (cit. on pp. 6, 17).

Wilkins, Stephen M., Neil Trentham, and Andrew M. Hopkins (2008). “The evolution of stellar mass and the implied star formation history.” In: *MNRAS* 385.2, pp. 687–694. DOI: `10.1111/j.1365-2966.2008.12885.x`. arXiv: `0801.1594 [astro-ph]` (cit. on pp. 22, 26).

Williams, R. E. et al. (1996). “The Hubble Deep Field: Observations, Data Reduction, and Galaxy Photometry.” In: *AJ* 112, p. 1335. DOI: `10.1086/118105`. eprint: `astro-ph/9607174` (cit. on p. 9).

Williams, Rik J., Ryan F. Quadri, Marijn Franx, Pieter van Dokkum, and Ivo Labbé (2009). “Detection of Quiescent Galaxies in a Bicolor Sequence from Z = 0-2.” In: *ApJ* 691.2, pp. 1879–1895. DOI: `10.1088/0004-637X/691/2/1879`. arXiv: `0806.0625 [astro-ph]` (cit. on pp. 23, 25, 90).

Willmer, C. N. A. (1997). “Estimating galaxy luminosity functions.” In: *AJ* 114, pp. 898–912. DOI: `10.1086/118522`. eprint: `astro-ph/9707246` (cit. on p. 32).

Wolf, C. (2009). “Bayesian photometric redshifts with empirical training sets.” In: *MNRAS* 397, pp. 520–533. DOI: `10.1111/j.1365-2966.2009.14953.x`. arXiv: `0904.3438 [astro-ph.IM]` (cit. on p. 12).

Wolf, C., K. Meisenheimer, and H.-J. Röser (2001). “Object classification in astronomical multi-color surveys.” In: *A&A* 365, pp. 660–680. DOI: `10.1051/0004-6361:20000474`. eprint: `astro-ph/0010092` (cit. on p. 36).

Wolf, C., K. Meisenheimer, H.-W. Rix, A. Borch, S. Dye, and M. Kleinheinrich (2003). “The COMBO-17 survey: Evolution of the galaxy luminosity function from 25 000 galaxies with 0.2< z <1.2.” In: *A&A* 401, pp. 73–98. DOI: `10.1051/0004-6361:20021513`. eprint: `astro-ph/0208345` (cit. on pp. 11, 12, 36).

Wolf, C. et al. (2004). “A catalogue of the Chandra Deep Field South with multi-colour classification and photometric redshifts from COMBO-17.” In: *A&A* 421, pp. 913–936. DOI: `10.1051/0004-6361:20040525`. eprint: `astro-ph/0403666` (cit. on pp. 11, 12, 35–37).

Wolfire, Mark G., David Hollenbach, and Christopher F. McKee (2010). “The Dark Molecular Gas.” In: *ApJ* 716.2, pp. 1191–1207. DOI: `10.1088/0004-637X/716/2/1191`. arXiv: `1004.5401 [astro-ph.GA]` (cit. on p. 99).

Wright, E. L. (2006). “A Cosmology Calculator for the World Wide Web.” In: *PASP* 118, pp. 1711–1715. DOI: `10.1086/510102`. eprint: `astro-ph/0609593` (cit. on p. 122).

Wu, Jingwen, II Evans Neal J., Yancy L. Shirley, and Claudia Knez (2010). “The Properties of Massive, Dense Clumps: Mapping Surveys of HCN and CS.” In: *ApJS* 188.2, pp. 313–357. DOI: `10.1088/0067-0049/188/2/313`. arXiv: `1004.0398 [astro-ph.GA]` (cit. on p. 99).

Wuyts, E., J. R. Rigby, K. Sharon, and M. D. Gladders (2012). “Constraints on the Low-mass End of the Mass-Metallicity Relation at z = 1-2 from Lensed Galaxies.” In: *ApJ* 755, 73, p. 73. DOI: `10.1088/0004-637X/755/1/73`. arXiv: `1202.5267` (cit. on p. 131).

Wylezalek, D. et al. (2013). “Galaxy Clusters around Radio-loud Active Galactic Nuclei at $1.3 < z < 3.2$ as Seen by Spitzer.” In: *ApJ* 769, 79, p. 79. DOI: `10.1088/0004-637X/769/1/79`. arXiv: `1304.0770` (cit. on pp. 15, 100–103, 123, 151, 152).

Wylezalek, D. et al. (2014). “The Galaxy Cluster Mid-infrared Luminosity Function at $1.3 < z < 3.2$.” In: *ApJ* 786, 17, p. 17. DOI: `10.1088/0004-637X/786/1/17`. arXiv: `1403.2390` (cit. on pp. 100, 102, 103).

Yèche, C. et al. (2010). “Artificial neural networks for quasar selection and photometric redshift determination.” In: *A&A* 523, A14, A14. DOI: `10.1051/0004-6361/200913508` (cit. on p. 12).

Yesuf, H. M., S. M. Faber, J. R. Trump, D. C. Koo, J. J. Fang, F. S. Liu, V. Wild, and C. C. Hayward (2014). "From Starburst to Quiescence: Testing Active Galactic Nucleus feedback in Rapidly Quenching Post-starburst Galaxies." In: *ApJ* 792, 84, p. 84. DOI: `10.1088/0004-637X/792/2/84`. arXiv: `1407.3834` (cit. on pp. 14, 142).

York, D. G. et al. (2000). "The Sloan Digital Sky Survey: Technical Summary." In: *AJ* 120, pp. 1579–1587. DOI: `10.1086/301513`. eprint: `astro-ph/0006396` (cit. on p. 9).

Yun, Min S., Naveen A. Reddy, and J. J. Condon (2001). "Radio Properties of Infrared-selected Galaxies in the IRAS 2 Jy Sample." In: *ApJ* 554.2, pp. 803–822. DOI: `10.1086/323145`. arXiv: `astro-ph/0102154 [astro-ph]` (cit. on p. 100).

Zamojski, M. A. et al. (2007). "Deep GALEX Imaging of the COSMOS HST Field: A First Look at the Morphology of z ˜ 0.7 Star-forming Galaxies." In: *ApJS* 172, pp. 468–493. DOI: `10.1086/516593`. eprint: `astro-ph/0701478` (cit. on p. 44).

Zeimann, G. R., S. A. Stanford, M. Brodwin, A. H. Gonzalez, G. F. Snyder, D. Stern, P. Eisenhardt, C. Mancone, and A. Dey (2012). "IDCS J1433.2+3306: An Infrared-selected Galaxy Cluster at z = 1.89." In: *ApJ* 756, 115, p. 115. DOI: `10.1088/0004-637X/756/2/115`. arXiv: `1207.4793` (cit. on p. 98).

Zeimann, G. R., S. A. Stanford, M. Brodwin, A. H. Gonzalez, C. Mancone, G. F. Snyder, D. Stern, P. Eisenhardt, A. Dey, and J. Moustakas (2013). "Hα Star Formation Rates of $z > 1$ Galaxy Clusters in the IRAC Shallow Cluster Survey." In: *ApJ* 779, 137, p. 137. DOI: `10.1088/0004-637X/779/2/137`. arXiv: `1310.6037` (cit. on pp. 129, 130).

Zucca, E. et al. (1997). "The ESO Slice Project (ESP) galaxy redshift survey. II. The luminosity function and mean galaxy density." In: *A&A* 326, pp. 477–488. eprint: `astro-ph/9705096` (cit. on p. 30).

Zwicky, F. (1933). "Die Rotverschiebung von extragalaktischen Nebeln." In: *Helvetica Physica Acta* 6, pp. 110–127 (cit. on p. 1).

RÉSUMÉ

Je développe un code Python pour déduire la fonction de masse stellaire (SMF) des galaxies en amas, en utilisant la méthode 1/Vmax et en ajustant la SMF avec un modèle choisi (la fonction de Schechter), pour la mission Euclid. Je teste le pipeline et déduire la SMF et l'ajustement de la SMF des galaxies de Flagship et de COSMOS2015 à 0.2 < z < 2.5. J'analyse l'évolution du SMF et je montre que la majeure partie de l'assemblage de la masse se produit à 1 < z < 2.5, et qu'il ralentit à z<1. Je détecte l'émission synchrotron et du gaz moléculaire dans le noyau de l'amas CARLA J1103+3449 à z ~ 1.44 avec NOEMA. La masse du gaz moléculaire est de M = 3.9 +/- 0.4 x 10^10 Mo, probablement d'origine du refroidissement du gaz. Je déduis les limites supérieures de la masse de gaz moléculaire, SFR, etc. des membres de l'amas. Pour la galaxie hôte RLAGN, nous trouvons SFR=30-140 Mo/an, et les SFR des autres membres de l'amas sont plus faibles, ce qui suggère un impact de l'environnement.

MOTS CLÉS

population stellaires des galaxies ; galaxies de type precoce ; galaxies-gaz moléculaire ; galaxies-formation d’étoiles ; evolution de galaxies

ABSTRACT

I develop a Python pipeline for deriving the stellar mass function (SMF) of cluster galaxies, using the 1/Vmax method and fitting the SMF with a chosen model (variations of the Schechter function), for the upcoming Euclid Mission. I test the pipeline and derive the SMF and SMF fit of the Flagship mock and COSMOS2015 galaxies at 0.2 < z < 2.5. I analyze the evolution of the SMF and stellar mass density, and show that most of the stellar mass assembly occurs at 1 < z < 2.5, and it slows down at z<1. I detect the synchrotron continuum emission and molecular gas structure in the CARLA J1103+3449 cluster core at z ~ 1.44 with NOEMA. The molecular gas reservoir mass is Mg = 3.9 +/- 0.4 x 10^10 Mo, probably originating from gas cooling. I derive the molecular gas mass upper limits, SFR, etc. of the cluster members. For the RLAGN host galaxy, I find SFR=30-140 Mo/yr, consistent with the MS galaxies, while the SFR of other cluster members are lower, suggesting an impact of the environment.

KEYWORDS

galaxies-stellar mass function ; galaxies-molecular gas ; cluster galaxies ; galaxies-star formation ; galaxies-quenching ; galaxy evolution